

KfK 5212
Januar 1994

**Behavior of a VVER Fuel
Element Tested under Severe
Accident Conditions in the
CORA Facility**
(Test Results of Experiment CORA-W1)

S. Hagen, P. Hofmann, V. Noack,
G. Schanz, G. Schumacher, L. Sepold
Hauptabteilung Ingenieurtechnik
Institut für Materialforschung
Institut für Neutronenphysik und Reaktortechnik
Projekt Nukleare Sicherheitsforschung

Kernforschungszentrum Karlsruhe

Kernforschungszentrum Karlsruhe
Hauptabteilung Ingenieurtechnik
Institut für Materialforschung
Institut für Neutronenphysik und Reaktortechnik
Projekt Nukleare Sicherheitsforschung

KfK 5212

**Behavior of a VVER Fuel
Element Tested under Severe Accident Conditions
in the CORA Facility**

(Test Results of Experiment CORA-W1)

S. Hagen, P. Hofmann, V. Noack, G. Schanz, G. Schumacher, L. Sepold

Kernforschungszentrum Karlsruhe GmbH, Karlsruhe

Als Manuskript gedruckt
Für diesen Bericht behalten wir uns alle Rechte vor

Kernforschungszentrum Karlsruhe GmbH
Postfach 3640, 76021 Karlsruhe

ISSN 0303-4003

Abstract

The "Severe Fuel Damage" (SFD) experiments of the Kernforschungszentrum Karlsruhe (KfK), Federal Republic of Germany, were carried out in the out-of-pile facility "CORA" as part of the international Severe Fuel Damage (SFD) research.

The experimental program was set up to provide information on the failure mechanisms of Light Water Reactor (LWR) fuel elements in a temperature range from 1200°C to 2000°C and in a few cases up to 2400°C.

Between 1987 and 1992 a total of 17 CORA experiments with two different bundle configurations, i.e. PWR (Pressurized Water Reactor) and BWR (Boiling Water Reactor) bundles were performed. These assemblies represented fuel elements of the type used in Western countries with the pertinent materials for fuel, cladding, grid spacer, absorber rod.

At the end of the experimental program two VVER-1000 specific tests were run in the CORA facility with identical objectives but with genuine VVER-type materials. The experiments, designated CORA-W1 and CORA-W2 were conducted on February 18, 1993 and April 21, 1993, respectively. Test bundle CORA-W1 was without absorber material whereas CORA-W2 contained one absorber rod (boron carbide/steel).

As in the earlier CORA tests the test bundles were subjected to temperature transients of a slow heatup rate in a steam environment. The transient phases of the tests were initiated with a temperature ramp rate of 1 K/s. With these conditions a so-called small-break LOCA was simulated. The temperature escalation due to the exothermal zirconium/niobium-steam reaction started at about 1200°C, leading the bundle to a maximum temperature of approximately 1900°C. The thermal response of bundle CORA-W2 is comparable to that of CORA-W1. In test CORA-W2, however, the temperature front moved faster from the top to the bottom as compared to test CORA-W1. The reason for this behavior may be an earlier melt formation and relocation of the absorber rod material in CORA-W2. With the movement of the melt also heat is transported to the lower region. Below 300 mm elevation the test bundle remained intact due to the axial temperature distribution. An essential portion of the absorber melt has resolidified at about 200 mm, i.e. at the second grid spacer, where a partial flow blockage had formed. The absorber rod and its pertinent guide tube have failed at ca. 200 mm, i.e. above this elevation the absorber rod is missing. Bundle CORA-

W2 is characterized by a strong oxidation above 300 mm elevation. Besides the severe oxidation the test bundle resulted in considerable fuel dissolution by ZrNb1/UO₂ interaction in the upper part, complete spacer destruction at 600 mm due to chemical interactions between steel and the ZrNb1 cladding.

The documentation of the experimental results is planned as a joint effort of the Russian and the German side. In particular, the posttest investigations will be documented by the participating institutions in Russia and Germany. The test data of CORA-W2 - provided with this report - are the contribution of the Karlsruhe Nuclear Research Center to serve as the basis for the posttest examinations to come.

Despite some specific features the material behavior of the VVER-1000 bundle is comparable to that observed in the PWR and BWR tests using fuel elements typical for Western countries.

Verhalten eines WWER-Brennelements, das unter Bedingungen von schweren Reaktorunfällen in der CORA-Anlage getestet wurde (Versuchsergebnisse des Experiments CORA-W1)

Kurzfassung

Die Severe-Fuel-Damage-(SFD)-Experimente des Kernforschungszentrums Karlsruhe (KfK) werden in der Out-of-pile-Versuchsanlage "CORA" durchgeführt.

Mit Hilfe der CORA-Versuche sollen die Versagensmechanismen von LWR (Leichtwasser-Reaktor)-Brennelementen im Temperaturbereich von 1200 bis 2000°C und in einigen Fällen bis 2400°C ermittelt werden.

In den Jahren 1987 bis 1992 wurden 17 CORA-Versuche mit zwei unterschiedlichen Typen von Brennstabbündeln, DWR (Druckwasserreaktor)- und SWR (Siedewasserreaktor)-Bündel, durchgeführt. Die Testbündel repräsentierten westliche Brennelemente mit Originalmaterialien bezüglich Brennstoff, Brennstabhüllen, Abstandshalter und Absorberstäben.

Am Ende des SFD-Versuchsprogramms standen zwei Experimente mit WWER-typischen Brennelementen (russische Bauart). Die Experimente CORA-W1 und CORA-W2 wurden am 18. Februar 1993 bzw. am 21. April 1993 durchgeführt. Versuchsbündel CORA-W1 hatte kein Absorberelement, CORA-W2 war mit einem Absorberstab ausgestattet.

Wie in den CORA-Versuchen zuvor wurden die Testbündel in Dampfatmosfera Temperaturtransienten mit langsamer Aufheizrate ausgesetzt. Damit wurde ein Unfallablauf für einen LWR simuliert, der sich aus einem Kühlmittelverluststörfall durch Auftreten eines sogenannten kleinen Lecks entwickeln kann.

Die Temperatureskalation - aufgrund der exothermen Zirkon/Niob-Wasserdampfreaktion - setzte ab ca. 1100°C ein. Die Höchsttemperaturen im Bündel betrugen 2000°C.

Die Dokumentation der experimentellen Ergebnisse ist als gemeinsame Aufgabe der russischen und der deutschen Seite geplant. In diesem Bericht werden die Versuchsdaten des Experiments CORA-W1 zusammen mit ersten Ergebnissen der

Nachuntersuchung dargelegt. Der Bericht ist der Beitrag des Kernforschungszentrums Karlsruhe.

Das Versuchsbündel weist eine starke Oxidation im oberen Bereich auf. Der untere Bündelabschnitt (bis 400 mm) blieb aufgrund der niedrigen Temperaturen in diesem Bereich unversehrt. Nach dem Versuch zeigte das Versuchsbündel ausschließlich im oberen Bündelbereich Brennstoffauflösung durch die Wechselwirkung ZrNb1/UO₂ und eine starke Zerstörung des Abstandshalters in der Höhe 600 mm aufgrund chemischer Wechselwirkungen zwischen Stahl und dem ZrNb1-Hüllrohrmaterial. Ebenso ergab sich eine Umverlagerung von Schmelzmassen aus dem oberen Bündelbereich in die mittlere Zone zwischen 400 und 650 mm unter Bildung einer Teilblockade des Kühlkanals in der Höhe von 420 mm.

Abgesehen von einigen spezifischen Merkmalen ist das Materialverhalten des WWER-1000-Bündels vergleichbar mit dem der DWR- und SWR-Versuche, in denen für westliche Reaktoren typische Brennstabbündel eingesetzt wurden.

Contents

1. Introduction	1
2. Test Description	2
2.1 Description of the Test Facility	2
2.2 Test Bundle Design	3
3. Test Conduct and Initial Boundary Conditions	6
4. Temperature Response, Hydrogen Generation, and Bundle End State ...	7
4.1 Temperature Measurements of the Bundle	7
4.2 Hydrogen Generation	9
4.3 Mass distribution and blockage formation	9
5. Posttest Appearance of the Bundle	11
6. Microstructural posttest evaluation of selected cross sections	13
7. Posttest Examination of the Bundle by SEM Analysis	16
7.1 General remarks	16
7.2 Preliminary SEM/EDX analytical results	16
7.2.1 Cross-section elevation W1-04 (389 mm)	16
7.2.2 Cross-section elevation W1-06 (612 mm)	18
7.3 Conclusions	19
8. Pre-transient Data	20
9. References	20
10. Acknowledgements	20
11. List of Tables	22
10. List of Figures	23

1. Introduction

Safety studies demonstrated that so-called small break loss-of-coolant accidents in Light-Water Reactors (LWR), in combination with failure of the required safety systems, can lead to overheating of the core and thus result in severe fuel damage (SFD) and fission product release.

In such an accident the nuclear fuel rods may be subjected to temperatures beyond the present design basis accident limit of 1200°C. The temperature transient, however, will not necessarily escalate to an uncontrolled core meltdown accident, as it was learned from the TMI accident in 1979.

The transient of a SFD-type accident is initiated by a slow temperature rise in the order of 0.5-1.0 K/s, followed by a rapid temperature escalation (about 10 to 20 K/s) due to the exothermal heat produced by the zirconium alloy cladding oxidation in steam environment. Besides oxidation and embrittlement of the fuel rod cladding, local melting of the cladding and interactions between solid and molten zirconium and uranium dioxide pellets occur and lead to the destruction of fuel rod elements and other core structures at temperatures far below the melting point of the fuel. The concern with melting of fuel rod materials in a SFD accident is relocation, solidification, and - as a result - the formation of coolant channel blockages.

To investigate the relevant damage mechanisms in an uncovered core, and to develop models for estimation of core damage initiation and propagation, research programs have been defined in various countries. In these programs in-pile and out-of-pile experiments are being performed under severe fuel damage conditions, i.e. temperature escalation to about 2000°C with termination of the transient before complete core meltdown.

At the Kernforschungszentrum Karlsruhe (KfK) a series of out-of-pile experiments on SFD research has been performed in the CORA facility. The entire experimental program is provided with Table 1 (CORA test matrix). As can be seen from this list, 17 experiments using bundle configurations of the Western design were conducted. All of these CORA experiments were performed with UO₂ as pellet material and with absorber materials (except for CORA-2 and -3). Two different absorber materials were used within the two different bundle configurations, i.e. (Ag,In,Cd) rods represented PWR (Pressurized Water Reactor)

conditions whereas boron carbide refers to the experiments simulating BWR (Boiling Water Reactor) fuel elements.

At the end of the experimental program two VVER-1000 specific tests were run in the CORA facility with analogous objectives but with genuine VVER-type materials. The experiments, designated CORA-W1 and CORA-W2 were conducted - under the same conditions as the previous tests - on February 18, 1993 and April 21, 1993, respectively. Test bundle CORA-W1 was without absorber material whereas CORA-W2 contained one absorber rod (boron carbide/ steel).

The documentation of the experimental results is planned to be a joint effort of the Russian and the German side. In particular, the posttest investigations are to be performed at different laboratories in Russia as well as at the Karlsruhe Nuclear Research Center, i.e. polished samples were distributed for the posttest examinations at the different institutions. This report describes the test data of the first CORA-VVER experiment CORA-W1 and some first results of destructive posttest examinations (extent of bundle oxidation and the chemical composition of the various solid and liquid phases).

2. Test Description

2.1 Description of the Test Facility

A detailed description of the CORA facility (see Figures 1 and 2) is given in reference /1/. The test bundle is surrounded by a high-temperature shield which is located within the pressure tube. The vertical and the horizontal cross-sections of the high-temperature shield are given in Figures 3 and 4. The high-temperature shield consists mainly of ceramic fibre plates. The inner layer of plates consists of ZrO_2 , and the outer one of Al_2O_3 . The fibre ceramics are excellent insulators and have a low density which results in a low heat capacity. The thermal shock behaviour of the fibre ceramics is also excellent.

The mechanical strength of the high temperature shield is provided by outer walls of stainless steel (0,9 mm). The fibre ceramic plates are attached to the stainless steel cover by ceramic nails. The inner ZrO_2 layer is 38 mm thick, and the outer Al_2O_3 layer is 76 mm thick, separated by a gap of 23 mm. The distance from the inner insulation surface to the centre of the bundle is 153 mm.

The test bundle is being inspected during the test by several video and still cameras through a number of holes in the shield.

Steam generator and steam superheater are placed inside the CORA containment. A maximum steam temperature of more than 800°C can be reached. The maximum steam flow rate amounts to 33 g/s.

Two different condensers are installed in the CORA facility: A vent condenser and a surge condenser. Under normal operating conditions the steam which is not consumed by oxidation of the bundle, is condensed in two vent condenser units. The surge condenser is physically separated from the high pressure system by four rupture disks. In case of emergency, e.g. due to an extremely high evaporation rate caused by quenching of the bundle, the void volume of the surge condenser serves as a pressure suppression system.

The condensate from the vent condensers and - in the case of emergency - the excess spray water of the surge condenser are collected in the condensate tank. After each test the amount of water in the condensate tank is determined to perform a water mass balance.

To avoid any hazard of hydrogen formed during the zirconium oxidation, the non-condensable gases are expanded and diluted in a mixing chamber (see [Fig.1](#)). In particular the hydrogen is diluted to a concentration below explosion limits by adding air to the gas.

The test facility has a quench capability which is activated by raising a water-filled quench cylinder into the test section at a controlled speed. This option was not used in the VVER-specific experiments. After a test the high-temperature shield can be lowered into the quench unit without moving the bundle. So, the tested bundle can be inspected and photographed in its original condition that existed at termination of the transient.

2.2 Test Bundle Design

Test bundle CORA-W1 consisted of 19 fuel rod simulators. The test rods were arranged within the bundle as shown in the schematic cross section of [Fig. 5](#). 13 of the 19 fuel rods were electrically heated by using tungsten pins as heating elements. The heated rods (fuel rod simulators) as well as the unheated rods were filled with annular UO₂ pellets of the same outer diameter but with different size of the central holes. The design of the heated and unheated types of rods used in the CORA-VVER test bundle is given with [Fig. 6](#). The rod claddings and the shroud

surrounding the rods are made of zirconium-1%niobium (Zr1%Nb). The shroud itself is insulated with a 20 mm-thick layer of ZrO_2 fiber material to guarantee a uniform radial temperature distribution.

Three grid spacers of 20 mm length were mounted below the heated region, in the lower bundle region, and above its axial center. All three grid spacers are made of stainless steel. Details on the location of the spacers and the fuel rod simulator design characteristics are given in Table 2.

The bundle head funnel (at the top of Fig. 3) is made of copper and is water-cooled by the double-walled outer chamber. To make the cooling more effective the space around the rods inside this chamber is filled with water. In consequence, the upper ends of the heated rods (the copper electrode inside the Zry-cladding) and the connectors for the pressure capillaries and thermocouples of the unheated rods are surrounded by water.

At the lower end the heated fuel rod simulators are cooled by the water inside the quench cylinder. The gross volume of water inside the quench cylinder (230 mm ID) amounts to about 70 l. The initial water level is at the -220 mm elevation.

The test train instrumentation comprised thermocouples and two-color pyrometers for the various temperature measurements. Besides the standard NiCr/Ni Al type thermoelements with stainless steel sheath the test section was instrumented with three different types of high-temperature thermocouples listed in Table 3. The Russian design - type 1 of this table - is additionally illustrated in Fig. 7. The exact positions of the thermocouples are provided with Table 4 and Table 5 (locations of the high-temperature shield).

Five videoscopes, at 200 mm, 400 mm, 600 mm, 800 mm, and 900 mm, were used in test CORA-W1 to observe the materials behavior and the relocation of material during transient testing. A schematic of the videoscope system with video camera and 35-mm still camera is given with Fig. 8.

The hydrogen produced during the test by the steam/Zr reaction is measured with means of two mass spectrometer systems at two different positions, i.e. above the test section and in the mixing chamber after the gas had passed the condenser (see Fig. 1). The gas at the test section outlet can contain a high steam partial pressure and has therefore to be diluted by helium before it enters the

analyser through the capillary tube. For this purpose a dilution chamber with flow meters is installed.

A schematic of the probes, gas lines, and gas analysis system is provided with Fig. 9. The off-gas mixture which contains hydrogen among other gases is being transported to the spectrometer via capillary tubes. It is analyzed by quadrupole mass spectrometers of the type Leybold PQ 100. The ion currents representing the concentrations of the respective gases are determined. The hydrogen generation rate is evaluated as follows:

$$R_m = 2 p_H \cdot F_{Ar} / 22.4 \cdot p_{Ar}$$

with

R_m = Mass production rate of hydrogen

p_H = Partial pressure of hydrogen

p_{Ar} = Partial pressure of argon

F_{Ar} = Volumetric argon flow through mixing chamber.

The mass production rate of hydrogen as well as of the other gases is calculated with the ratio of the partial pressure of the particular gas to that one of argon (carrier gas) and multiplied by the argon flow rate through the test bundle.

Based on a calibration test with bundle CORA-7 in which a mixture of argon and 30 % hydrogen was radially injected in the test section the delay time of monitoring the gas was estimated to be 80 s. This time was taken into account for the measured hydrogen production of all CORA experiments.

From the same calibration test, however, it was learned that the measured gas concentration showed lower slopes of the hydrogen production rate than it had to be expected from the injected gas flow. For this reason the measured data were corrected based on the real gas concentration, i.e. on the gas input during the calibration test. A transfer function was determined and applied to the measured data. The result is a corrected curve that better represents the H₂ production rate in the test section.

3. Test Conduct and Initial Boundary Conditions

In the CORA experiments one can generally distinguish the following phases for the test sequence:

- Pre-heating 0000 - 3000 s (argon only)
- Heat-up 3000 - 3900 s (argon; argon + steam from 3300 s)
- Escalation 3900 - 4850 s (argon + steam)
- Cool-down > 4850 s (argon only).

The test sequence of the experiment CORA-W1 can be taken from Table 6. During the preheating phase argon of about 500 °C entered the test bundle with a flow rate of 8 g/s (Figures 10 and 11). Between 3000 s and 4850 s the electric power was increased from 2 kW to 16.5 kW with a ramp rate of approx. 0.01 kW/s to achieve the initial heatup rate of 1 K/s. At 3300 s within the test a constant flow of superheated steam of 4 g/s was added to the argon flow of 6 g/s. At about 4000 s the slow temperature rise was followed by a rapid increase caused by increasing electric power input and additional energy from the exothermal zirconium - steam reaction.

The electric power supply was turned off at 4850 s (termination by slow cooldown) together with the steam supply.

The power input history for test CORA-W1 together with the coolant data as argon flow, steam flow (provided as mass flow of the injected water into the evaporator), and coolant pressure are given in Figs. 10 through 13.

The measured voltage input during the transient phase, the total electric energy input, the total current, and the total electric resistance of the bundle are given in Figs. 14 through 17. The variation of currents of the individual rods plotted per rod group can be found in Fig. 18. The resistances of the three rod groups are given in Fig. 19 and the resistances of the individual heaters are given in Figs. 20 through 22.

The water temperature in the quench cylinder at -250 and -350 mm elevation is shown in Fig. 23. During the transient the water temperatures increase to 90 and 60°C, respectively, due to heat conduction of the heated fuel rod simulators that

immerse into the water of the quench cylinder and due to the radiation from the bundle.

In Fig. 24 four measured steam tube temperatures at -50 mm elevation are provided. The steam inlet temperature at 0 mm elevation is given with Fig. 25. During the heatup the temperature increases from 500 to about 640°C. The rod internal pressure during test CORA-W1 can be obtained from Fig. 25 a.

4. Temperature Response, Hydrogen Generation, and Bundle End State

4.1 Temperature Measurements of the Bundle

The initial temperatures of the different components at 0 s and at the onset of the transient, i.e. at 3000 s, are provided with Tables 7 and 8.

The temperature measurements are presented as a function of time in the following way: On one hand, the temperatures of the components (heated rods, unheated rods, spacers, shroud, high-temperature shield) are given, on the other hand - for comparative reasons - the temperature measurements for different components are grouped for the same axial elevations (Figs. 36 through 47). Moreover, best-estimate temperatures at different elevations (Fig. 46) and axial temperature distributions for different time steps (Fig. 47) are presented.

Different thermocouples were installed in test bundle CORA-W1 (Table 3):

- In the center and at the outer surface of unheated rods
- At the outer surface of heated rods
- At the outer surface of the shroud and its insulation
- Above the shroud and at the bundle flange (gas temperature)
- At the grid spacer
- At the steam entrance.

The thermocouple locations listed in Tables 4 and 5 are in addition illustrated in Figures 26, 31, and 48.

The course of the rod temperatures during the CORA-W1 transient at different locations and elevations is provided with Figs. 27 through 29. The temperatures of the heated rods show fairly consistent traces from 450 mm to 1150 mm. The data for the lower as well as for the upmost locations of 1250 mm, 1350 mm, and 1450 mm differ significantly. There is more variance in the recorded temperatures of the unheated rods (Figs. 28 and 29). In the range of 450 mm to 650 mm, however, the scatter is not very large.

Temperatures at locations from 450 mm upward continued to rise more rapidly (temperature escalation at about 1100 °C) due to the zirconium-steam reaction with the strongest heatup at 750 mm. At this location the maximum measured temperature amounts to 1900 °C.

The temperature escalation can also be found in Fig. 30 which depicts the temperatures of the three grid spacers and in Figs. 32 and 33 with shroud and shroud insulation temperature. While the temperatures of the grid spacers at the low elevations, i.e. at -15 mm and 200 mm, do not show any escalation - as was expected - the 600 mm level exhibits a sharp temperature rise.

The start of rod failure was indicated by the measured rod internal pressure (Fig. 25a). At the time of the pressure loss (4185 s, upper graph) the maximum temperature was at 950 mm elevation and amounted to ca. 1900 °C. This temperature indicates melting of the cladding. In addition, there was no grid spacer located at the upper part of the bundle. Thus, an interaction between spacer and cladding can be excluded as initiating mechanism for the onset of failure.

The gas temperatures at four elevations are given in Figs. 34 and 35, those of the high-temperature shield for elevations between 50 mm and 1270 mm in Figs. 49 through 68. The temperatures of the high-temperature (HTS) shield are compared to each other either for different axial elevations or for different azimuthal positions. The high-temperature shield has measurement planes at 153 mm (inner surface), 172 mm, 192 mm, 255 mm, 293 mm and 380 mm (outer surface). Temperatures at different radial positions (different components) but at individual elevations are shown in Figs. 36 through 45, axial temperature distributions in Figs. 46 and 47. The best-estimate values used for evaluating the axial temperature profiles have the following uncertainties: ± 100 K in maximum up to the time of temperature escalation. Beyond the escalation the uncertainties are often larger. As thermocouples usually fail before the maximum temperature is reached an exact number cannot be given. Uncertainties due to eccentricities of

the rod arrangements that can form during the course of the transient are included in the error range.

4.2 Hydrogen Generation

The hydrogen production rate during test CORA-W1 and the integral hydrogen production (measured and corrected* data) are given in Fig. 69 as a function of time. The measured data are obtained from the gas probes at the mixing chamber. The total hydrogen amounts to 96 g. This value corresponds to an average of 39 % oxidation based on 5.545 kg zirconium, i.e. 3.361 kg of cladding and 2.184 kg of shroud (1.2 m length). With the total hydrogen of 96 g H₂ and the time at temperatures above 1400 °C - estimated to be 750 s - the fraction of steam consumed is calculated to be 29 % of the total steam flow of 4 g/s injected into the test section.

4.3 Mass Distribution and Blockage Formation

An axial profile of voids and structure material, respectively, can be obtained by using the epoxying process. As can be seen in Fig. 70 the epoxy resin is filled into the mould from the bottom end. By weighing the resin left in the supply container after each step, i.e. when the resin level has raised in the bundle by 1 cm, the difference of mass allows the calculation of the void volume of the bundle as a function of axial height. The filling process is slow enough so that the reading at the scale can be taken per cm providing a specific mass in (g/cm). The error of this method amounts to about 15 % with respect to readings of the epoxy level at 1 cm increments. It is too large to give reliable results. The error, however, is alternating, i.e. epoxy mass not measured at one step is certainly included in the next reading at the scale.

The data of the specific mass of resin as a function of elevation (g/cm) in Fig. 71 demonstrate the scatter (crosses). The smoothed solid-line curve in Fig. 71 was obtained from the data (crosses) by filtering, i.e. by using a Fourier transformation where higher frequencies were cut off by a low-pass filter. This filtering method has an additional advantage in reducing the uncertainty when dealing with alternating errors. The smoothed curve is used for further evaluation.

*. Corrected data are based on the CORA-7 calibration test.

The axial distribution in Fig. 71 is a distribution of voids because a higher amount of resin is equivalent to a larger void volume.

Fig. 72 presents the axial distribution of the structural material. For the evaluation of this profile the cut bundle segments were weighed. These data represent the mass of the structure and the mass of the heater elements. The masses of the epoxy resin and of the shroud are eliminated:

Specific mass = Mass of weighed samples - Epoxy mass - Mass of shroud remnants referred to the pertinent axial segment.

As the shroud of the axial center (hot region) was removed together with the fiber insulation after the test, the remnants of the shroud which were present during the filling process were excluded in the evaluation. It was assumed that there had been no shroud.

Concerning the uncertainty the measurement of the epoxy mass contains the same absolute error as the volume distribution, however, the relative error is only one fifth because the epoxy resin is referred to a 5-cm block compared to the reference of 1 cm for the volume method. So, if one compares the uncertainty of the axial volume distribution with the axial mass distribution one obtains an error band referred to the epoxy resin filled into the bundle of $\pm 15\%$ and $\pm 3\%$, respectively, i.e. the method using the weighed samples is the more accurate.

In Fig. 74 the axial mass distribution is compared with the axial volume distribution. Both curves show a similar behavior and particularly the blockage between 400 and 500 mm. In Fig. 73 the axial mass distribution is depicted together with the axial temperature distribution (best-estimate values), for various time steps. From this distribution it can be learned that the higher temperatures, i.e. temperatures above $1500\text{ }^{\circ}\text{C}$ existed in the upper half (between 800 to 1000 mm) and the central zone (from 600 to 1200 mm) for times of 4200 s and 4400 s, respectively. At these times the material relocated from the region between 850 and 1150 mm to lower elevations. The partial blockage - as a result of this material relocation - had formed above the 400-mm elevation although about $1900\text{ }^{\circ}\text{C}$ were reached at 400 mm prior to the termination of the transient, i.e. at 4800 s. Apparently, this late temperature escalation at 400 mm did not lead to an additional relocation of molten material. In general, however, the material deposition is a temperature-controlled process due to the solidification of the materials.

5. Posttest Appearance of the Bundle

Overall views of test bundle CORA-W1 after the test at different orientations are given in Figs. 75 through 78 with the first pictures demonstrating the condition of the bundle prior to the removal of the shroud. From approx. 350 mm to 950 mm the shroud insulation is glued to the shroud. This interaction is caused by the temperature effect. In the lower bundle portion the insulation could easily be taken off (relatively cold region). More detailed views are presented with the photographs of Figs. 79 through 109.

The following description of the posttest appearance with an insight into the interior of the test bundle was made possible with the additional help of cross sections (Figs. 110 through 113). The positions of the cross sections can be taken from Table 9. After visual inspection of the horizontal sections some 50-mm slabs were vertically cut according to Fig. 114. The vertical sections are shown in Figs. 115 through 119.

To obtain cross sections a mould was set up around the bundle that was filled with epoxy resin (see also Fig. 70). For encapsulation of the bundle the epoxy system Rütapox 0273 with the hardener designated LC (Epoxy resin and hardener manufactured by Bakelite GmbH, Iserlohn) was chosen. The bundle was filled starting from the bottom, through the steam inlet line, to avoid air entrainment in the encapsulant. In general, the epoxy shows some heating during the curing stage but the shrinkage effect is negligible. After epoxying the bundle the resin was allowed to harden for one week. A saw with a 2.3 mm-thick diamond blade (mean diamond size 138 μm) of 500 mm OD was used to cut the slabs at 3200 rpm.

Those sections that were selected for metallographic examination (Table 10) were infiltrated by "Araldit" resin to close up residual pores then ground and polished. The entire procedure of the preparation for the metallographic examination is given with Table 11). The steps described in the list were performed using a semi-automatic machine with a closed water circuit for grinding and an automatic lubricant feeder for the polishing steps.

From the posttest photography and the cross sections one can recognize that

- the test bundle is intact up to an elevation of 300 mm to 400 mm (shroud and rods are only slightly oxidized -- black color),

- the severely oxidized part of the bundle lies above 400 mm,
- the central grid spacer is intact (see cross section at 203 mm) due to a local temperature of below 1000 C,
- the upper grid spacer was either completely converted to oxide as detected in the outer region of cross sections 612 and 614 mm, or was molten away in other parts (central region of cross sections 612 and 614 mm) due to chemical interactions with the ZrNb1 cladding and by reaching the melting point,
- a partial flow blockage has formed between 400 mm and 610 mm due to relocated melt from upper bundle elevations with the relatively largest flow channel blockage at 420 mm elevation,
- the radial deformation of the cladding, the so-called "flowering" is evident from 610 mm upward,
- a strong variation of the oxide layer thickness of the cladding has been evaluated,
- a localized strong increase in the wall thickness of the shroud had occurred as a result of melt relocations and solidifications .

Moreover, the video observation revealed

- that only a relatively small amount of melt relocated downward,
- that the flame front (severe oxidation, temperature escalation) commenced at the 950 mm elevation,
- that the first droplets of melt were visible at 4198 s at the 900-mm observation window (at 4202 s → 800 mm, at 4224 s → 600 mm, at 4447 s → 400 mm, at 4472 → 200 mm),
- that the first lump of melt was detected at 4223 s at the 900-mm observation window (at 4230 s → 800 mm, at 4418 s → 600 mm),
- that the stainless steel grid spacer melted away from 4445 s to 4500 s, i.e. within 55 s.

In general, the material behavior of this VVER-1000-type bundle is comparable to that of a PWR of Western design /2/.

6. Microstructural Posttest Evaluation of Selected Cross Sections

At the elevation 374 mm (cross section W1-10, top) the status of the bundle is documented by the macrographs of Fig. 120 and the micrographs of Fig. 121 through 125 as a still preserved arrangement of the components despite their strong interactions: The pellets have remained intact apart from crack formation and beginning interaction with molten cladding. Void formation within some central fuel rods indicates local and internal relocation of cladding melt, whereas at the 300 ° orientation considerable metallic melt has accumulated between the shroud and neighboring rods. The strongest fuel rod cladding and shroud oxidation is observed at this bundle side, which was obviously the hottest during the test.

Microstructures from different rods illustrate the extent of cladding oxidation across the bundle (Fig. 121). The scales are composed of columnar grains. A thin external sublayer shows either features of early scale spalling or has to be interpreted at some positions as adherent metallic melt subsequently oxidized. For growth above 1500 °C an internal sublayer contains α -Zr(O) grain boundary phase after decomposition of the cubic high-temperature oxide modification. The oxidation proceeds into molten cladding and fuel containing melt; the resulting ZrO_2 or $(Zr,U)O_2$ cannot be distinguished by visual observation alone. Artefacts, resulting from the metallographic specimen preparation (loss of fragments, edge rounding) may even support further interpretation of the microstructures.

The shroud oxidation (Fig. 122) is generally comparable to that of the cladding, since both structures are of the same material. Whereas equal scale thickness on both shroud surfaces is found at the cooler side of the bundle, the internal surface is much more oxidized at the hotter bundle side compared to the external scale. Their growth must have been effectively retarded by steam supply rate limitation (steam starvation) and possibly by scale thinning due to dissolution into the metallic matrix as well. At the azimuthal angle 300 ° the external scale indicates lateral cracking and spalling of partial layers (Fig. 123). This behavior which is similar to the "breakaway phenomenon", an effect of scale protection loss observed during long-term oxidation of zirconium alloys, might be induced prematurely by the uranium content within the original shroud wall. This modification by uranium uptake is indicated by ceramic precipitates and has been analytically confirmed.

Fig. 124 illustrates beginning fuel pellet degradation by crack system formation and chemical attack. According to Fig. 125 the thermocouples could have still worked if not destroyed at other elevations.

At the elevation 389 mm (cross section W1-04, top), only 15 mm higher, the bundle component interactions are much more advanced (Fig. 126 through 131): Especially fuel rods towards the hotter 300° direction are connected via bridges of metallic melt, which has continued to oxidize by formation of thick scales. Most of the originally present melt has relocated downward, leaving behind void regions inward of the scales, in which rubble fragments have been caught. At several places the shroud wall has thickened by solidifying melt, relocated from above (Fig. 126).

The extent of cladding oxidation depends strongly on the rod position within the bundle (Fig. 127). Externally adhering metallic melt can effectively protect the cladding from continued oxidation or even reduce the scale along its elongated grain boundaries (Fig. 128). The observed oxidation, melting and interaction of the shroud with uranium-containing melt (Fig. 129) confirm the already discussed interpretations. The pellet attack is more advanced at this bundle elevation, not only from the external side by dissolution of fuel into cladding melt, but also by beginning reaction with tungsten heater rods (Fig. 130) or a fuel centerline thermocouple (Fig. 131).

All the observations made at this elevation are confirmed by the adjacent cross section at 391 mm (W1-j, bottom), for which macrographs are given in Fig. 132.

The extent of cladding tube oxidation at the elevations 374 and 389 mm was quantified by measuring the ZrO_2 scale thickness at both opposite sides of a rod along three directions across the bundle. Fig. 133 illustrates the result for the direction from 330 ° to 150 ° and three parallel measurement lines through four or five rods, respectively. The given values include the thickness of subsequently oxidized pellet/cladding reaction zones. The strong azimuthal dependence of scale thickness, thus depicted, compares to an estimated difference in peak temperatures across the bundle of ca. 300 to 400 K. Such high values have been reported up to now only for the bundle CORA-13 /2/, whereas all other CORA tests developed flatter lateral temperature profiles, at least at the examined elevations. The observation can be interpreted as the result of the downward movement of an oblique oriented escalation front, which has reached only parts of the given cross sections.

The oxidation profiles around the shroud at 374 and 389 mm elevation (Fig. 134) are in agreement with the profiles measured across the fuel rods. The scale thickness curves for the internal side with maxima around 300 ° are comparable with the measurement results for adjacent fuel rods. (In the 389 mm elevation at 330 ° and 290 ° the comparatively small values measured are due to scale growth limitation by temporal isolation from steam and by contact with metallic melt.) The profile of the external scales is comparatively low and flat. The variance between the internal and the external scale thickness cannot be explained by a temperature gradient across the shroud wall, but only by steam starvation conditions that establish between the shroud and its fiber material insulation during the individual temperature escalation periods of the given bundle elevation.

Estimation of an axial temperature profile through the bundle would require more evaluated cross sections. Clear is, however, that the cladding oxidation must be essentially complete at any elevation above 400 mm.

At the elevation 612 mm (W1-06, top) the bundle components are found seriously attacked, destroyed or converted (Figs. 135 - 137). The macrographs and micrographs show, apart from the heater rods, only tiny, isolated metallic residues (Fig. 136, Pos. 2). Some fuel pellets have been dissolved or fragmented to a great part, whereas others are essentially intact. The cladding after partial melting, fuel interaction, and "flowering" deformation is completely converted to oxide. The same holds for the residual parts of the spacer grid. A considerable amount of melt is distributed between the rods, enclosing pores and larger voids, some of the latter containing loose rubble particles. The melt has got completely oxidized to ceramic material. The part of the shroud, which was not removed is essentially converted to oxide (Fig. 137). It may have thickened not only by melt agglomeration (70 °) but also by reaction with the surrounding ZrO₂ fiber material (220 °). The observations concerning this elevation are confirmed by cross section W1-n, bottom, at 614 mm (Fig. 138).

At the elevation 783 mm (cross section W1-07, top) the shroud has not been preserved. Compared to the previous elevation the bundle itself looks qualitatively similar (Figs. 139 through 142). The microstructures illustrate residual bundle components (Fig. 140), pellet interaction with the tungsten heater (Fig. 141), morphology and distribution of molten material (Fig. 142). Fig. 143 shows macrographs from 785 mm of the adjacent cross section W1-q, bottom.

7. Posttest Examination of the Bundle by SEM Analysis

7.1 General Remarks

Two cross-sections of the bundle CORA-W1 were chemically analyzed by SEM/EDX (scanning electron microscope, energy dispersive X-ray) examinations to

- describe the high-temperature reaction behavior among the bundle components, and to
- provide reference chemical compositions of some typical phases (reaction products).

The measurements were performed with a SEM type JEOL 6100. For the EDX examination a newly developed light element detector was used (Quantum 3600 - 19, KeveX).

At the examined bundle cross-section elevation W1-04 (389 mm) the reaction phases are either metallic or ceramic in nature. At the other examined cross-section elevation W1-06 (612 mm) all phases are ceramic; the fuel rod cladding and the once molten and relocated materials are completely oxidized. The chemical composition of the various examined phases is given in the following chapters.

The cross-sections W1-04 and W1-06 will be examined once more in Russia. Therefore, the results have to be considered as preliminary. In addition, all the other available cross-sections of the bundle will be analysed by SEM/EDX examinations later in time in Germany and Russia.

7.2 Preliminary SEM/EDX Analytical Results

7.2.1 Cross-section Elevation W1-04 (389 mm)

The cross-section W1-04 is shown in Figure 144. The examined locations are indicated by arrows; the numbers correspond with the metallographically examined locations, which have been more extensive than the analytical SEM/EDX examinations.

At the cross-section location # 2 a metallic "melt-bridge" has formed between two adjacent fuel rods. The melt is kept at place by an oxide layer on its surface. Figure 145 shows an electron backscatter image of the metallic melt. One can recognize different phases of various chemical compositions. The integral composition exhibits mainly Zr (~ 63 wt. %), U (~ 13 wt. %), and oxygen (~ 9 wt %); but also all the other elements of the bundle components. The SEM/EDX examination results of the individual phases are given in Figure 146. The phases # 1 and # 3 are ceramic; phase # 1 corresponds to UO_2 with some dissolved Zr and phase # 3 corresponds to an $(\text{U}, \text{Zr})\text{O}_2$ solid solution. The other two phases are metallic in nature, but they contain also some oxygen.

The cross-section location # 12 shows part of the solidified metallic melt and the oxide layer which acted as a crucible and which kept the molten material at place (Figure 147). The chemical compositions of three regions a, b, and c are indicated. The oxide layer corresponds to an $(\text{U}, \text{Zr})\text{O}_2$ solid solution.

The cross-section location # 9 reflects a part of the partially oxidized ZrNb1 cladding (phases # 1 and 2; pure ZrO_2) and a part of an UO_2 pellet (phase # 5, UO_2); see Figure 148. Between the oxide layer and the UO_2 fuel two $(\text{U}, \text{Zr})\text{O}_2$ phases (# 3 and # 4) of different chemical compositions have formed. The appearance of phase # 4 indicates that it was probably molten during the test (formation of pores on cooldown). Details of the phases are shown in Figure 149; they look rather homogeneous composed, except phase # 4. The individual phases which form a phase mixture (phase # 4) are shown in Figure 150. One has to keep in mind that some of these phases are only present in very small quantities; for example phase # 1 in Figure 150 which corresponds to oxygen-stabilized $\alpha\text{-Zr(O)}$.

The cross-section location # 17 shows a part of a still "intact" looking fuel rod (Figure 151). A detailed examination reveals that the temperature at this location has not exceeded the melting temperature of oxygen-stabilized $\alpha\text{-Zr(O)}$ of about 2050°C . The ZrO_2 oxide layer looks very dense (phase a), the $\alpha\text{-Zr(O)}$ layer adjacent to the ZrO_2 (phase b) is still present. The $\alpha\text{-Zr(O)}$ phase in contact with the UO_2 contains some U (phase d), reflecting some UO_2 dissolution. Phase c is rather complex chemically composed, it contains beside Zr and O also U, Fe, and Nb. This is a clear indication that this was once molten material and must have formed as a result of stainless steel spacer grid/ZrNb1 fuel rod cladding eutectic interactions at higher bundle elevations. A detailed description of the various phases which

form phase c is given in [Figure 152](#). Phase region d is also composed of different individual phases as shown in [Figure 153](#).

The cross-section location # 20 corresponds to a fuel rod which exhibits partial ZrNb1 cladding melting and relocation under formation of a large void ([Figure 154](#)). It was interesting to compare the analytical results of this location with those of the cross-section location # 17 ([Figure 151](#)). In principle, the same chemical interactions, occurred, but, as a result of the higher temperatures the reactions were more extensive. The presence of the stainless steel elements Fe, Cr, and Ni indicates interactions of the cladding with the spacer grid at some other location. In addition, UO_2 dissolution by the metallic melt takes place. Details of the various phases observed are given in [Figure 155](#).

The cross-section location # 29 represents a part of the ZrNb1 shroud which has thickened due to partial melting and melt relocation from higher elevations. The initial wall thickness increased by a factor of two and more at this location. [Figure 156](#) shows the once molten shroud kept at place by $(\text{U, Zr})\text{O}_2$ oxide layers which act as a crucible (phases a and d). The oxide layers are not homogeneous as demonstrated by the result given in [Figure 157](#). In between the oxide layers the solidified metallic melt can be recognized. On solidification different oxidic and metallic phases form that are shown in [Figure 158](#). The oxidic phases are all of the type $(\text{U, Zr})\text{O}_2$ of various UO_2 and ZrO_2 concentrations. The fact that the shroud contains U means either interactions with the neighbouring fuel rods or interactions with "fuel rod" melts which have formed at higher elevations, relocated and solidified at the examined cross-section location.

7.2.2 Cross-section Elevation W1-O6 (612 mm)

The cross-section W1-O6 is shown in [Figure 159](#). At this elevation only three locations were examined by SEM/EDX examinations since the various reaction products looked metallographically similar. At this elevation also a strong increase in wall thickness of the shroud can be recognized.

At the cross-section location #2 the integral chemical composition of the ceramic material (reaction product) is given in [Figure 160](#). The ceramic matrix looks inhomogeneous and contains a few voids; it consists of $(\text{U,Zr})\text{O}_2$ with some dissolved W from the heated rods. Similar chemical conditions prevail at the cross-section location # 19 ([Figure 161](#)). In the vicinity of this location a more detailed phase analysis was performed. The results are given in [Figures 162 and 163](#). The

ceramic reaction products correspond to $(U, Zr)O_2$ of different U/Zr ratios, which, in addition, contains sometimes other elements like Fe and W.

7.3 Conclusions

The chemical analytical results of all examined (U, Zr, O) phases of the cross-sections W1-04 and W1-06 are summarized in Table 12. The results are arranged in a sequence with increasing U concentration. The location of the phases is also indicated. At the cross-section elevation W1-04 two types of (U, Zr, O) phases can be recognized

- a) a metallic α -Zr(O) phase which contains some U; the oxygen concentration is generally below 30 at. %, and a
- b) ceramic $(U, Zr)O_2$ phase of various U/Zr ratios with an oxygen concentration between 61.4 and 68.2 at. %.

At the cross-section elevation W1-06 only ceramic phases of the type b) could be determined.

The chemical analytical results reflect the temperature conditions which existed during the test. At the cross-section elevation W1-04 (389 mm) the temperature was high enough to melt the remaining metallic part of the cladding which in most cases did not relocate because it was kept at place by oxide layers. However, in the gap between the external ZrO_2 layer and the UO_2 pellet a mixing in the melt must have taken place over large distances. At the cross-section elevation W1-06 (612 mm) the temperatures were much higher resulting in cladding failure, melt relocation and complete oxidation of all metallic components. At this elevation also strong UO_2 dissolution by molten ZrNb1 cladding can be noticed.

Final statements concerning the physico-chemical behavior of the bundle CORA-W1 will be possible when all SEM/EDX examination results of the other cross-sections are available. This will be done in a separate joint German/Russian post-test result report.

8. Pre-transient Data

Pre-transient data, i.e. data measured before 3000 s (begin of the transient) are provided in the Appendix.

9. References

- /1/ S. Hagen, K. Hain, "Out-of-pile Bundle Experiments on Severe Fuel Damage (CORA Program): Objectives, Test Matrix, and Facility Description", KfK 3677 (1986)
- /2/ S. Hagen, V. Noack, L. Sepold, P. Hofmann, G. Schanz, G. Schumacher, "Results of SFD Experiment CORA-13 (OECD International Standard Problem 31)", KfK 5054 (1993)

10. Acknowledgements

The CORA-VVER program is a joint effort of the Kernforschungszentrum Karlsruhe (KfK) and the Kurchatov Institute Moscow. It is part of a bi-lateral agreement on scientific-technical cooperation between the Russian Federation and the Federal Republic of Germany. For the efforts to realize this cooperation the authors would like to express their thanks to the project managers at the Kurchatov Institute Drs. V. Pavchuk and L. Yegorova.

At the Kernforschungszentrum Karlsruhe a variety of support needed for preparation, conduct, and evaluation of the experiment is gratefully acknowledged:

The fuel elements were designed by Mr. H. Junker. The test rods were assembled by Mr. E. Mackert, the test bundles by Messrs. H. Giesmann and R. Röder. The authors would like to thank Messrs. H. Benz, C. Grehl, and H.J. Röhling for test preparations and conduct.

Mr. K.P. Wallenfels is acknowledged for arrangement of camera and video systems and for the preparation of temperature measurements. Messrs. R. Huber

and H. Malauschek prepared and conducted the on-line measurements of the off-gas composition.

The authors would like to thank Mr. L. Anselment for sectioning of the epoxied bundle and for preparation of the metallographic samples, Mr. H. Metzger for investigation of the metallographic samples by optical microscope, and Mr. J. Burbach for the SEM investigations.

11. List of Tables

1. CORA test matrix
2. Design characteristics of test bundle CORA-W1
3. Thermocouples used in the CORA-VVER Test CORA-W1 (without absorber rod)
4. CORA-W1; Position of thermocouples of test bundle CORA-W1
5. CORA-W1; Position of thermocouples in the high-temperature shield
6. CORA-W1; Sequence of events
7. Temperatures of test CORA-W1 for different components at 0 seconds
8. Temperatures of test CORA-W1 for different components at 3000 seconds
9. Cross sections of test bundle CORA-W1
10. CORA-W1; Polished samples
11. Procedure of the preparation of the samples for the metallographic examination
12. Summary of O-Zr-U molten phases found, arranged as to uranium contents

10. List of Figures

- Fig. 1: SFD test facility CORA, main components
- Fig. 2: CORA test section
- Fig. 3: CORA bundle arrangement
- Fig. 4: Horizontal cross section of the high-temperature shield
- Fig. 5: Rod arrangement and test rod designation of bundle CORA-W1
- Fig. 6: Rod types used in the CORA / VVER experiments
- Fig. 7: The high-temperature thermoelectric transducer (HTT) of Russian design used in test CORA-W1
- Fig. 8: Videoscope system for the CORA test bundle
- Fig. 9: Hydrogen measurement
- Fig. 10: CORA-W1; System pressure, argon flow, steam input and power
- Fig. 11: Argon flow through bundle and videoscopes
- Fig. 12: CORA-W1; System pressure (gauge)
- Fig. 13: CORA-W1; Total power input
- Fig. 14: CORA-W1; Voltage input for the 3 rod groups
- Fig. 15: CORA-W1; Total electric energy input
- Fig. 16: CORA-W1; Total current
- Fig. 17: CORA-W1; Resistance of bundle (Voltage group1 / total current)
- Fig. 18: CORA-W1; Variation of currents within the rod groups
- Fig. 19: CORA-W1; Resistance of the rod groups
- Fig. 20: CORA-W1; Resistance of rod group 1
- Fig. 21: CORA-W1; Resistance of rod group 2
- Fig. 22: CORA-W1; Resistance of rod group 3
- Fig. 23: CORA-W1; Water temperature in the quench cylinder
- Fig. 24: CORA-W1; Temperature in and on steam tube at -50 mm elevation
- Fig. 25: CORA-W1; Temperatures at steam inlet
- Fig. 25a: CORA-W1; Internal rod pressure

- Fig. 26: Thermocouple locations within the bundle (CORA-W1)
- Fig. 27: CORA-W1; Temperatures of heated rods
- Fig. 28: CORA-W1; Temperatures of unheated rods (TCs in central position)
- Fig. 29: CORA-W1; Temperatures of unheated rod (TCS on outer surface)
- Fig. 30: Temperatures of the three spacers used in test CORA-W1
- Fig. 31: CORA-W1; Location of the thermocouples at shroud and shroud insulation
- Fig. 32: CORA-W1; Temperatures of the outer side of the shroud
- Fig. 33: CORA-W1; Temperatures of the shroud insulation
- Fig. 34: CORA-W1; Gas temperatures above the heated zone (1150, 1250, 1350 mm)
- Fig. 35: CORA-W1; Gas temperature measured in the bundle head plate (1491, 1451 mm)
- Fig. 36: CORA-W1; Temperatures at elevations given (1450, 1350 mm)
- Fig. 37: CORA-W1; Temperatures at elevations given (1250, 1150 mm)
- Fig. 38: CORA-W1; Temperatures at elevations given (1050, 950 mm)
- Fig. 39: CORA-W1; Temperatures at elevations given (850, 750 mm)
- Fig. 40: CORA-W1; Temperatures at elevations given (650, 600 mm)
- Fig. 41: CORA-W1; Temperatures at elevations given (550, 450 mm)
- Fig. 42: CORA-W1; Temperatures at elevations given (350, 250 mm)
- Fig. 43: CORA-W1; Temperatures at elevations given (200, 150 mm)
- Fig. 44: CORA-W1; Temperatures at elevations given (50, 0 mm)
- Fig. 45: CORA-W1; Temperatures at elevations given (-15, -50 mm)
- Fig. 46: CORA-W1; Best-estimate bundle temperatures at different elevations
- Fig. 47: Axial temperature distribution during the transient of test CORA-W1
- Fig. 48: CORA-W1; Locations of thermocouples in the high-temperature shield
- Fig. 49: CORA-W1; Temperatures of HTS at inner surface, 153 mm radius

- Fig. 50: CORA-W1; Temperatures of HTS, inner surface at 153 mm radius (550 mm)
- Fig. 51: CORA-W1; Temperatures of HTS, inner surface at 153 mm radius (950mm)
- Fig. 52: CORA-W1; Temperatures of HTS, inner surface at 153 mm radius
- Fig. 53: CORA-W1; Temperatures of HTS, inner surface at 153 mm radius (50mm)
- Fig. 54: CORA-W1; Temperatures of HTS, Temperatures of the HT shield at 172 mm radius
- Fig. 55: CORA-W1; Temperatures of HTS, Temperatures of the HT shield at 172 mm radius (0 - 15000 s)
- Fig. 56: CORA-W1; Temperatures of HTS, Temperatures of the HT shield at 192 mm radius
- Fig. 57: CORA-W1; Temperatures of HTS, Temperatures of the HT shield at 255 mm radius
- Fig. 58: CORA-W1; Temperatures of HTS, Temperatures of the HT shield at 192 mm radius (0 - 20000 s)
- Fig. 59: CORA-W1; Temperatures of HTS, Temperatures of the HT shield at 255 mm radius (0 - 20000 s)
- Fig. 60: CORA-W1; Temperatures of HTS, Temperatures of the HT shield at 293 mm radius
- Fig. 61: CORA-W1; Temperatures of HTS, Temperatures at the outer surface of the HT shield, 380 mm radius
- Fig. 62: CORA-W1; Temperatures of HTS, Temperatures of the HT shield at 293 mm radius (0 - 15000 s)
- Fig. 63: CORA-W1; Temperatures of HTS, Temperatures at the outer surface of the HT shield at 380 mm radius (0 - 15000 s)
- Fig. 64: CORA-W1; Temperatures of HTS, HT shield temperature at 950 mm elevation, at different radii (0 - 10000s)
- Fig. 65: CORA-W1; Temperatures of HTS, HT shield temperature at 550 mm elevation, at different radii (0 - 10000s)
- Fig. 66: CORA-W1; Temperatures of HTS, HT shield temperature at 950 mm elevation, at different radii (3000 - 6000s)
- Fig. 67: CORA-W1; Temperatures of HTS, HT shield temperature at 550 mm elevation, at different radii (3000 - 6000s)
- Fig. 68: CORA-W1; Temperatures of HTS, HT shield temperatures at 50 mm elevation (3000 - 6000s)

- Fig. 69: Hydrogen production in test CORA-W1; production rate (top) and integral values (bottom)
- Fig. 70: CORA-W1; Epoxying process of the tested bundle
- Fig. 71: CORA-W1; Axial distribution of the bundle fill-up with epoxy resin
- Fig. 72: CORA-W1; Axial mass distribution of bundle segments filled with epoxy resin
- Fig. 73: CORA-W1; Axial volume distribution after the test, relative blockage inside the shroud and axial temperature distribution during the test
- Fig. 74: CORA-W1; Axial volume distribution (relative blockage within the shroud) and axial mass distribution after the tests
- Fig. 75: CORA-W1; Posttest view of the inner side of the shroud insulation
- Fig. 76: CORA-W1; Posttest appearance of the entire bundle length after removal of the shroud insulation
- Fig. 77: Enlarged posttest view of bundle CORA-W1 after removal of the shroud insulation
- Fig. 78: Posttest view of the bundle CORA-W1 after partial removal of the shroud
- Fig. 79: CORA-W1; Posttest view, 0° orientation
- Fig. 80: CORA-W1; Posttest view, 0° orientation
- Fig. 81: CORA-W1; Posttest view, 0° orientation
- Fig. 82: CORA-W1; Posttest view, 0° orientation
- Fig. 83: CORA-W1; Posttest view, 60° orientation
- Fig. 84: CORA-W1; Posttest view, 60° orientation
- Fig. 85: CORA-W1; Posttest view, 60° orientation
- Fig. 86: CORA-W1; Posttest view, 60° orientation
- Fig. 87: CORA-W1; Posttest view, 120° orientation
- Fig. 88: CORA-W1; Posttest view, 120° orientation
- Fig. 89: CORA-W1; Posttest view, 120° orientation
- Fig. 90: CORA-W1; Posttest view, 120° orientation
- Fig. 91: CORA-W1; Posttest view, 160° orientation
- Fig. 92: CORA-W1; Posttest view, 160° orientation
- Fig. 93: CORA-W1; Posttest view, 160° orientation

- Fig. 94: CORA-W1; Posttest view, 160° orientation
- Fig. 95: CORA-W1; Posttest view, 180° orientation
- Fig. 96: CORA-W1; Posttest view, 180° orientation
- Fig. 97: CORA-W1; Posttest view, 180° orientation
- Fig. 98: CORA-W1; Posttest view, 210° orientation
- Fig. 99: CORA-W1; Posttest view, 210° orientation
- Fig. 100: CORA-W1; Posttest view, 210° orientation
- Fig. 101: CORA-W1; Posttest view, 210° orientation
- Fig. 102: CORA-W1; Posttest view, 240° orientation
- Fig. 103: CORA-W1; Posttest view, 240° orientation
- Fig. 104: CORA-W1; Posttest view, 240° orientation
- Fig. 105: CORA-W1; Posttest view, 240° orientation
- Fig. 106: CORA-W1; Posttest view, 300° orientation
- Fig. 107: CORA-W1; Posttest view, 300° orientation
- Fig. 108: CORA-W1; Posttest view, 300° orientation
- Fig. 109: CORA-W1; Posttest view, 300° orientation
- Fig. 110: Horizontal cross sections of bundle CORA-W1, top view (1125 - 664 mm)
- Fig. 111: Horizontal cross sections of bundle CORA-W1, top view (612-203 mm)
- Fig. 112: Horizontal cross sections of bundle CORA-W1, bottom view (1112-614 mm)
- Fig. 113: Horizontal cross sections of bundle CORA-W1, bottom view (599-173 mm)
- Fig. 114: CORA-W1; Longitudinal cut through samples W1-j, W1-k, W1-l, W1-m, W1-n (top view)
- Fig. 115: ORA-W1; Longitudinal sections (overview)
- Fig. 116: CORA-W1; Longitudinal section 443-493 mm
- Fig. 117: CORA-W1; Longitudinal section 510-560 mm
- Fig. 118: CORA-W1; Longitudinal section 562-597 mm
- Fig. 119: CORA-W1; Longitudinal section 614-664 mm

- Fig. 120: Cross section W1-10 (top), elevation 374 mm, overview
- Fig. 121: Cross section W1-10 (top), elevation 374 mm, cladding oxidation, melting, interaction with fuel
- Fig. 122: Cross section W1-10 (top), elevation 374 mm, shroud oxidation
- Fig. 123: Cross section W1-10 (top), elevation 374 mm, shroud melting and interaction with melt
- Fig. 124: Cross section W1-10 (top), elevation 374 mm, heated and unheated fuel rod
- Fig. 125: Cross section W1-10 (top), elevation 374 mm, thermocouples
- Fig. 126: Cross section W1-04 (top), elevation 389 mm, overview
- Fig. 127: Cross section W1-04 (top), elevation 389 mm, fuel rod cladding oxidation
- Fig. 128: Cross section W1-04 (top), elevation 389 mm, external cladding attack, scale reduction by melt
- Fig. 129: Cross section W1-04 (top), elevation 389 mm, shroud at different orientations
- Fig. 130: Cross section W1-04 (top), elevation 389 mm, heated and unheated fuel rods
- Fig. 131: Cross section W1-04 (top), elevation 389 mm, thermocouples
- Fig. 132: Cross section W1-j (bottom), elevation 391 mm, overview
- Fig. 133: ZrO₂ scale thickness profiles across the fuel rod bundle CORA-W1 in the azimuthal direction 330 ° to 150 ° at the elevations 389 mm (cross section W1-04, top) and 374 mm (cross section W1-10, top)
- Fig. 134: ZrO₂ scale thickness profiles around the shroud of bundle CORA-W1 at the elevations 389 mm and 374 mm, measured at external and internal surface
- Fig. 135: Cross section W1-06 (top), elevation 612 mm, overview
- Fig. 136: Cross section W1-06 (top), elevation 612 mm, heated and unheated fuel rods
- Fig. 137: Cross section W1-06 (top), elevation 612 mm, shroud at different orientations
- Fig. 138: Cross section W1-n (bottom), elevation 614 mm, overview
- Fig. 139: Cross section W1-07 (top), elevation 783 mm, overview
- Fig. 140: Cross section W1-07 (top), elevation 783 mm, degradation of test bundle components

- Fig. 141: Cross section W1-07 (top), elevation 783 mm, fuel pellet interaction with tungsten heater rod
- Fig. 142: Cross section W1-07 (top), elevation 783 mm, distribution and microstructure of metallic or subsequently oxidized melts
- Fig. 143: Cross section W1-q (bottom), elevation 785, overview
- Fig. 144: Results of the SEM/EDX analysis of sample CORA-W1-04; Overview of the positions analyzed
- Fig. 145: Results of the SEM/EDX analysis of sample CORA-W1-04, position 2
- Fig. 146: Results of the SEM/EDX analysis of sample CORA-W1-04, position 2, SEM analyses positions 1 - 4
- Fig. 147: Results of the SEM/EDX analysis of sample CORA-W1-04, position 12, SEM analyses positions a - c
- Fig. 148: Results of the SEM/EDX analysis of sample CORA-W1-04, position 9, SEM analyses positions 1 - 5
- Fig. 149: Results of the SEM/EDX analysis of sample CORA-W1-04, position 9, micro-photographs of SEM positions 1 - 5
- Fig. 150: Results of the SEM/EDX analysis of sample CORA-W1-04, position 9, SEM sub-position 4, SEM analyses positions 1 - 5
- Fig. 151: Results of the SEM/EDX analysis of sample CORA-W1-04, position 17, SEM analyses positions a - e
- Fig. 152: Results of the SEM/EDX analysis of sample CORA-W1-04, position 17, SEM sub-position c, SEM analyses positions 1 - 4
- Fig. 153: Results of the SEM/EDX analysis of sample CORA-W1-04, position 17, SEM sub-position d, SEM analyses positions 1 - 3
- Fig. 154: Results of the SEM/EDX analysis of sample CORA-W1-04, position 20, SEM analyses positions 1 - 6
- Fig. 155: Results of the SEM/EDX analysis of sample CORA-W1-04, position 20, micro-photographs of SEM positions 2 - 4
- Fig. 156: Results of the SEM/EDX analysis of sample CORA-W1-04, position 29, SEM analyses positions a - d
- Fig. 157: Results of the SEM/EDX analysis of sample CORA-W1-04, position 29, SEM sub-position a, SEM analyses positions 1 - 2
- Fig. 158: Results of the SEM/EDX analysis of sample CORA-W1-04, position 29, SEM sub-position b, SEM analyses positions 1 - 4
- Fig. 159: Results of the SEM/EDX analysis of sample CORA-W1-06; Overview of the positions analyzed
- Fig. 160: Results of the SEM/EDX analysis of sample CORA-W1-06, position 2, mean value of five SEM analyses positions

- Fig. 161: Results of the SEM/EDX analysis of sample CORA-W1-06, position 19, mean value of five SEM analyses positions
- Fig. 162: Results of the SEM/EDX analysis of sample CORA-W1-06, position 19, SEM sub-position a, SEM analyses positions 1,2, and 4
- Fig. 163: Results of the SEM/EDX analysis of sample CORA-W1-06, position 19, SEM sub-position a/3, SEM analyses positions 1 - 6

APPENDIX

- Fig. A1: CORA-W1; Argon flow through bundle and videoscopes, pre-heat phase
- Fig. A2: CORA-W1; Temperature at steam inlet, pre-heat phase
- Fig. A3: CORA-W1; Temperature of steam superheater prior to transient
- Fig. A4: CORA-W1: Temperatures of heated rods, pre-heat phase
- Fig. A5: CORA-W1: Temperatures of unheated rods, pre-heat phase
- Fig. A6: CORA-W1: Temperatures of unheated rods, pre-heat phase
- Fig. A7: CORA-W1: Temperatures of the spacers; pre-heat phase
- Fig. A8: CORA-W1: Temperatures of outer side of shroud, pre-heat phase
- Fig. A9: CORA-W1: Temperatures of shroud insulation, pre-heat phase
- Fig. A10: CORA-W1: Gas temperature above the shroud; pre-heat phase
- Fig. A11: CORA-W1: Gas temperature of the bundle heat plate; pre-heat phase
- Fig. A12: CORA-W1: Temperatures measured in and on the steam tube at -50 mm elevation; pre-heat phase
- Fig. A13: CORA-W1: Temperatures at fixed elevations, pre-heat phase (1450, 1350 mm)
- Fig. A14: CORA-W1: Temperatures at fixed elevations, pre-heat phase (1250, 1150 mm)
- Fig. A15: CORA-W1: Temperatures at fixed elevations, pre-heat phase (1050, 950 mm)
- Fig. A16: CORA-W1: Temperatures at fixed elevations, pre-heat phase (850, 750 mm)
- Fig. A17: CORA-W1: Temperatures at fixed elevations, pre-heat phase (650, 600 mm)
- Fig. A18: CORA-W1: Temperatures at fixed elevations, pre-heat phase (550, 450 mm)
- Fig. A19: CORA-W1: Temperatures at fixed elevations, pre-heat phase (350, 250 mm)
- Fig. A20: CORA-W1: Temperatures at fixed elevations, pre-heat phase (200, 150 mm)
- Fig. A21: CORA-W1: Temperatures at fixed elevations, pre-heat phase (50, 0 mm)

Fig.A22: CORA-W1: Temperatures at fixed elevations, pre-heat phase (-15 mm)

Fig.A23: CORA-W1: Temperatures at fixed elevations, pre-heat phase (-50, -200, -300 mm)

Tab.1: CORA test matrix

Test No.	Max. Cladding Temperatures	Absorber Material	Other Test Conditions	Date of Test
2	≈ 2000°C	-	UO ₂ refer., inconel spacer	Aug. 6, 1987
3	≈ 2400°C	-	UO ₂ refer., high temperature	Dec. 3, 1987
5	≈ 2000°C	Ag, In, Cd	PWR-absorber	Febr. 26, 1988
12	≈ 2000°C	Ag, In, Cd	quenching	June 9, 1988
16	≈ 2000°C	B ₄ C	BWR-absorber	Nov. 24, 1988
15	≈ 2000°C	Ag, In, Cd	rods with internal pressure	March 2, 1989
17	≈ 2000°C	B ₄ C	quenching	June 29, 1989
9	≈ 2000°C	Ag, In, Cd	10 bar system pressure	Nov. 9, 1989
7	< 2000°C	Ag, In, Cd	<u>57-rod bundle</u> , slow cooling	Febr. 22, 1990
18	< 2000°C	B ₄ C	<u>59-rod bundle</u> , slow cooling	June 21, 1990
13	≈ 2200°C	Ag, In, Cd	OECD/ISP; quench initiation at higher temperature	Nov. 15, 1990
29*	≈ 2000°C	Ag, In, Cd	pre-oxidized,	April 11, 1991
31*	≈ 2000°C	B ₄ C	slow initial heat-up (≈ 0.3 K/s)	July 25, 1991
30*	≈ 2000°C	Ag, In, Cd	slow initial heat-up (≈ 0.2 K/s)	Oct. 30, 1991
28*	≈ 2000°C	B ₄ C	pre-oxidized	Febr. 25, 1992
10	≈ 2000°C	Ag, In, Cd	cold lower end 2 g/s steam flow rate	July 16, 1992
33	≈ 2000°C	B ₄ C	dry core conditions, no extra steam input	Oct. 1, 1992
W1	≈ 2000°C	-	WWER-test	Febr. 18, 1993
W2	≈ 2000°C	B ₄ C	WWER-test with absorber	April 21, 1993

Tab.2: Design characteristics of test bundle CORA-W1

Bundle type:		VVER
Bundle size:		19
Number of heated rods:		13
Number of unheated rods:		6
Pitch:		12.75 mm
Cladding outside diameter		9.13 mm
Cladding inside diameter:		7.72 mm
Cladding material:		Zr-1%Nb
Heater:	- material	Tungsten (W)
	- diameter	4 mm
Fuel pellets:	- heated rods	UO ₂ annular pellets
	- outer diameter (nominal)	7.57 mm
	- diameter of central void	4.2 mm
	- unheated rods	UO ₂ annular pellets
	- diameter of central void	2.4 mm
Pellets stack:	- heated rods	0 to 1000 mm
	- unheated rods	-142/-192 to 1400 mm
U-235 enrichment		0.3%
Grid spacer	- material	Stainless steel (06X18H10T and 08X18H10T)
	- height	20 mm
	- number	3
	- location by elevation of upper edges (from level 0 mm)	-5; 210; 610 mm
Shroud	- material	Zr-1%Nb
	- wall thickness	1.2 mm
	- outer dimension	68 mm
	- length	1195 mm

Tab. 3: Thermocouples used in the CORA-VVER Test CORA-W1 (without absorber rod)

	1. *)	2.	3.	4.
Thermoelement wire	WRe 5 % - WRe 20 %	WRe 5 % - WRe 26 %	WRe 5 % - WRe 26 %	NiCr/Ni Al (Type K)
Insulation	BeO	HfO ₂	HfO ₂	Al ₂ O ₃
Cladding	Mo-ZrC- Mo-MoSi ₂	Niobium + Zry-4	Niobium	Stainless steel
Outer Diameter [mm]	2.3	2.3	1.5	1.0
Positions for measurements	In the center and outer surface of unheated rods	At the outer surface of heated rods, of the shroud and of the shroud insulation	At the grid spacer	At the lower part of heated rods, of grid spacer, of the shroud and insulation, for gas temperature, temperature of the bundle flange and of the steam entrance

*) Russian design

Tab. 4: Positions of thermocouples of test bundle CORA-W1

Positions of thermocouples in unheated rods (CORA -W 1)		
Slot Number	Elevation [mm]	Rod Number
101	1250	2.8
102	1150	2.2
103	1050	2.4
104	950	3.0
105	850	2.6
106	750	2.0
221	650	3.0
222	550	2.6
223	450	2.0
224	350	2.2
225	250	2.4
226	150	2.8

Positions of thermocouples at heated rods (CORA- W 1)		
Slot Number	Elevation [mm]	Rod Number
117	950	4.9
118	850	4.1
119	750	5.3
249	650	3.3
250	550	1.1
251	550	4.1
252	450	4.9
253	350	3.1
254	250	4.3
255	150	4.7
231	50	3.7
232	-50	4.5

Positions of thermocouples at shroud outer surface(W1)		
Slot Number	Elevation [mm]	Direction of TE
215	150	300°
235	50	120°

Positions of thermocouples at shroud insulation(CORA-W 1)		
Slot Number	Elevation [mm]	Direction of TE
128	950	120°
129	850	240°
130	750	0°
216	650	240°
217	550	240°
236	450	240°
237	350	300°
238	250	300°
239	150	300°
261	50	300°
262	950	0°
263	850	0°
264	750	0°

Positions of thermocouples at unheated rods (CORA-W 1)		
Slot Number	Elevation [mm]	Rod Number
107	1250	2.8
108	1150	2.2
109	1050	2.4
110	950	3.0
111	850	2.6
112	750	2.0
227	750	2.2
228	750	3.0
229	650	2.4
230	650	3.0
241	550	2.6
242	550	2.0
243	450	2.6
244	450	2.0
245	350	2.2
246	350	2.8
247	250	2.4
248	150	2.8

Positions of thermocouples at grid spacer (CORA- W 1)		
Slot Number	Elevation [mm]	Direction of TE
256	600	60°
257	600	240°
258	200	60°
259	200	240°
233	-15	60°
234	-15	240°

Positions of thermocouples for gas (CORA- W1)		
Slot Number	Elevation [mm]	Direction of TE
120	1350	353°
121	1250	210°
122	1150	150°

Positions of thermocouples at shroud outer surface (W1)		
Slot Number	Elevation [mm]	Direction of TE
123	1150	300°
124	1050	240°
125	950	120°
126	850	180°
127	750	60°
260	650	180°
211	550	0°
212	450	240°
213	350	60°
214	250	0°

Positions of thermocouples steam distribution tube(C-W1)		
Slot Number	Elevation [mm]	Direction of TE
265	0	180°
266	0	180°
267	50	360°
268	-50	15°
269	-50	195°
270	-50	165°
271	-50	345°
272	-250	300°
62	-300	180°
135	1491	60°

Positions of thermocouples at heated rods (CORA-W 1)		
Slot Number	Elevation [mm]	Rod Number
131	1450	3.1
132	1350	4.3
113	1250	3.3
114	1150	4.5
115	1050	3.7
116	950	1.1

Table 5: CORA-W1; Positions of thermocouples in the high-temperature shield

ANGLE \angle	30°	55°	75°	120°	145°	165°	210°	235°	255°	300°	345°				
RADIUS	153	153	153	153	153	153	153	153	153	153	153	172	192	255	293
(mm)															
1250											174 33Ni				
1150											175 56Ni				
1050											176 55Ni				
950		162 54Ni			166 53Ni			170 52Ni			177 51Ni	188 29Ni	191 30Ni	194 38Ni	197 39Ni
850											178 24Ni				
750											179 23Ni				
650											180 22Ni				
550	slot161 19Ni		163 18Ni	165 17Ni		167 16Ni	169 15Ni		171 14Ni	173 13Ni	181 12Ni	189 20Ni	192 21Ni	195 36Ni	198 37Ni
450											182 11Ni				
350											183 10Ni				
250											184 9Ni				
150											185 8Ni				
50			164 5Ni			168 4Ni			172 3Ni		186 2Ni	190 6Ni	193 7Ni	196 34Ni	199 35Ni
-50											187 1Ni				

Table 6: Sequence of events in test CORA-W1

- 10 500 s	Start of the argon injection of 3 g/s into the bundle (F408)
- 8 400 s	Argon injection increased to 8 g/s
- 8 400 s	Begin of the argon injection (F402) for videoscopes and bundle head plate
- 6 300 s	Argon injection (F408) increased to 10 g/s
- 1 740 s	Argon injection in the bundle reduced to 8 g/s
- 300 s	Total argon injection (F402) 6 g/s: 1.18 g/s for videoscopes and 4.82 g/s for the bundle head plate
0 s	Start of the bundle heating (0.52 KW)
2 700 s	Argon injection in the bundle reduced to 6 g/s
3 000 s	Start of the transient with a linear electric power input rate (Initial value 1.6 kW, final value 16.5 KW)
3 700 s	Begin of the steam injection: 4 g/s
4 100 s	Begin of the temperature escalation
4 850 s	Electric power reduced to 0.52 KW
4 900 s	Heating of evaporator and superheater turned off
7 200 s	Argon injection in the bundle (F408) increased to 10 g/s

**Table 7: Temperatures [°C] of test CORA-W1 for
different components at 0 seconds**

Elevation [mm]	Components					
	Heated rod	Unheated rod		Shroud	Shroud insulation	HTS 153 mm
		Central position	Outer surface			
1450	37					
1350	75					
1250	146	78	125			79
1150	317	284	307	241		93
1050	312	342	344	302		94
950	366	372	370	312	(133)	92
850	378	378	380	323	128	88
750	376	381	381	325	128	85
650	384	392	384		124	84
550	403	397	403	337	156	83
450	395	401	393	360	125	81
350	394	406	405	351	134	77
250	420	417	437	365	127	75
150	420	413	415	394	173	72
50	443			382	231	72
-50	311					65

**Table 8: Temperatures [°C] of test CORA-W1 for
different components at 3000 seconds**

Elevation [mm]	Components					
	Heated rod	Unheated rod		Shroud	Shroud insulation	HTS 153 mm
		Central position	Outer surface			
1450	38					
1350	95					
1250	159	77	114			84
1150	374	331	363	278		105
1050	399	423	425	370		105
950	469	463	463	392	(151)	102
850	472	469	470	401	144	97
750	467	469	467	398	144	94
650	471	470	463		137	92
550	477	466	466	397	174	91
450	472	464	456	409	135	87
350	457	461	459	396	145	83
250	464	460	476	398	134	77
150	444	439	440	411	181	77
50	454			387	222	76
-50	322					69

Tab. 9: Cross sections of test bundle CORA-W1

Sample	Sample length	Axial position bottom	top	Remarks
W1-a	xxx mm	-xxx mm	-67 mm	
W1-b	50 mm	-65 mm	-15 mm	
W1-01	13 mm	-13 mm	0 mm	
W1-c	50 mm	2 mm	52 mm	
Cut	2 mm			
W1-d	50 mm	54 mm	104 mm	
W1-02	13 mm	106 mm	119 mm	
W1-e	50 mm	121 mm	171 mm	
Cut	2 mm			
W1-f	30 mm	173 mm	203 mm	
Cut	2 mm			Central grid spacer
W1-03	13 mm	205 mm	218 mm	Cross section
Cut	2 mm			
W1-g	50 mm	220 mm	270 mm	
Cut	2 mm			
W1-h	50 mm	272 mm	322 mm	
Cut	2 mm			
W1-i	35 mm	324 mm	359 mm	
Cut	2 mm			
W1-10	13 mm	361 mm	374 mm	Cross section
Cut	2 mm			
W1-04	13 mm	376 mm	389 mm	Cross section
Cut	2 mm			
W1-j	50 mm	391 mm	441 mm	Additional longitudinal cut
Cut	2 mm			
W1-k	50 mm	443 mm	493 mm	Additional longitudinal cut

Cut	2 mm			
W1-05	13 mm	495 mm	508 mm	Cross section
Cut	2 mm			
W1-l	50 mm	510 mm	560 mm	Additional longitudinal cut
Cut	2 mm			
W1-m	35 mm	562 mm	597 mm	Additional longitudinal cut
Cut	2 mm			Upper grid spacer
W1-06	13 mm	599 mm	612 mm	Cross section
Cut	2 mm			
W1-n	50 mm	614 mm	664 mm	Additional longitudinal cut
Cut	2 mm			
W1-o	50 mm	666 mm	716 mm	
Cut	2 mm			
W1-11	13 mm	718 mm	731 mm	Cross section
Cut	2 mm			
W1-p	35 mm	733 mm	768 mm	
Cut	2 mm			
W1-07	13 mm	770 mm	783 mm	Cross section
Cut	2 mm			
W1-q	50 mm	785 mm	835 mm	
Cut	2 mm			
W1-r	50 mm	837 mm	887 mm	
Cut	2 mm			
W1-s	50 mm	889 mm	939 mm	
Cut	2 mm			
W1-08	13 mm	941 mm	954 mm	Cross section
Cut	2 mm			

W1-t	35 mm	956 mm	991 mm	
Cut	2 mm			
W1-12	13 mm	993 mm	1006 mm	Cross section
Cut	2 mm			Top of heated zone
W1-u	50 mm	1008 mm	1058 mm	
Cut	2 mm			
W1-v	50 mm	1060 mm	1110 mm	
Cut	2 mm			
W1-09	13 mm	1112 mm	1125 mm	Cross section
Cut	2 mm			
W1-w	xxx mm	1127 mm	xxxx mm	Remnant

Tab. 10: CORA-W1; Polished samples

- W1-03 top 218 mm (central grid spacer)
- W1-10 top 374 mm
- W1-04 top 389 mm
- W1-05 top 508 mm
- W1-06 top 612 mm
- W1-11 top 731 mm
- W1-07 top 783 mm
- W1-08 top 954 mm
- W1-12 top 1006 mm
- W1-09 top 1125 mm (above the heated zone)

-
- W1-j bottom 391 mm (to be compared with W1-04 top) → KfK
 - W1-n bottom 614 mm (to be compared with W1-06 top) → KfK
 - W1-q bottom 785 mm (to be compared with W1-07 top) → KfK

Table 11: Procedure of the preparation of the samples for the metallographic examination

	Horizontal grinding	Grinding	Lapping	Polishing		
Abrasive	Corrundum disc 120 μm Diamond disc 64 μm	Diamond disc 20 μm	Petrodisc-M or DP Net*)	PAW cloth	PAN-W	NAP cloth
Particle size			Diamond spray 6 μm	6 μm	3 μm	1 μm
Lubricant	Water	Water	W. lubric. **)	W. lub.	W. lub.	W. lub.
Revolutions of disc	300 rpm	300 rpm	150 rpm (Net) or 300 rpm (Petrod.)	150 U/min	150 U/min	150 U/min
Pressure	200-400 N	200-300 N	200 N	100 N	100 N	100 N
Time	to level	25 min	30 min	30 min	60 min	60 min

*) Petrodisc-M and DP Net are registered trade marks of Struers company

***) "White lubricant" of Struers; liquid on an oil/alcohol/glycerin basis

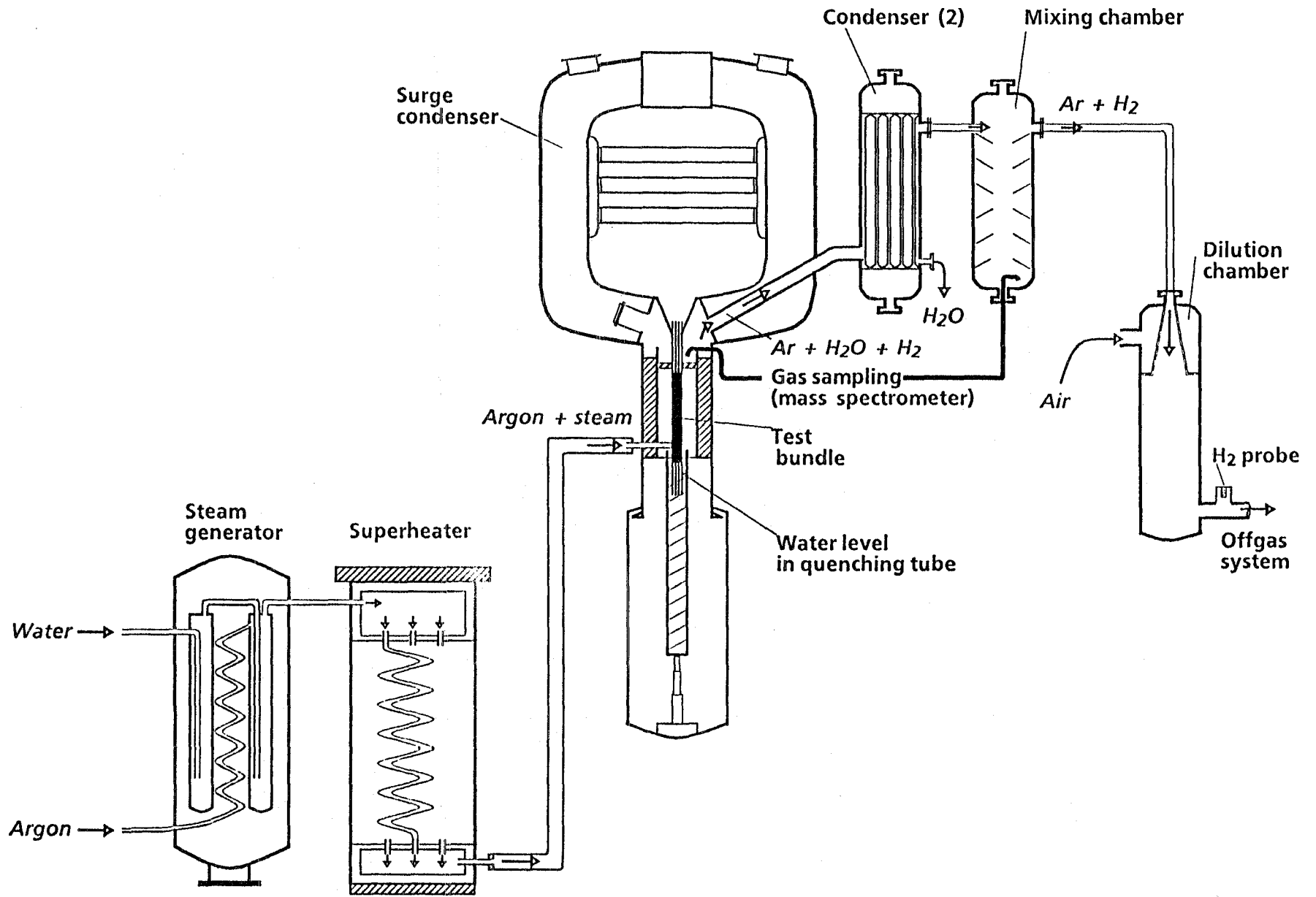
Tab. 12: Summary of O-Zr-U molten phases found, arranged as to uranium contents

Sauerstoff		Zirkon		Uran		Analysenposition-Nr.
Gew.-%	Atom %	Gew.-%	Atom %	Gew.-%	Atom %	
5.9	26.3	93.9	73.6	0.2	0.1	04-29-REM b-3
5.8	26.0	94.0	74.0	0.2	0.1	04-20-REM 5
5.4	24.7	93.3	74.9	1.3	0.4	04-17-REM c-2
24.9	65.9	72.7	33.7	2.4	0.4	04-9-REM 4-5
26.7	68.2	69.1	31.0	4.2	0.7	04-29-REM a-1
26.4	68.3	67.6	30.7	6.0	1.0	04-29-REM d
6.5	29.4	87.3	68.8	6.2	1.9	04-9-REM 4-4
24.6	67.3	63.6	30.6	11.8	2.2	04-12-REM c
22.2	64.4	65.1	33.1	12.7	2.5	04-2-REM 3
21.5	63.4	65.7	34.0	12.8	2.5	04-9-REM 4-3
23.7	66.7	61.7	30.5	14.6	2.8	04-29-REM b-1
9.4	39.8	74.8	55.7	15.8	4.5	04-9-REM 4-1
20.5	65.8	49.0	27.6	30.5	6.6	04-9-REM 3
12.5	61.9	17.0	14.7	70.5	23.4	04-9-REM 4-2
11.3	61.4	10.8	10.2	77.9	28.4	04-29-REM b-2
12.5	65.6	6.2	5.7	81.3	28.7	04-2-REM 1
23.1	67.4	55.6	28.4	21.3	4.2	06-19-REM a-3-2
23.0	67.8	53.1	27.5	23.8	4.7	06-19-REM a-1
21.4	66.8	49.6	27.1	29.0	6.1	06-19-REM a-3-6
19.7	67.9	36.3	21.9	44.0	10.2	06-19-REM a-3-5
11.5	65.7	0.7	0.7	87.8	33.6	06-19-REM a-4
10.1	62.1	1.1	1.2	88.8	36.7	*06-19-REM a-3-3

* Erklärung zur Analysenpositionierung :

Probe Nr.	Lichtopt. Nr.	REM Pos.	REM Teilbereich	Analysen Pos.
06	-	19	-	a
			-	3
				3

Fig. 1: SFD Test Facility (Simplified flow diagram)



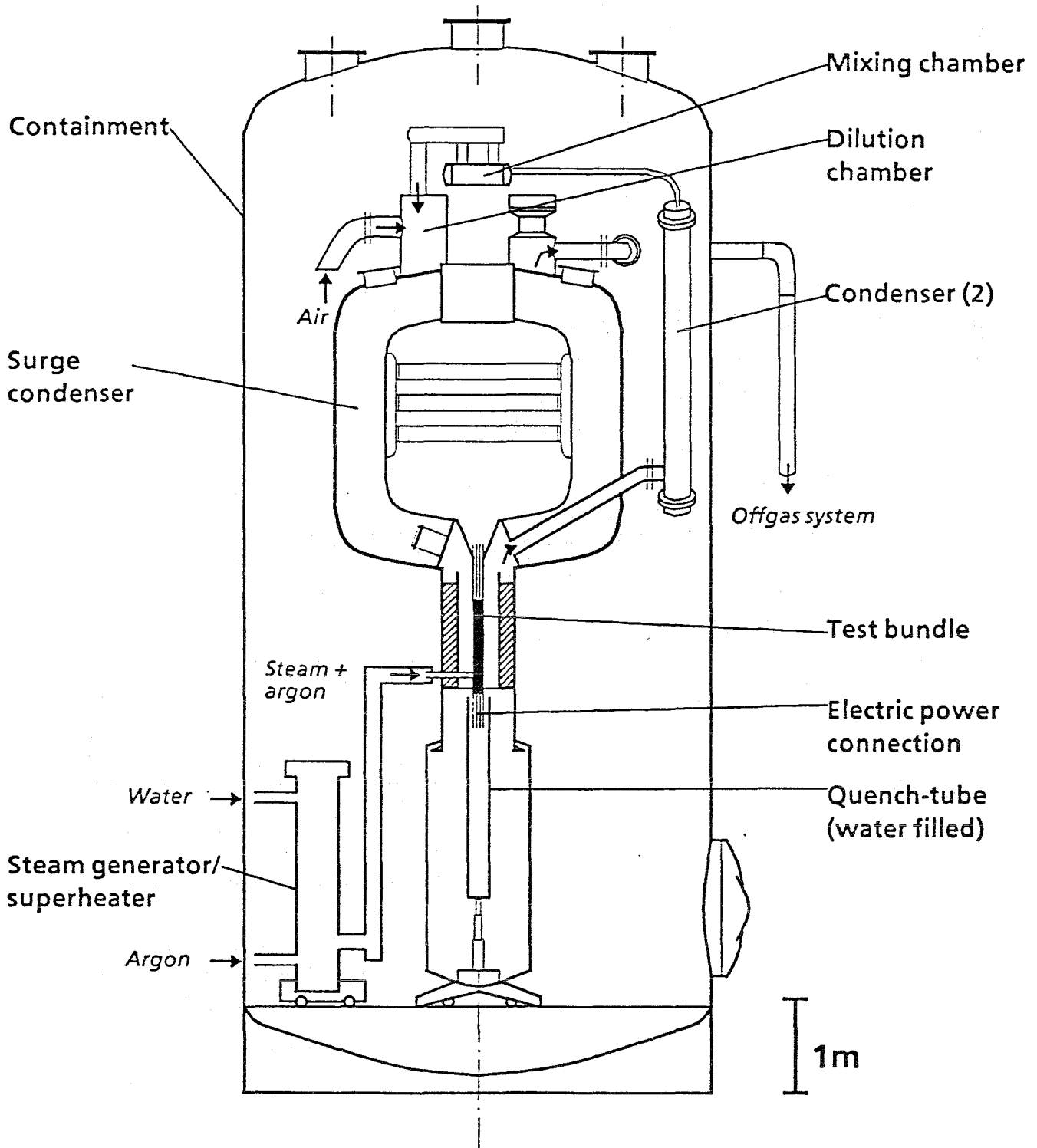


Fig. 2: SFD Test Facility CORA (Main components)

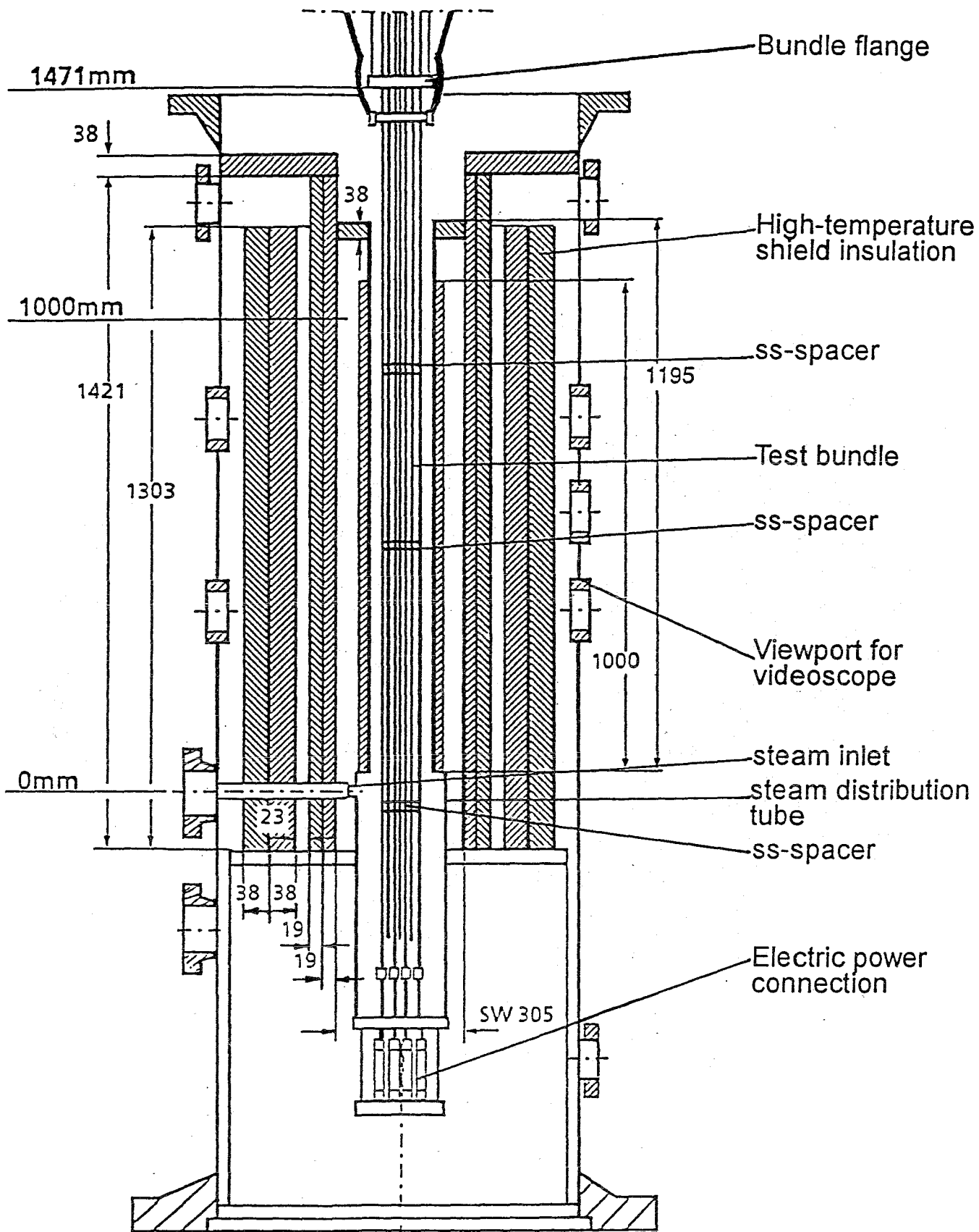


Fig. 3: CORA bundle arrangement

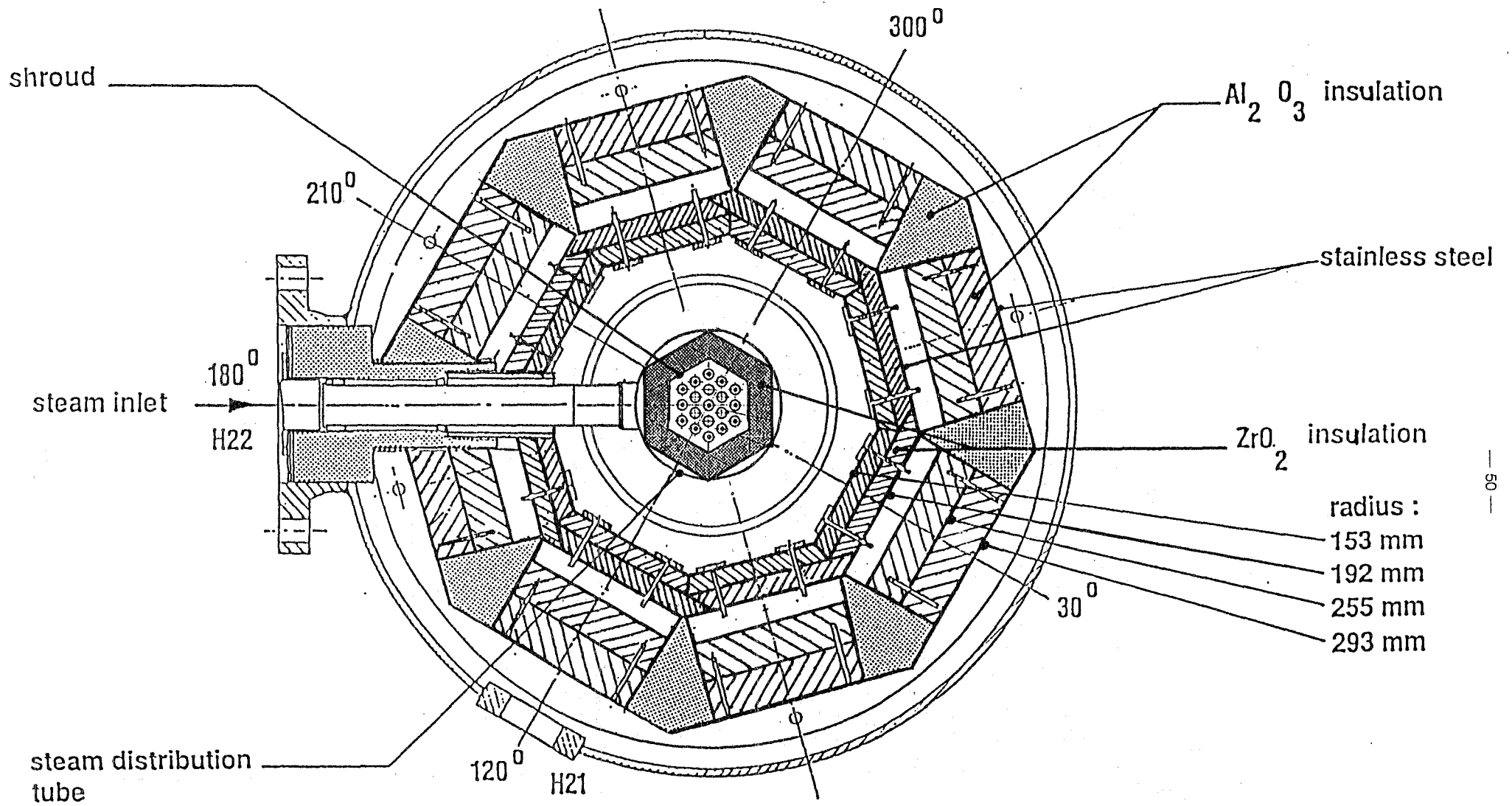


Fig. 4: Horizontal cross section of the high-temperature shield

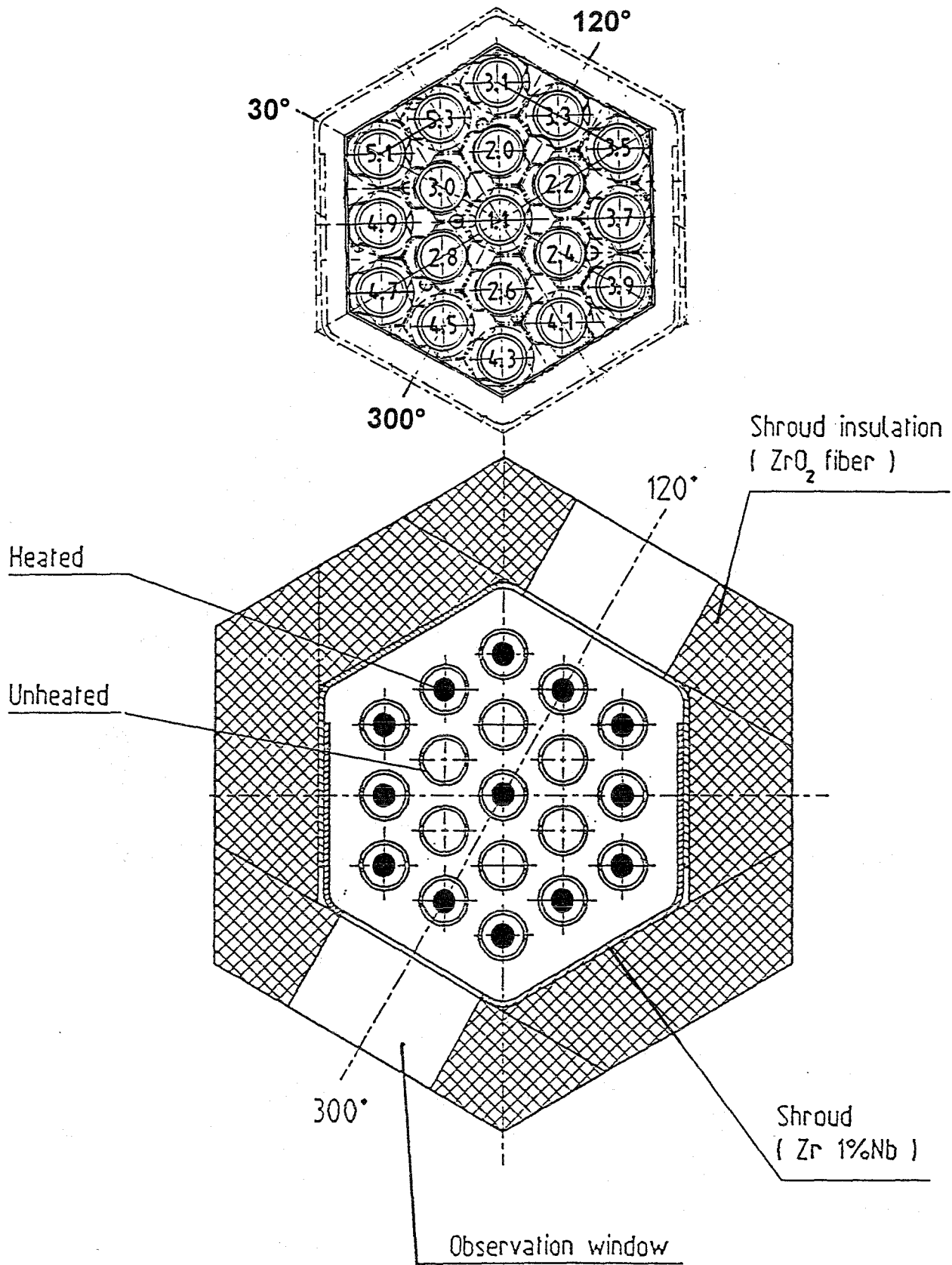


Fig. 5: Rod arrangement and test rod designation of bundle CORA-W1

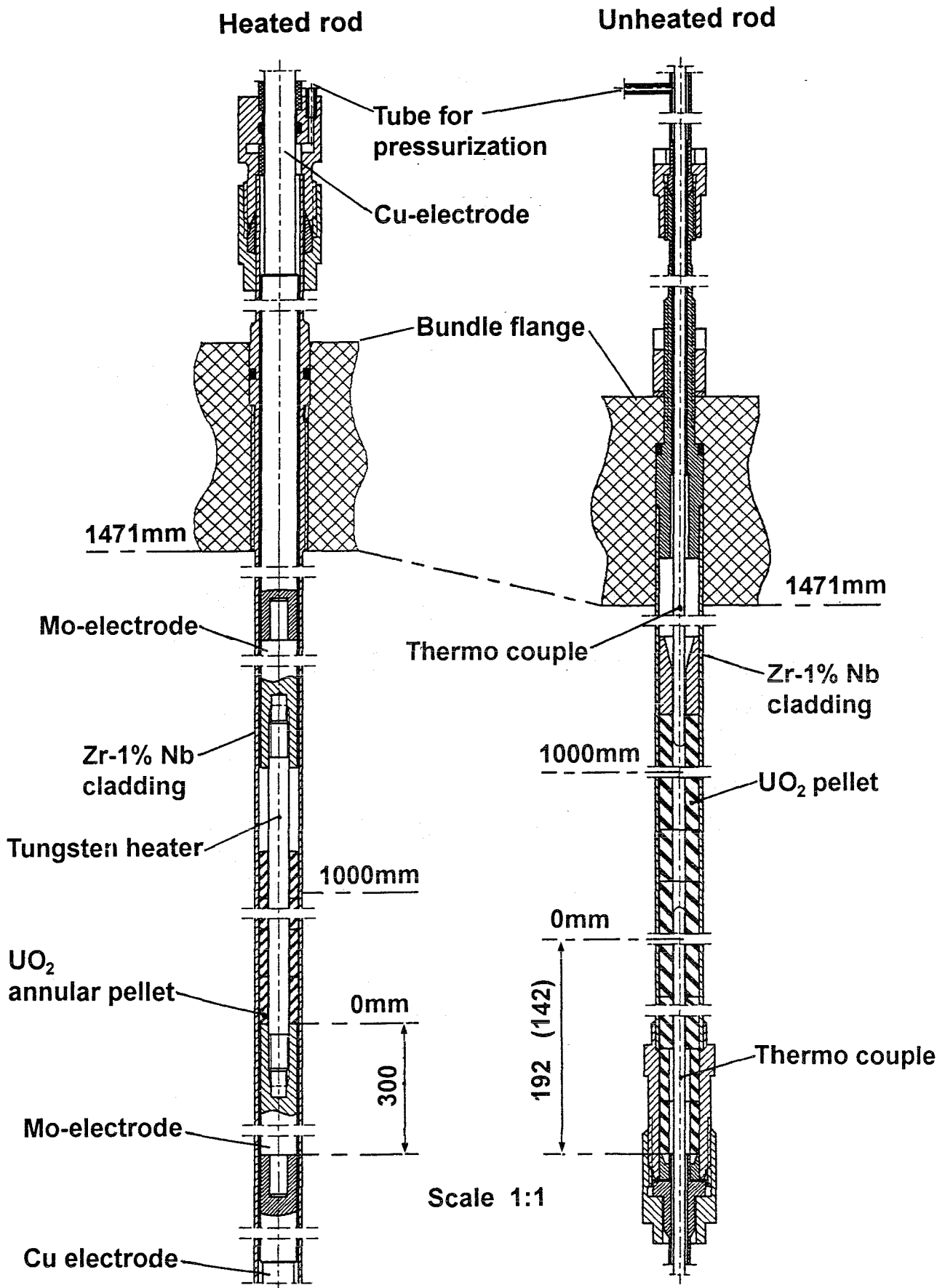


Fig. 6: Rod types used in the CORA / VVER experiments

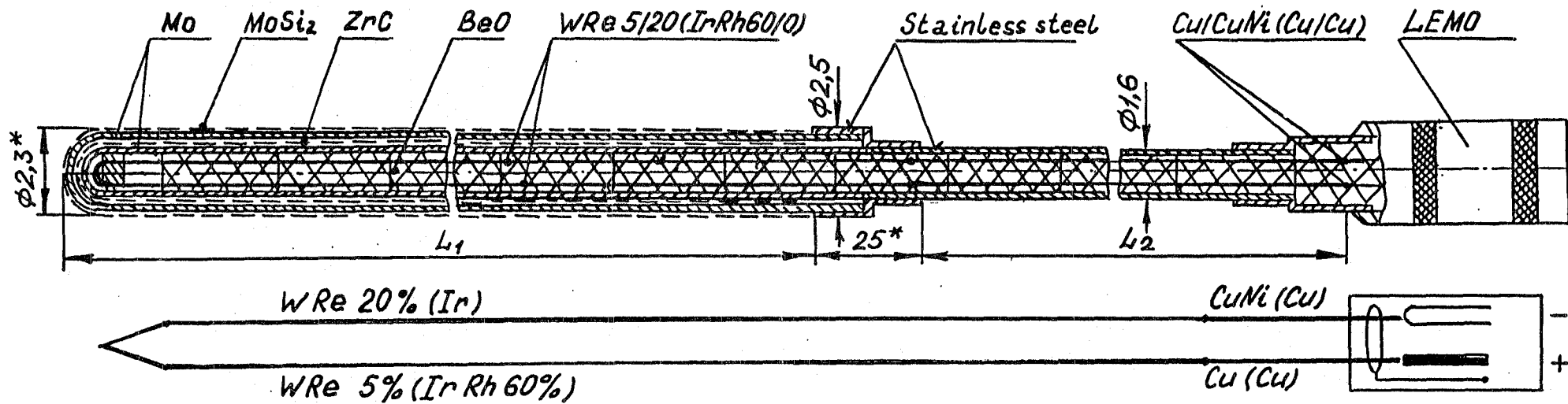


Fig. 7: The high-temperature thermoelectric transducer (HTT) of Russian design used in test CORA-W1

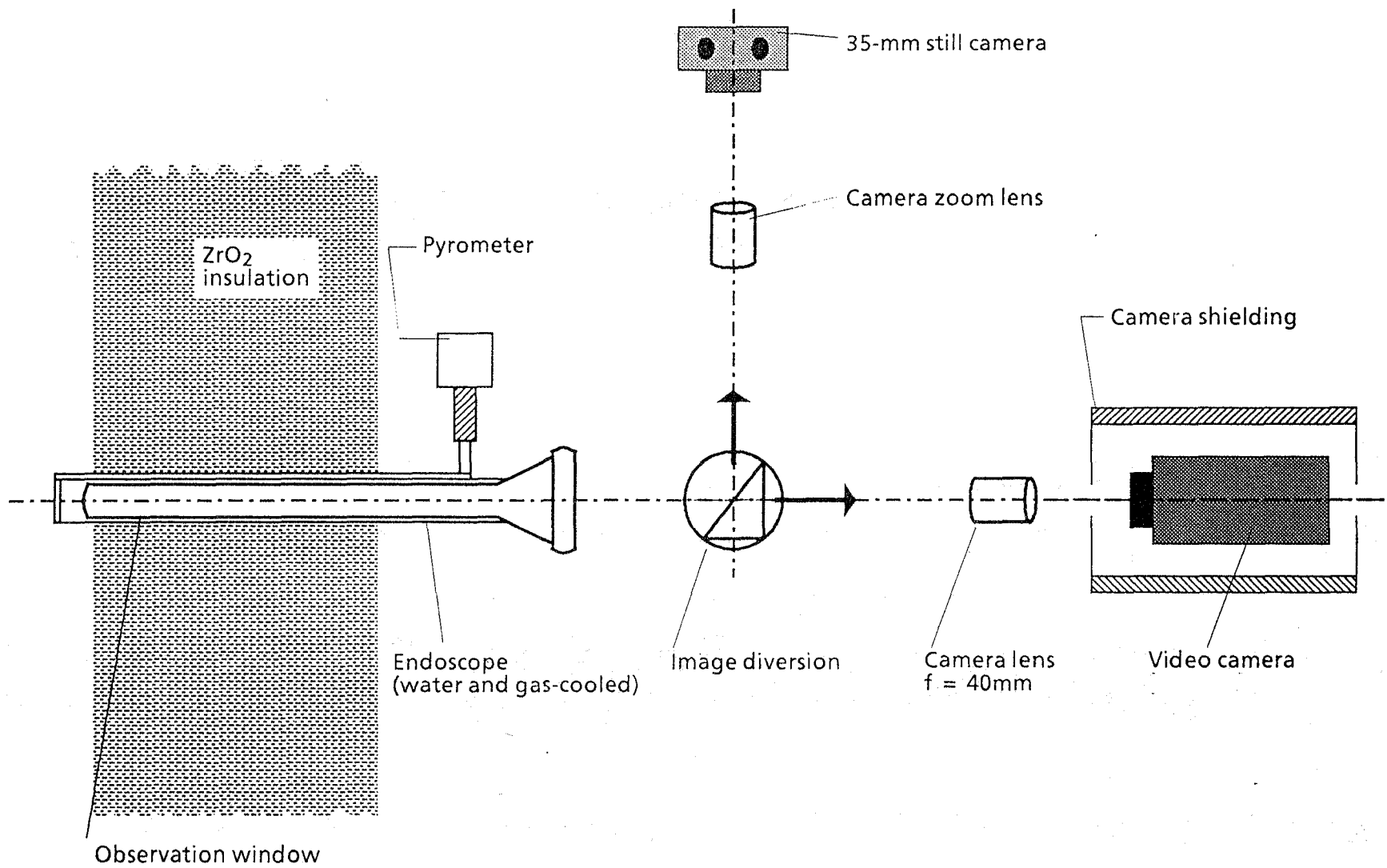
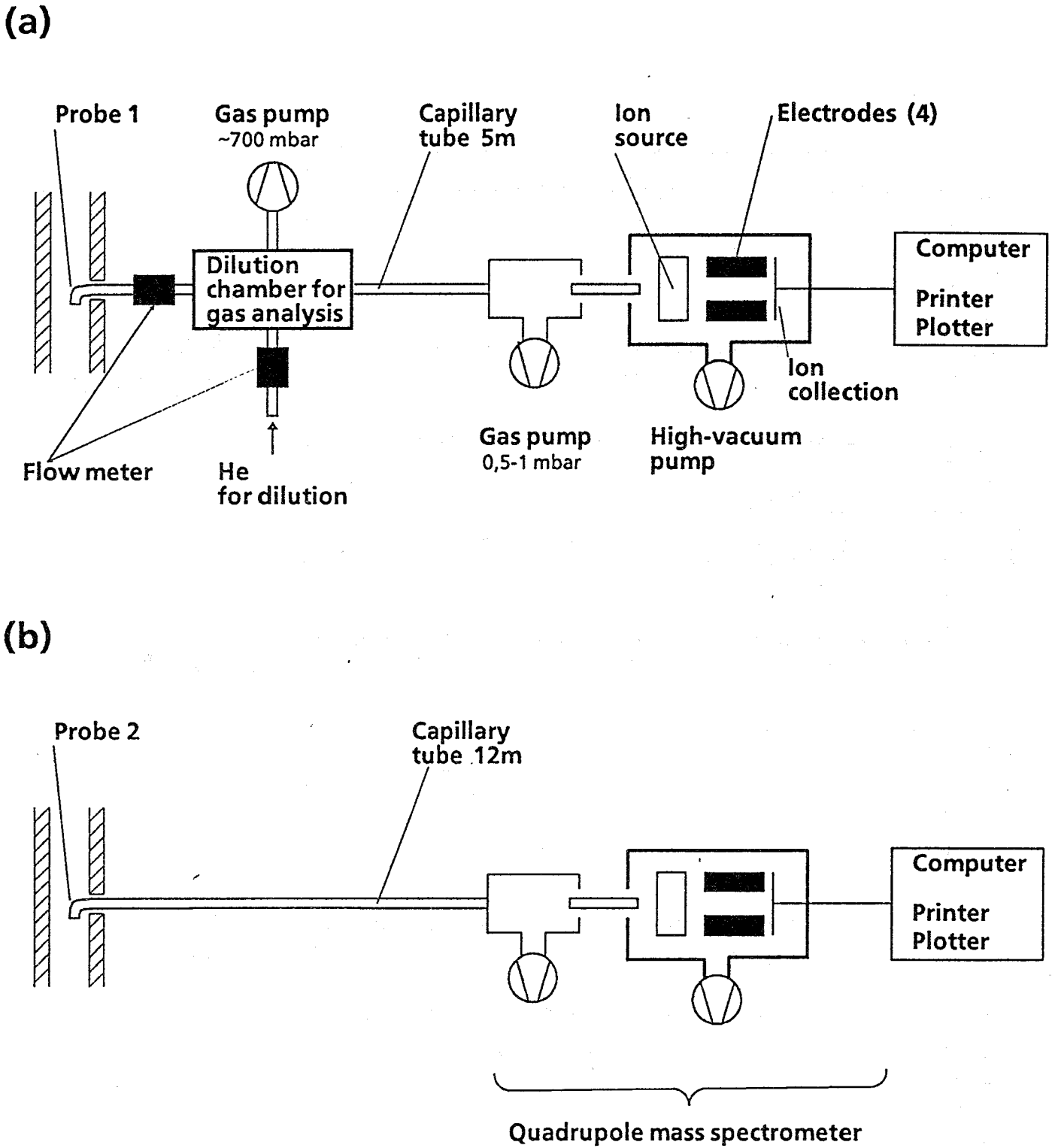


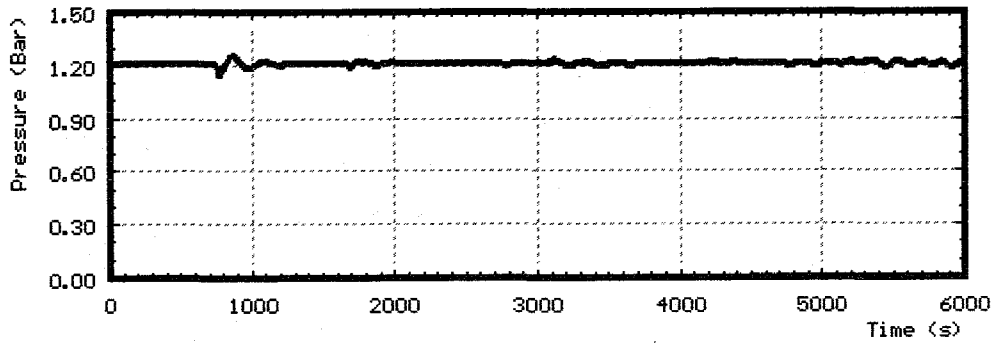
Fig. 8: Videoscope system for the CORA test bundle



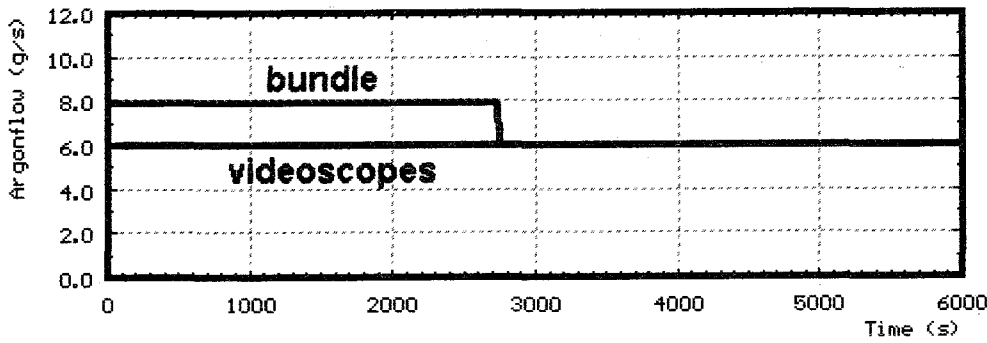
Location (a) : Outlet of test section

Location (b) : Mixing chamber

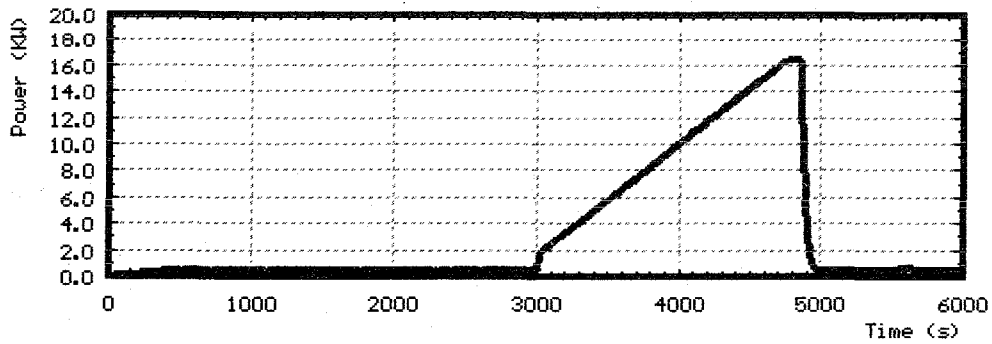
Fig. 9: Hydrogen measurement



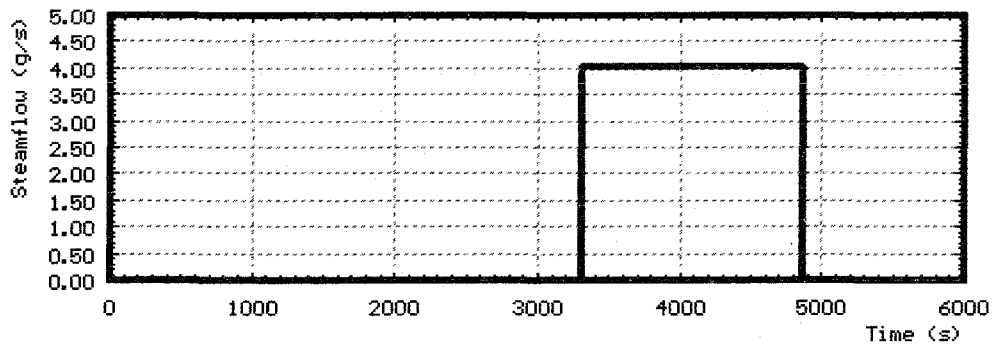
System Overpressure



Argonflow



Power



Steam Input

Fig. 10: CORA-W1; System pressure, argon flow, steam input and power

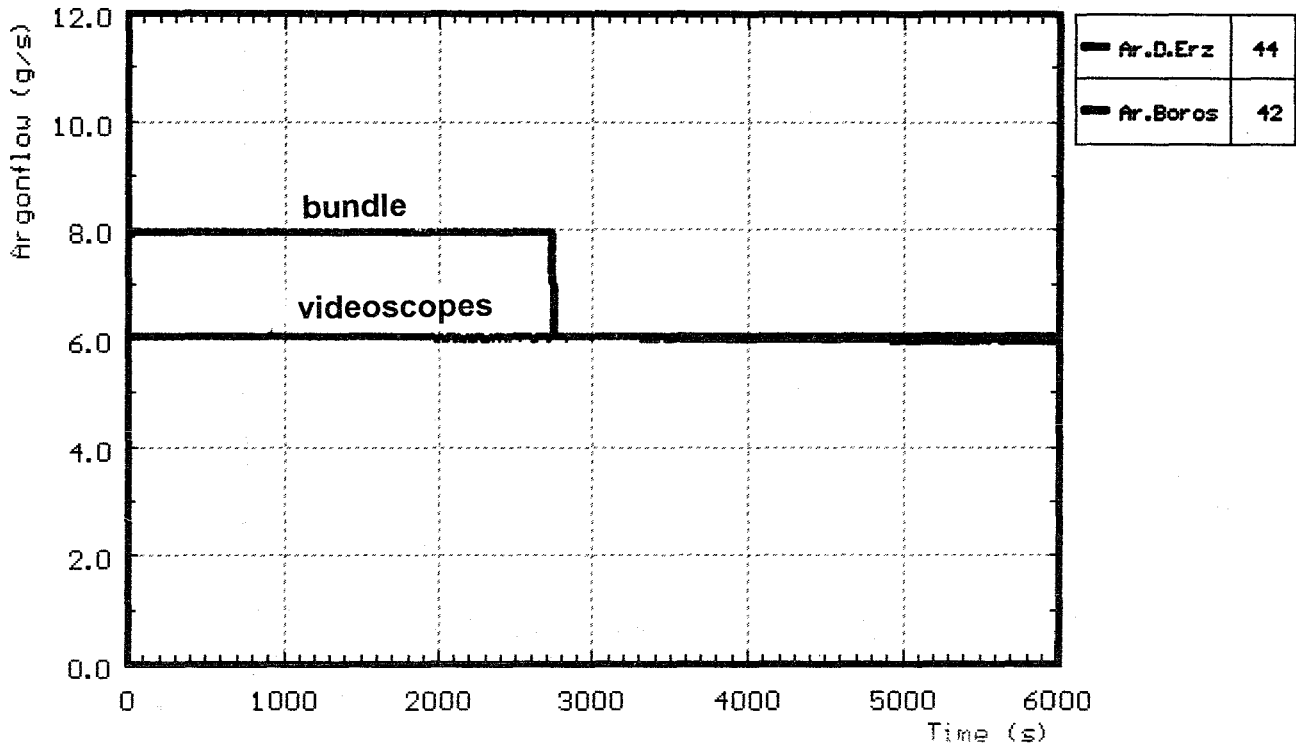


Fig. 11: Argon flow through bundle and videoscopes

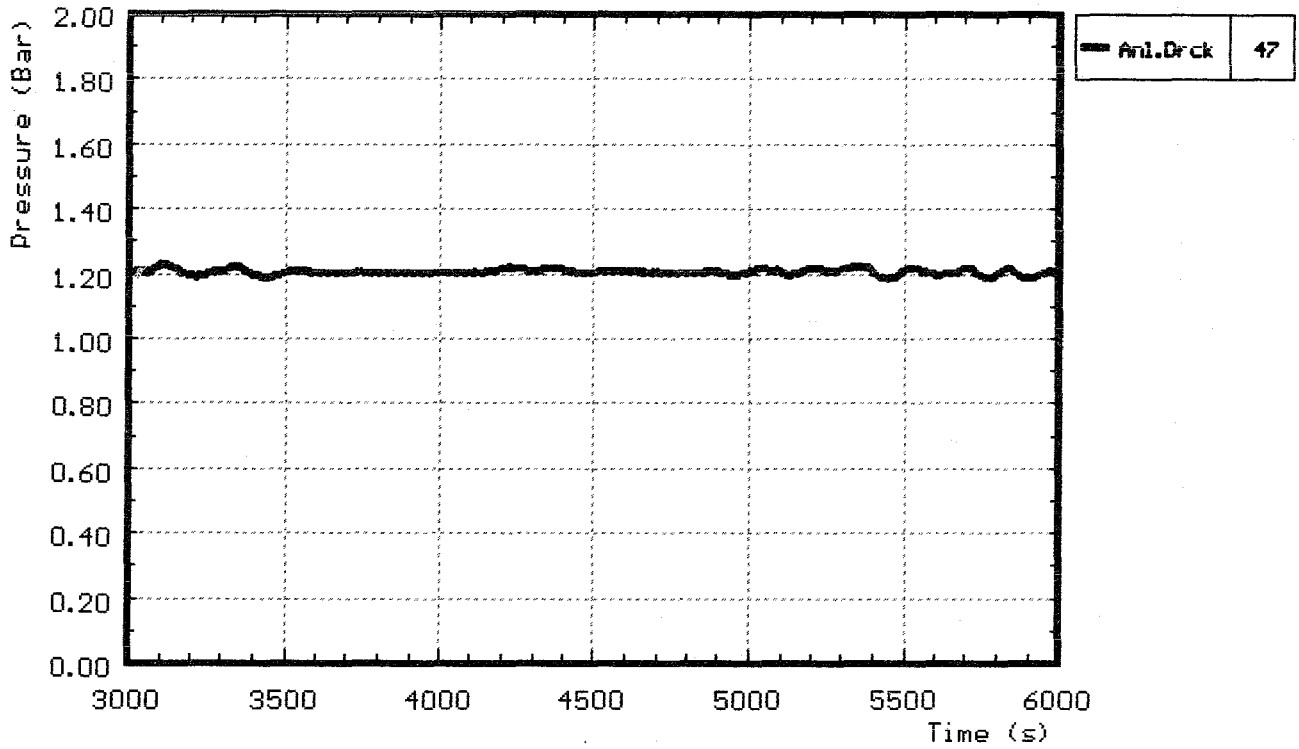


Fig. 12: CORA-W1; System pressure (gauge)

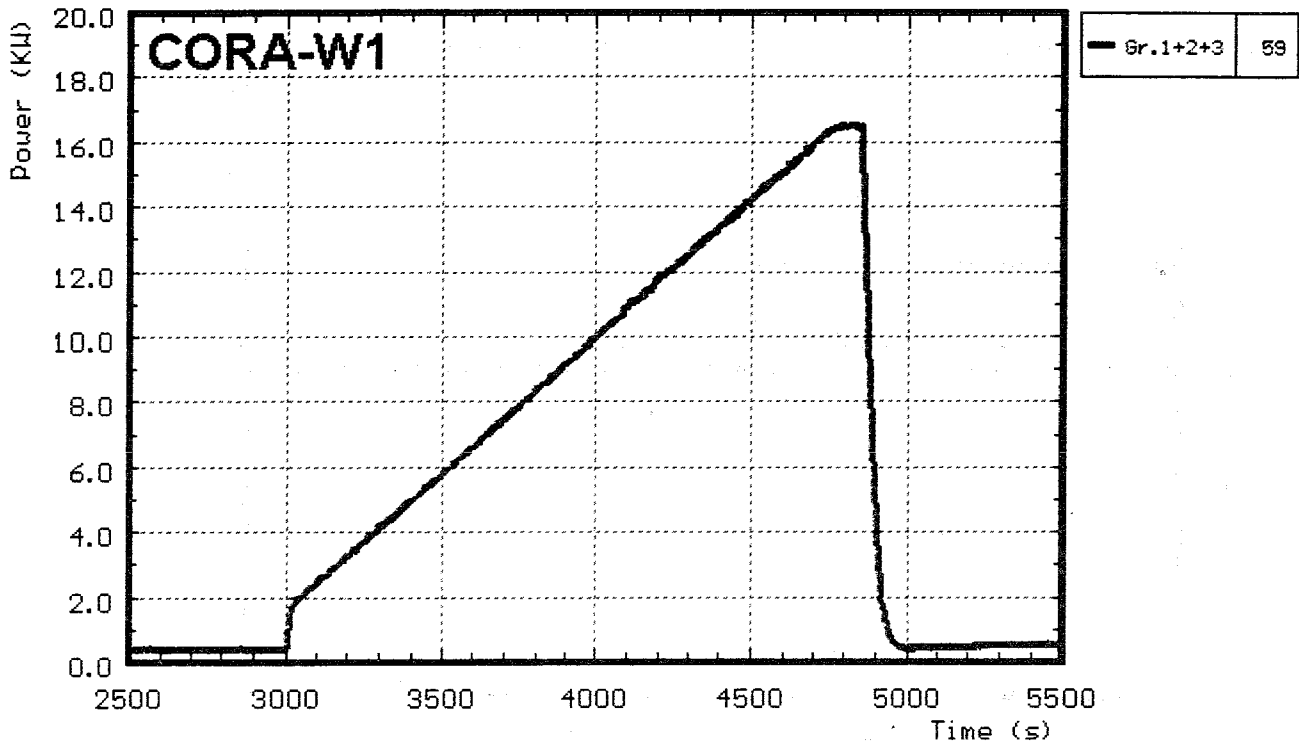


Fig. 13: CORA-W1; Total power input

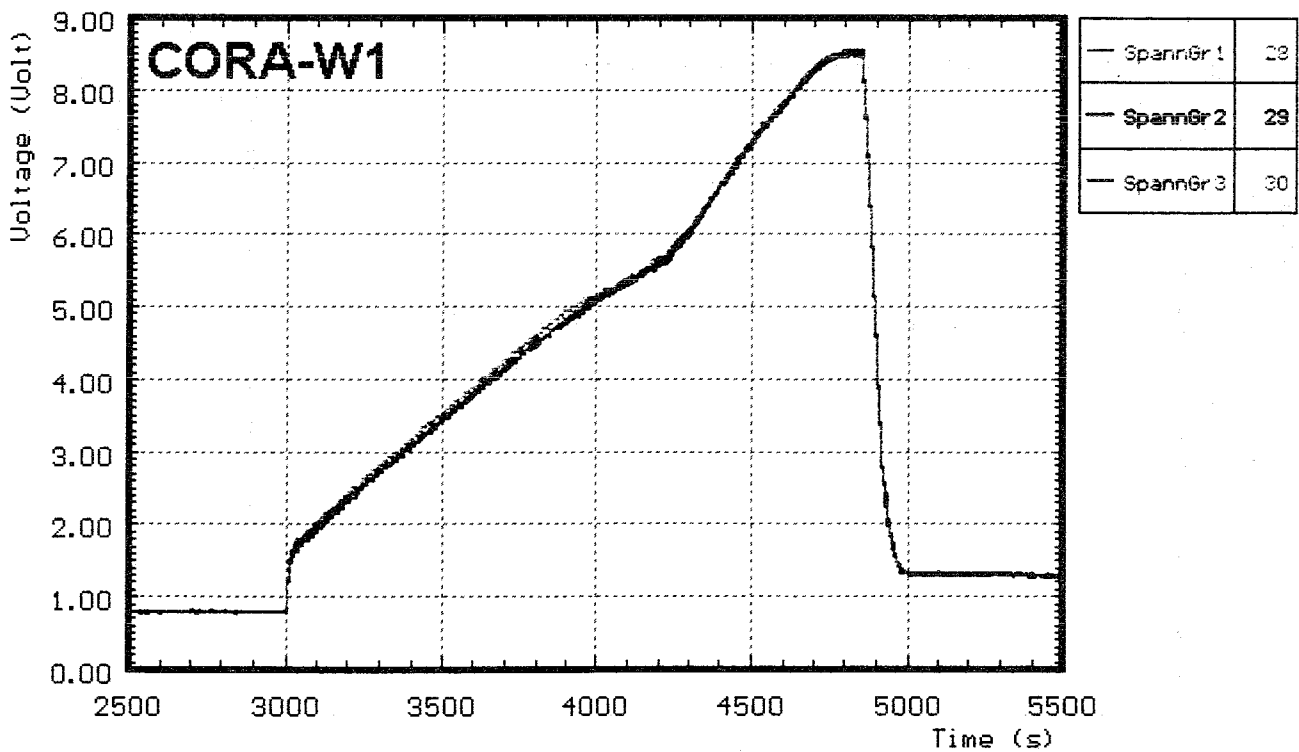


Fig. 14: CORA-W1; Voltage input for the 3 rod groups

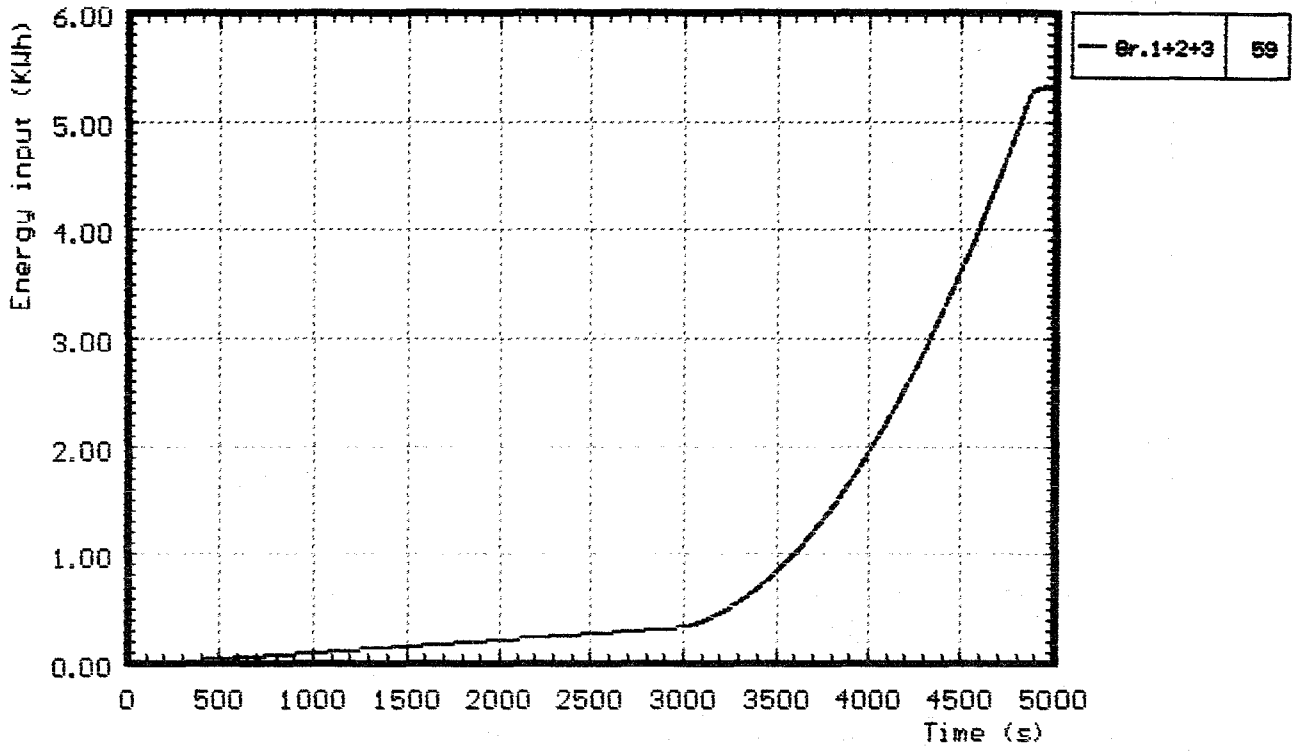


Fig. 15: CORA-W1; Total electric energy input

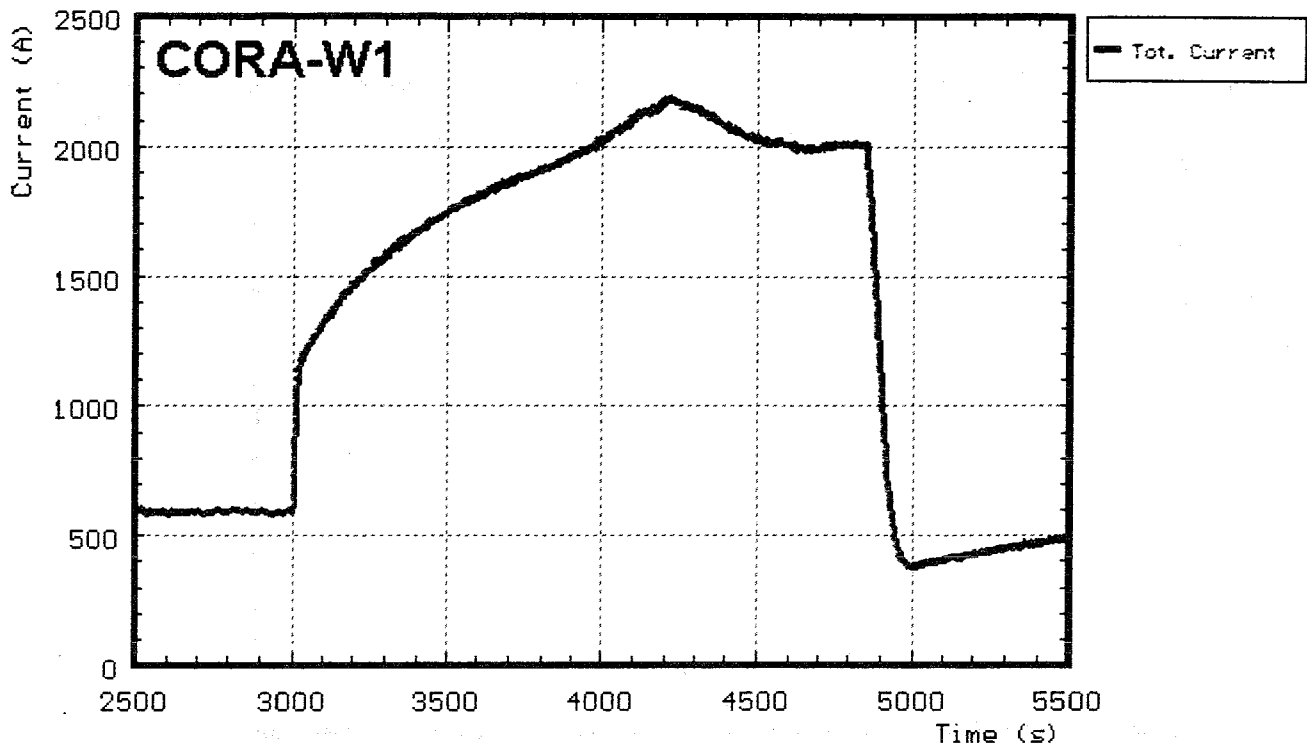


Fig. 16: CORA-W1; Total current

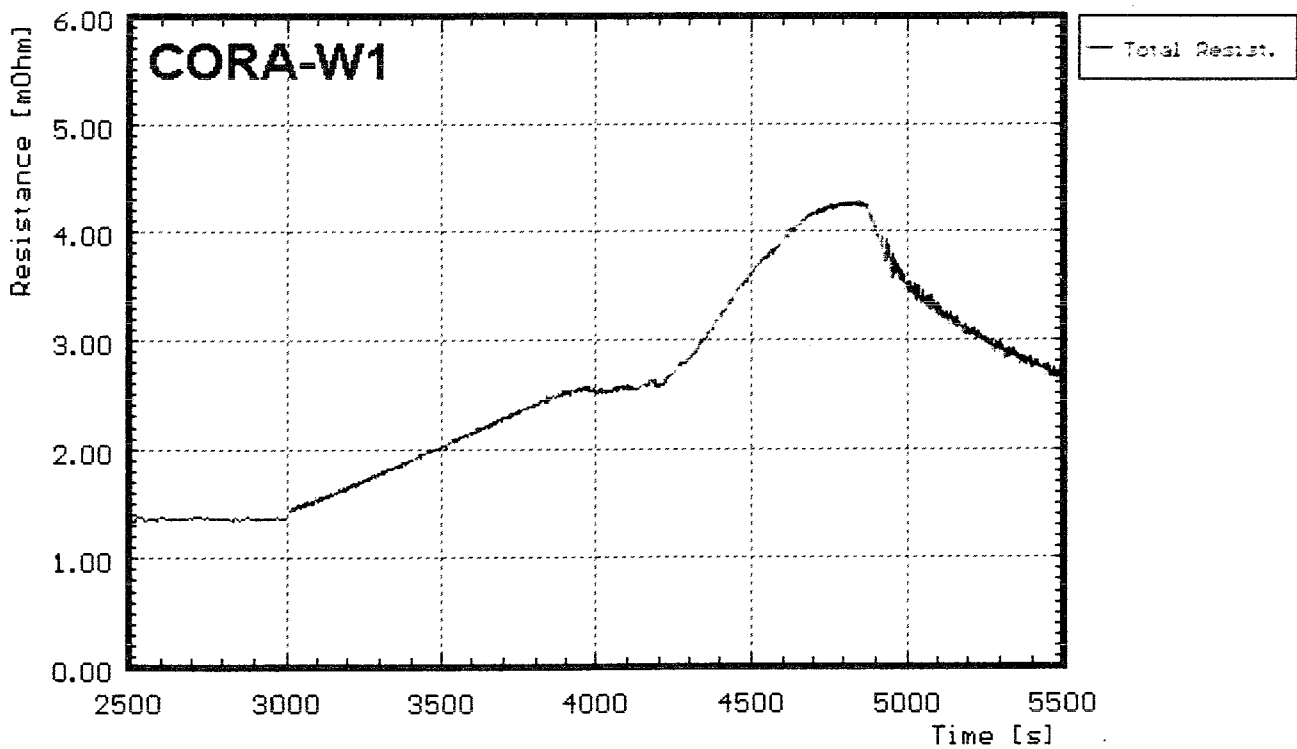


Fig. 17: CORA-W1; Resistance of bundle (Voltage group1 / total current)

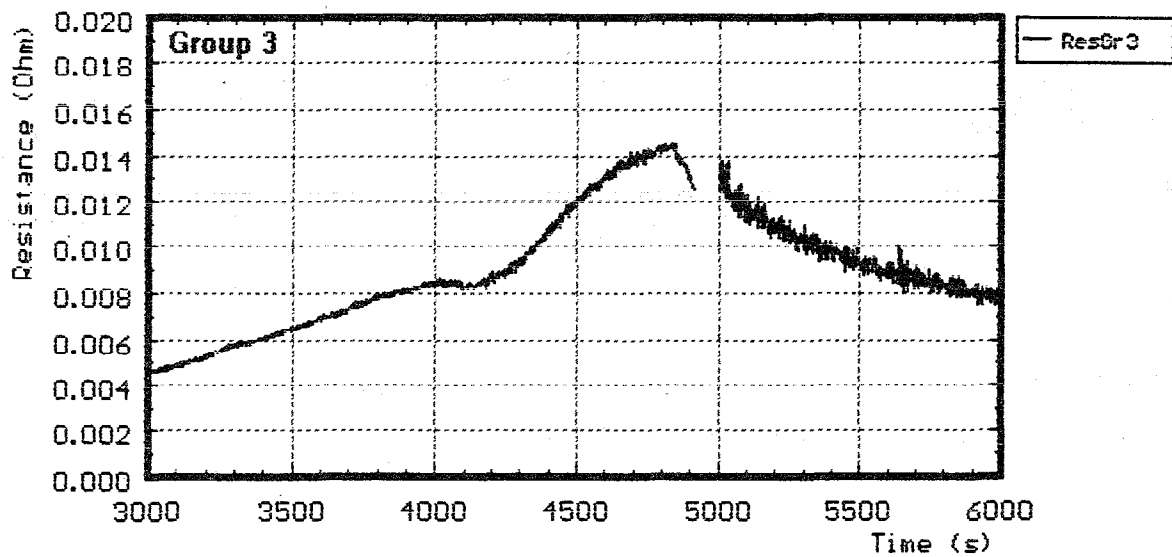
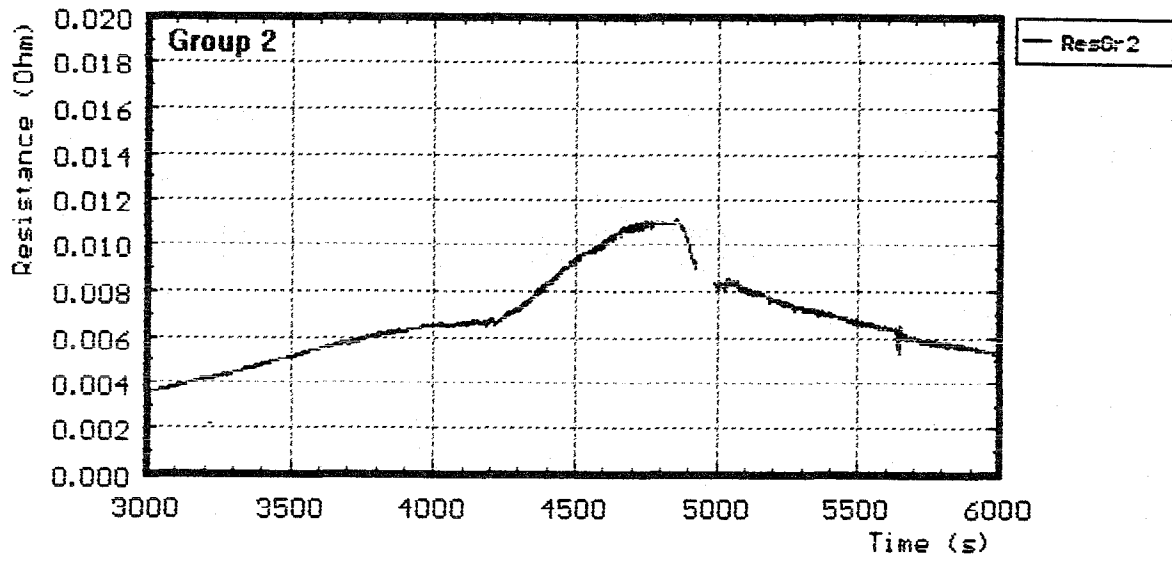
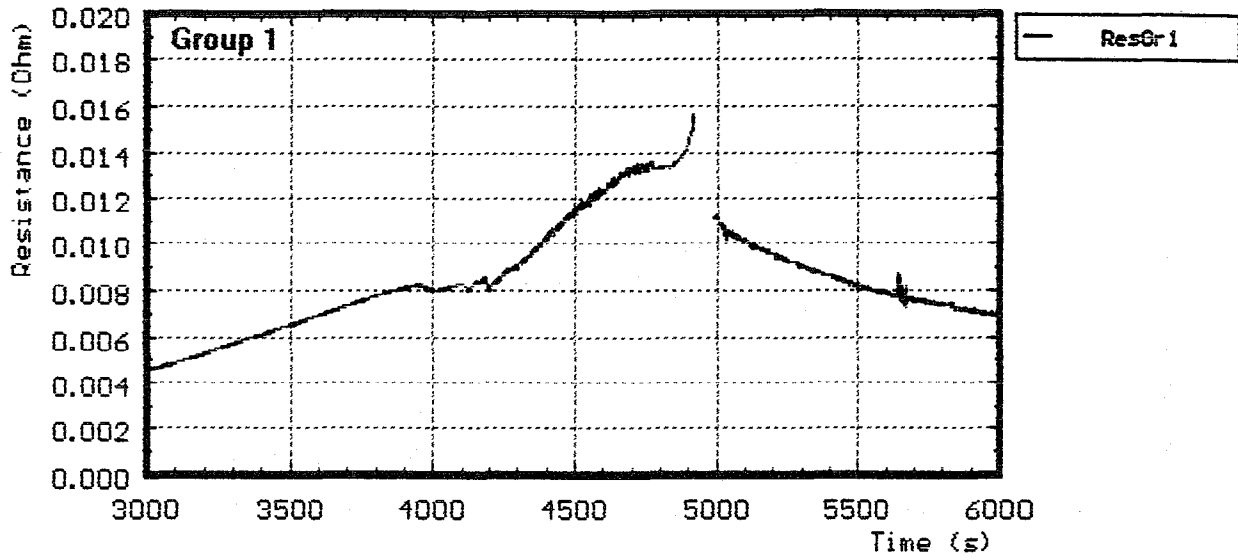


Fig. 19: CORA-W1; Resistance of the rod groups

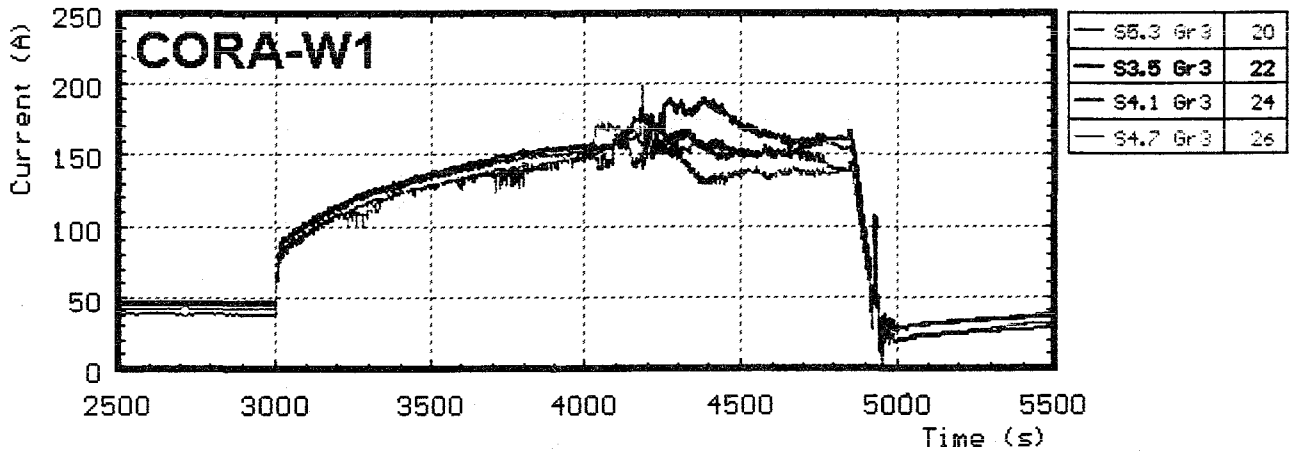
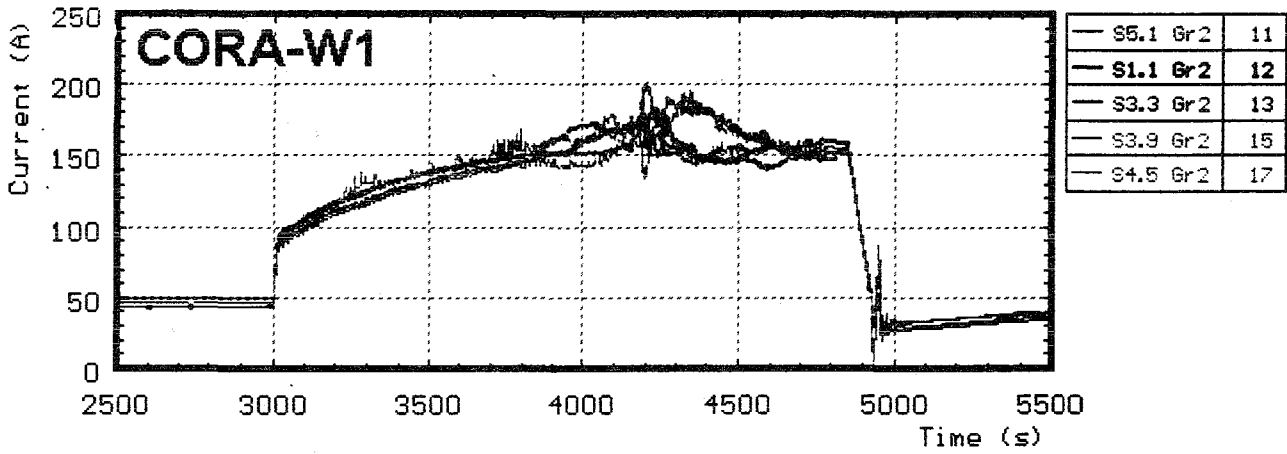
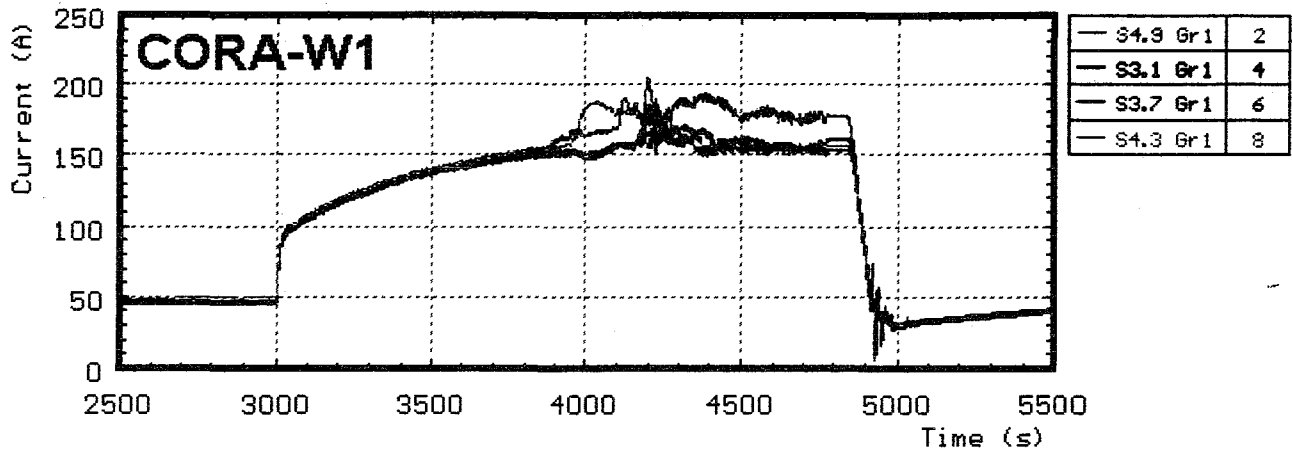


Fig. 18: CORA-W1; Variation of currents within the rod groups

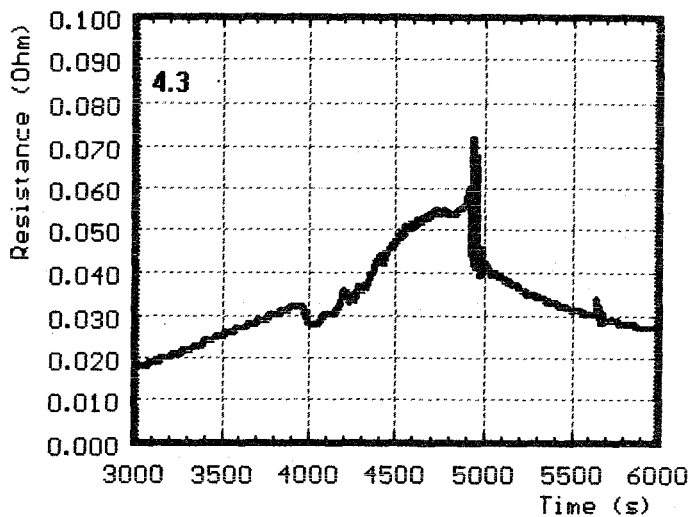
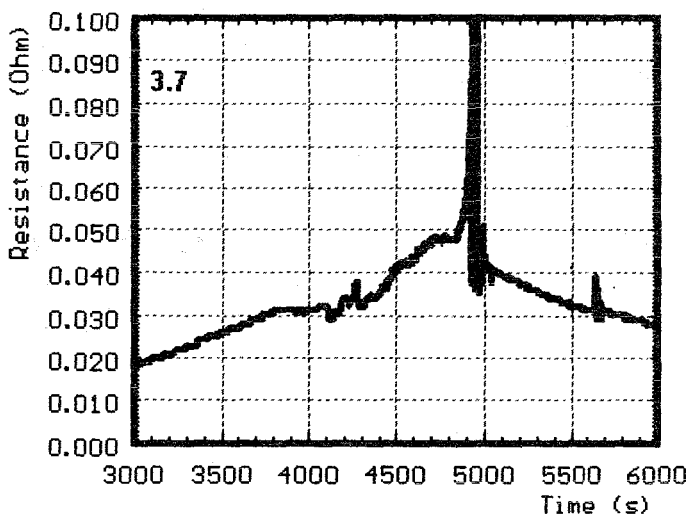
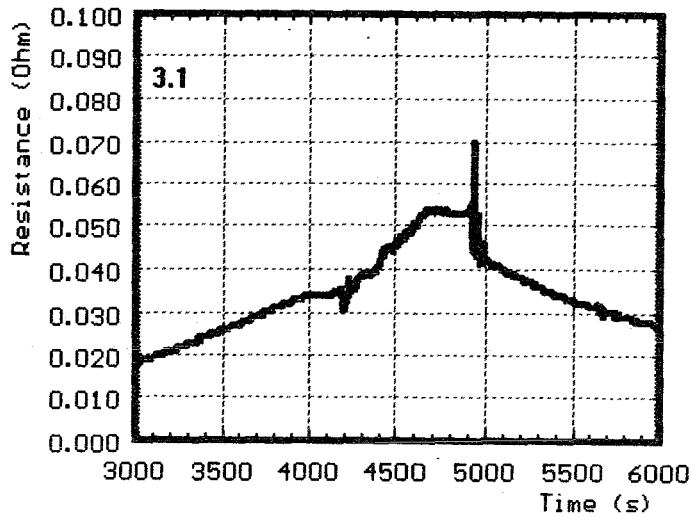
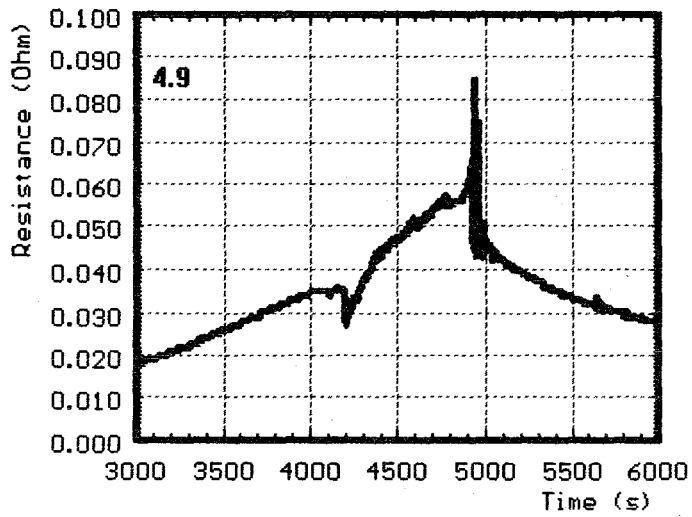


Fig. 20: CORA-W1; Resistance of rod group 1

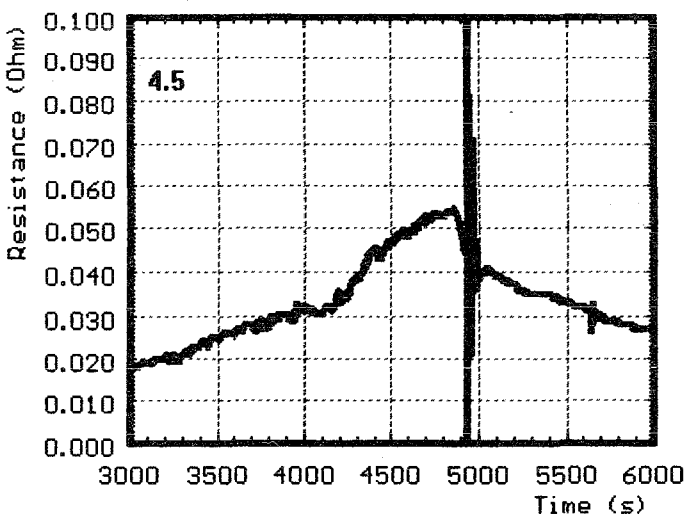
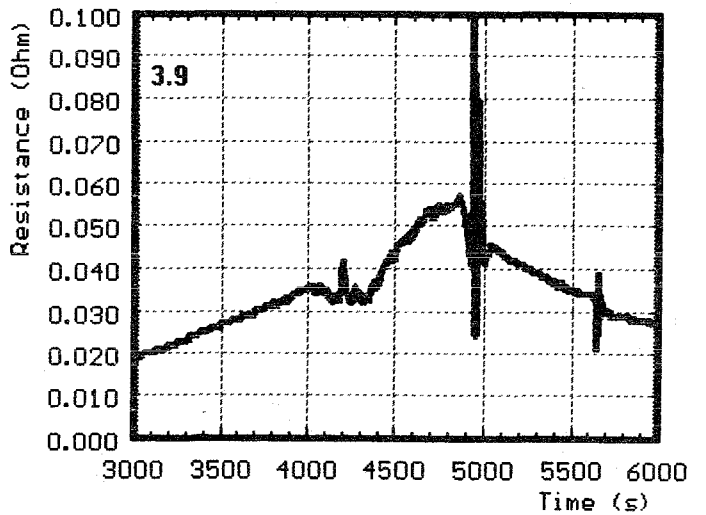
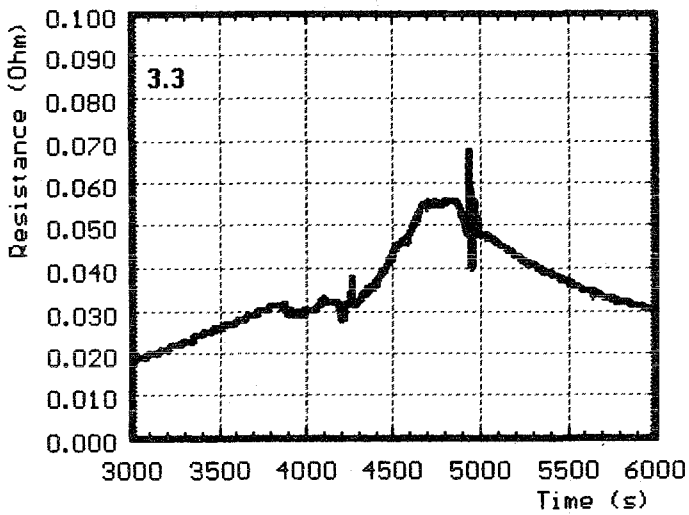
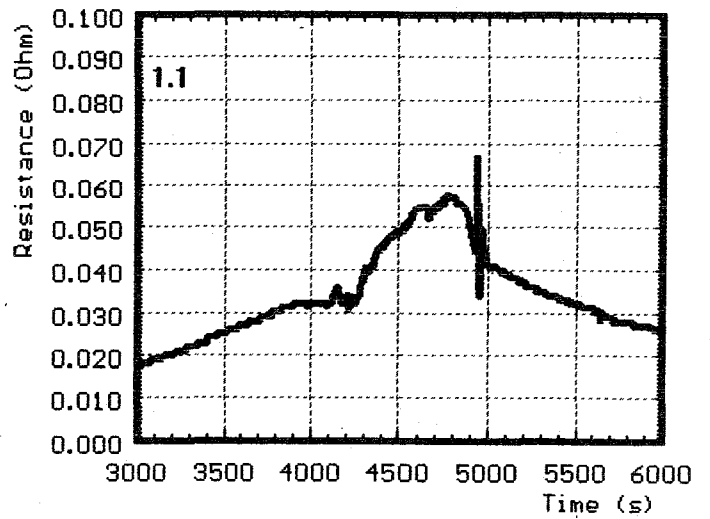
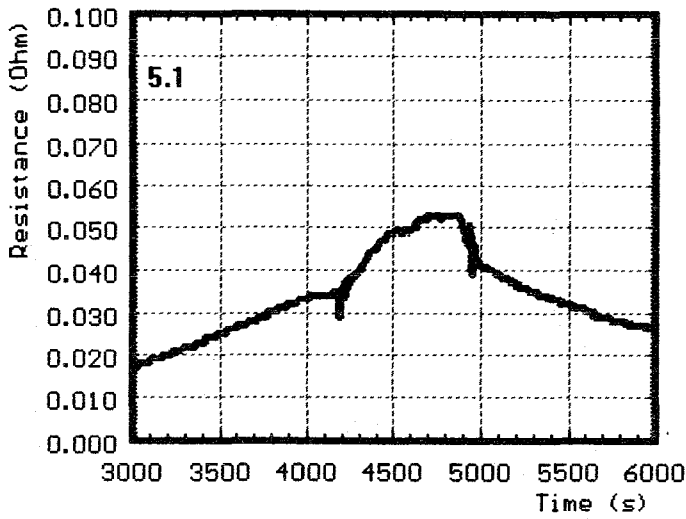


Fig. 21: CORA-W1;
Resistance of rod group 2

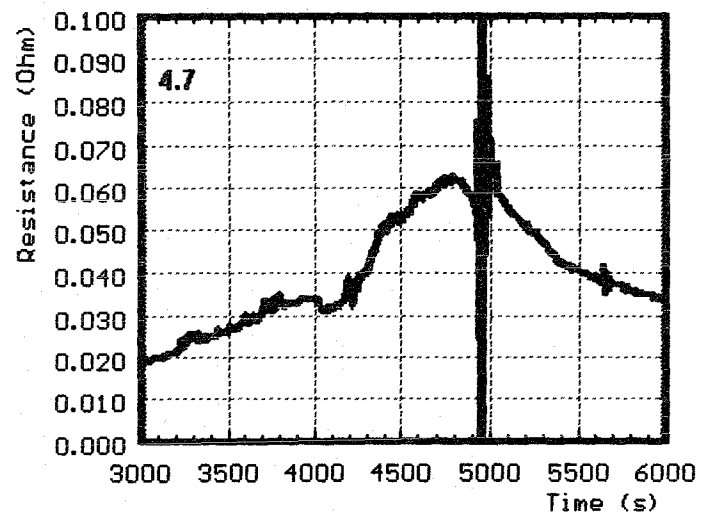
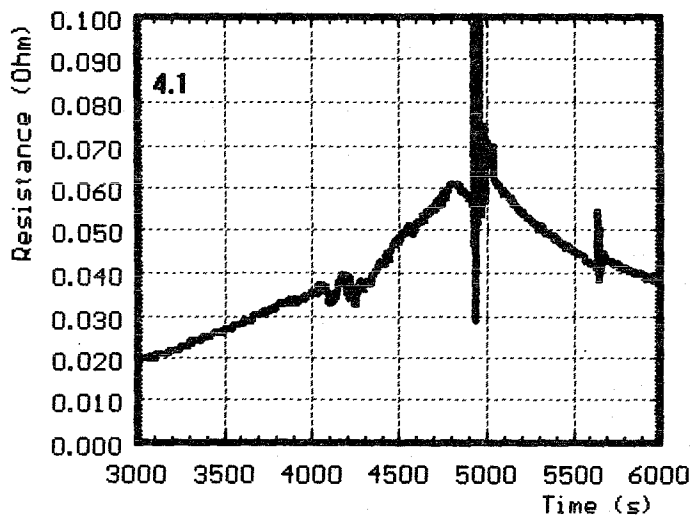
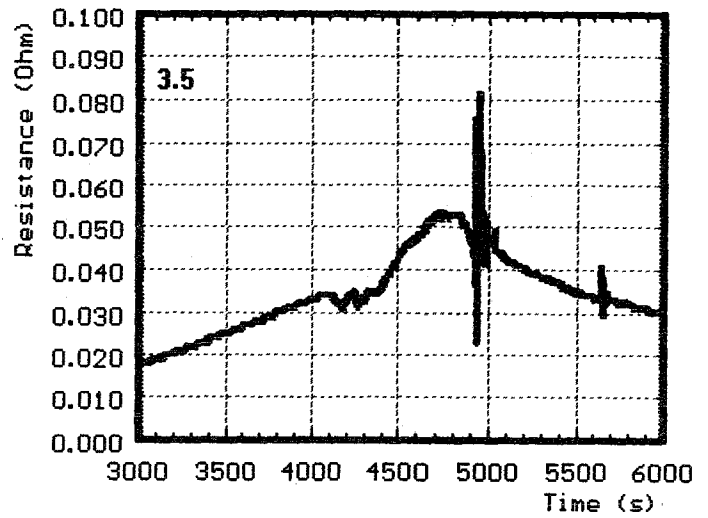
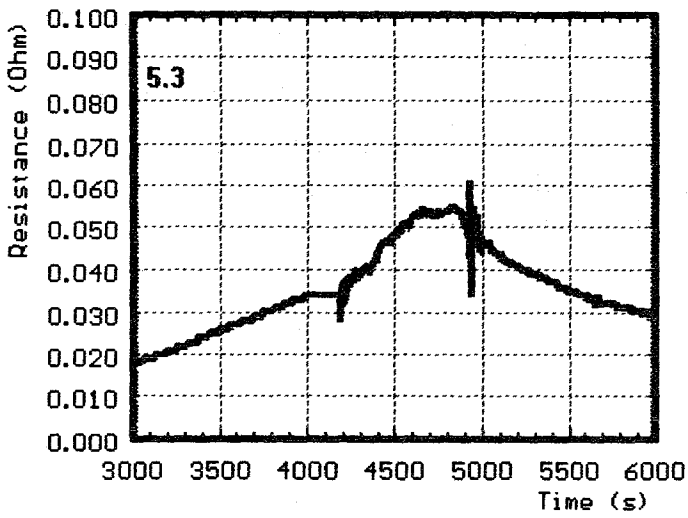


Fig. 22: CORA-W1; Resistance of rod group 3

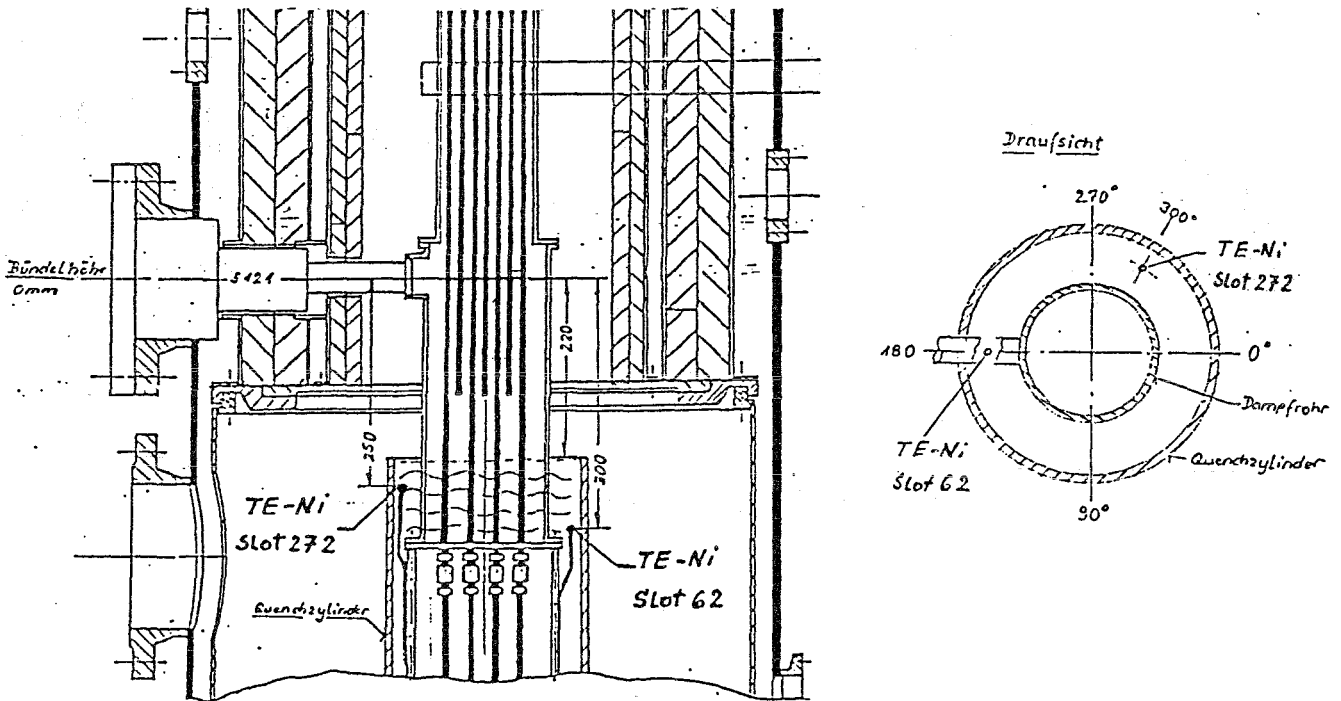
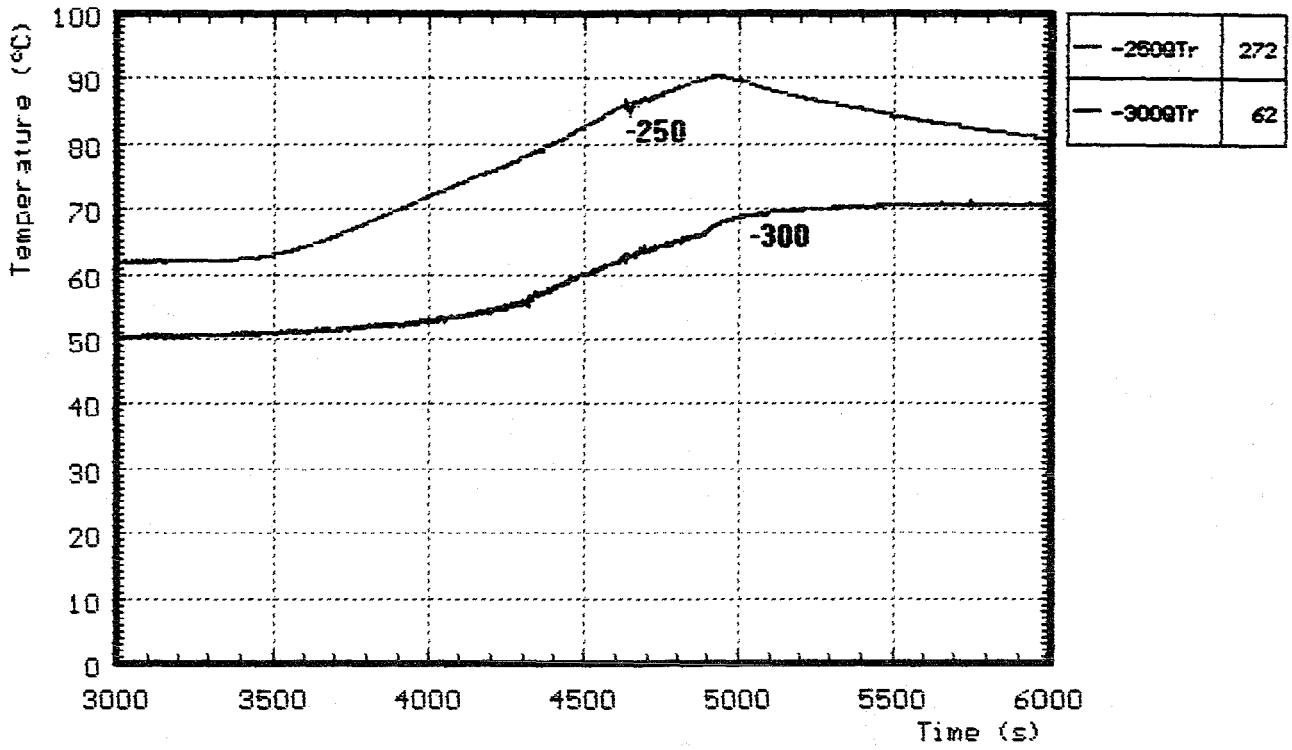


Fig. 23: CORA-W1; Water temperature in the quench cylinder

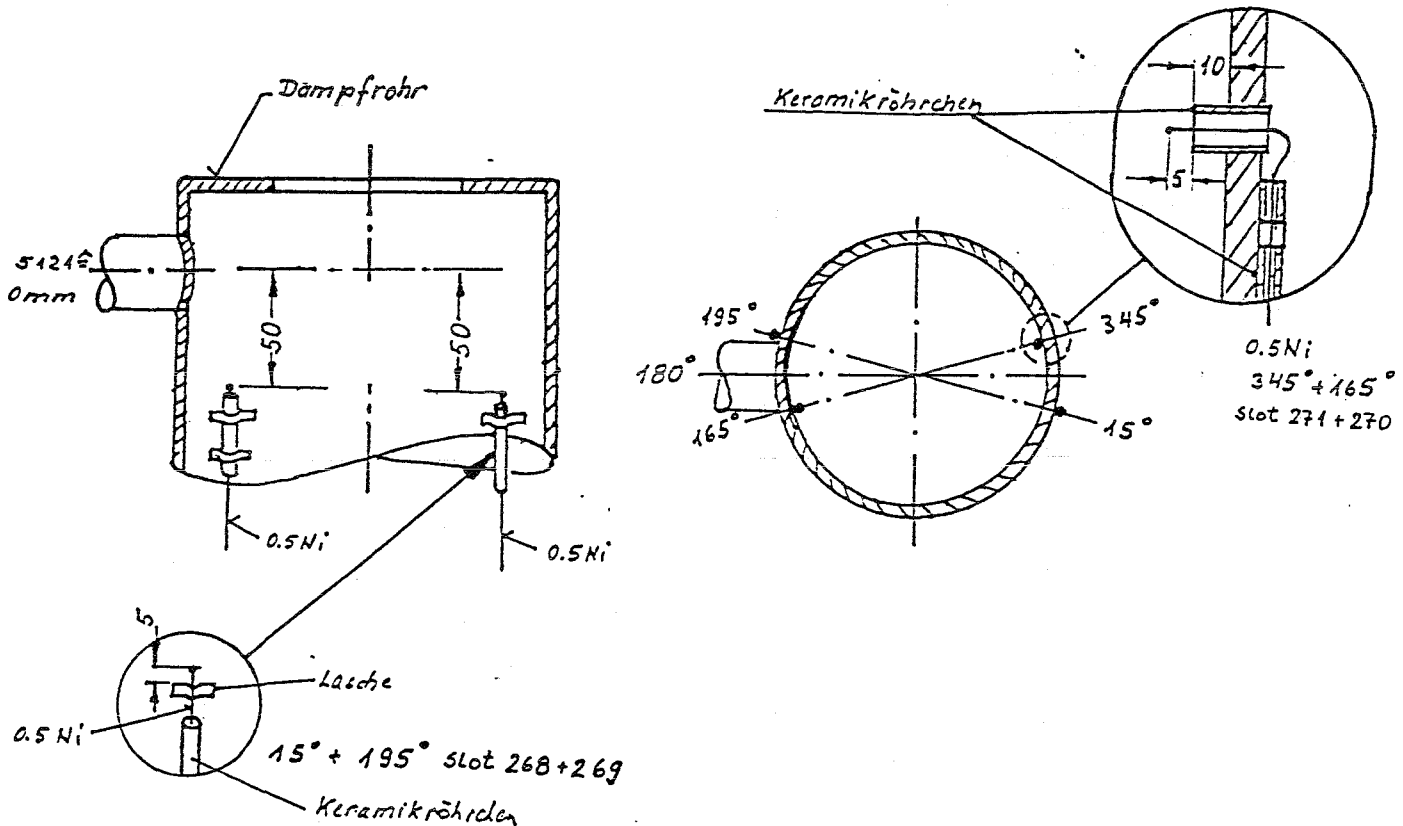
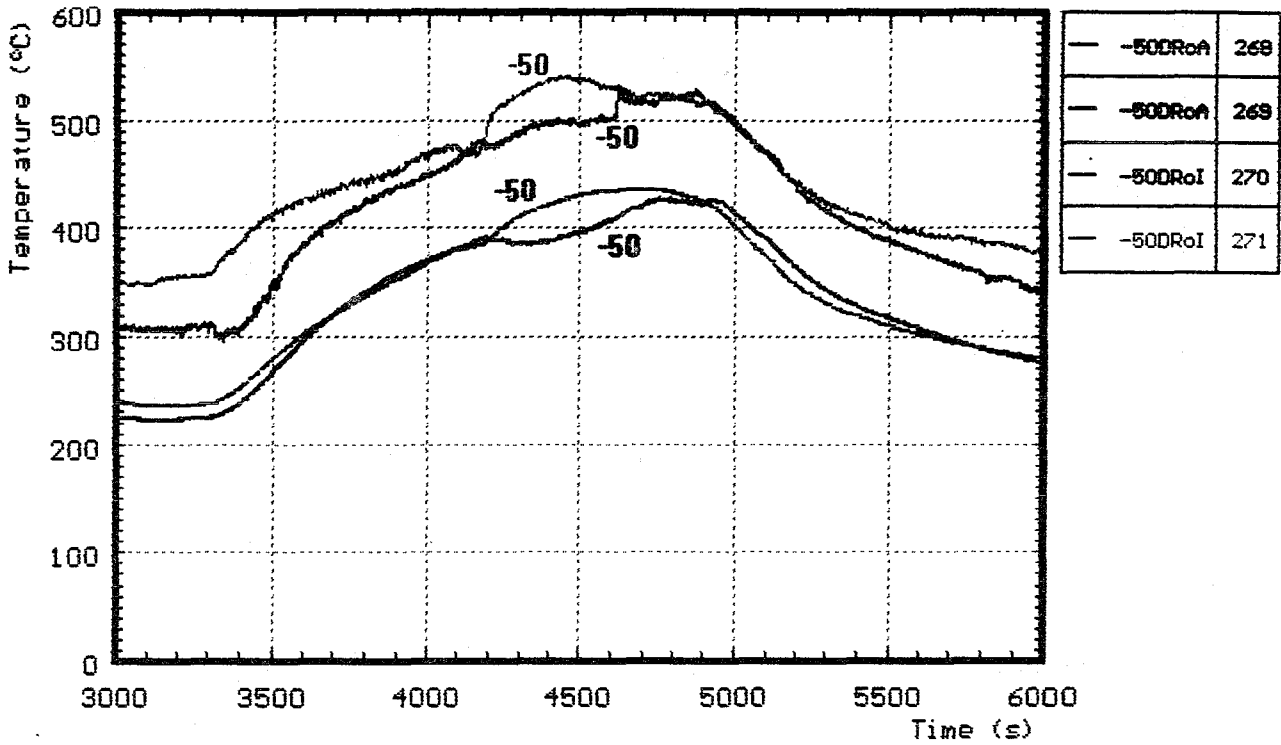


Fig. 24: CORA-W1; Temperature in and on steam tube at -50 mm elevation

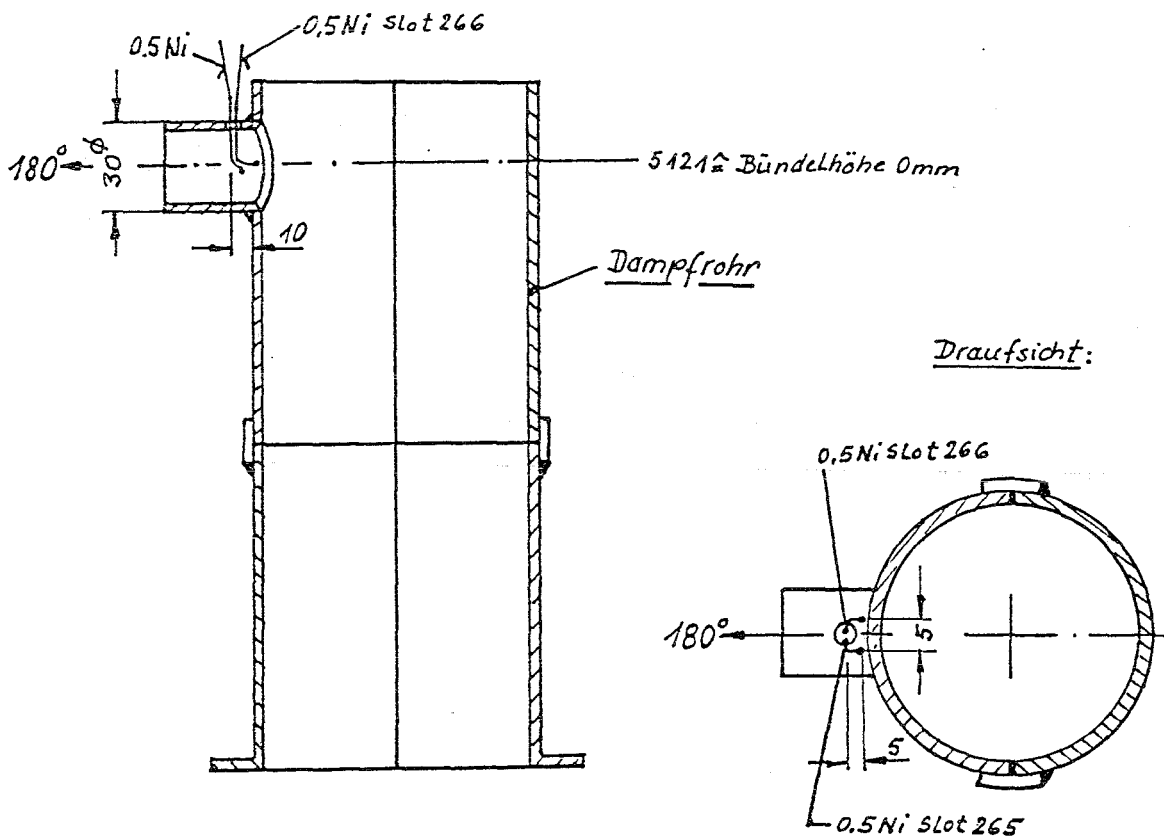
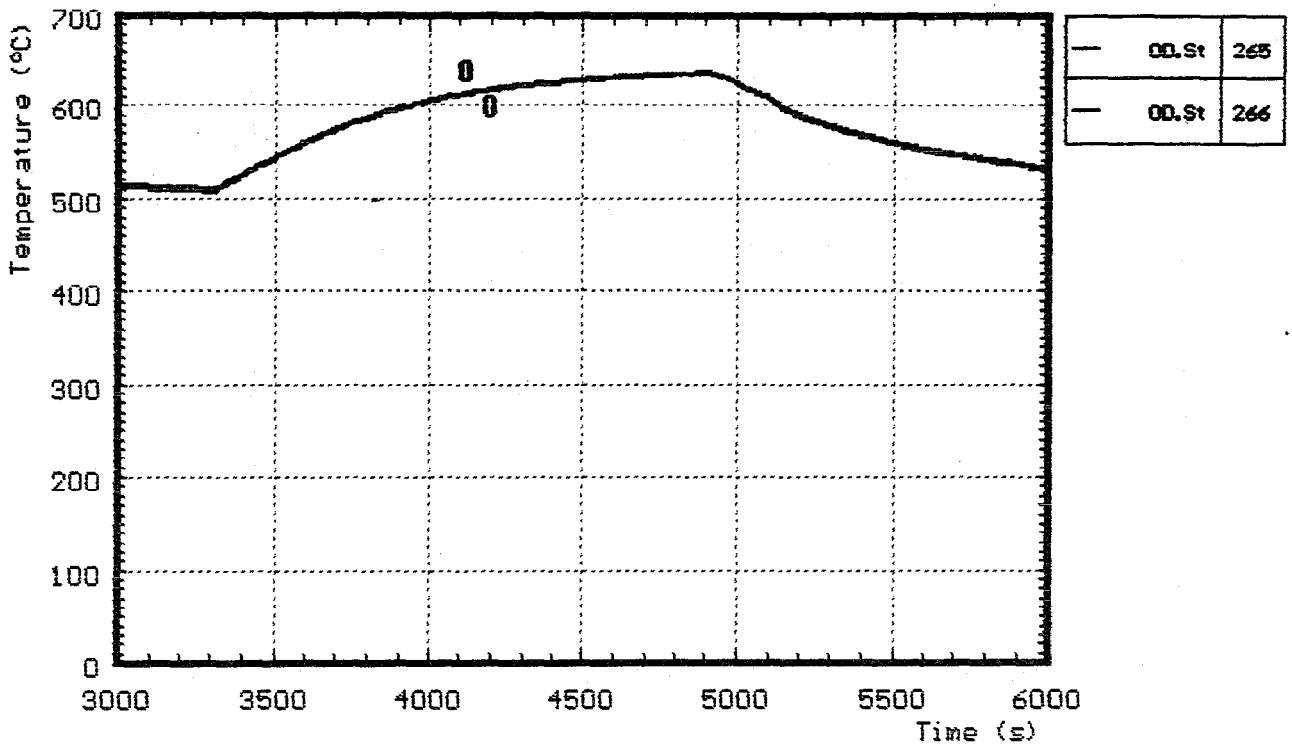


Fig. 25: CORA-W1; Temperatures at steam inlet

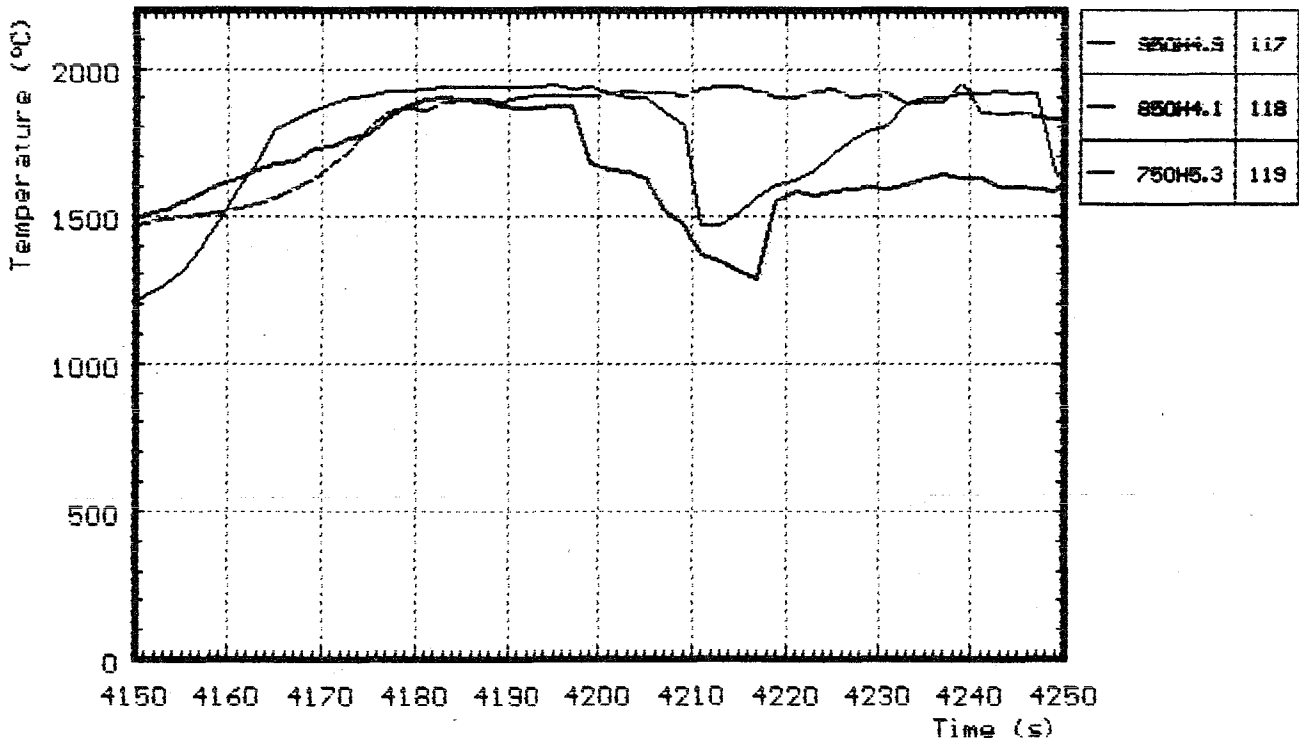
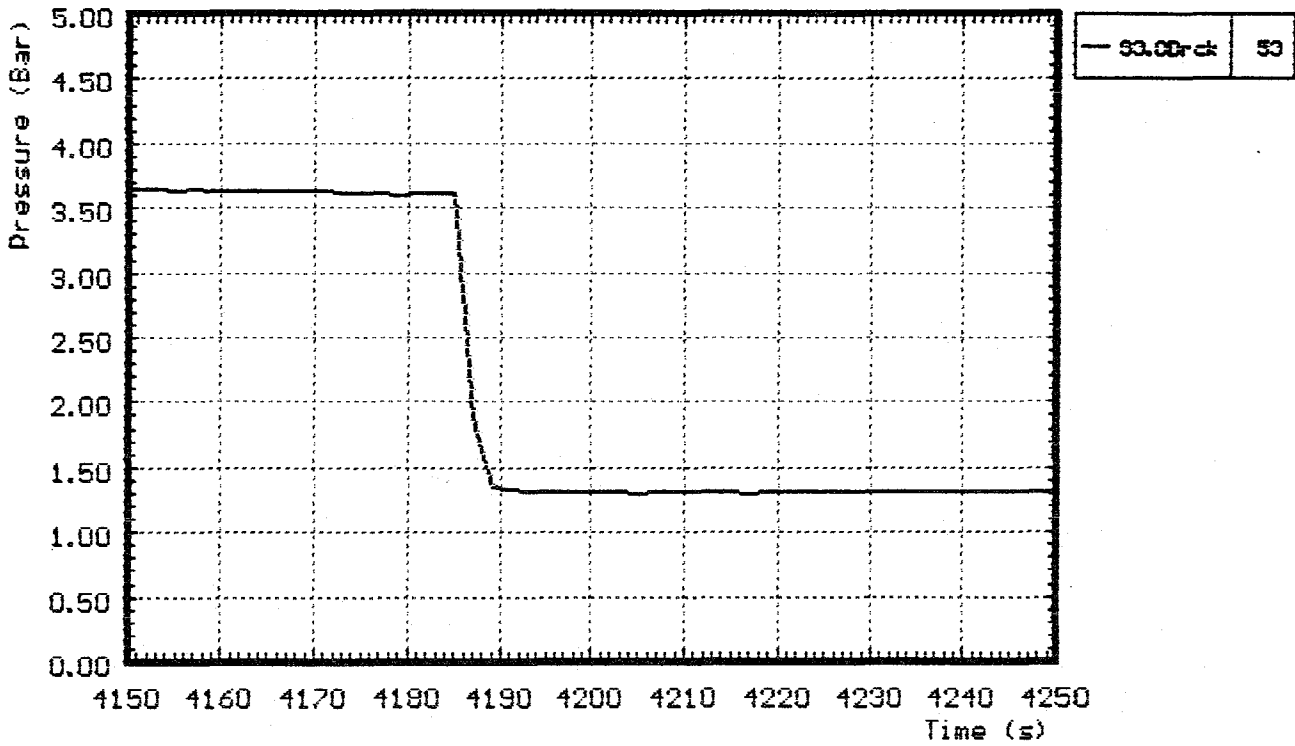


Fig. 25a: Comparison of internal rod pressure with temperatures of heated rods (750, 850 and 950 mm)

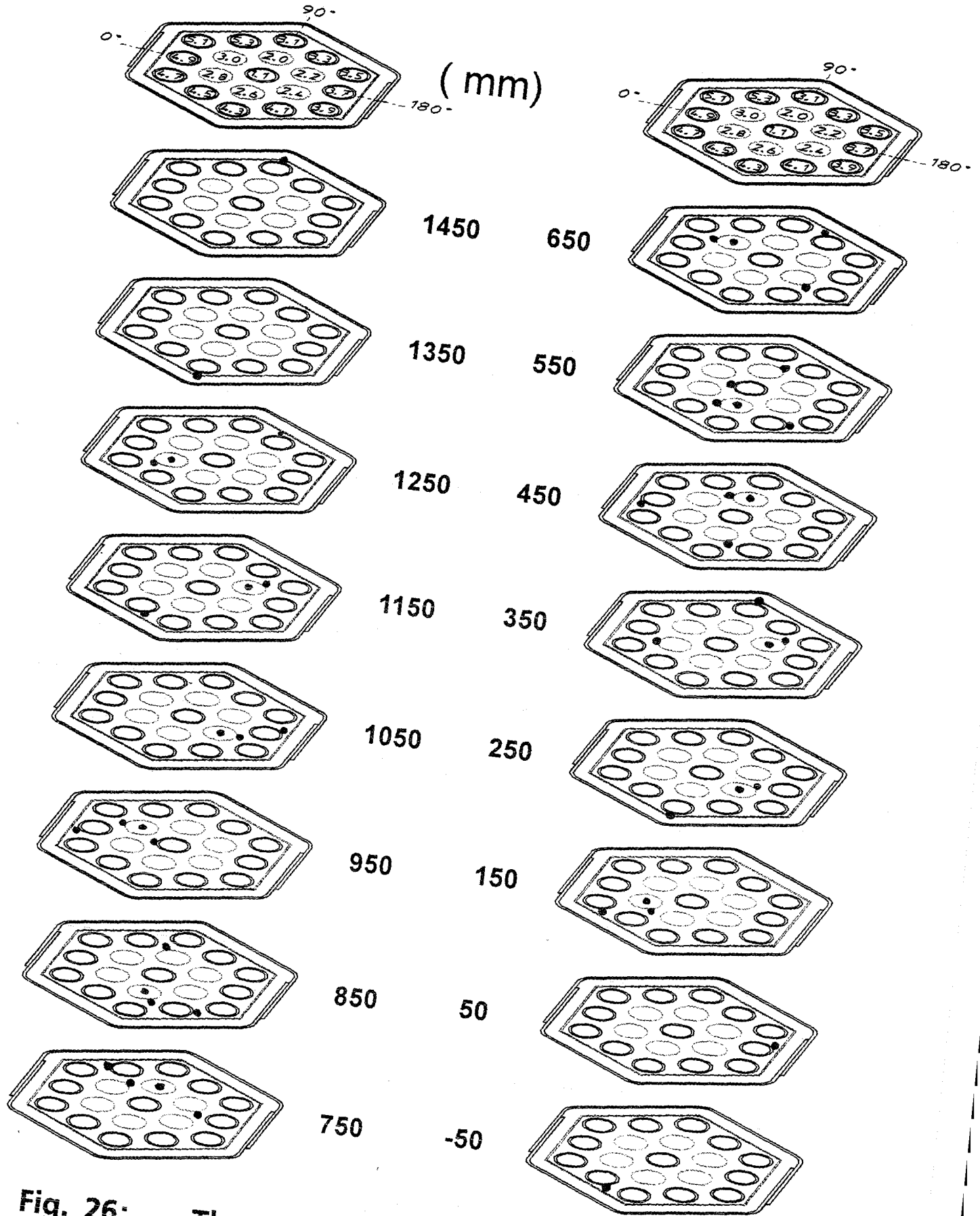


Fig. 26: Thermocouple locations within the bundle (CORA-W1)

CORA-W1: Temperatures on heated rods

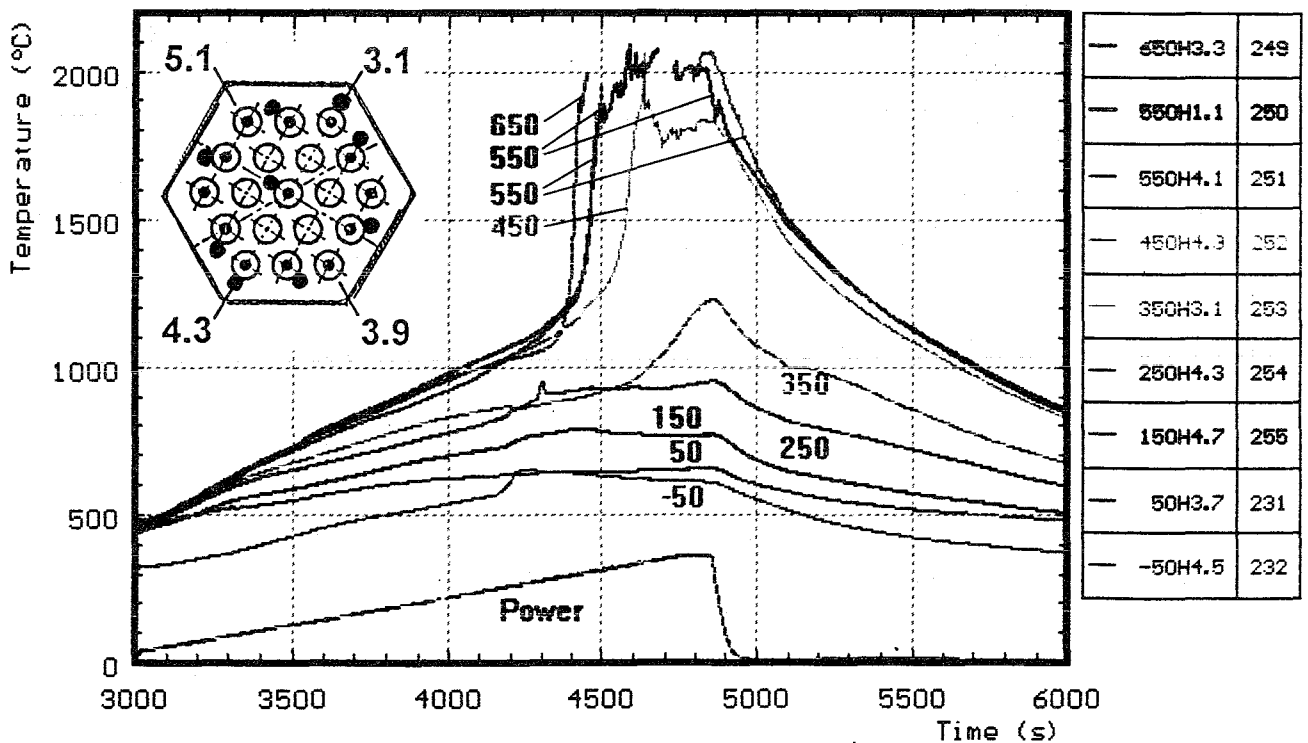
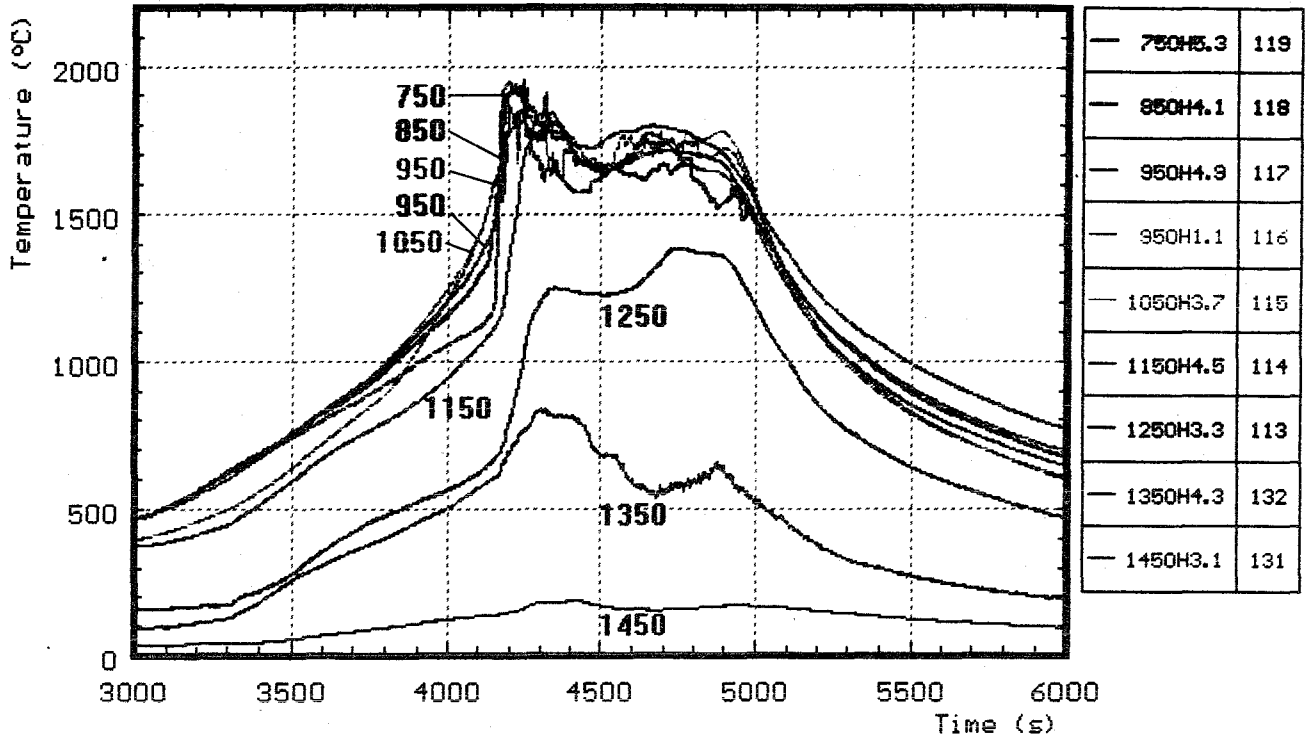


Fig. 27:

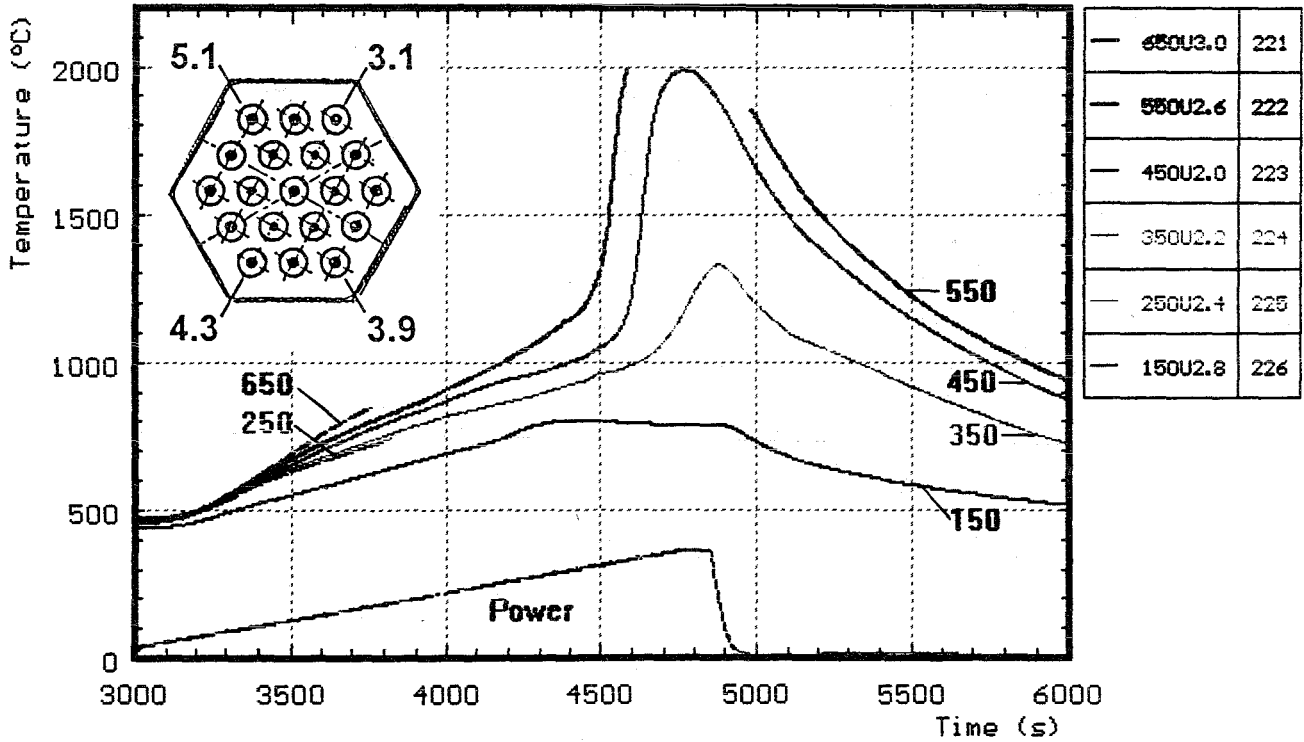
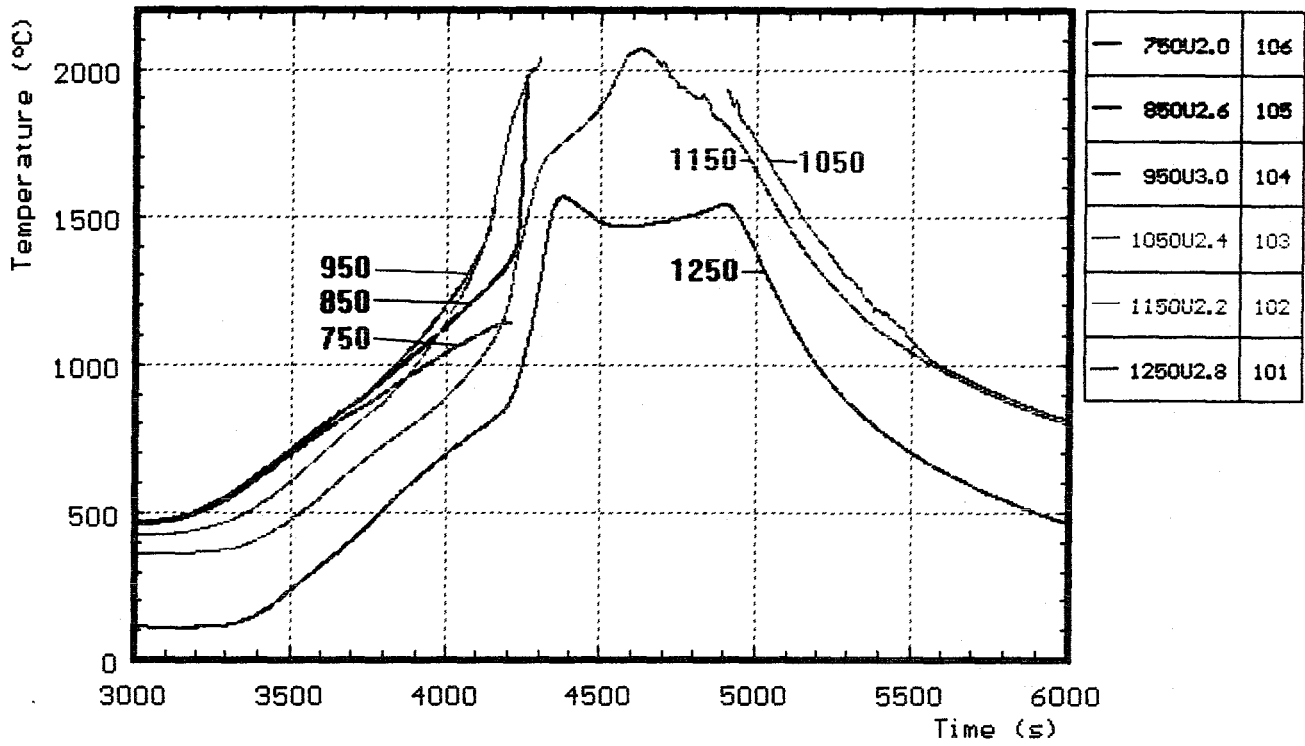


Fig. 28: CORA-W1; Temperatures of unheated rods (TCs in central position)

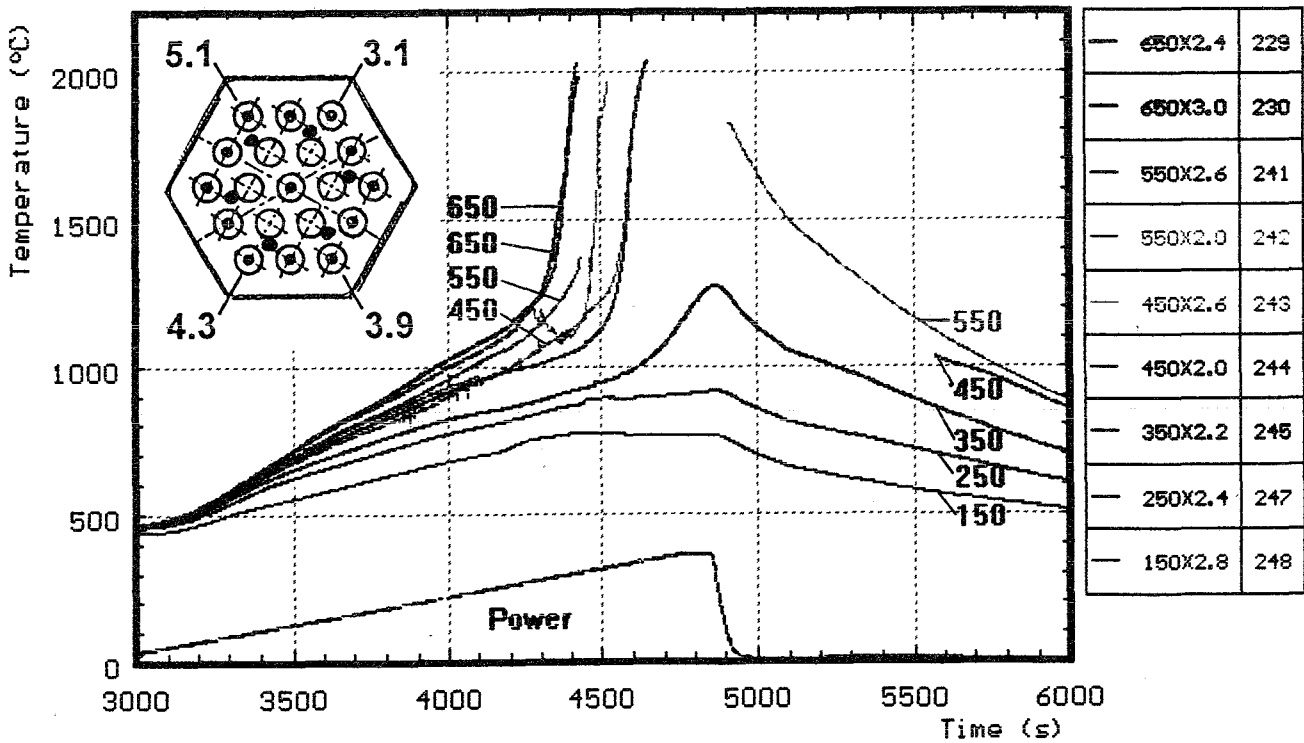
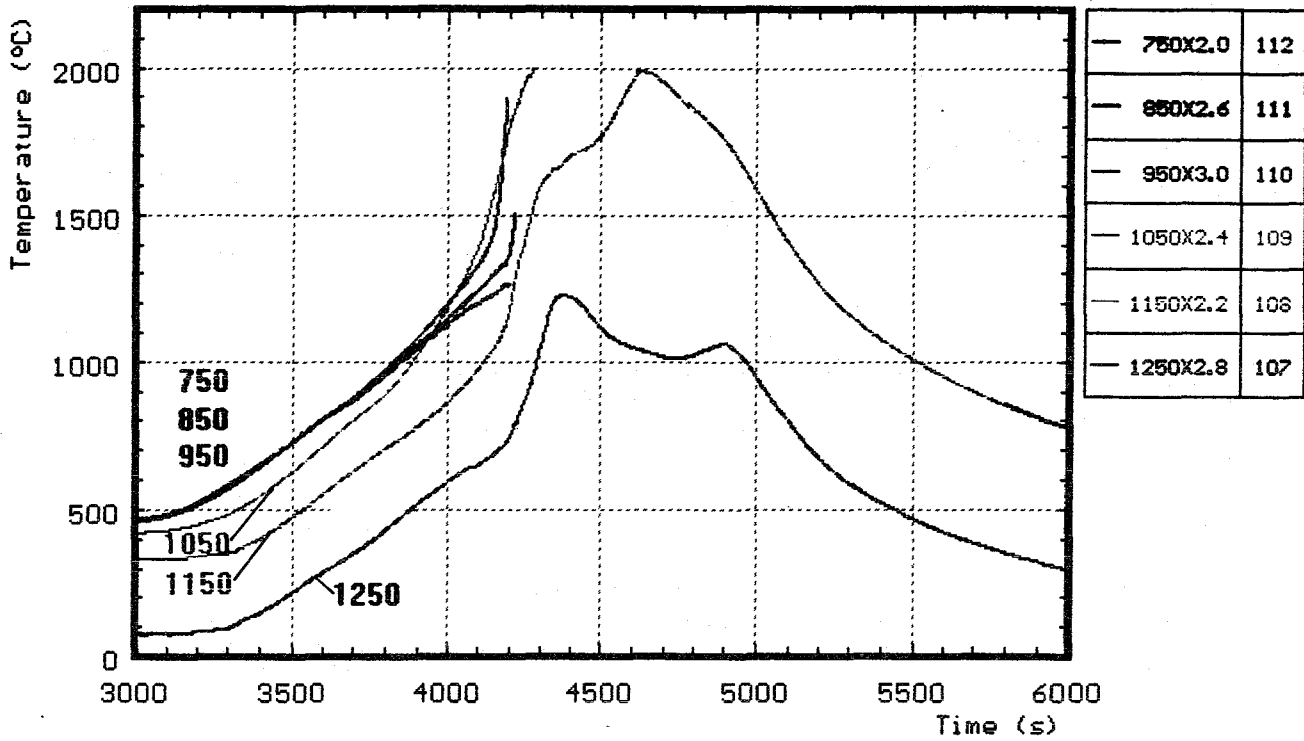


Fig. 29: CORA-W1; Temperatures of unheated rods (TCs on outer surface)

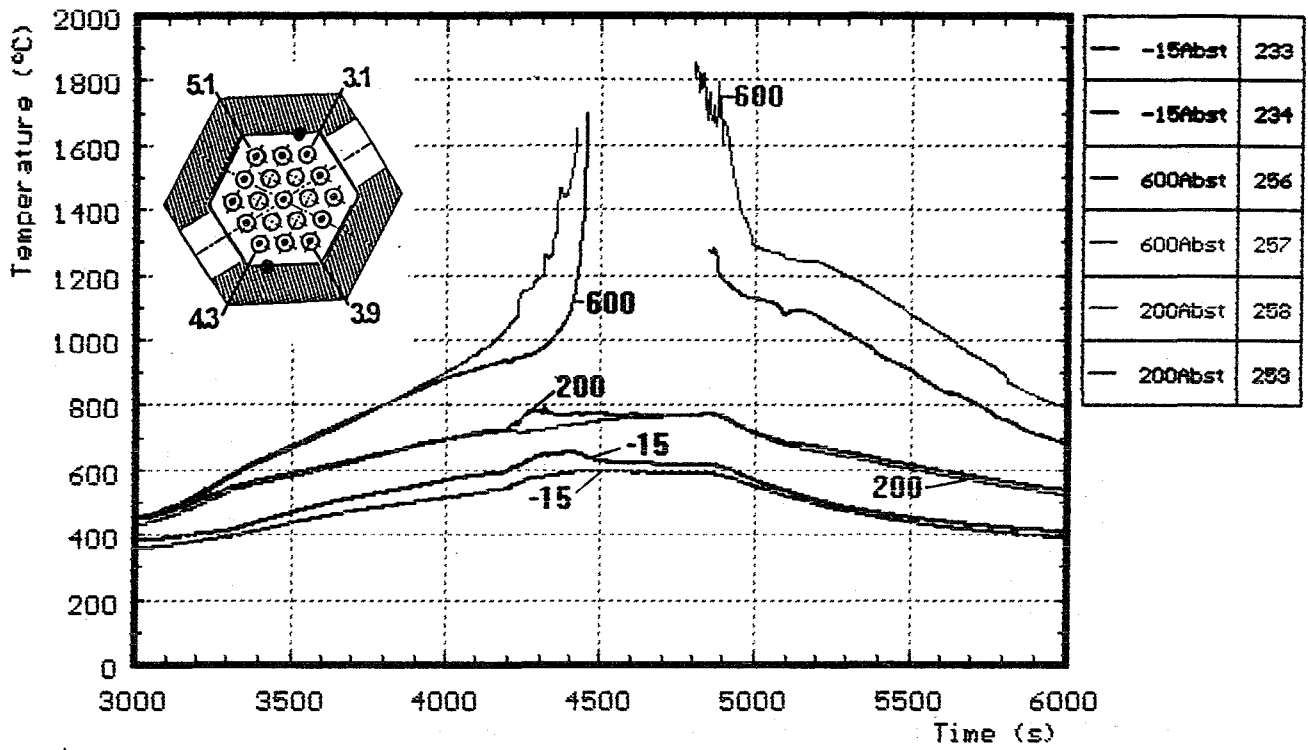


Fig. 30: Temperatures of the three spacers used in test CORA-W1

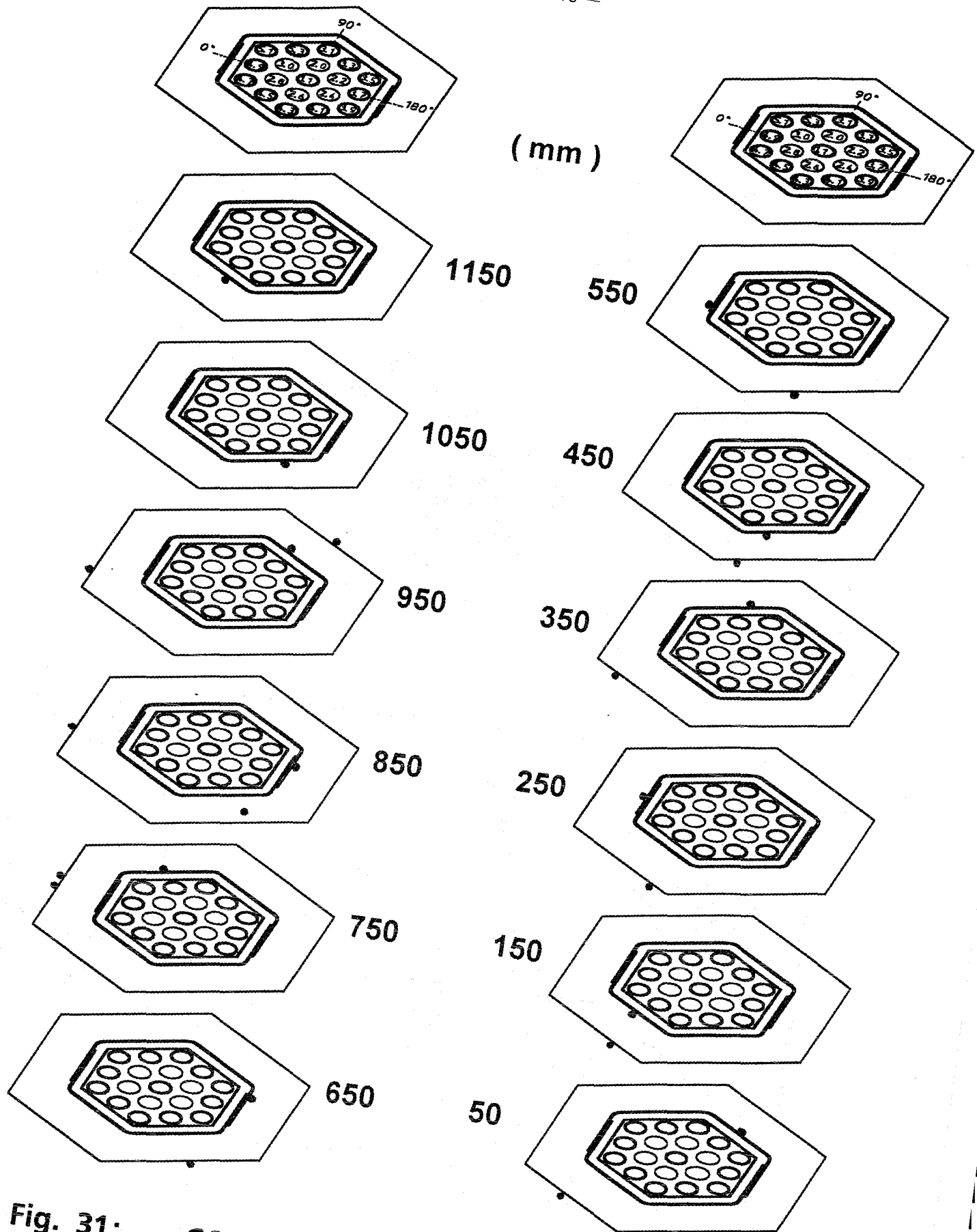


Fig. 31: CORA-W1; Location of the thermocouples at shroud and shroud insulation

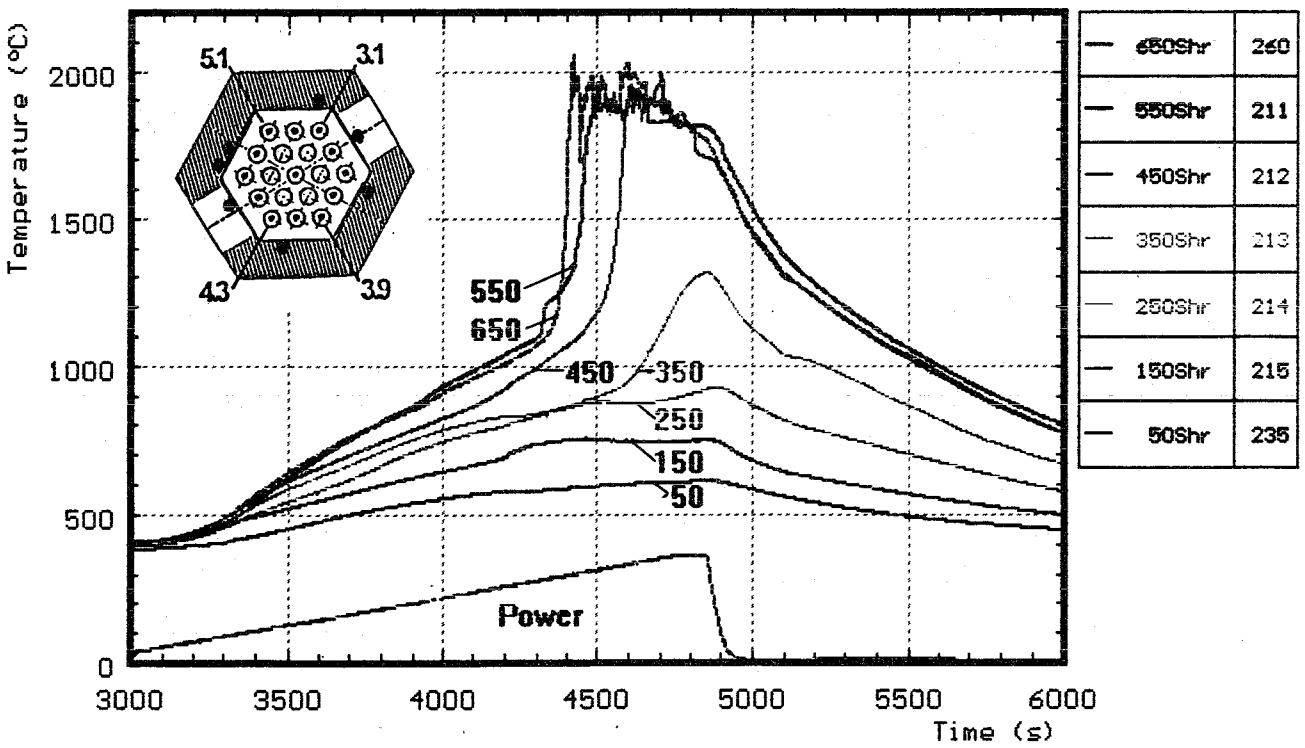
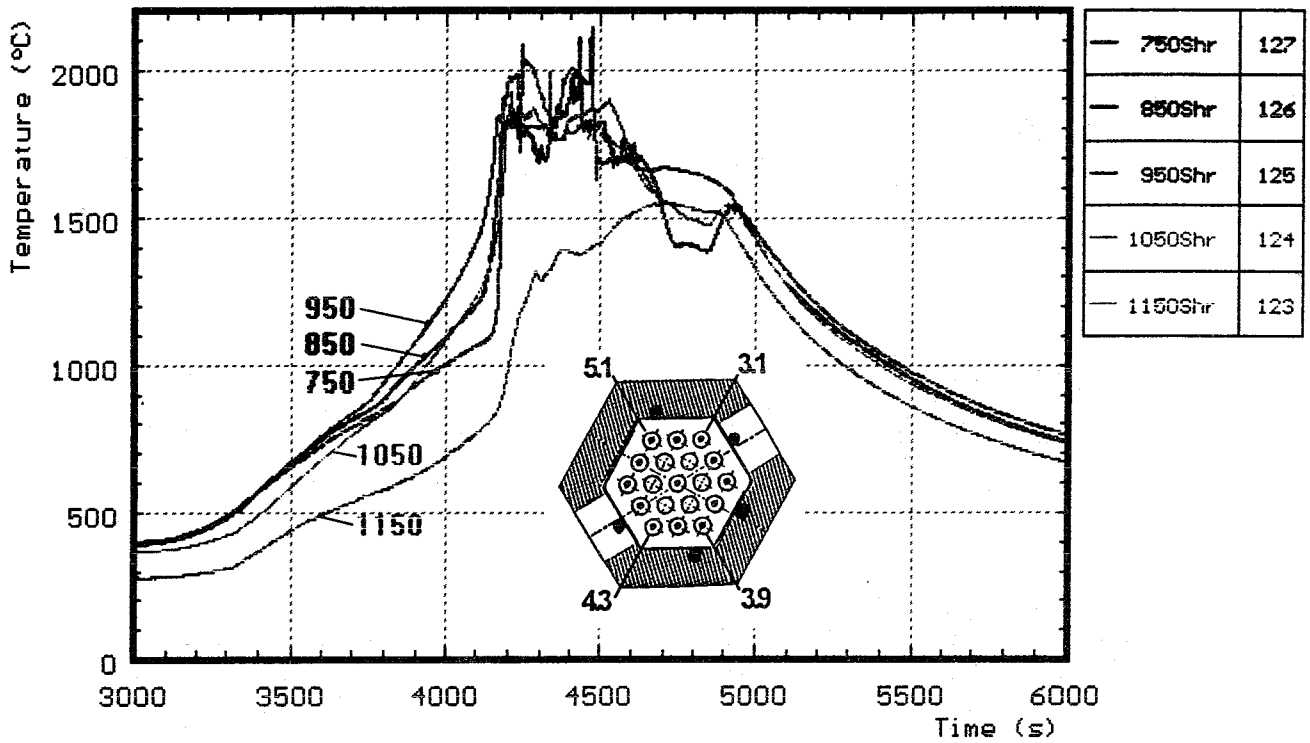


Fig. 32: CORA-W1; Temperatures of the outer side of the shroud

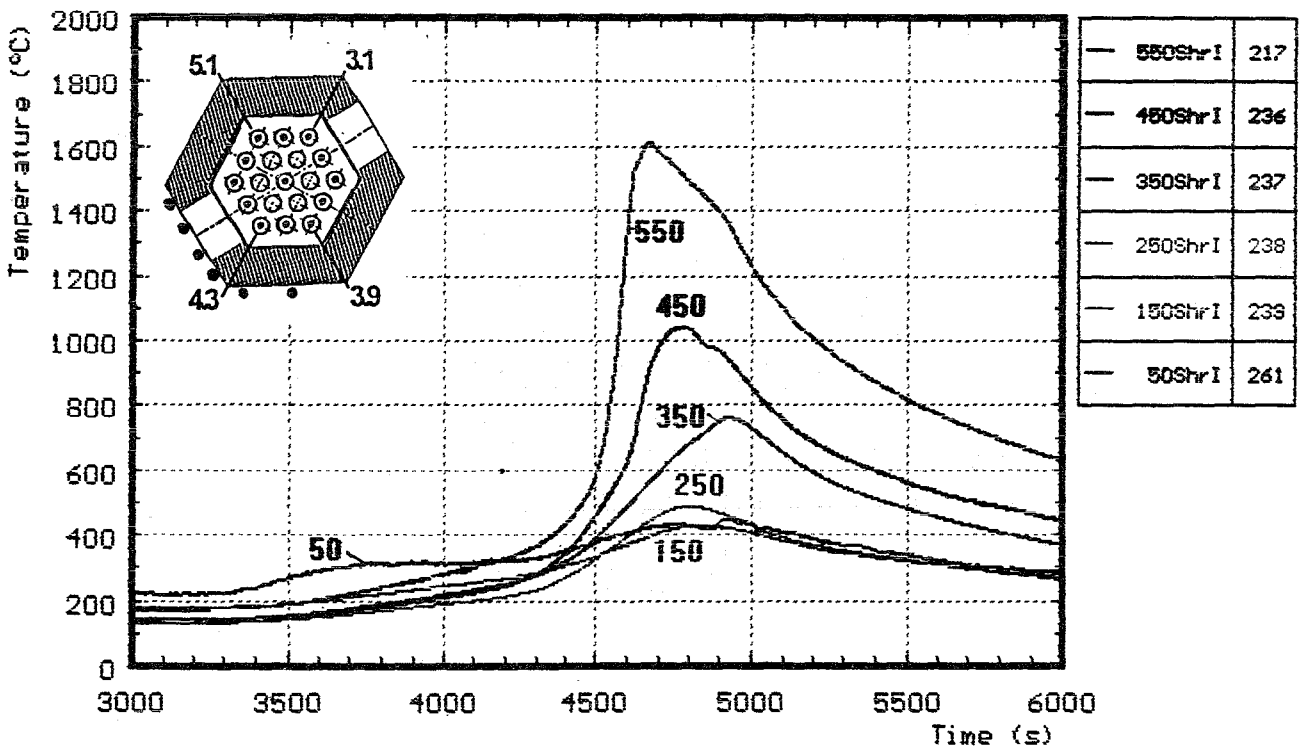
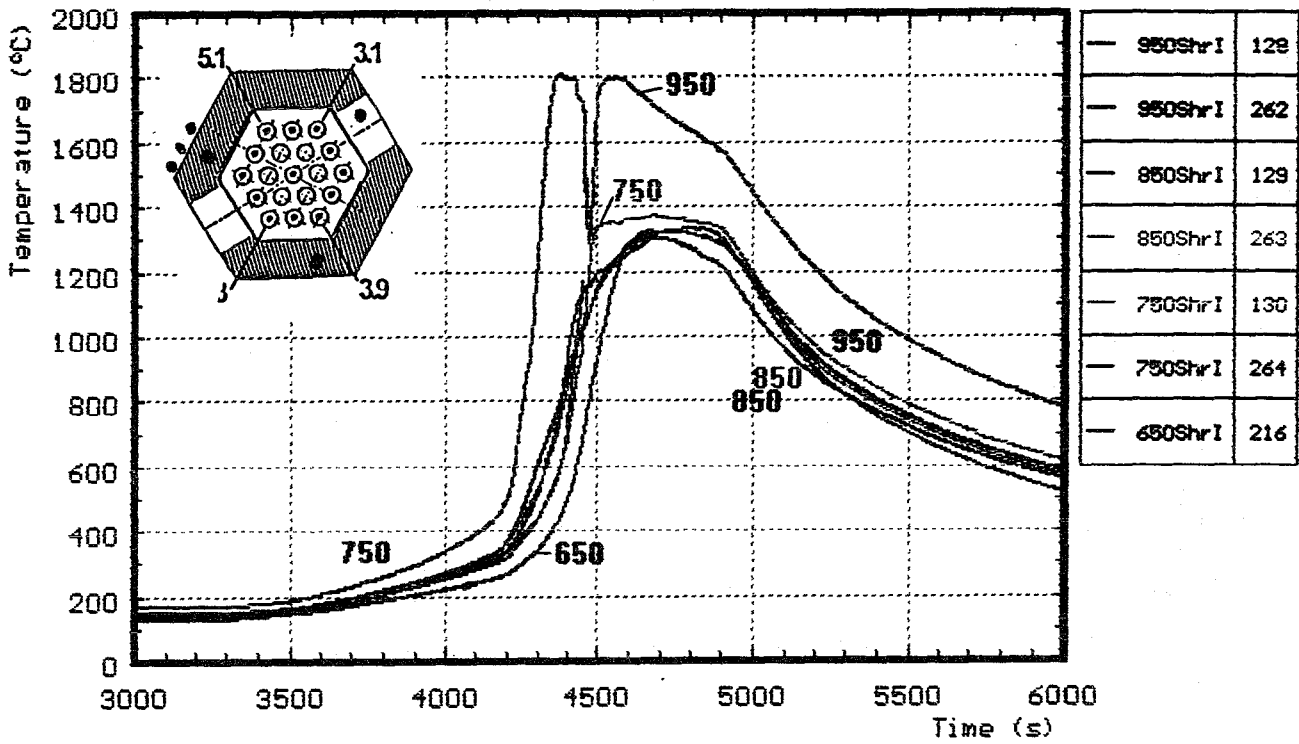


Fig. 33: CORA-W1; Temperatures of the shroud insulation

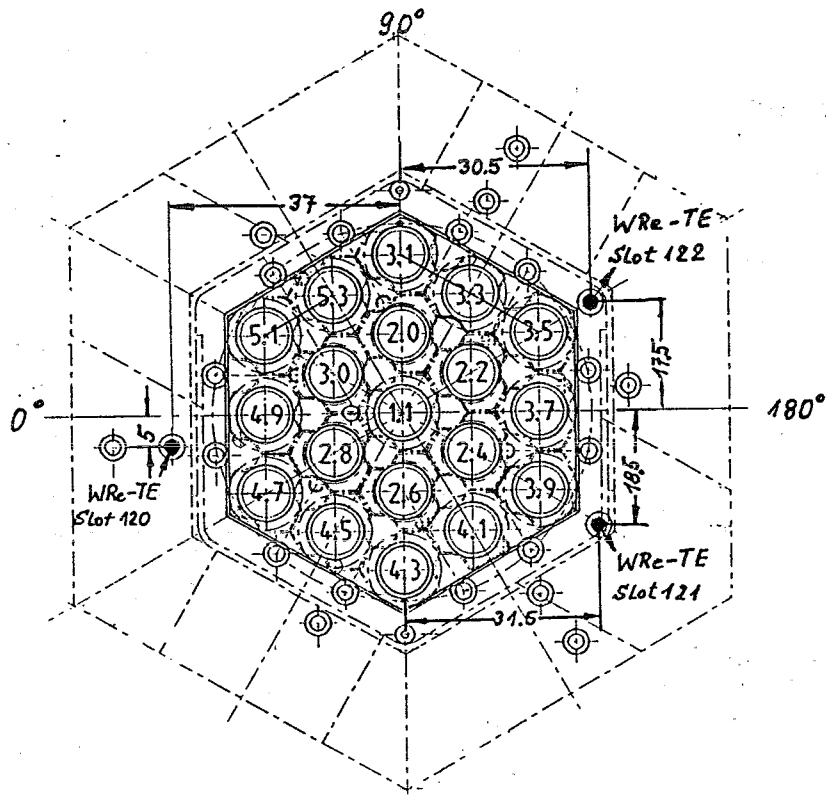
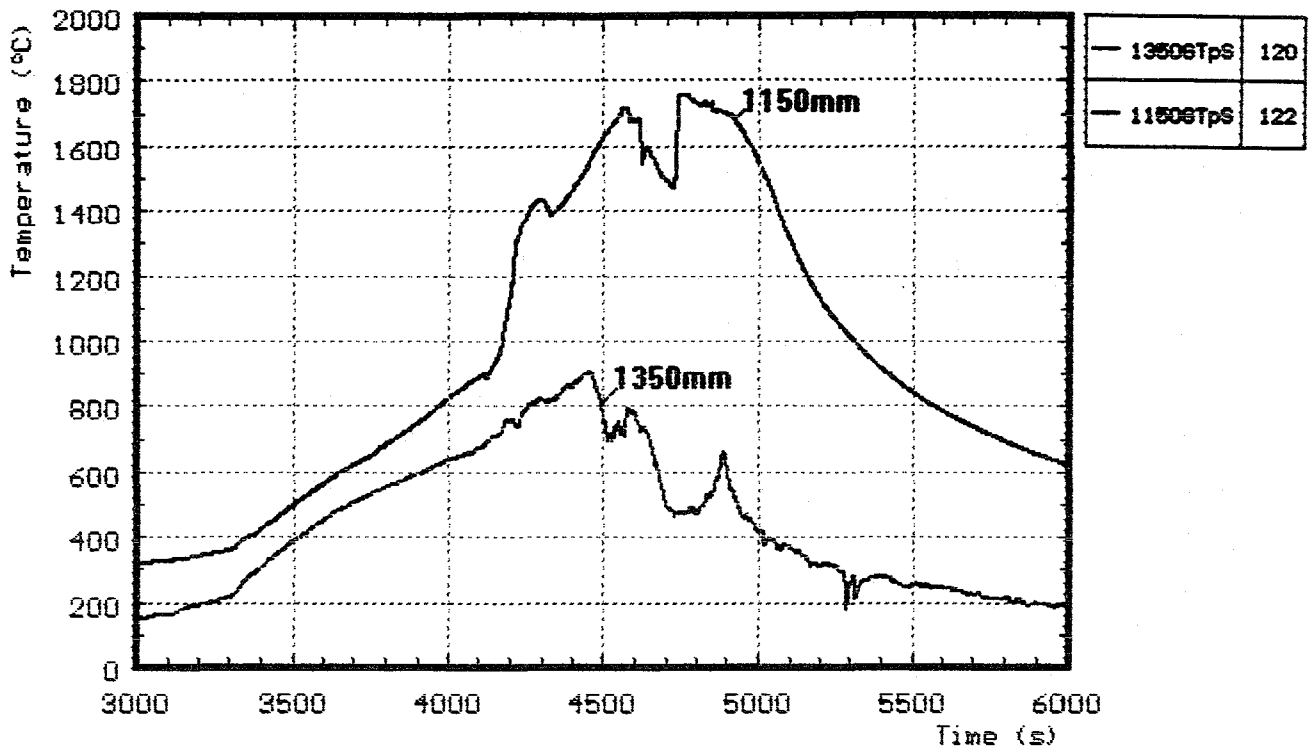


Fig. 34: CORA-W1; Gas temperatures above the heated zone (1150, 1250, 1350 mm)

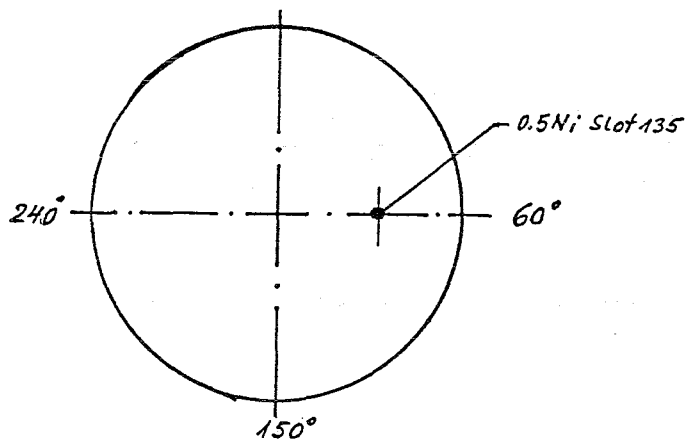
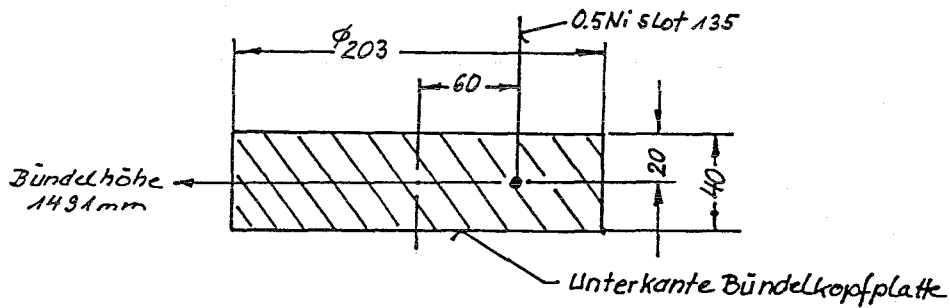
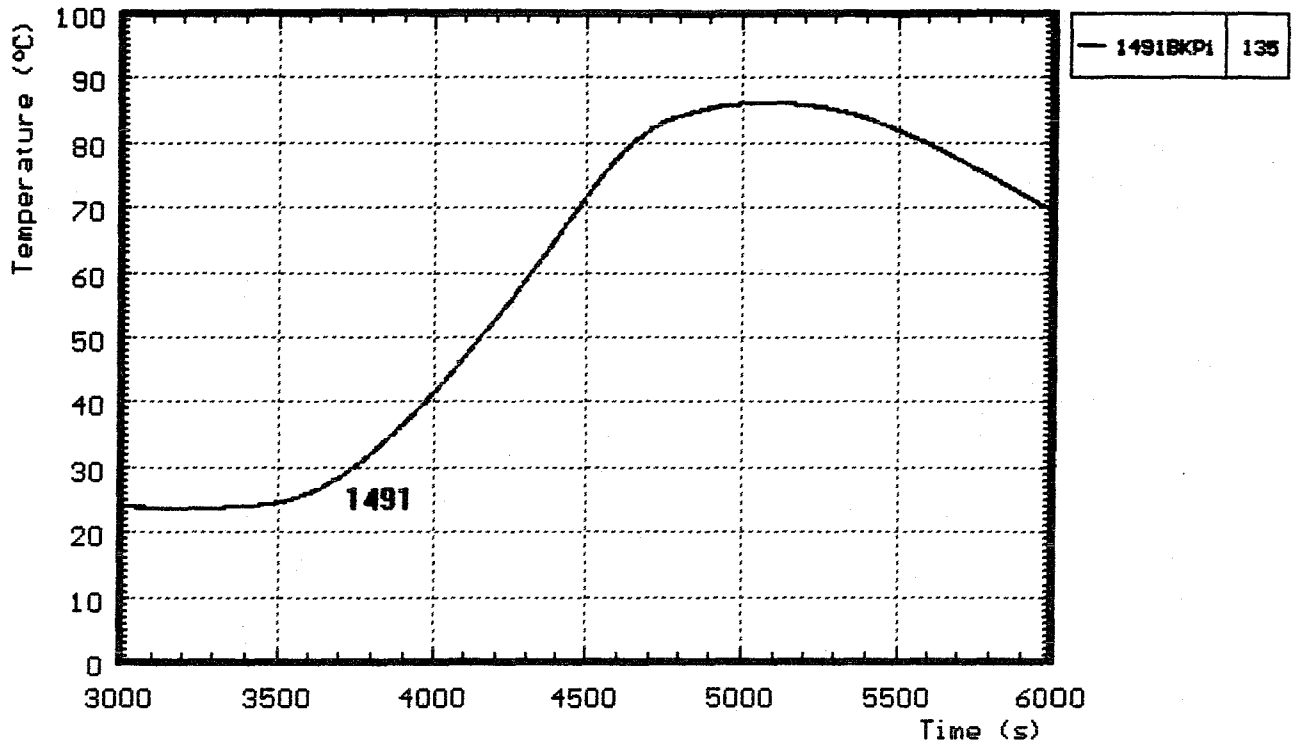
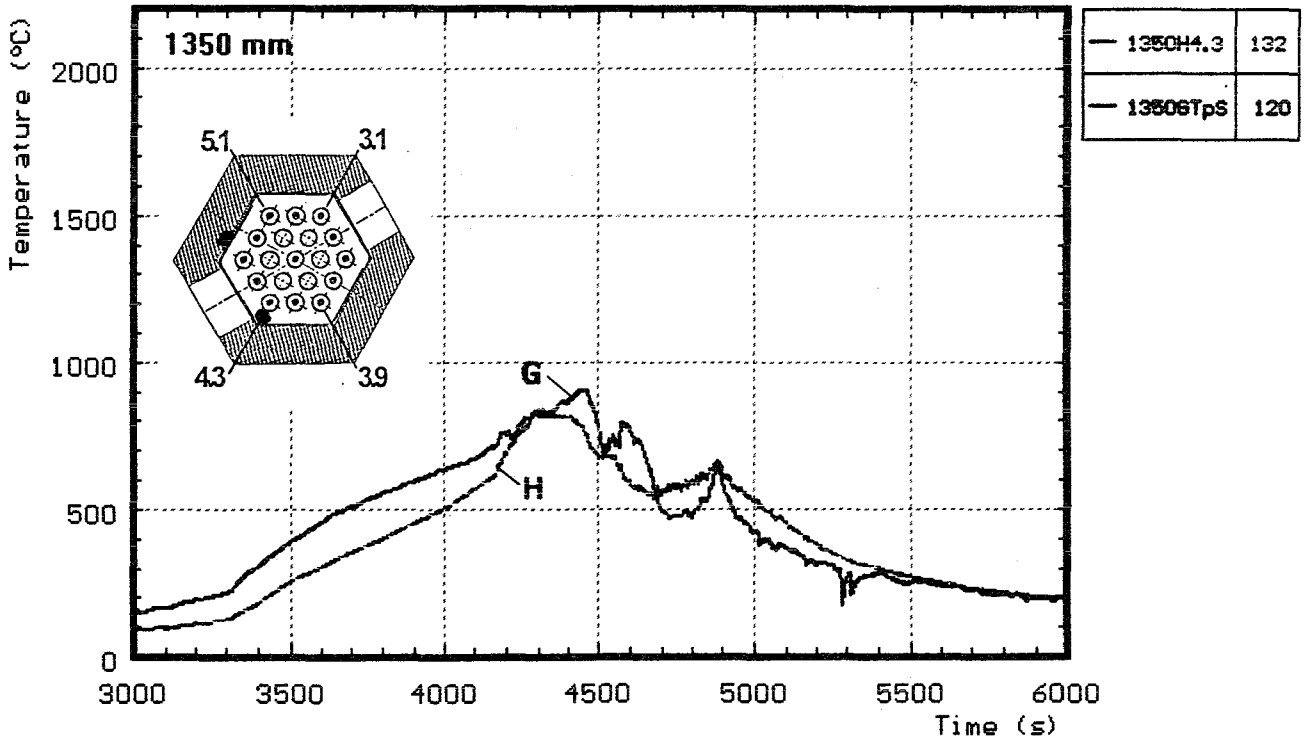
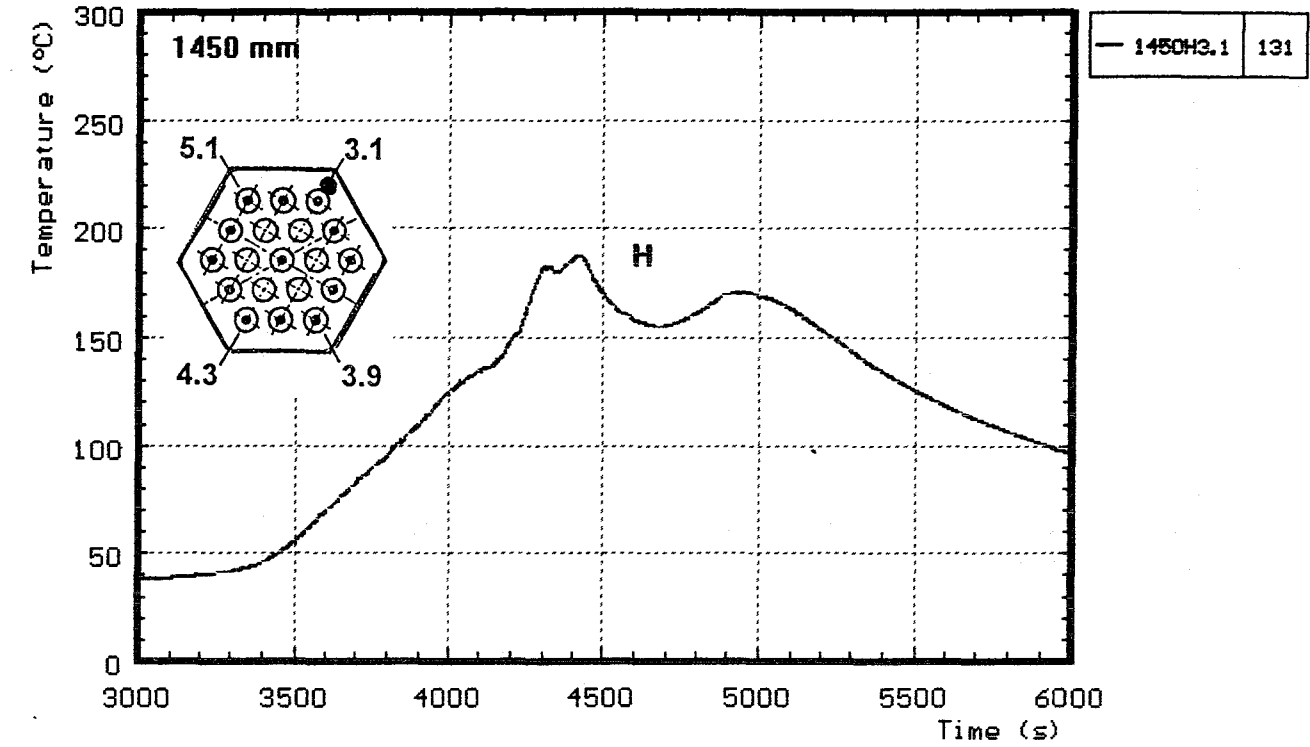
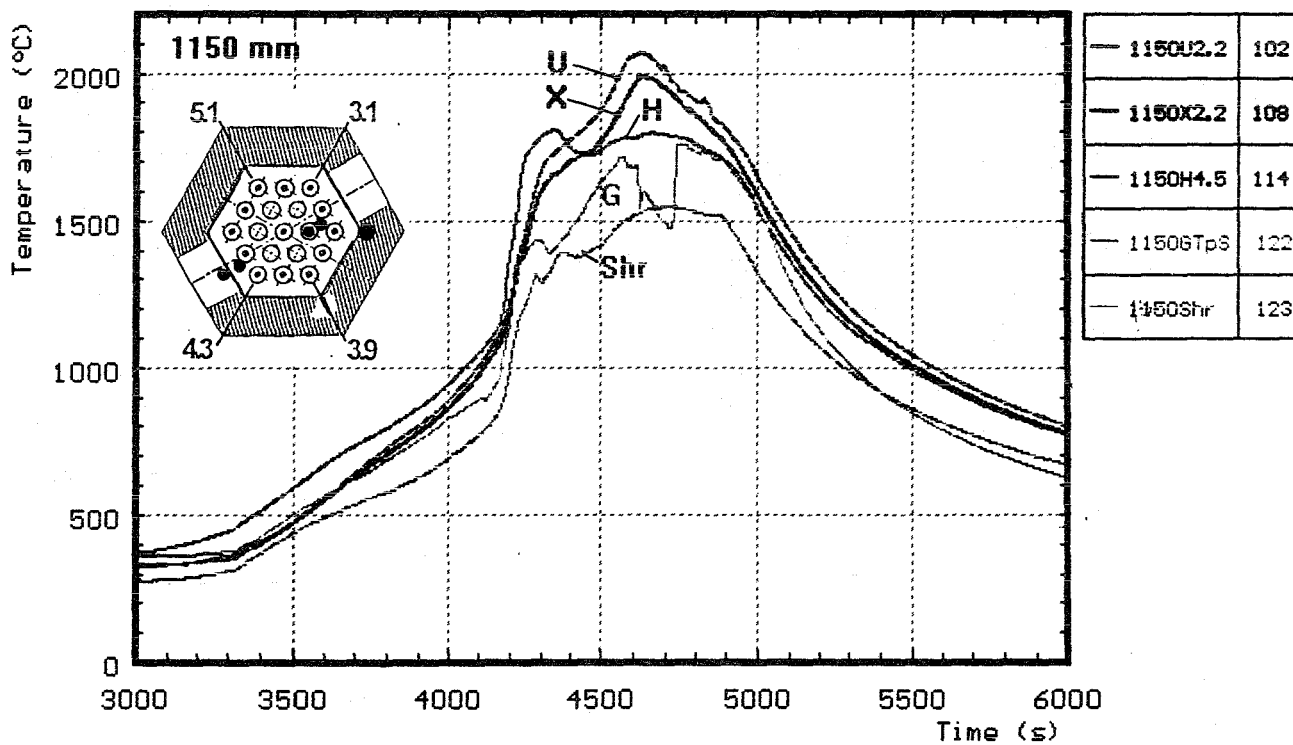
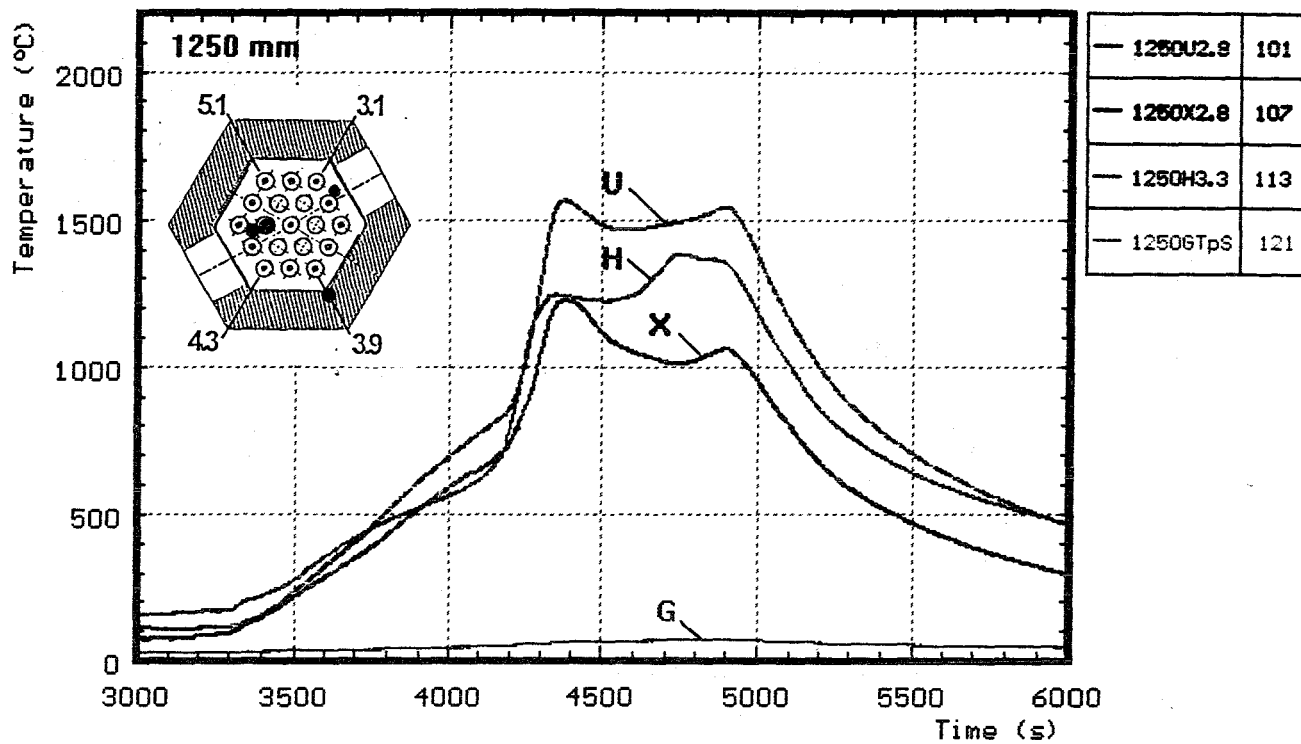


Fig. 35: CORA-W1: Temperature measured in the bundle head plate (1491 mm)



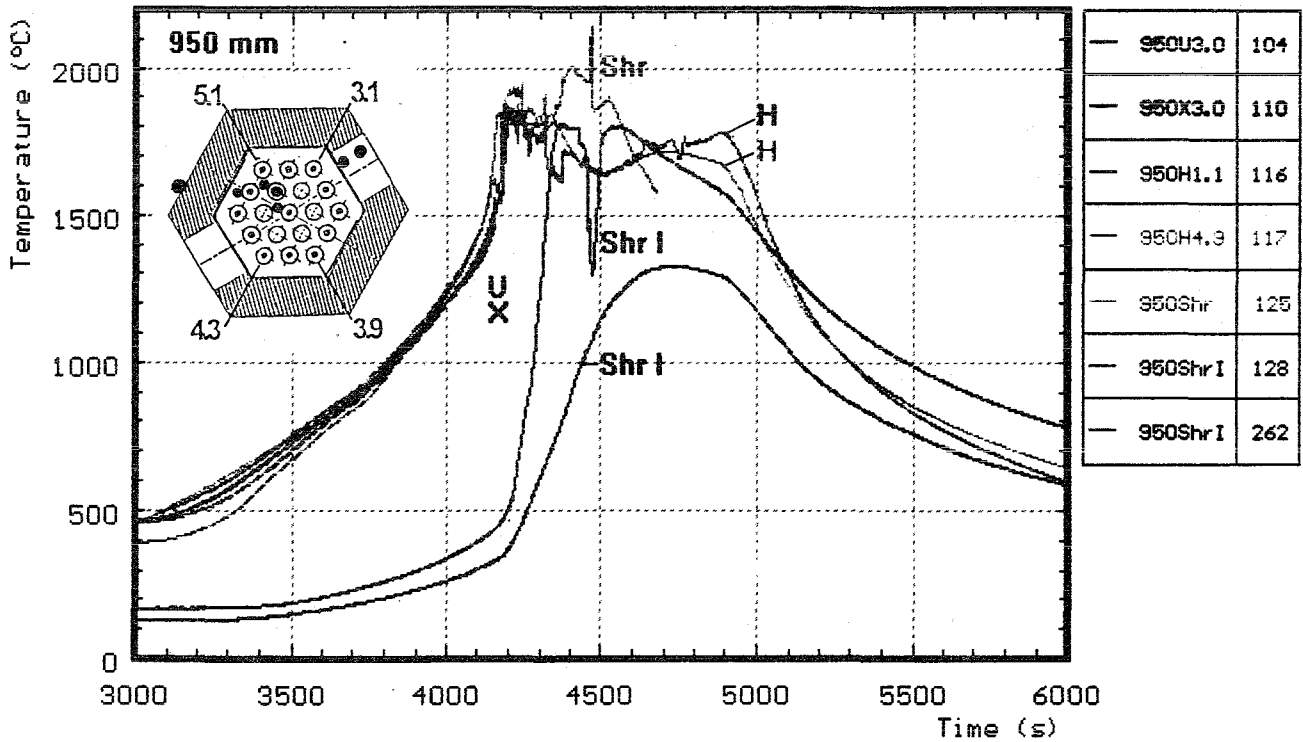
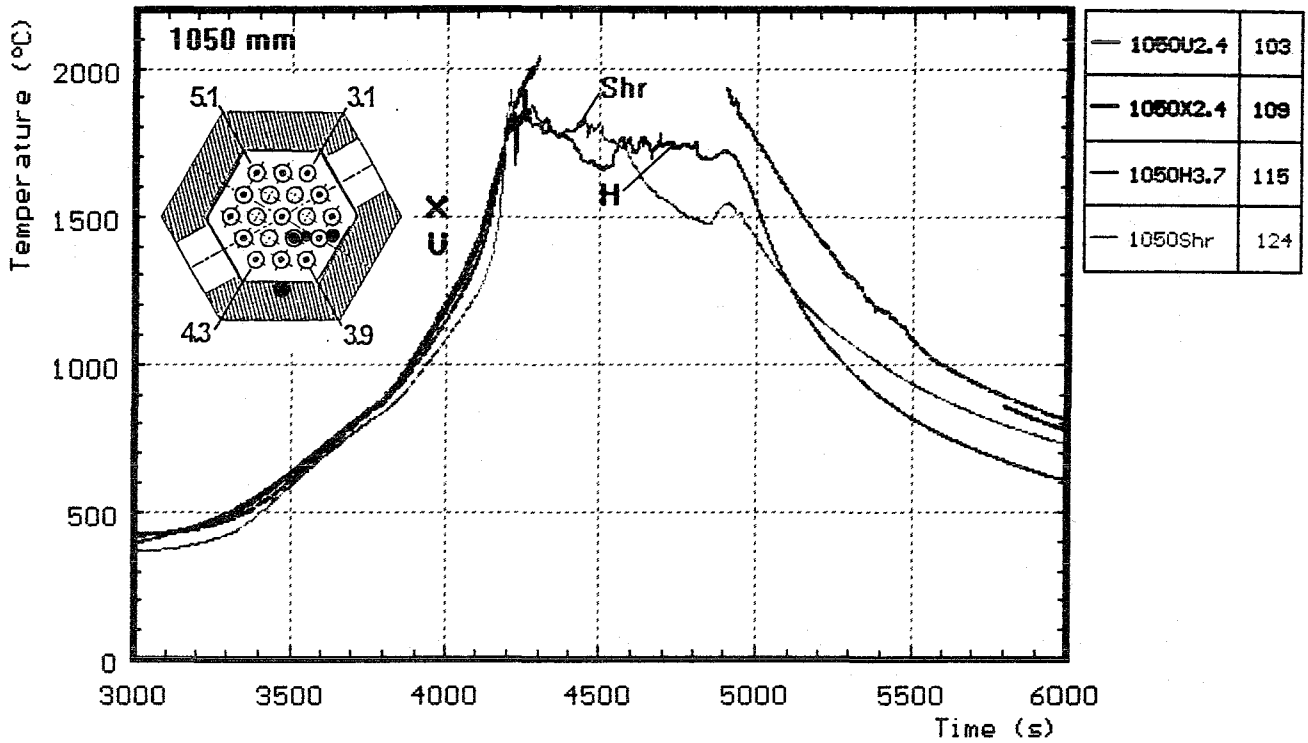
H : Heated rods
 G : Gas temperature

Fig. 36: CORA-W1; Temperatures at elevations given (1450, 1350 mm)



<p>H : Heated rods</p> <p>U : Unheated rods</p> <p>G : Gas temperature</p>	<p>Shr : On shroud</p> <p>X : On unheated rods</p>
--	--

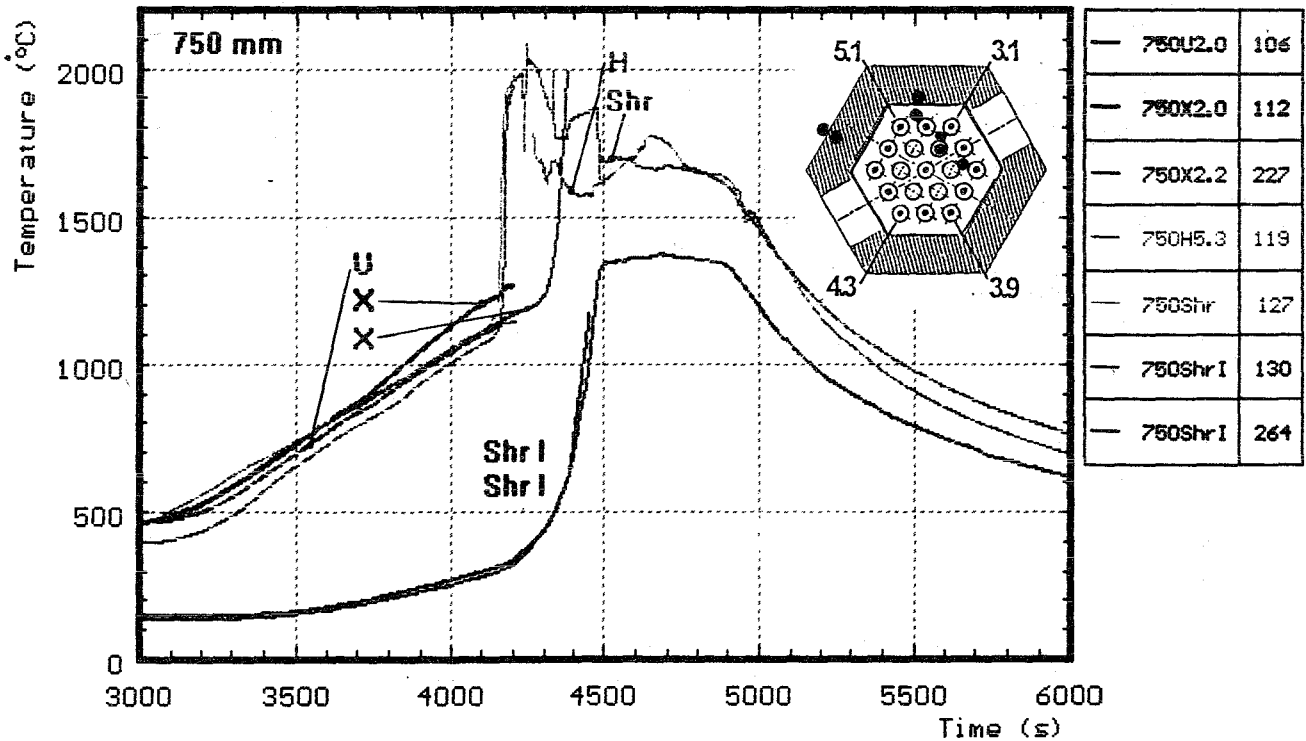
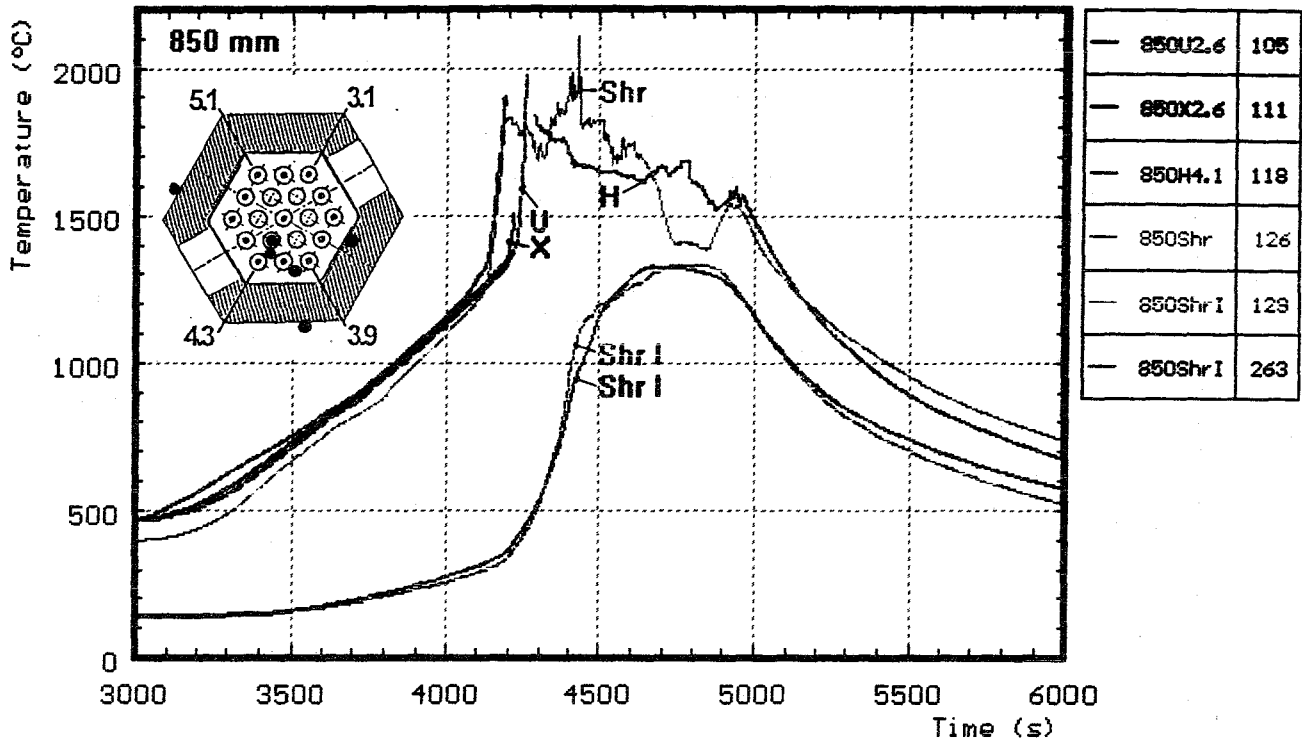
Fig. 37: CORA-W1; Temperatures at elevations given (1250, 1150 mm)



H : Heated rods
 U : Unheated rods
 X : On unheated rods

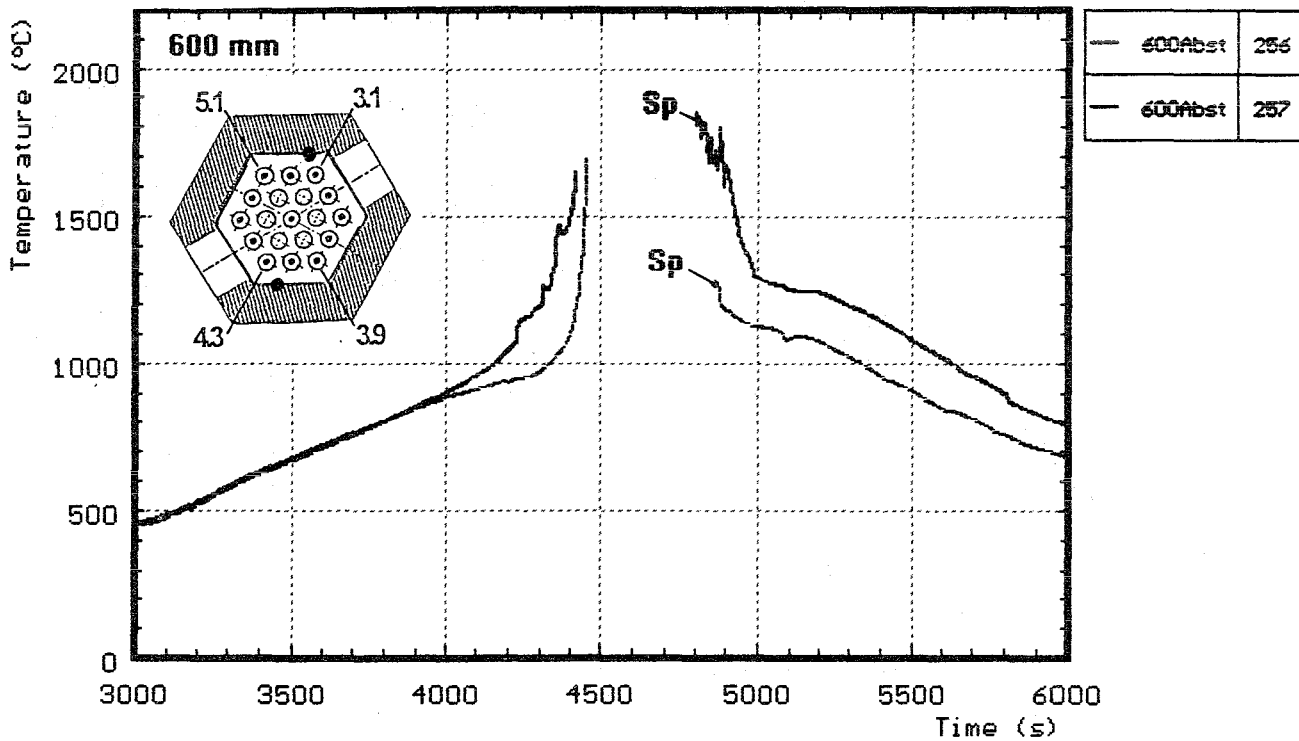
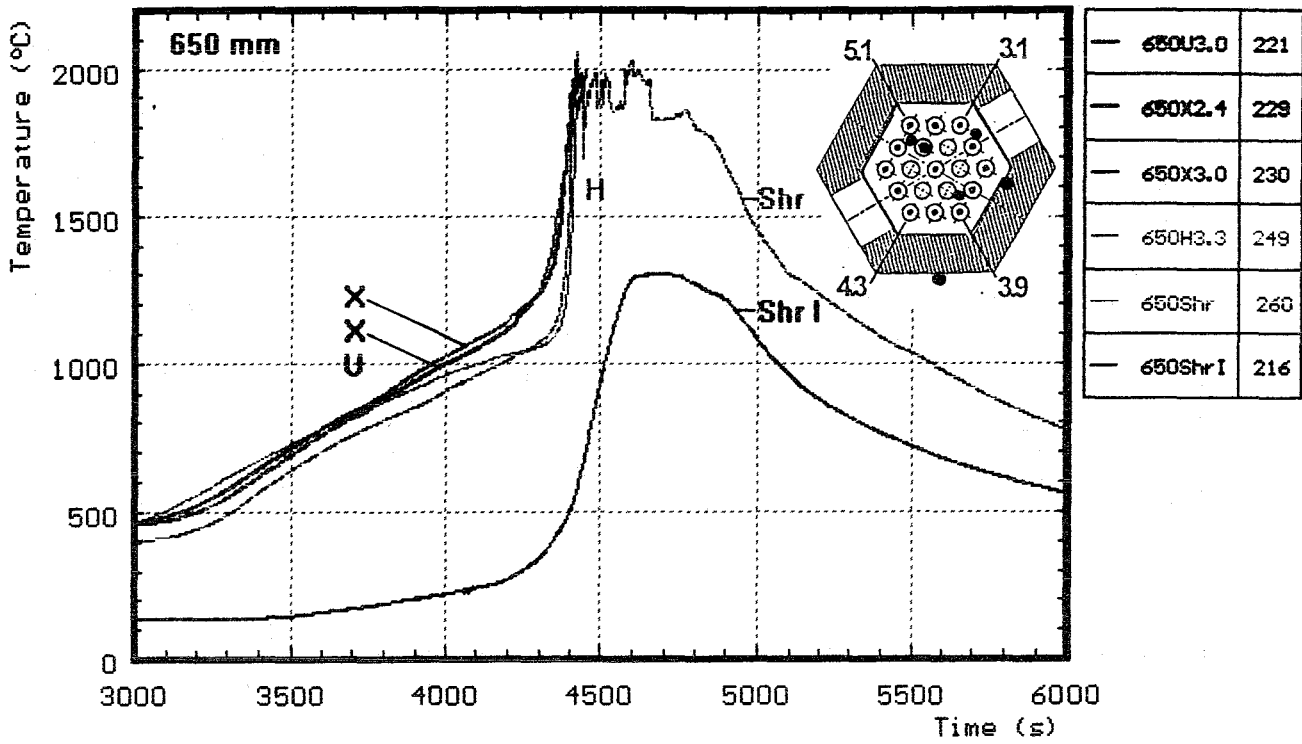
Shr I: Shroud insulation
 Shr : On shroud

Fig. 38: CORA-W1; Temperatures at elevations given (1050, 950 mm)



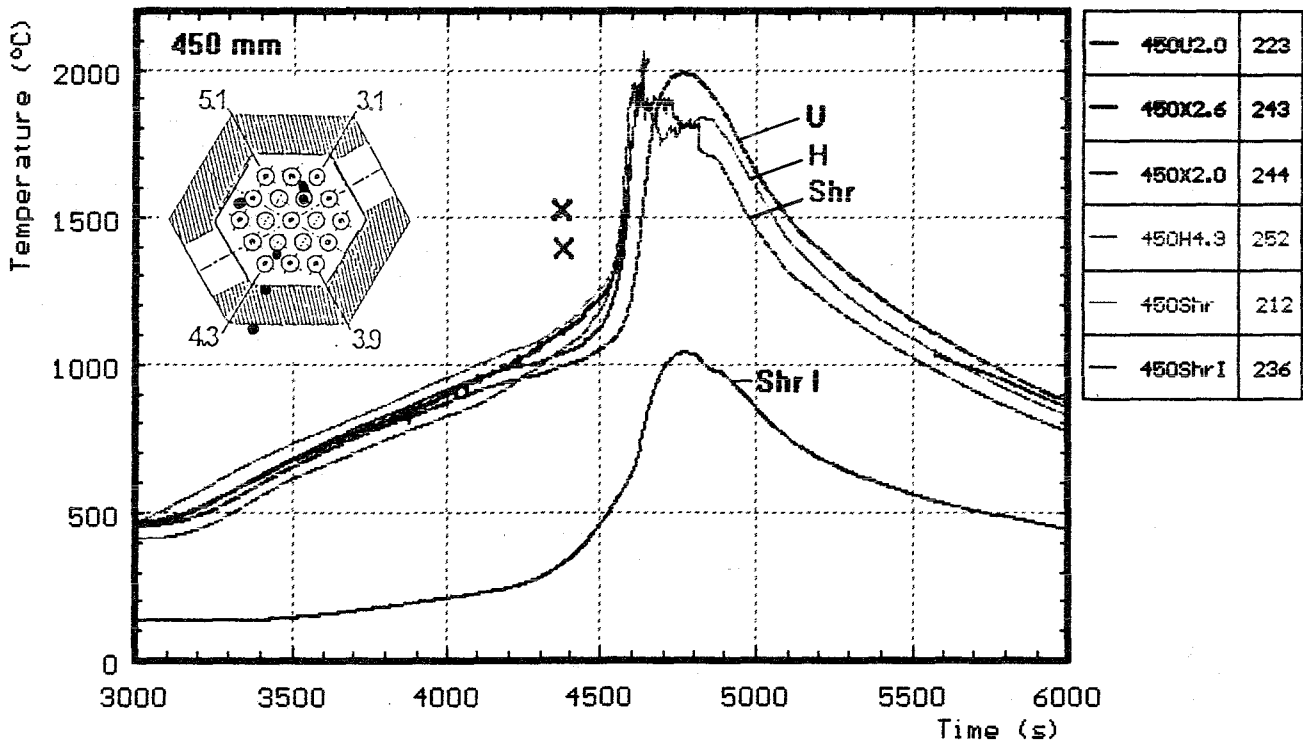
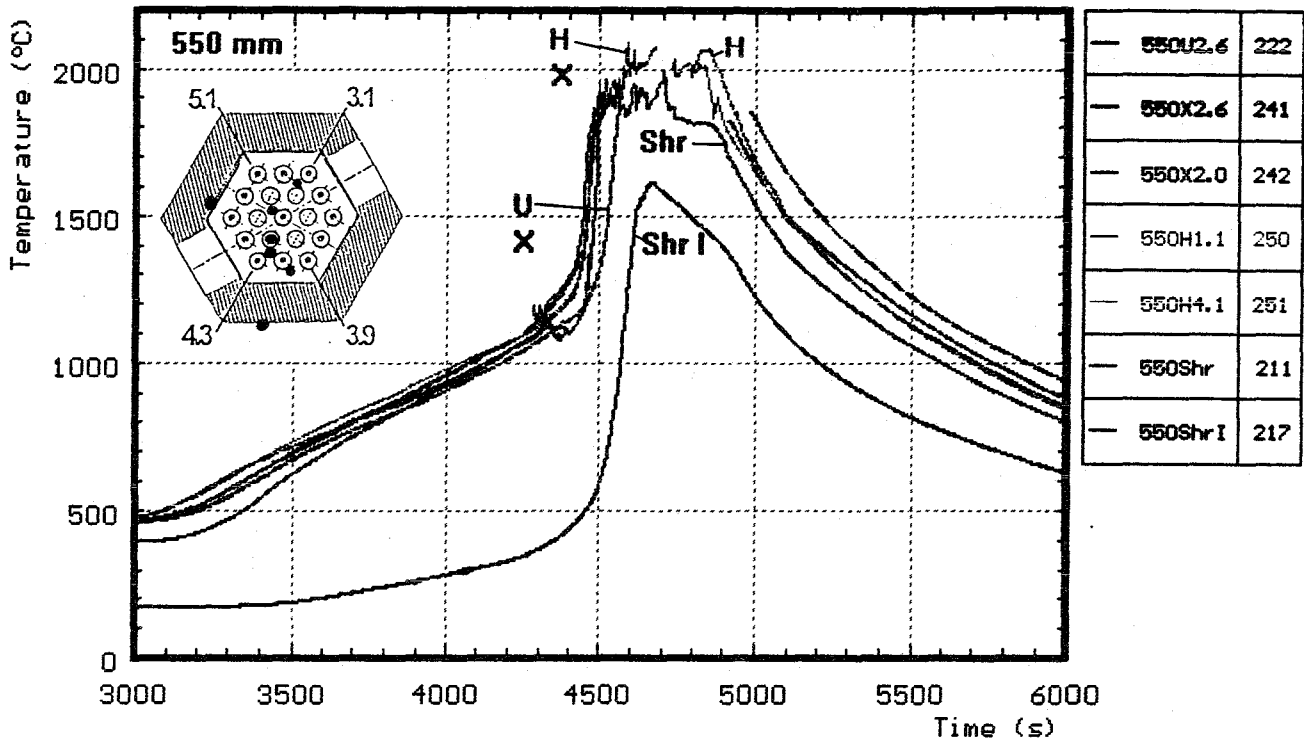
H : Heated rods
 U : Unheated rods
 X : On unheated rods
 Shr I: Shroud insulation
 Shr : On shroud

Fig. 39: CORA-W1; Temperatures at elevations given (850, 750 mm)



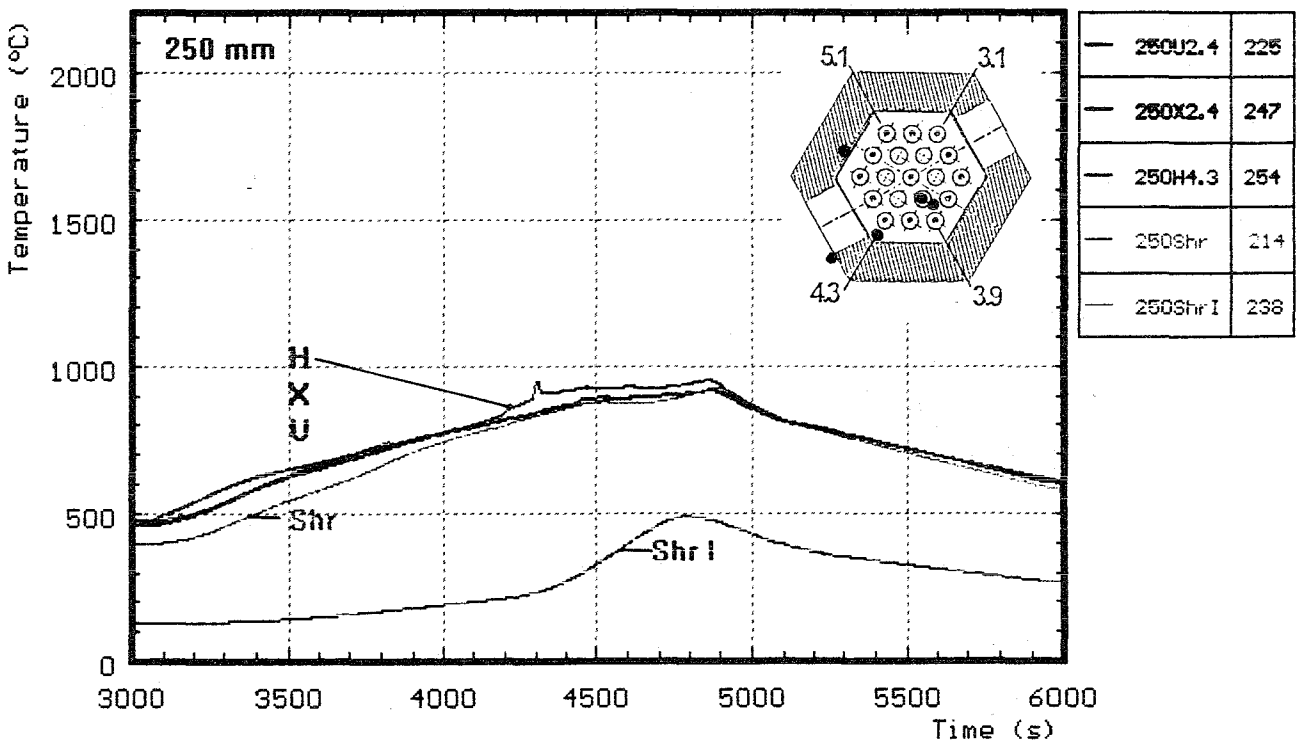
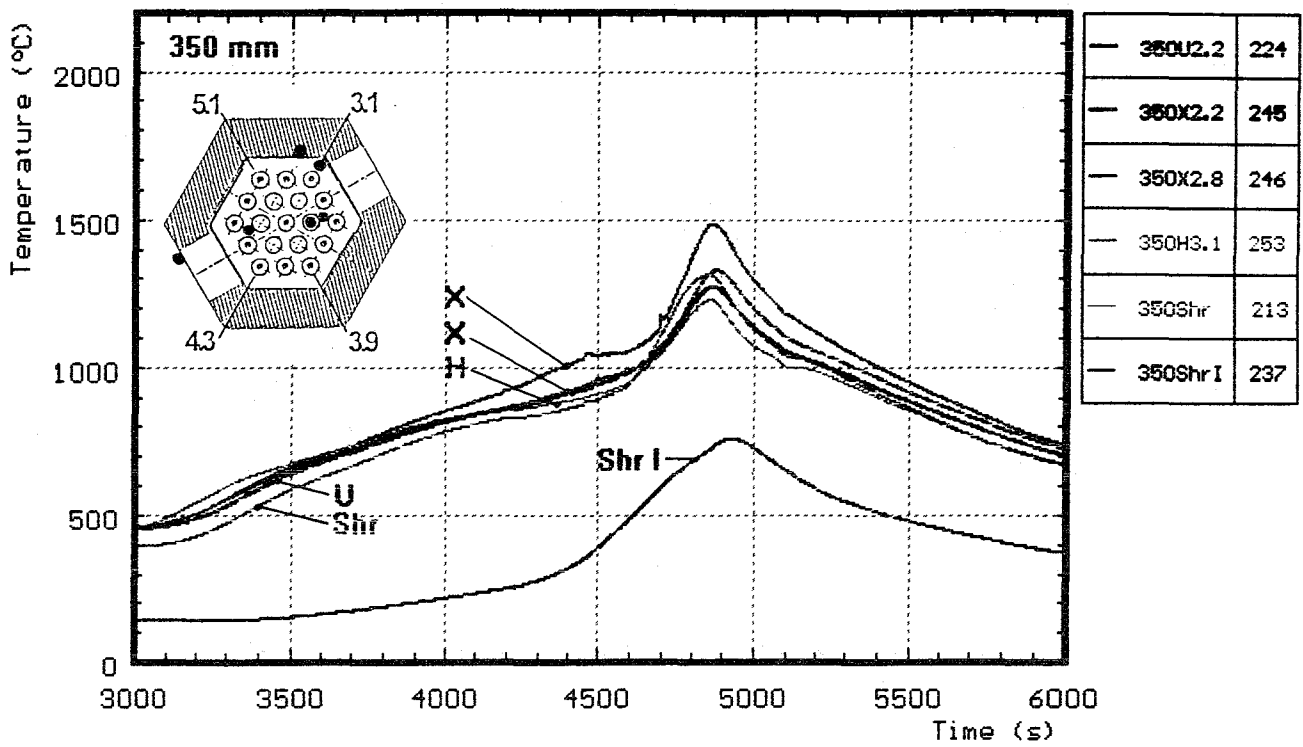
- | | | | |
|---|--------------------|--------|-------------------|
| H | : Heated rods | Shr I: | Shroud insulation |
| U | : Unheated rods | Shr : | On shroud |
| X | : On unheated rods | Sp : | Spacer |

Fig. 40: CORA-W1; Temperatures at elevations given (650, 600 mm)



H : Heated rods
U : Unheated rods
X : On unheated rods
Shr I: Shroud insulation
Shr : On shroud

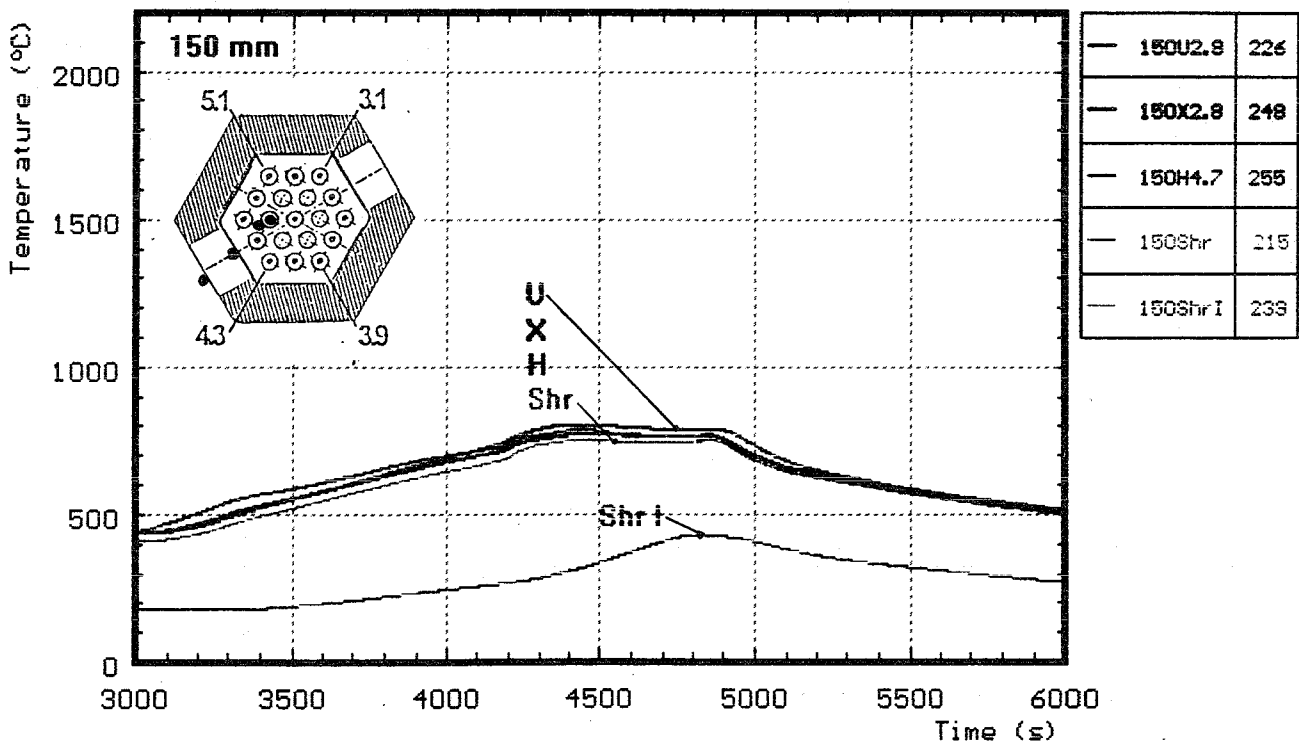
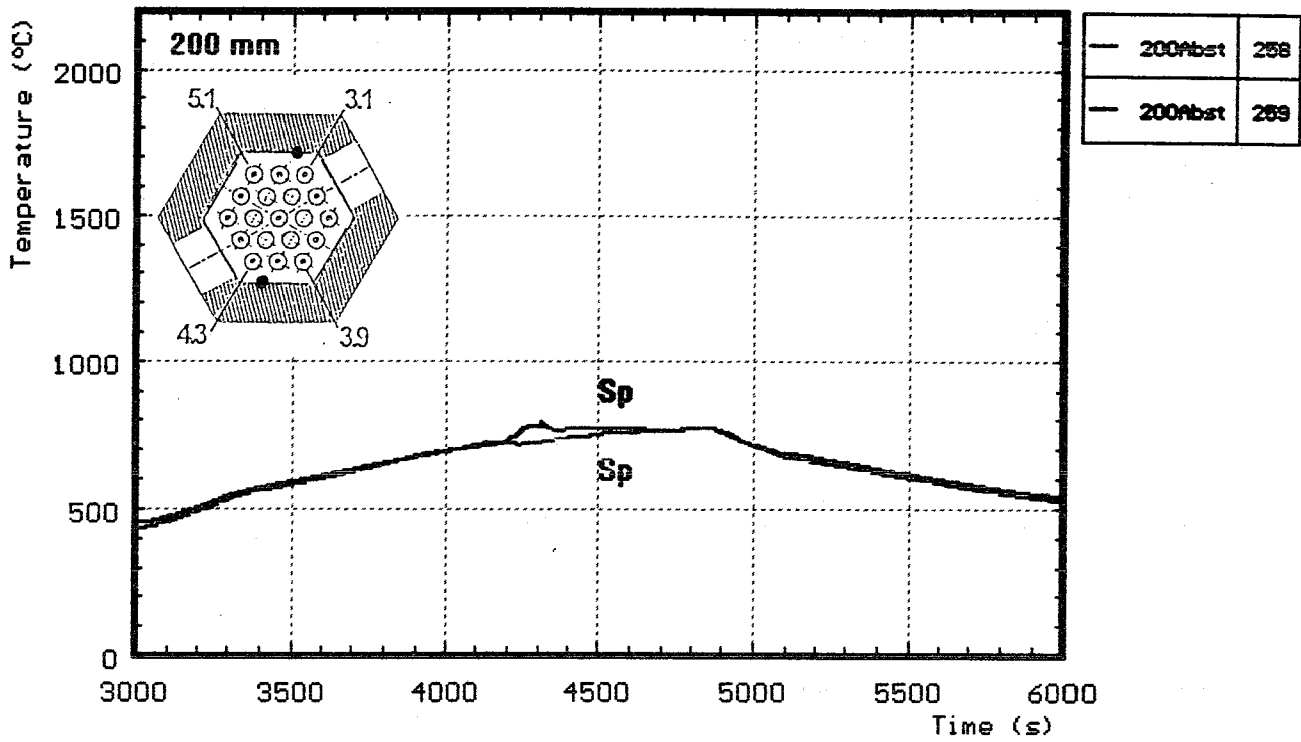
Fig. 41: CORA-W1; Temperatures at elevations given (550, 450 mm)



H : Heated rods
 U : Unheated rods
 X : On unheated rods

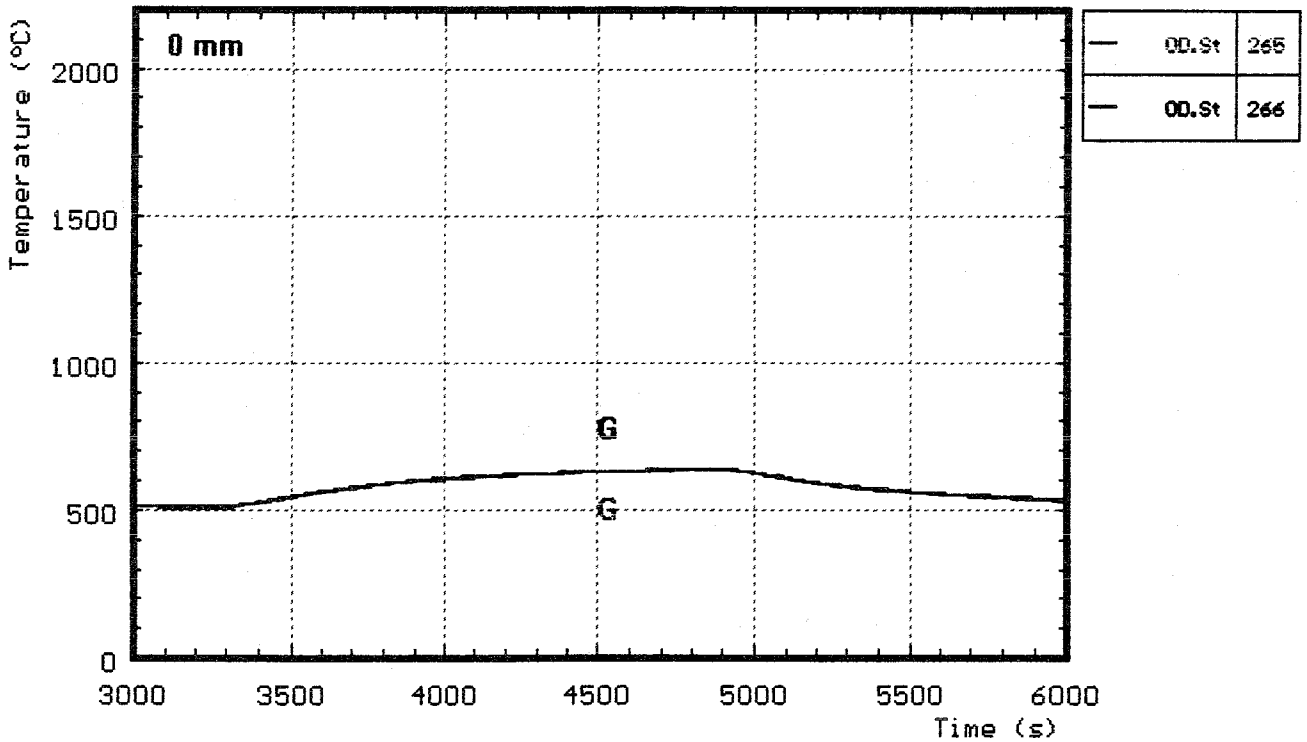
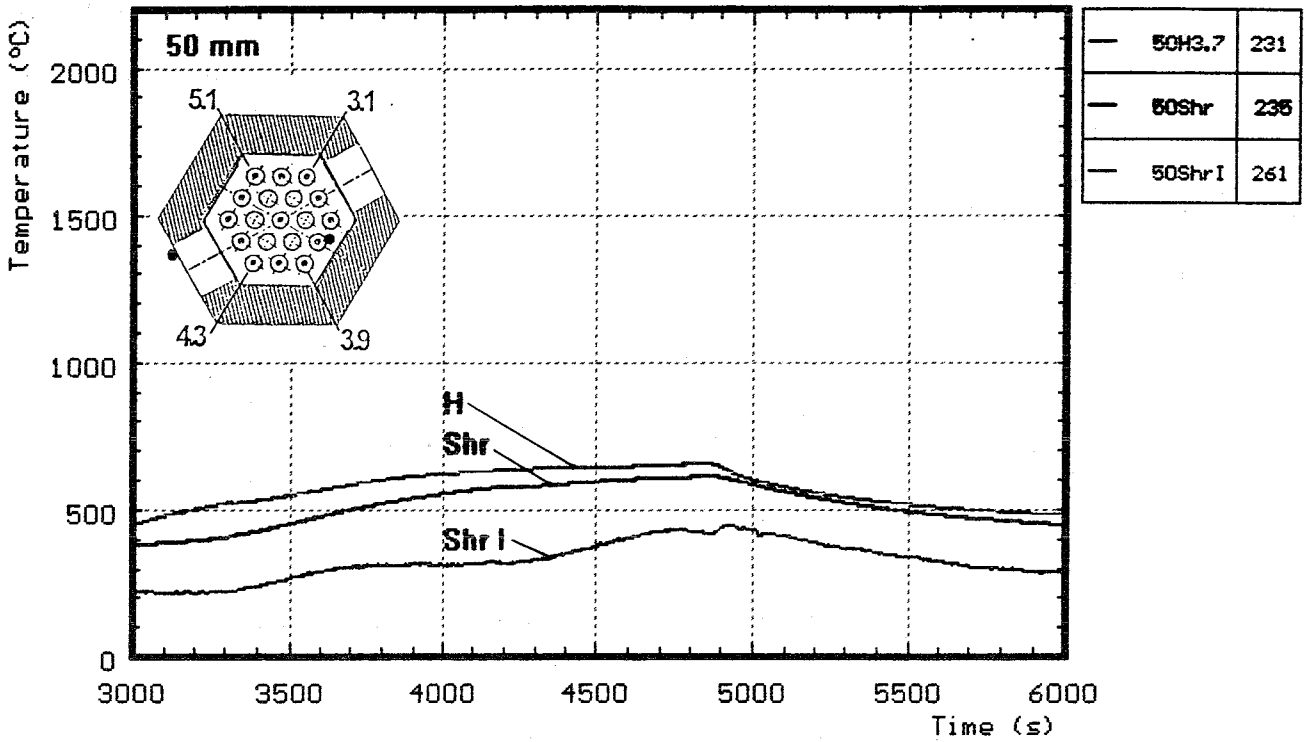
Shr I: Shroud insulation
 Shr : On shroud

Fig. 42: CORA-W1; Temperatures at elevations given (350, 250 mm)



- | | | | |
|---|--------------------|--------|-------------------|
| H | : Heated rods | Shr I: | Shroud insulation |
| U | : Unheated rods | Shr : | On shroud |
| X | : On unheated rods | Sp : | Spacer |

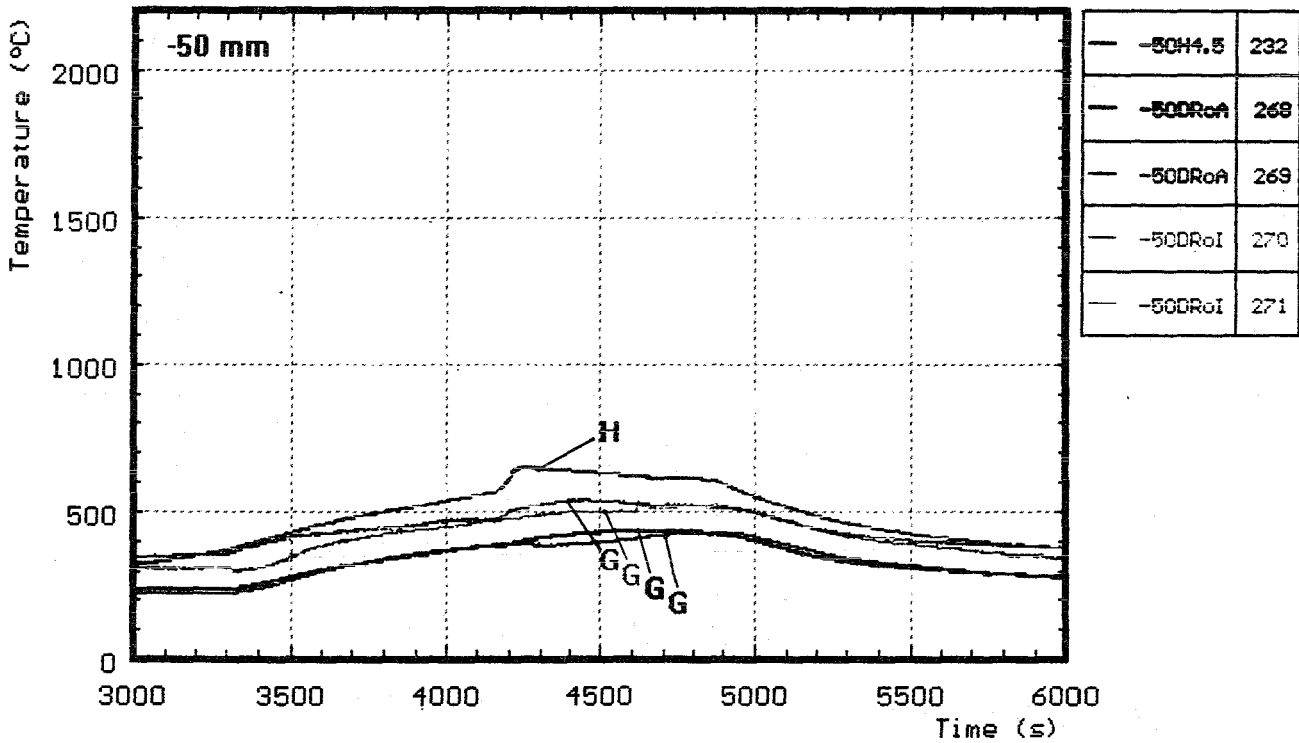
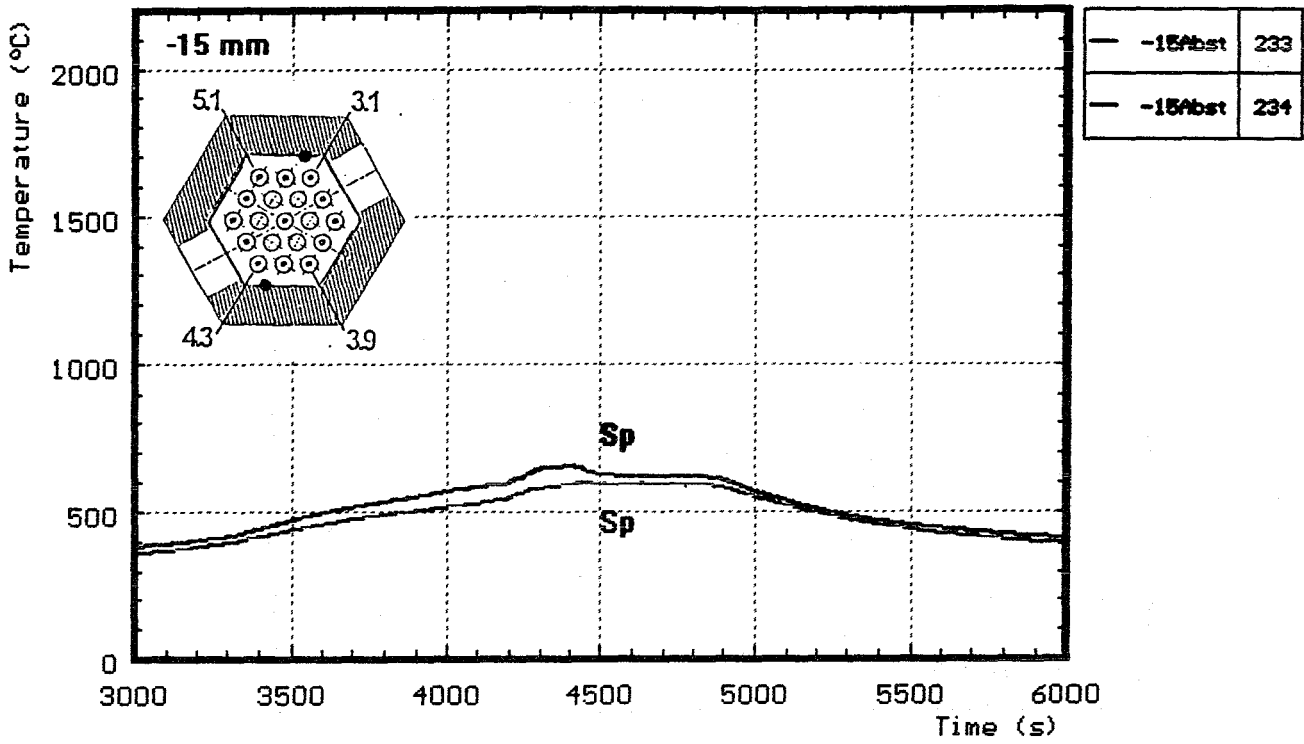
Fig. 43: CORA-W1; Temperatures at elevations given (200, 150 mm)



H : Heated rods
 G : Gas temperature

Shr I: Shroud insulation
 Shr : On shroud

Fig. 44: CORA-W1; Temperatures at elevations given (50, 0 mm)



H : Heated rods
 G : Gas temperature
 Sp : Spacer

Fig. 45: CORA-W1; Temperatures at elevations given (-15, -50 mm)

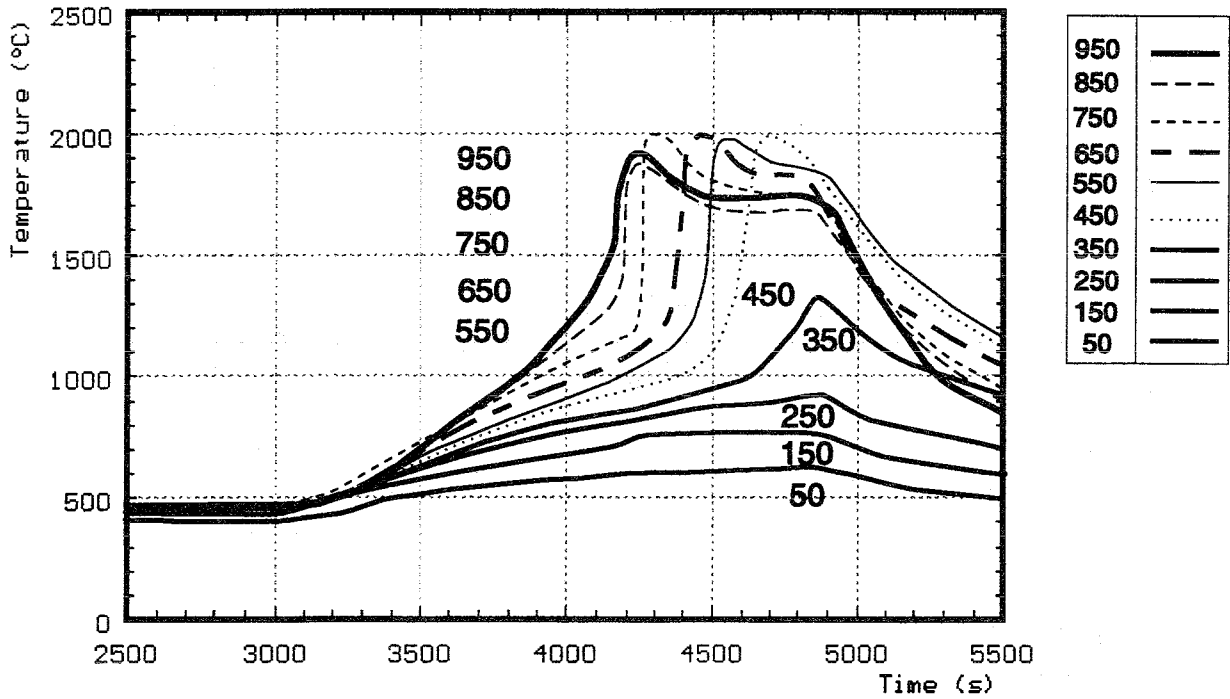
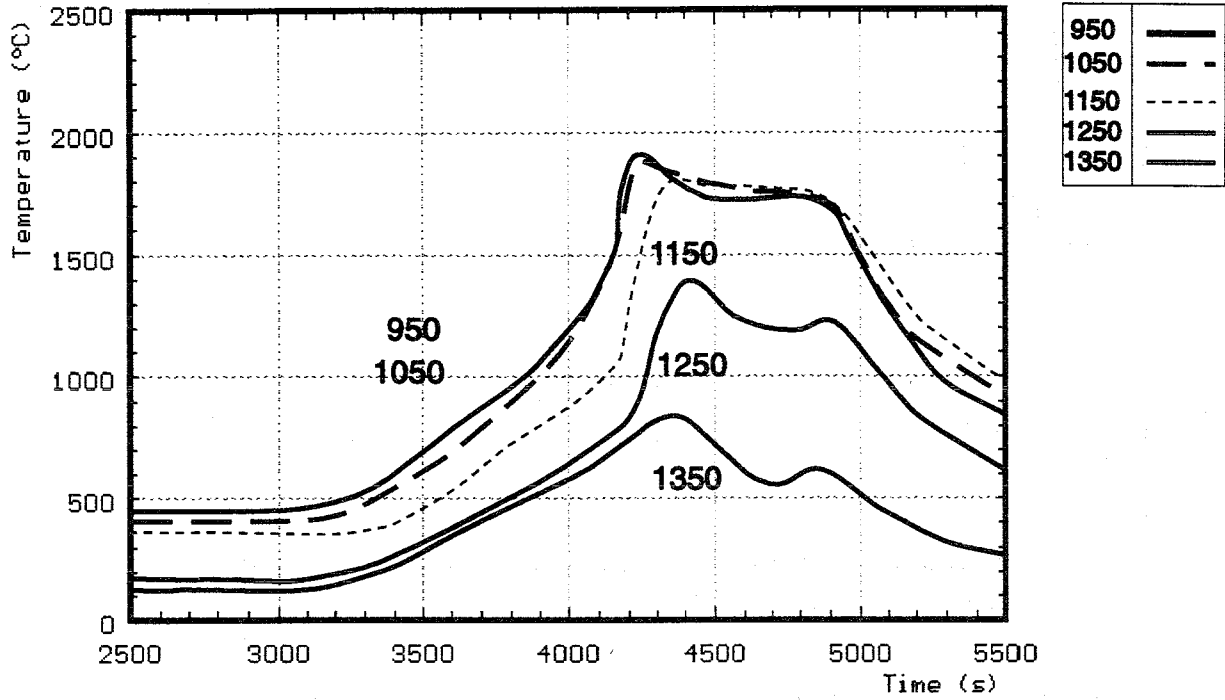


Fig. 46: CORA-W1; Best-estimate bundle temperatures at different elevations

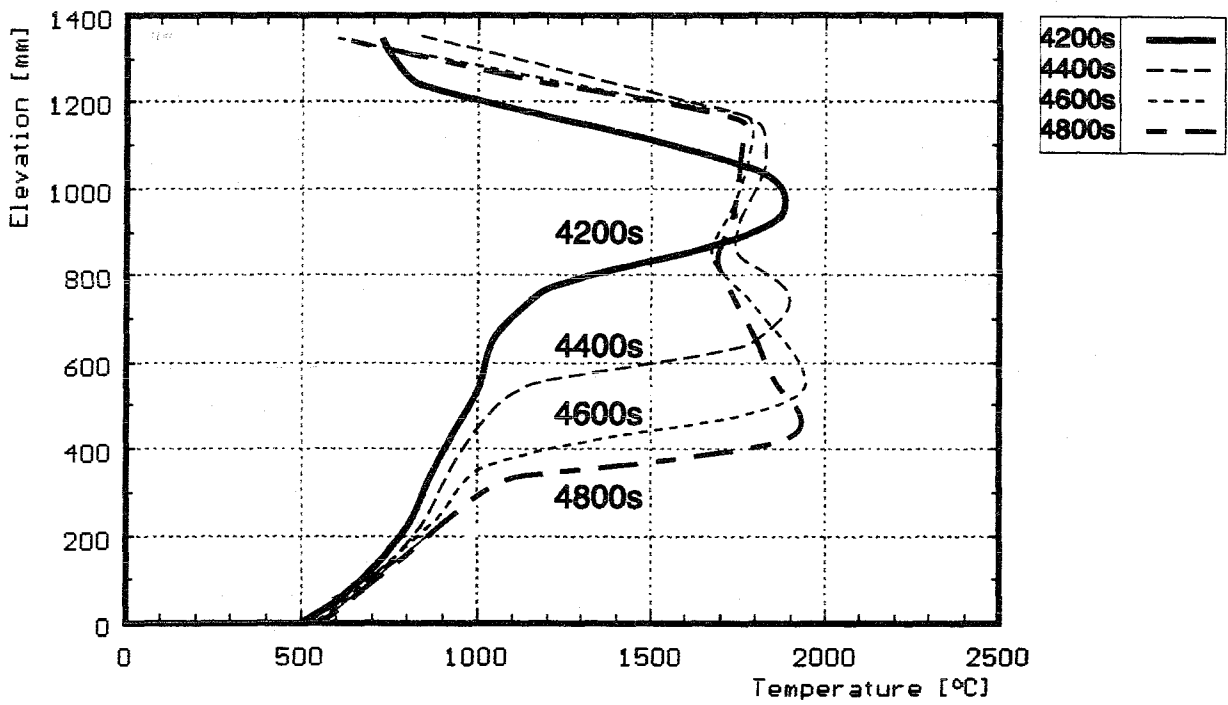
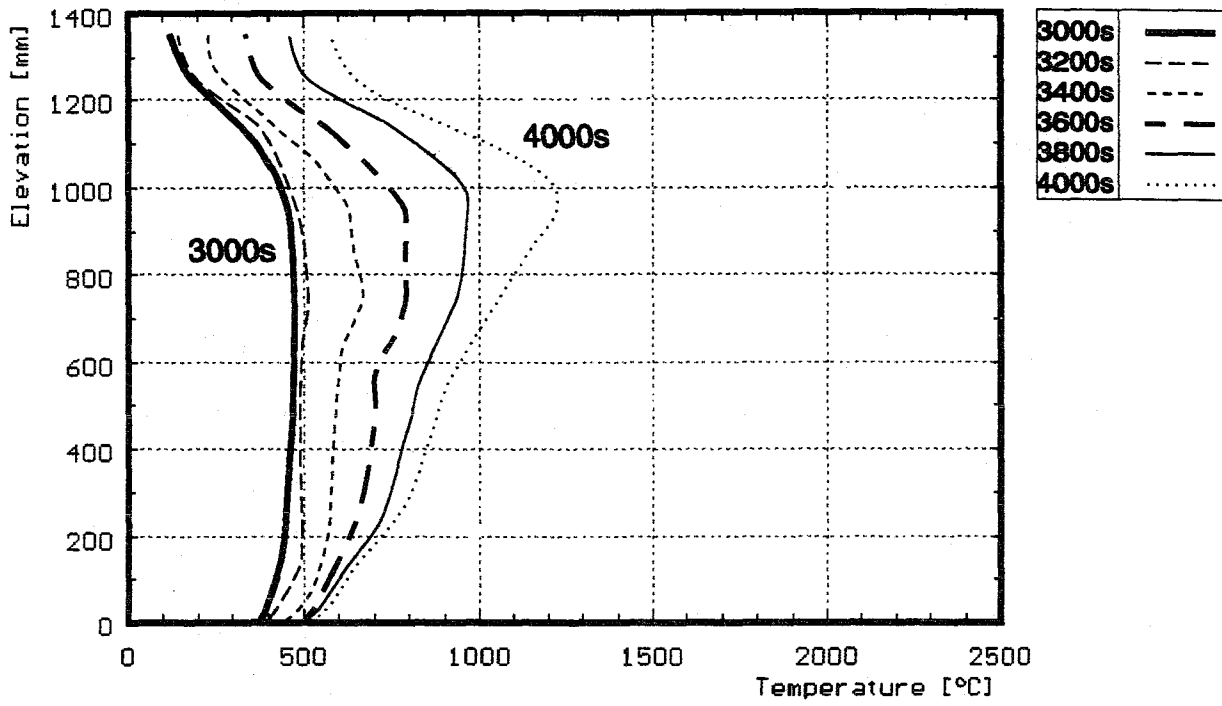


Fig. 47: Axial temperature distribution during the transient of test CORA-W1

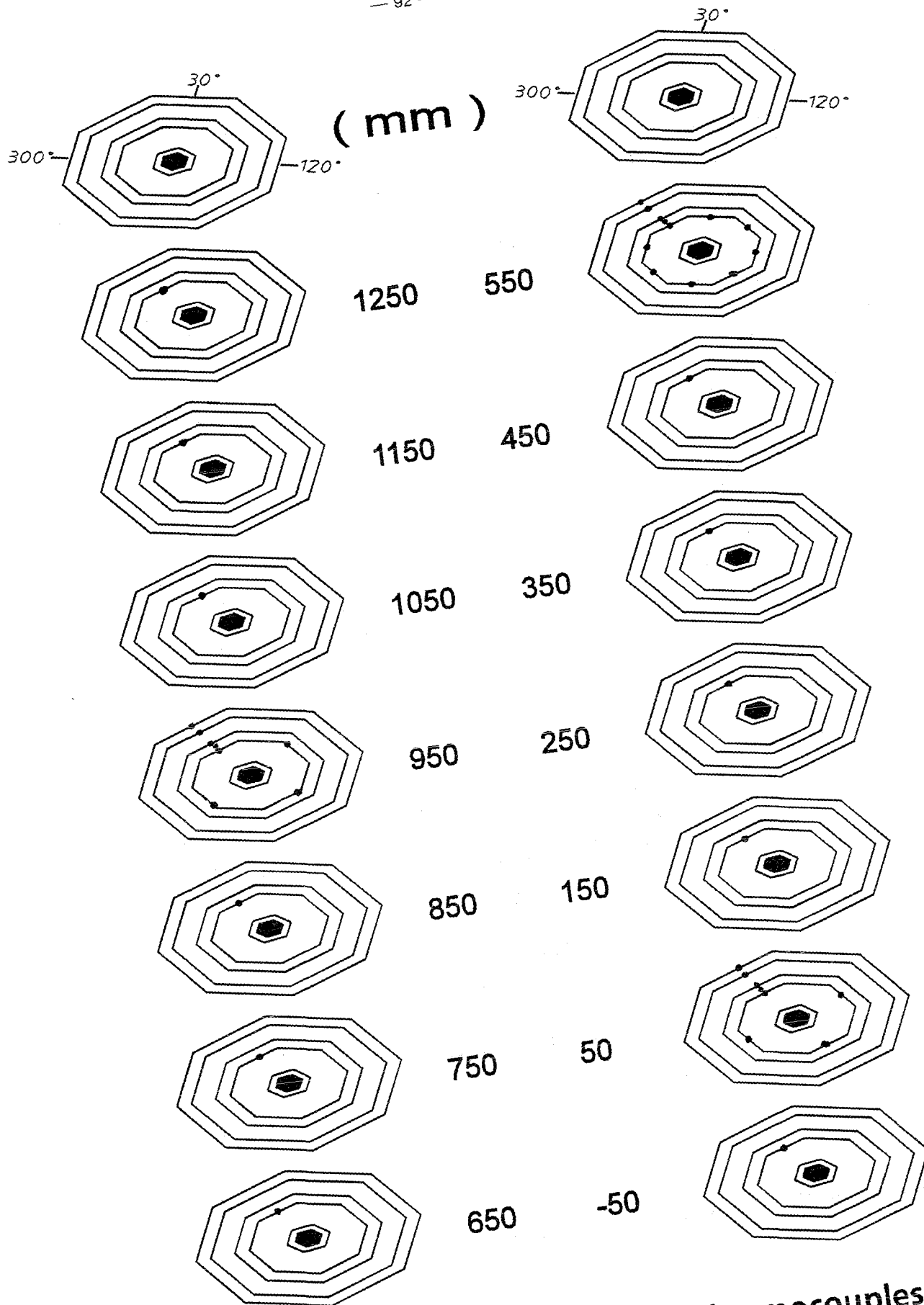


Fig. 48: CORA-W1; Locations of thermocouples in the high-temperature shield

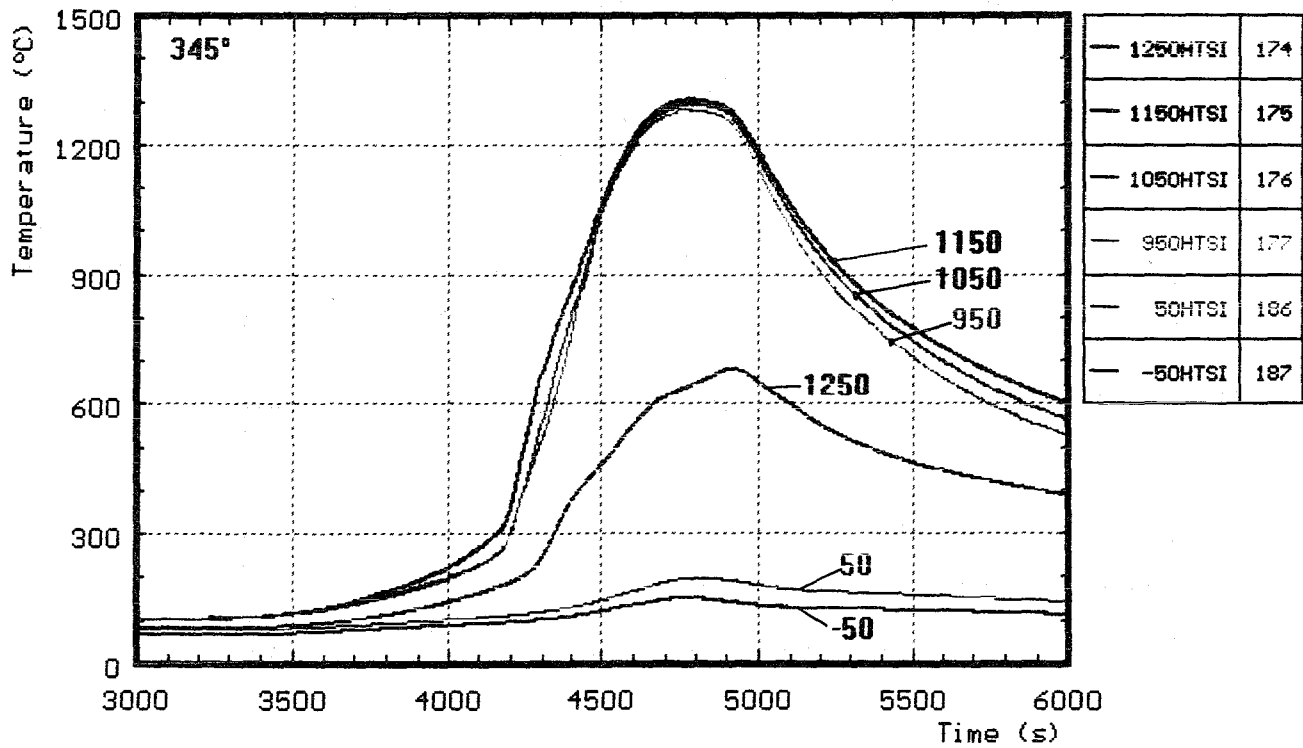
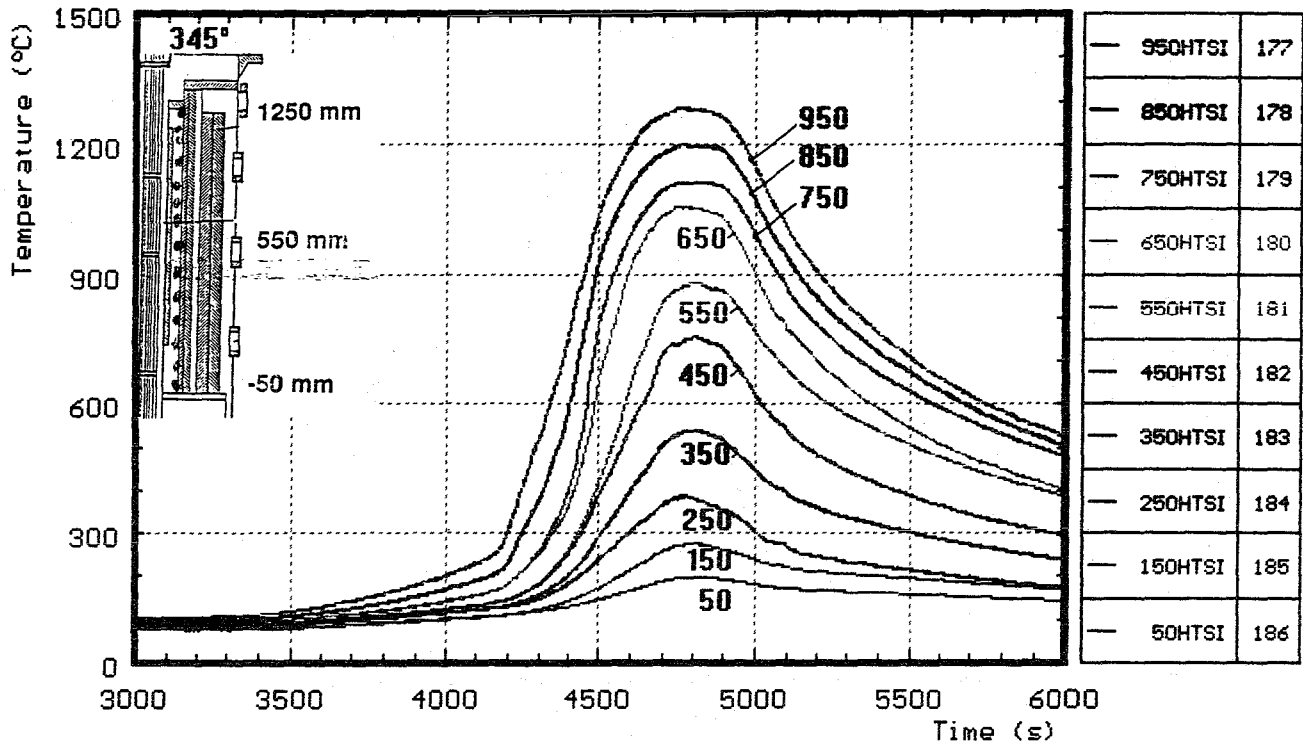


Fig. 49: CORA-W1; Temperatures of HTS at inner surface, 153 mm radius

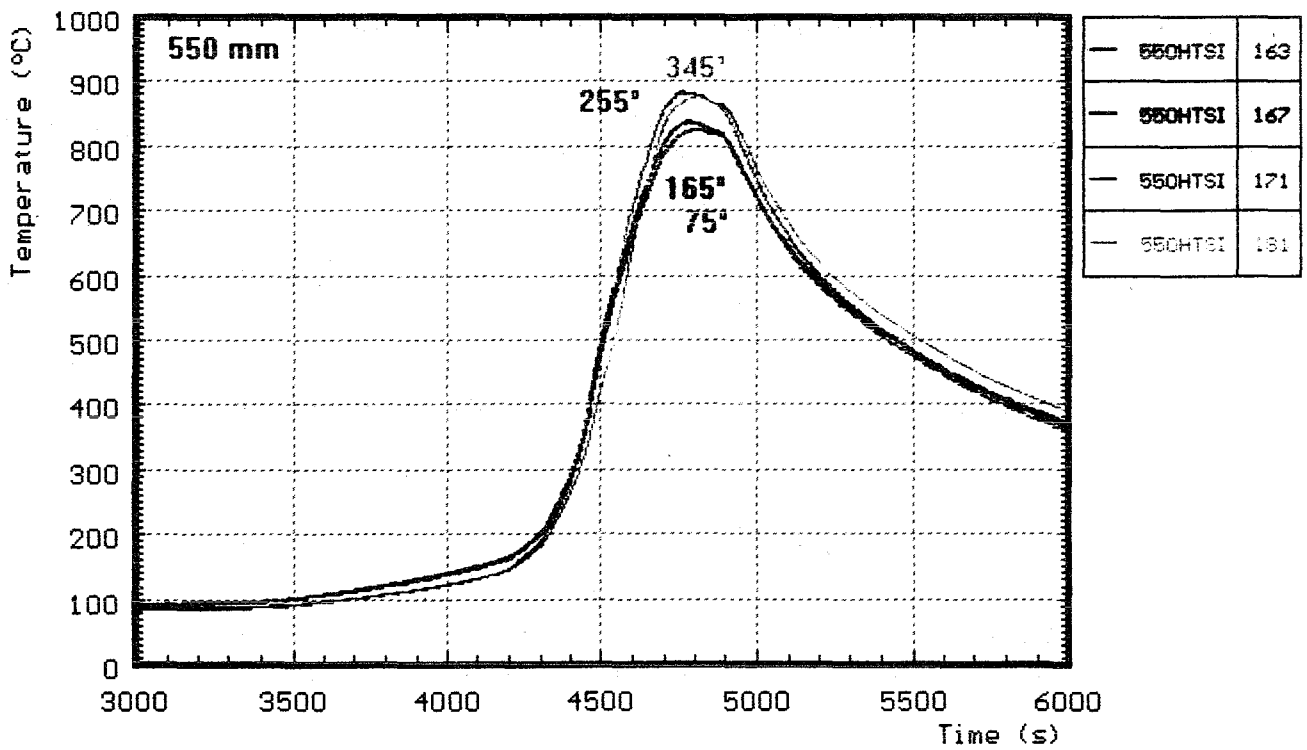
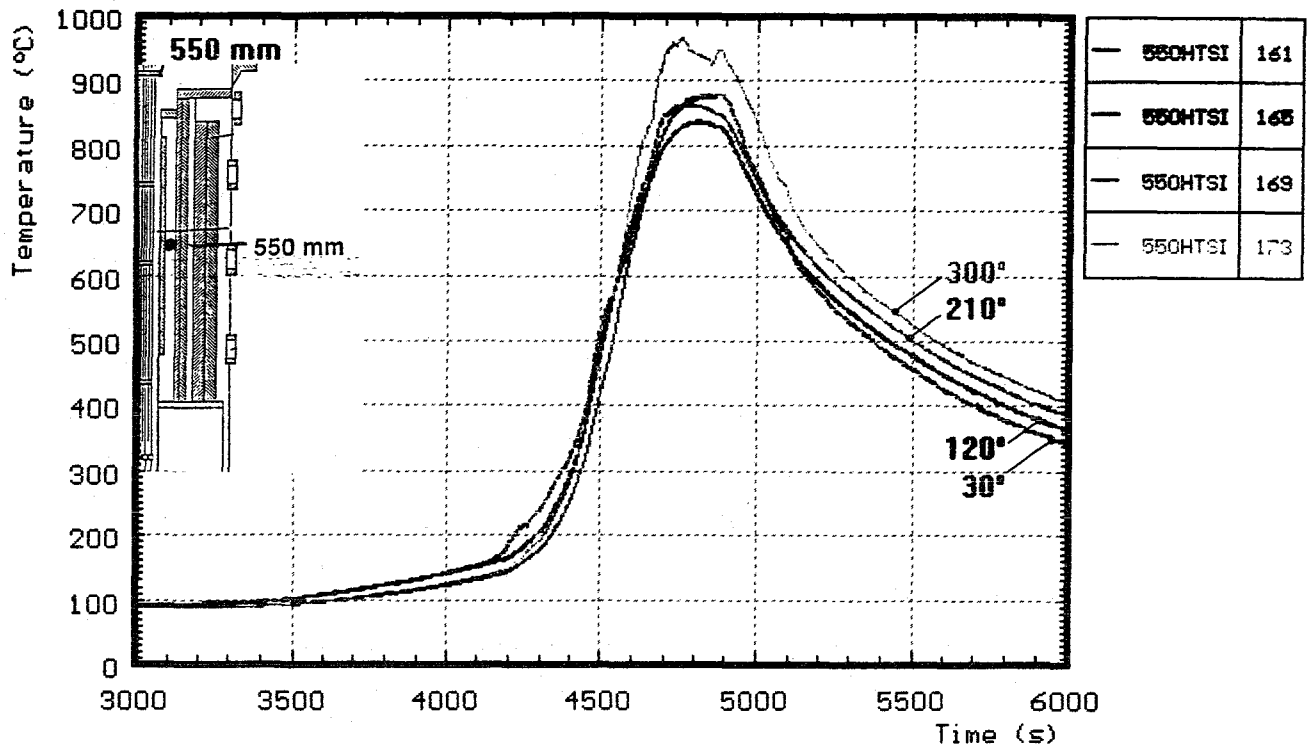


Fig. 50: CORA-W1; Temperatures of HTS, inner surface at 153 mm radius (550 mm)

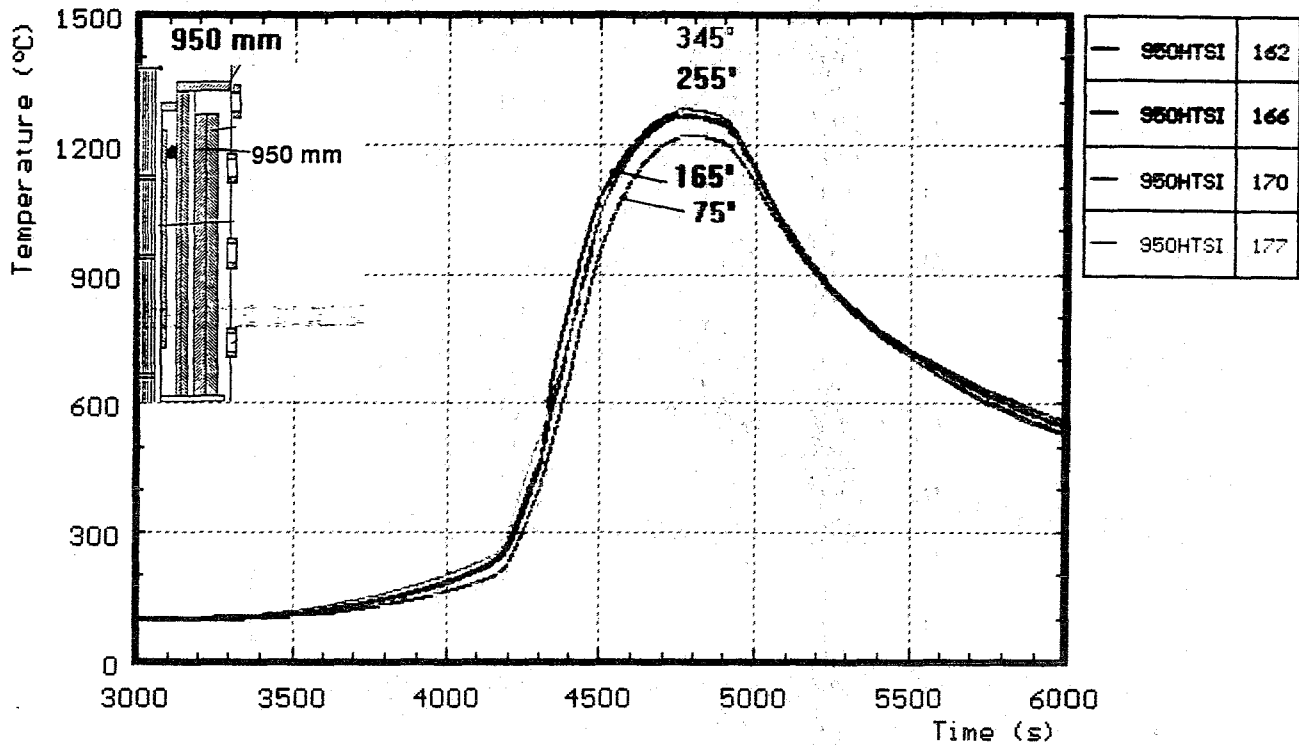


Fig. 51: CORA-W1; Temperatures of HTS, inner surface at 153 mm radius (950mm)

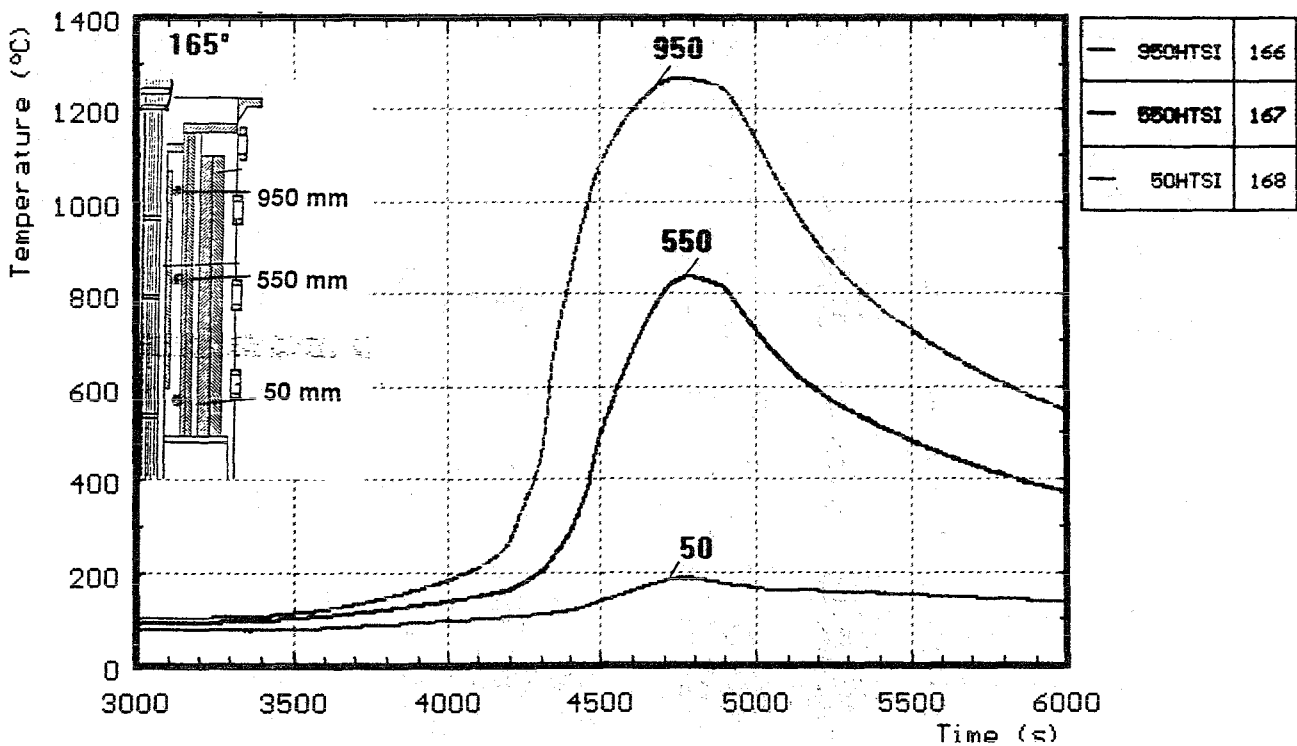


Fig. 52: CORA-W1; Temperatures of HTS, inner surface at 153 mm radius

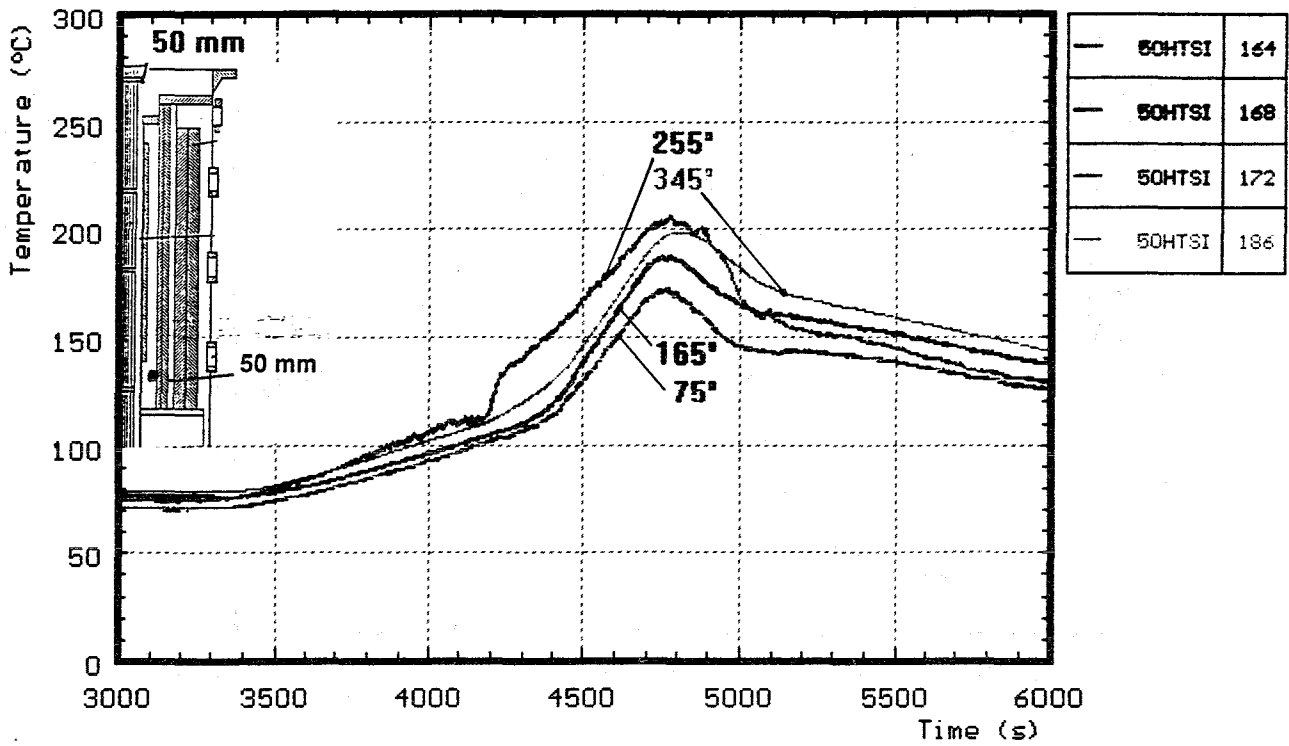


Fig. 53: CORA-W1; Temperatures of HTS, inner surface at 153 mm radius (50mm)

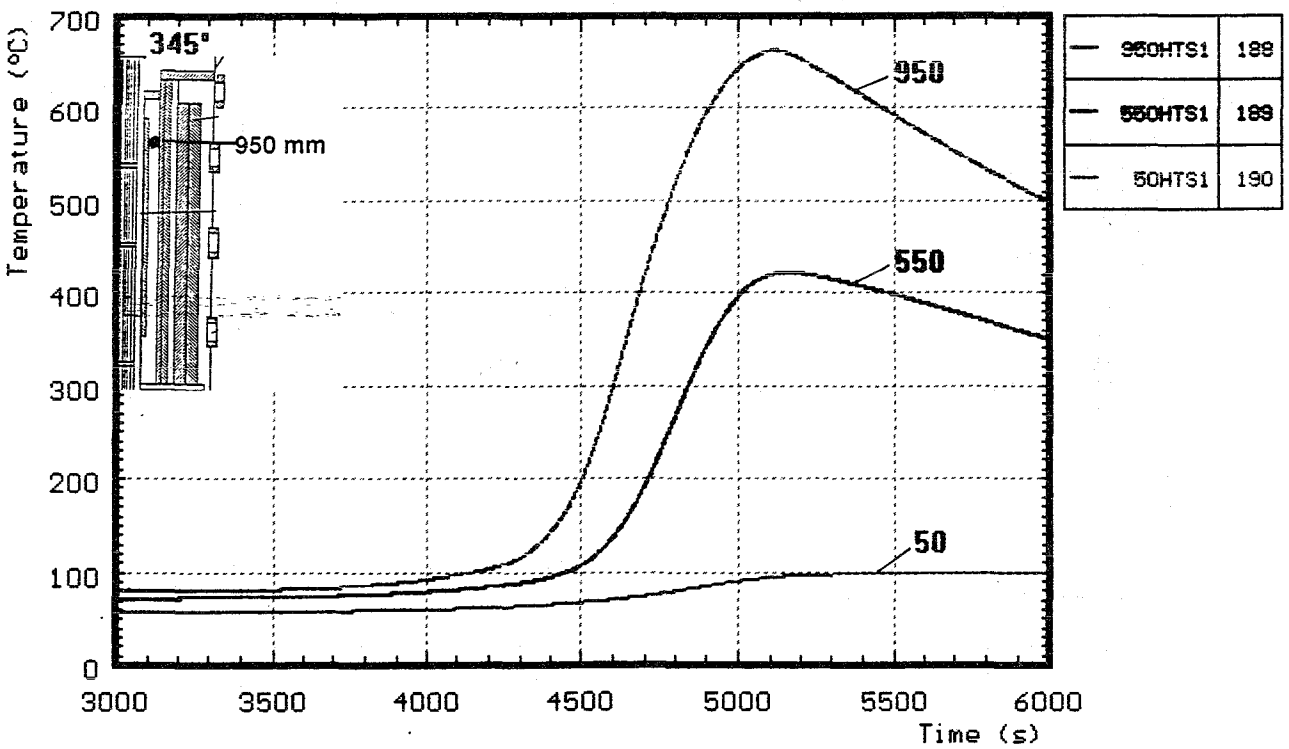


Fig. 54: CORA-W1; Temperatures of HTS, Temperatures of the HT shield at 172 mm radius

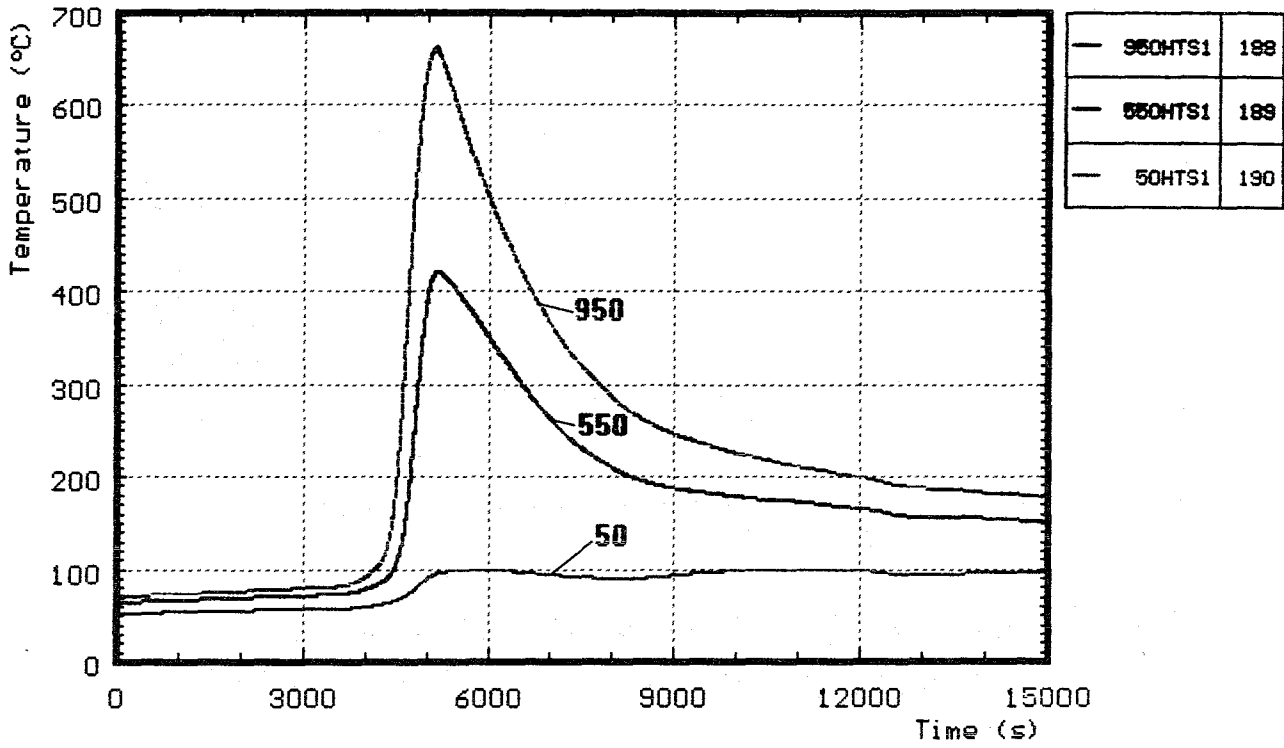


Fig. 55: CORA-W1; Temperatures of HTS, Temperatures of the HT shield at 172 mm radius (0 - 15000 s)

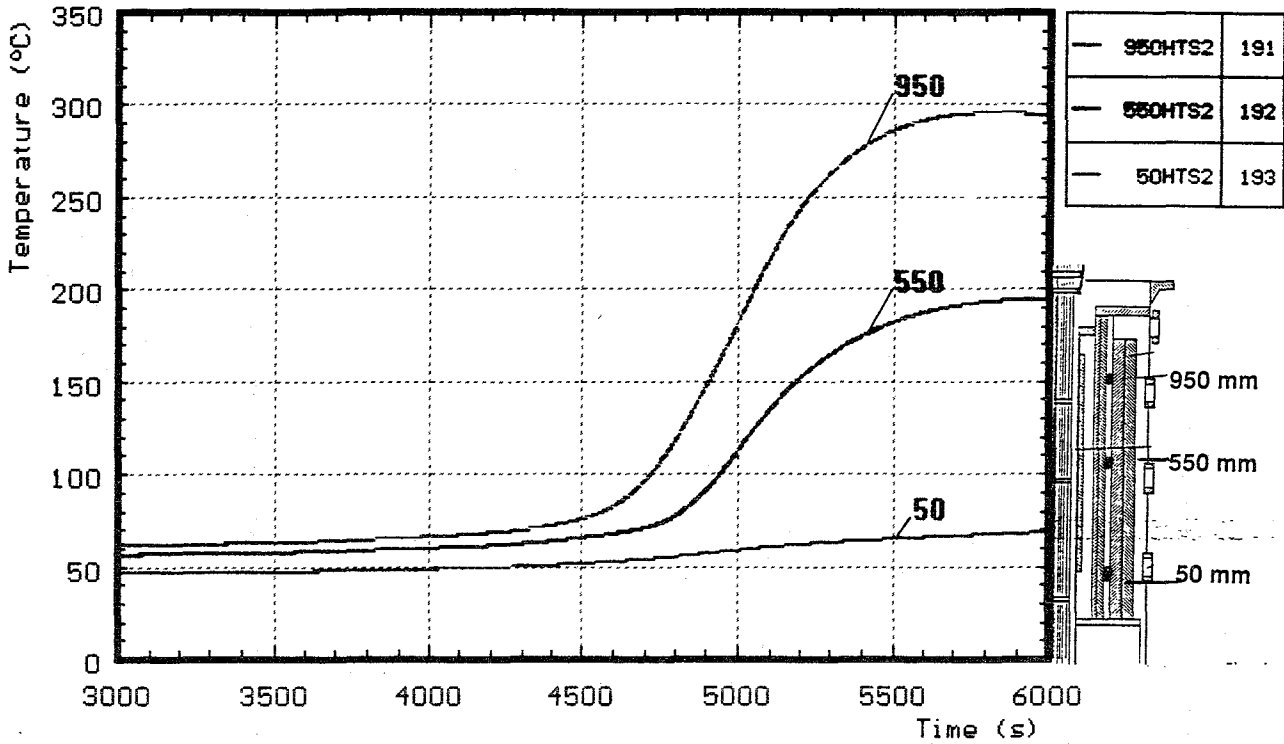


Fig. 56: CORA-W1; Temperatures of HTS, Temperatures of the HT shield at 192 mm radius

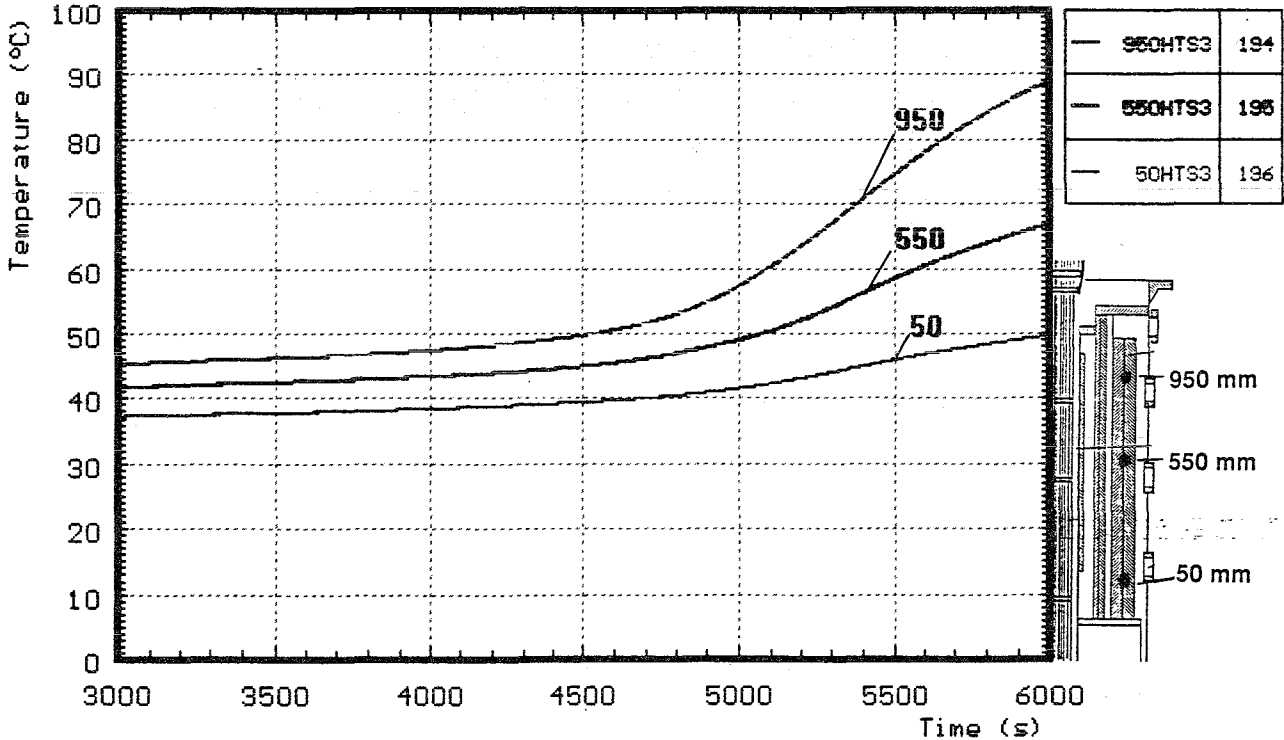


Fig. 57: CORA-W1; Temperatures of HTS, Temperatures of the HT shield at 255 mm radius

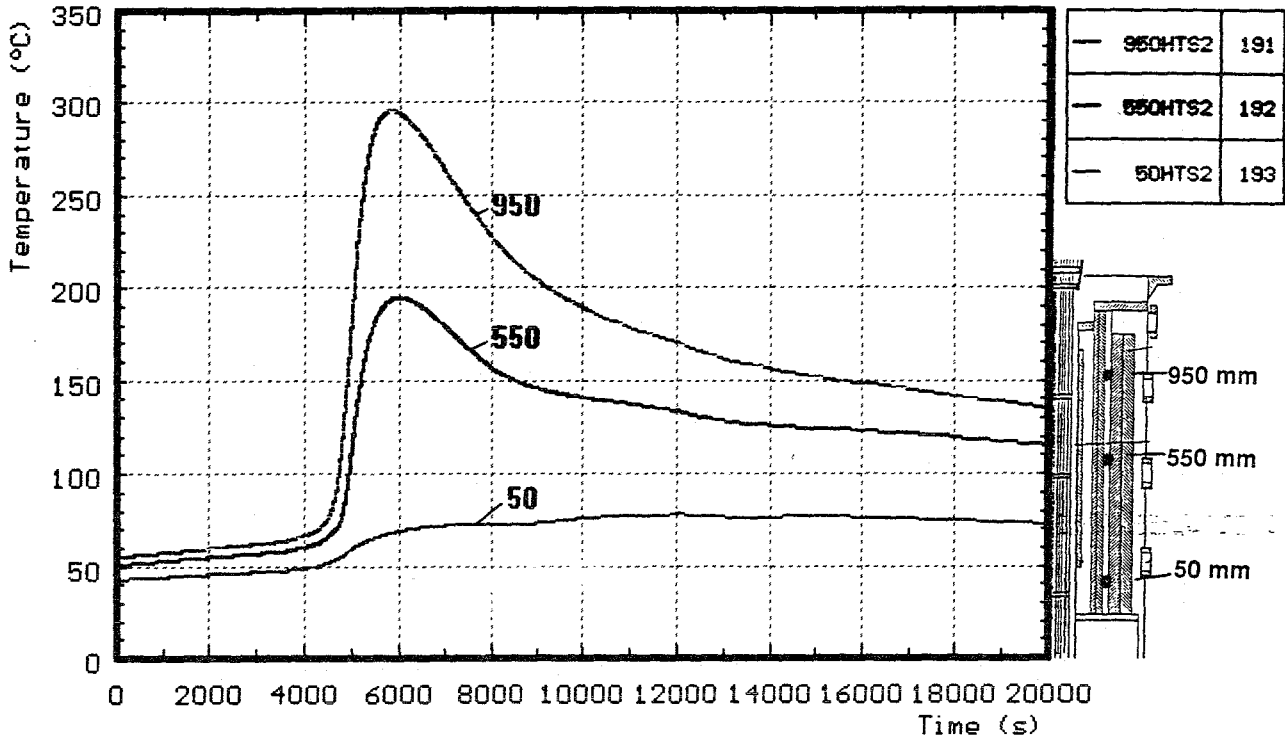


Fig. 58: CORA-W1; Temperatures of HTS, Temperatures of the HT shield at 192 mm radius (0 - 20000 s)

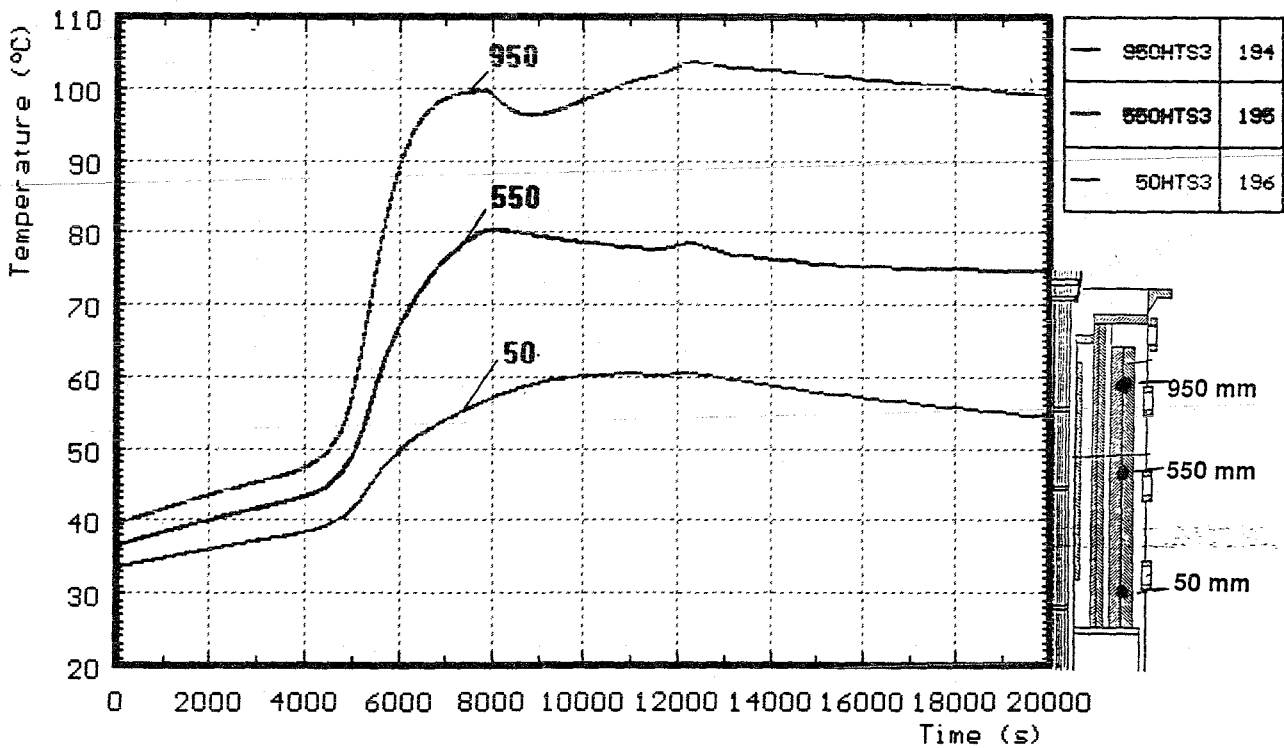


Fig. 59: CORA-W1; Temperatures of HTS, Temperatures of the HT shield at 255 mm radius (0 - 20000 s)

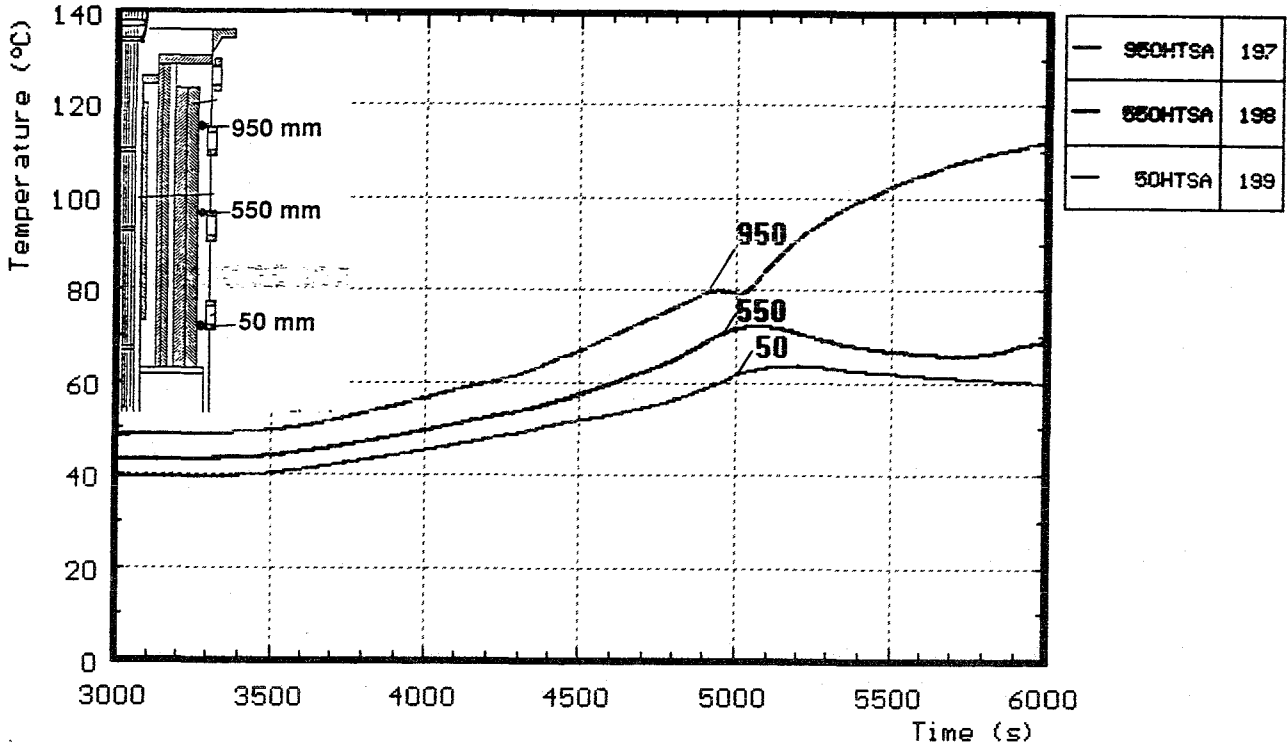


Fig. 60: CORA-W1; Temperatures of HTS, Temperatures of the HT shield at 293 mm radius

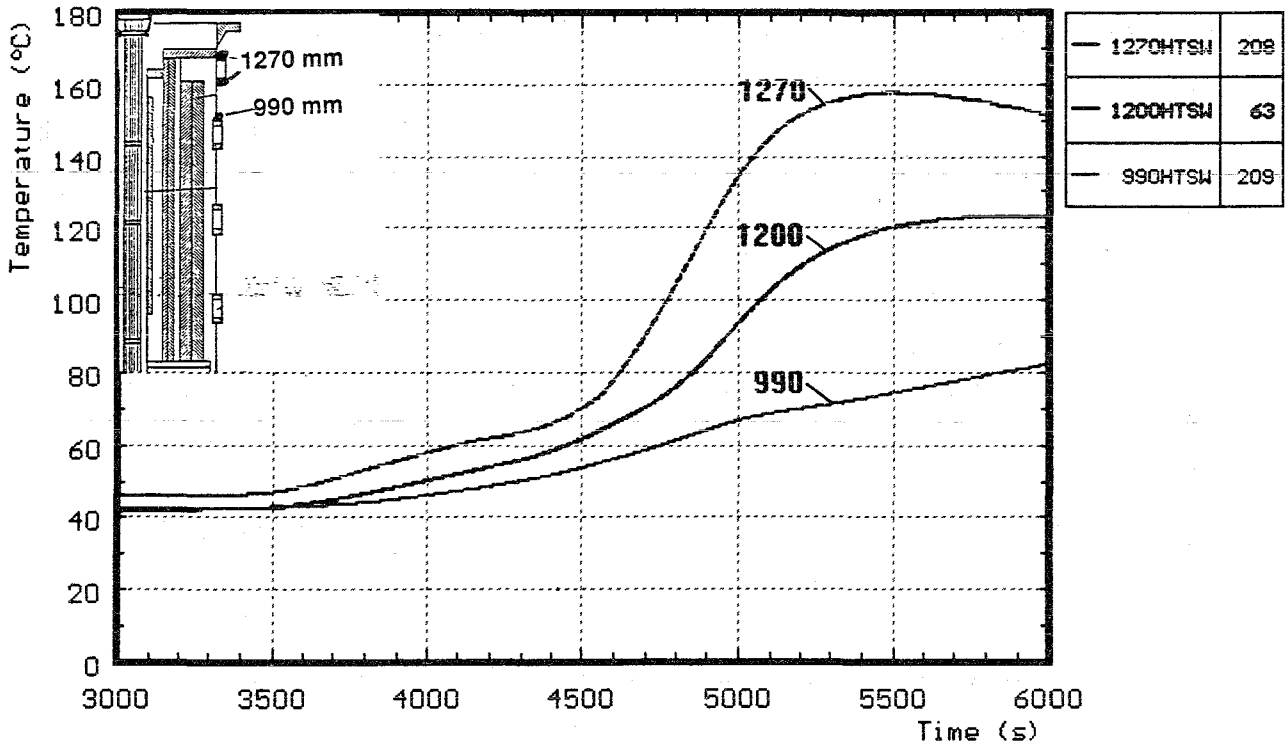


Fig. 61: CORA-W1; Temperatures of HTS, Temperatures at the outer surface of the HT shield, 380 mm radius

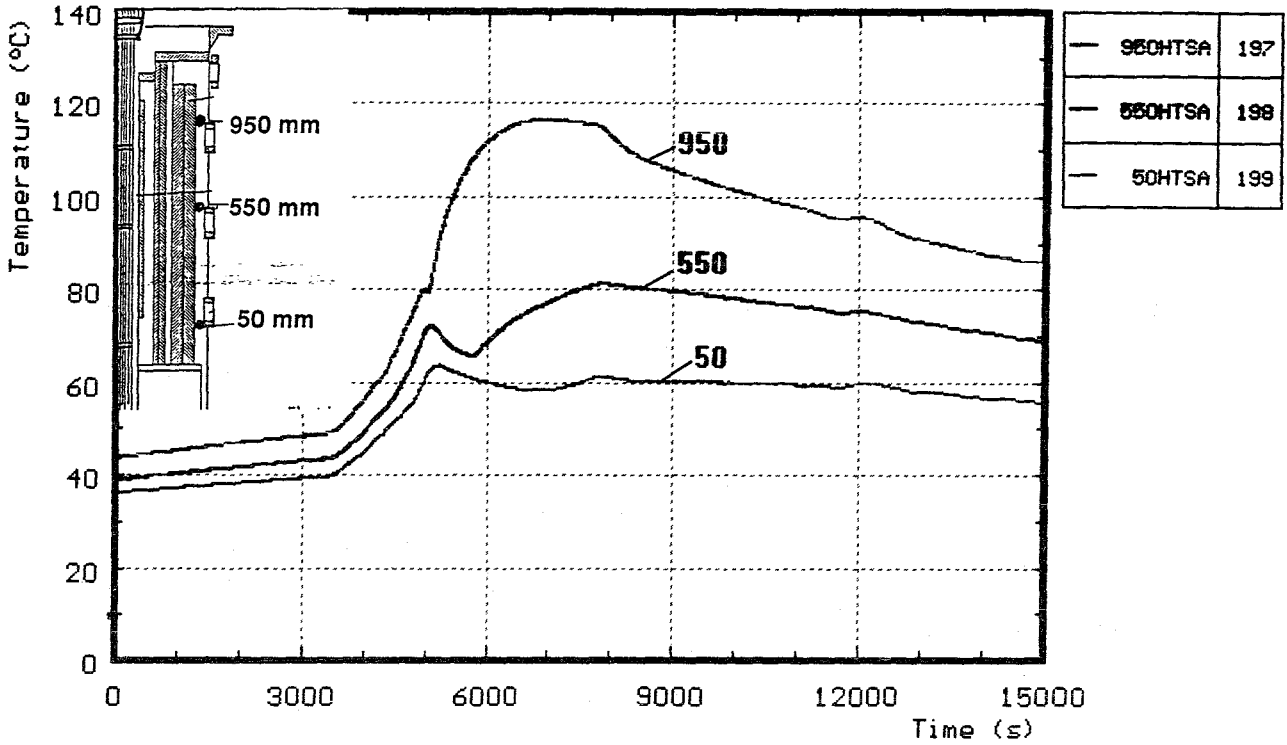


Fig. 62: CORA-W1; Temperatures of HTS, Temperatures of the HT shield at 293 mm radius (0 - 15000 s)

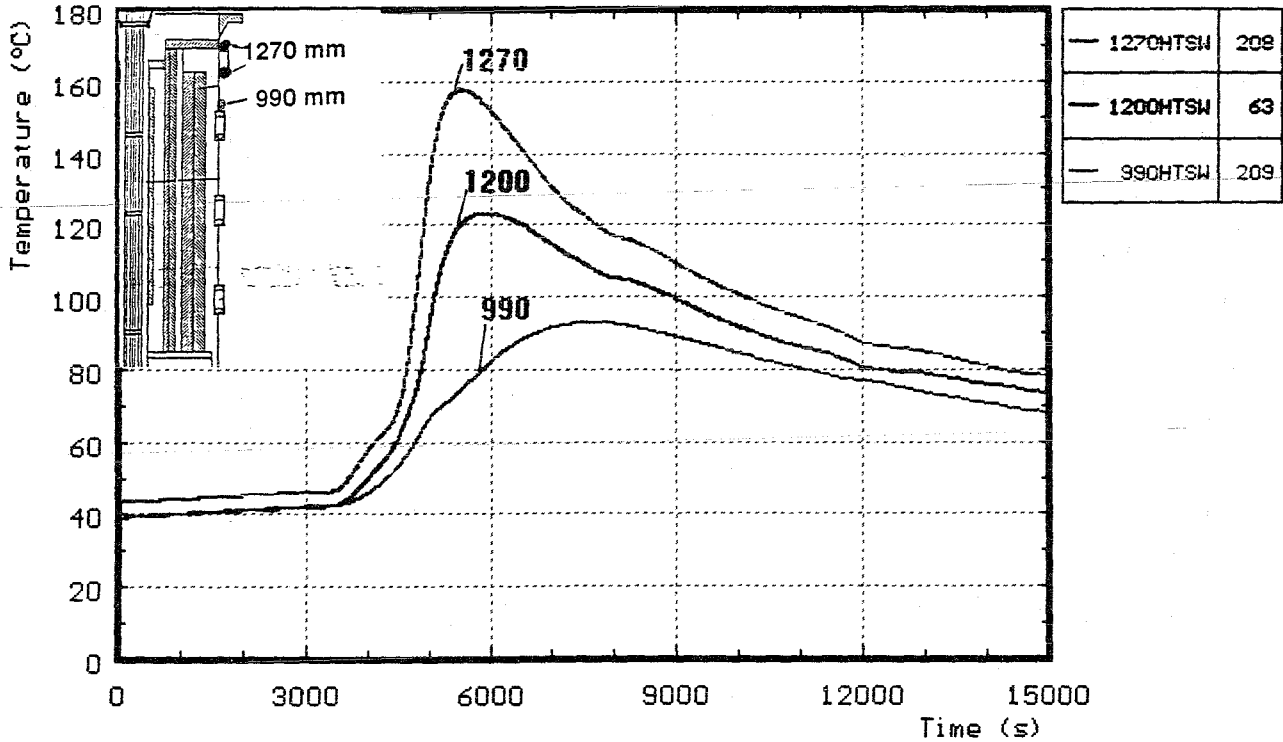


Fig. 63: CORA-W1; Temperatures of HTS, Temperatures at the outer surface of the HT shield at 380 mm radius (0 - 15000 s)

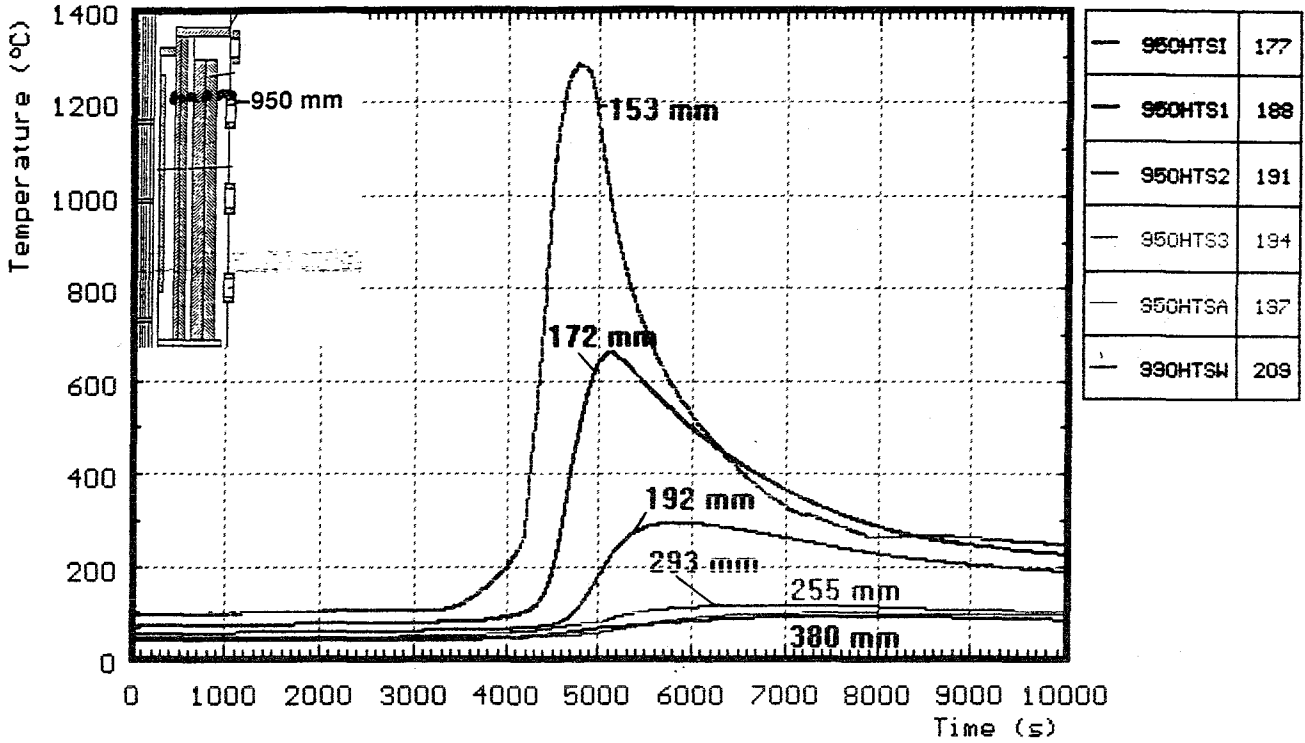


Fig. 64: CORA-W1; Temperatures of HTS, HT shield temperature at 950 mm elevation, at different radii (0 - 10000s)

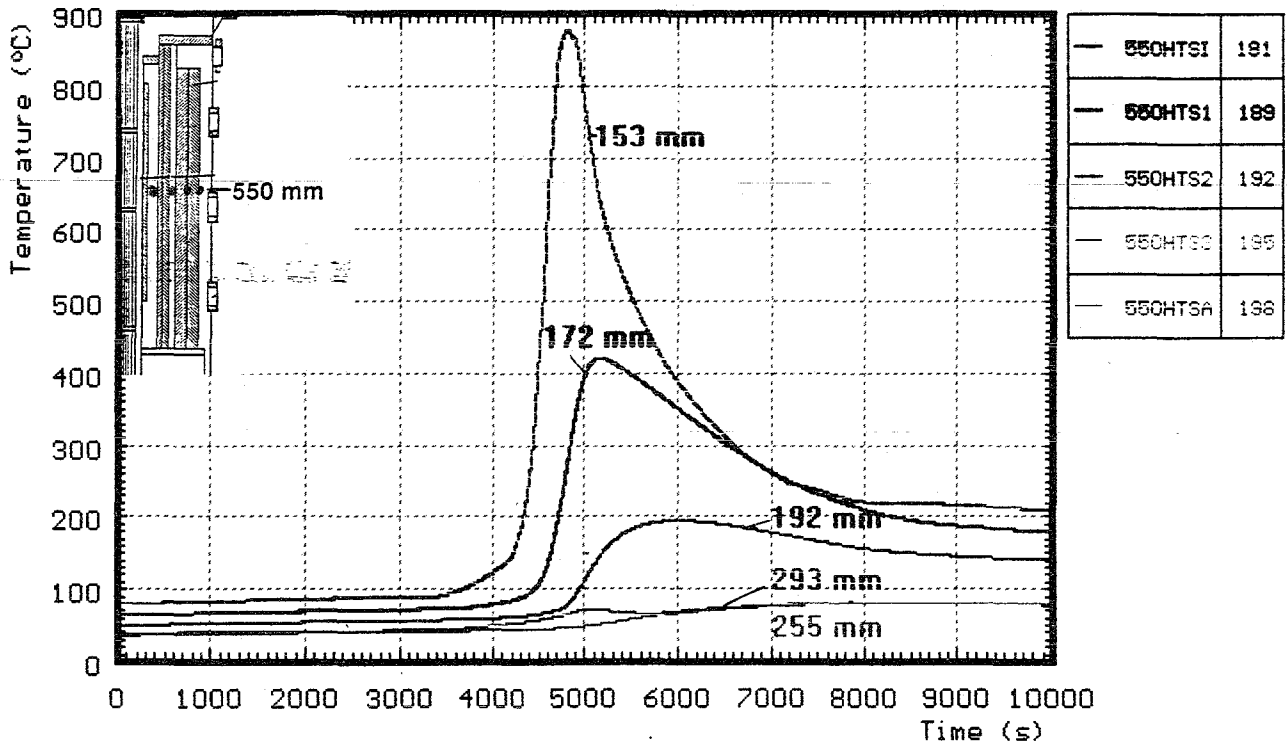


Fig. 65: CORA-W1; Temperatures of HTS, HT shield temperature at 550 mm elevation, at different radii (0 - 10000s)

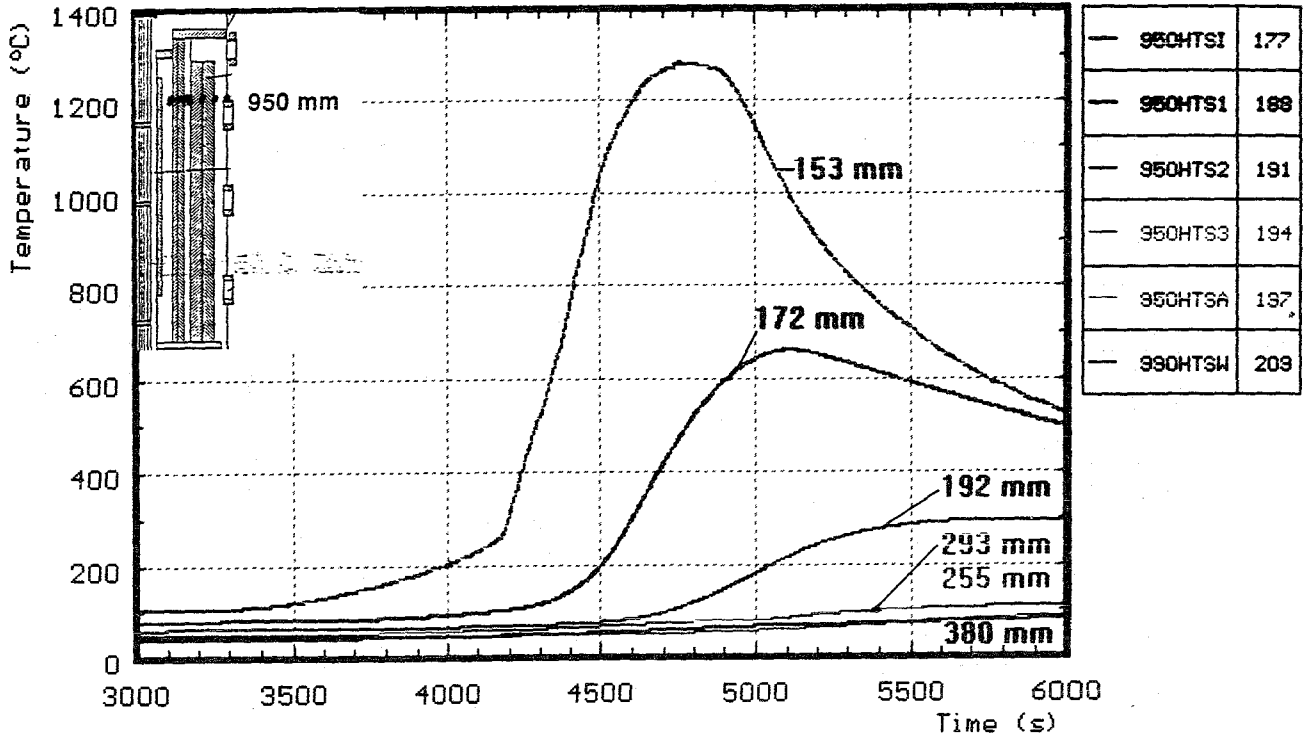


Fig. 66: CORA-W1; Temperatures of HTS, HT shield temperature at 950 mm elevation, at different radii (3000 - 6000s)

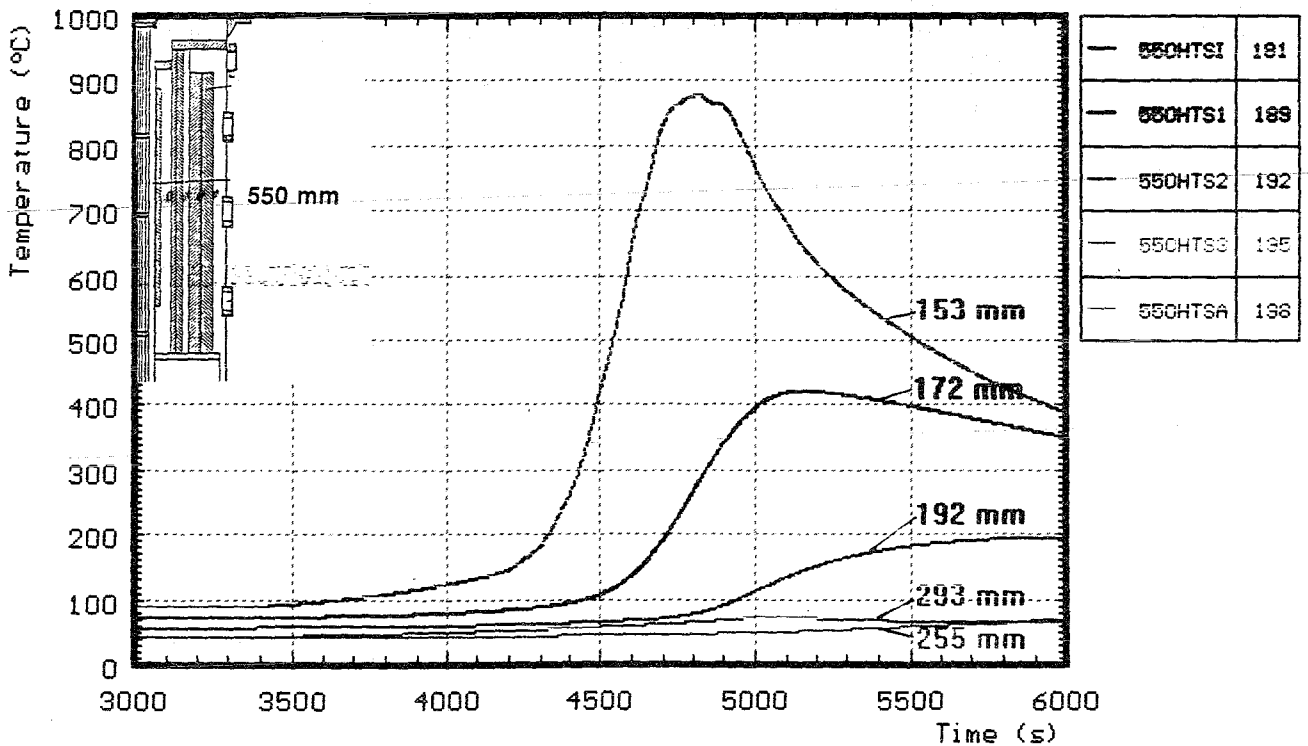


Fig. 67: CORA-W1; Temperatures of HTS, HT shield temperature at 550 mm elevation, at different radii (3000 - 6000s)

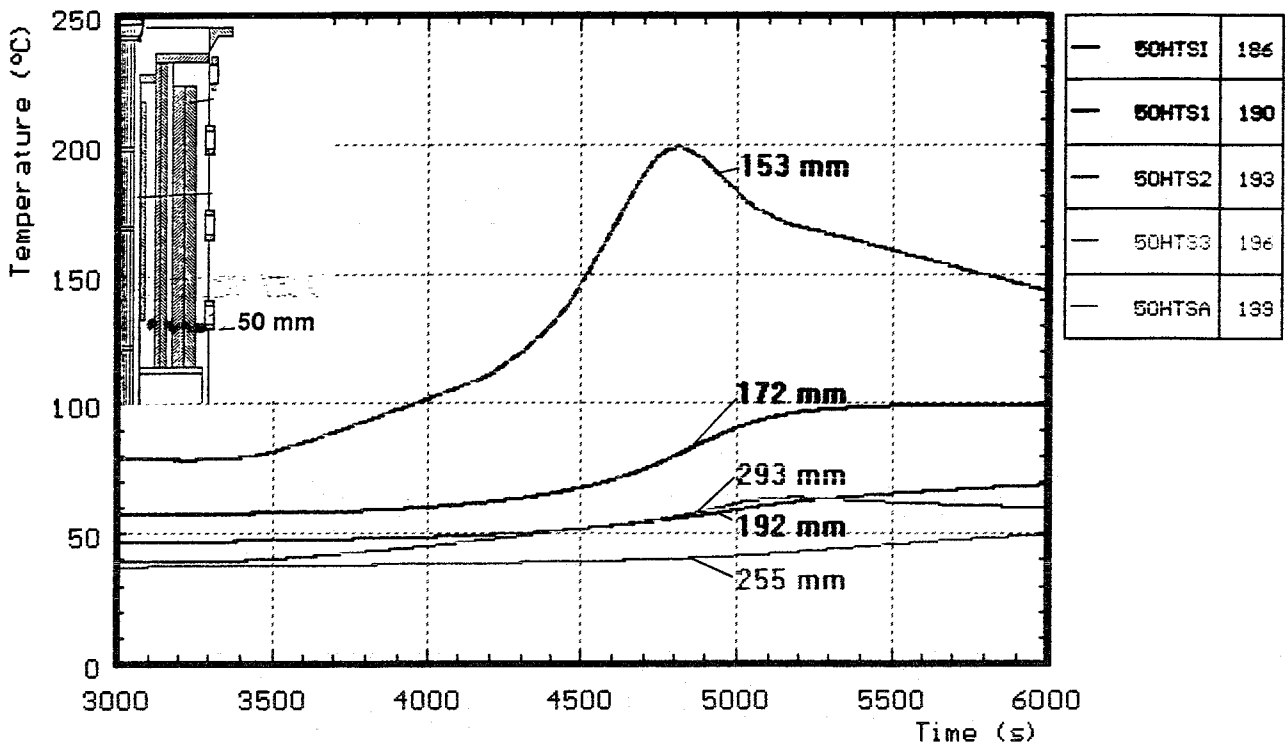


Fig. 68: CORA-W1; Temperatures of HTS, HT shield temperatures at 50 mm elevation (3000 - 6000s)

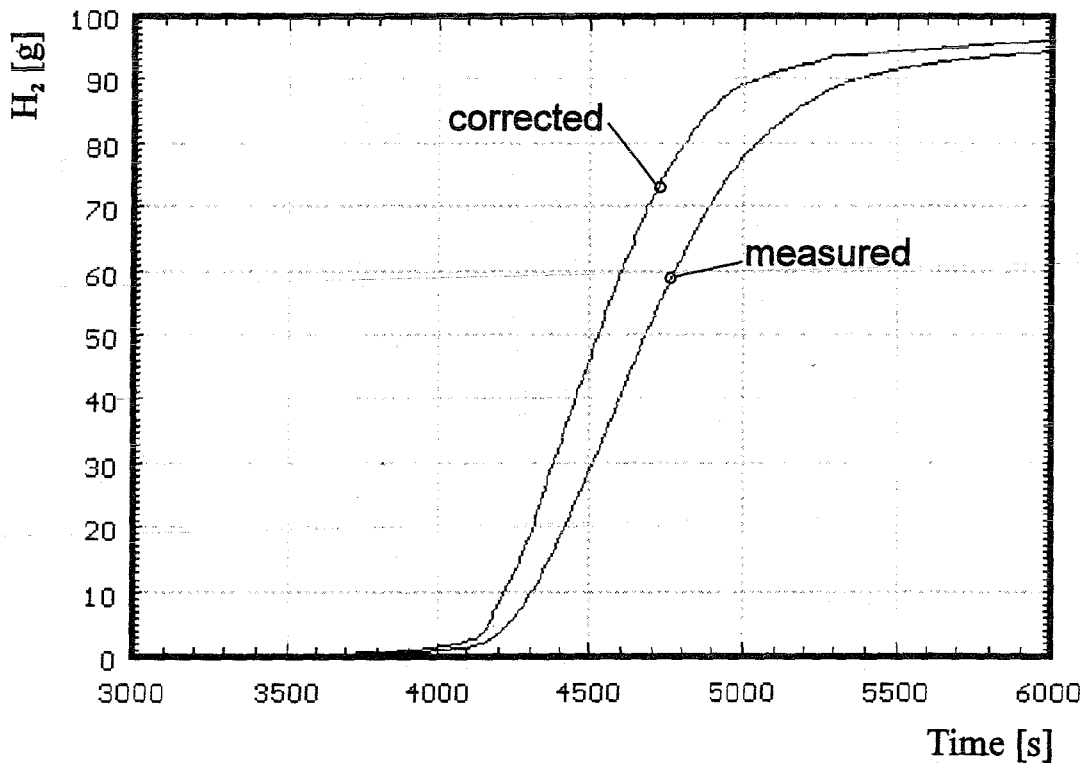
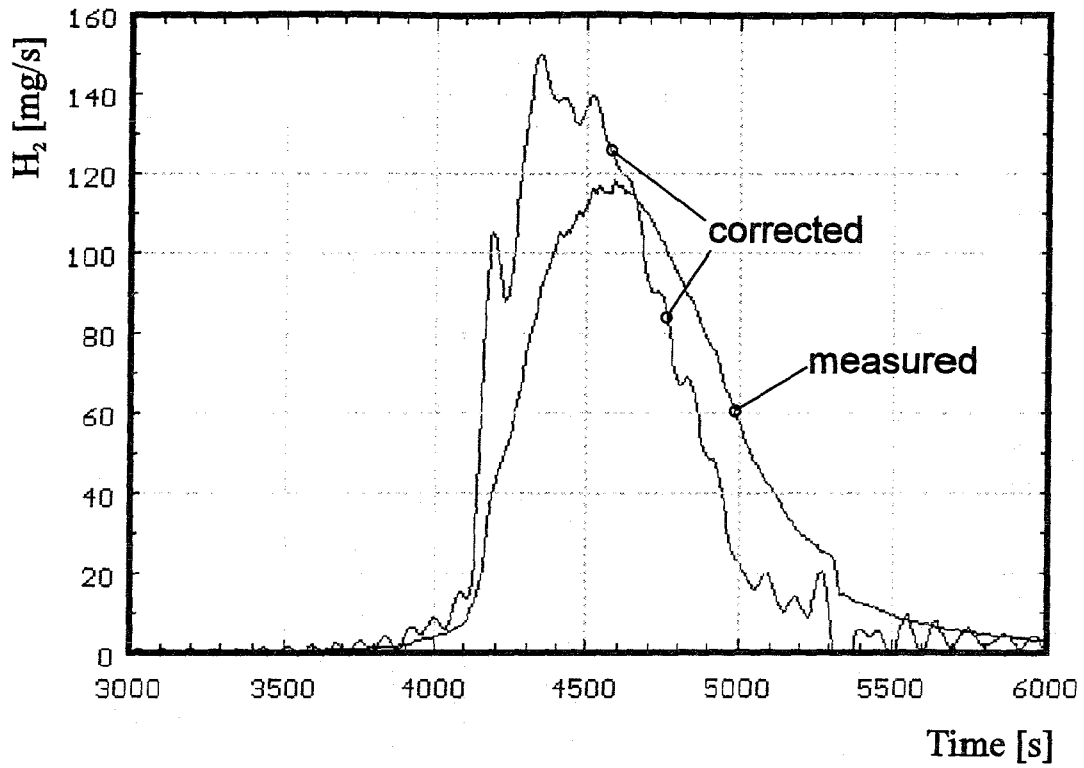


Fig. 69: Hydrogen production in test CORA-W1; production rate (top) and integral values (bottom)

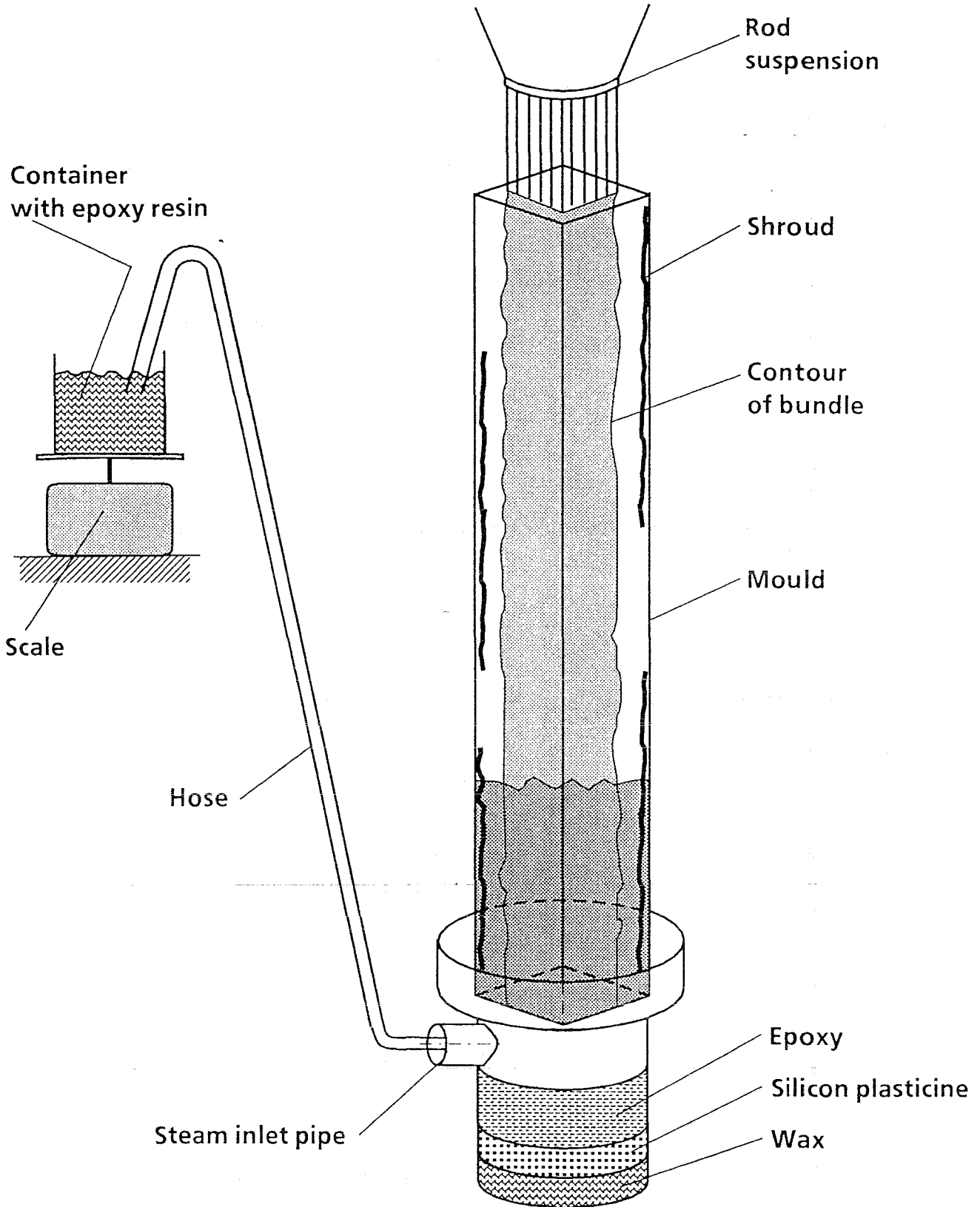


Fig. 70: CORA-W1; Epoxying process of the tested bundle

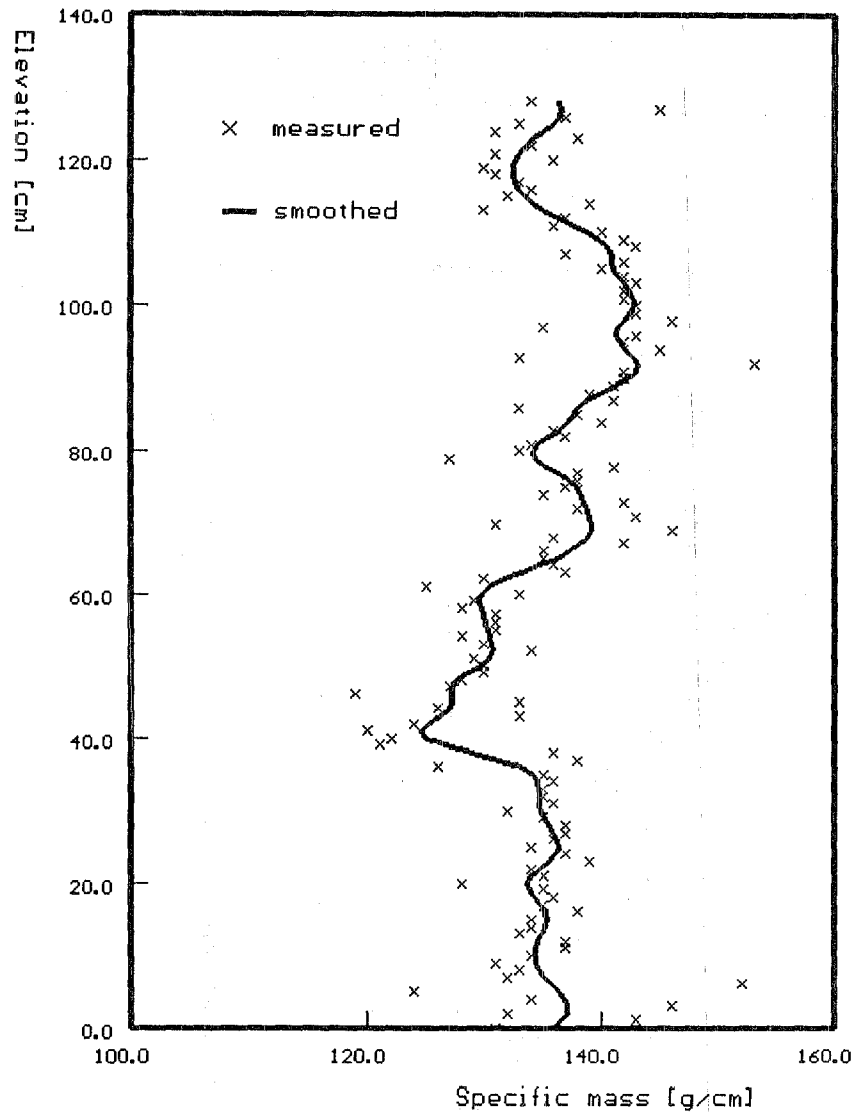


Fig. 71: CORA-W1; Axial distribution of the bundle fill-up with epoxy resin

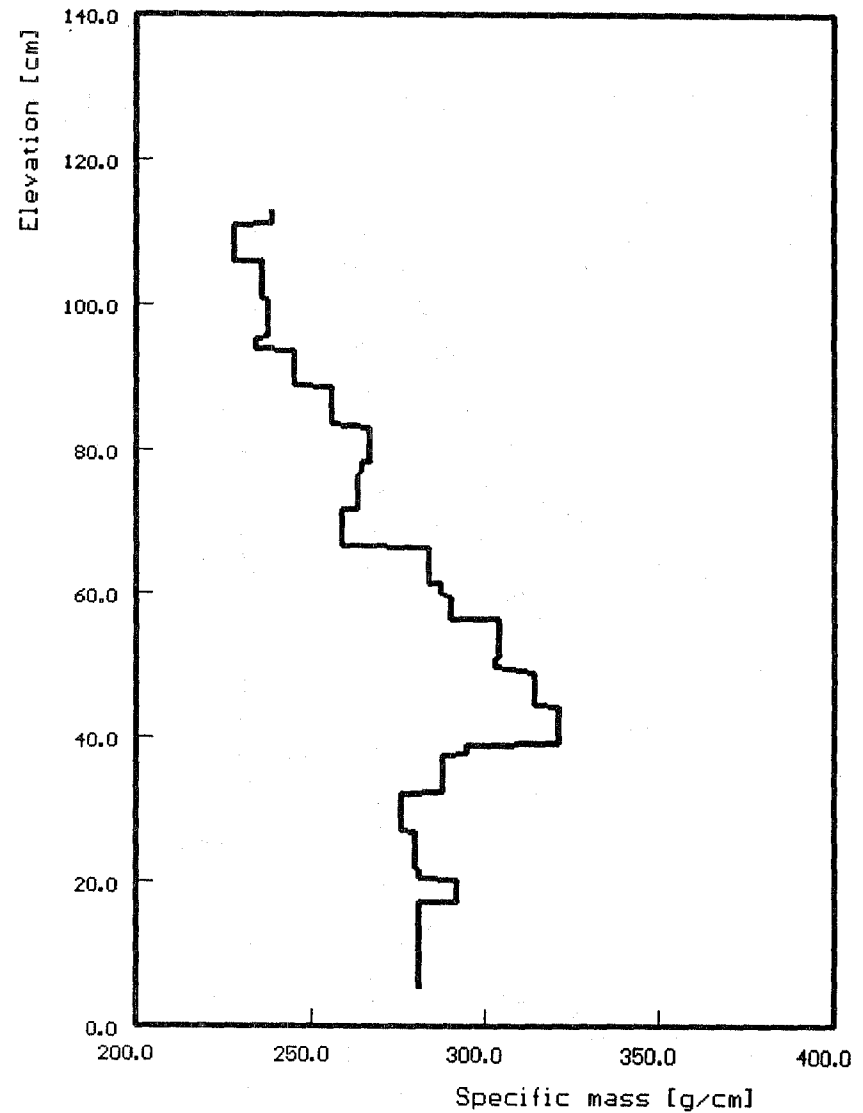


Fig. 72: CORA-W1; Axial mass distribution bundle segments filled with epoxy resin

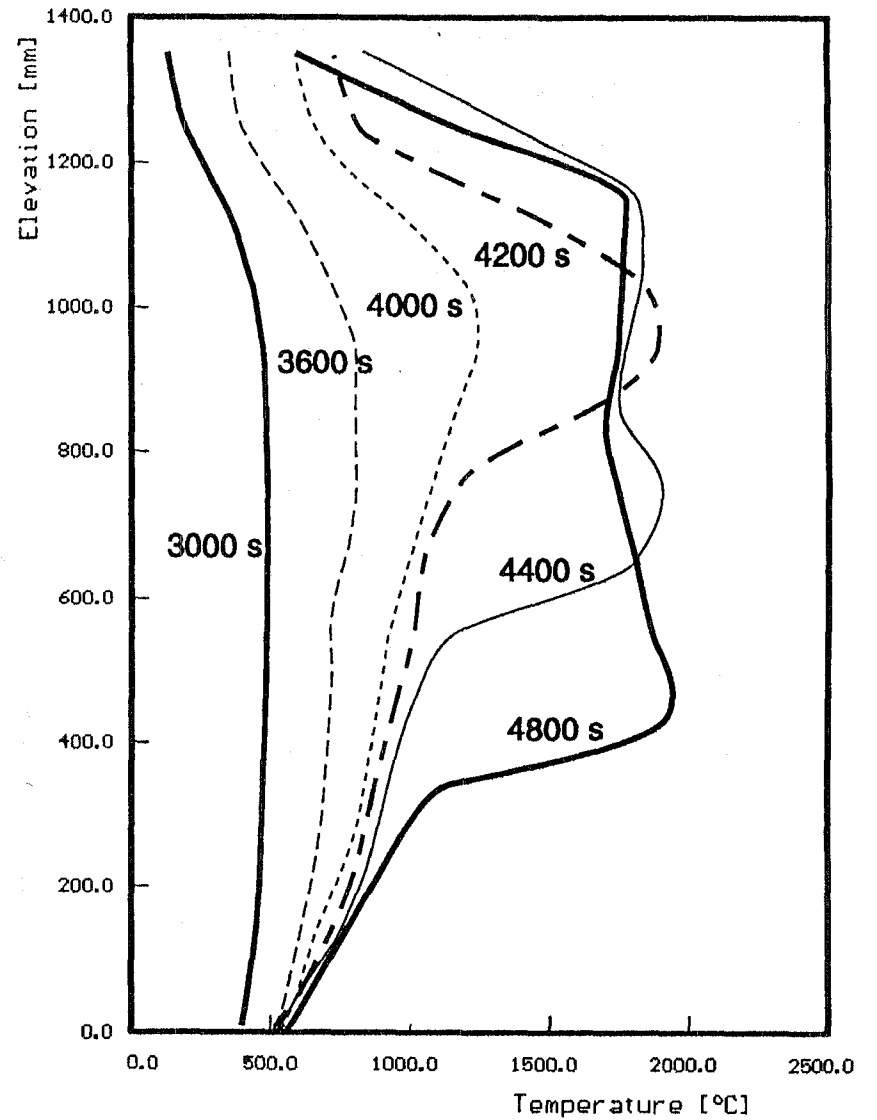
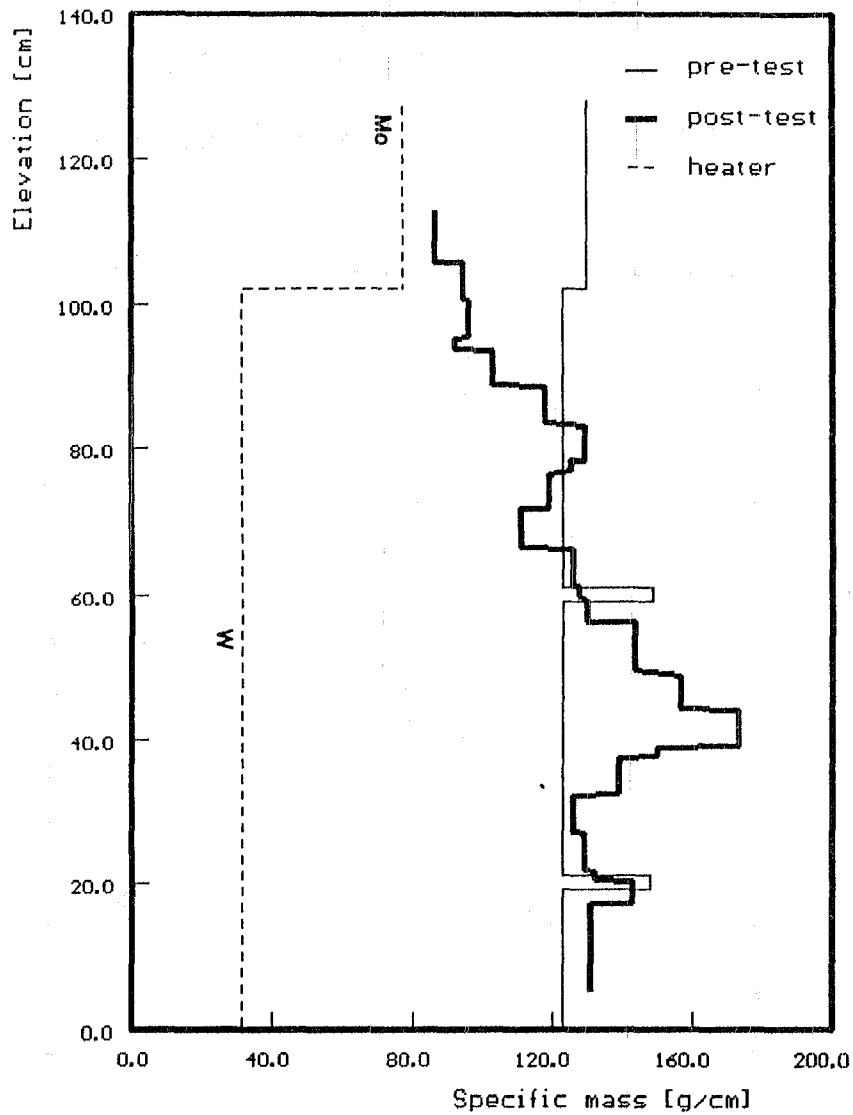


Fig. 73: CORA- W1: Axial mass distribution after the test and axial temperature distribution during the test

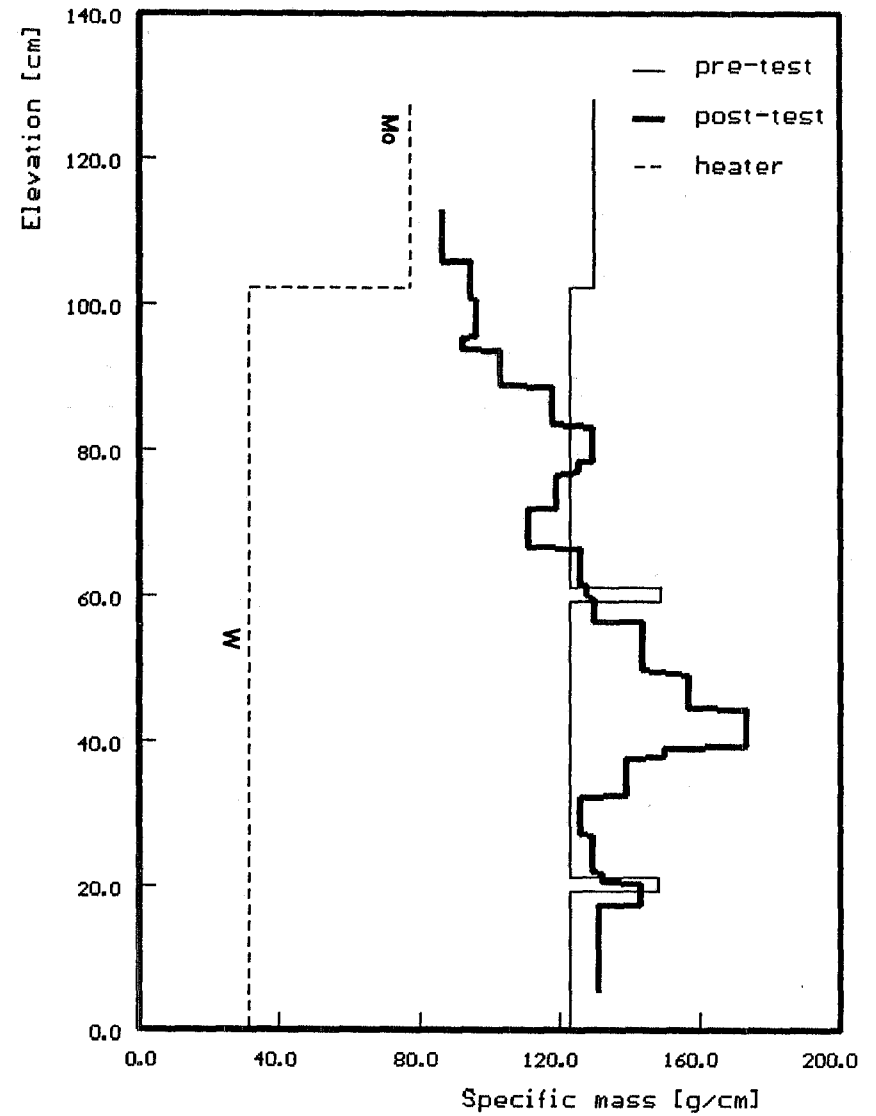
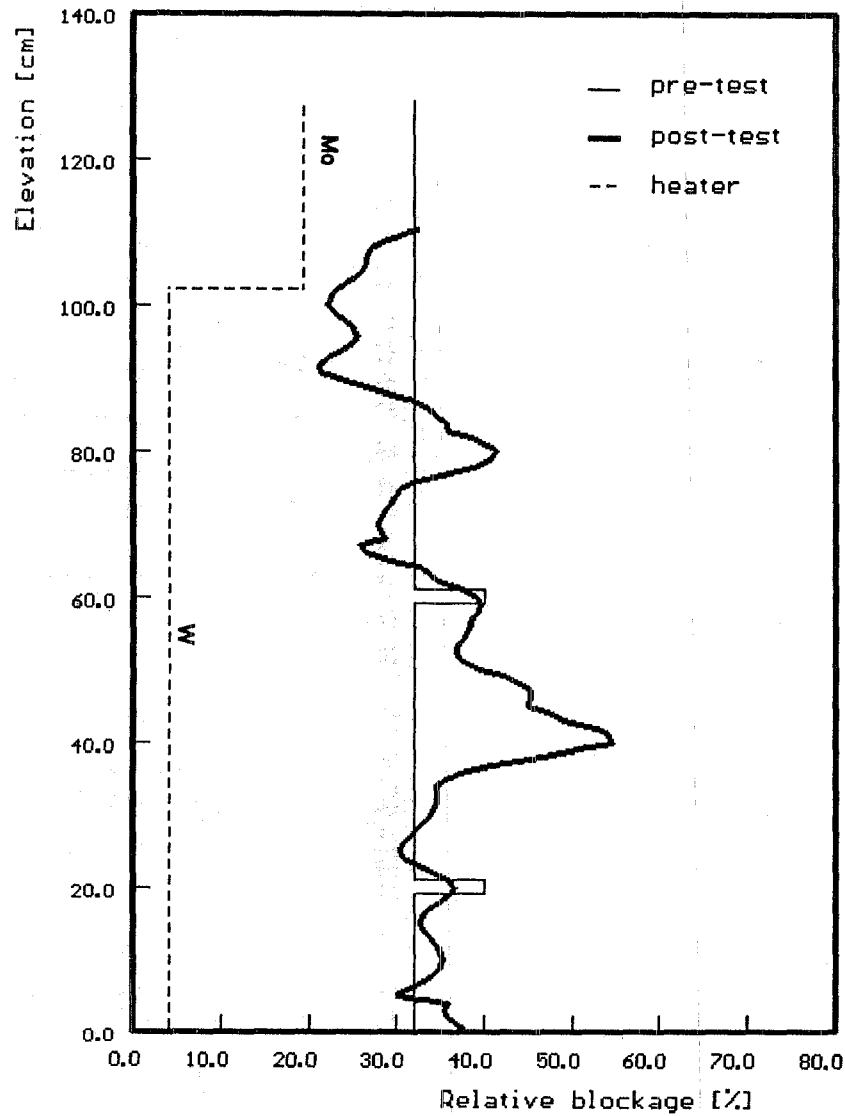


Fig. 74: CORA-W1; Axial volume distribution (relative blockage within the shroud) and axial mass distribution after the test

0°

60°

120°

180°

240°

300°

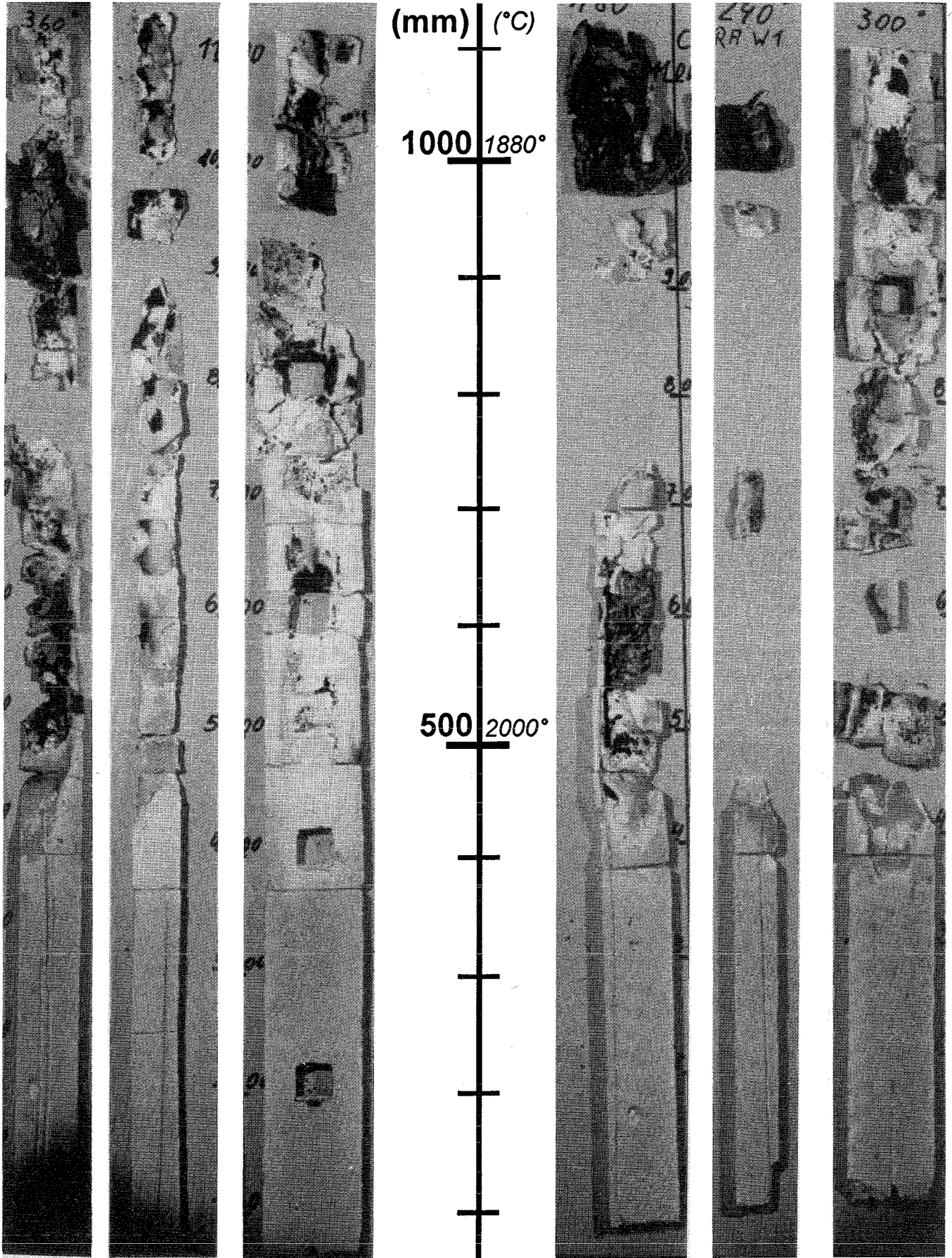


Fig. 75: CORA-W1; Posttest view of the inner side of the shroud insulation

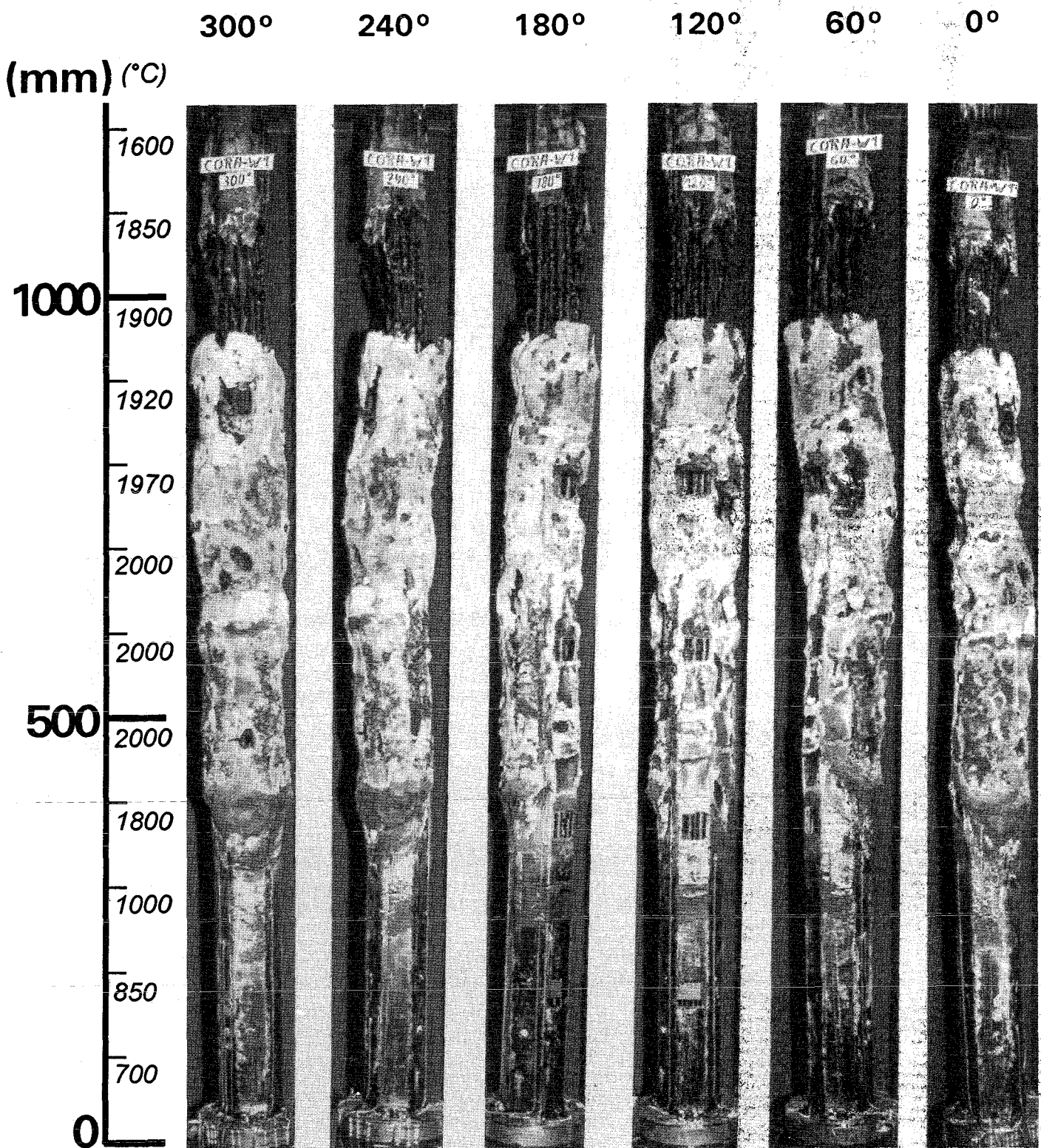


Fig. 76: CORA-W1; Posttest appearance of the entire bundle length after removal of the shroud insulation

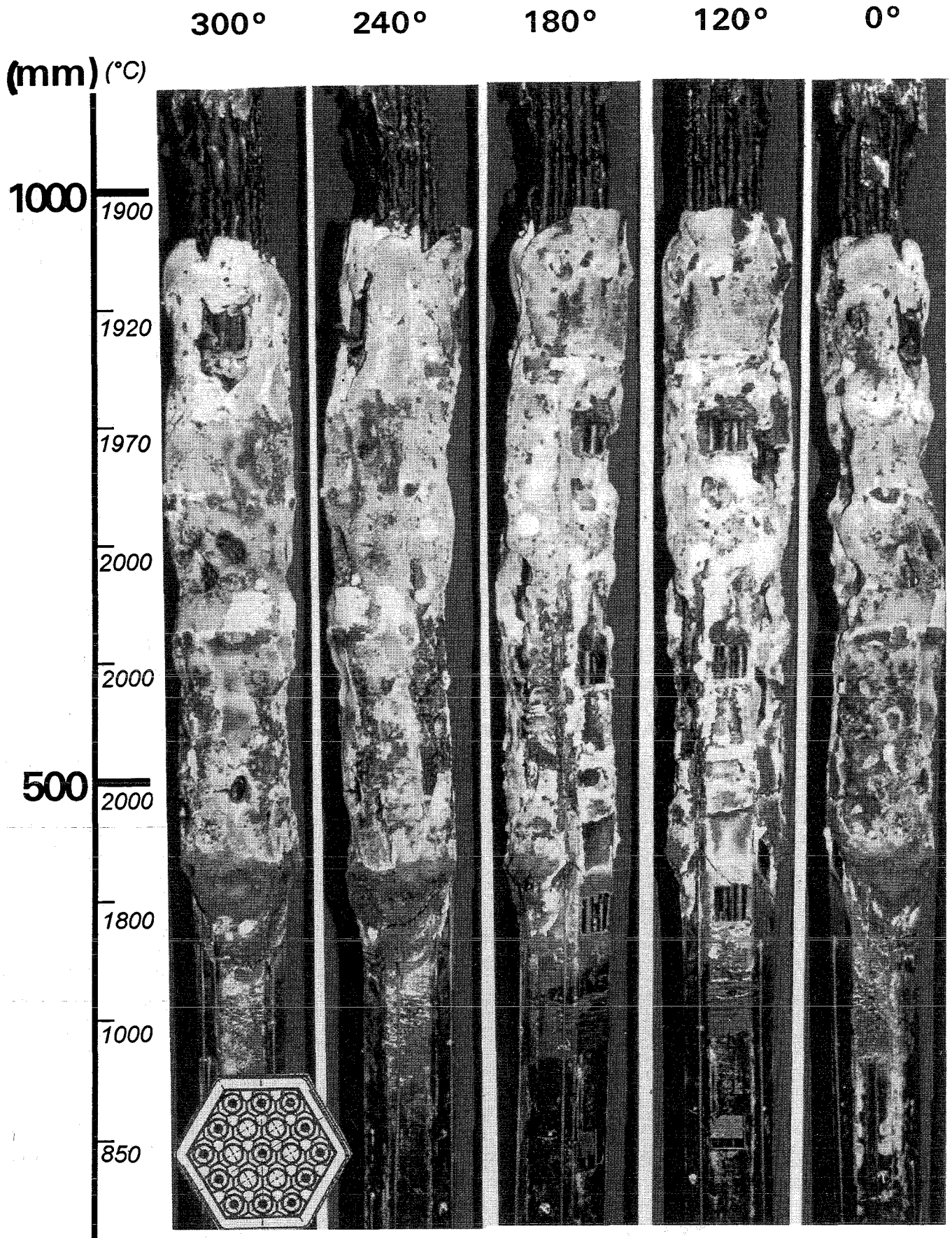


Fig. 77: Enlarged posttest view of bundle CORA-W1 after removal of the shroud insulation

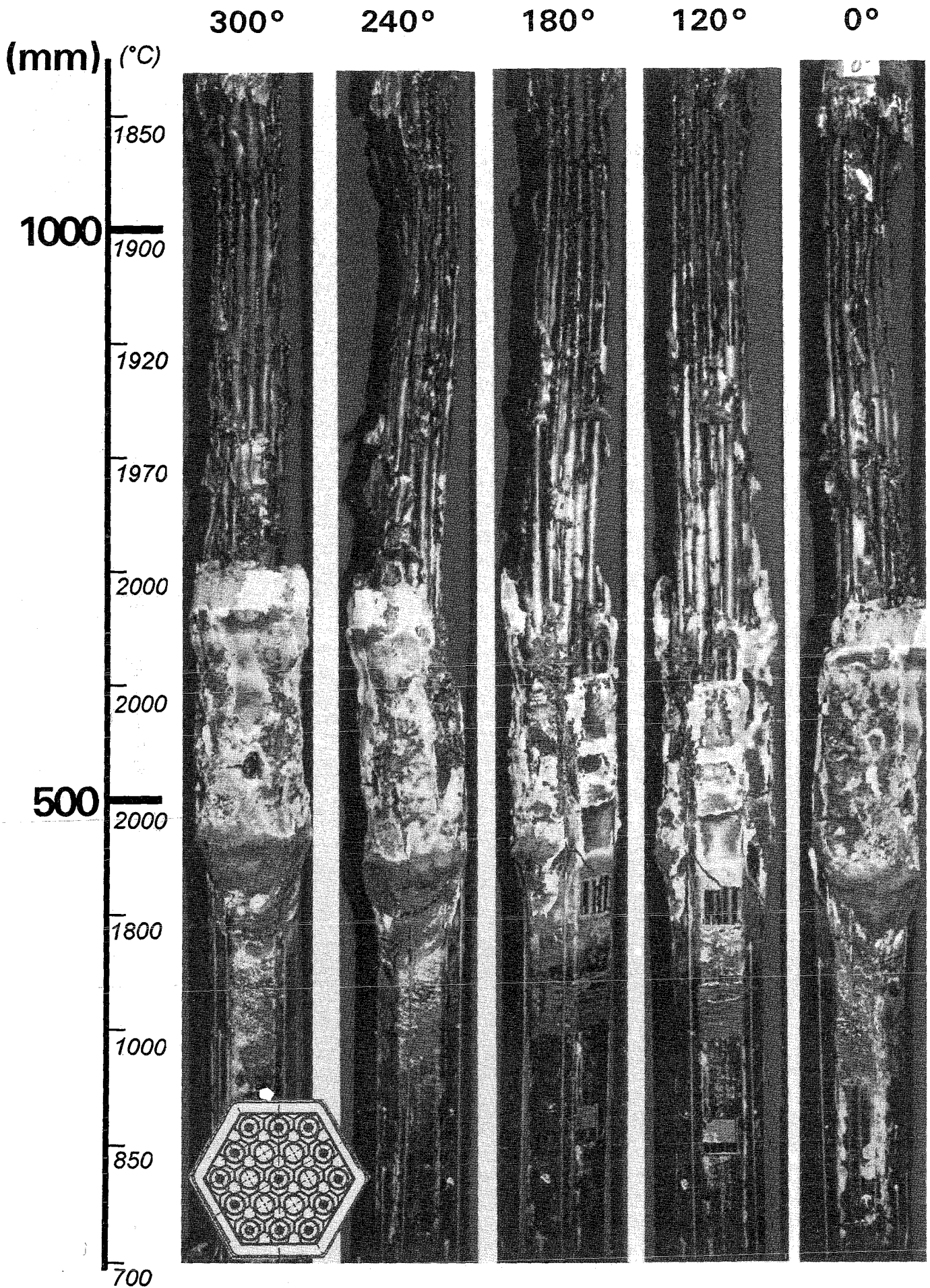


Fig. 78: Posttest view of the bundle CORA-W1 after partial removal of the shroud

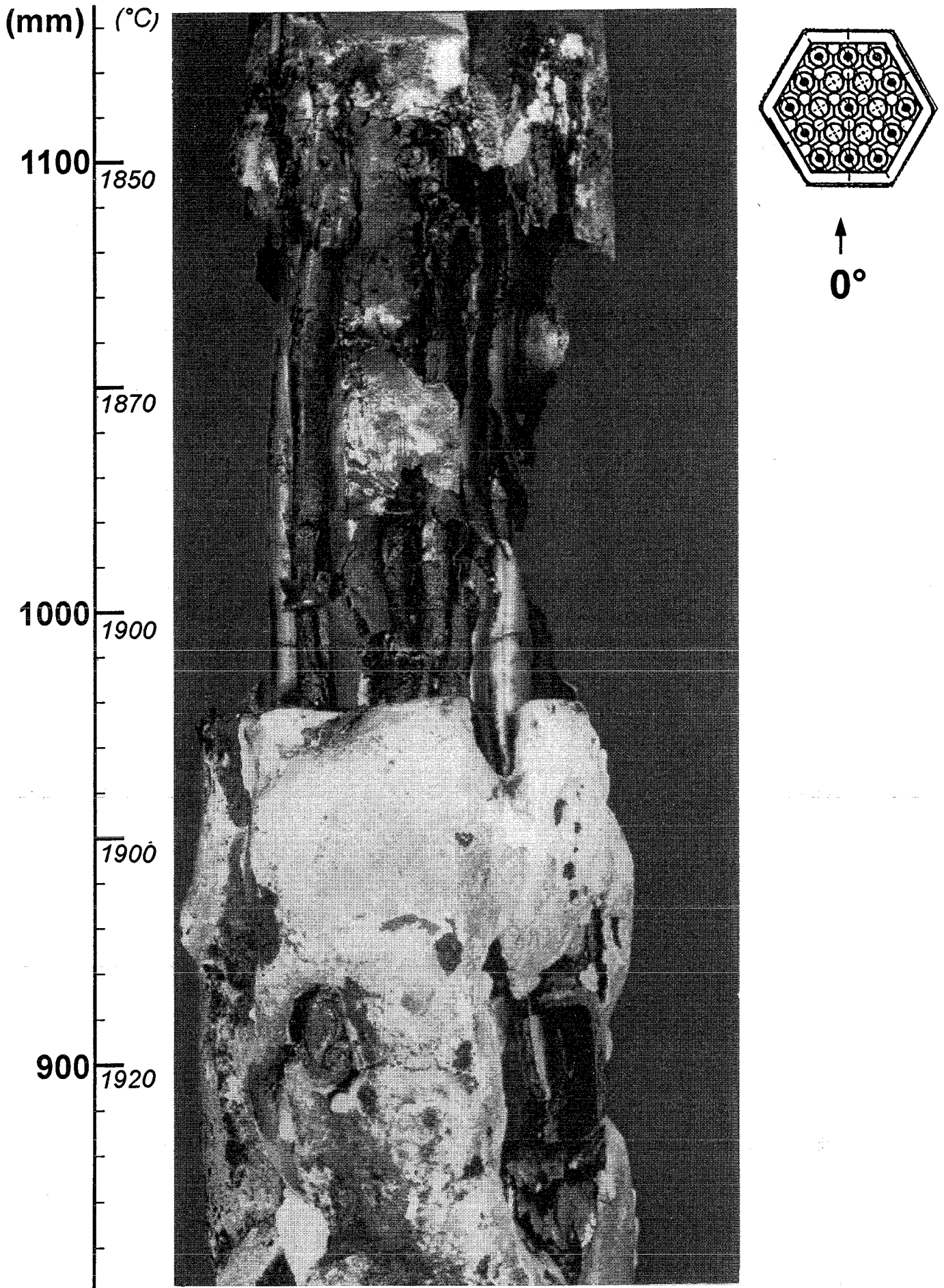


Fig. 79: CORA-W1; Posttest view, 0° orientation

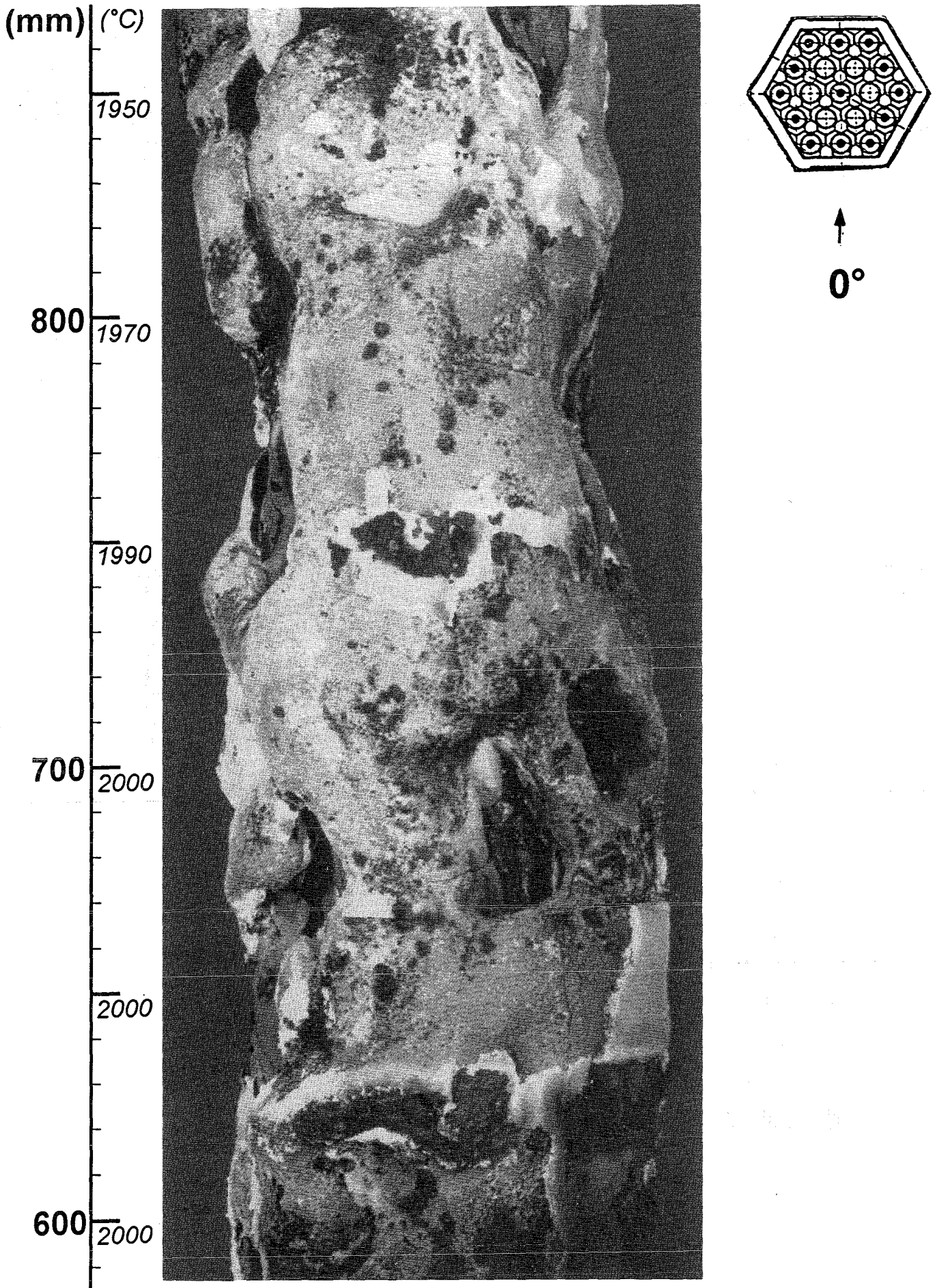


Fig. 80: CORA-W1; Posttest view, 0° orientation

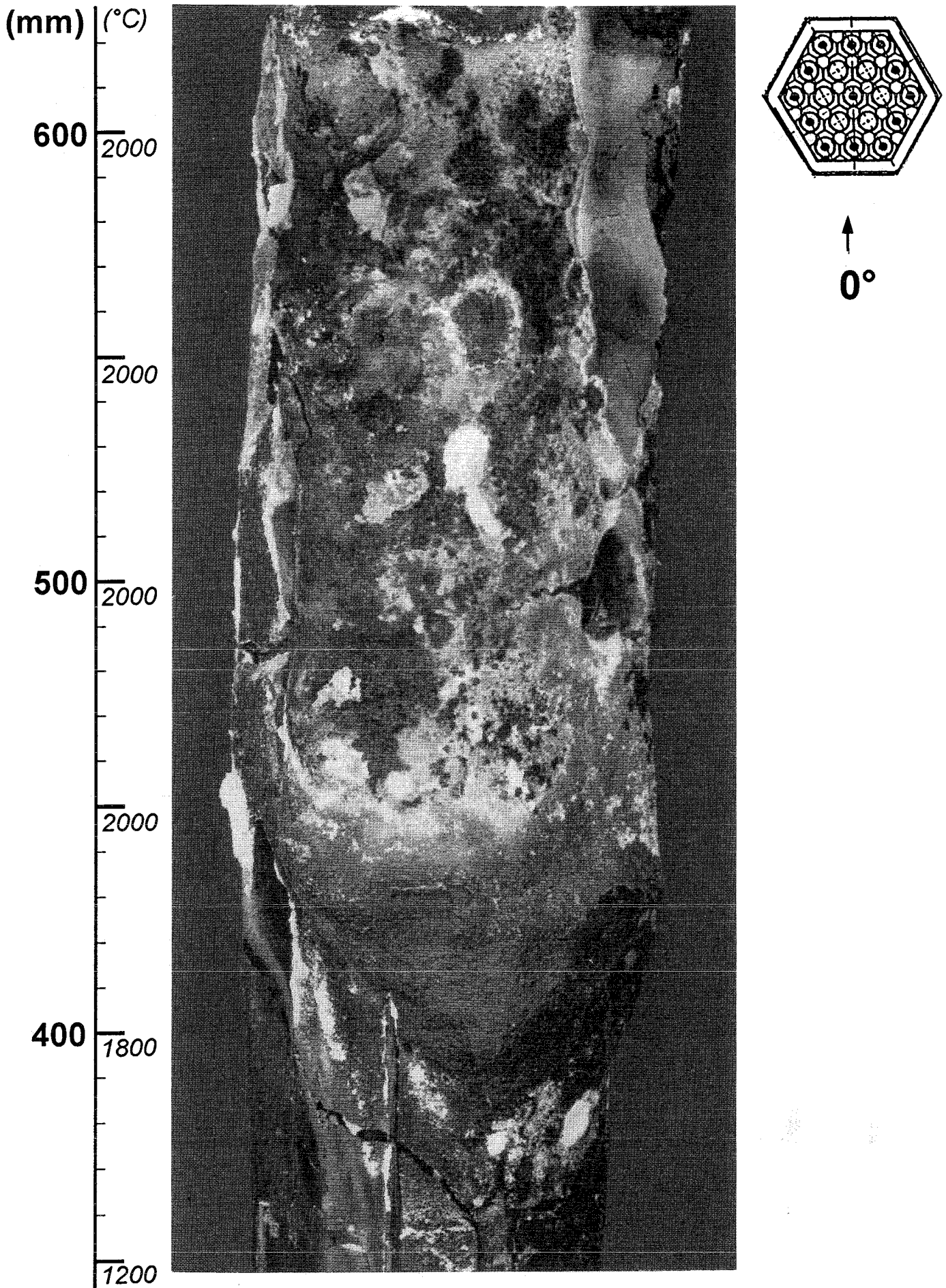


Fig. 81: CORA-W1; Posttest view, 0° orientation

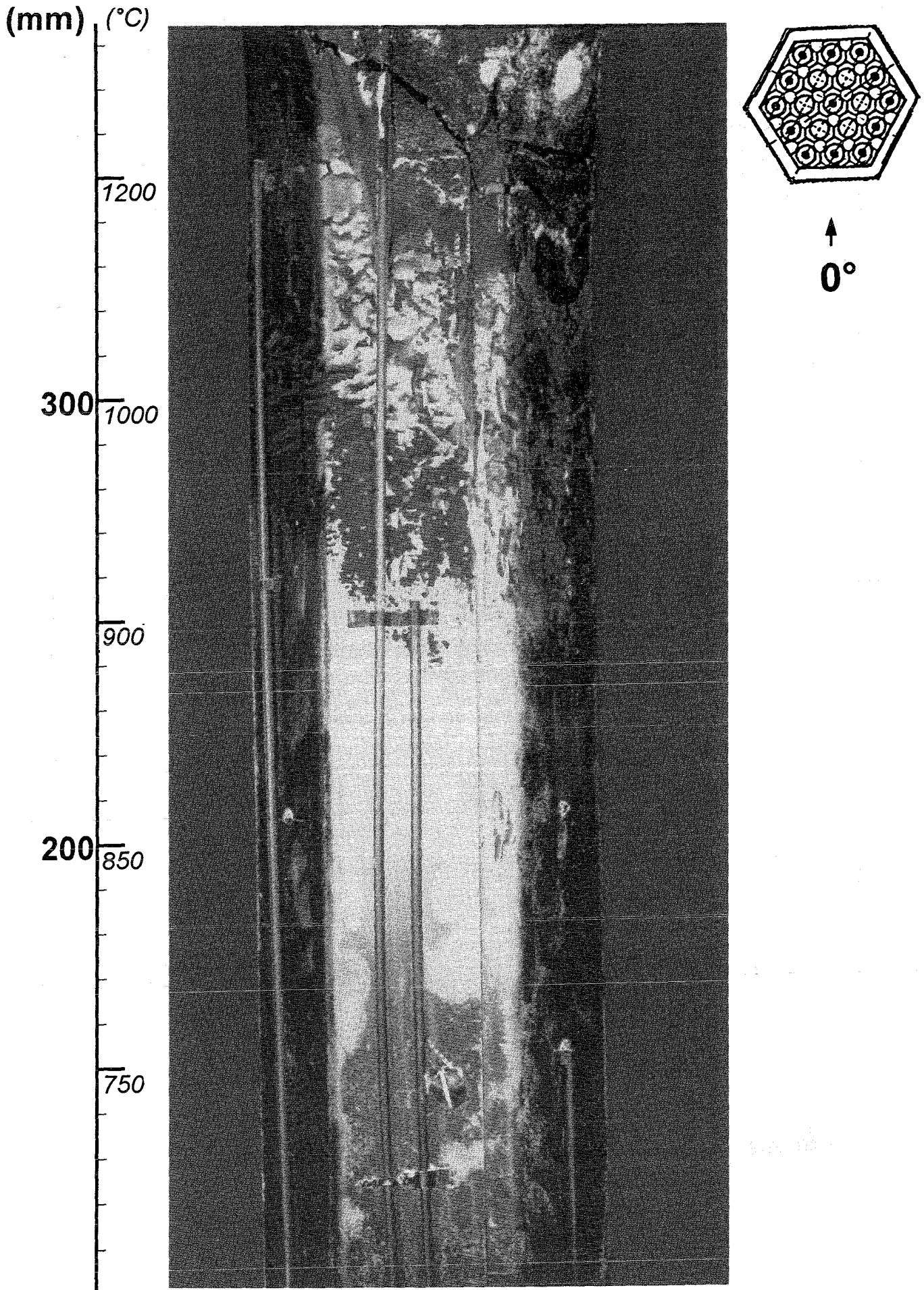


Fig. 82: CORA-W1; Posttest view, 0° orientation

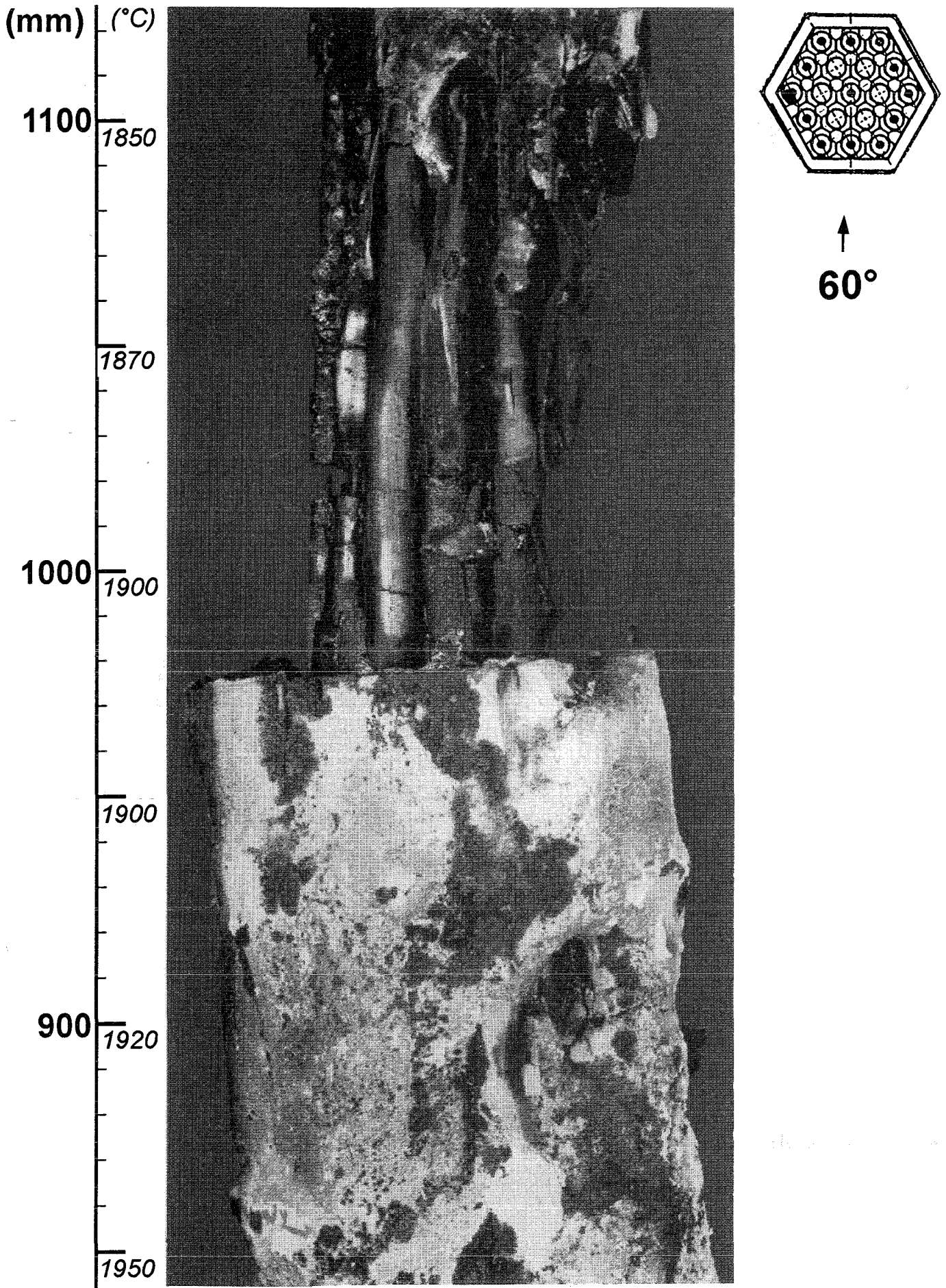


Fig. 83: CORA-W1; Posttest view, 60° orientation

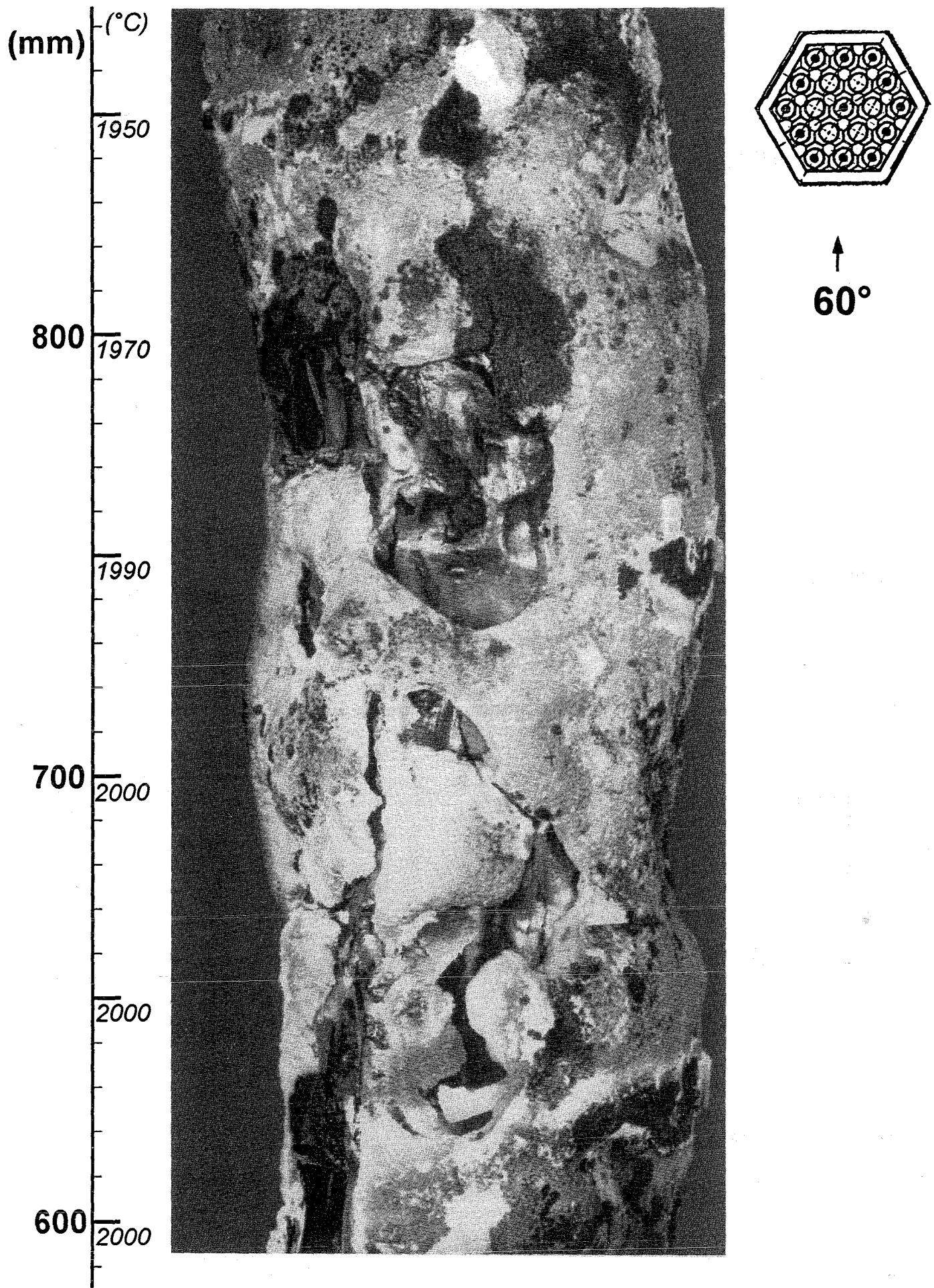


Fig. 84: CORA-W1; Posttest view, 60° orientation

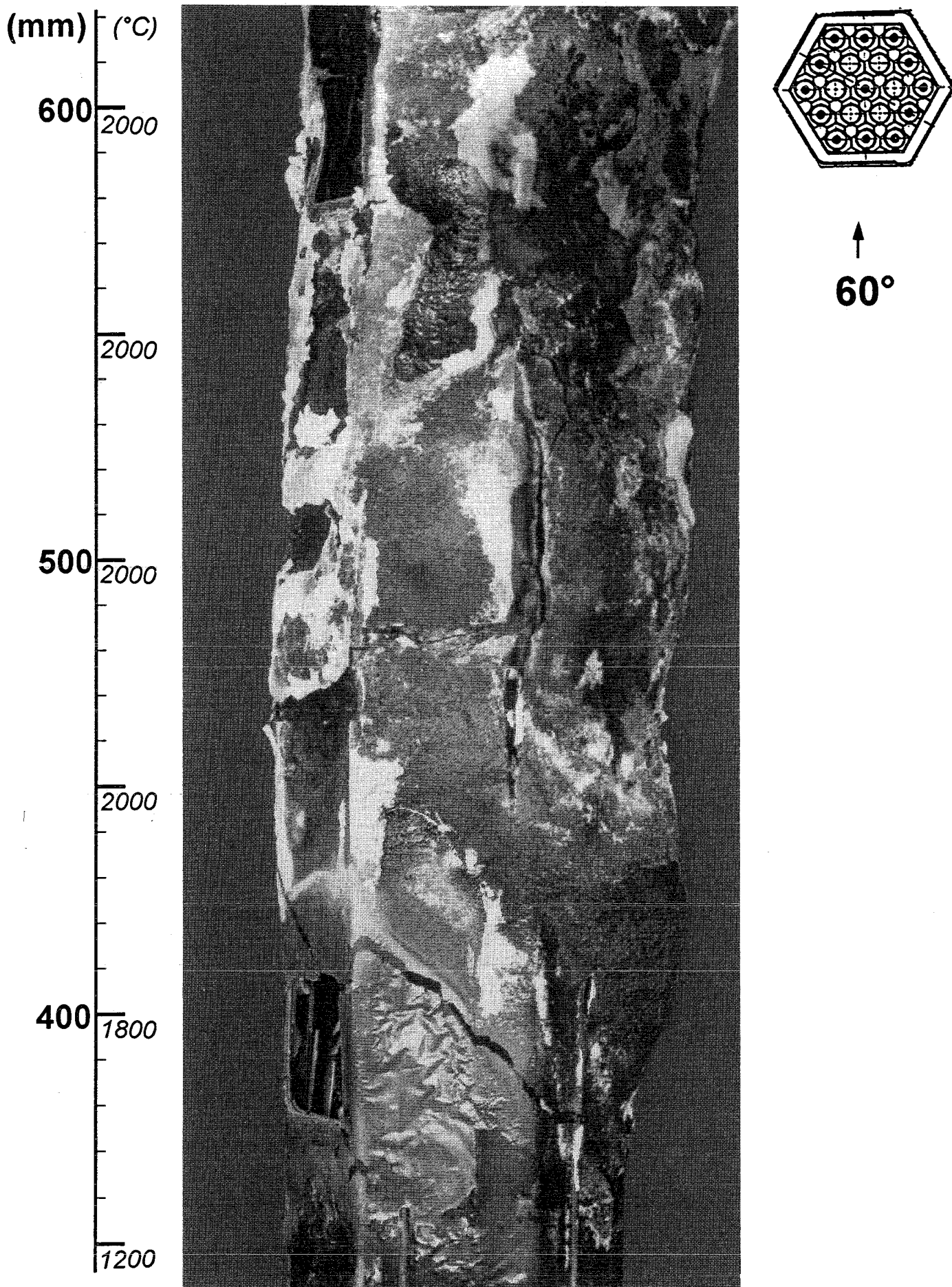


Fig. 85: CORA-W1; Posttest view, 60° orientation

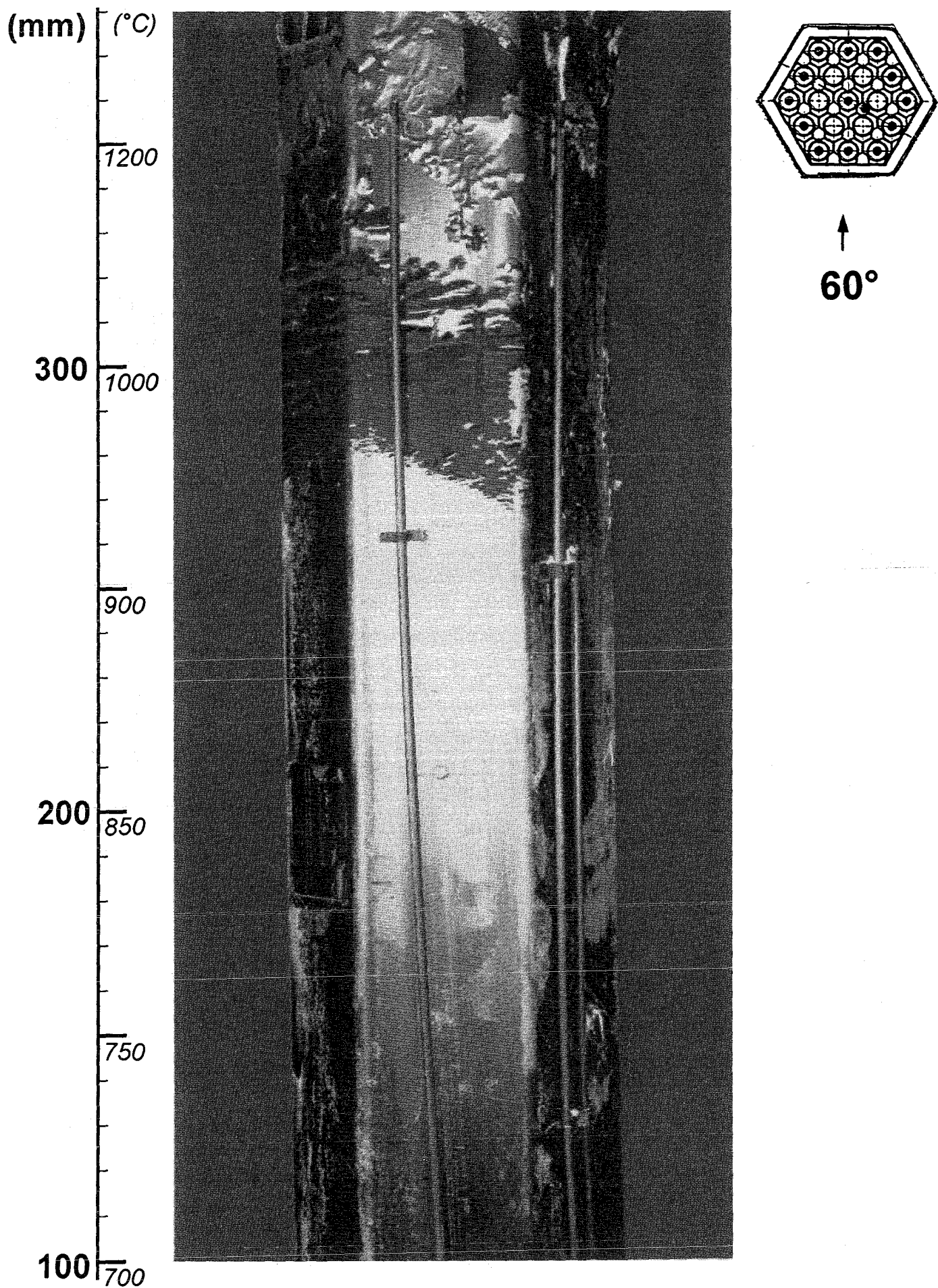


Fig. 86: CORA-W1; Posttest view, 60° orientation

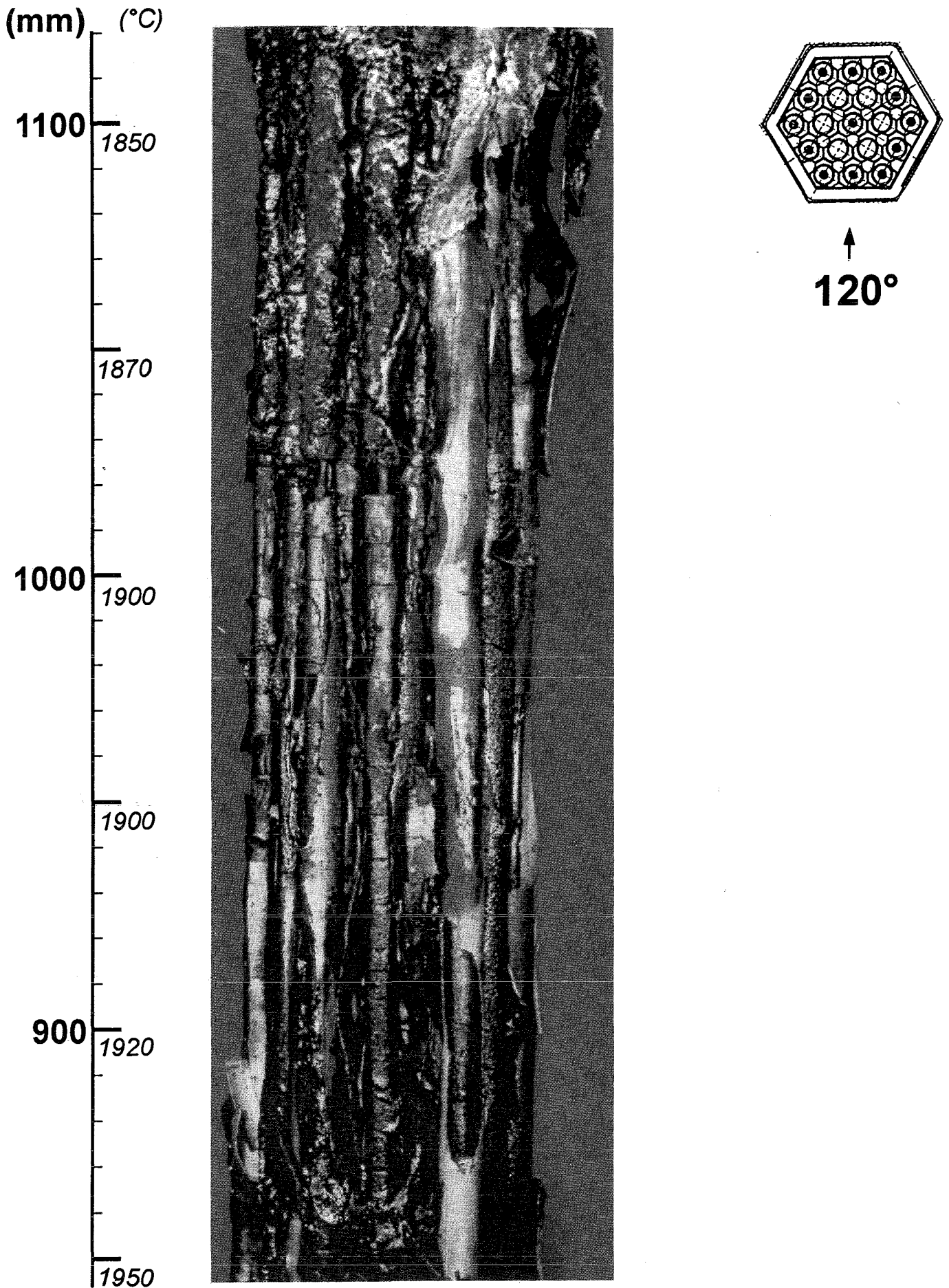


Fig. 87: CORA-W1; Posttest view , 120° orientation

(mm) (°C)

1950

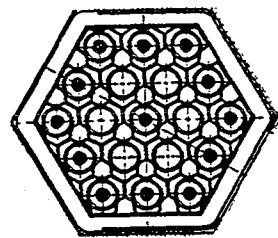
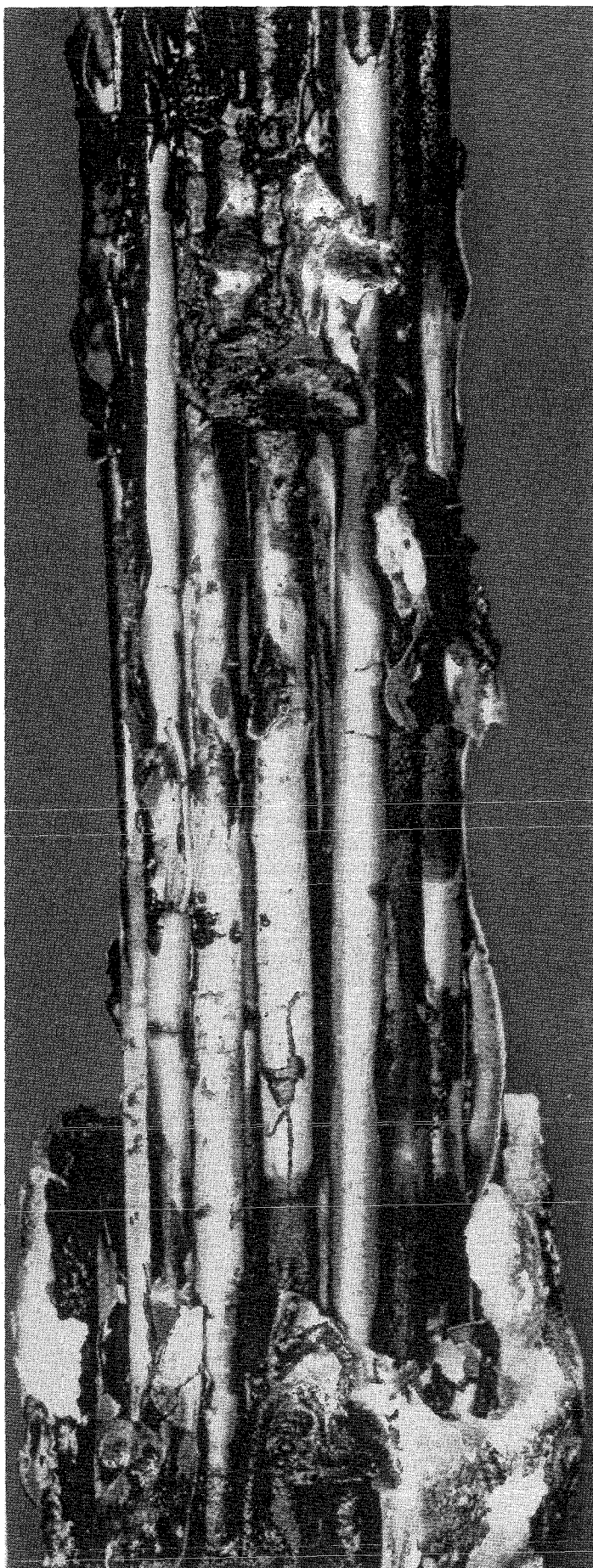
800 1970

1990

700 2000

2000

600 2000



120°

Fig. 88: CORA-W1; Posttest view , 120° orientation

(mm) (°C)

600 2000

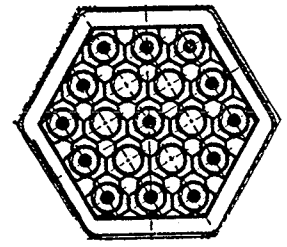
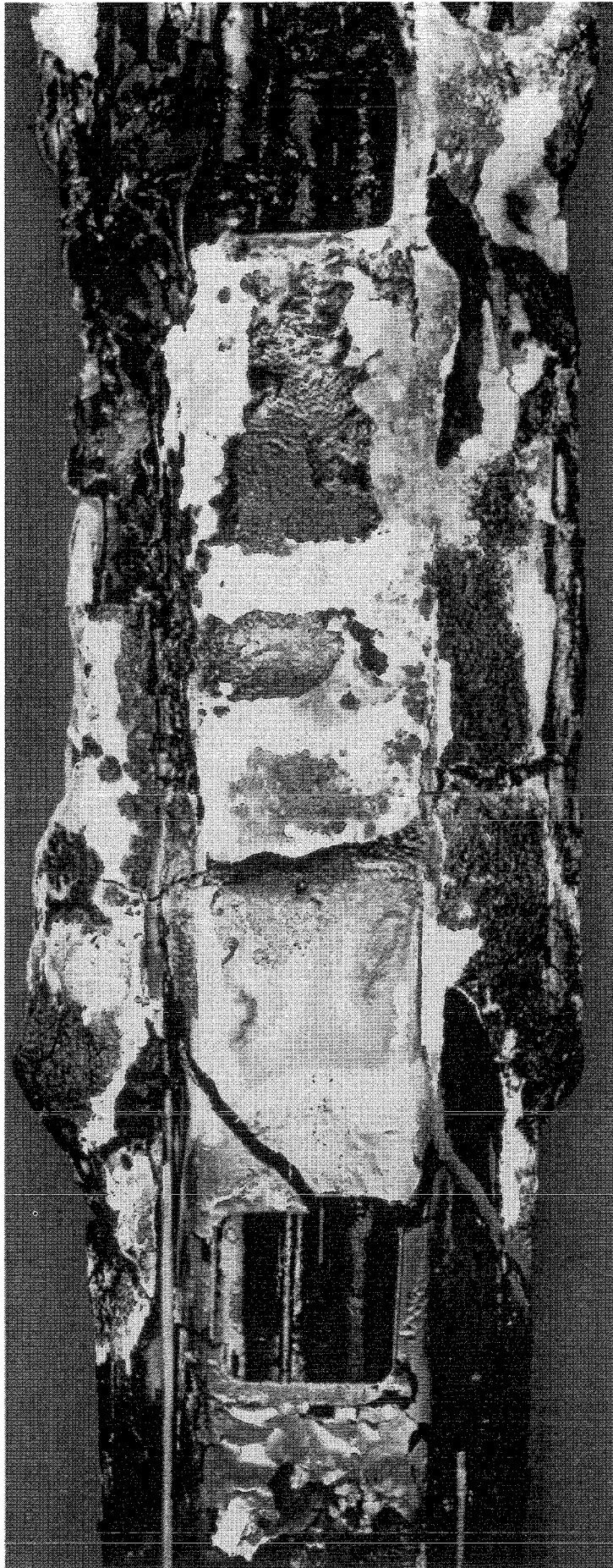
2000

500 2000

2000

400 1800

1200



120°

Fig. 89: CORA-W1; Posttest view , 120° orientation

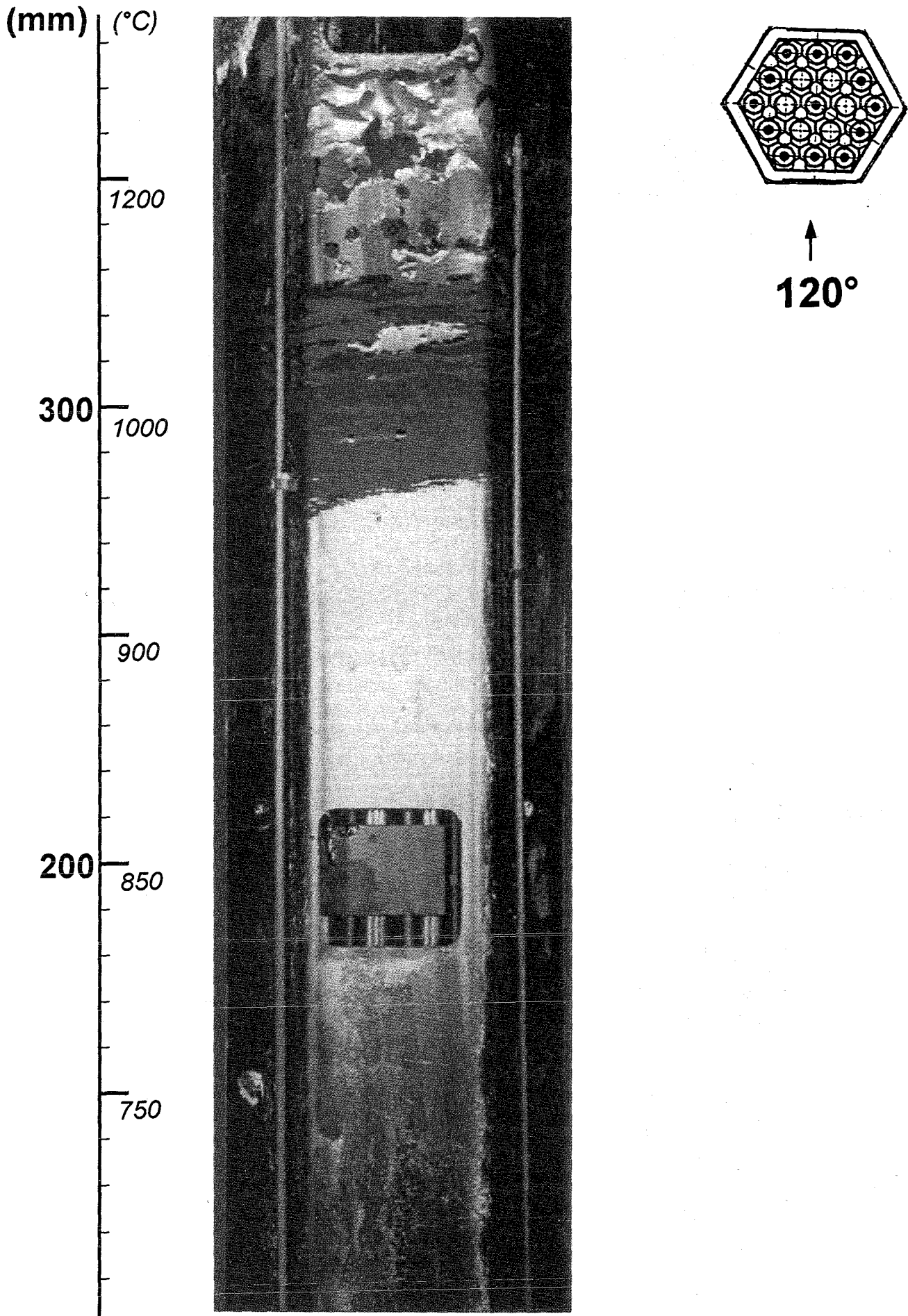


Fig. 90: CORA-W1; Posttest view , 120° orientation

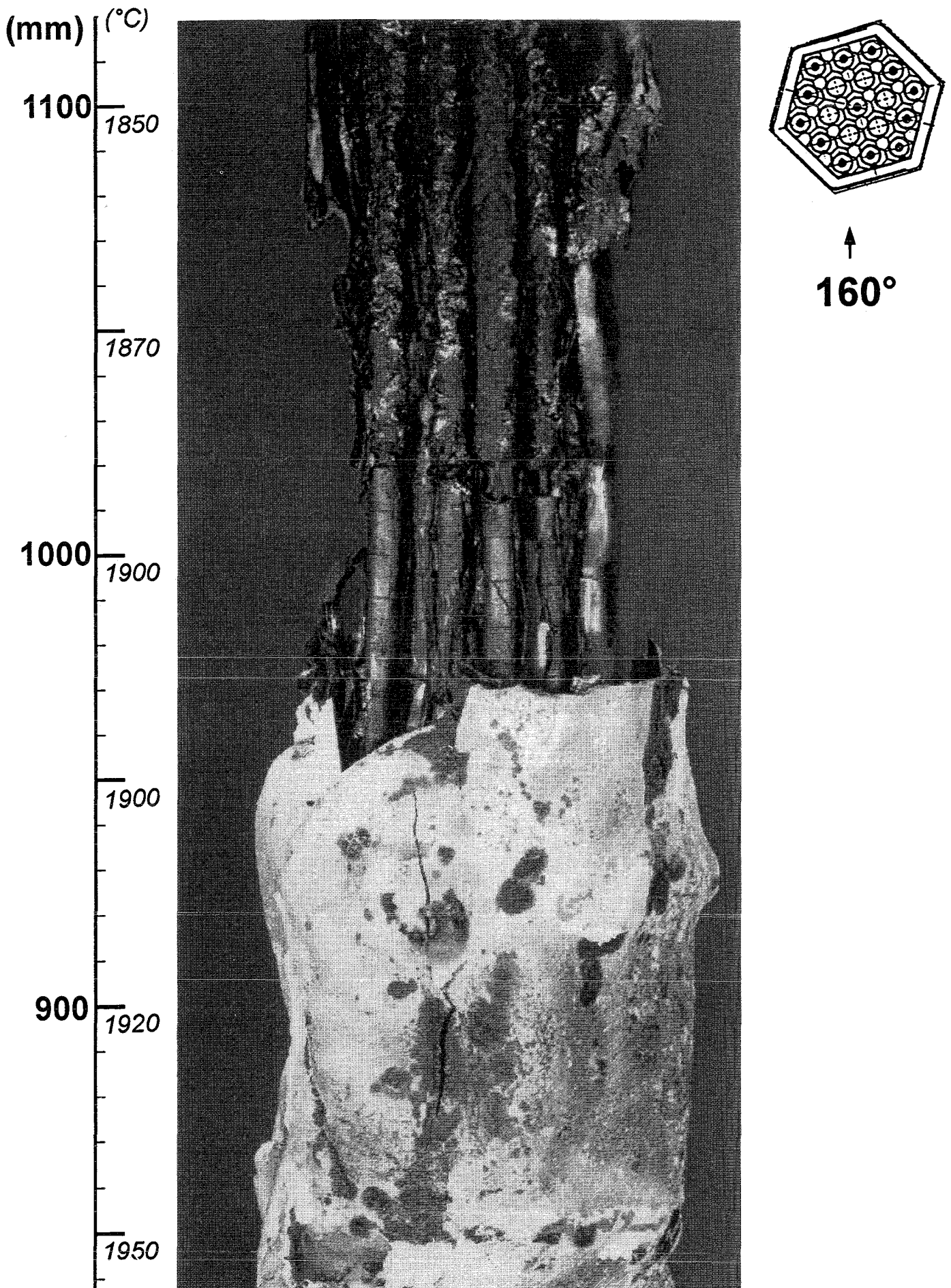


Fig. 91: CORA-W1; Posttest view, 160° orientation

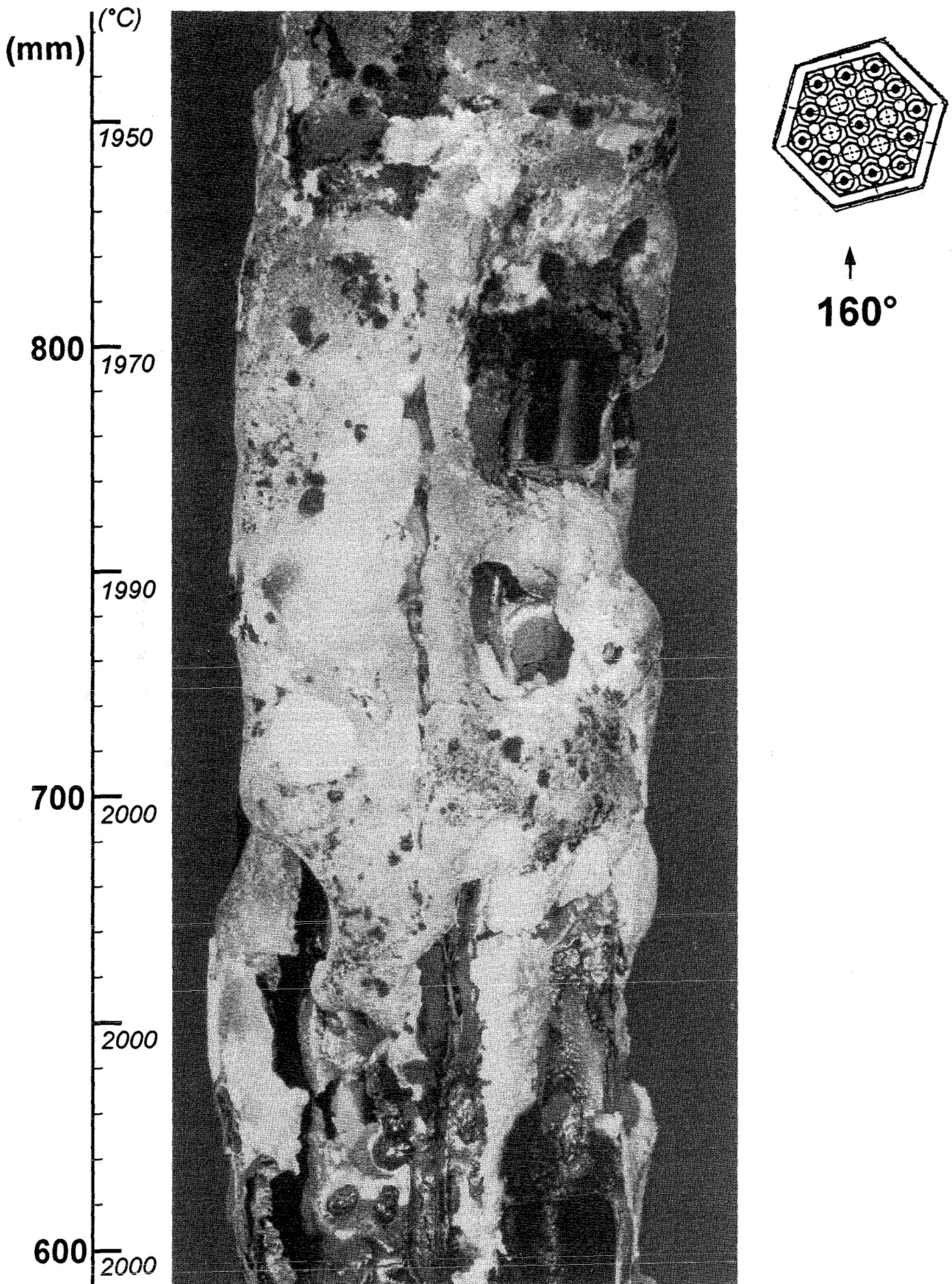


Fig. 92: CORA-W1; Posttest view, 160° orientation

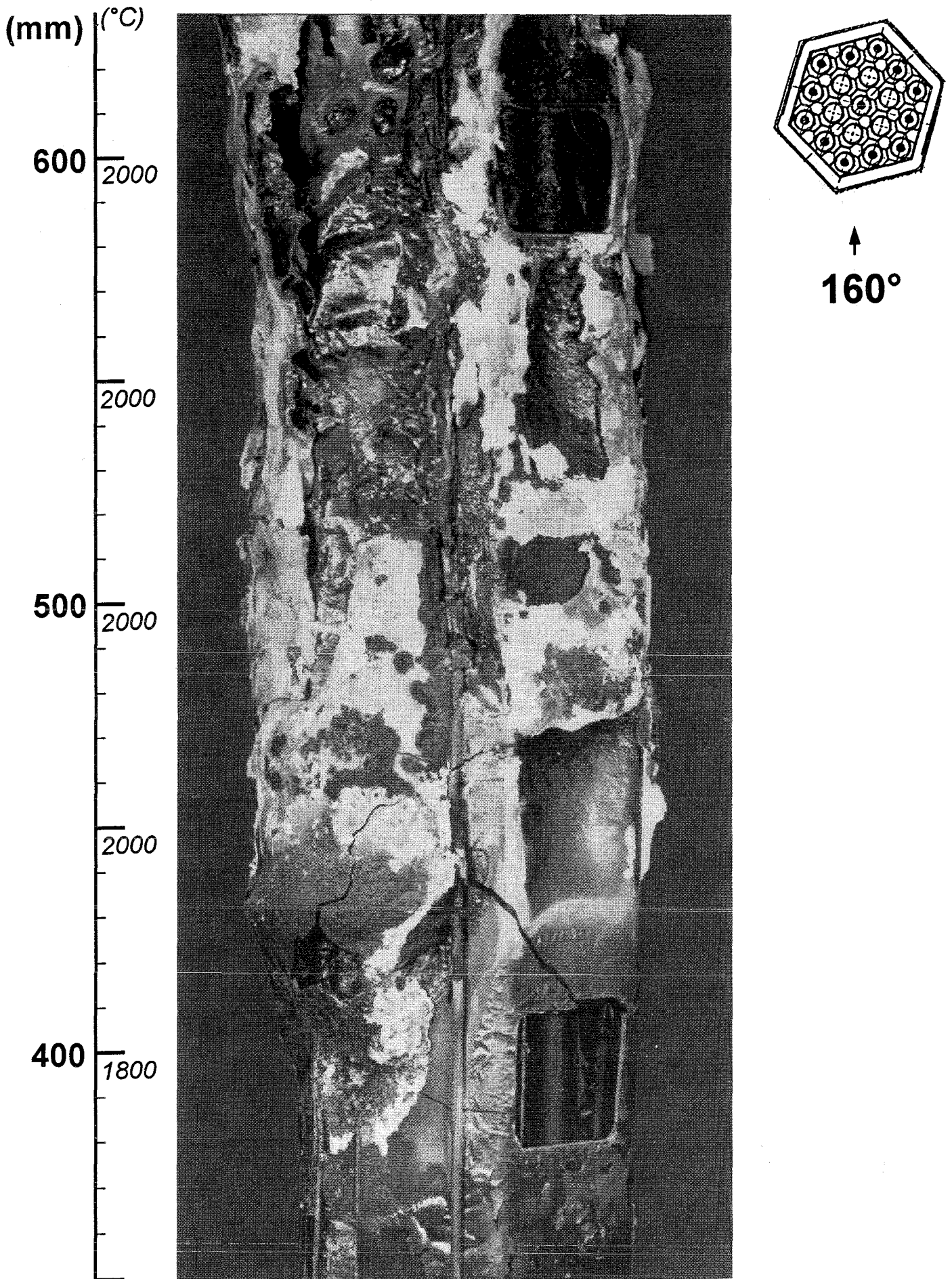


Fig. 93: CORA-W1; Posttest view, 160° orientation

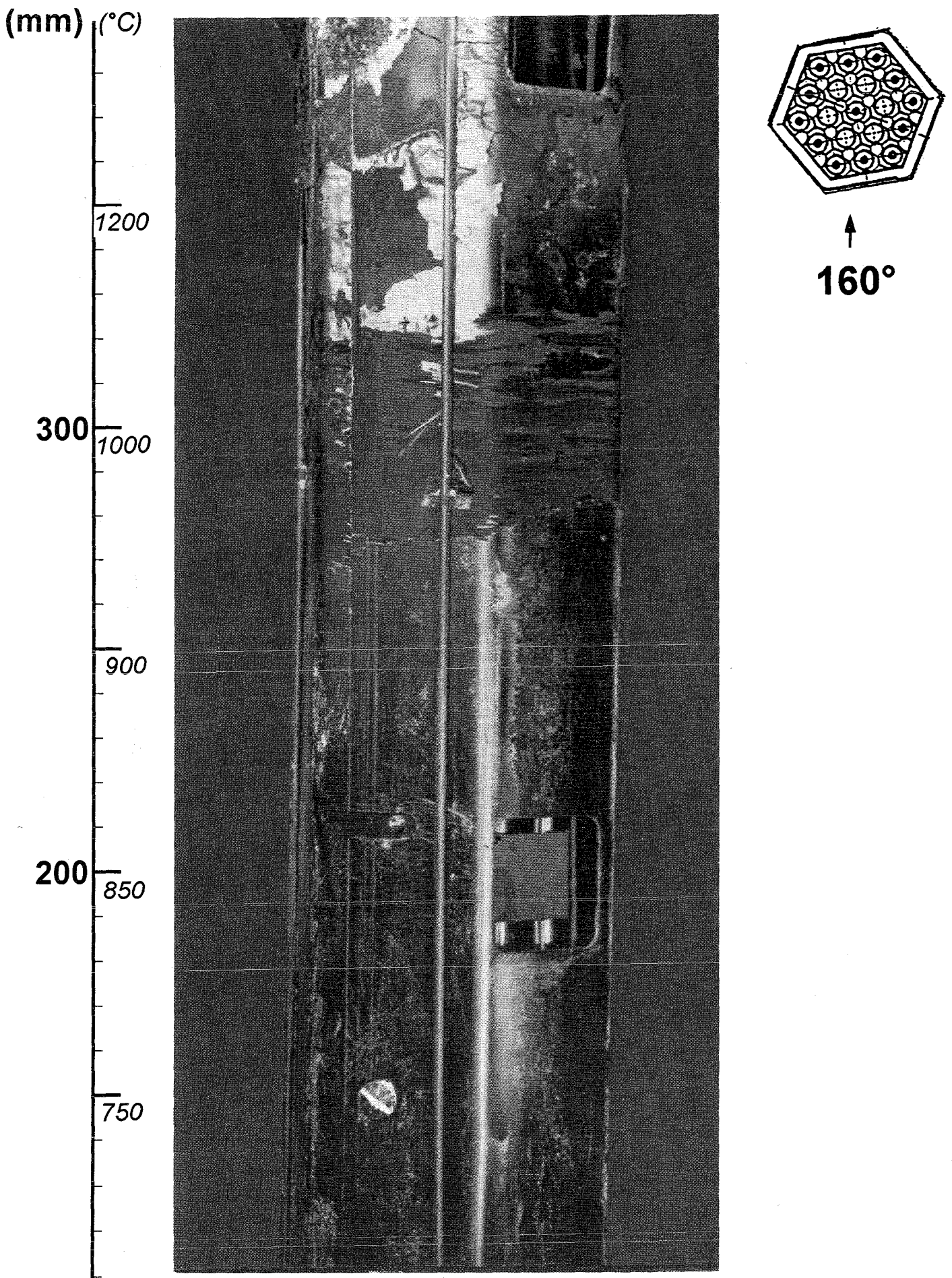


Fig. 94: CORA-W1; Posttest view, 160° orientation

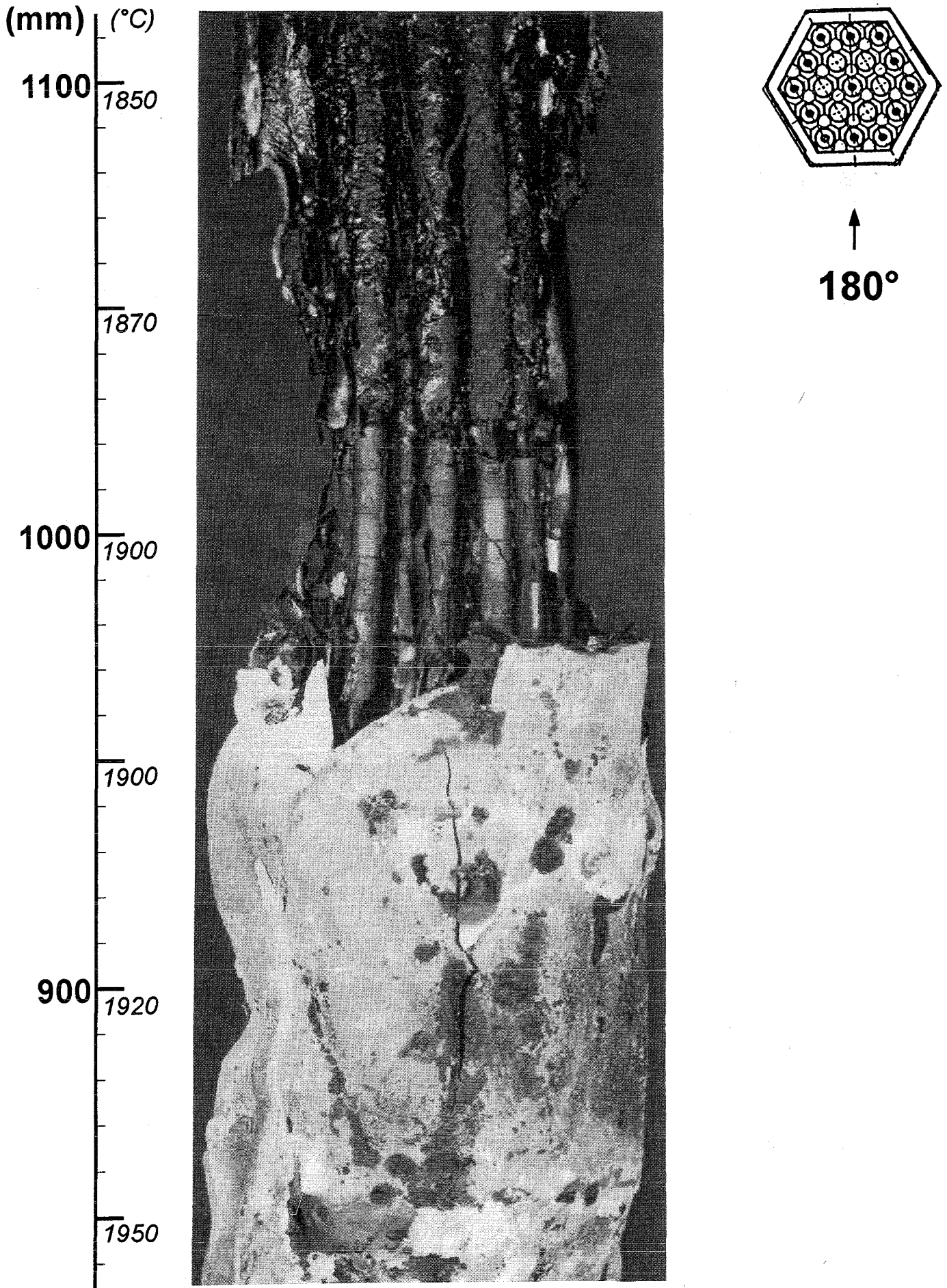


Fig. 95: CORA-W1; Posttest view , 180° orientation

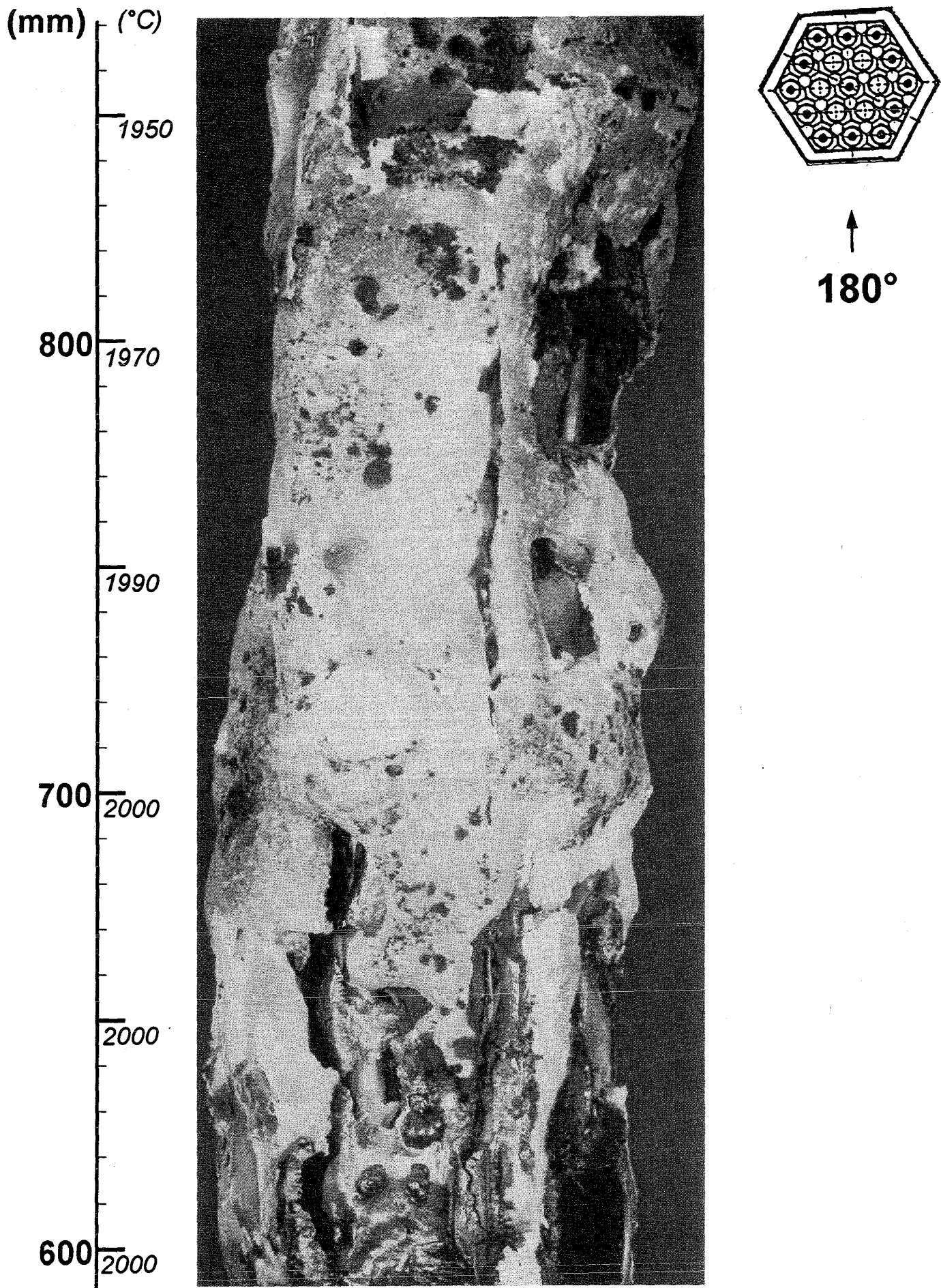


Fig. 96: CORA-W1; Posttest view , 180° orientation

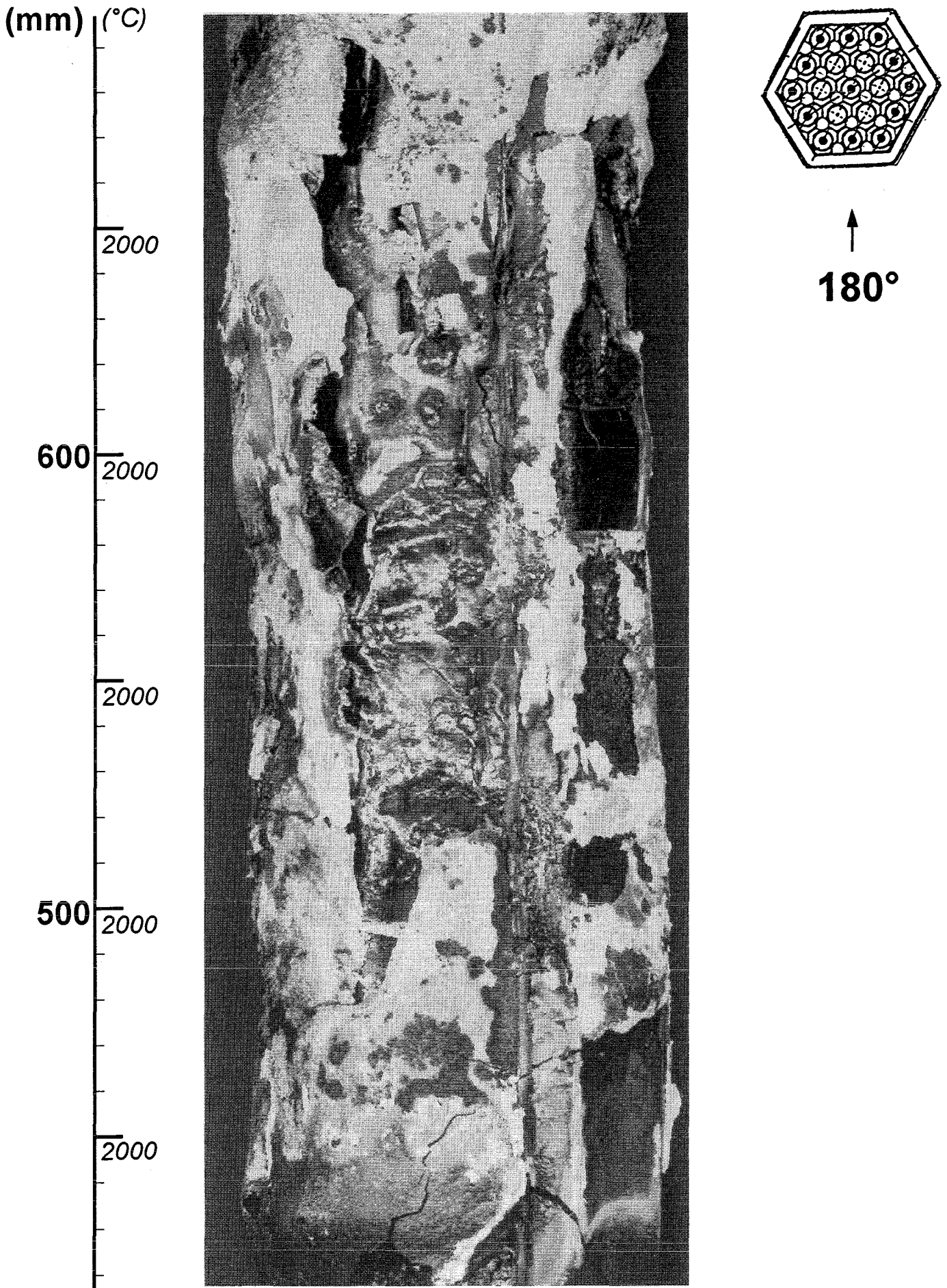


Fig. 97: CORA-W1; Posttest view , 180° orientation

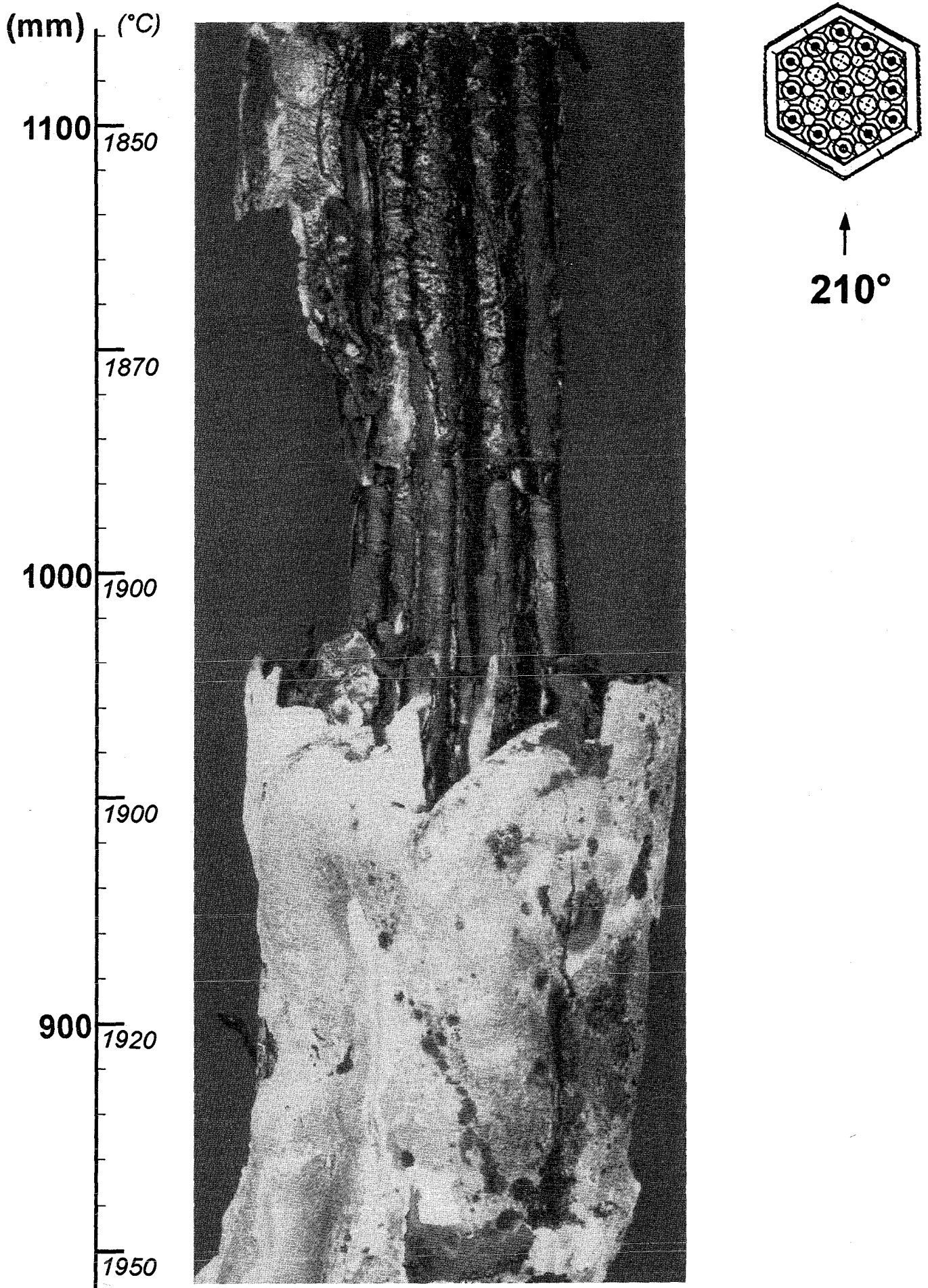


Fig. 98: CORA-W1; Posttest view , 210° orientation

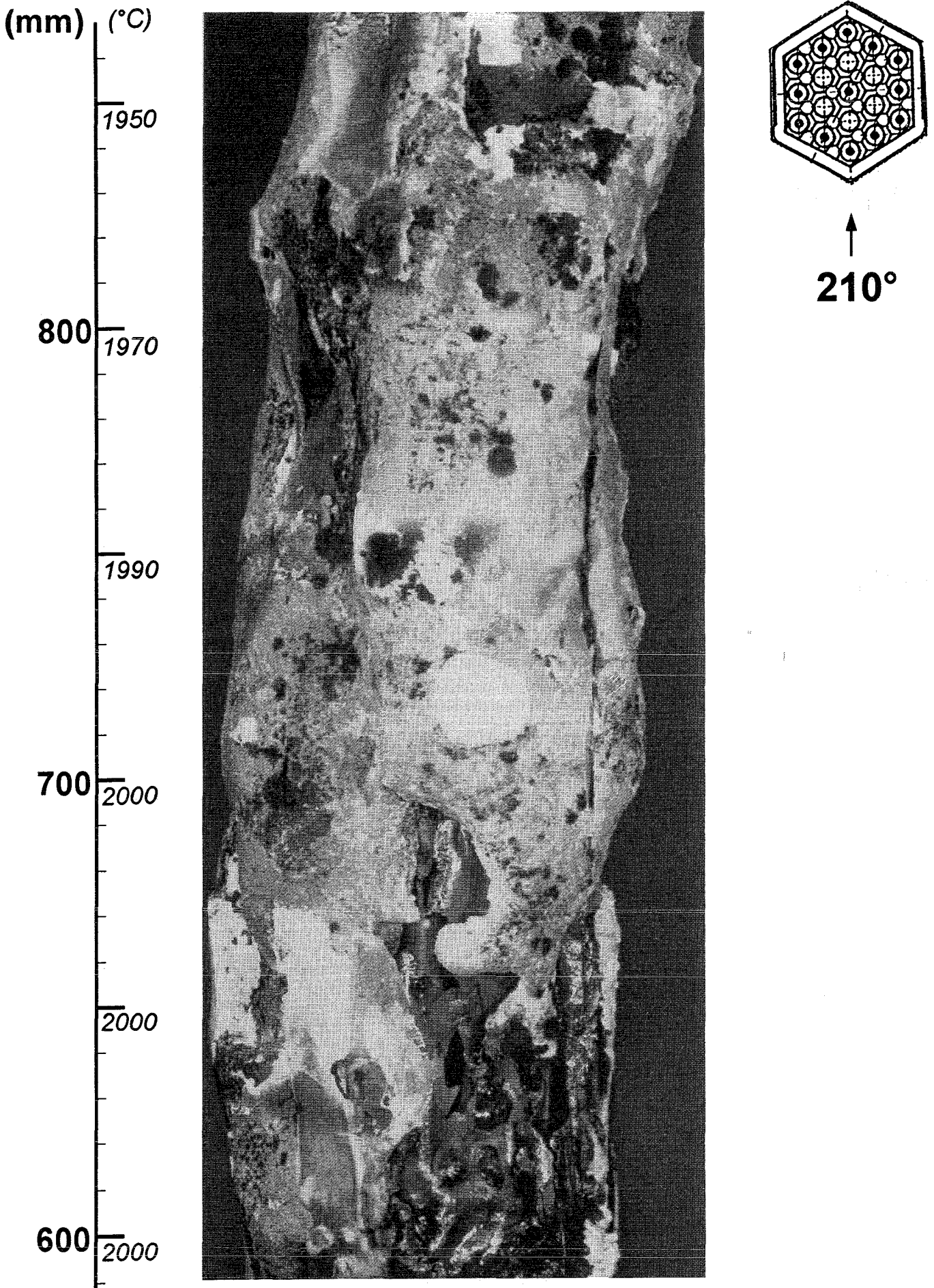


Fig. 99: CORA-W1; Posttest view , 210° orientation

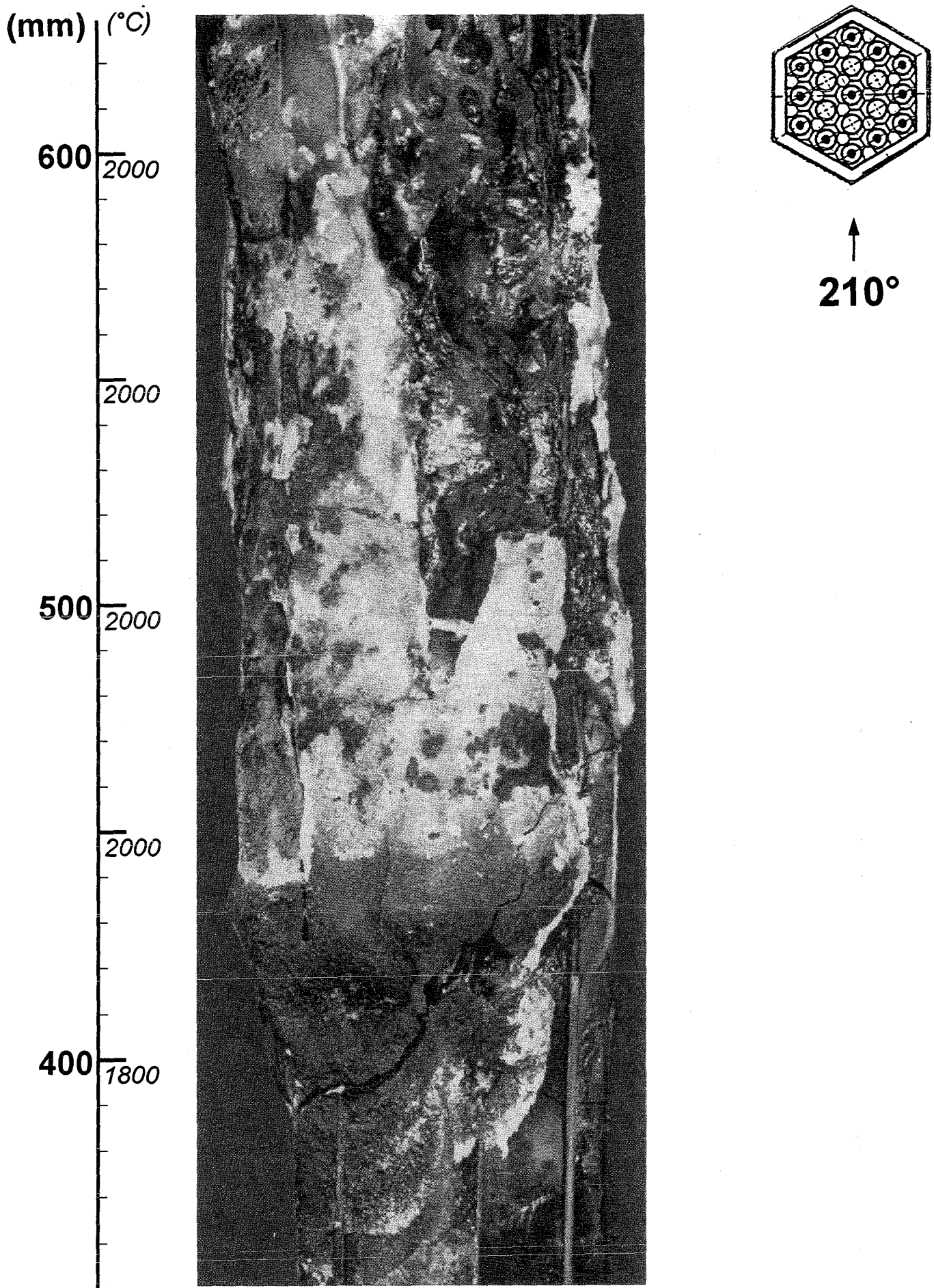


Fig.100: CORA-W1; Posttest view , 210° orientation

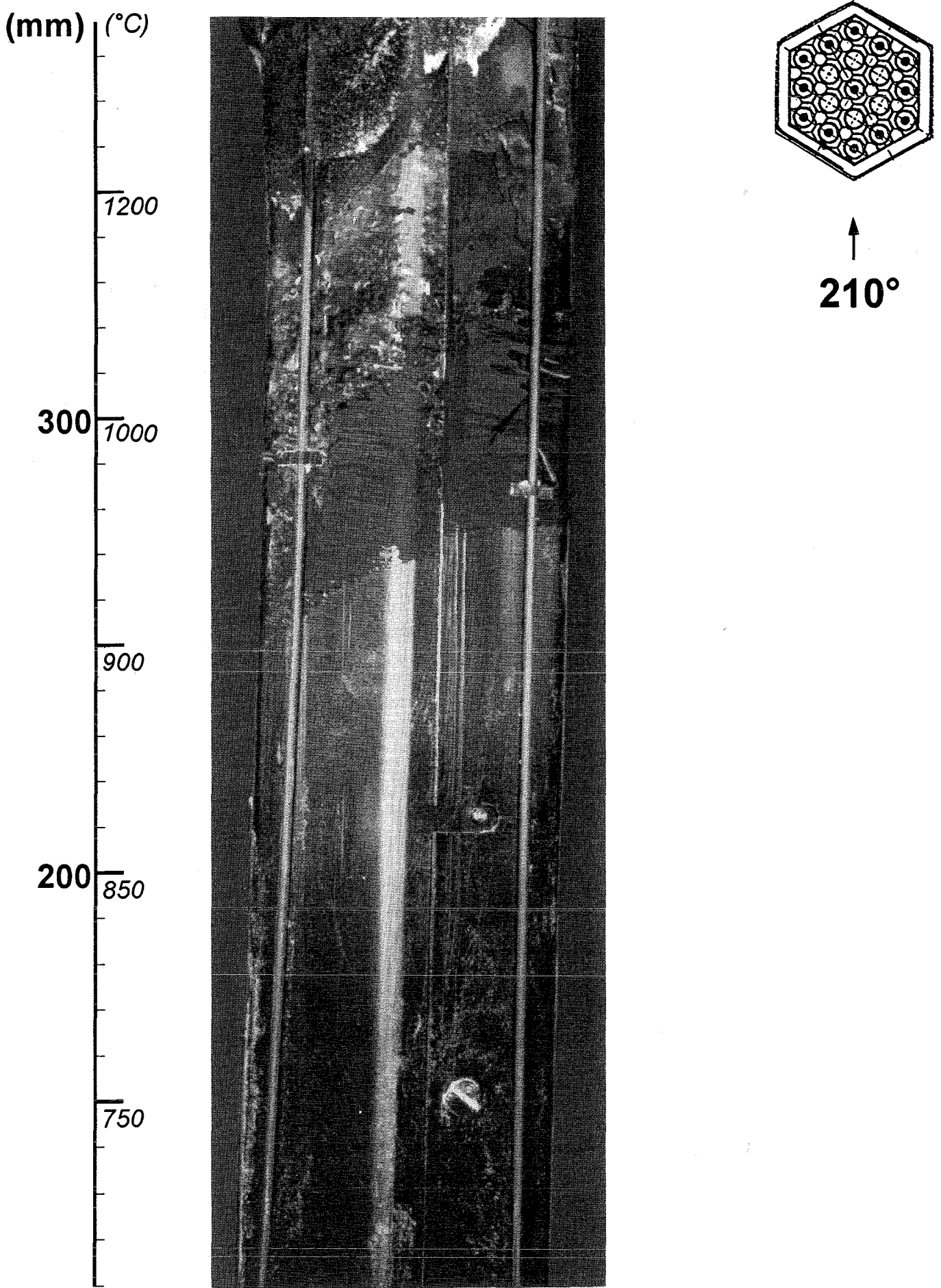


Fig.101: CORA-W1; Posttest view , 210° orientation

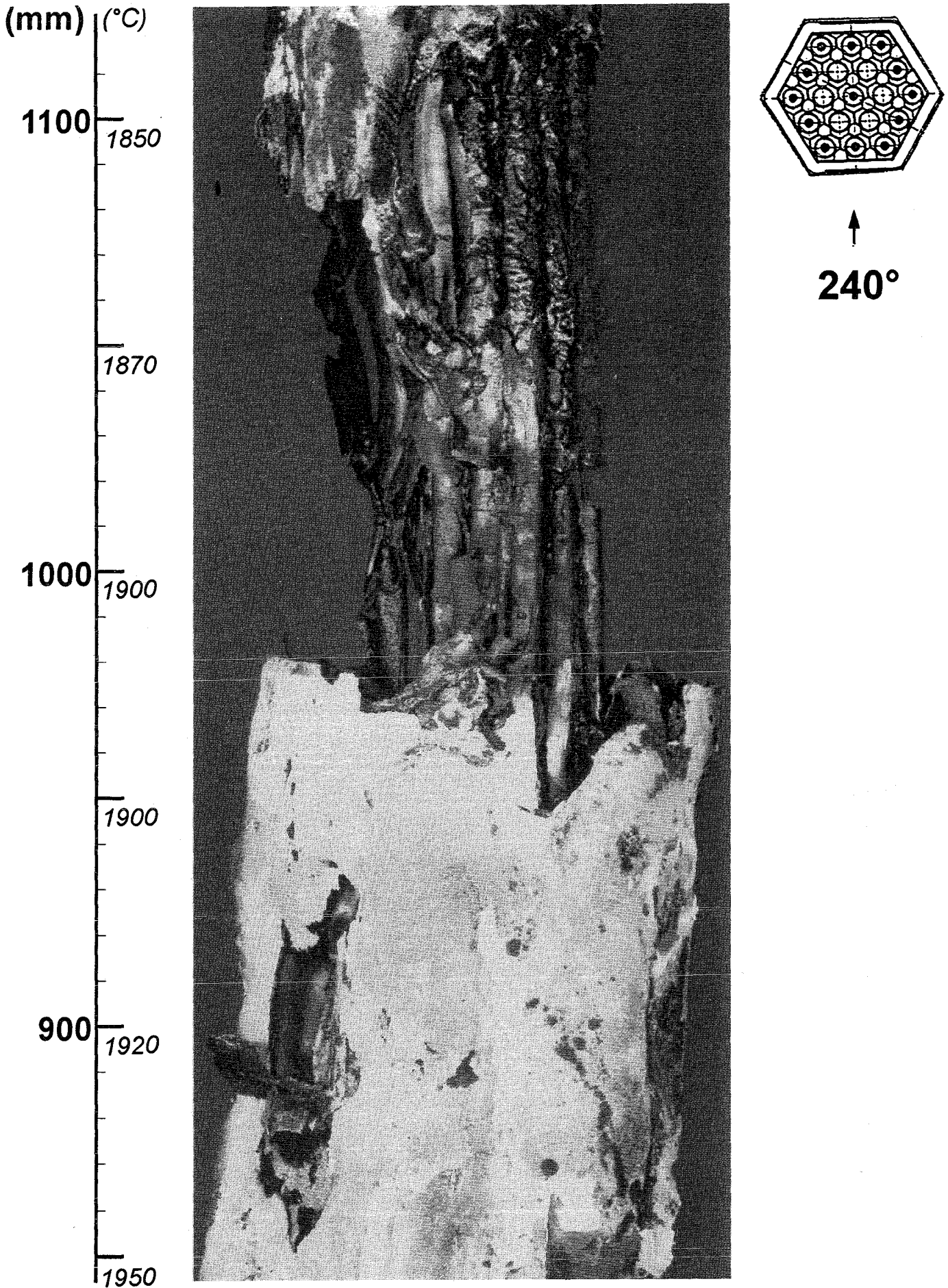


Fig.102: CORA-W1; Posttest view , 240° orientation

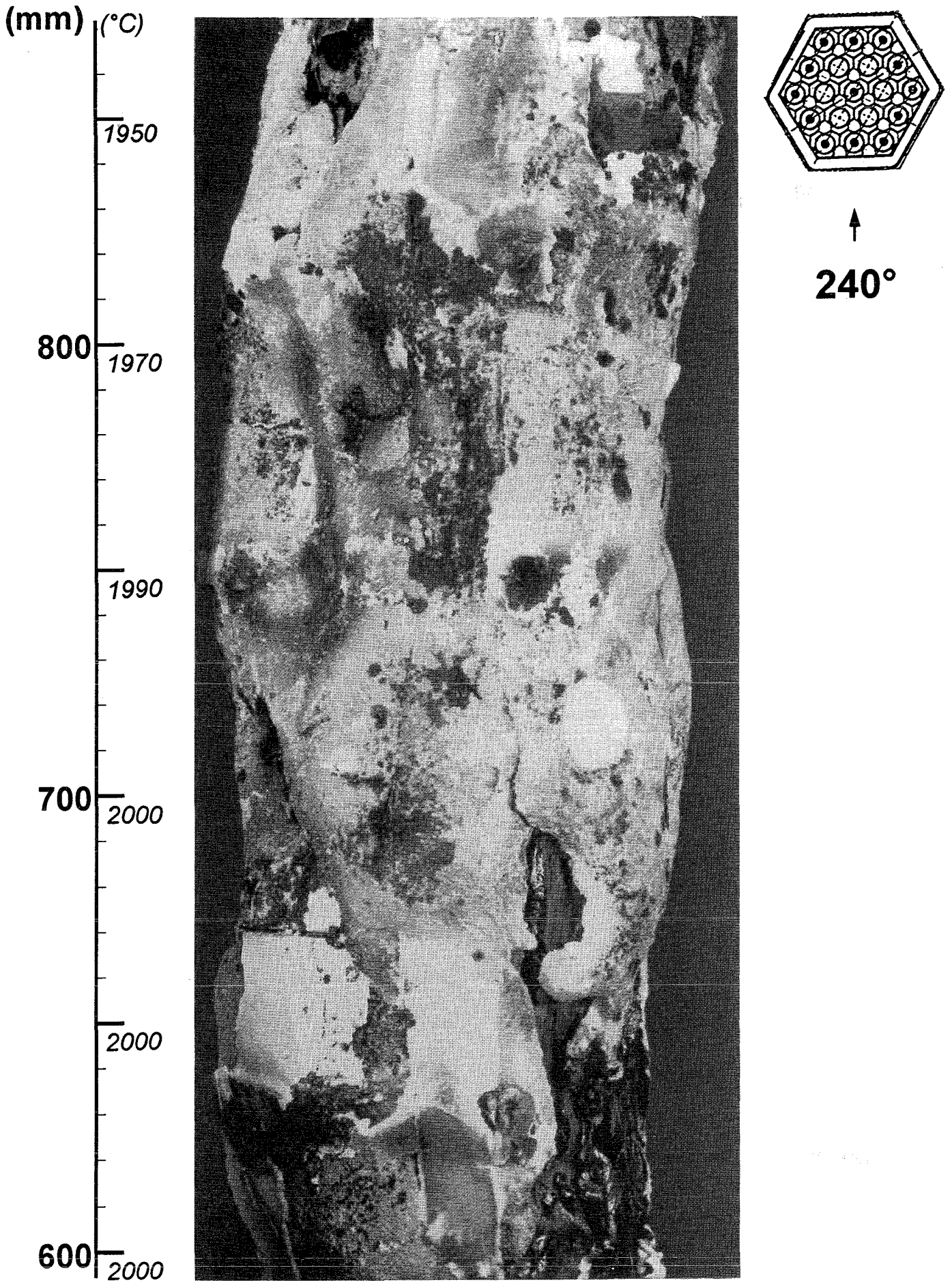


Fig.103: CORA-W1; Posttest view , 240° orientation

(mm) (°C)

600 2000

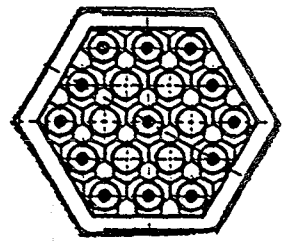
2000

500 2000

2000

400 1800

1200



240°

Fig.104: CORA-W1; Posttest view , 240° orientation

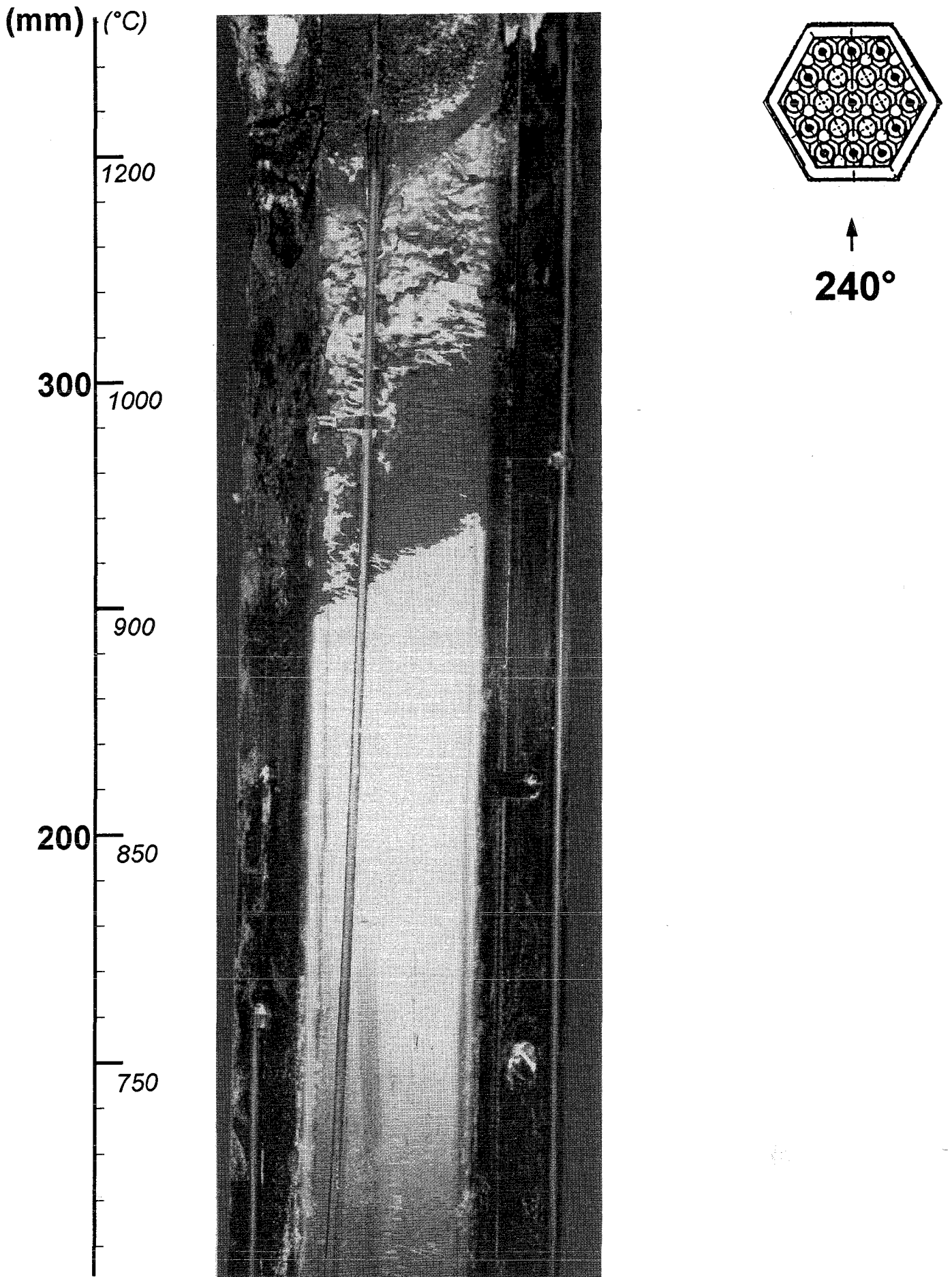


Fig.105: CORA-W1; Posttest view , 240° orientation

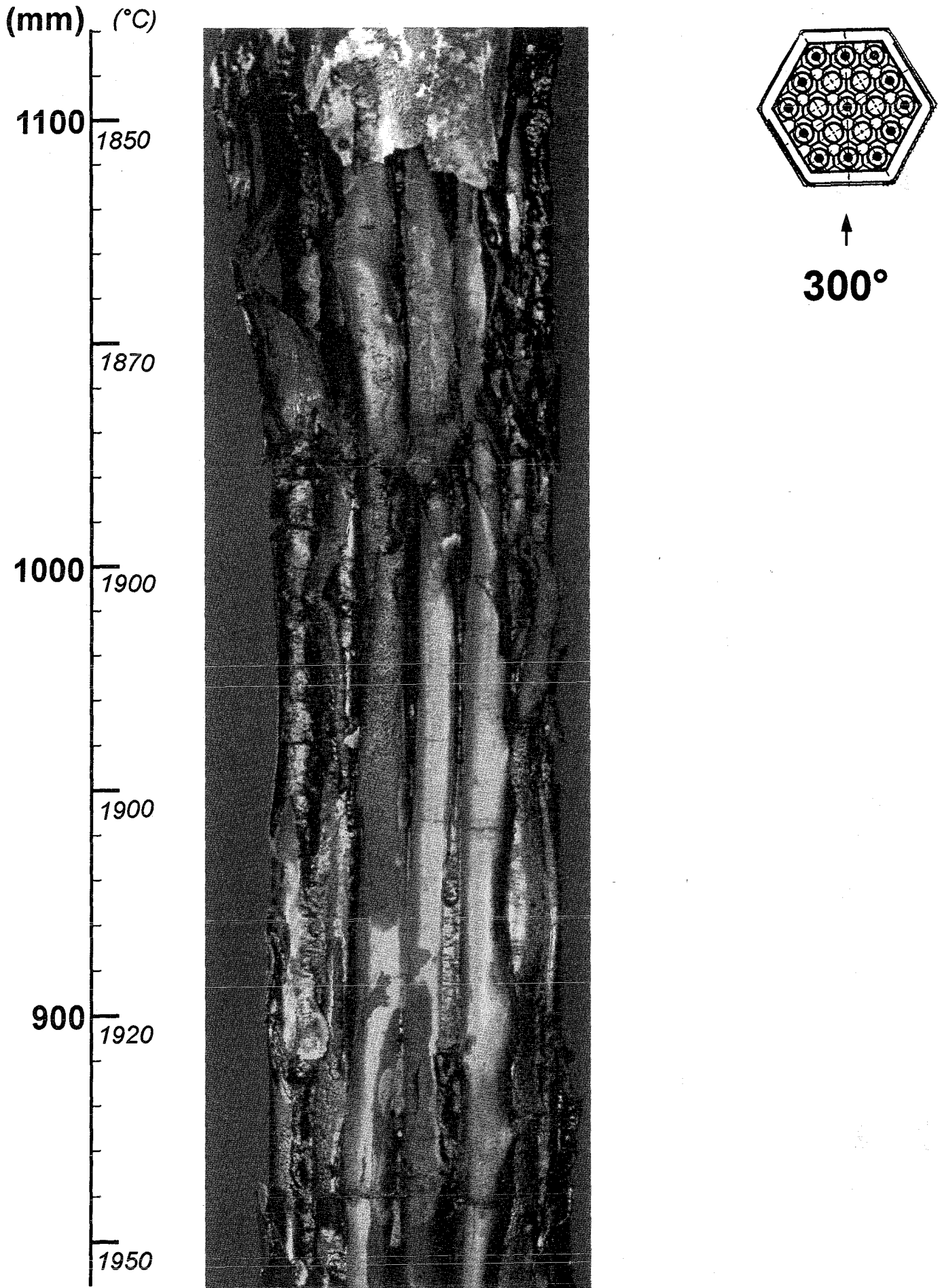
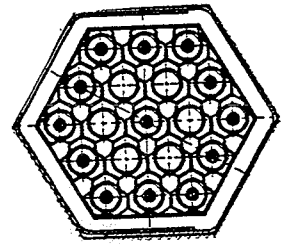
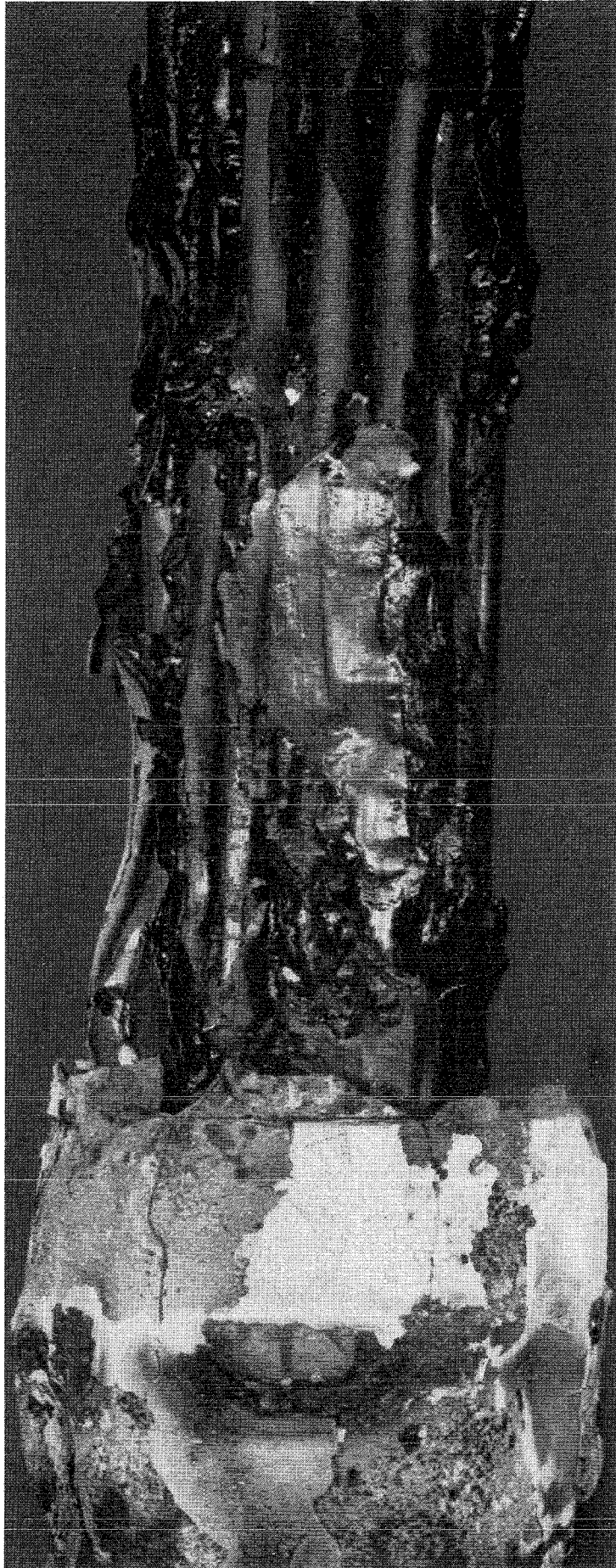
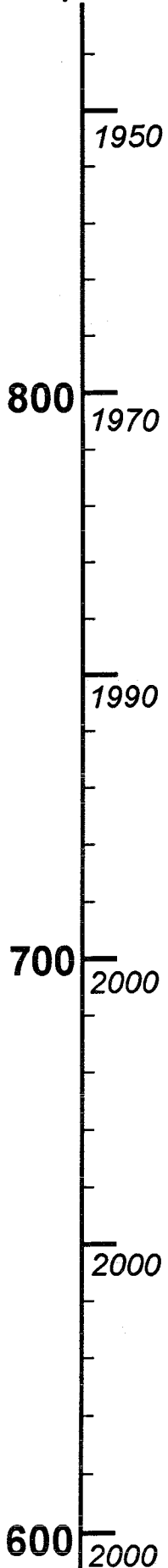


Fig.106: CORA-W1; Posttest view , 300° orientation

(mm) (°C)



↑
300°

Fig.107: CORA-W1; Posttest view , 300° orientation

(mm) (°C)

600 2000

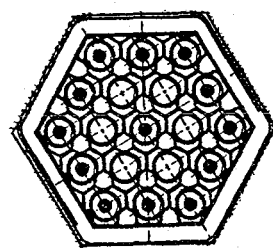
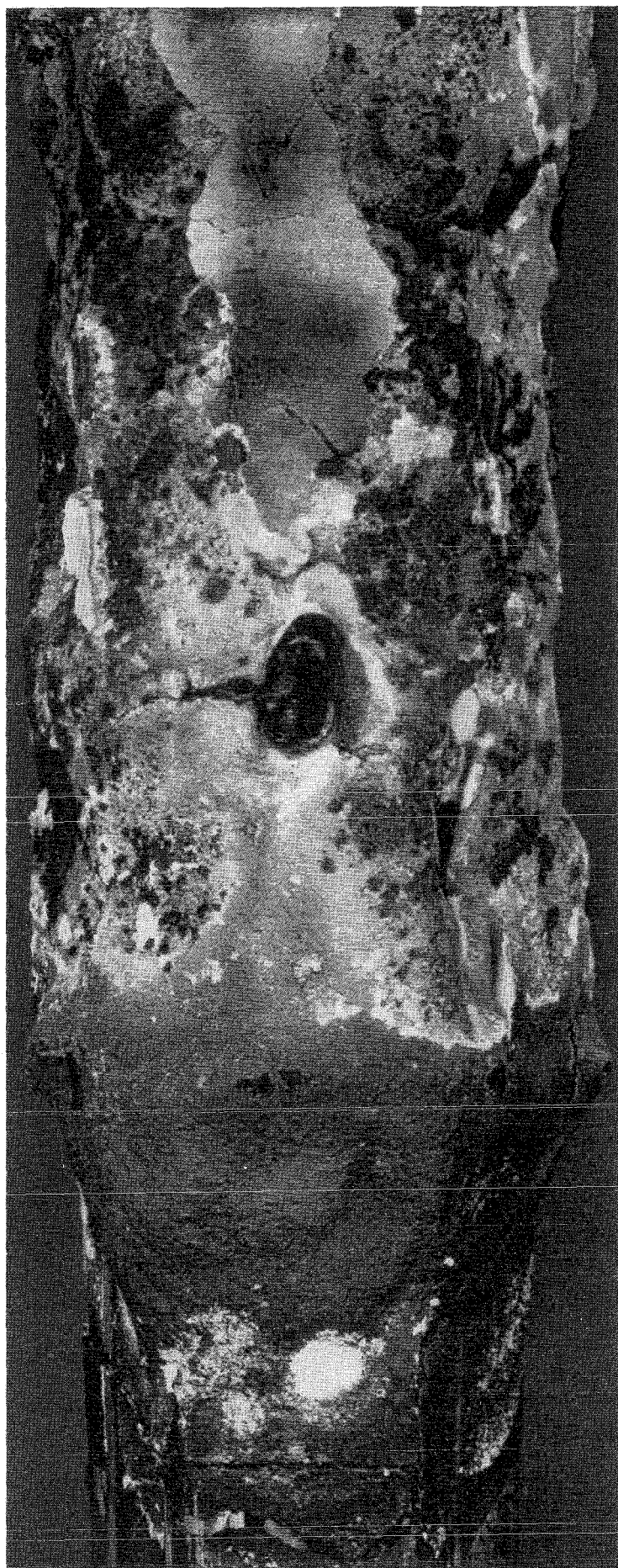
2000

500 2000

2000

400 1800

1200



300°

Fig.108: CORA-W1; Posttest view , 300° orientation

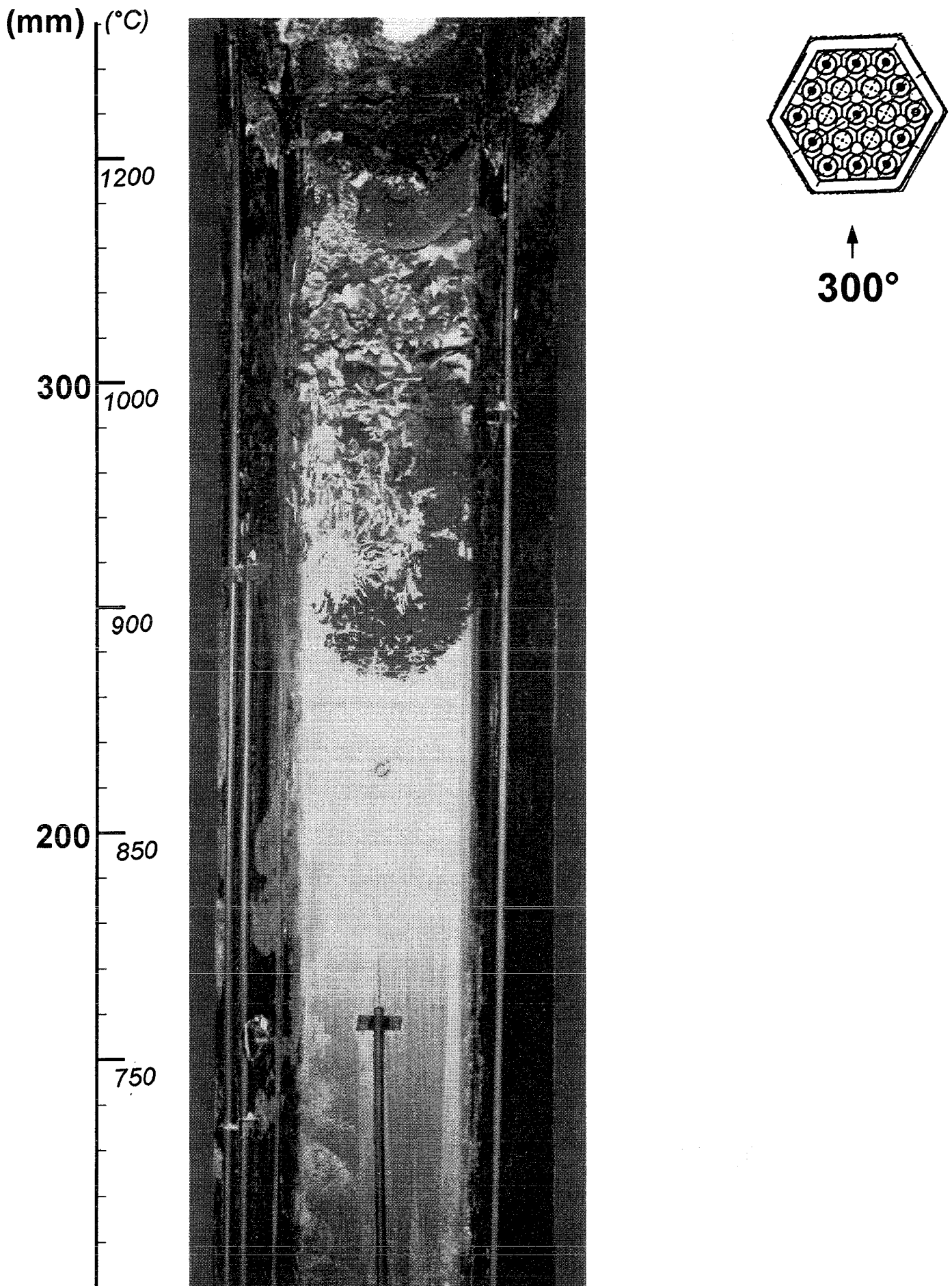
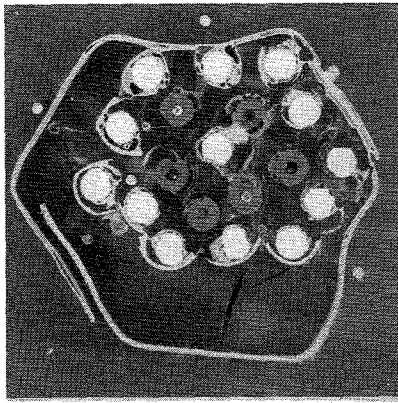
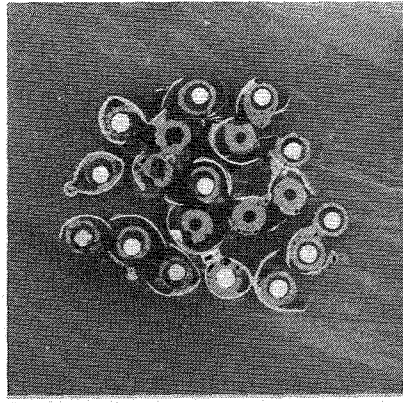


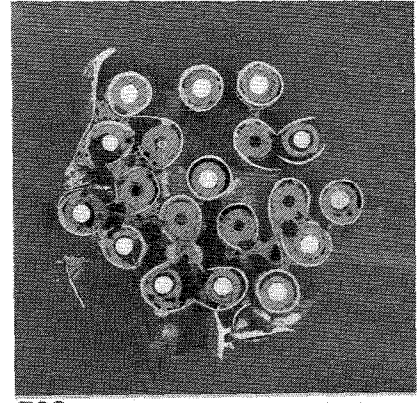
Fig.109: CORA-W1; Posttest view , 300° orientation



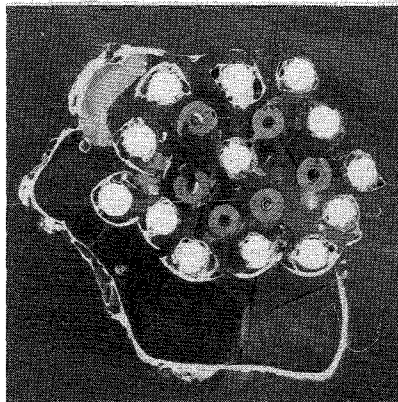
1125 mm



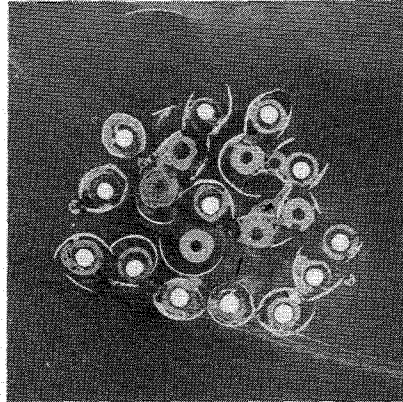
954 mm



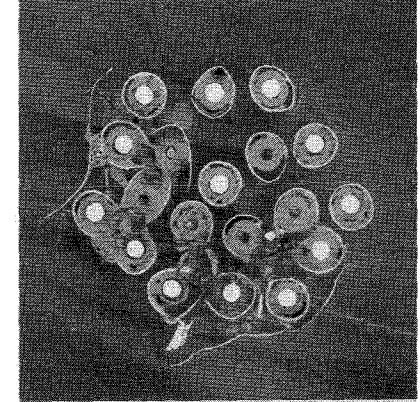
783 mm



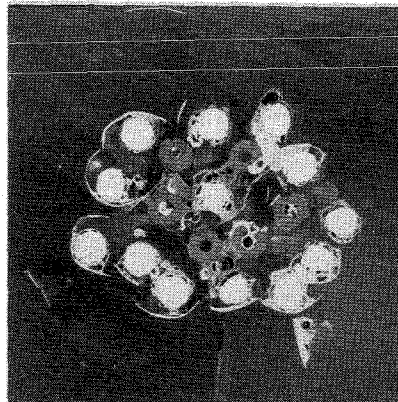
1110 mm



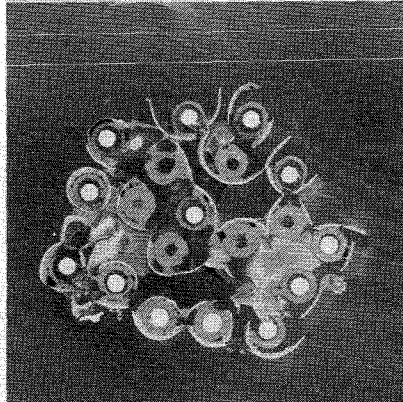
939 mm



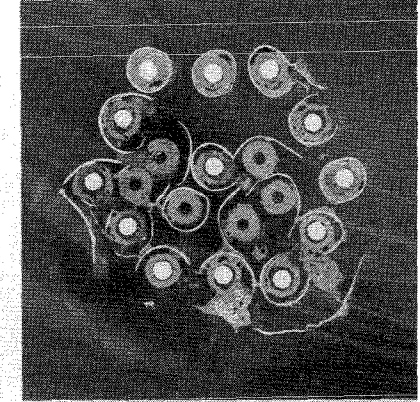
768 mm



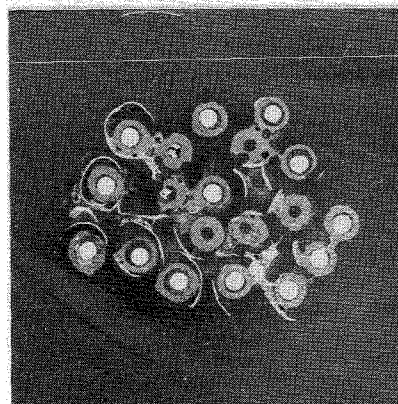
1058 mm



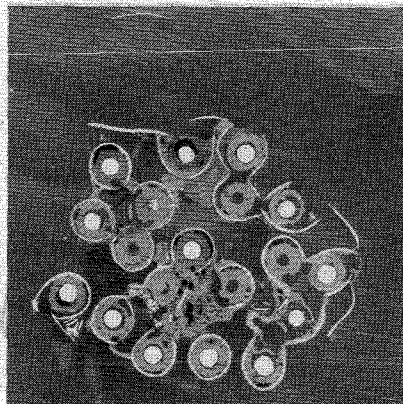
887 mm



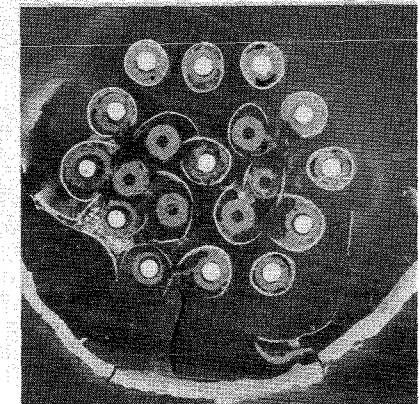
716 mm



1006 mm



835 mm



664 mm

Fig.110: Horizontal cross sections of bundle CORA-W1, top view (1125 - 664 mm)

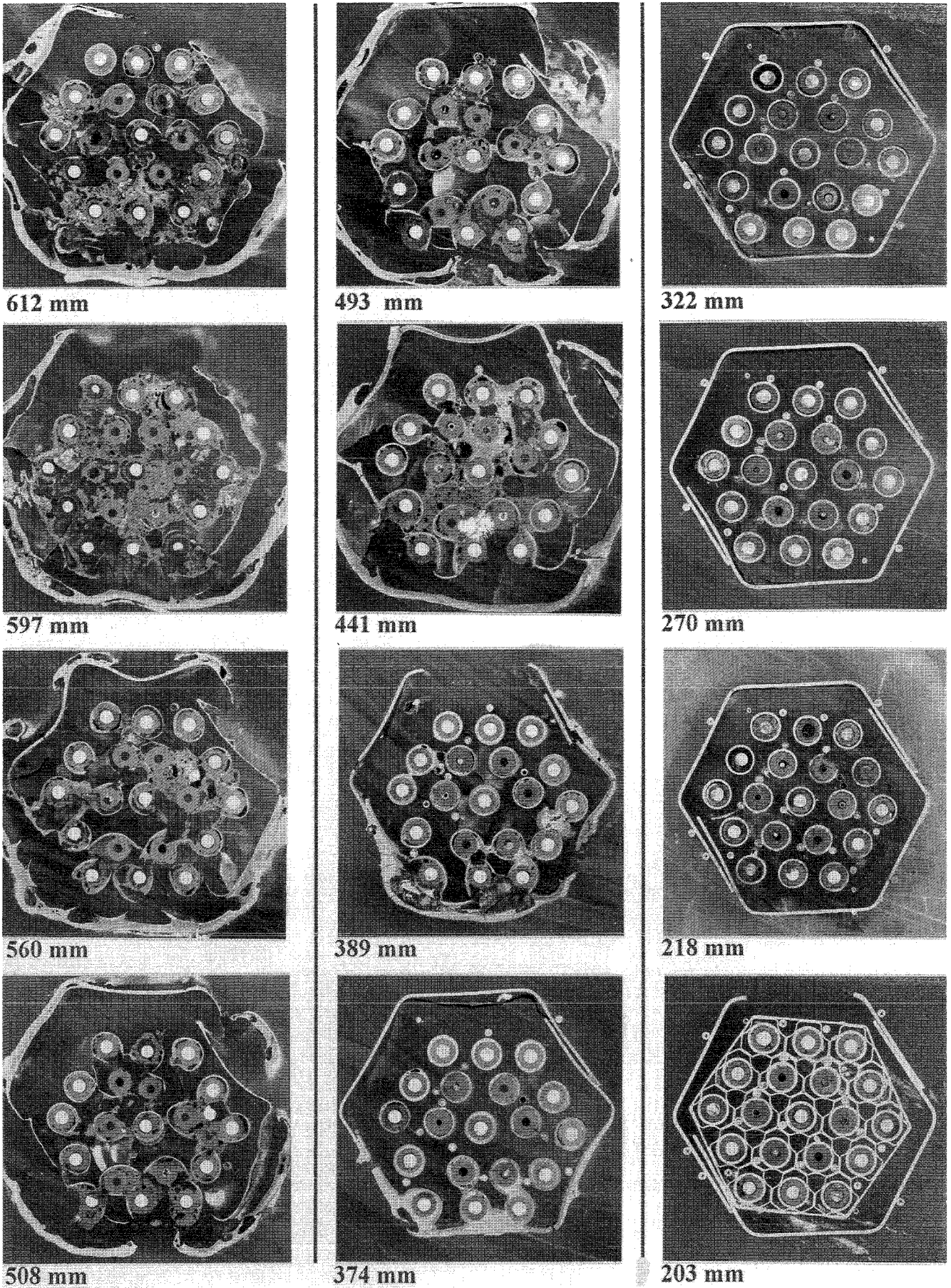


Fig.111: Horizontal cross sections of bundle CORA-W1, top view (612-203 mm) (top)

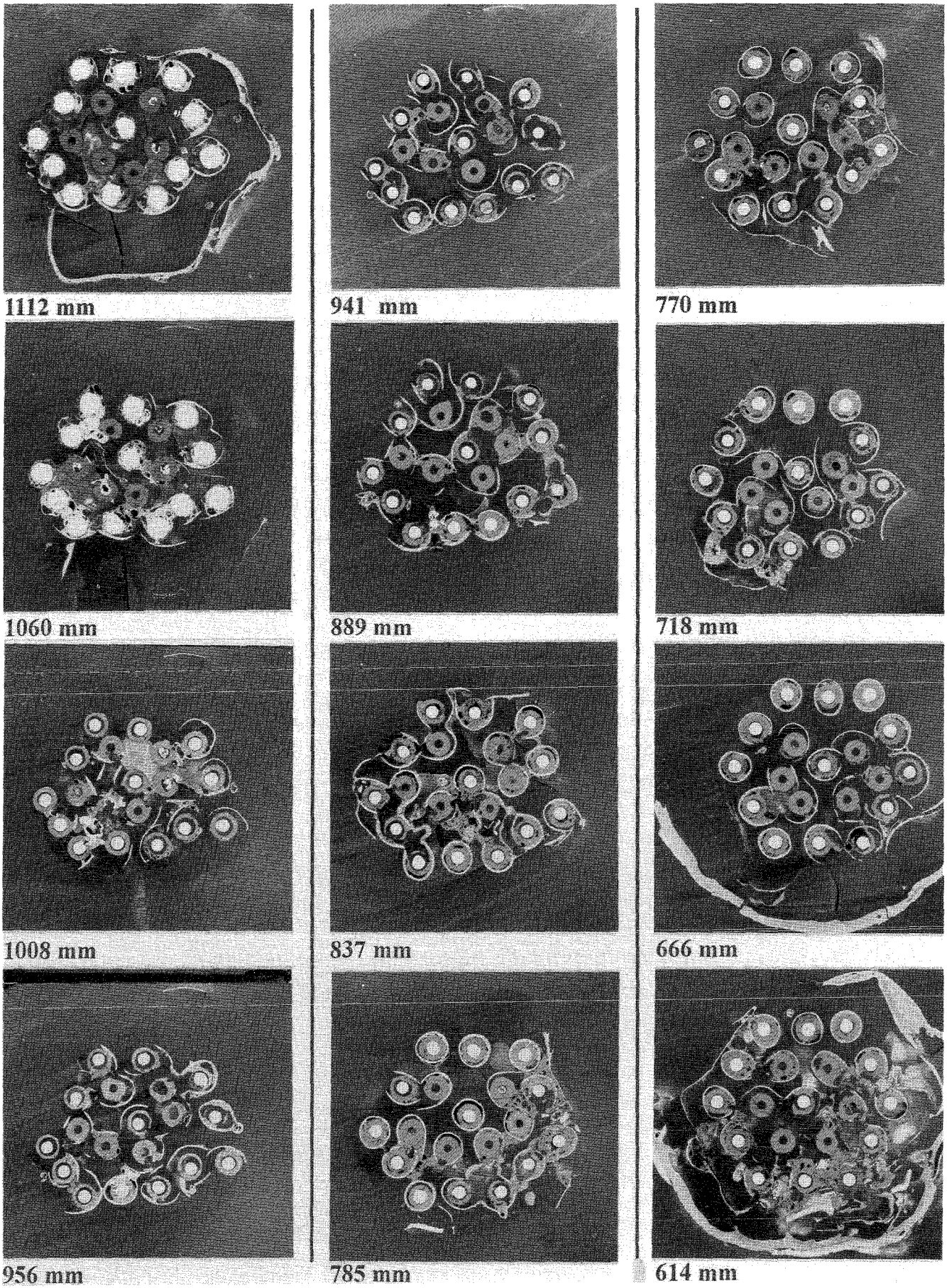


Fig.112: Horizontal cross sections of bundle CORA-^(bottom) W1, bottom view (1112-614 mm)

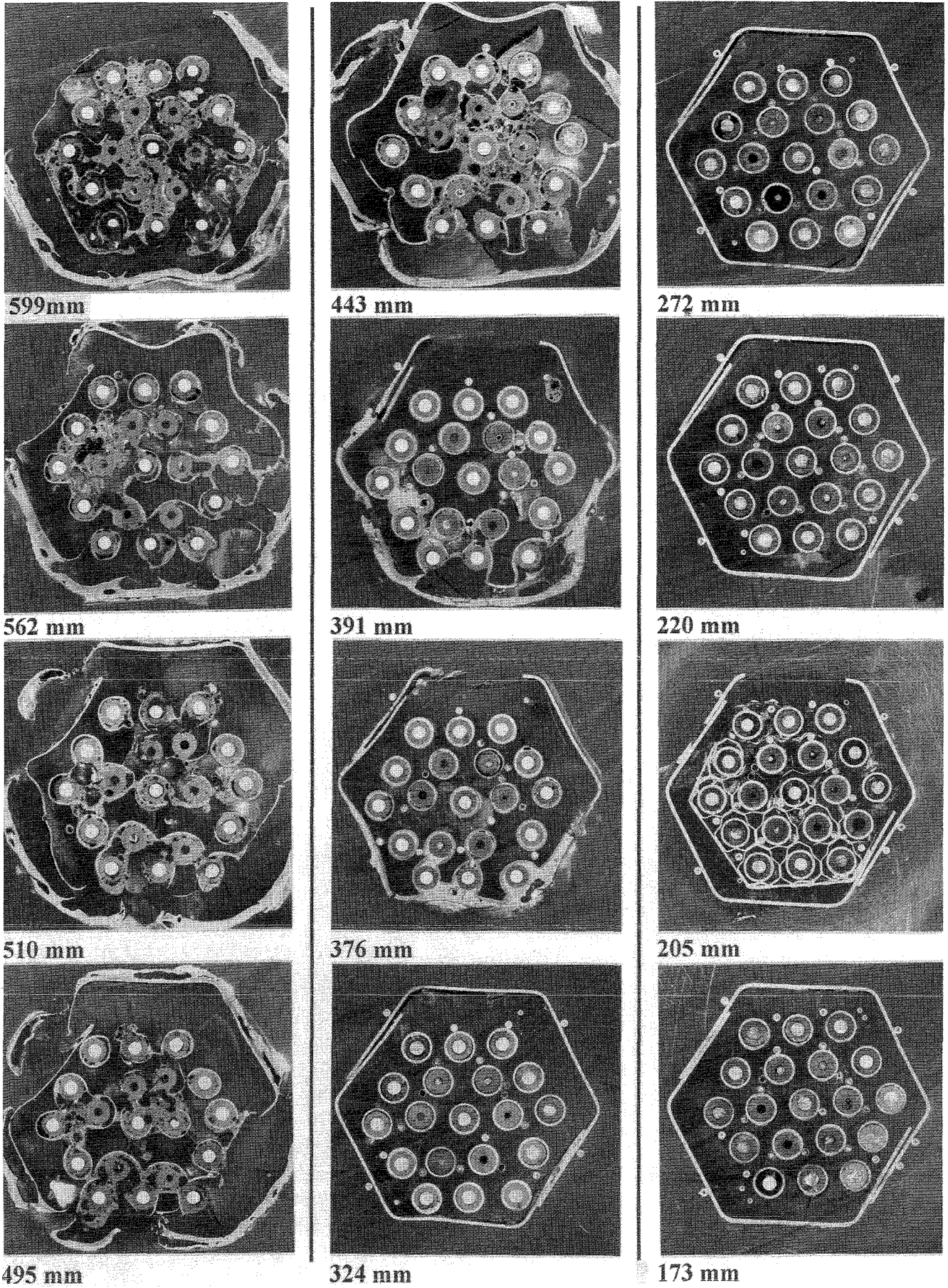


Fig.113: Horizontal cross sections of bundle CORA-W1, bottom view (599-173 mm) (bottom)

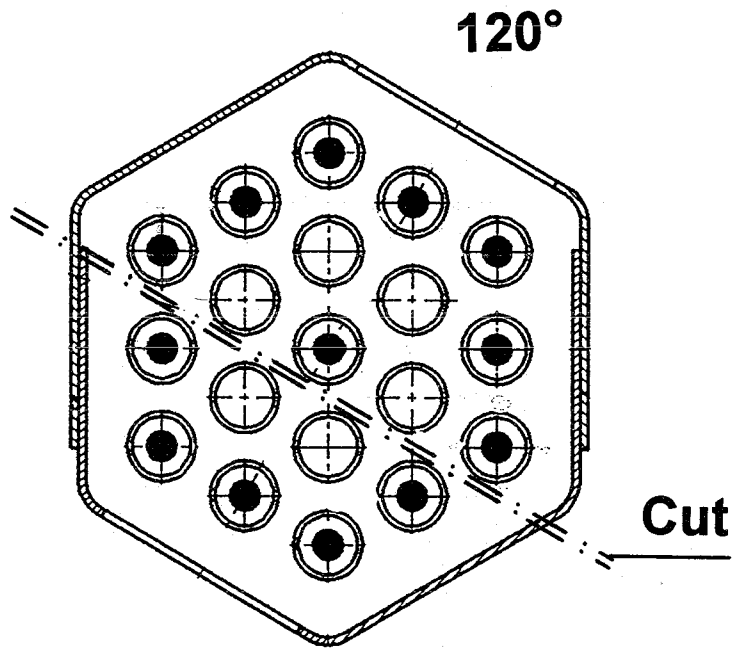


Fig.114: CORA-W1; Longitudinal cut through samples W1-j, W1-k, W1-l, W1-m, W1-n (top view)

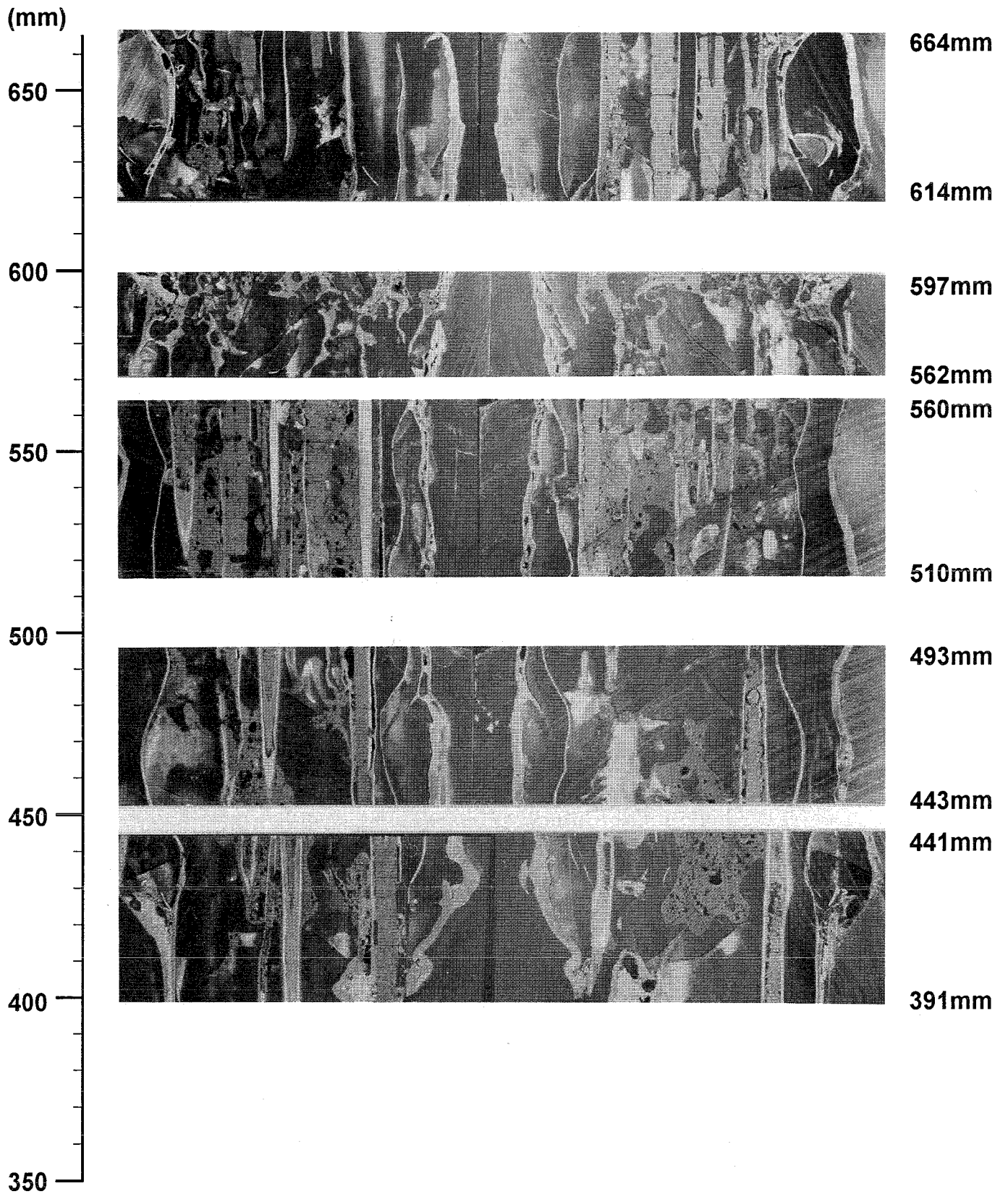
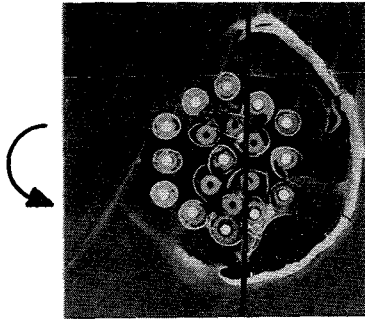
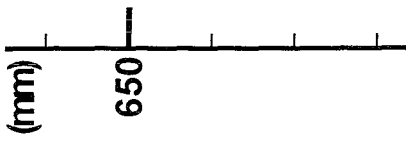


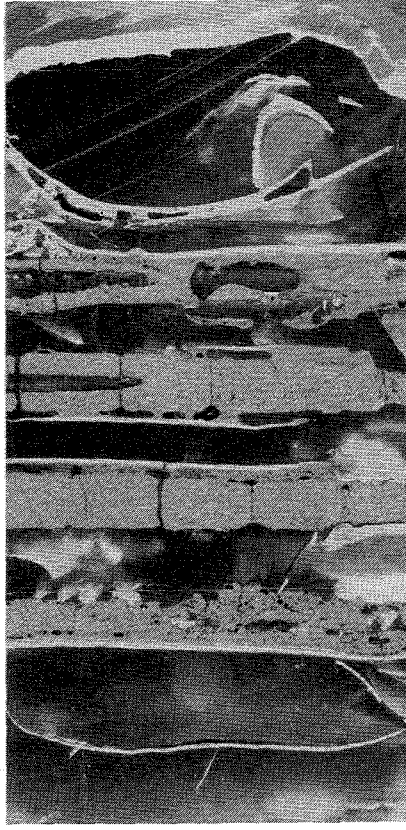
Fig.115: CORA-W1; Longitudinal sections (overview)



614 mm
(bottom)



664



614

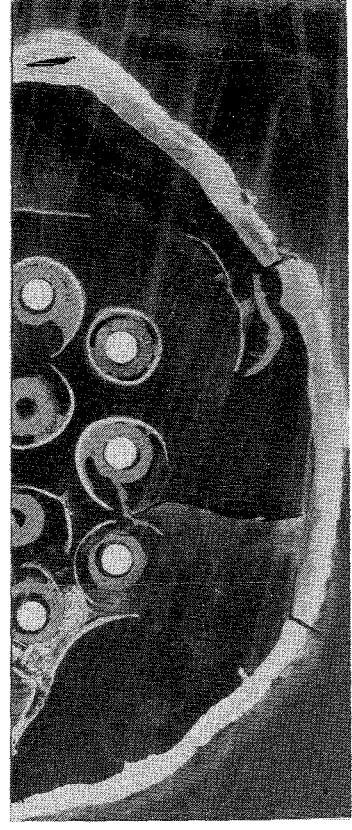
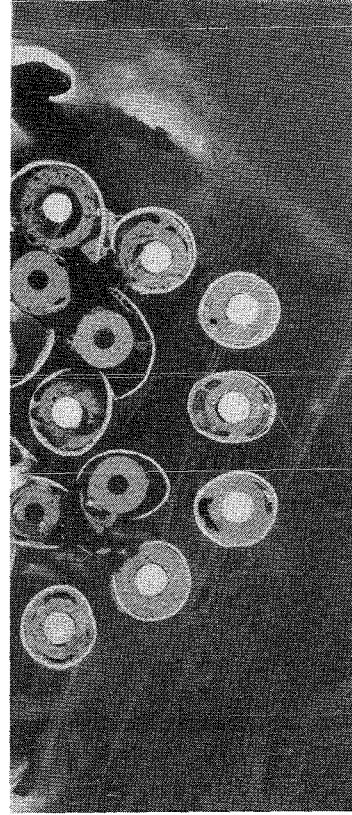
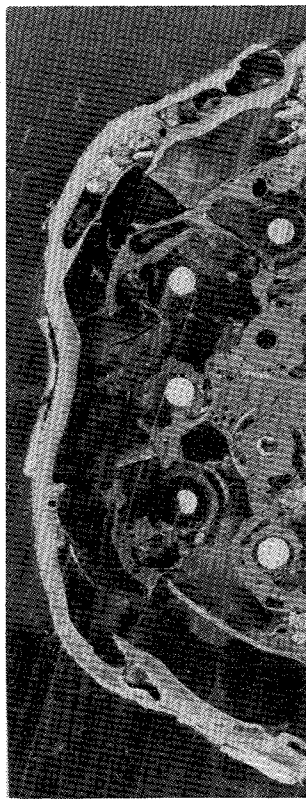
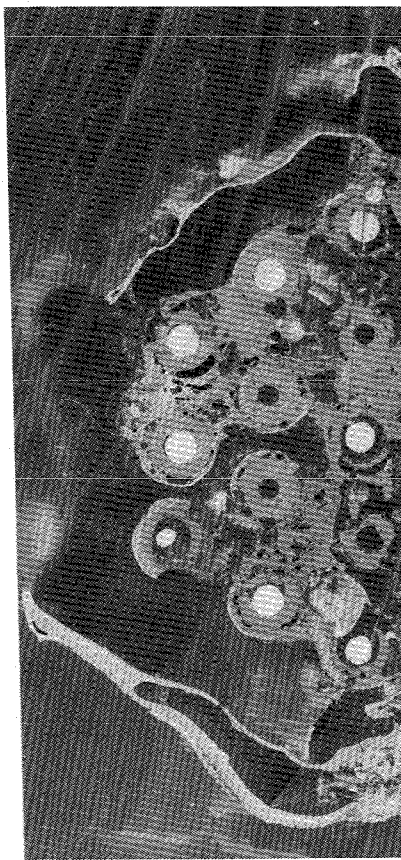
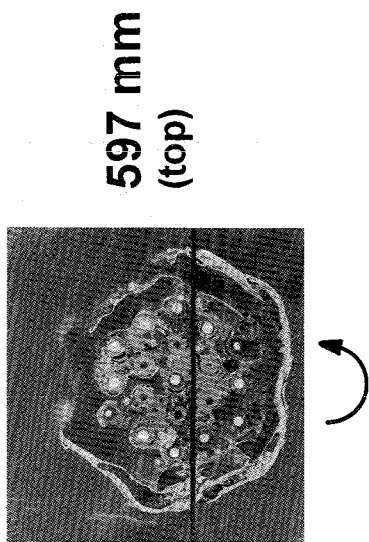


Fig.116: CORA-W1; Longitudinal section 443-493 mm



(mm)
580

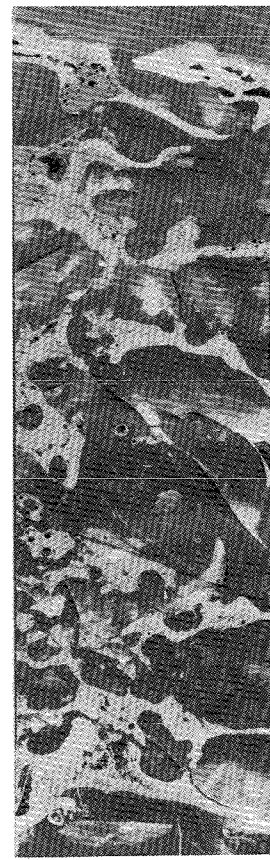
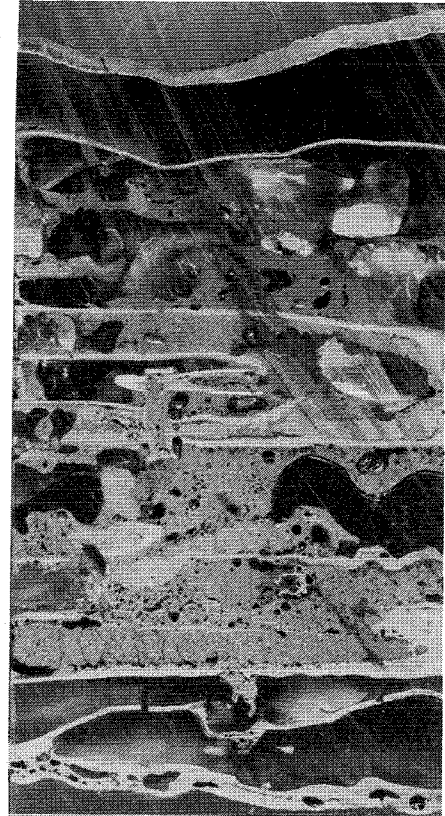
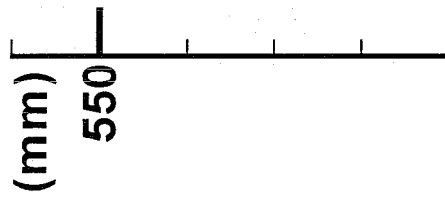
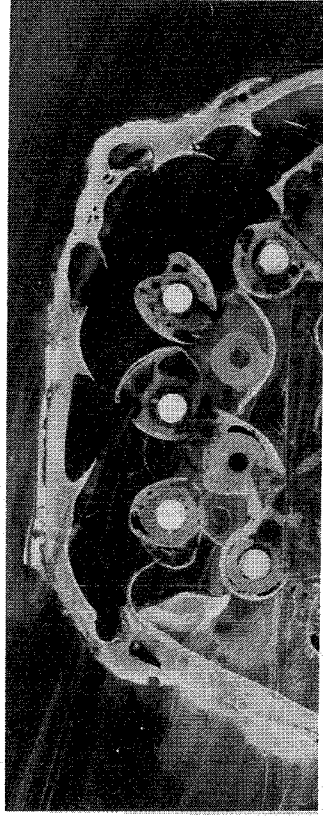
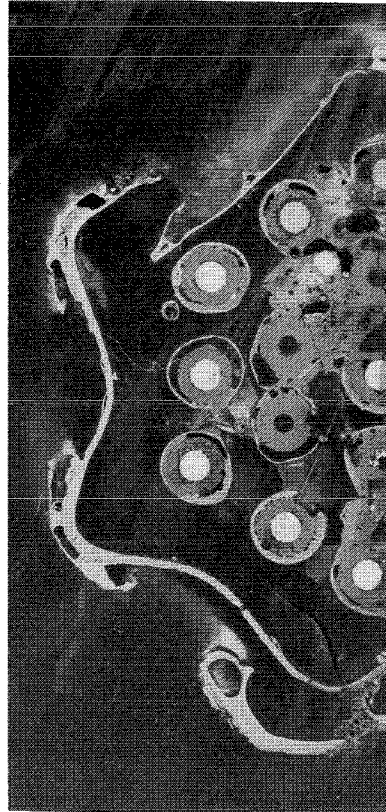
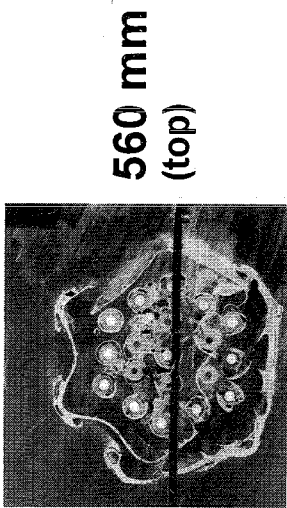


Fig.117: CORA-W1; Longitudinal section 510-560 mm



560

510

Fig.118: CORA-W1; Longitudinal section 562-597 mm

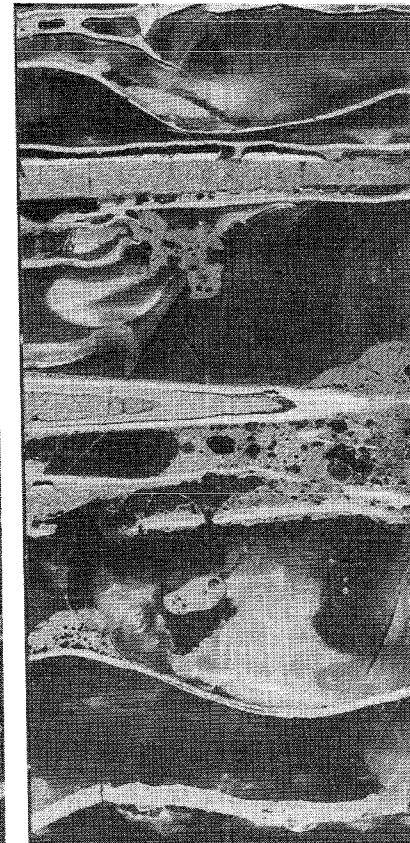
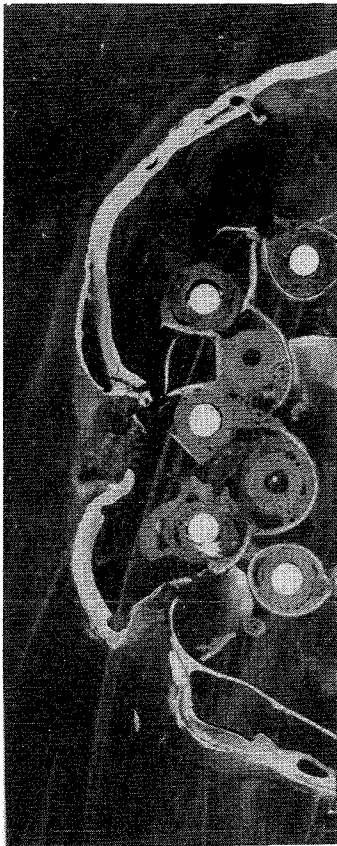
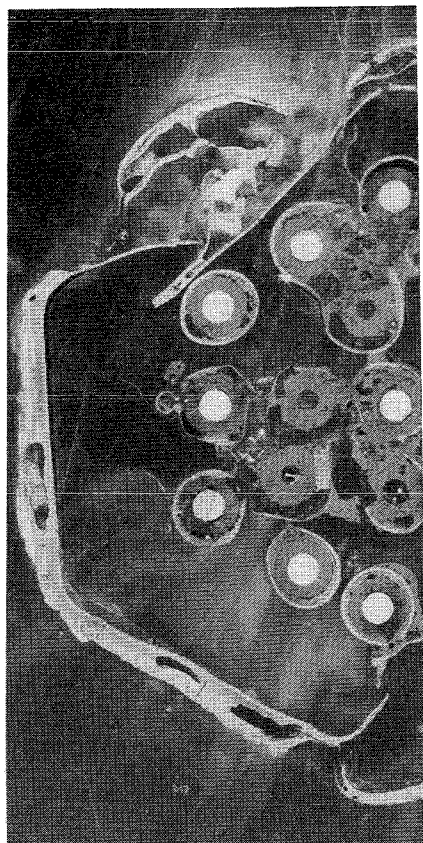
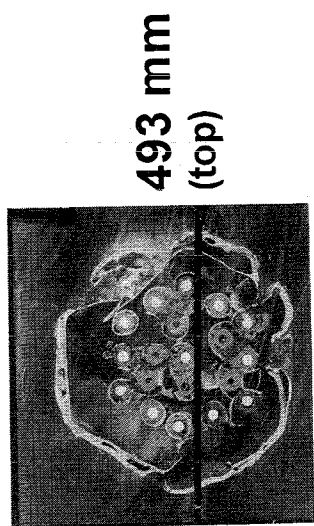
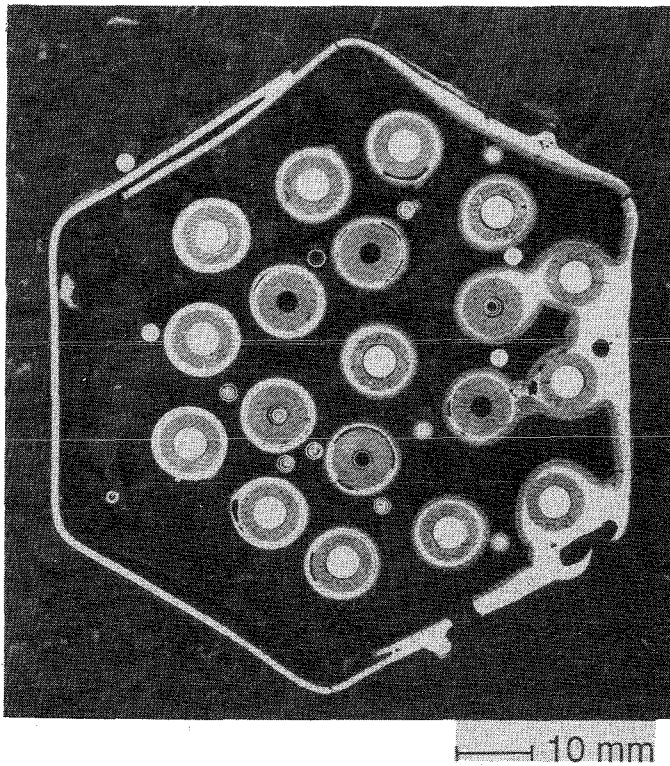
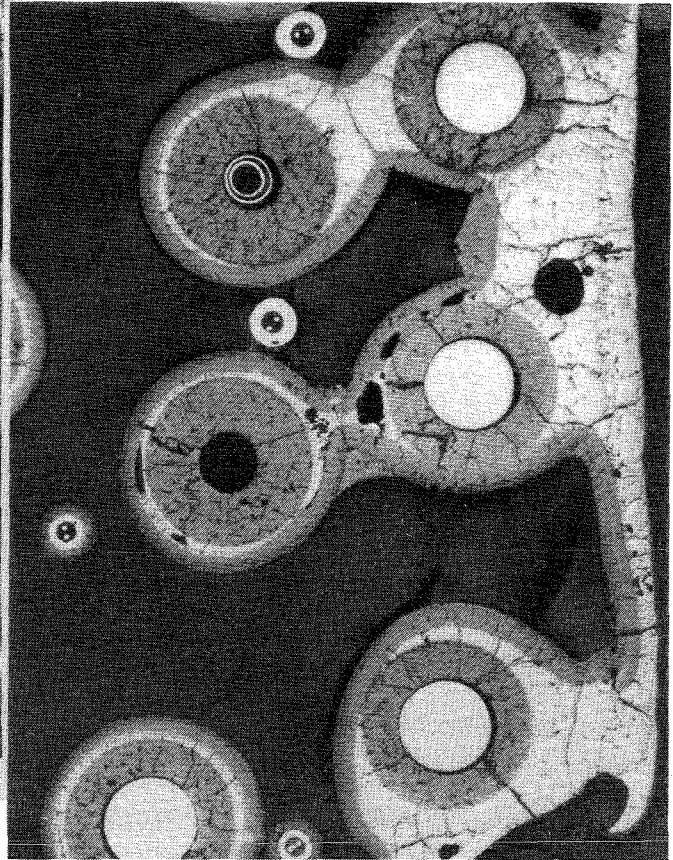
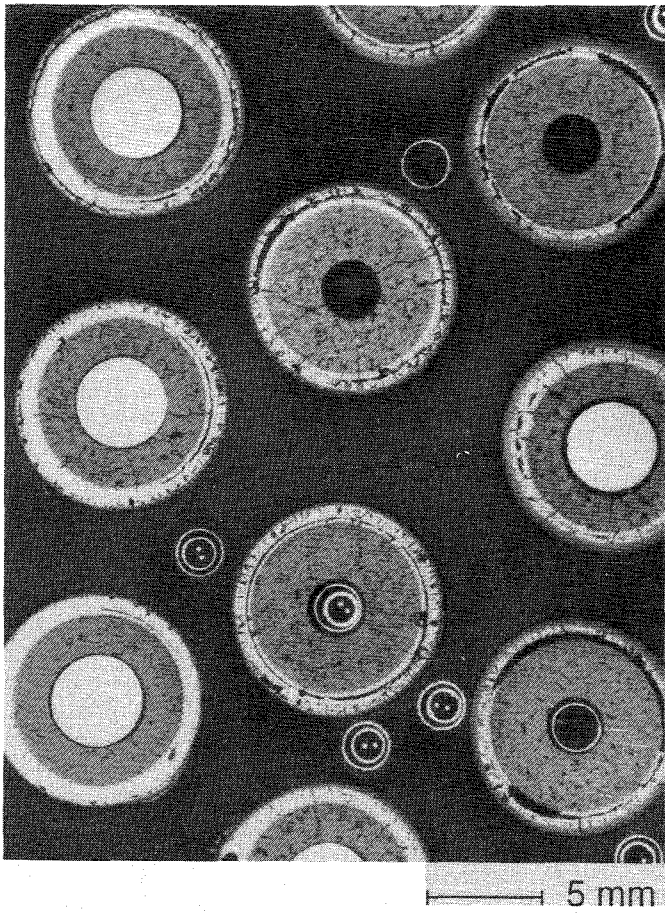


Fig.119: CORA-W1; Longitudinal section 614-664 mm



W1-10 (top), 374 mm

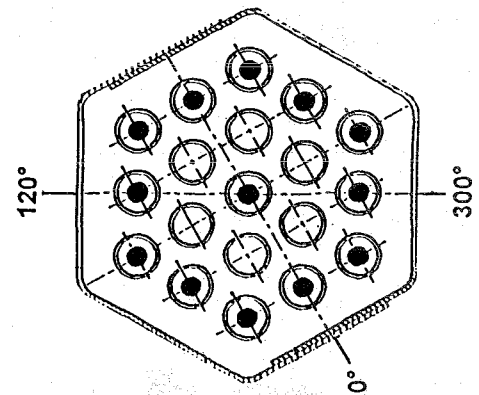


Fig. 120:
Cross Section W1-10 (top), Elevation 374 mm
Overview

W1-10 (top), 374 mm

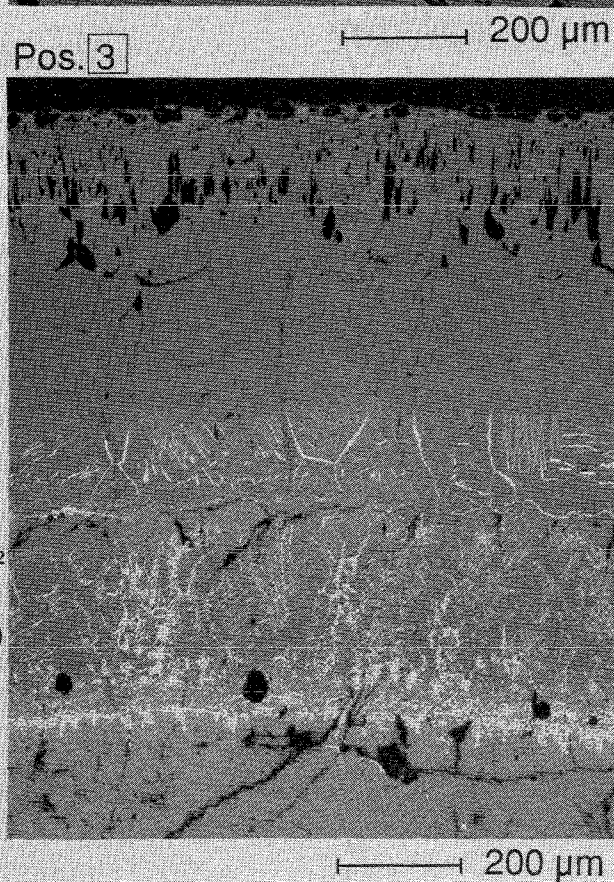
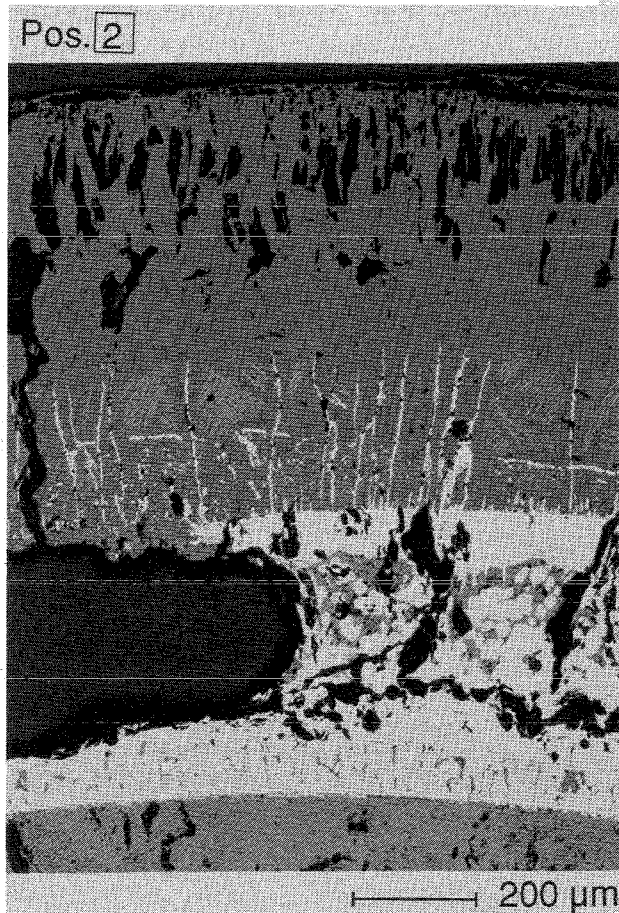
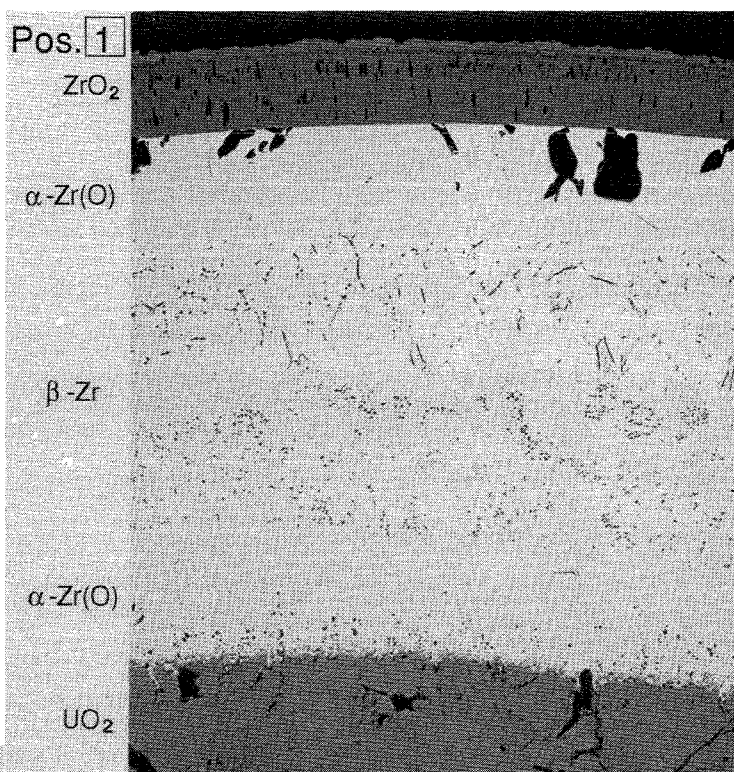
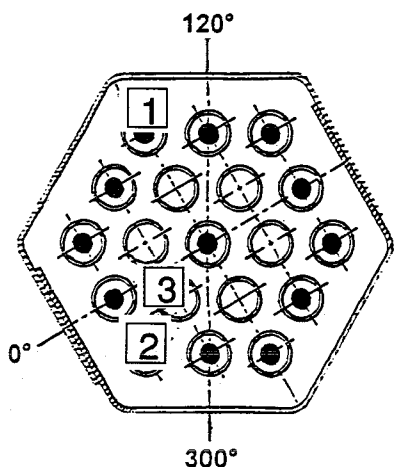
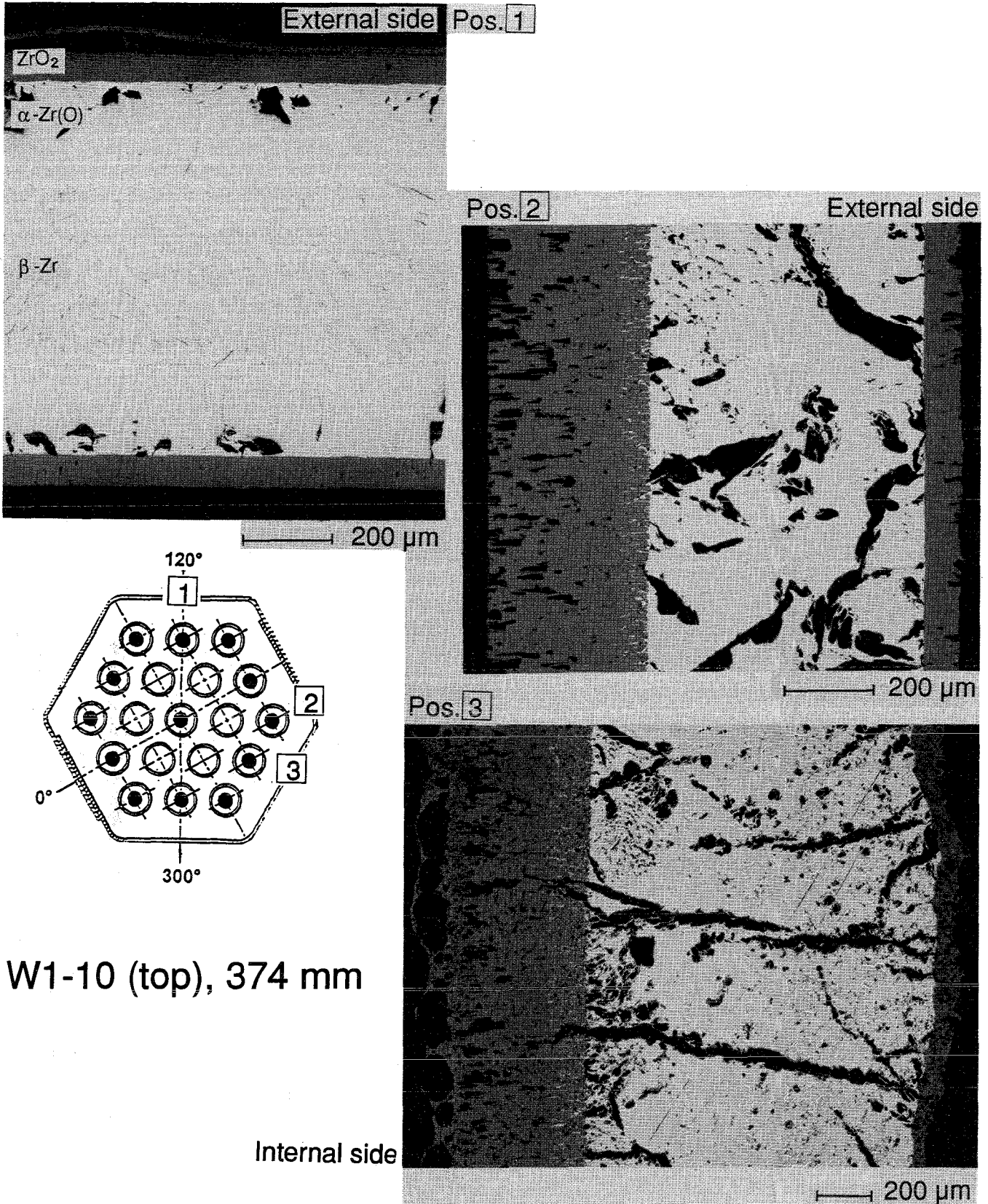


Fig. 121:

Cross Section W1-10 (top), Elevation 374 mm
Cladding Oxidation, Melting, Interaction With Fuel

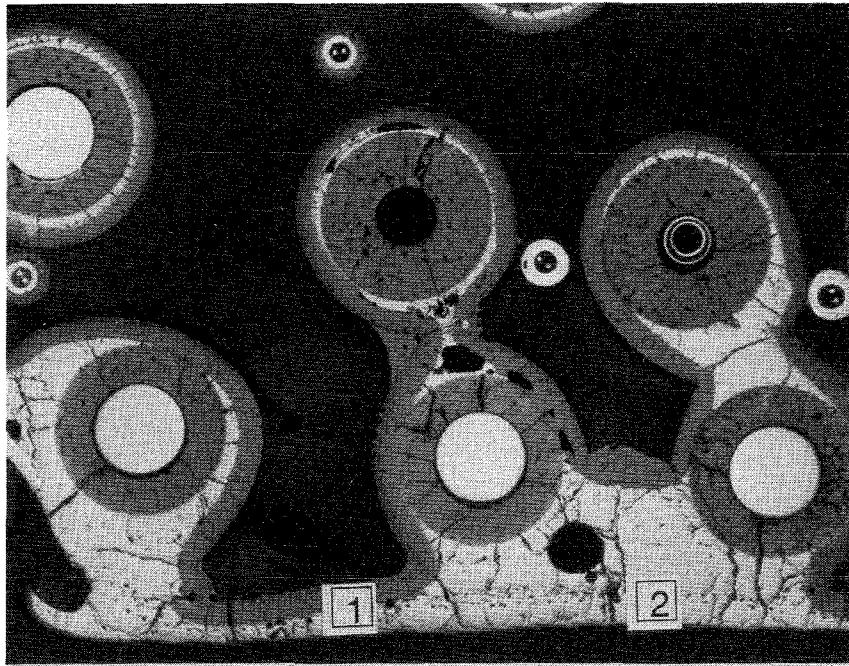


W1-10 (top), 374 mm

Internal side

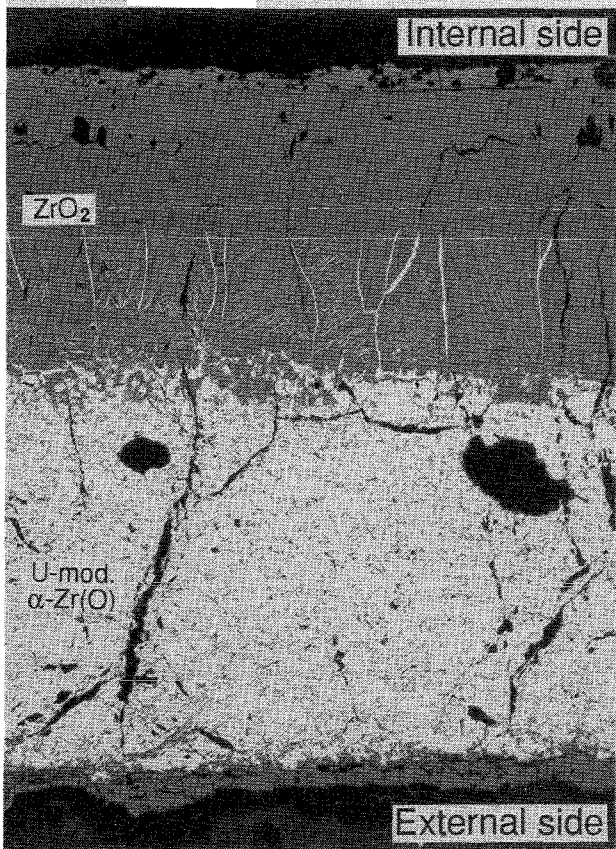
Fig. 122:

Cross Section W1-10 (top), Elevation 374 mm
Shroud Oxidation

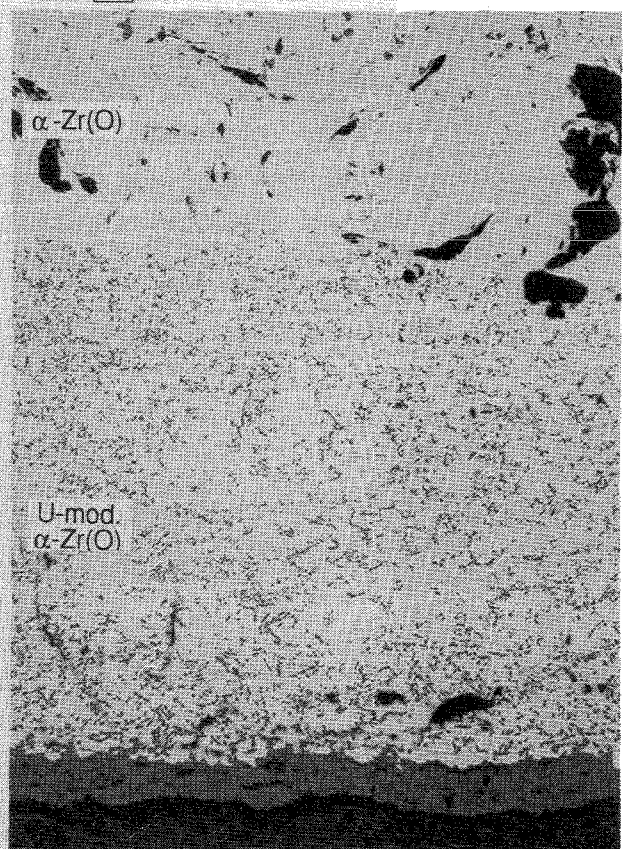


5 mm

Pos. 1



Pos. 2

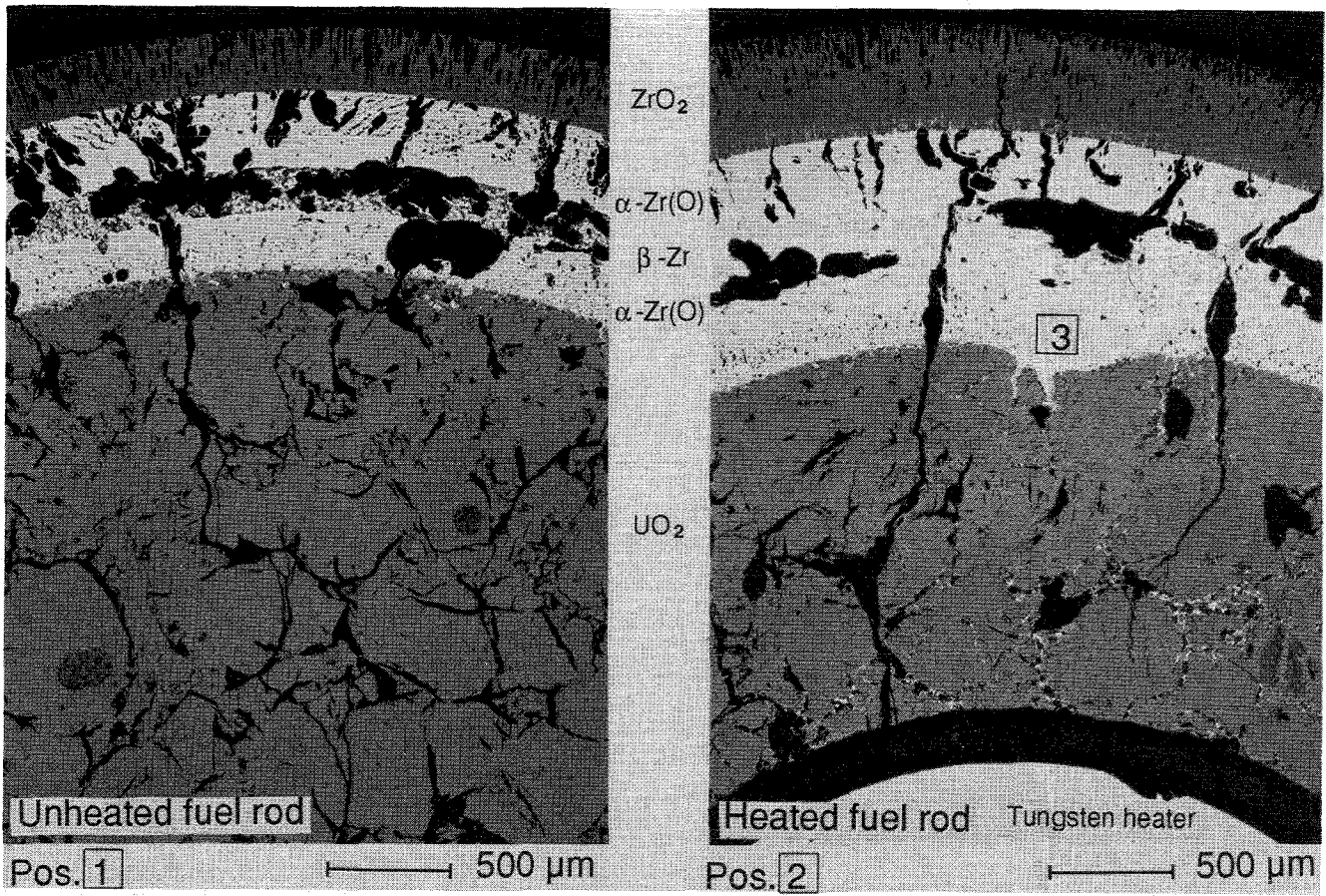


ZrO_2

W1-10 (top), 374 mm

Fig. 123:

Cross Section W1-10 (top), Elevation 374 mm
Shroud Melting and Interaction With Melt



W1-10 (top), 374 mm

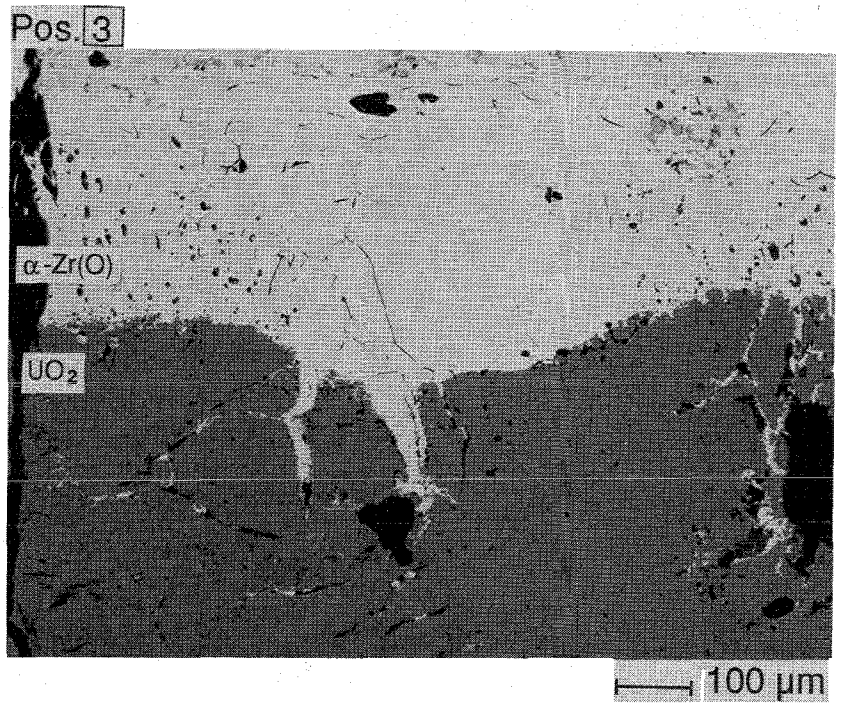
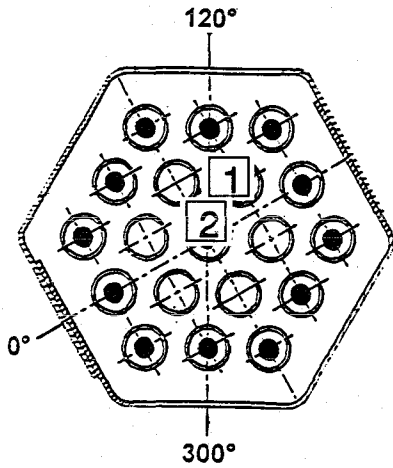
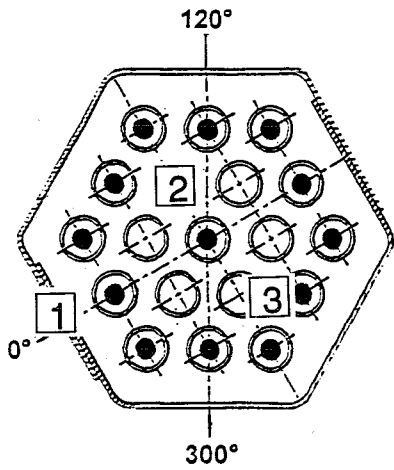
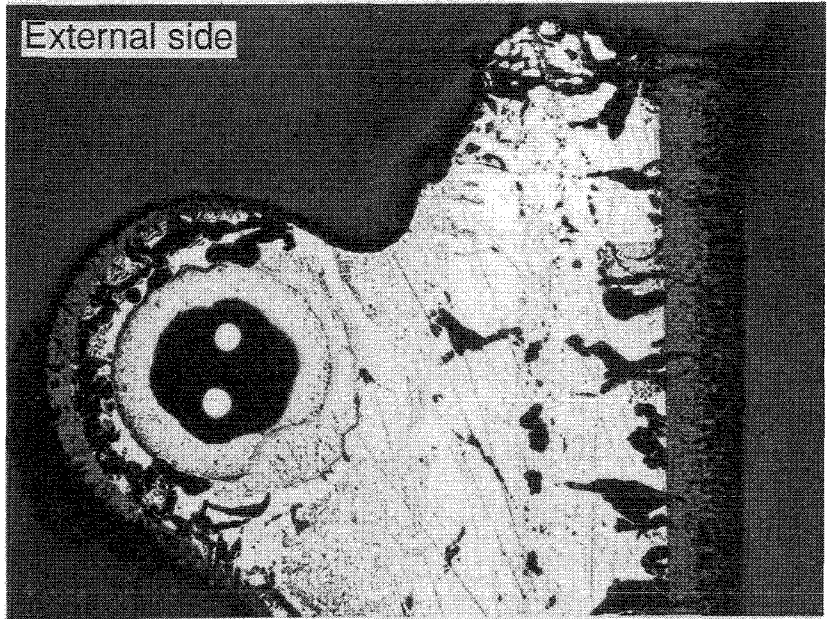


Fig. 124:
Cross Section W1-10 (top), Elevation 374 mm
Heated and Unheated Fuel Rod

W1-10 (top), 374 mm

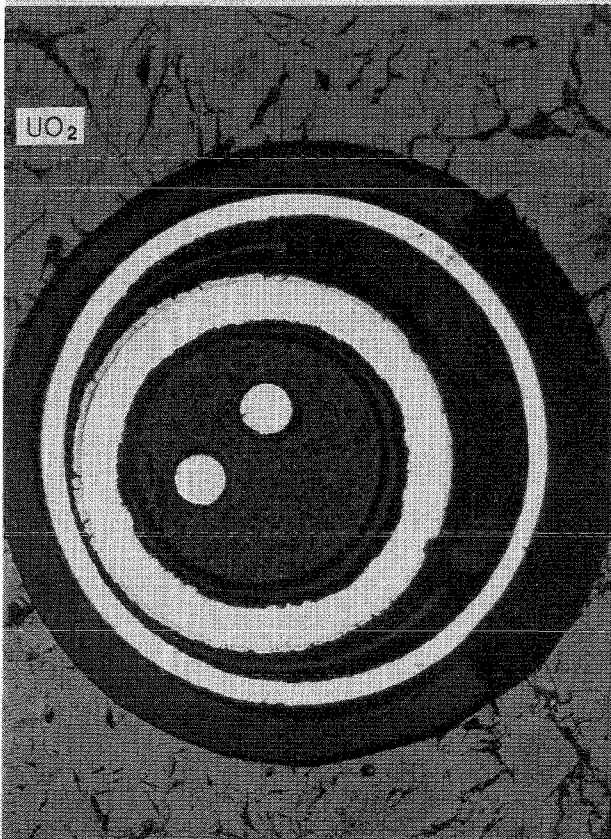


Pos. 1 Shroud TC, external



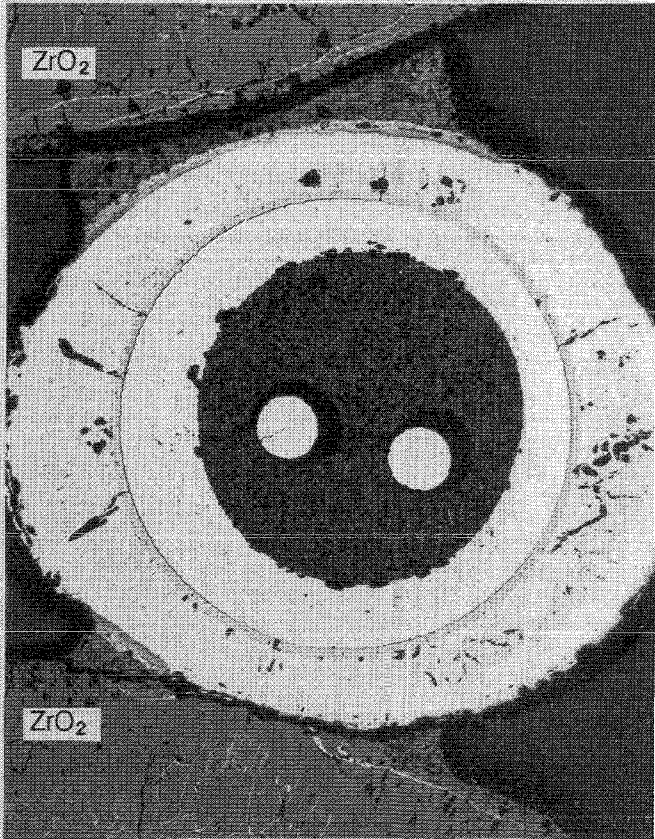
500 μm

Pos. 2 Fuel TC



500 μm

Pos. 3 Cladding TC



250 μm

Fig. 125:
Cross Section W1-10 (top), Elevation 374 mm
Thermocouples

W1-04 (top), 389 mm

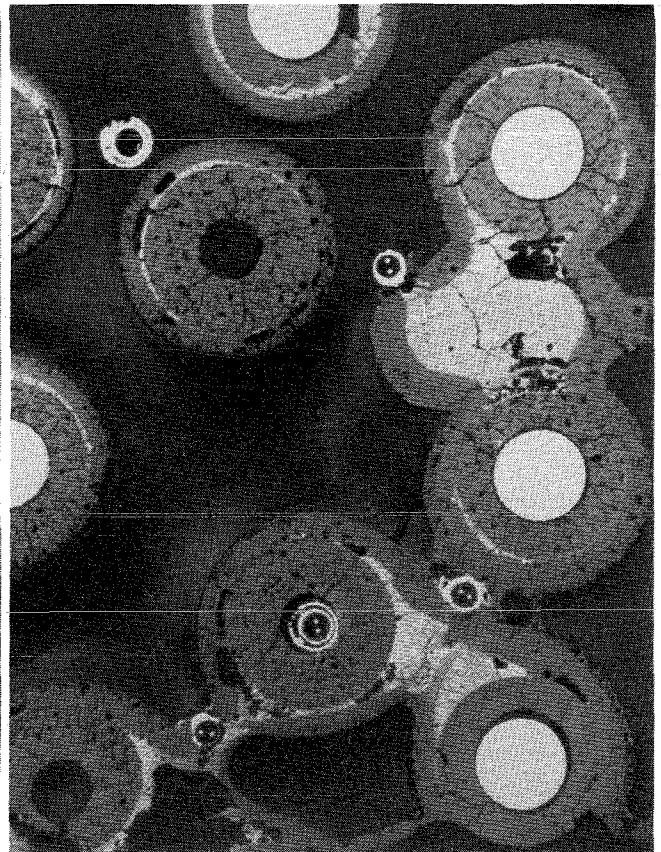
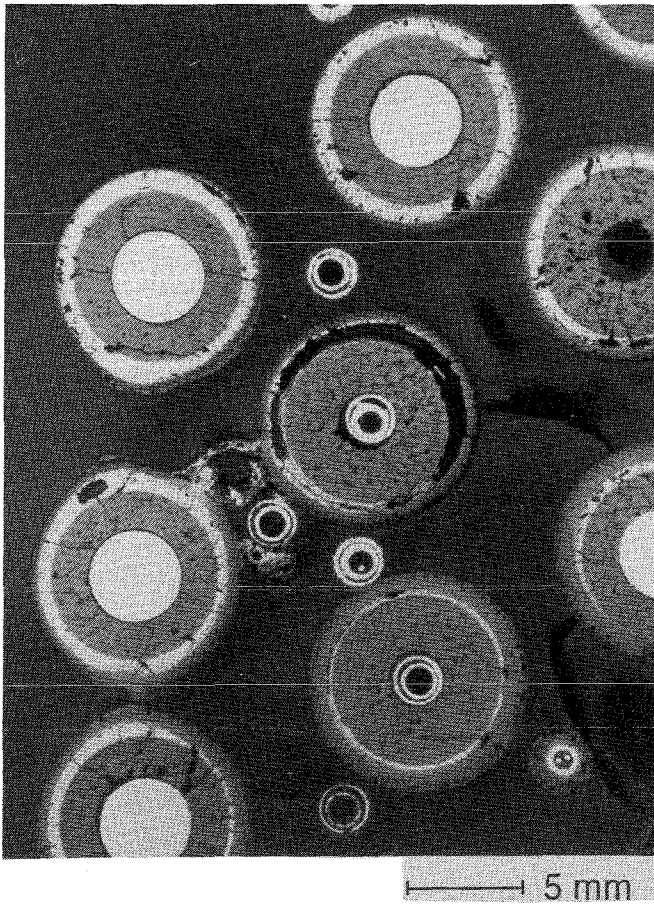
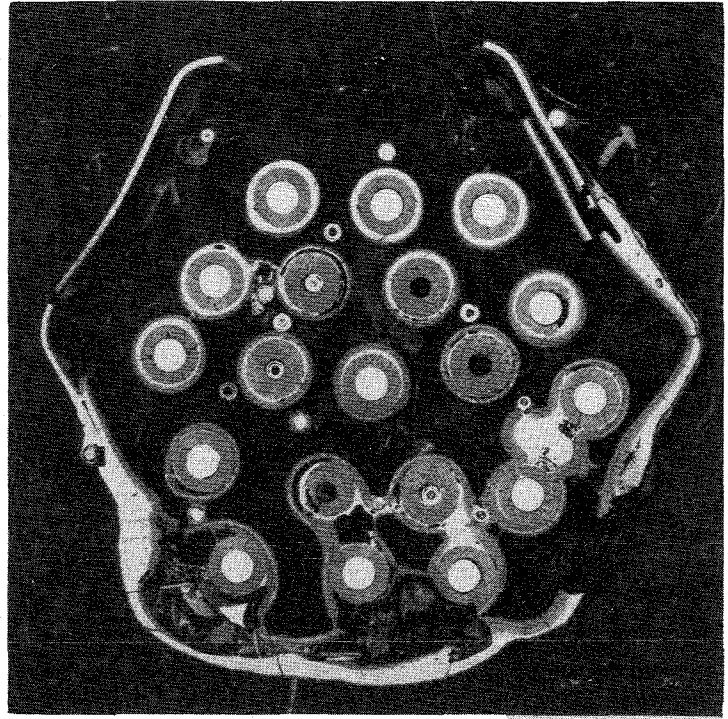
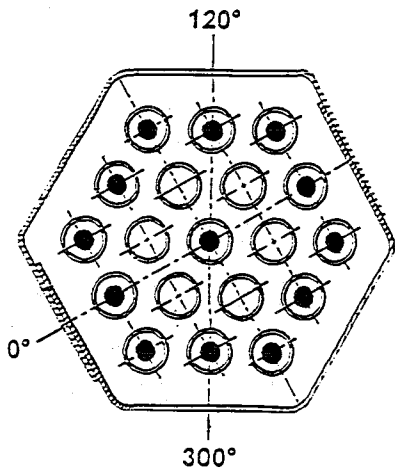
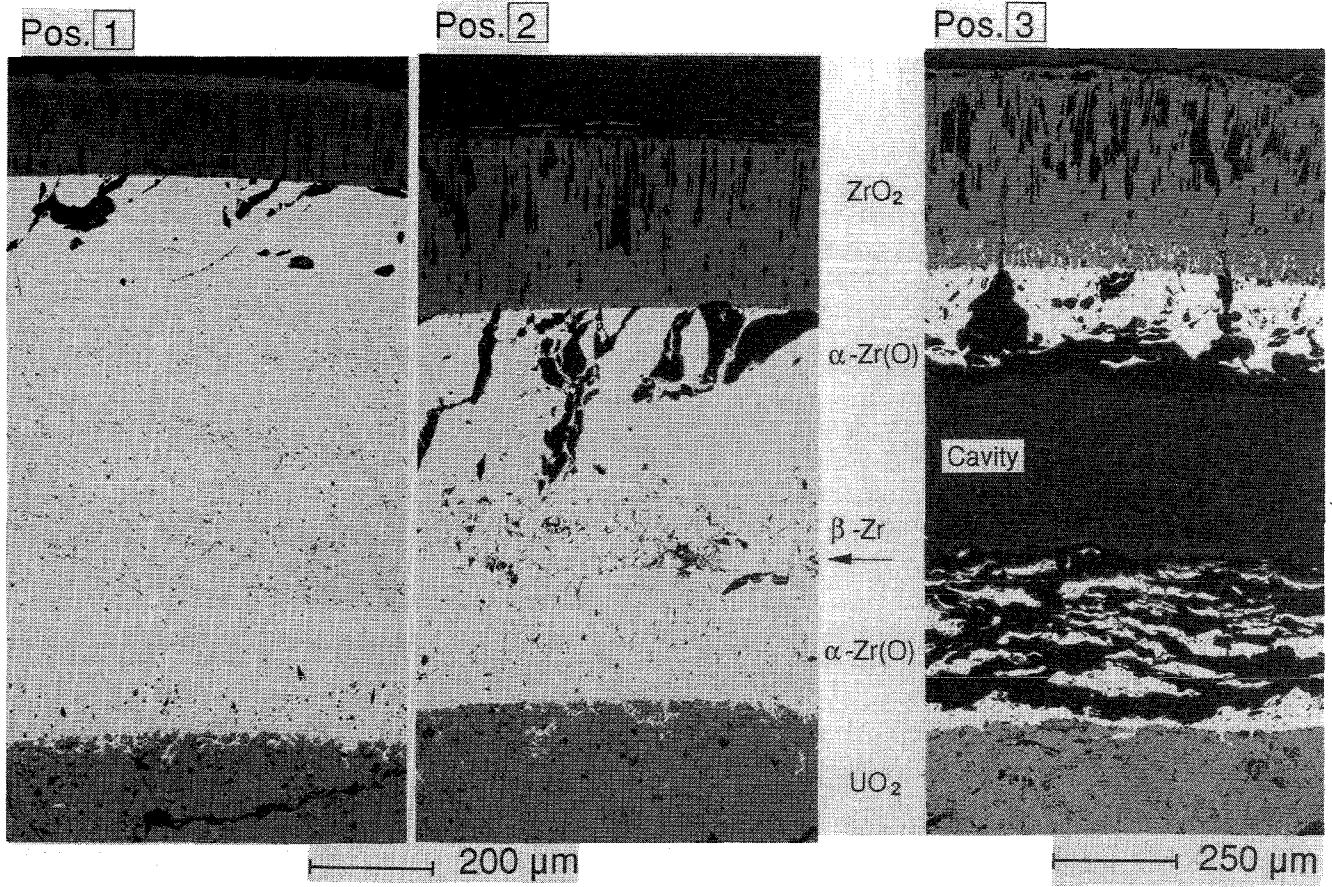


Fig. 126:

Cross Section W1-04 (top), Elevation 389 mm
Overview



W1-04 (top), 389 mm

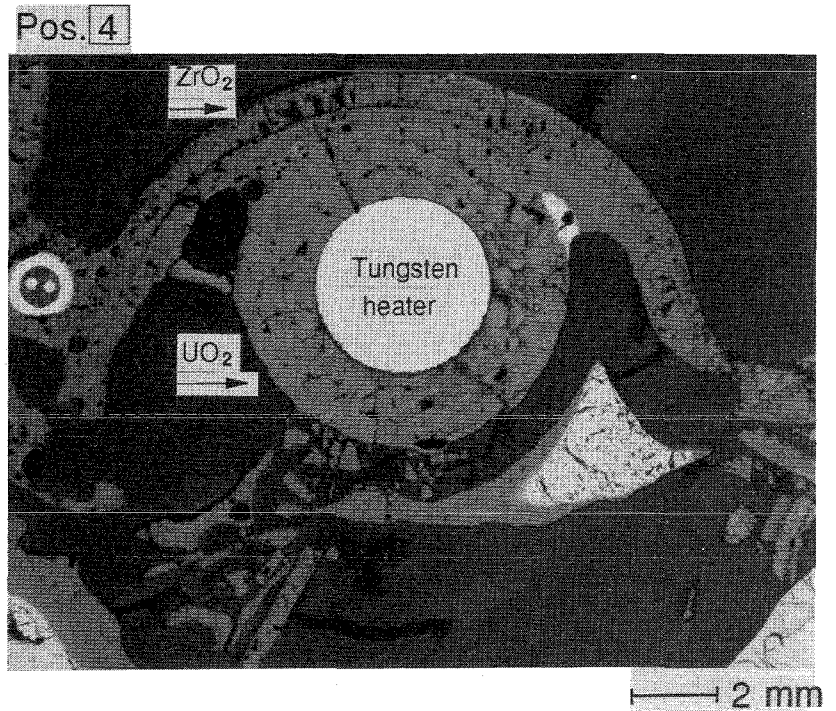
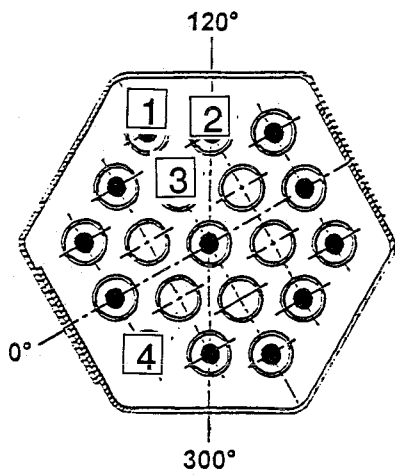
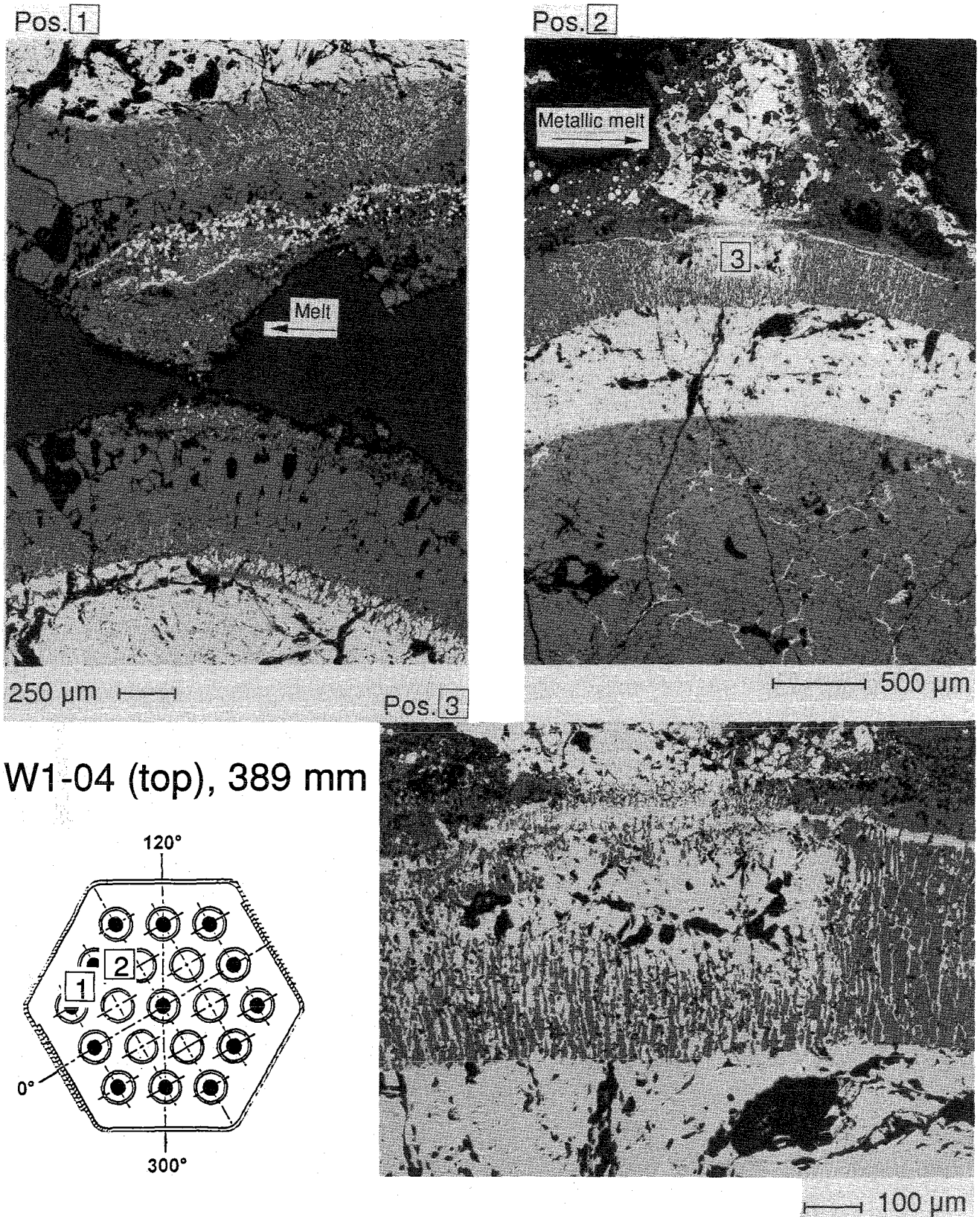


Fig. 127:

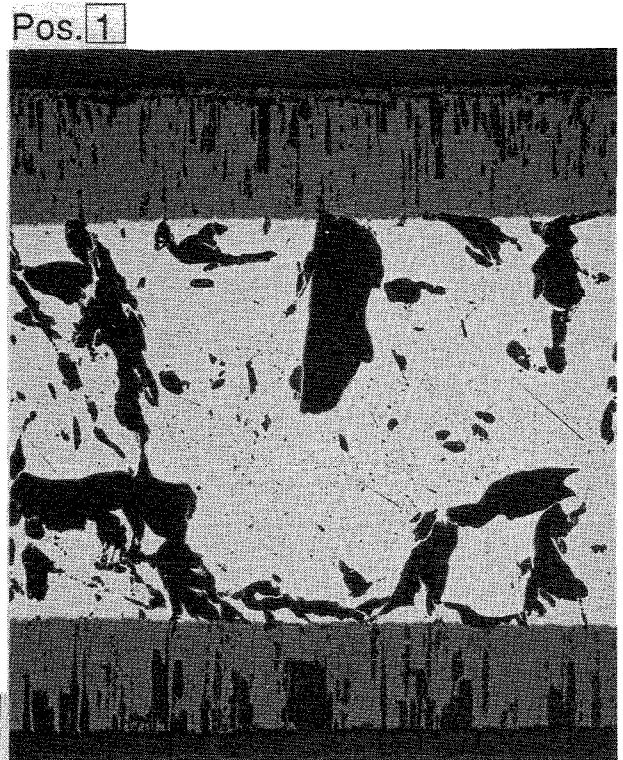
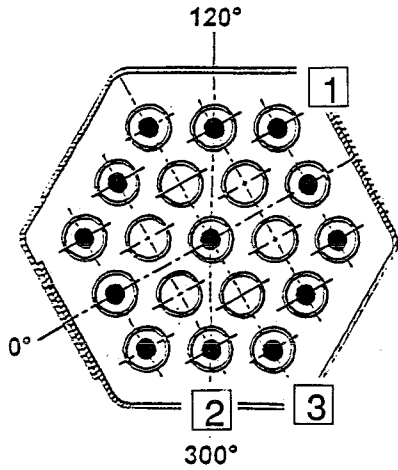
Cross Section W1-04 (top), Elevation 389 mm
Fuel Rod Cladding Oxidation



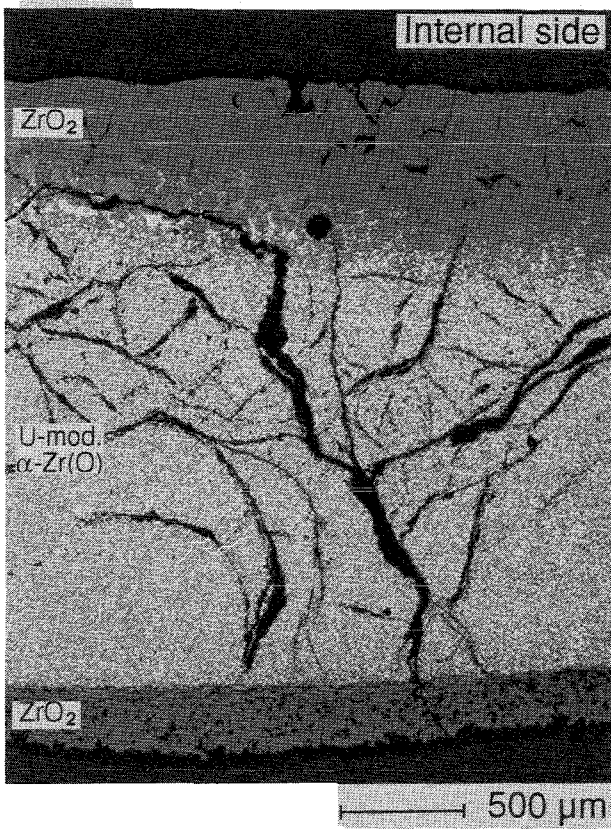
W1-04 (top), 389 mm

Fig. 128:
Cross Section W1-04 (top), Elevation 389 mm
External Cladding Attack, Scale Reduction by Melt

W1-04 (top), 389 mm



Pos. 2



Pos. 3

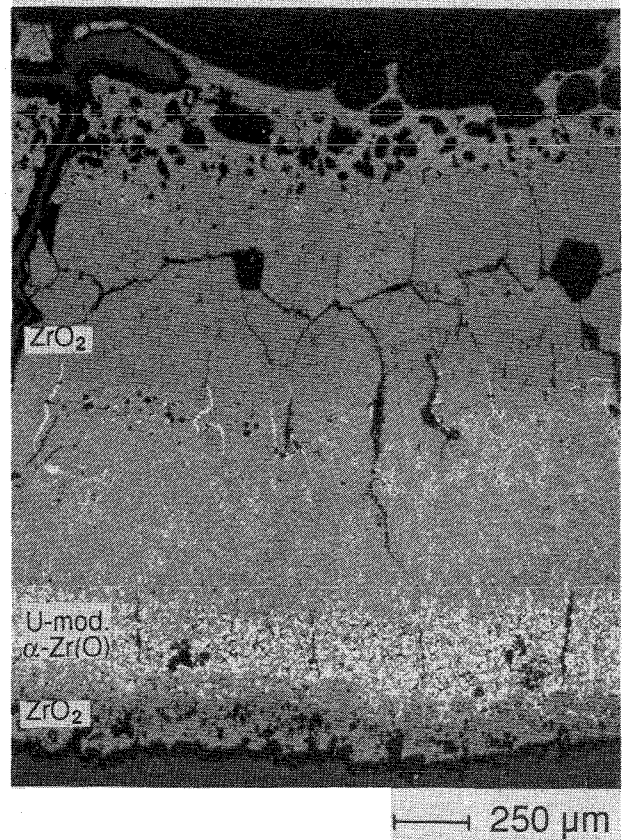


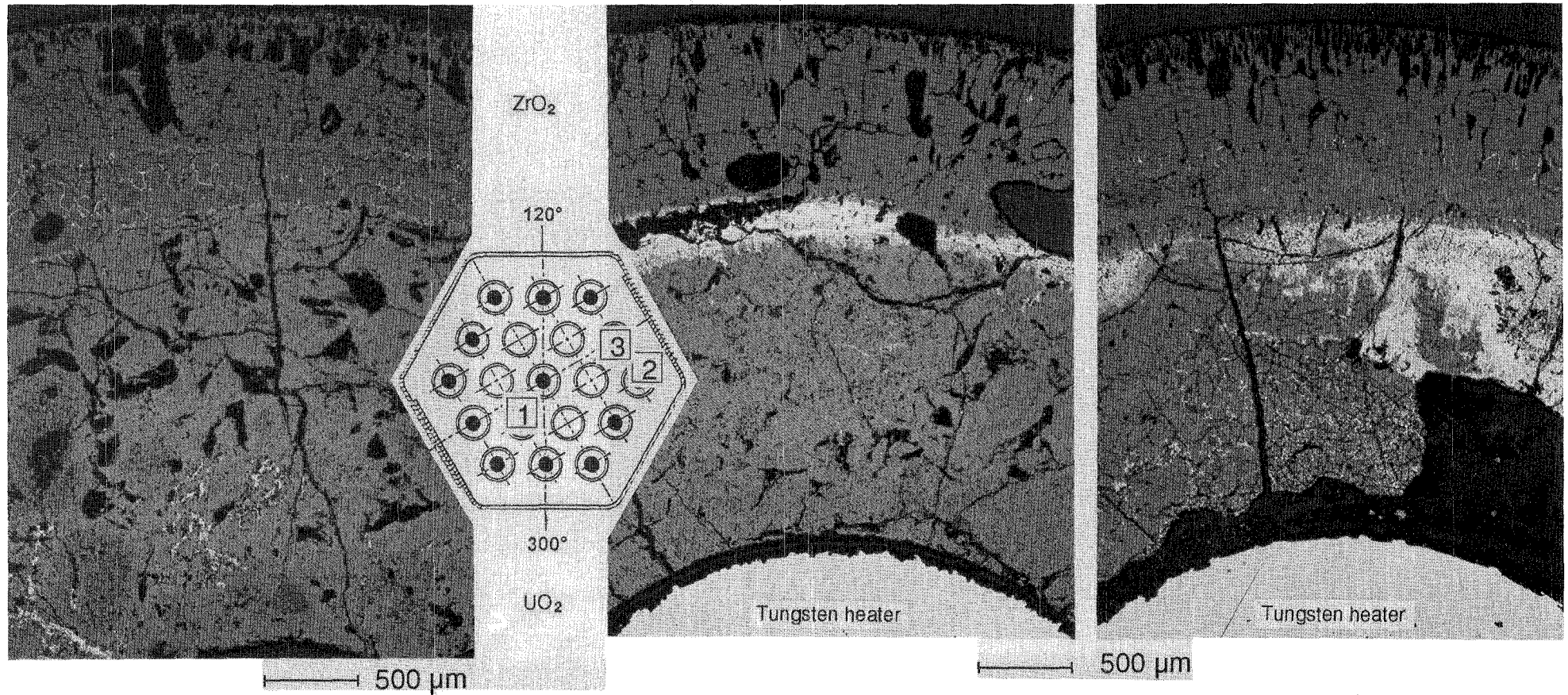
Fig. 129:
Cross Section W1-04 (top), Elevation 389 mm
Shroud at Different Orientations

Pos. 1 Unheated fuel rod

Pos. 2

Heated fuel rods

Pos. 3



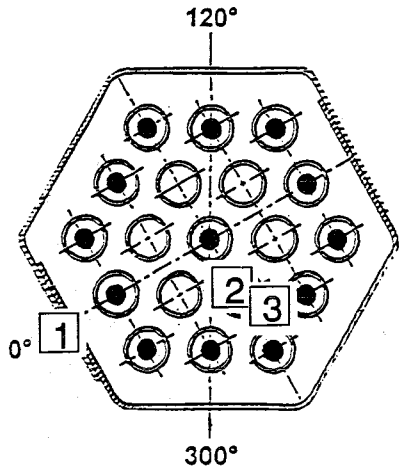
W1-04 (top), 389 mm



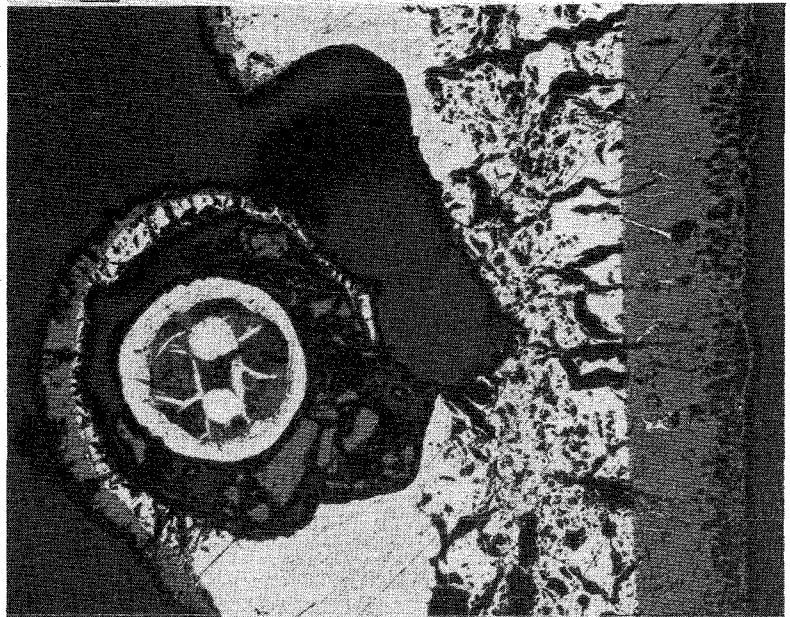
Fig. 130:

Cross Section W1-04 (top), Elevation 389 mm. Heated and Unheated Fuel Rods

W1-04 (top), 389 mm



Pos. 1 Shroud TC, external



Pos. 2 Fuel TC



Pos. 3 Cladding TC

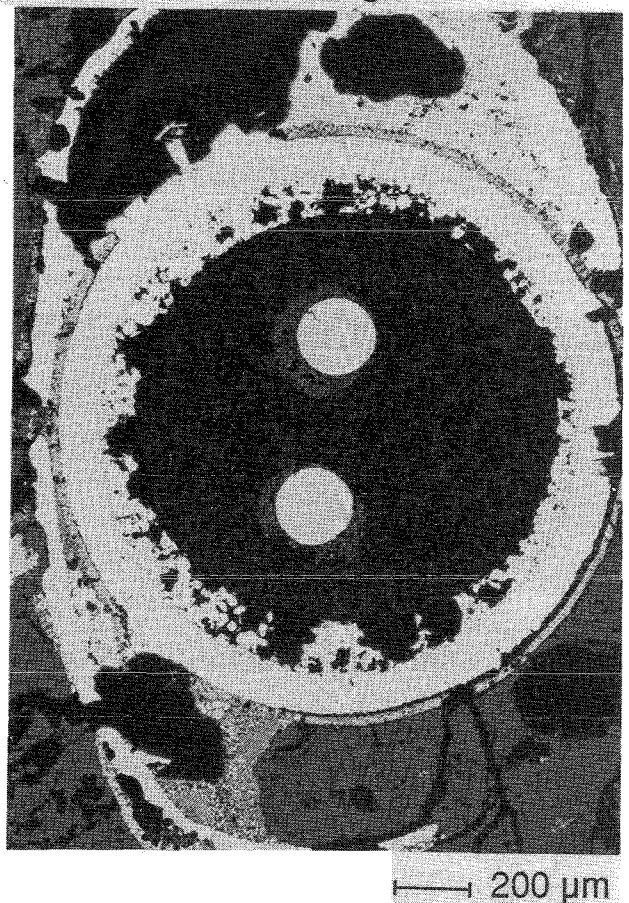
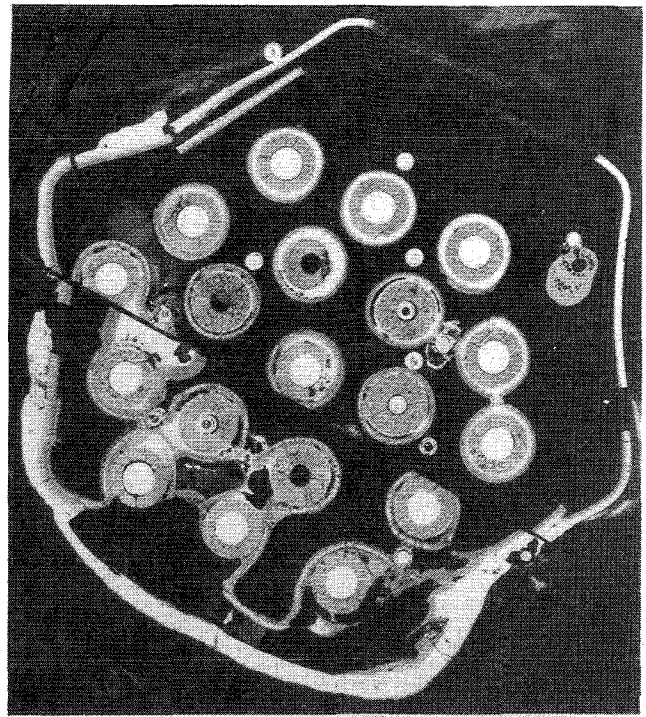
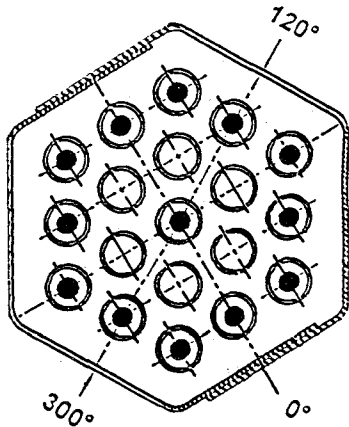
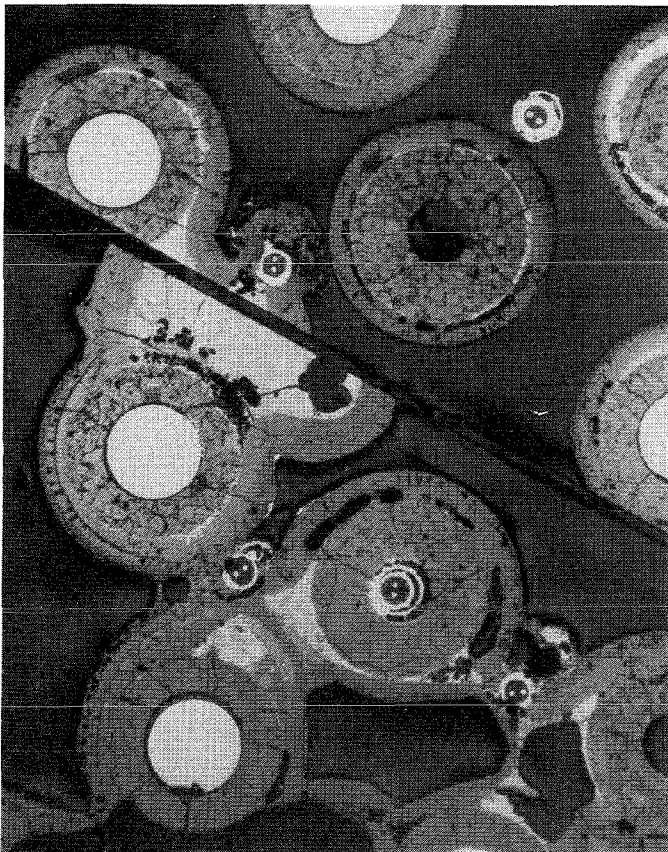


Fig. 131:
Cross Section W1-04 (top), Elevation 389 mm
Thermocouples

W1-j (bottom), 391 mm



10 mm



5 mm

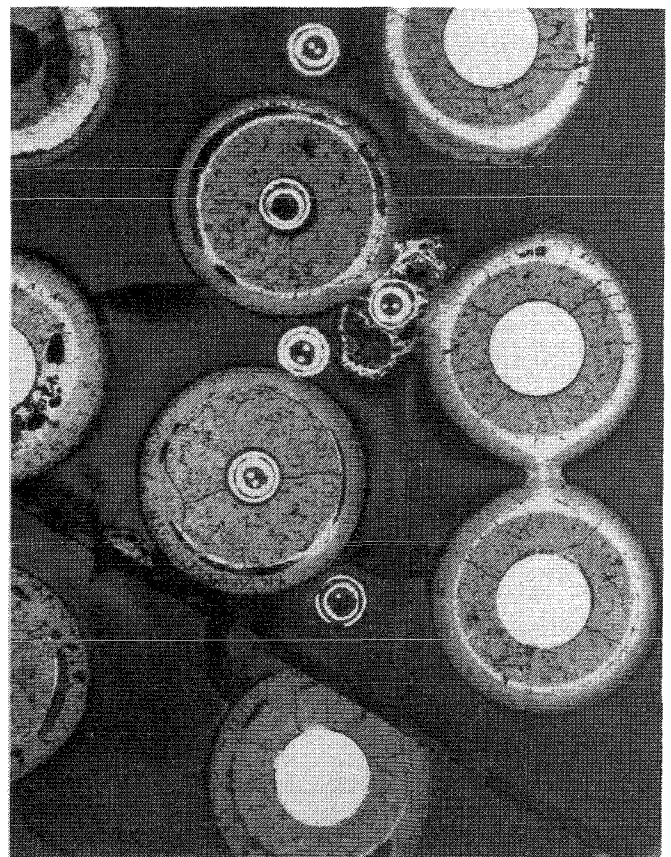


Fig. 132:
Cross Section W1-j (bottom), Elevation 391 mm
Overview

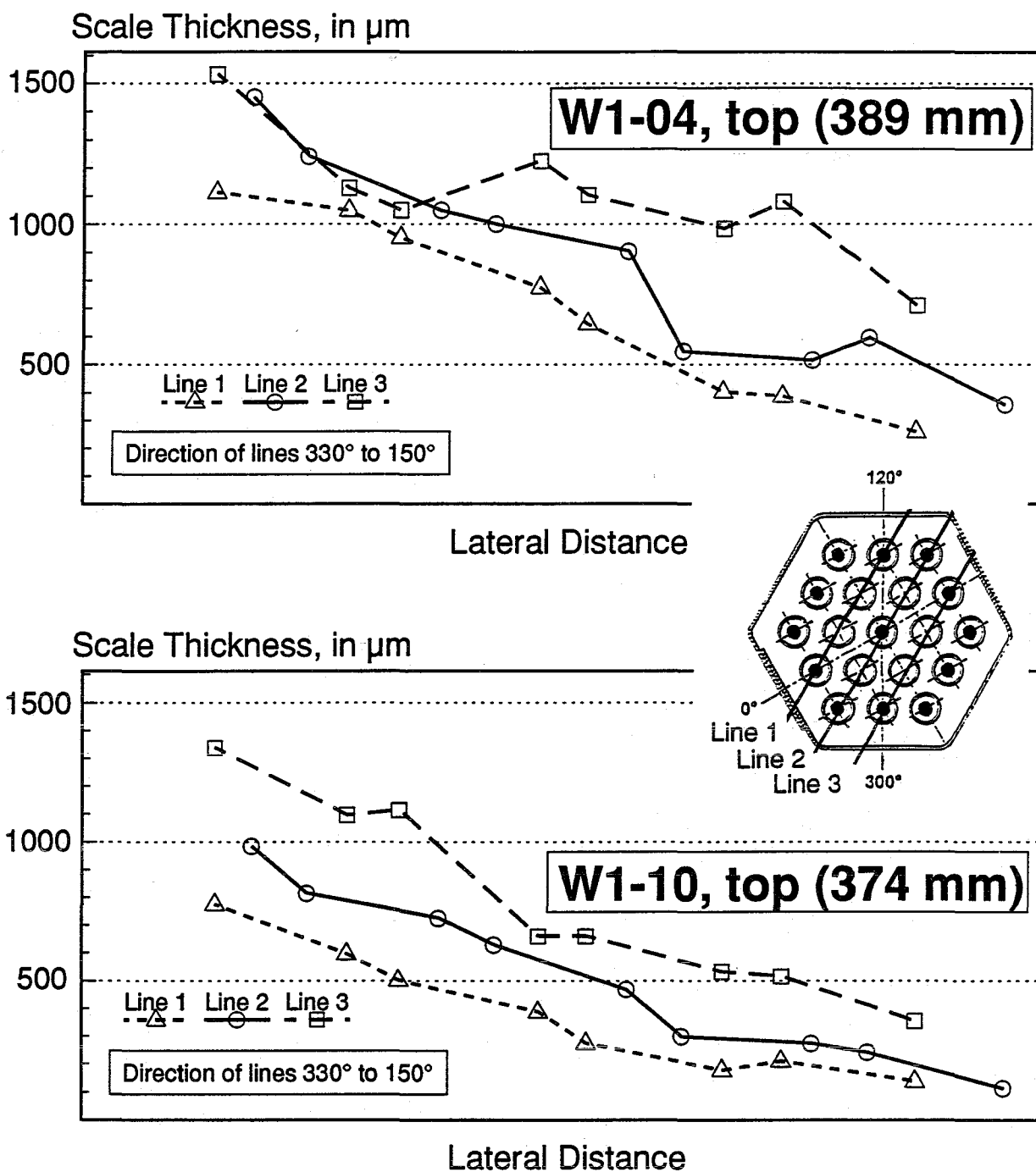


Fig. 133:



IMF-III/KOR

ZrO₂ Scale Thickness Profiles across the Fuel Rod Bundle CORA-W1 in the Azimuthal Direction 330° to 150° at the Elevations 389 mm (Cross Section W1-04, Top) and 374 mm (Cross Section W1-10, Top)

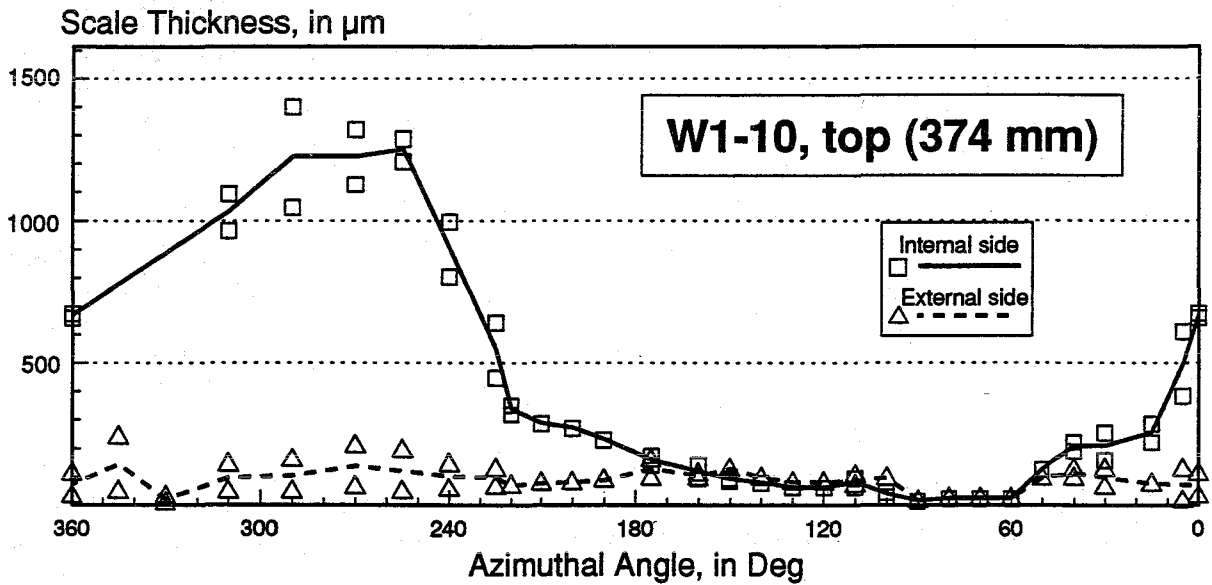
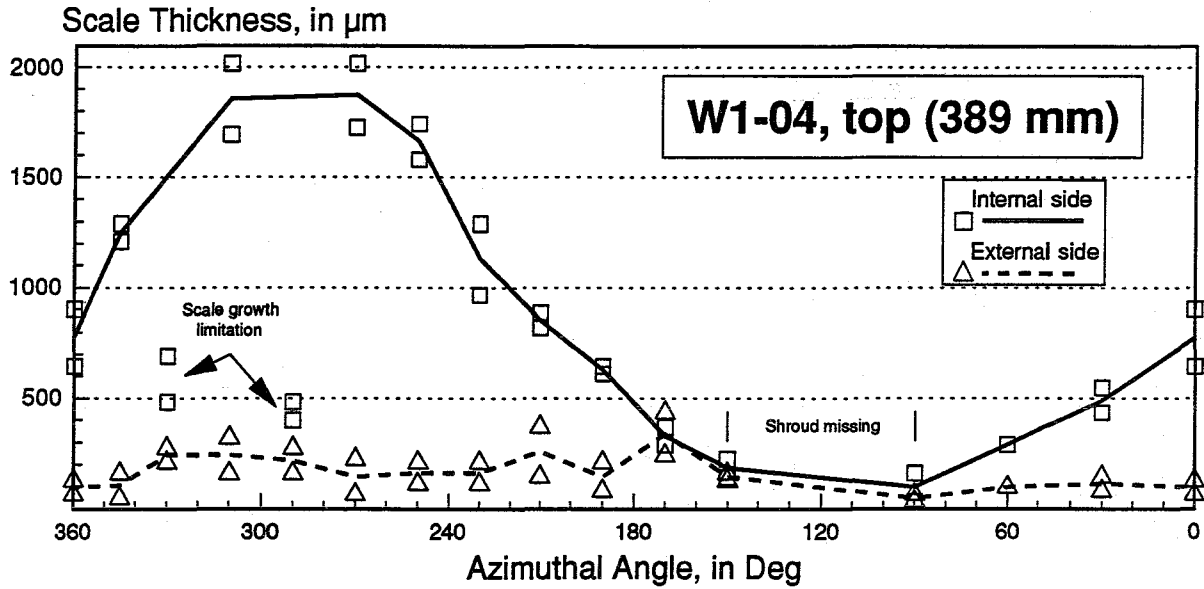

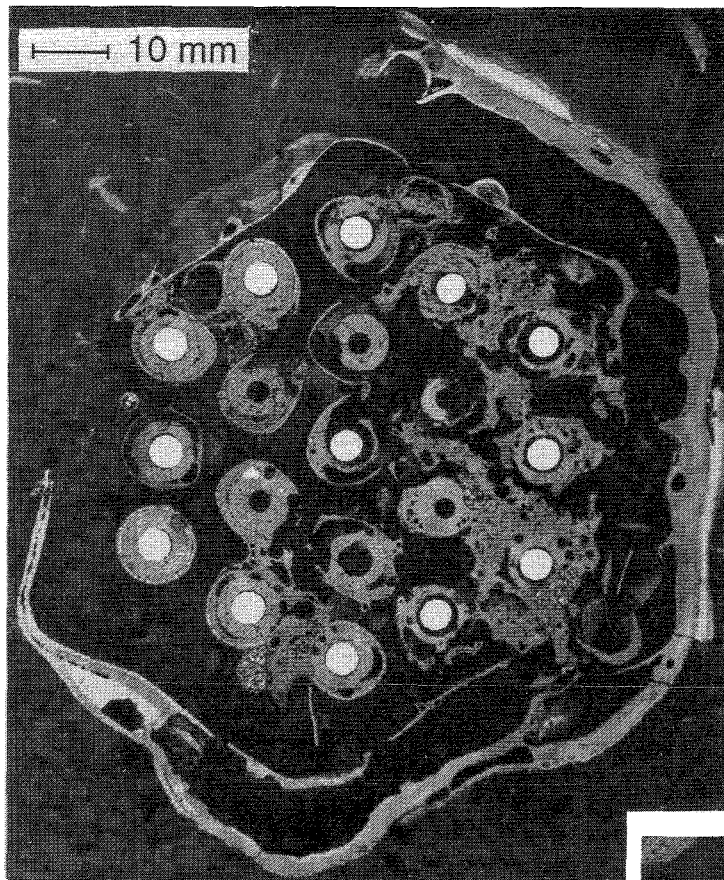


Fig. 134:  IMF-II/KOR
ZrO₂ Scale Thickness Profiles around the Shroud of Bundle CORA-W1 at the Elevations 389 mm and 374 mm, measured at External and Internal Surface



W1-06 (top), 612 mm

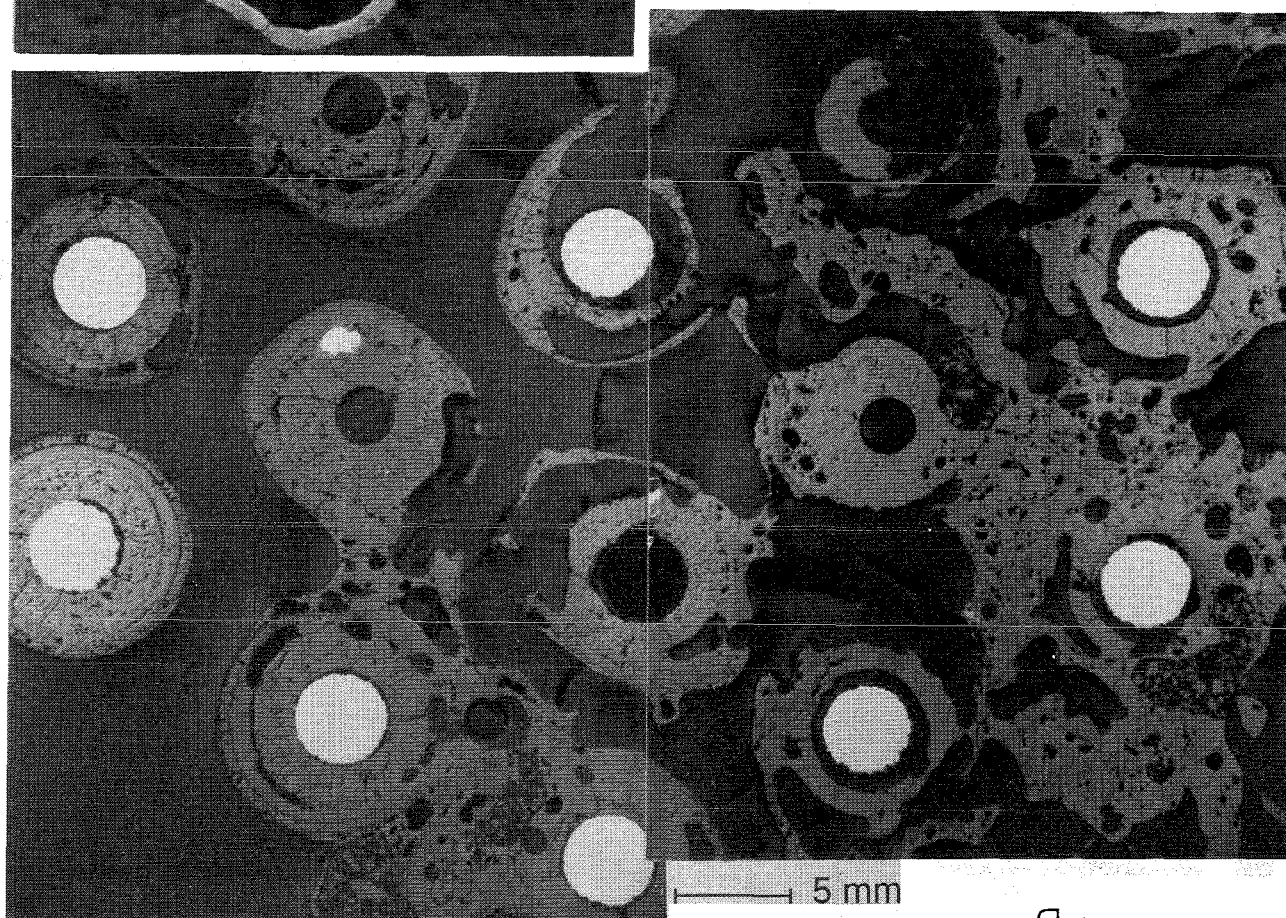
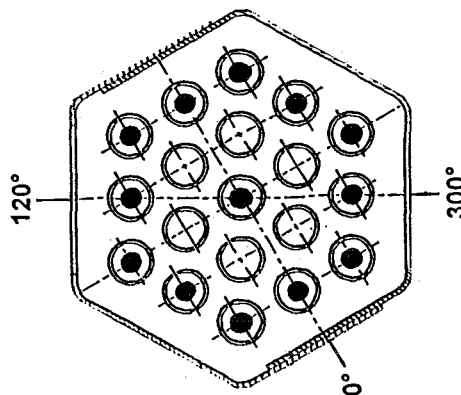
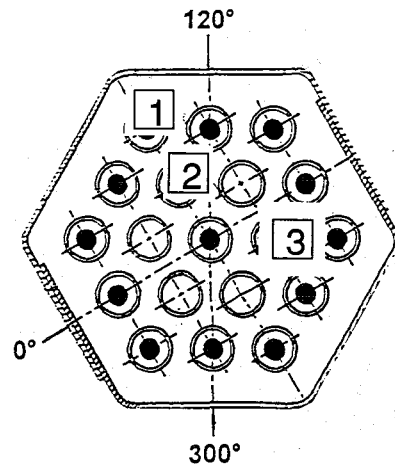
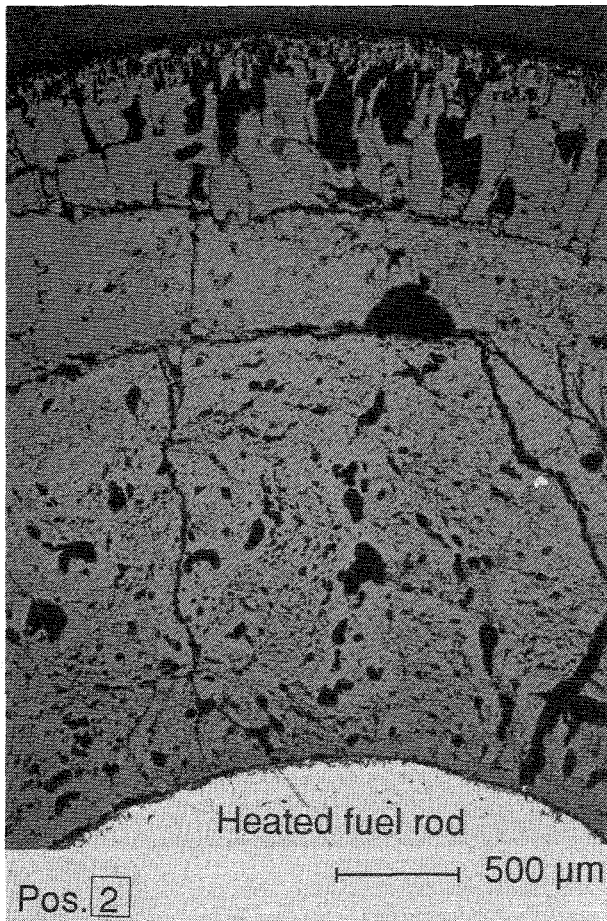


Fig. 135:
Cross Section W1-06 (top), Elevation 612 mm
Overview

Pos. 1

W1-06 (top), 612 mm



Pos. 3

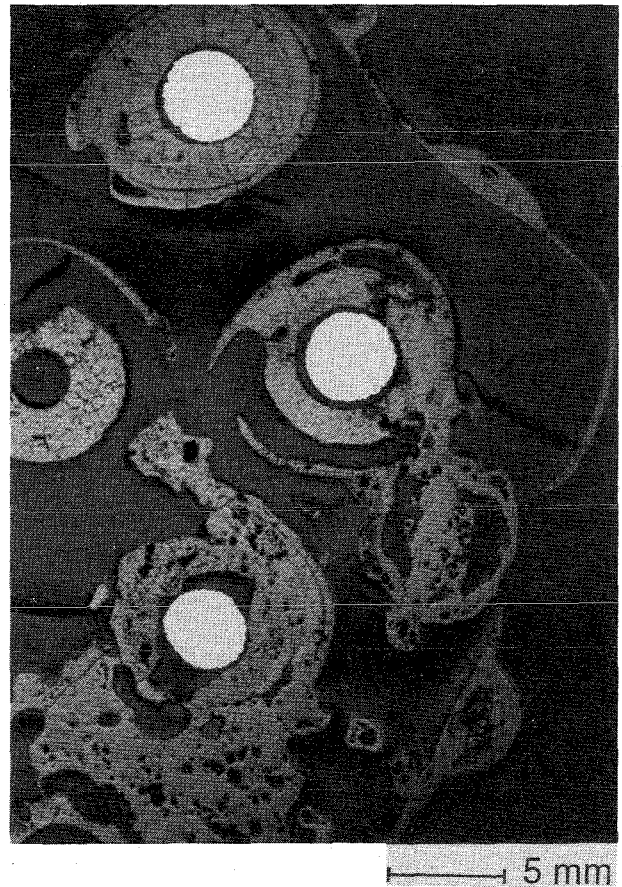
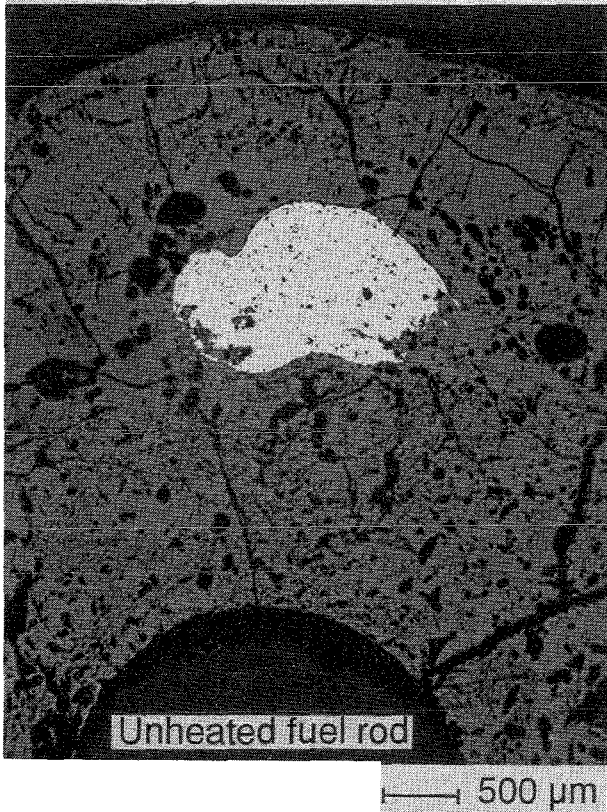


Fig. 136:

Cross Section W1-06 (top), Elevation 612 mm
Heated and Unheated Fuel Rods

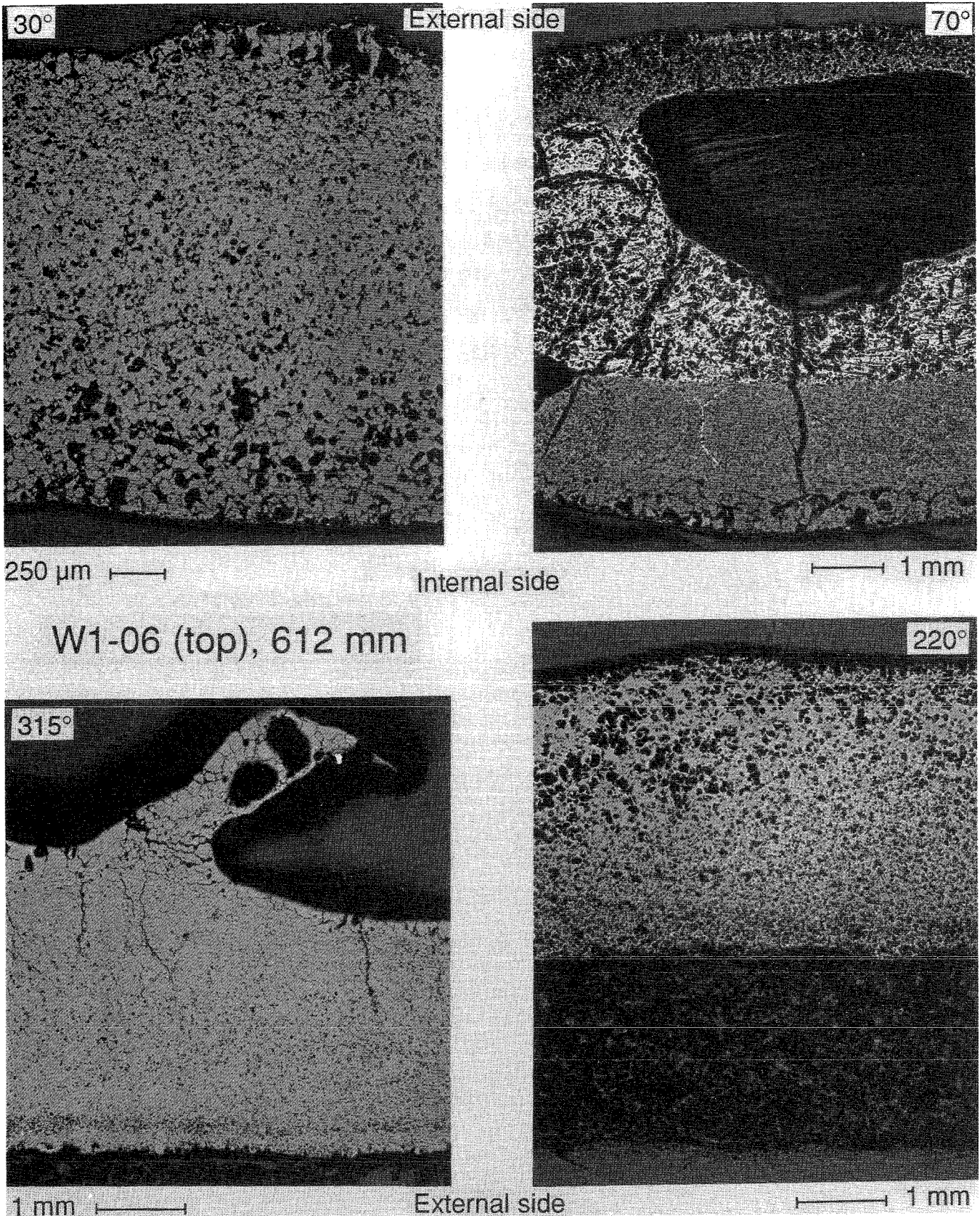
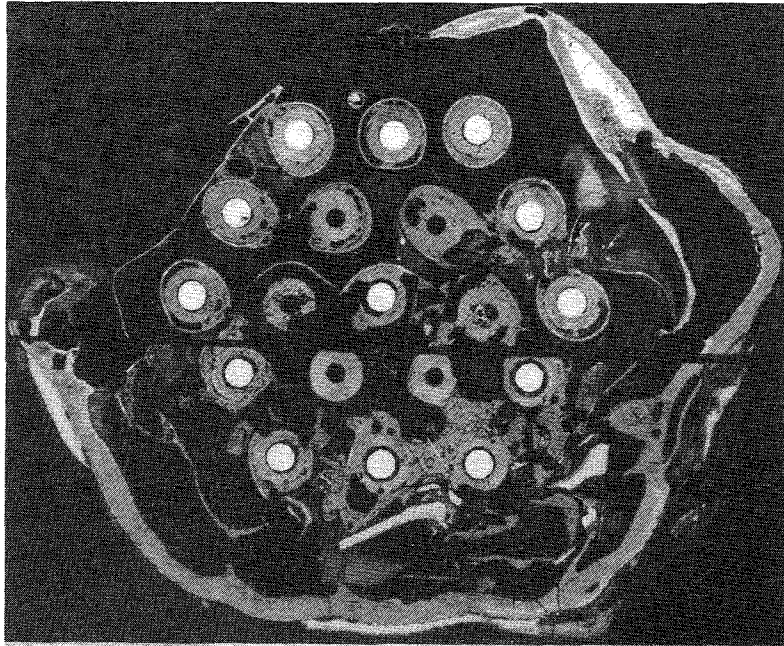


Fig. 137:
Cross Section W1-06 (top), Elevation 612 mm
Shroud at Different Orientations



W1-n (bottom), 614 mm

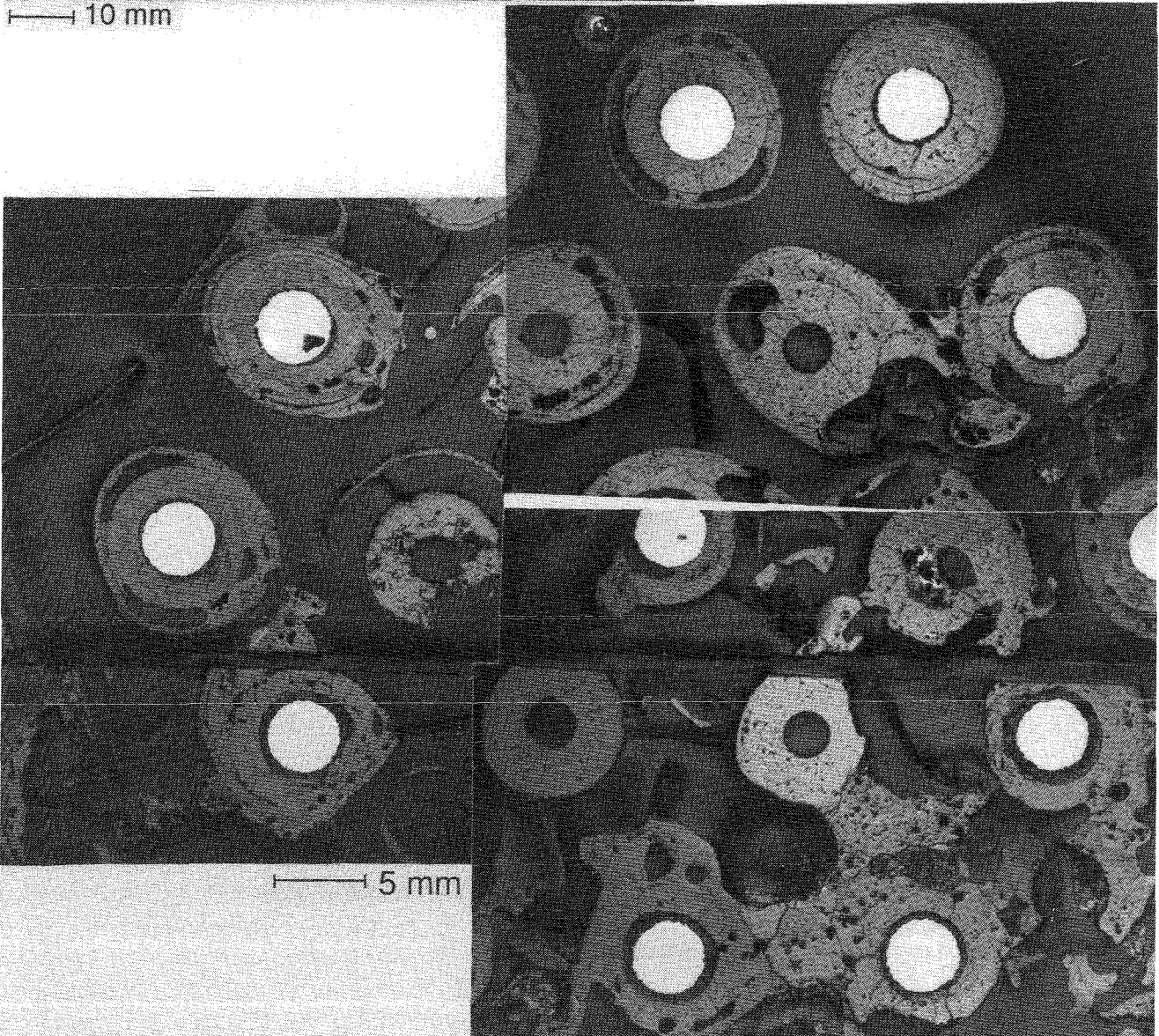
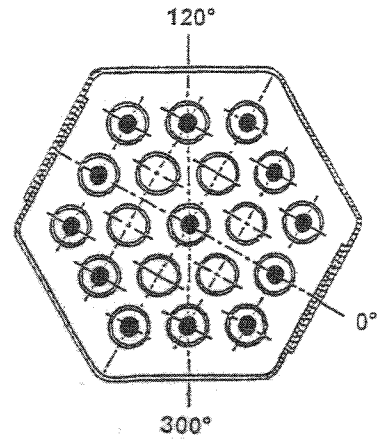
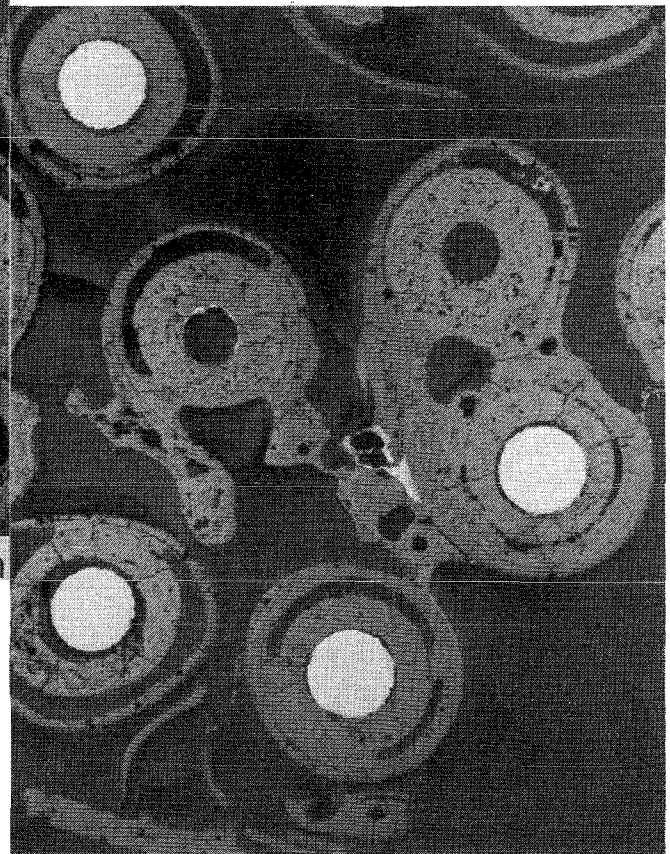
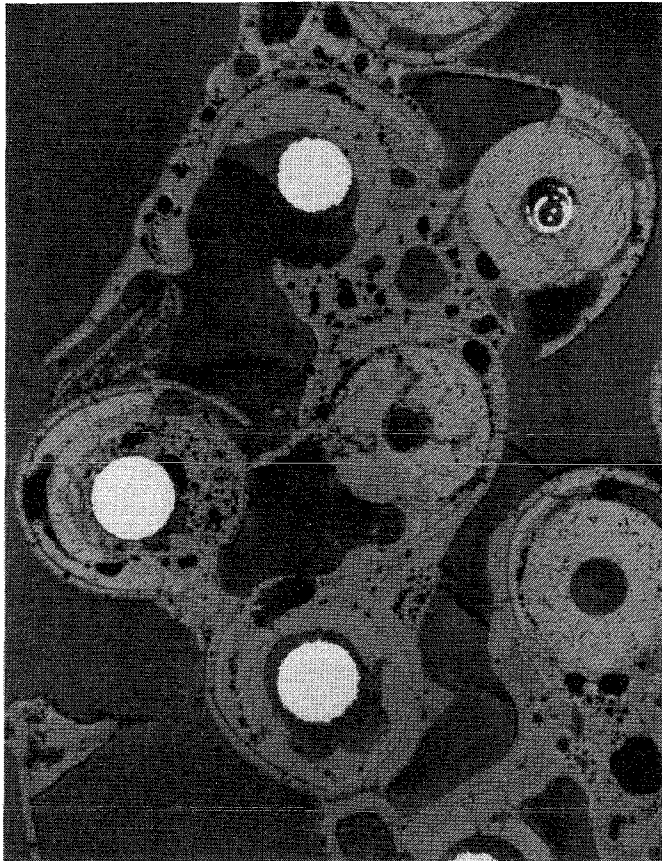
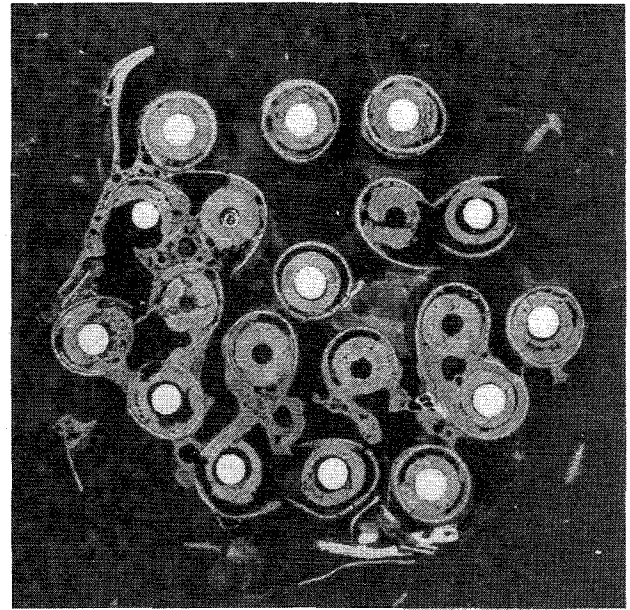
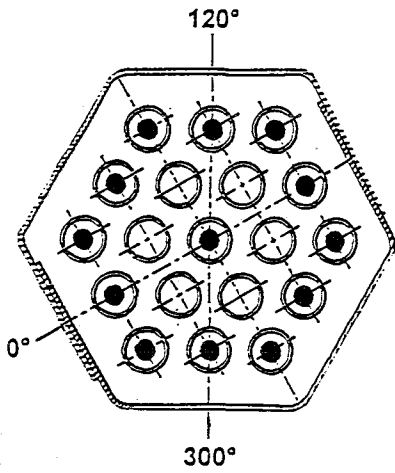


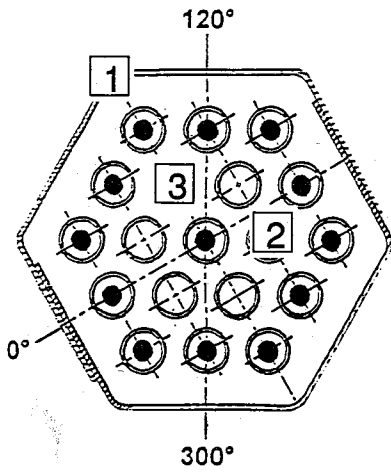
Fig. 138: Cross Section W1-n (bottom), Elevation 614 mm; Overview



W1-07 (top), 783 mm

Fig. 139:
Cross Section W1-07 (top), Elevation 783 mm
Overview

W1-07 (top), 783 mm



Pos. 1 Shroud

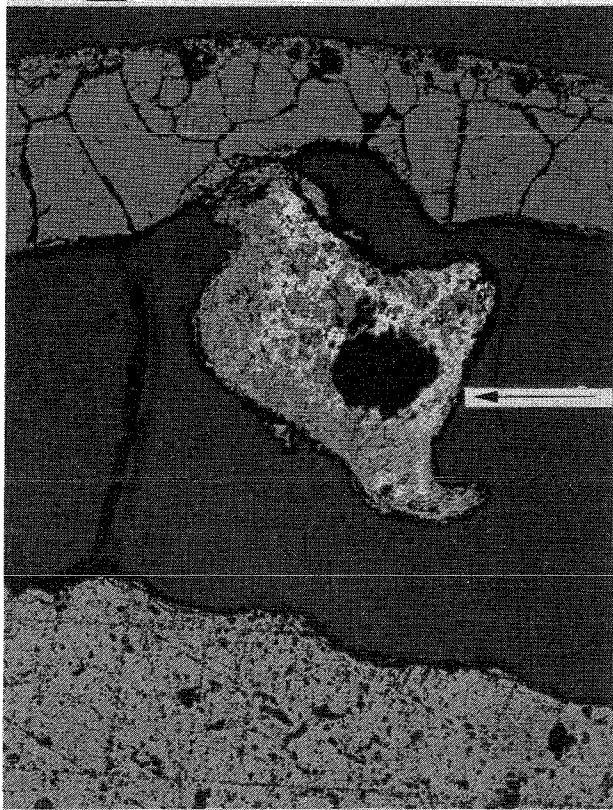
External side



ZrO₂

Internal side

Pos. 2 Unheated fuel rod



ZrO₂

Melt

Void

UO₂

Pos. 3 Fuel TC

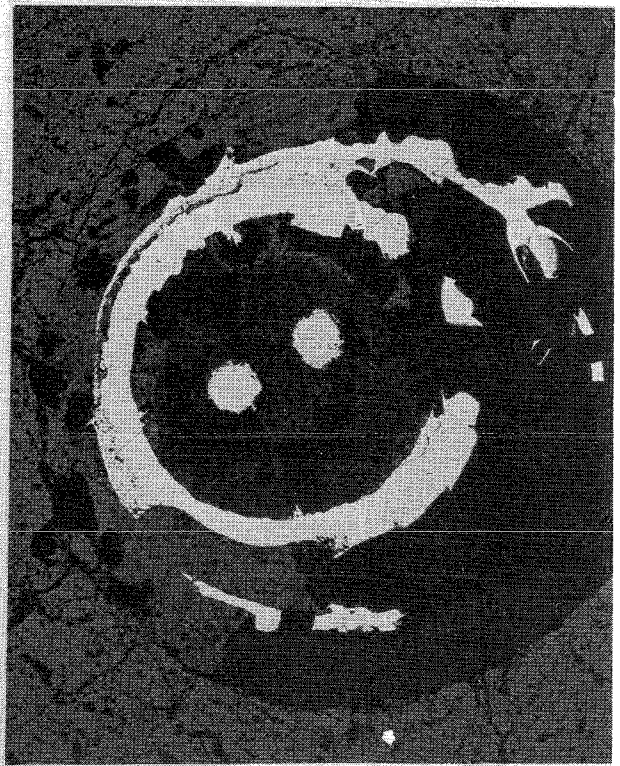


Fig. 140:
Cross Section W1-07 (top), Elevation 783 mm
Degradation of Test Bundle Components

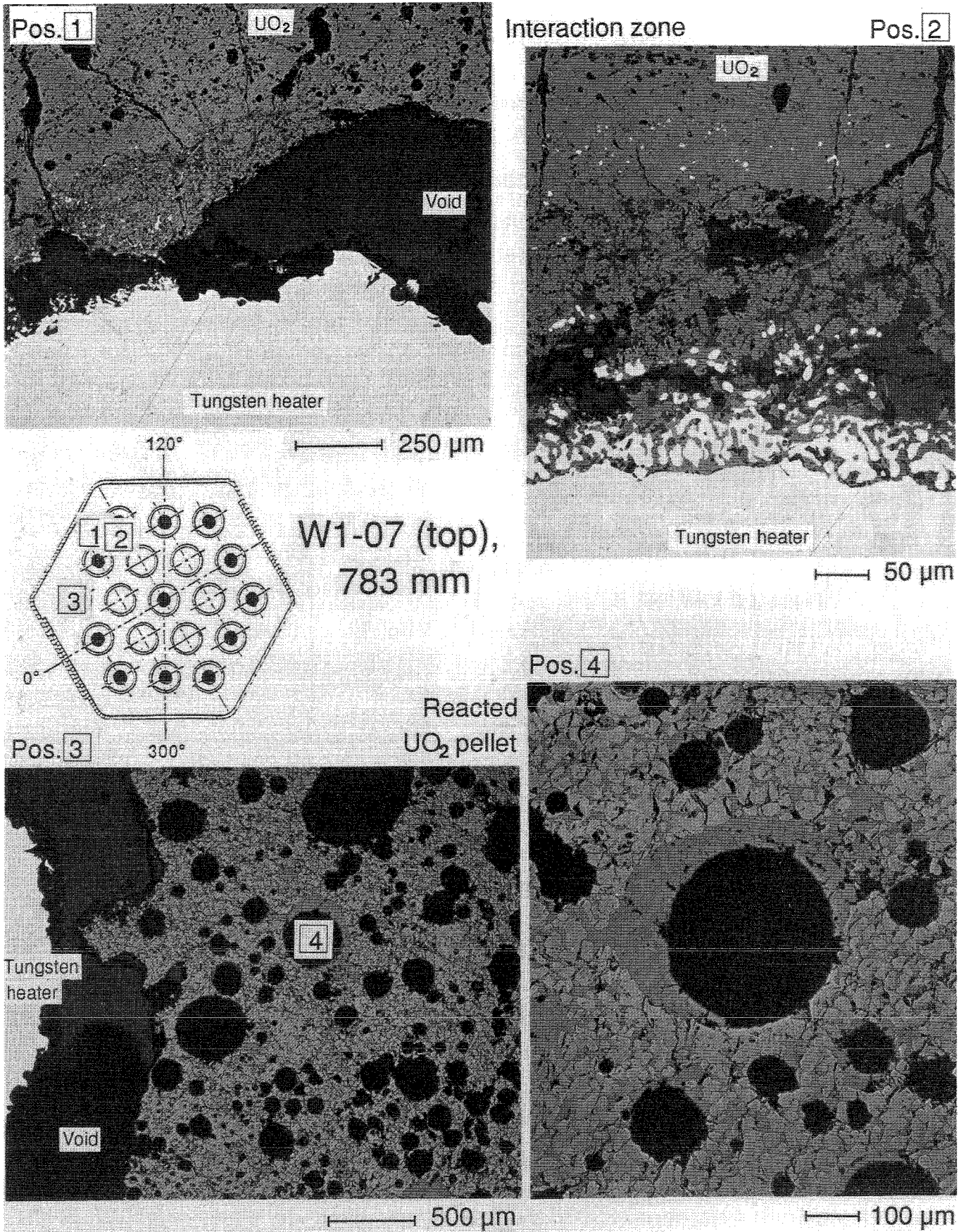
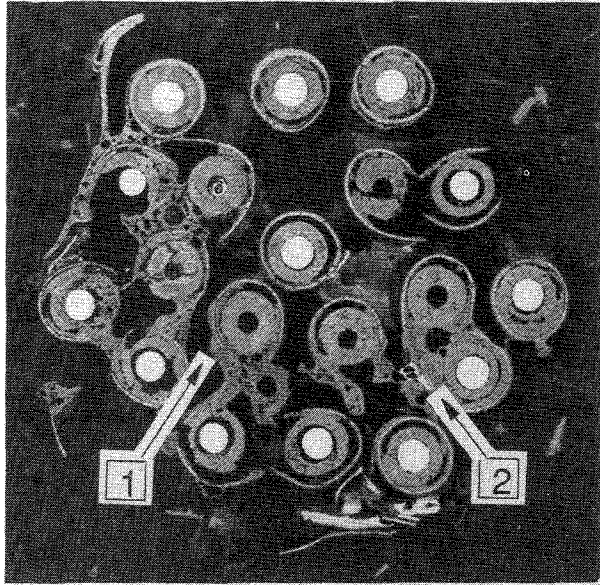


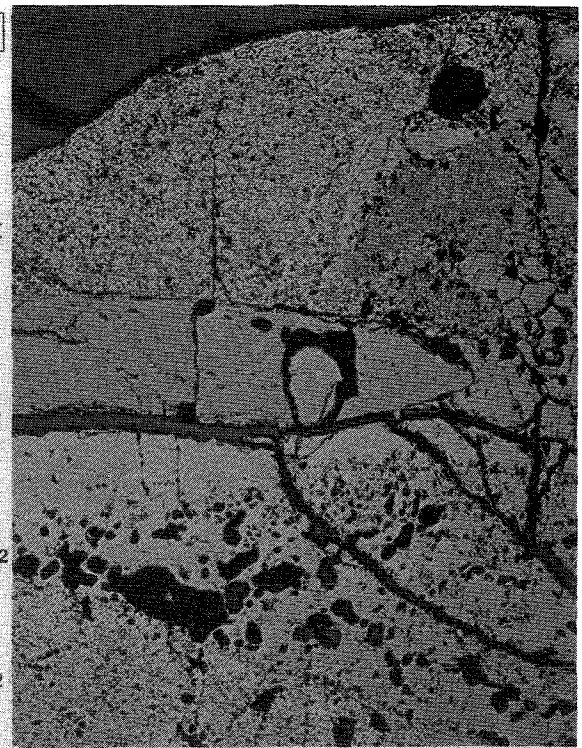
Fig. 141: Cross Section W1-07 (top), Elevation 783 mm; Fuel Pellet Interaction with Tungsten Heater Rod

W1-07 (top), 783 mm



10 mm

Pos. 1



Melt

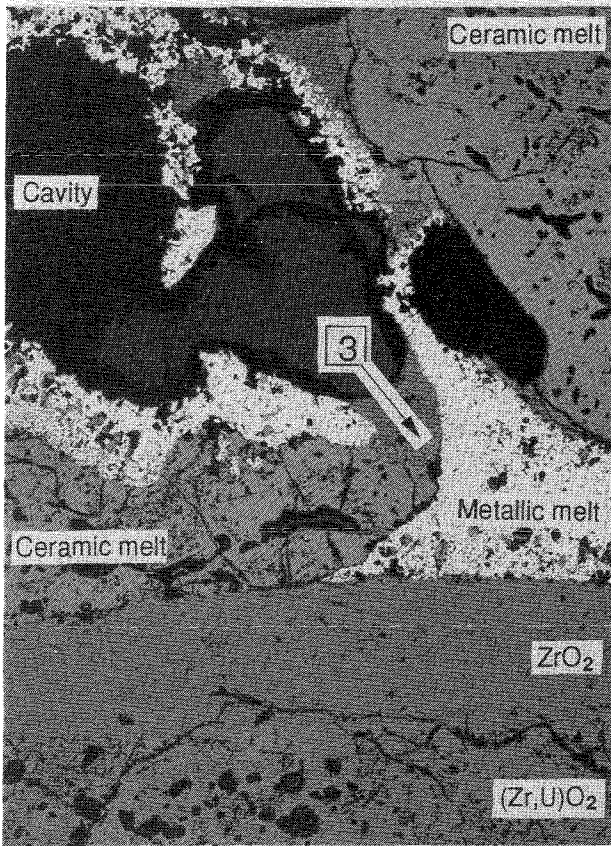
ZrO₂

(Zr,U)O₂

UO₂

500 μm

Pos. 2



Ceramic melt

Cavity

3

Metallic melt

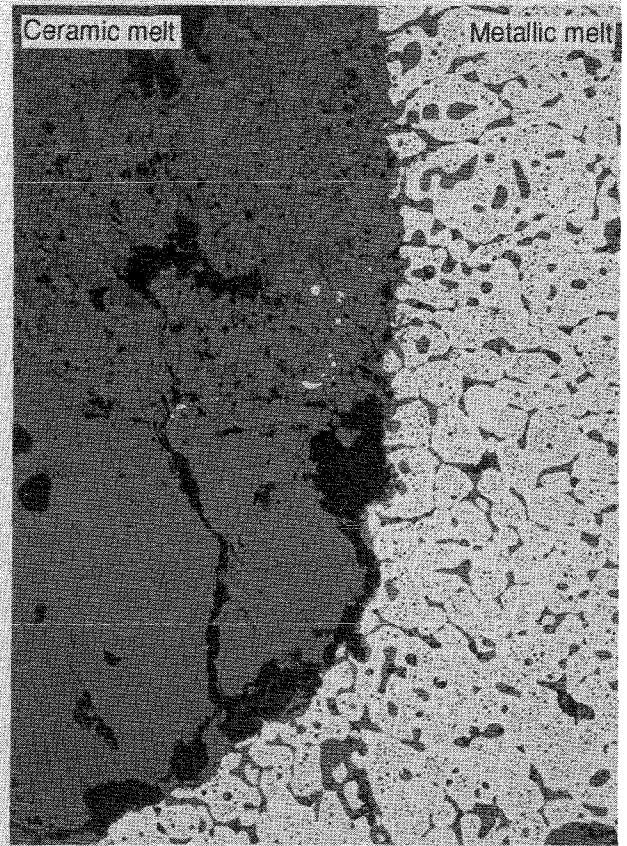
Ceramic melt

ZrO₂

(Zr,U)O₂

500 μm

Pos. 3



Ceramic melt

Metallic melt

50 μm



IMF-III/KOR

Fig. 142:

Cross Section W1-07 (top), Elevation 783 mm; Distribution and Microstructure of Metallic or Subsequently Oxidized Melts

W1-q (bottom), 785 mm

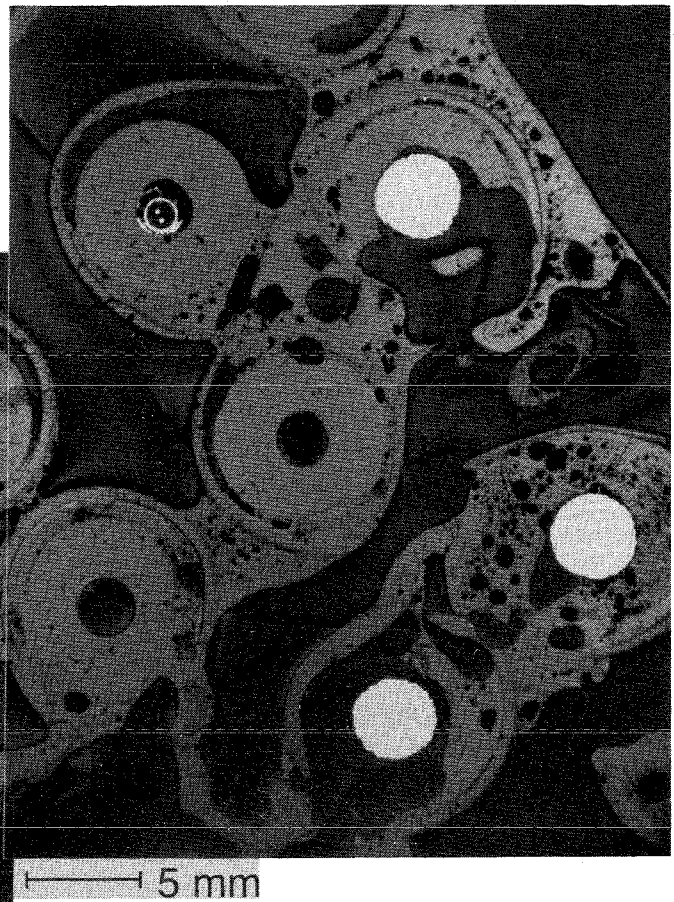
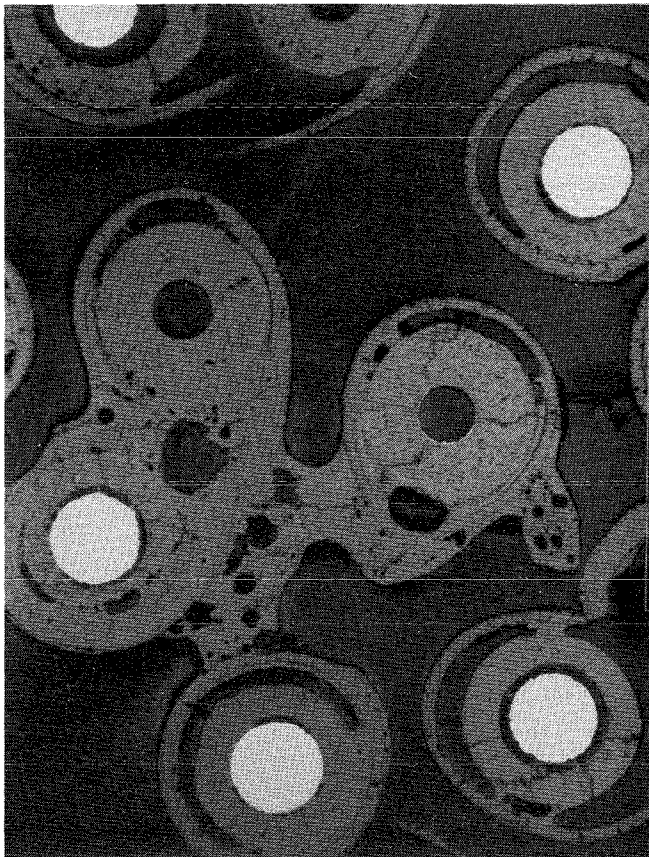
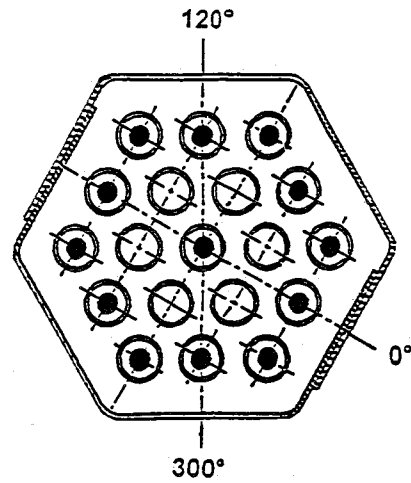
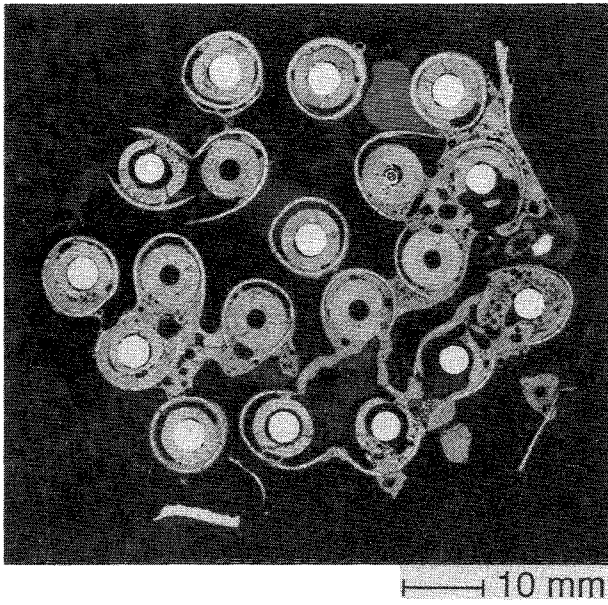


Fig. 143:
Cross Section W1-q (bottom), Elevation 785 mm
Overview

REM / EDX - Analysenpositionen

(Die Nummerierung stammt von den lichtoptischen Untersuchungen)

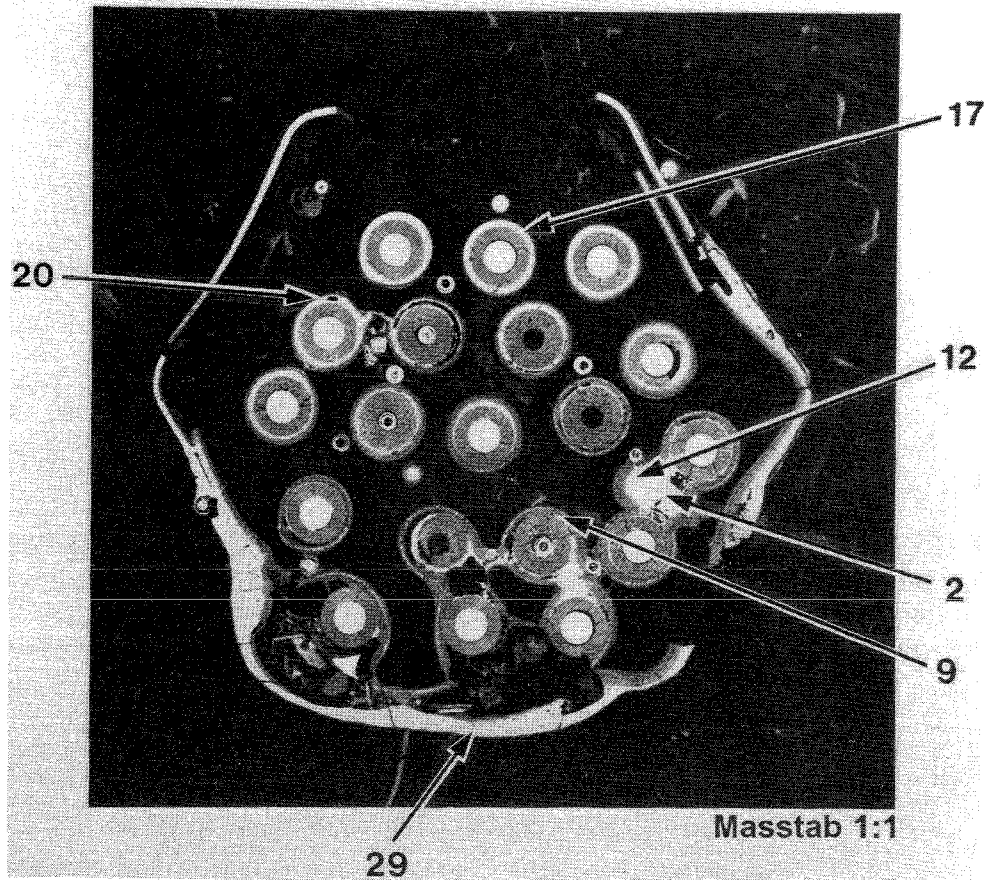


Fig. 144: Results of the SEM/EDX analysis of sample CORA-W1-04; Overview of the positions analyzed

Lichtoptische Position Nr.: 2 (5 verschiedene REM-Ausschnitte)

Anmerkung: Integralanalysen bei 500-facher Vergrößerung

Mittelwertbildung der Schmelzzone

Element	Linie	Mittelwert Gew.- %	Standard- Abweichung
O	Ka	9.48	1.91
Si	Ka	0.15	0.10
Cr	Ka	0.58	0.12
Fe	Ka	5.69	1.14
Ni	Ka	1.10	0.26
Zr	La	63.22	5.60
Nb	La	1.71	0.45
Mo	La	5.15	1.38
U	Ma	12.92	3.78

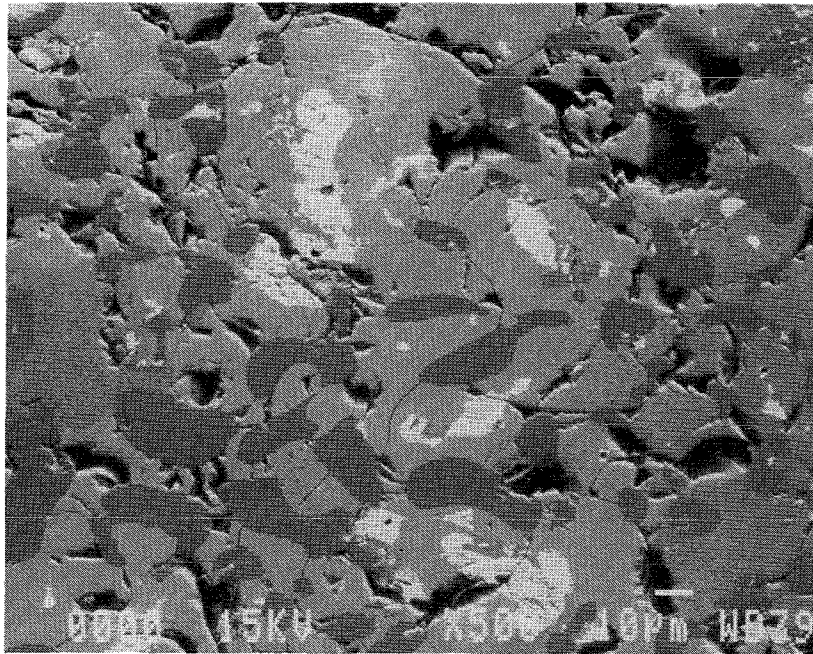


Fig. 145: Results of the SEM/EDX analysis of sample CORA-W1-04, position 2

Lichtoptische Position Nr.: 2

REM-Analysenpos. Nr.	Element u. Linie		Gewichts- Prozent	Atom- * Prozent
1	O	Ka	12.5	65.6
	Zr	La	6.2	5.7
	U	Ma	81.3	28.7
2	O	Ka	6.8	29.3
	Zr	La	93.2	70.7
3	O	Ka	22.2	64.4
	Zr	La	65.1	33.1
	U	Ma	12.7	2.5
4	O	Ka	3.9	18.3
	Si	Ka	0.2	0.5
	Cr	Ka	1.3	1.9
	Fe	Ka	12.6	16.8
	Ni	Ka	2.2	2.8
	Zr	La	56.5	46.1
	Nb	La	6.3	5.1
	Mo	La	7.2	5.6
	U	Ma	9.7	3.0

Anmerkung: Punktanalysen
* auf 100% normalisiert

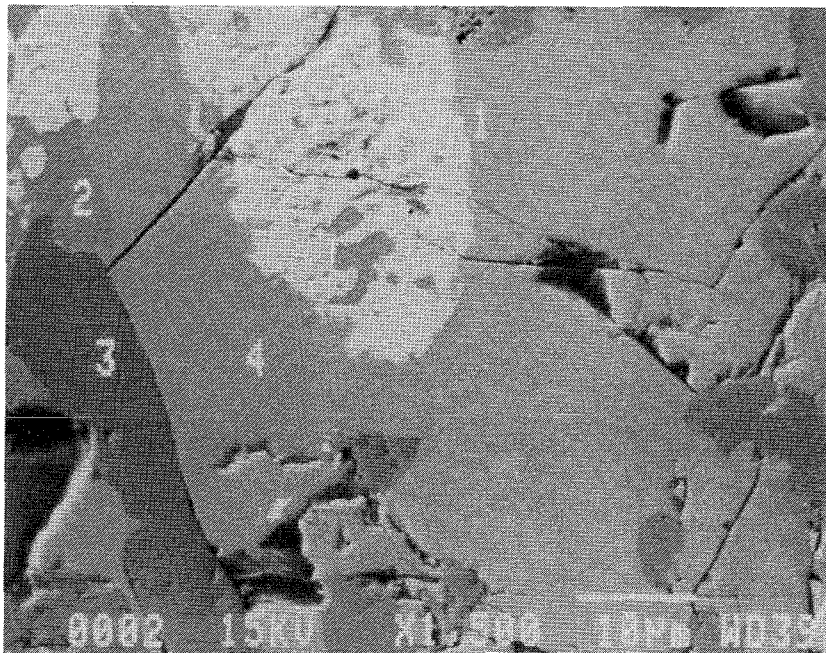


Fig. 146: Results of the SEM/EDX analysis of sample CORA-W1-04, position 2, SEM analyses positions 1 - 4

Lichtoptische Position Nr.: 12

REM-Analysenpos. Nr.	Element u. Linie	Gewichts-Prozent	Atom- * Prozent
a	O Ka	7.6	31.9
	Cr Ka	1.3	1.7
	Fe Ka	11.0	12.3
	Ni Ka	1.7	2.0
	Zr La	52.8	38.8
	Nb La	3.3	2.4
	Mo La	9.0	6.3
	U Ma	13.2	3.7
b	O Ka	24.2	66.8
	Fe Ka	0.5	0.4
	Zr La	63.0	30.5
	U Ma	12.3	2.3
c	O Ka	24.6	67.3
	Zr La	63.6	30.6
	U Ma	11.8	2.2

Anmerkung: Integralanalysen bei 1000-facher Vergrößerung
* auf 100% normalisiert

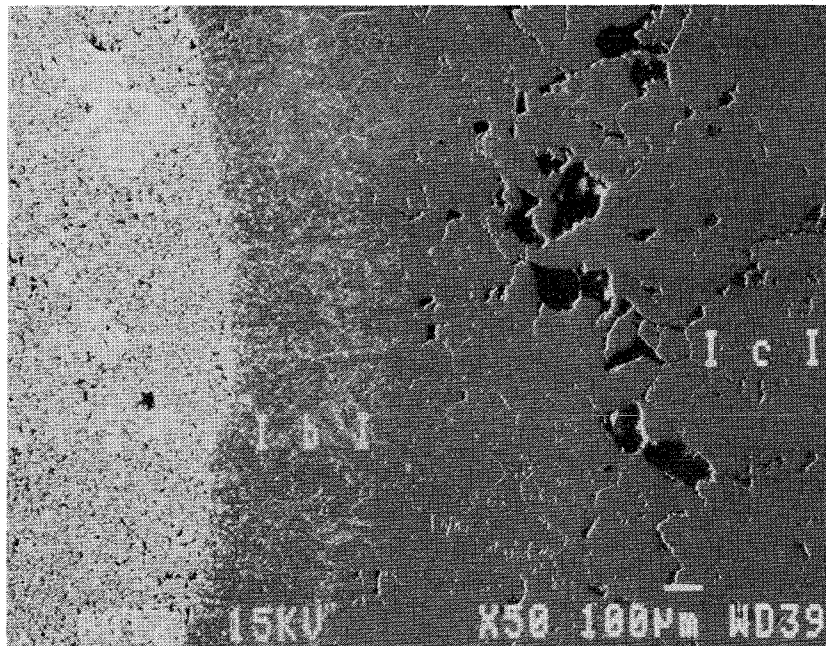


Fig. 147: Results of the SEM/EDX analysis of sample CORA-W1-04, position 12, SEM analyses positions a - c

Lichtoptische Position Nr.: 9

REM-Analysenpos. Nr.	Element u. Linie	Gewichts-Prozent	Atom- * Prozent
1	O Ka	27.1	67.9
	Zr La	72.9	32.1
2	O Ka	26.3	67.0
	Zr La	73.7	33.0
3	O Ka	20.5	65.8
	Zr La	49.0	27.6
	U Ma	30.5	6.6
4	O Ka	22.7	65.4
	Zr La	62.9	31.8
	U Ma	14.4	2.8
5	O Ka	12.0	67.0
	U Ma	88.0	33.0

Anmerkung: Integralanalysen bei 1000-facher Vergrößerung
 * auf 100% normalisiert

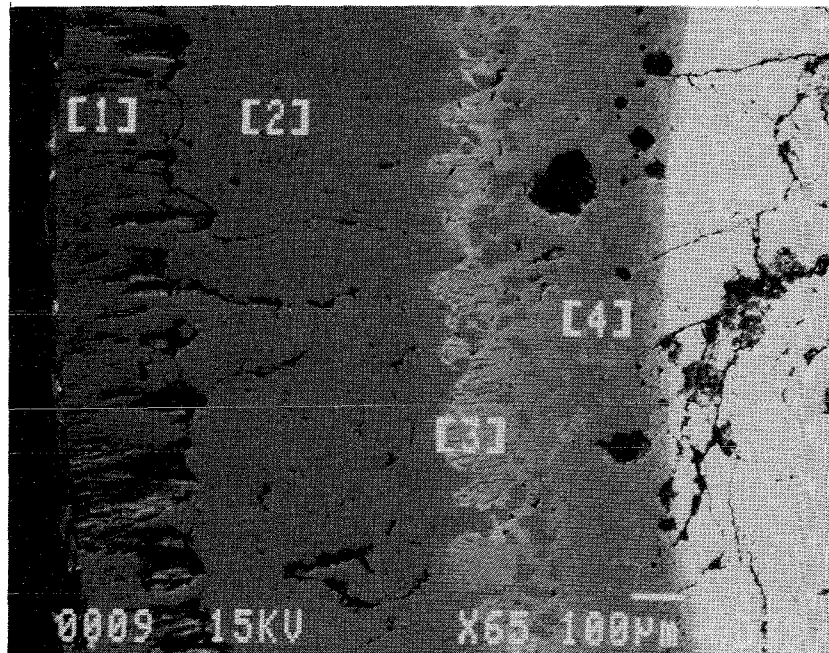
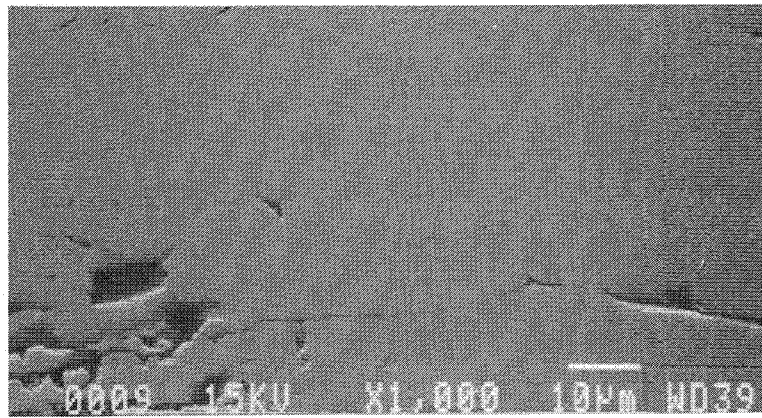


Fig. 148: Results of the SEM/EDX analysis of sample CORA-W1-04, position 9, SEM analyses positions 1 - 5

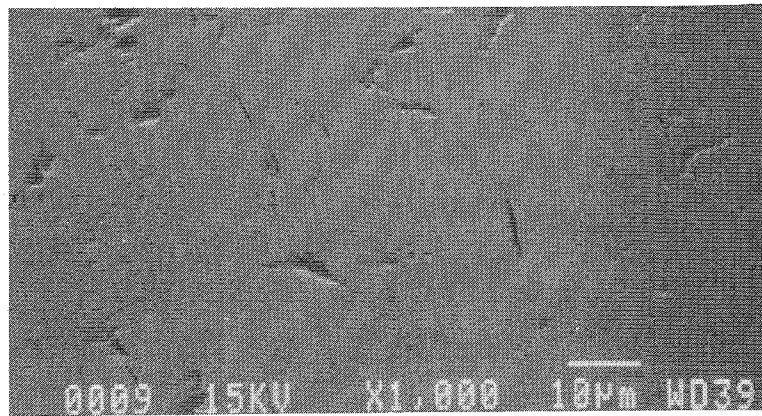
Lichtoptische Position Nr.: 9

REM-Analysenpos.
Nr.

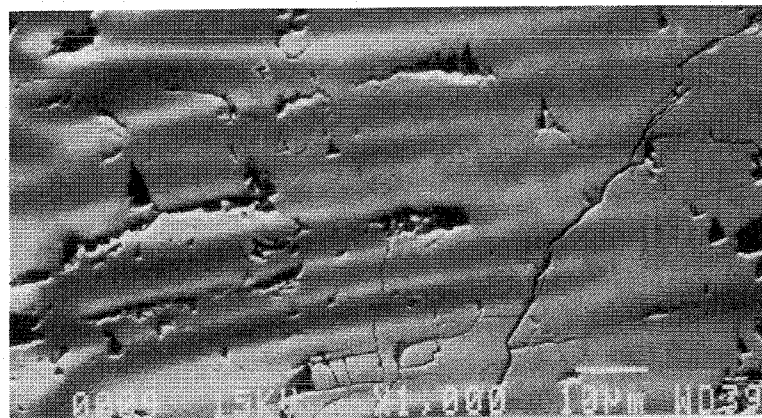
1



2



3



5

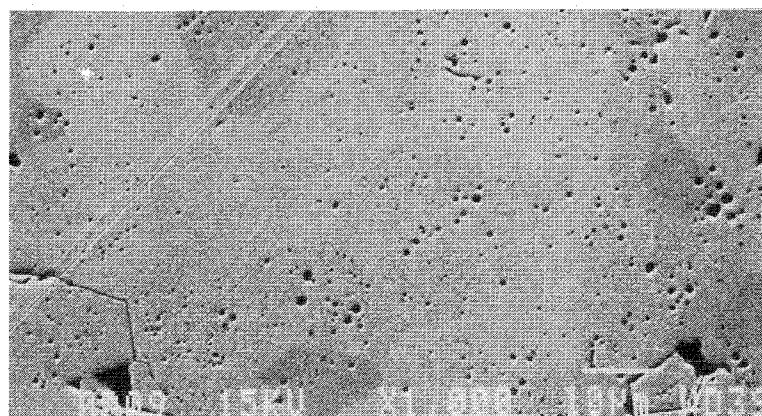


Fig. 149: Results of the SEM/EDX analysis of sample CORA-W1-04, position 9, micro-photographs of SEM positions 1 - 5

Lichtoptische Position Nr.: 9 / REM-Ausschnitt Nr. 4

REM-Analysenpos. Nr.	Element u. Linie	Gewichts- Prozent	Atom- * Prozent
1	O Ka	9.4	39.8
	Zr La	74.8	55.7
	U Ma	15.8	4.5
2	O Ka	12.5	61.9
	Zr La	17.0	14.7
	U Ma	70.5	23.4
3	O Ka	21.5	63.4
	Zr La	65.7	34.0
	U Ma	12.8	2.5
4	O Ka	6.5	29.4
	Zr La	87.3	68.8
	U Ma	6.2	1.9
5	O Ka	24.9	65.9
	Zr La	72.7	33.7
	U Ma	2.4	0.4

Anmerkung: Punktanalysen
* auf 100% normalisiert

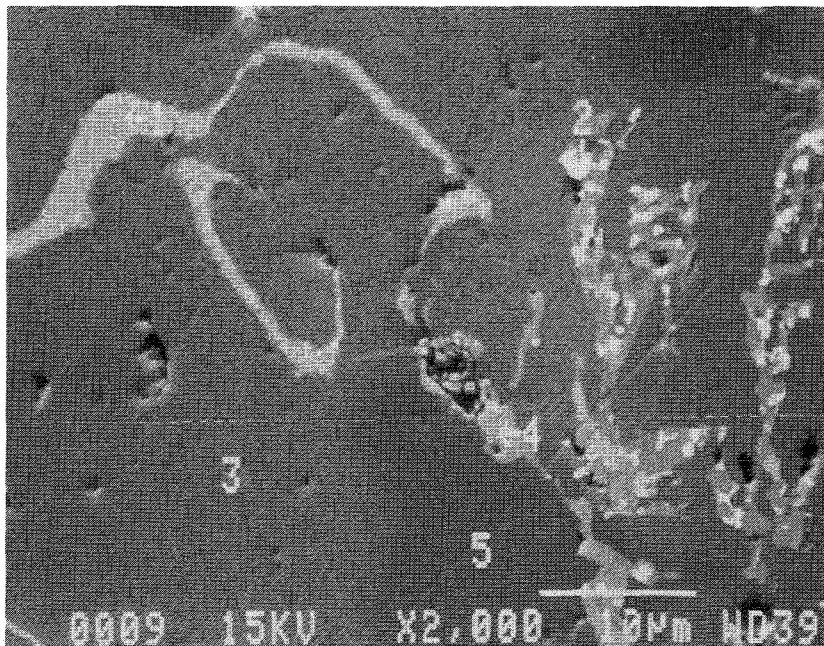


Fig. 150: Results of the SEM/EDX analysis of sample CORA-W1-04, position 9, SEM sub-position 4, SEM analyses positions 1 - 5

Lichtoptische Position Nr.: 17

REM-Analysenpos. Nr.	Element u. Linie		Gewichts- Prozent	Atom- Prozent *
a	O	Ka	26.8	67.6
	Zr	La	73.2	32.4
b	O	Ka	8.3	33.9
	Zr	La	91.7	66.1
c	O	Ka	3.9	22.2
	Fe	Ka	4.8	7.8
	Zr	La	55.9	55.4
	Nb	La	2.1	2.0
	U	Ma	33.3	12.6
d	O	Ka	5.6	25.9
	Fe	Ka	0.9	1.2
	Zr	La	86.7	70.7
	U	Ma	6.8	2.1
e	O	Ka	10.9	64.6
	U	Ma	89.1	35.4

Anmerkung: Integralanalysen bei 1000-facher Vergrößerung
* auf 100% normalisiert

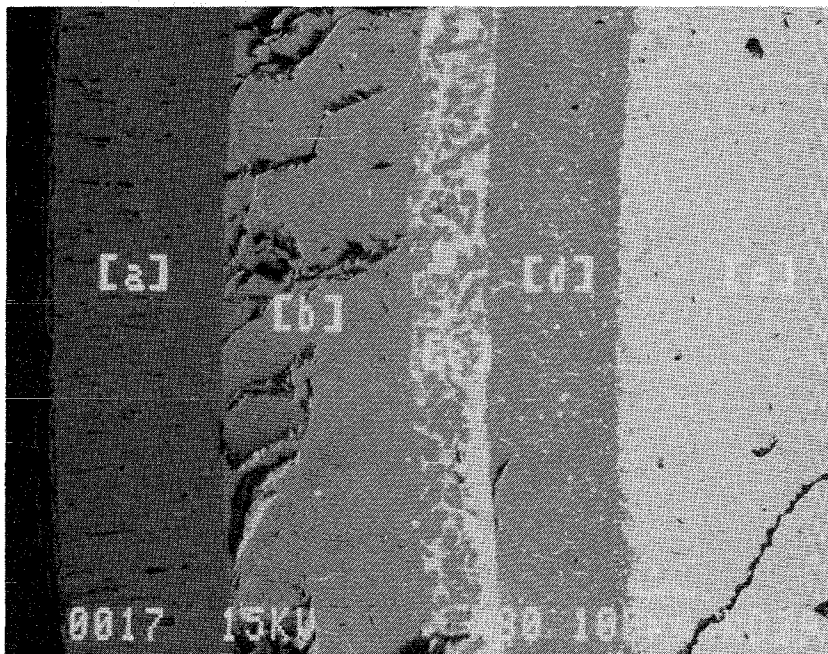


Fig. 151: Results of the SEM/EDX analysis of sample CORA-W1-04, position 17, SEM analyses positions a - e

Lichtoptische Position Nr.: 17 / REM-Ausschnitt Nr. c

REM-Analysenpos. Nr.	Element u. Linie	Gewichts-Prozent	Atom- * Prozent
1	O Ka	1.6	16.5
	Zr La	19.7	31.7
	Nb La	5.6	8.9
	U Ma	73.0	44.9
2	O Ka	5.4	24.7
	Zr La	93.3	74.9
	U Ma	1.3	0.4
3	O Ka	1.5	10.1
	Fe Ka	13.3	25.8
	Ni Ka	1.8	3.4
	Zr La	31.3	37.1
	U Ma	52.1	23.7
4	O Ka	3.5	17.2
	Cr Ka	1.3	2.0
	Fe Ka	11.1	15.5
	Ni Ka	3.1	4.2
	Zr La	55.6	47.6
	Nb La	10.1	8.5
	U Ma	15.2	5.0

Anmerkung: Punktanalyse
* auf 100% normalisiert

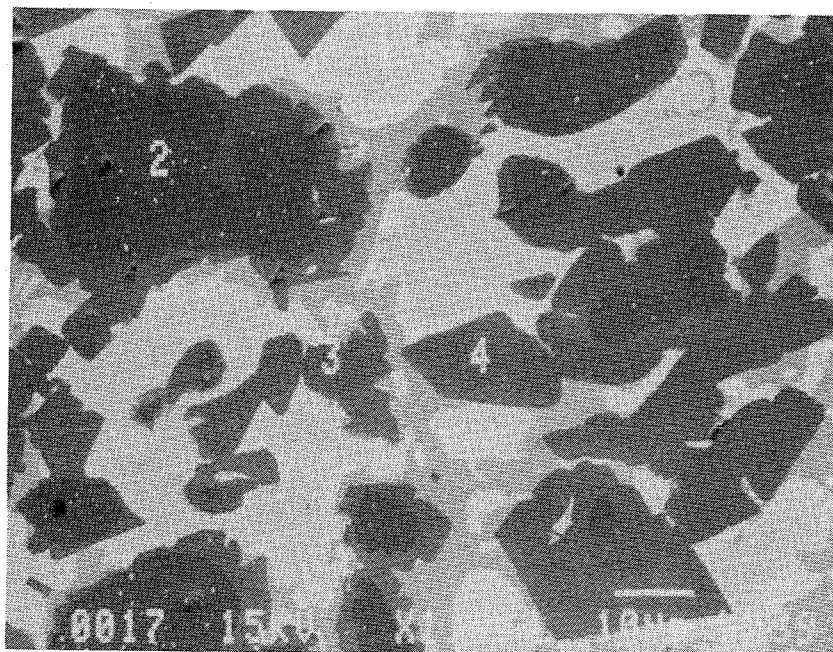


Fig. 152: Results of the SEM/EDX analysis of sample CORA-W1-04, position 17, SEM sub-position c, SEM analyses positions 1 - 4

Lichtoptische Position Nr.: 17 / REM-Ausschnitt Nr. d

REM-Analysenpos. Nr.	Element u. Linie	Gewichts- Prozent	Atom- Prozent *
1	O Ka	3.6	17.5
	Cr Ka	1.1	1.7
	Fe Ka	11.3	15.9
	Ni Ka	2.7	3.6
	Zr La	54.7	47.2
	Nb La	10.4	8.8
	U Ma	16.3	5.4
2	O Ka	6.5	50.2
	Zr La	0.5	0.7
	Nb La	0.7	1.0
	U Ma	92.3	48.1
3	O Ka	5.8	26.0
	Zr La	94.2	74.0

Anmerkung: Punktanalysen
* auf 100% normalisiert

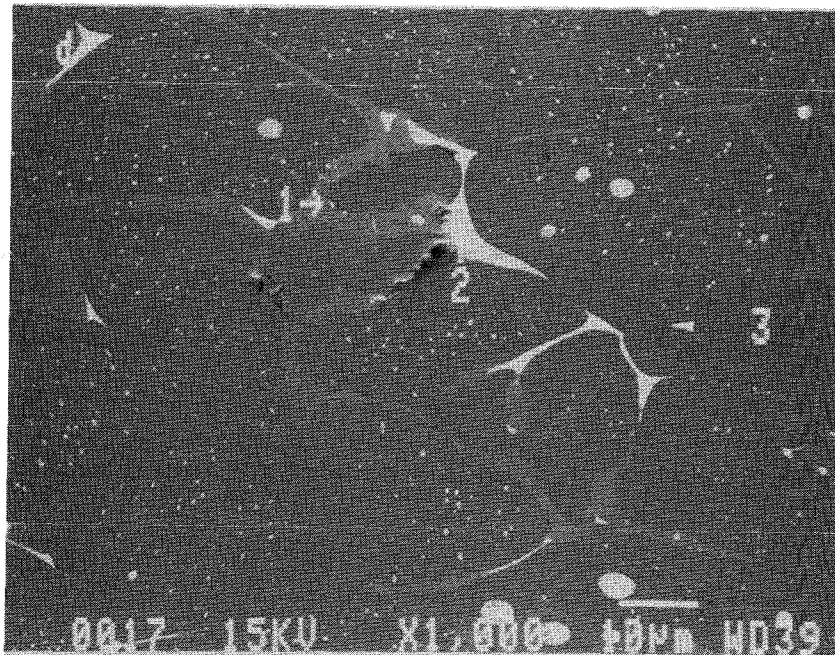


Fig. 153: Results of the SEM/EDX analysis of sample CORA-W1-04, position 17, SEM sub-position d, SEM analyses positions 1 - 3

Lichtoptische Position Nr.: 20

REM-Analysenpos. Nr.	Element u. Linie	Gewichts-Prozent	Atom- * Prozent
1	O Ka	11.5	66.0
	U Ka	88.5	34.0
2	O Ka	5.4	25.2
	Cr Ka	0.6	0.8
	Fe Ka	4.7	6.2
	Ni Ka	0.9	1.1
	Zr La	78.1	63.5
	U Ma	10.4	3.3
3	O Ka	6.1	27.1
	Cr Ka	0.2	0.3
	Fe Ka	1.5	2.0
	Ni Ka	0.4	0.5
	Zr La	88.5	69.2
	U Ma	3.3	1.0
4	O Ka	3.2	16.3
	Cr Ka	1.0	1.5
	Fe Ka	8.7	12.6
	Ni Ka	1.5	2.0
	Zr La	69.1	61.8
	U Ma	16.6	5.7
5	O Ka	5.8	26.0
	Zr La	94.0	74.0
	U Ma	0.2	0.1
6	O Ka	25.6	66.2
	Zr La	74.4	33.8

Anmerkung: Integralanalysen bei 1000-facher Vergrößerung
* auf 100% normalisiert

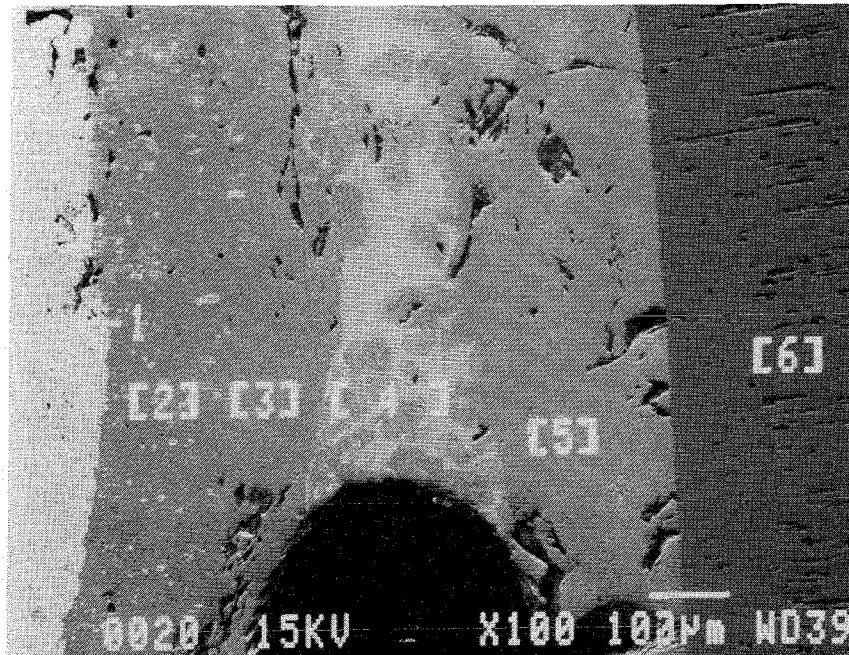
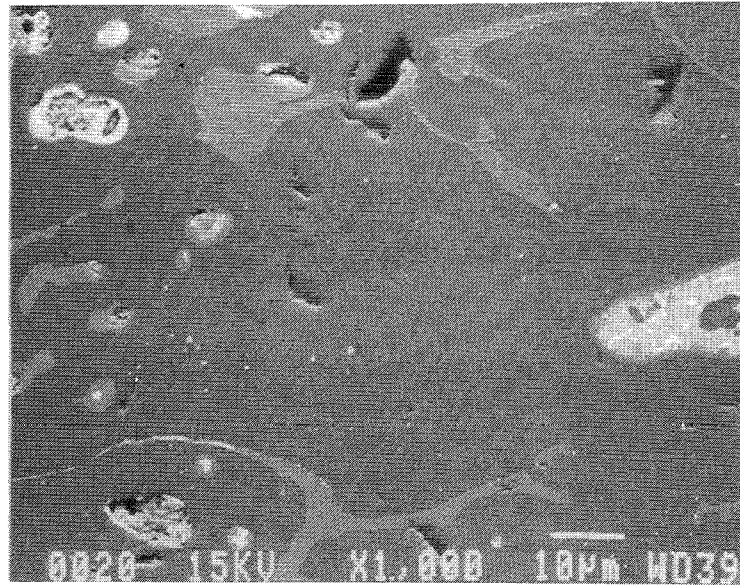


Fig. 154: Results of the SEM/EDX analysis of sample CORA-W1-04, position 20, SEM analyses positions 1 - 6

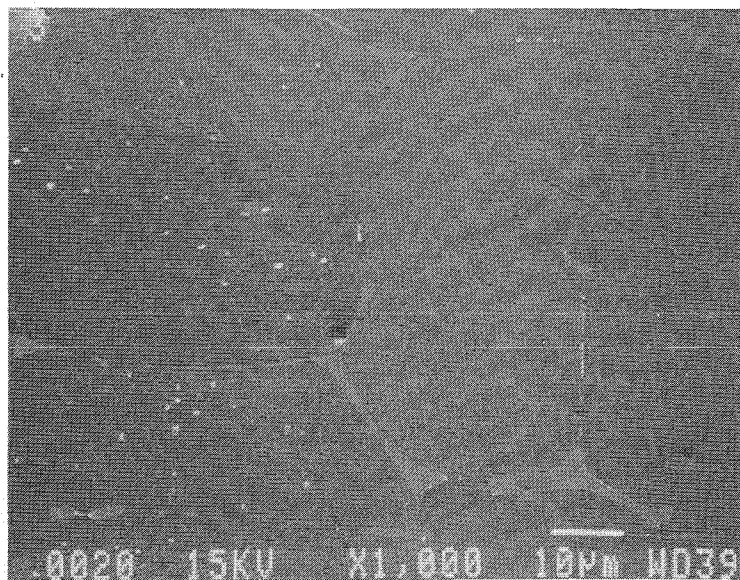
Lichtoptische Position Nr.: 20

REM-Analysenpos.
Nr.

2



3



4

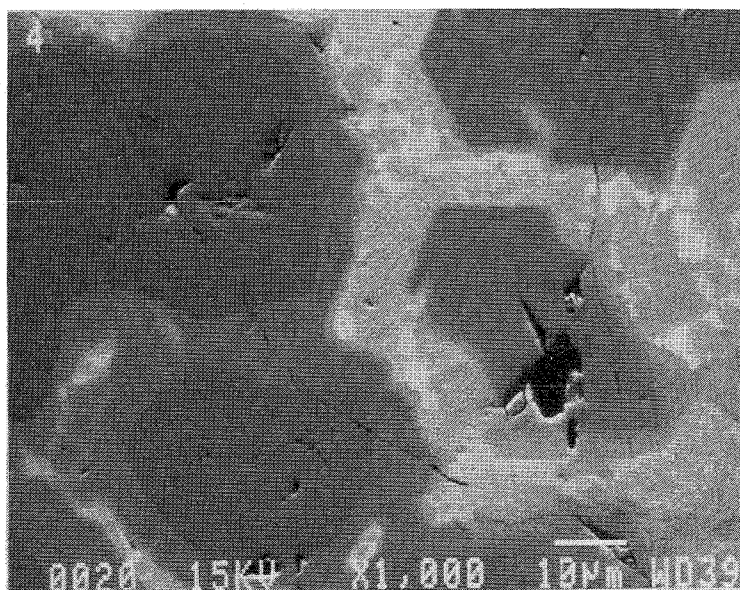


Fig. 155: Results of the SEM/EDX analysis of sample CORA-W1-04, position 20, micro-photographs of SEM positions 2 - 4

Lichtoptische Position Nr.: 29

REM-Analysenpos. Nr.	Element u. Linie	Gewichts-Prozent	Atom- * Prozent
a	O Ka	27.3	68.7
	Zr La	69.8	30.8
	U Ma	2.9	0.5
b	O Ka	14.5	50.9
	Zr La	74.0	45.7
	Nb La	1.6	1.0
	U Ma	9.9	2.3
c	O Ka	25.6	66.9
	Zr La	70.8	32.4
	U Ma	3.6	0.6
d	O Ka	26.4	68.3
	Zr La	67.6	30.7
	U Ma	6.0	1.0

Anmerkung: Integralanalysen bei 1000-facher Vergrößerung
 * auf 100% normalisiert

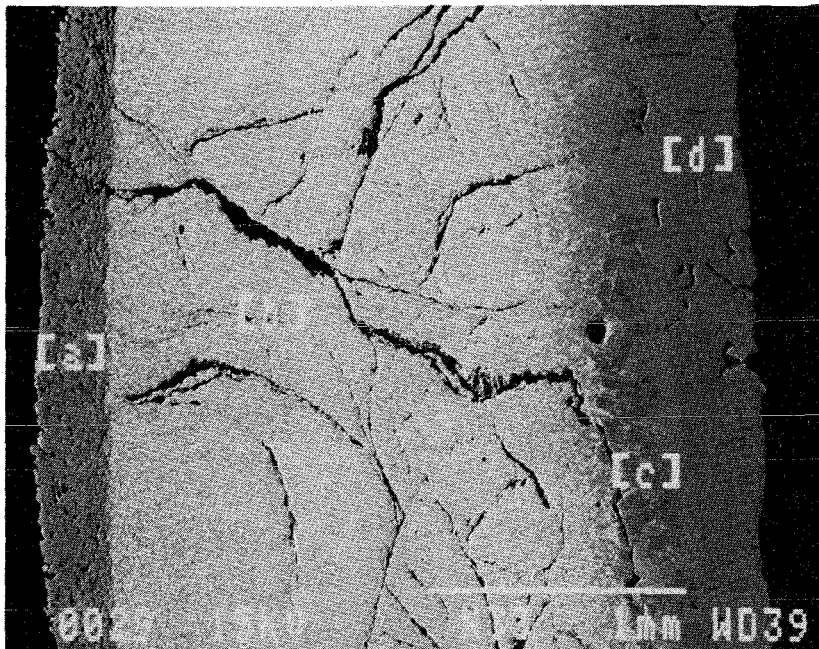


Fig. 156: Results of the SEM/EDX analysis of sample CORA-W1-04, position 29, SEM analyses positions a - d

Lichtoptische Position Nr.: 29 / REM-Ausschnitt Nr.a

REM-Analysenpos. Nr.	Element u. Linie	Gewichts- Prozent	Atom- Prozent *
1	O Ka	26.7	68.2
	Zr La	69.1	31.0
	U Ma	4.2	0.7
2	O Ka	26.9	67.7
	Zr La	73.1	32.3

Anmerkung: Punktanalysen
* auf 100% normalisiert

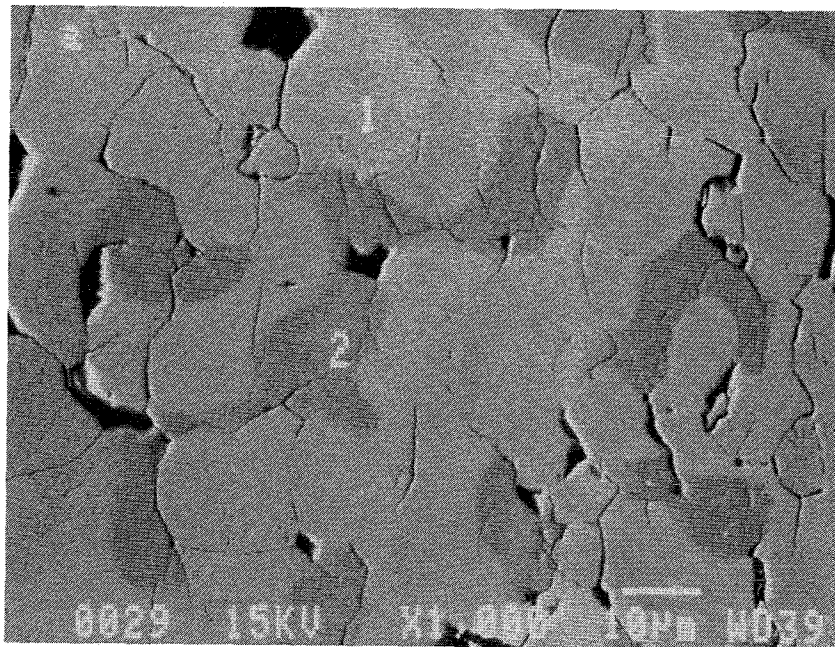


Fig. 157: Results of the SEM/EDX analysis of sample CORA-W1-04, position 29, SEM sub-position a, SEM analyses positions 1 - 2

Lichtoptische Position Nr.: 29 / REM-Ausschnitt Nr.b

REM-Analysenpos. Nr.	Element u. Linie	Gewichts-Prozent	Atom- * Prozent
1	O Ka	23.7	66.7
	Zr La	61.7	30.5
	U Ma	14.6	2.8
2	O Ka	11.3	61.4
	Zr La	10.8	10.2
	U Ma	77.9	28.4
3	O Ka	5.9	26.3
	Zr La	93.9	73.6
	U Ma	0.2	0.1
4	O Ka	4.1	19.1
	Cr Ka	1.7	2.3
	Fe Ka	11.8	15.7
	Ni Ka	1.3	1.6
	Zr La	57.8	47.1
	Nb La	8.9	7.1
	Mo La	5.4	4.2
	U Ma	9.1	2.9

Anmerkung: Punktanalysen
* auf 100% normalisiert

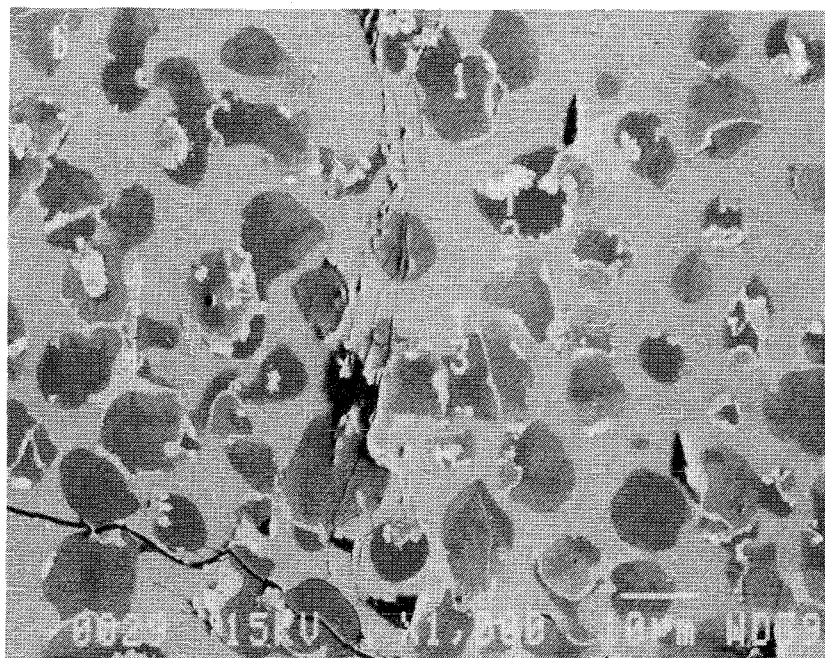


Fig. 158: Results of the SEM/EDX analysis of sample CORA-W1-04, position 29, SEM sub-position b, SEM analyses positions 1 - 4

REM / EDX - Analysenpositionen

(Die Nummerierung stammt von den lichtoptischen Untersuchungen)

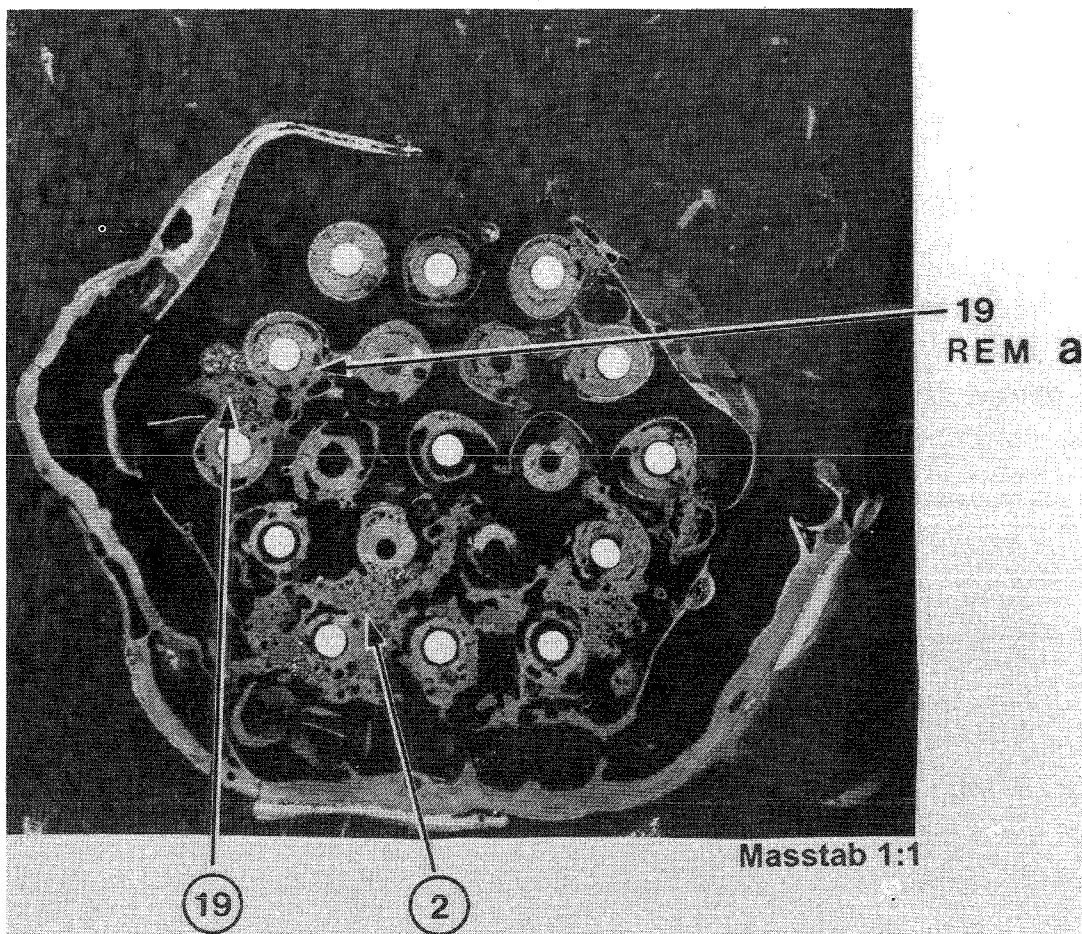


Fig. 159: Results of the SEM/EDX analysis of sample CORA-W1-06, Overview of the positions analyzed

Lichtoptische Position Nr.: ~ 2 (Schmelzzone)

Analysenfeld : 1mm X 1mm

Mittelwertsbildung von fuenf verschiedenen Analysenfelder

Element	Linie	Mittelwert Gew.- %	Standard- Abweichung
O	Ka	20.26	1.92
Zr	La	37.28	9.98
W	Ma	6.74	3.82
U	Ma	35.72	10.58

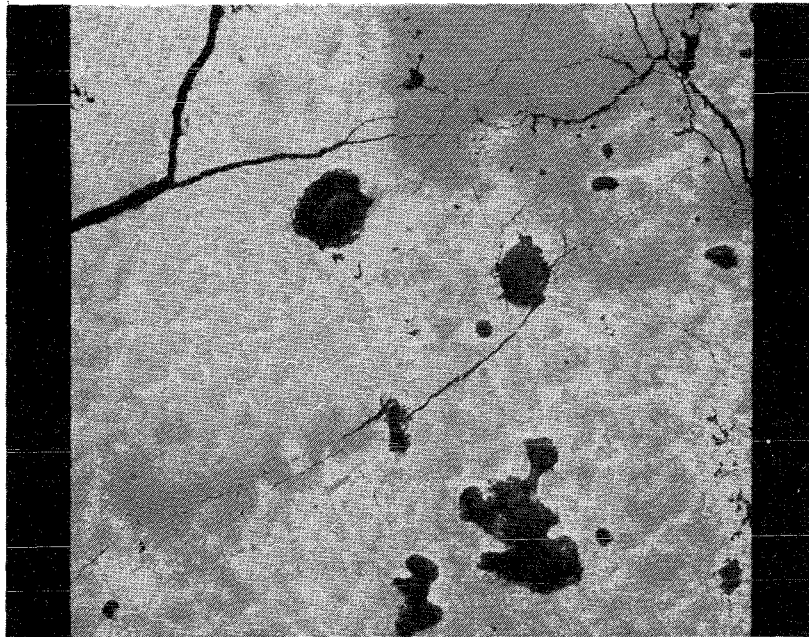


Fig. 160: Results of the SEM/EDX analysis of sample CORA-W1-06, position 2, mean value of five SEM analyses positions

Lichtoptische Position Nr.: ~ 19 (Schmelzzone)

Analysenfeld : 1mm X 1mm

Mittelwertbildung von fuenf verschiedenen Analysenfelder

Element	Linie	Mittelwert Gew.- %	Standard- Abweichung
O	Ka	21.37	1.35
Zr	La	52.83	4,85
W	Ma	1.25	0.62
U	Ma	25.55	5.55

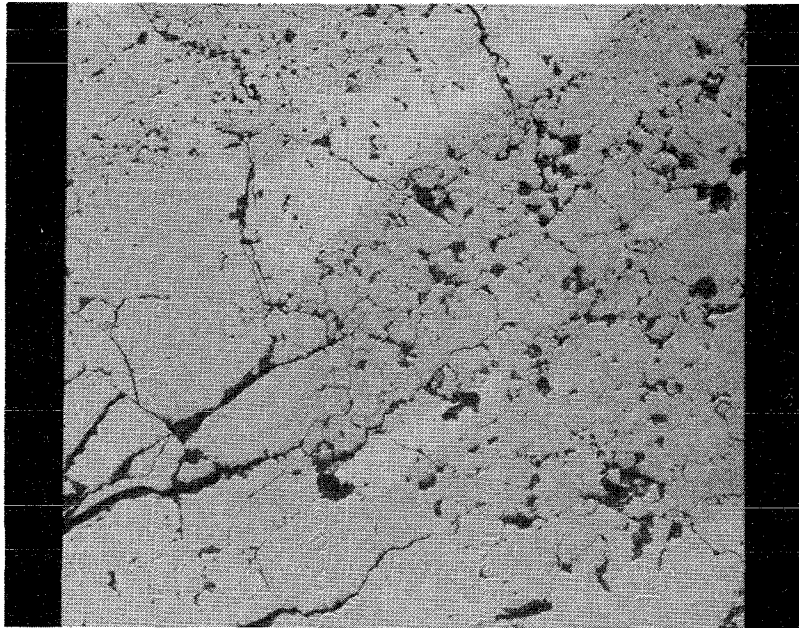


Fig. 161: Results of the SEM/EDX analysis of sample CORA-W1-06, position 19, mean value of five SEM analyses positions

Lichtoptische Position Nr.: 19 / REM-Ausschnitt Nr.a

REM-Analysenpos. Nr.	Element u. Linie	Gewichts- Prozent	Atom- Prozent *
1	O Ka	23.0	67.8
	Zr La	53.1	27.5
	U Ma	23.8	4.7
2	O Ka	15.9	66.7
	Zr La	19.6	14.4
	W Ma	10.2	3.7
	U Ma	54.2	15.2
4	O Ka	11.5	65.7
	Zr La	0.7	0.7
	U Ma	87.8	33.6

Anmerkung: Integralanalysen bei 1000-facher Vergrößerung
* auf 100% normalisiert

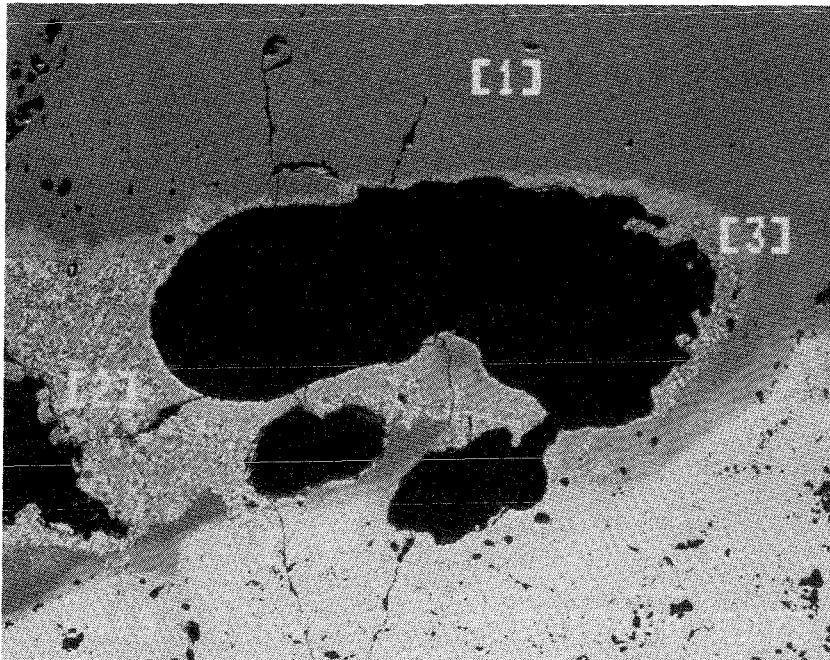


Fig. 162: Results of the SEM/EDX analysis of sample CORA-W1-06, position 19, SEM sub-position a, SEM analyses positions 1,2 and 4

Lichtoptische Position Nr.: 19 / REM-Ausschnitt Nr.a , Pos.3

REM-Analysenpos. Nr.	Element u. Linie	Gewichts-Prozent	Atom- * Prozent
1	O Ka	17.1	60.2
	Cr Ka	1.0	1.1
	Mn Ka	1.9	1.9
	Fe Ka	14.5	14.7
	Ni Ka	3.0	2.9
	W Ma	62.5	19.2
2	O Ka	23.1	67.4
	Zr La	55.6	28.4
	U Ma	21.3	4.2
3	O Ka	10.1	62.1
	Zr La	1.1	1.2
	U Ma	88.8	36.7
4	O Ka	20.5	67.3
	Fe Ka	0.9	0.8
	Zr La	41.1	23.6
	U Ma	37.5	8.3
5	O Ka	19.7	67.9
	Zr La	36.3	21.9
	U Ma	44.0	10.2
6	O Ka	21.4	66.8
	Zr La	49.6	27.1
	U Ma	29.0	6.1

Anmerkung: Pos. 1 bis 3 = Punktanalysen
 Pos. 4 bis 6 = Bereichsanalysen
 * auf 100% normalisiert

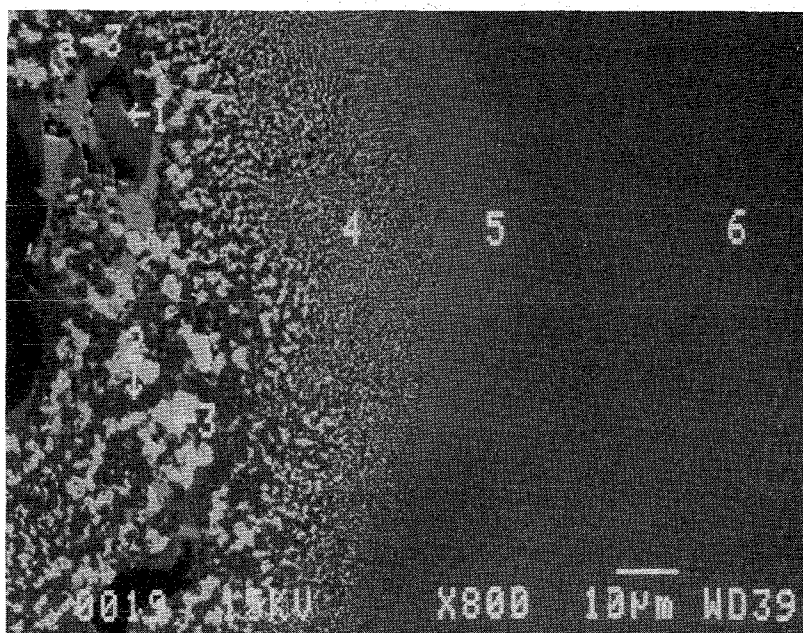


Fig. 163: Results of the SEM/EDX analysis of sample CORA-W1-06, position 19, SEM sub-position a/3, SEM analyses positions 1 - 6

Appendix

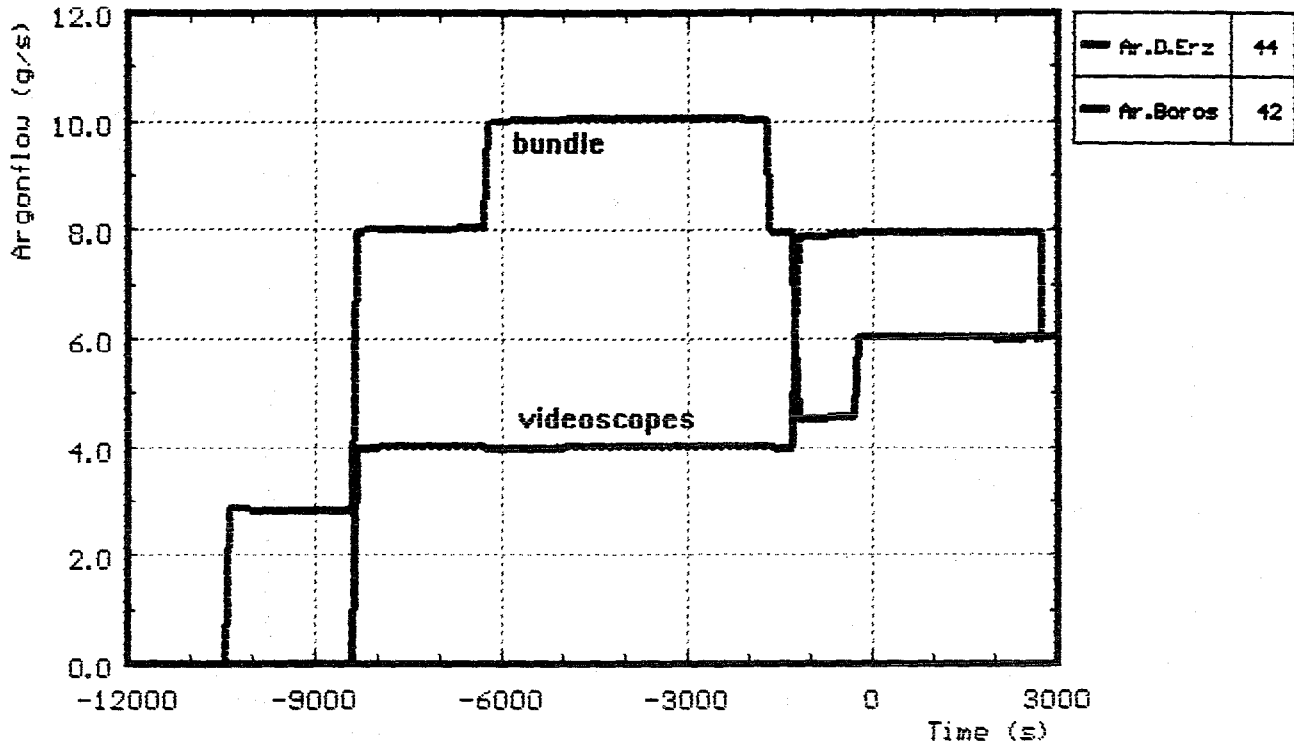


Fig. A1: CORA-W1; Argon flow through bundle and videoscopes, pre-heat phase

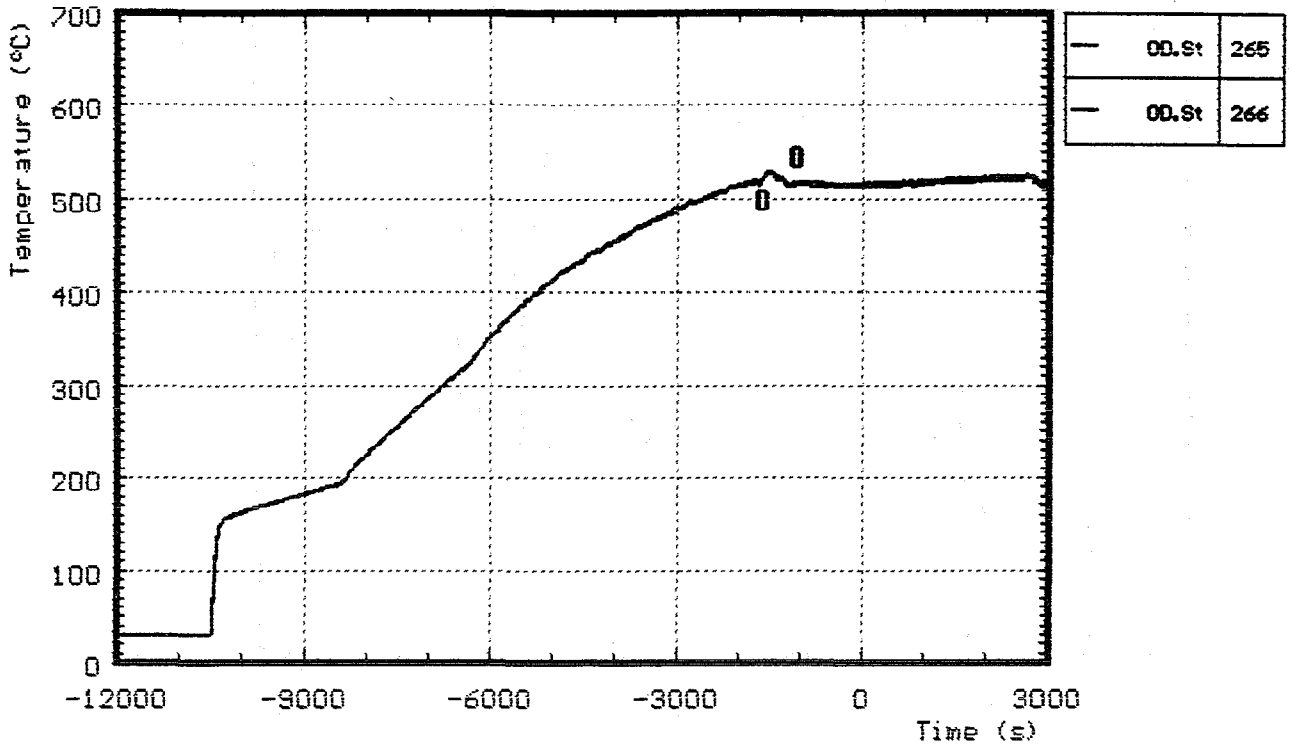


Fig. A2: CORA-W1; Temperature at steam inlet, pre-heat phase

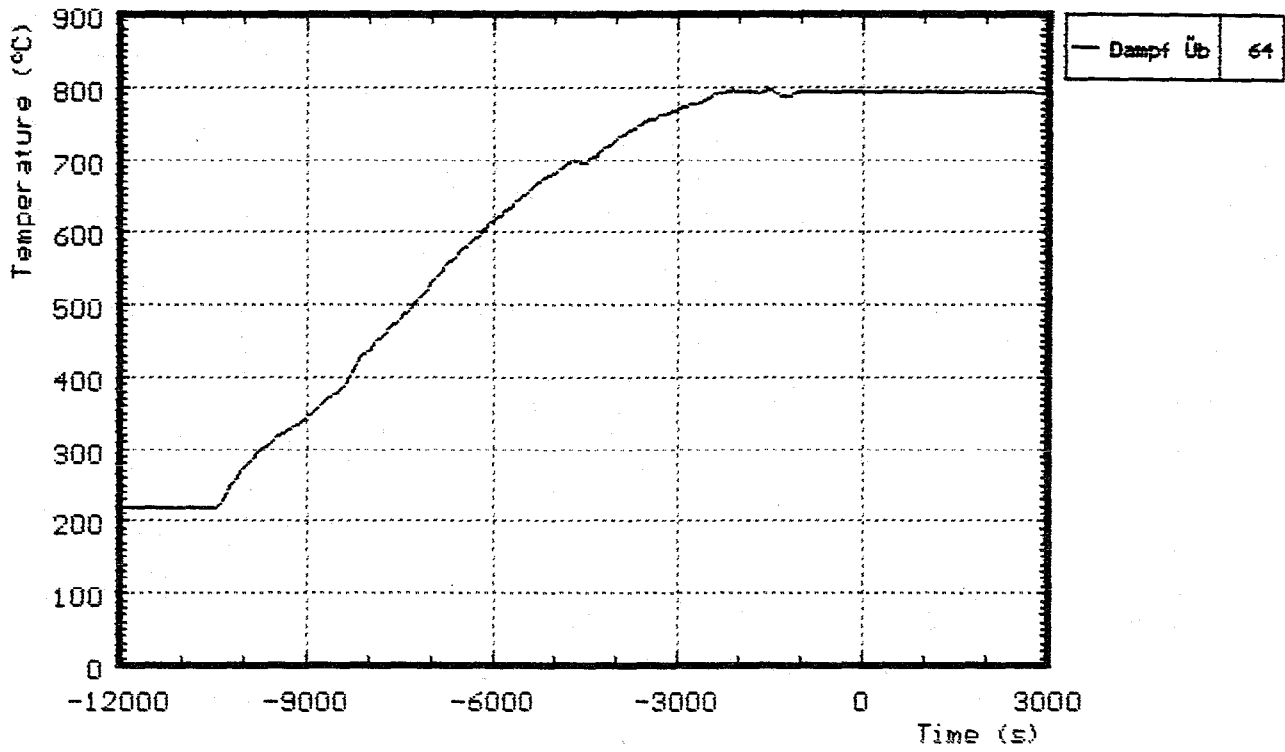


Fig. A3: CORA-W1; Temperature of steam superheater prior to transient

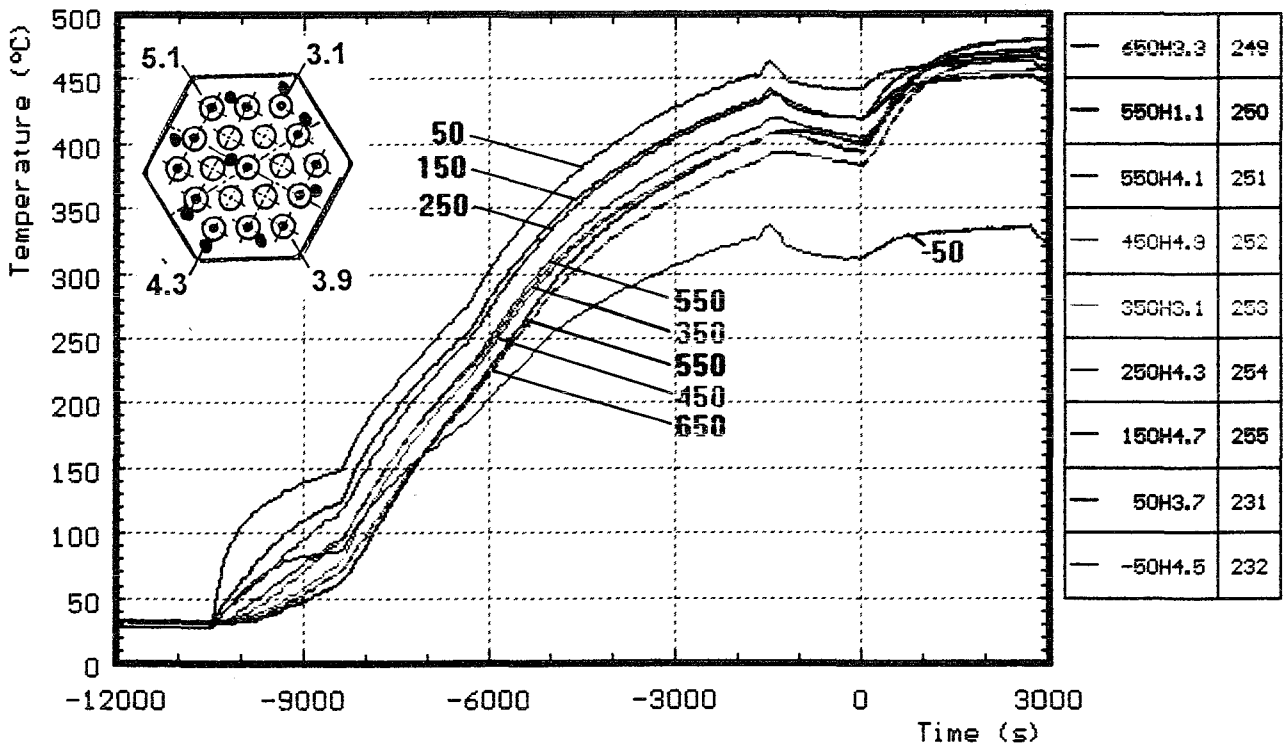
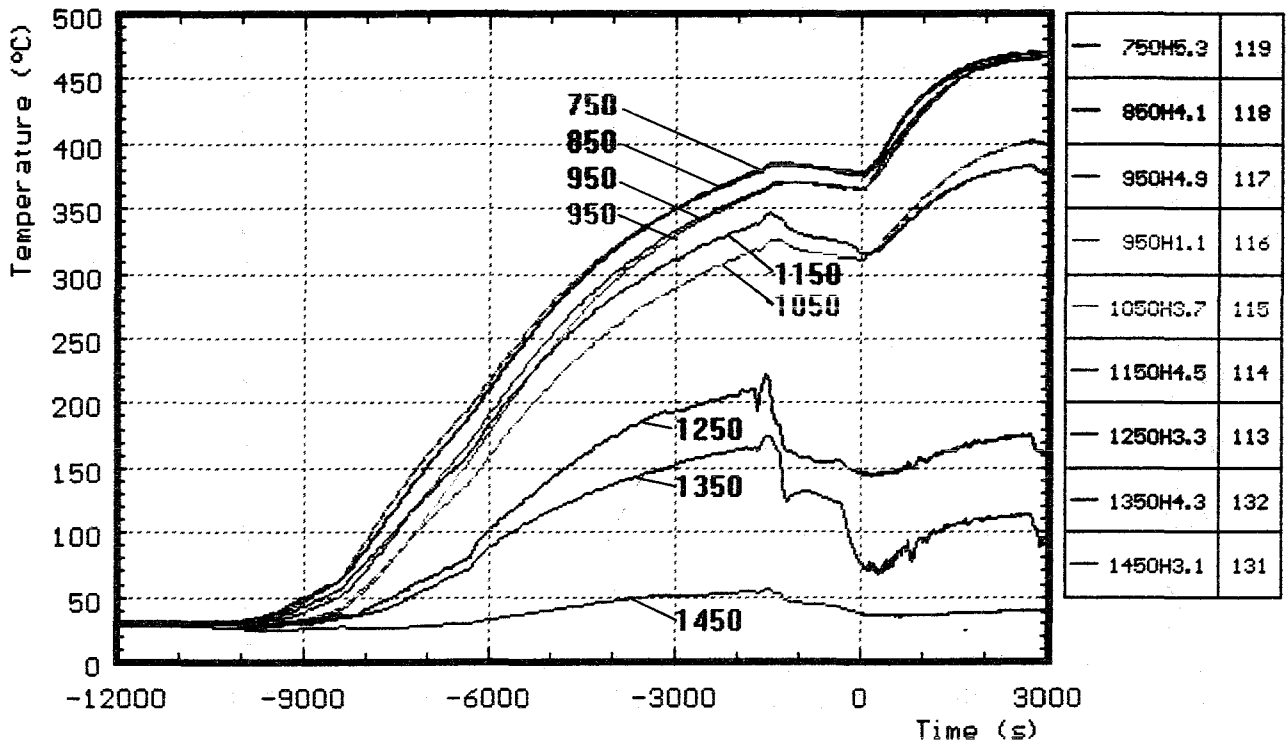


Fig. A4: CORA-W1: Temperatures of heated rods, pre-heat phase

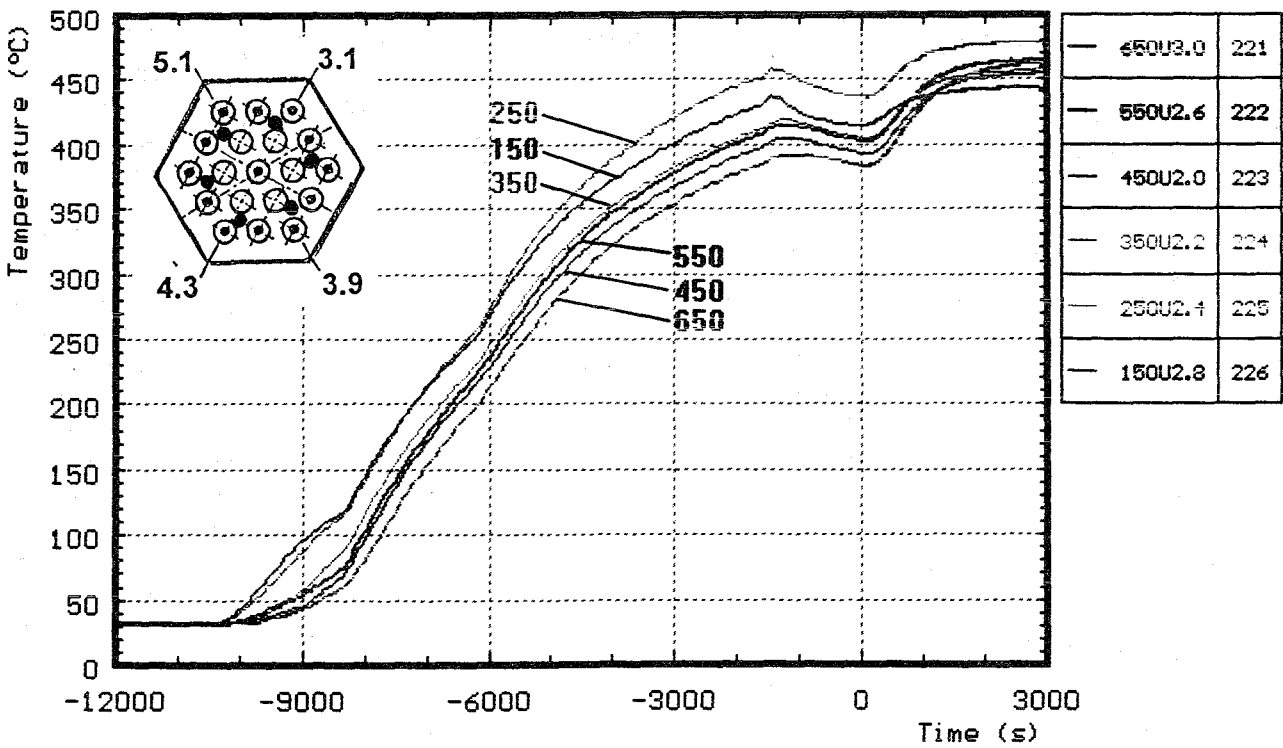
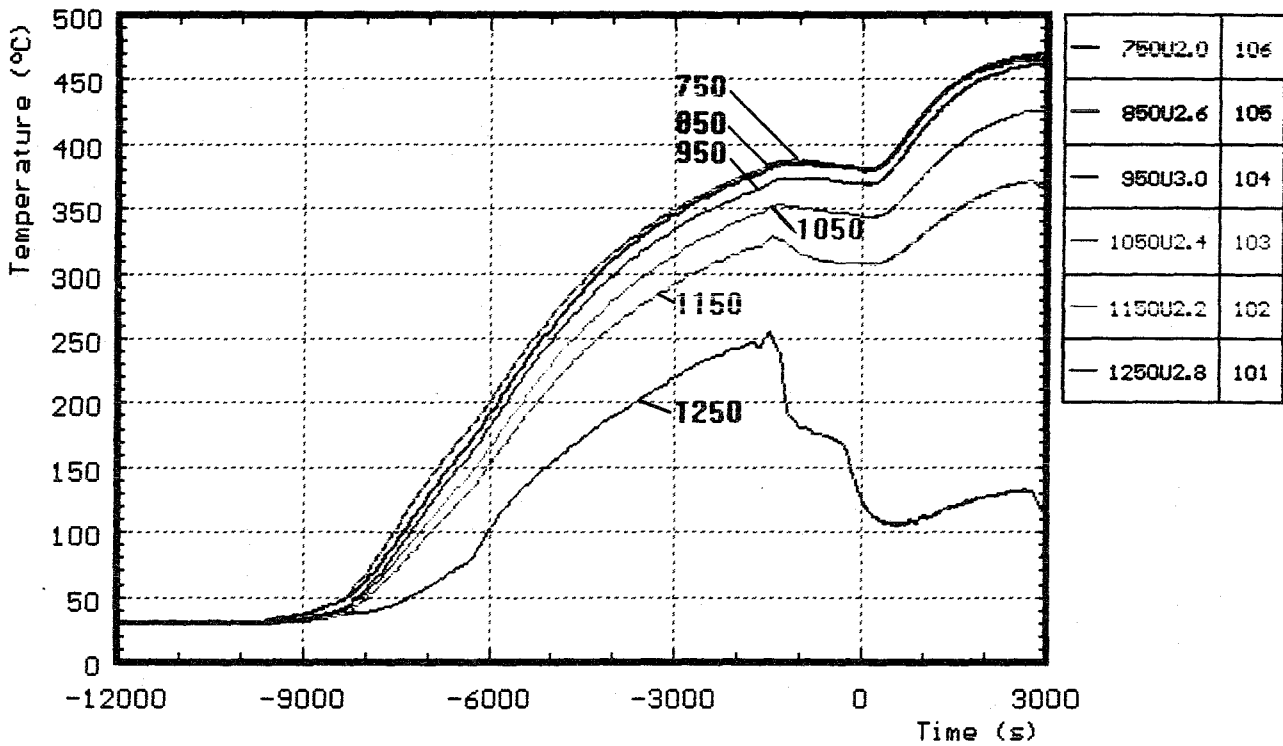


Fig. A5: CORA-W1: Temperatures of unheated rods, pre-heat phase

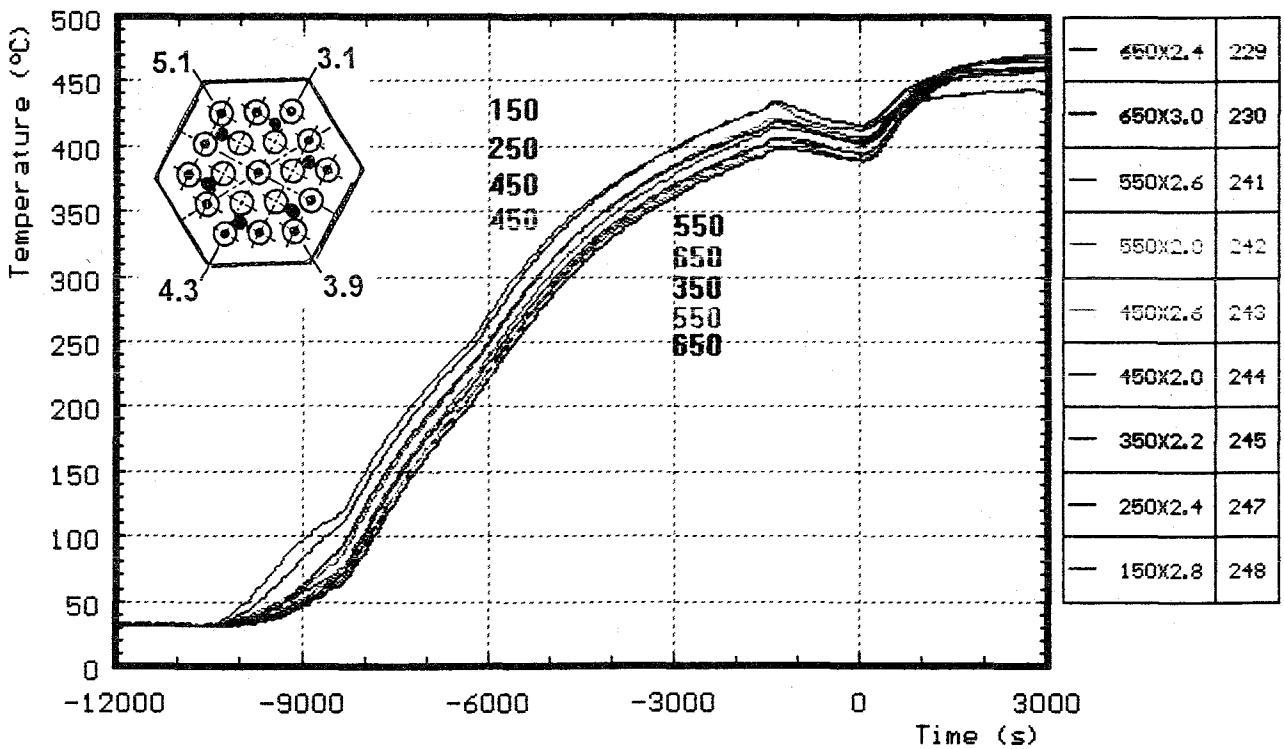
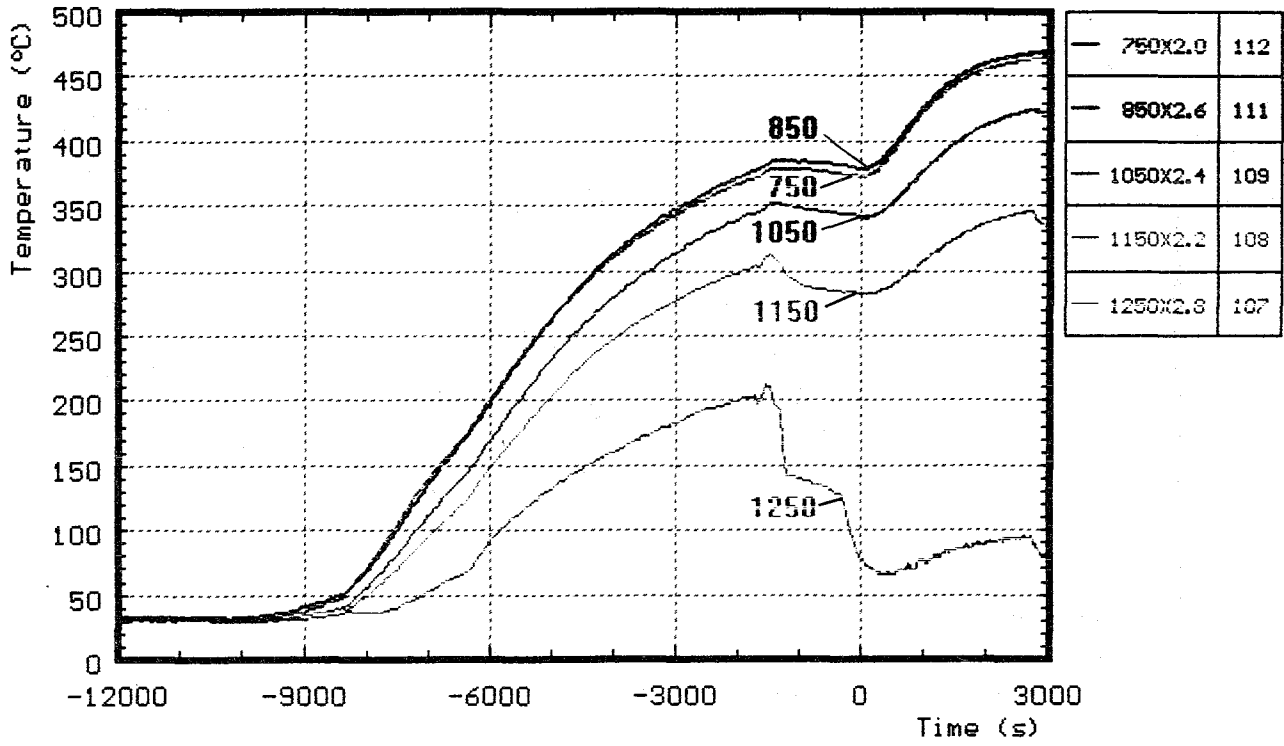


Fig. A6: CORA-W1: Temperatures of unheated rods, pre-heat phase

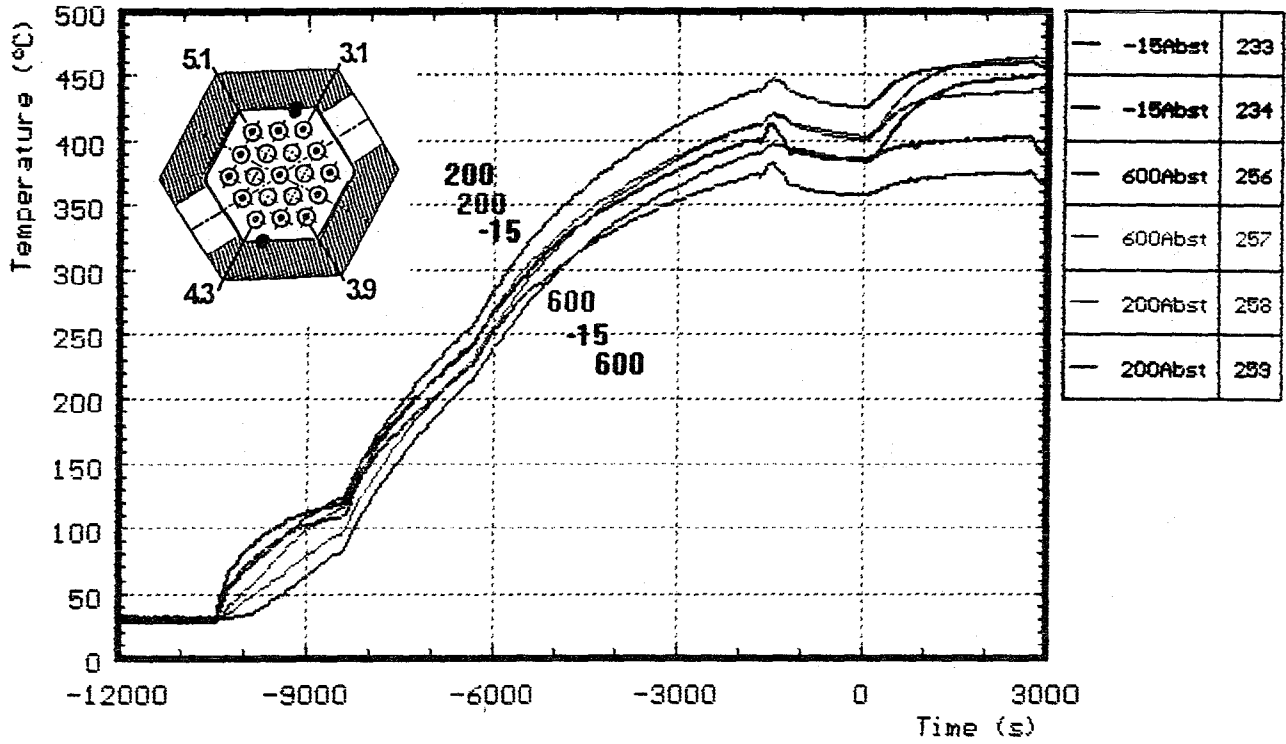


Fig. A7: CORA-W1: Temperatures of the spacers; pre-heat phase

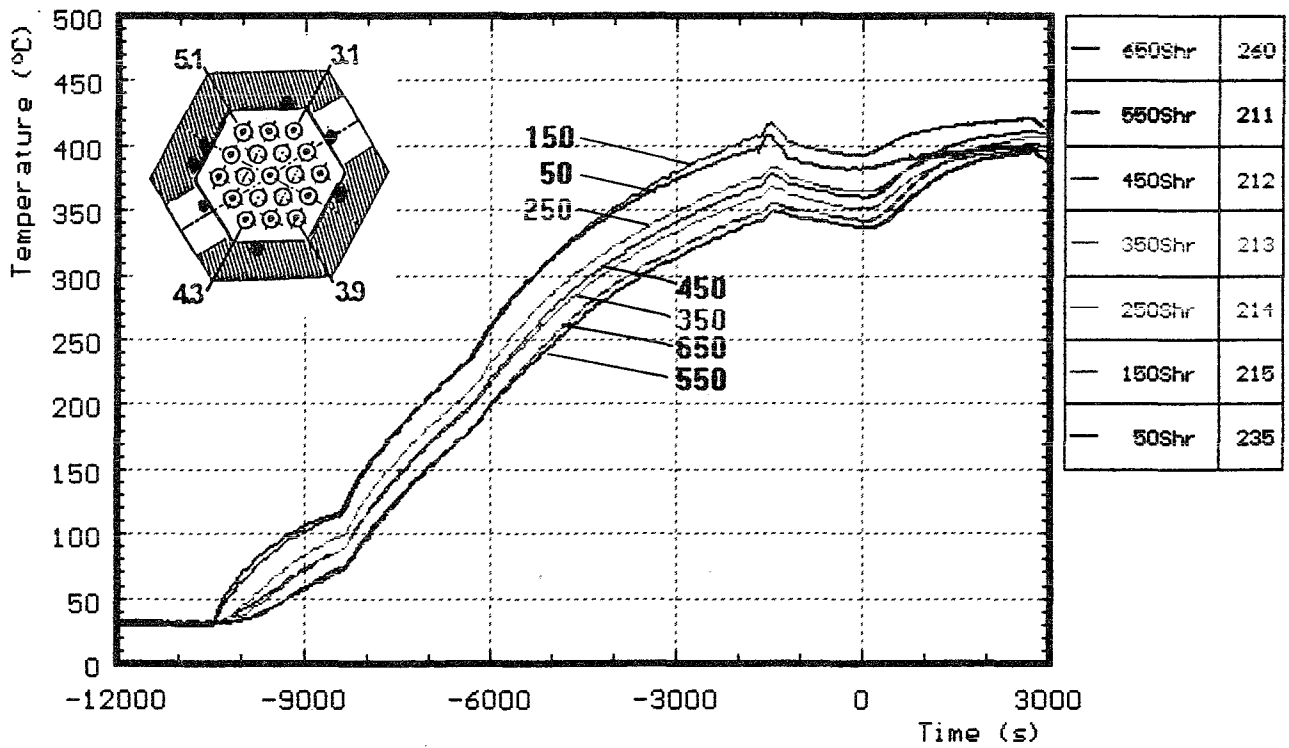
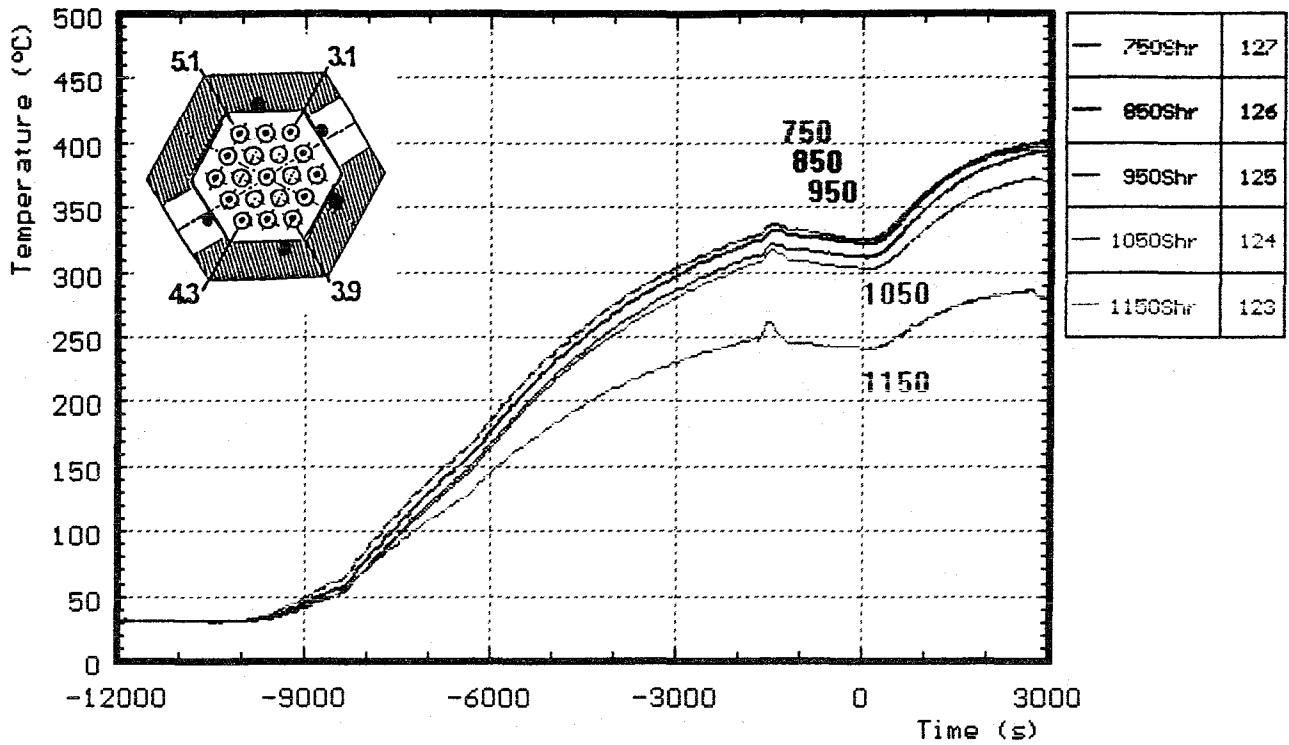


Fig. A8: CORA-W1: Temperatures of outer side of shroud, pre-heat phase

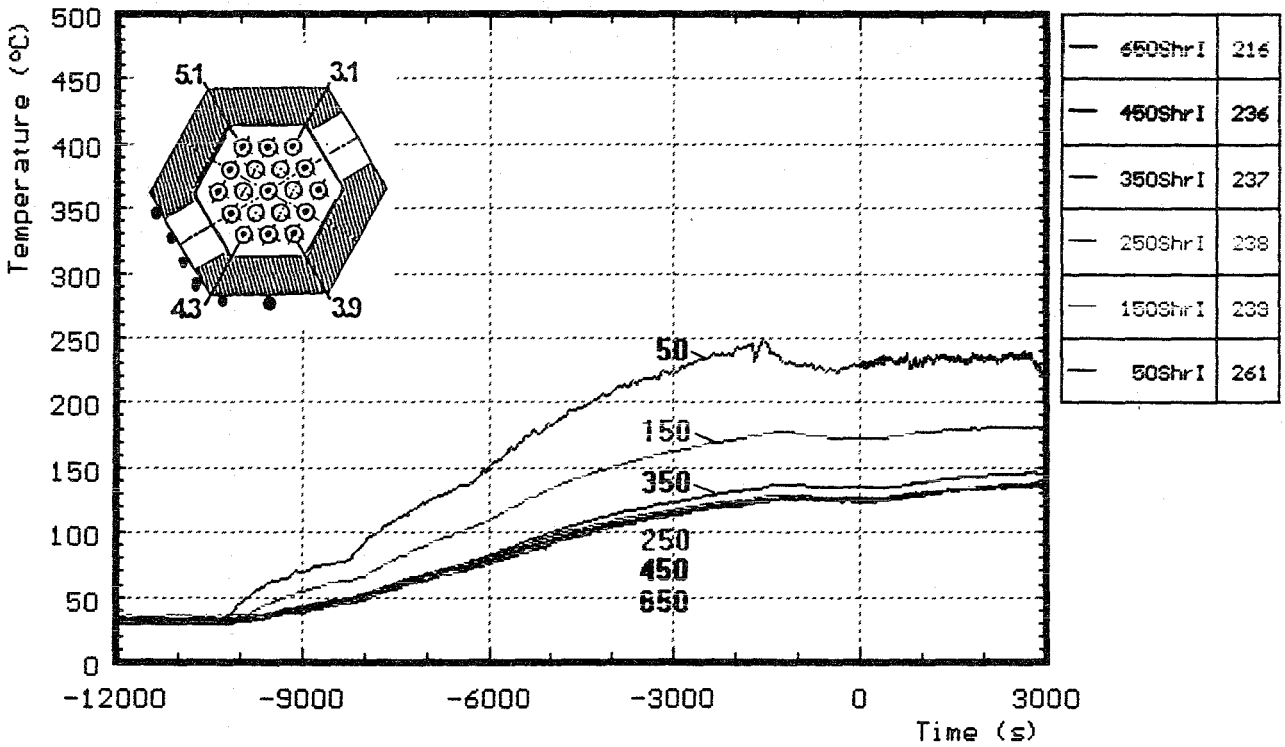
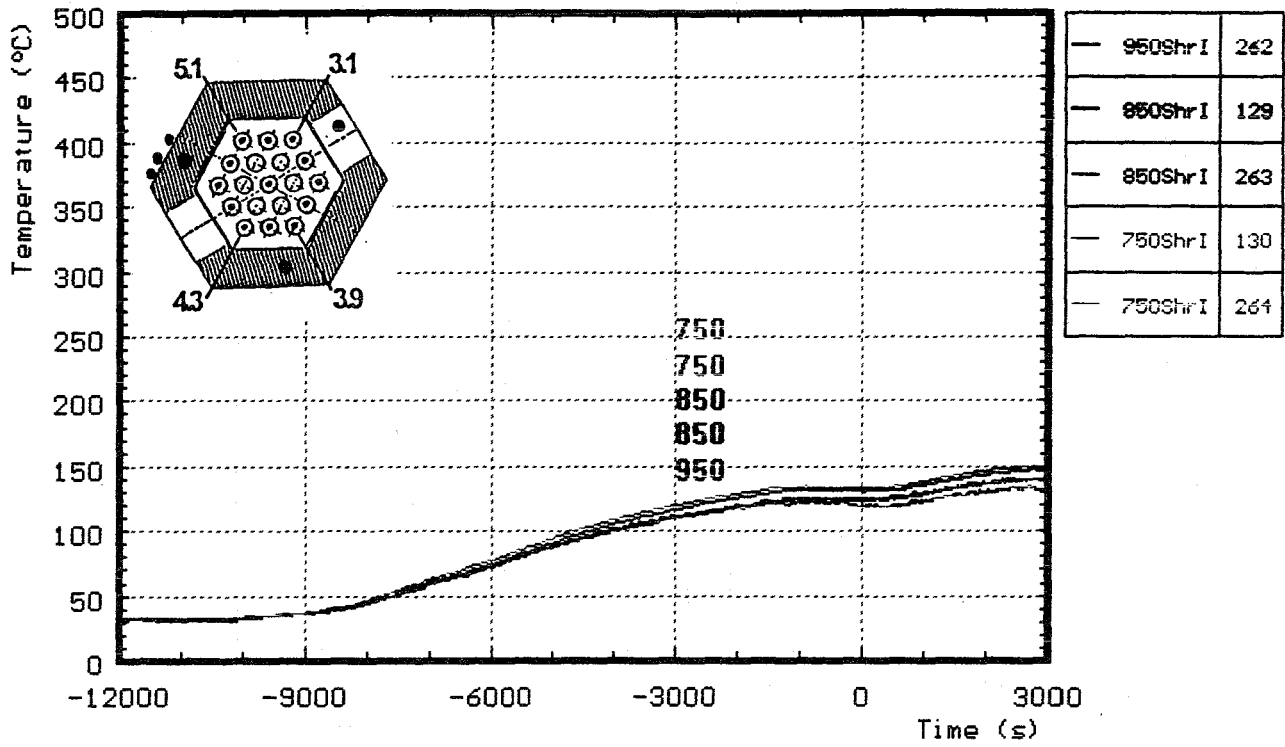


Fig. A9: CORA-W1: Temperatures of shroud insulation, pre-heat phase

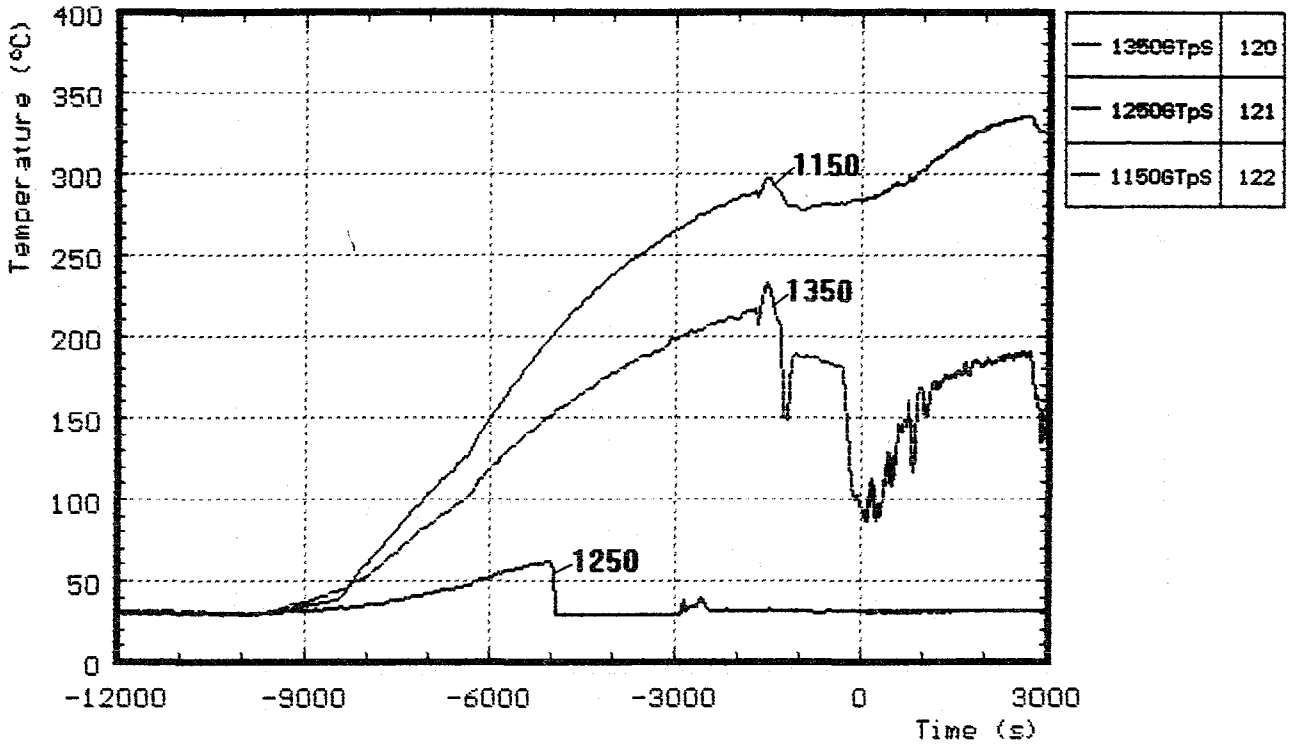


Fig.A10: CORA-W1: Gas temperature above the shroud; pre-heat phase

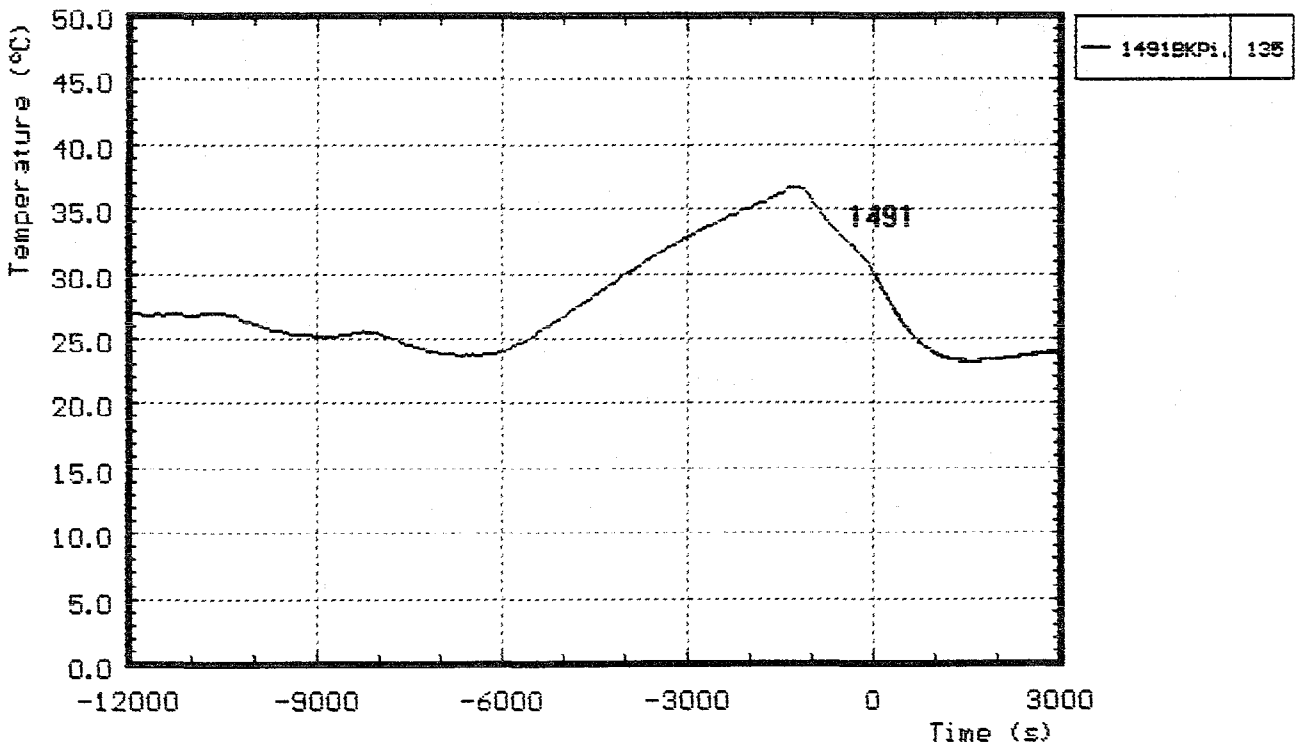


Fig.A11: CORA-W1: Gas temperature of the bundle heat plate; pre-heat phase

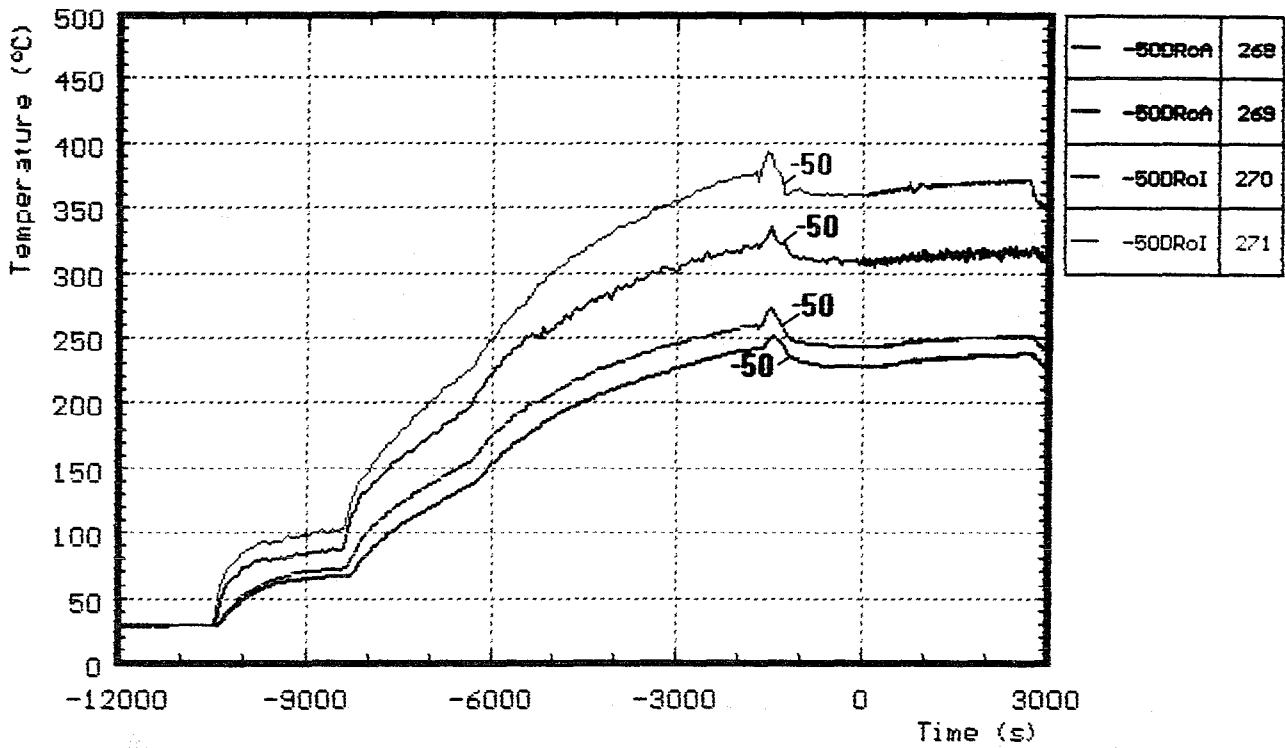
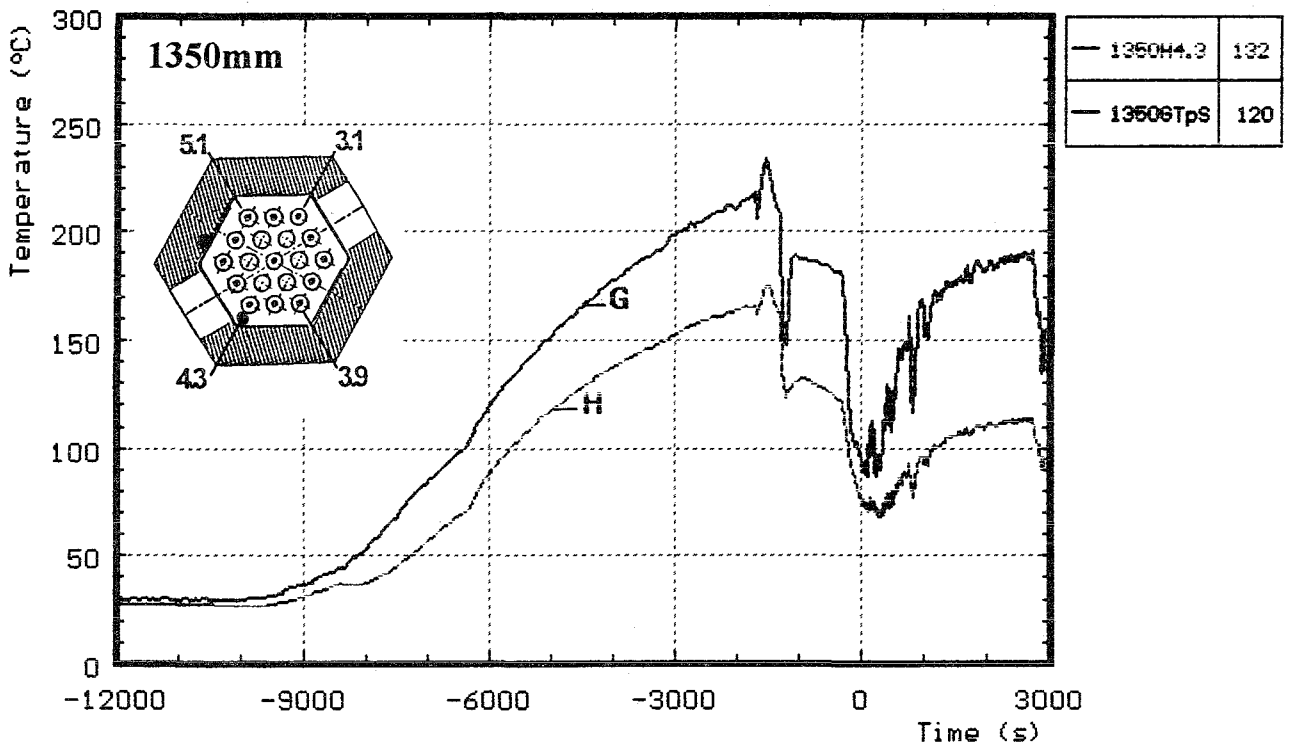
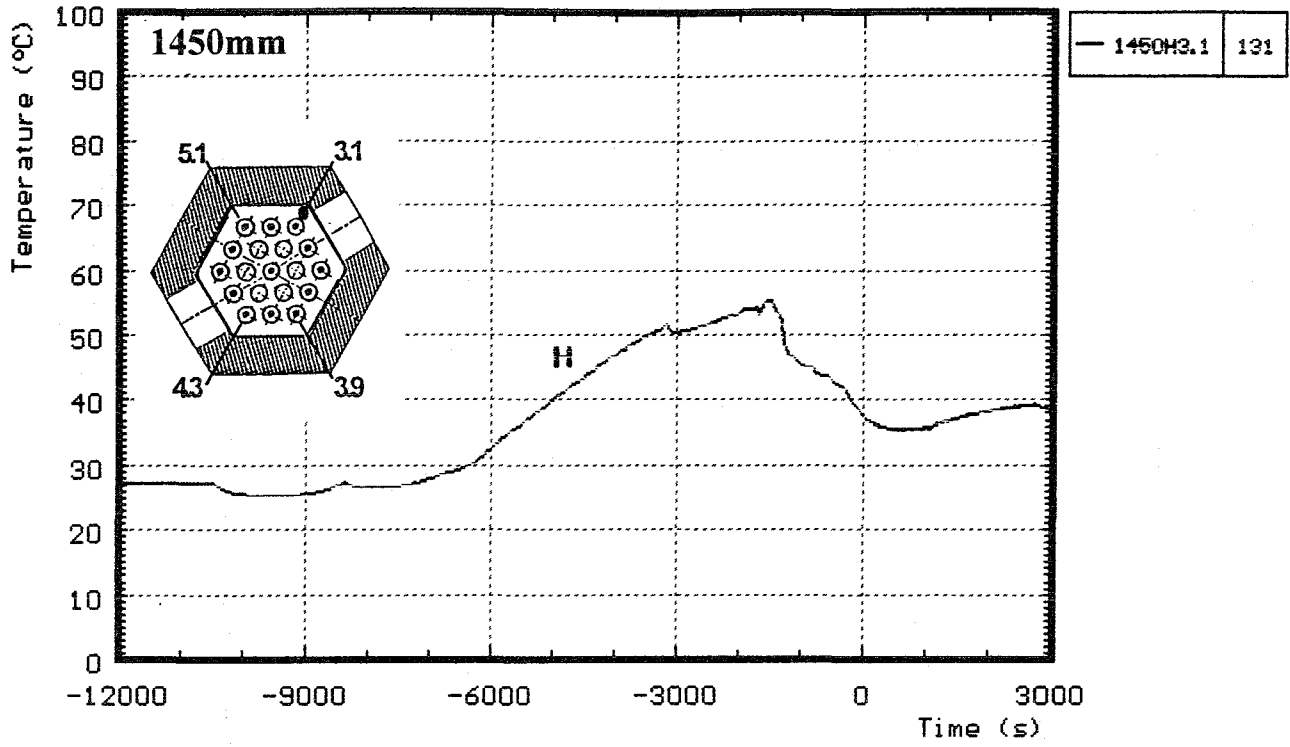
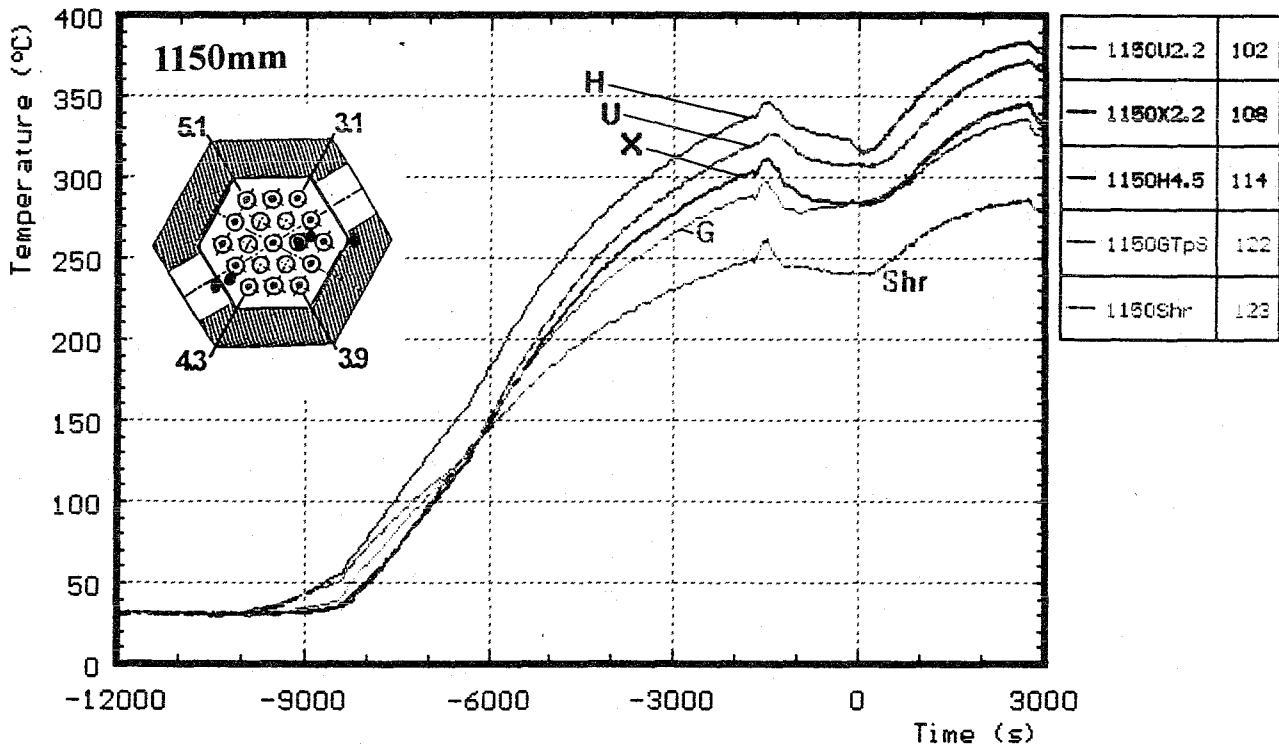
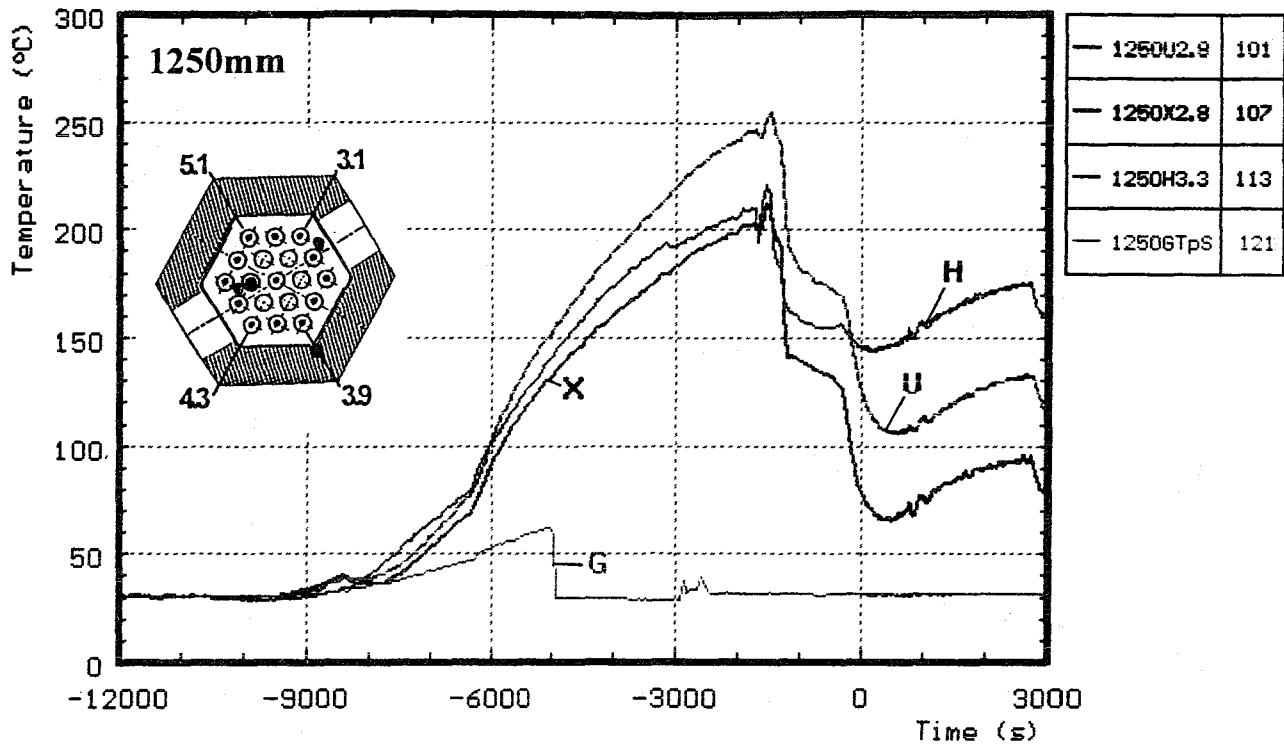


Fig.A12: CORA-W1:Temperatures measured in and on the steam tube at -50 mm elevation; pre-heat phase



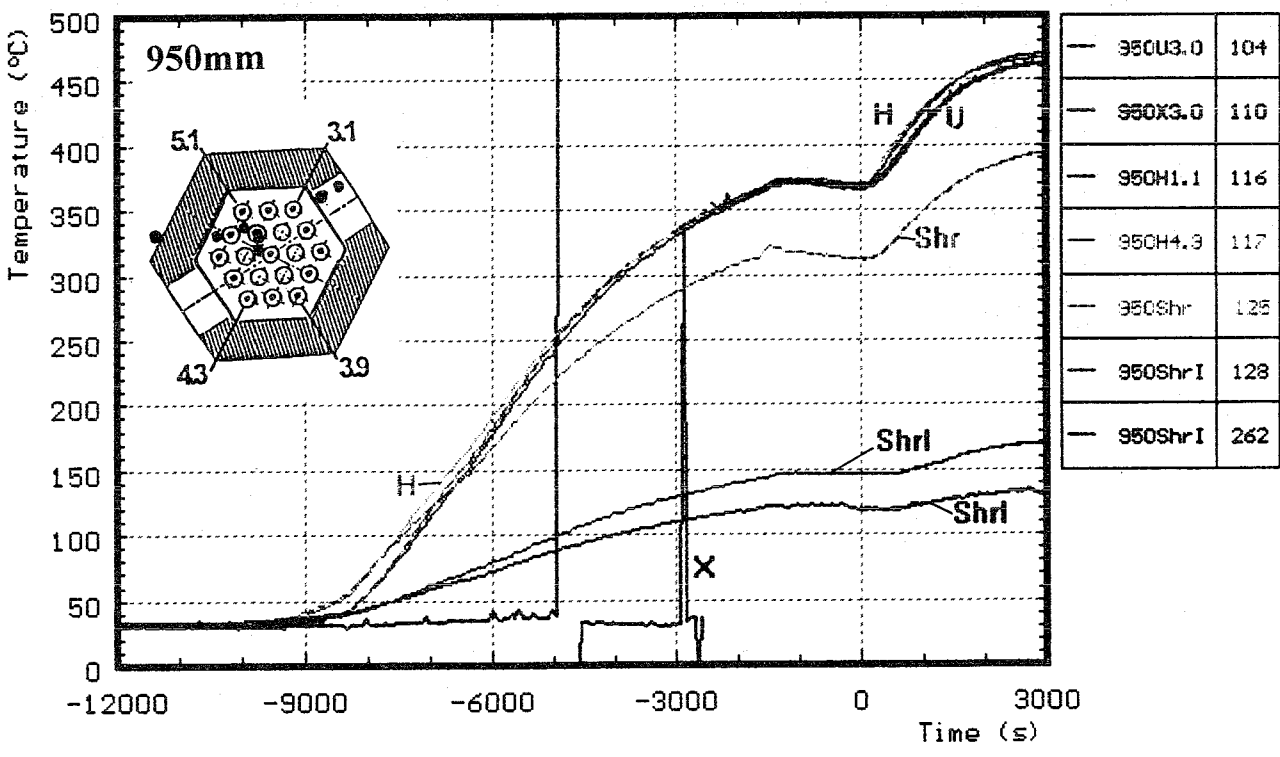
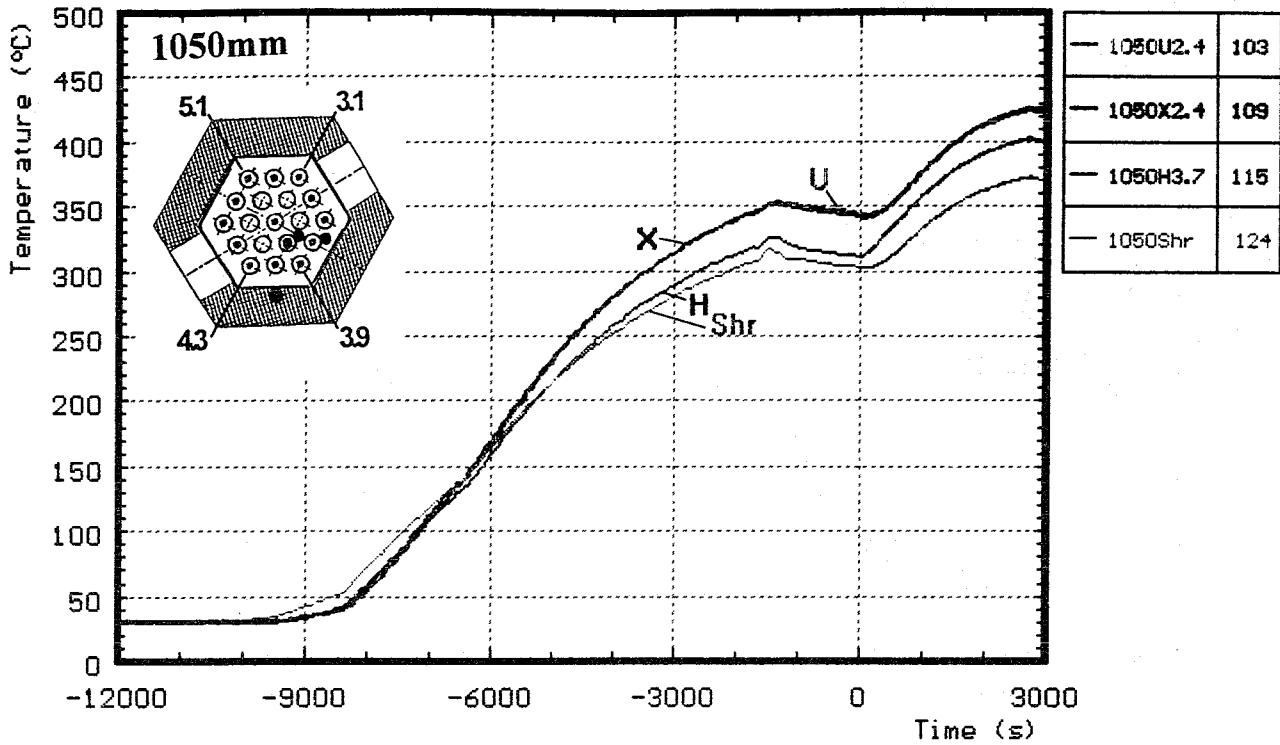
H : heated rods
G : gas temperature

Fig.A13: CORA-W1: Temperatures at fixed elevations, pre-heat phase (1450, 1350 mm)



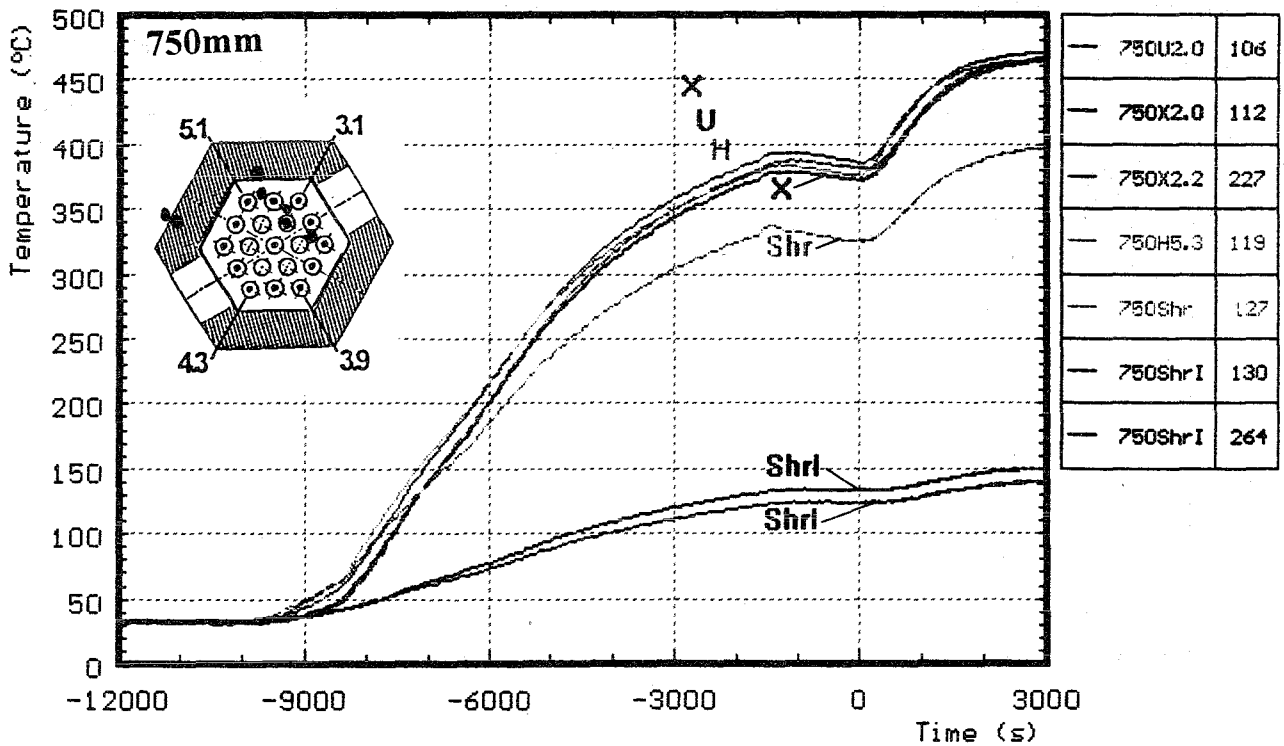
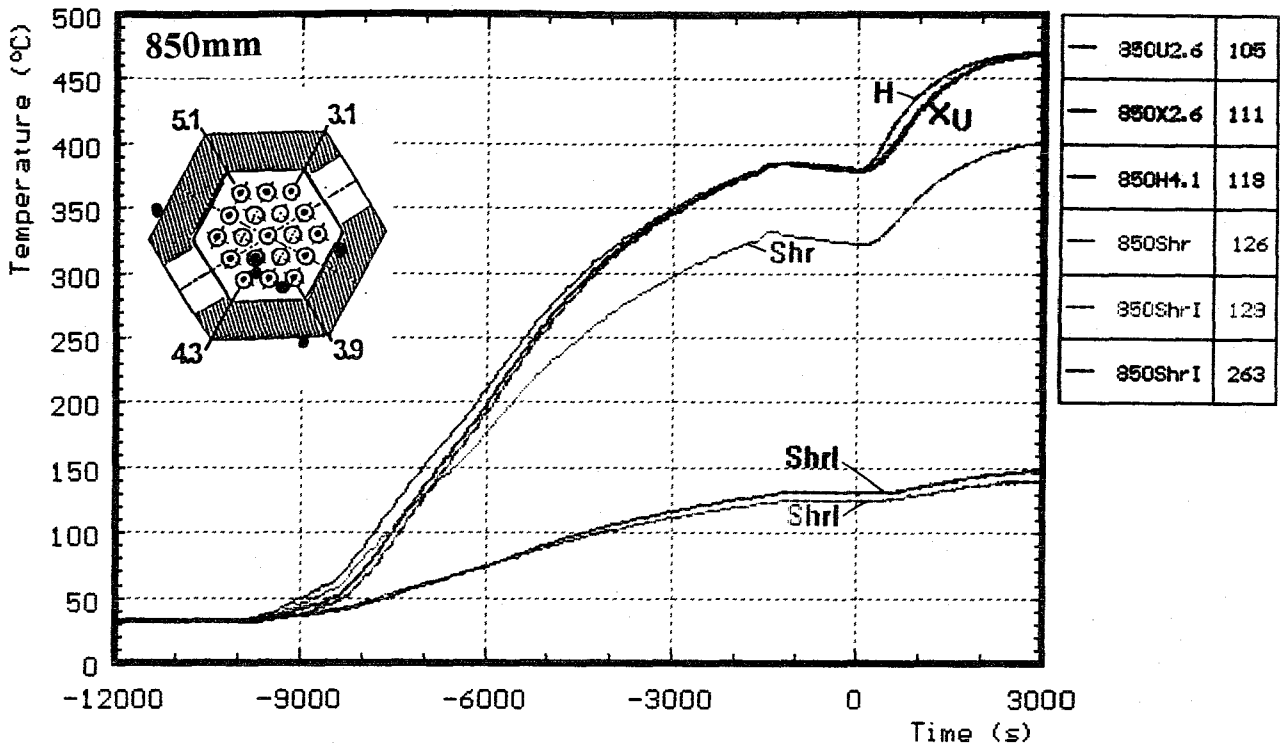
U : in absorber
 H : heated rods
 X : on unheated rods
 Shr : on shroud
 G : gas temperature

Fig.A14: CORA-W1: Temperatures at fixed elevations, pre-heat phase (1250, 1150 mm)



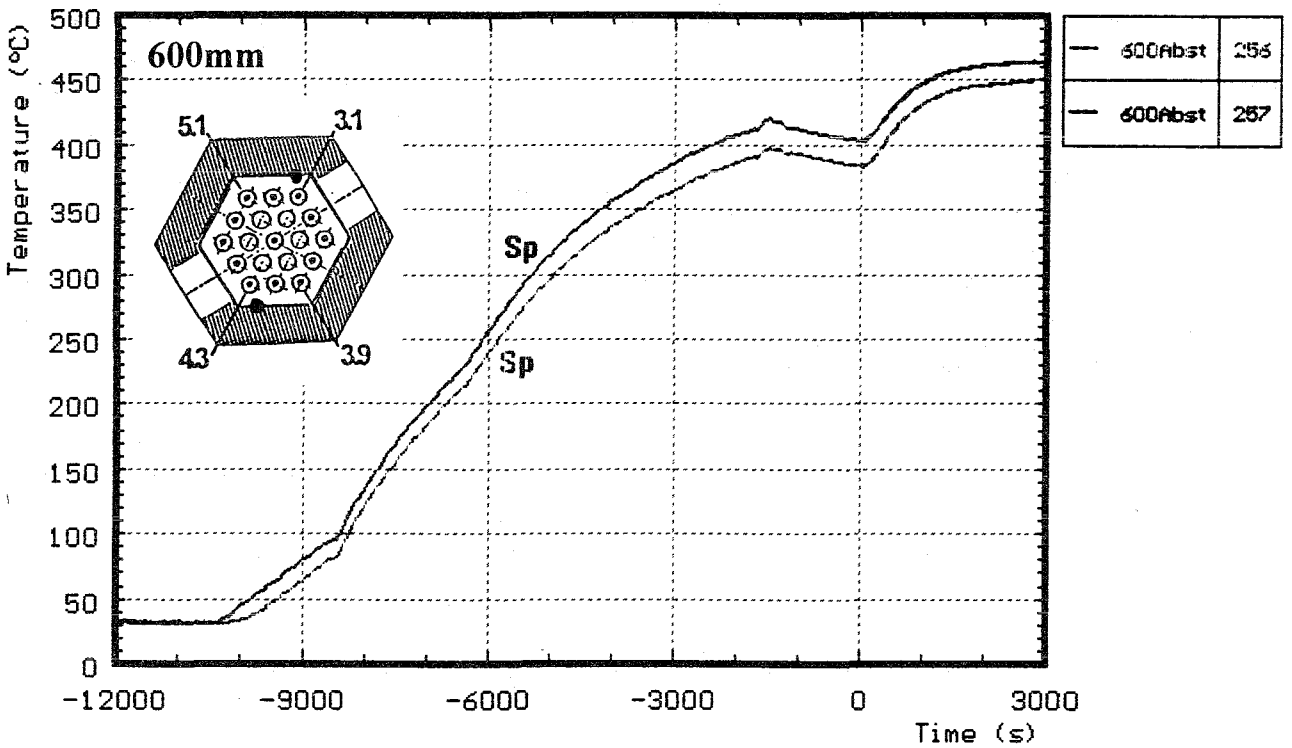
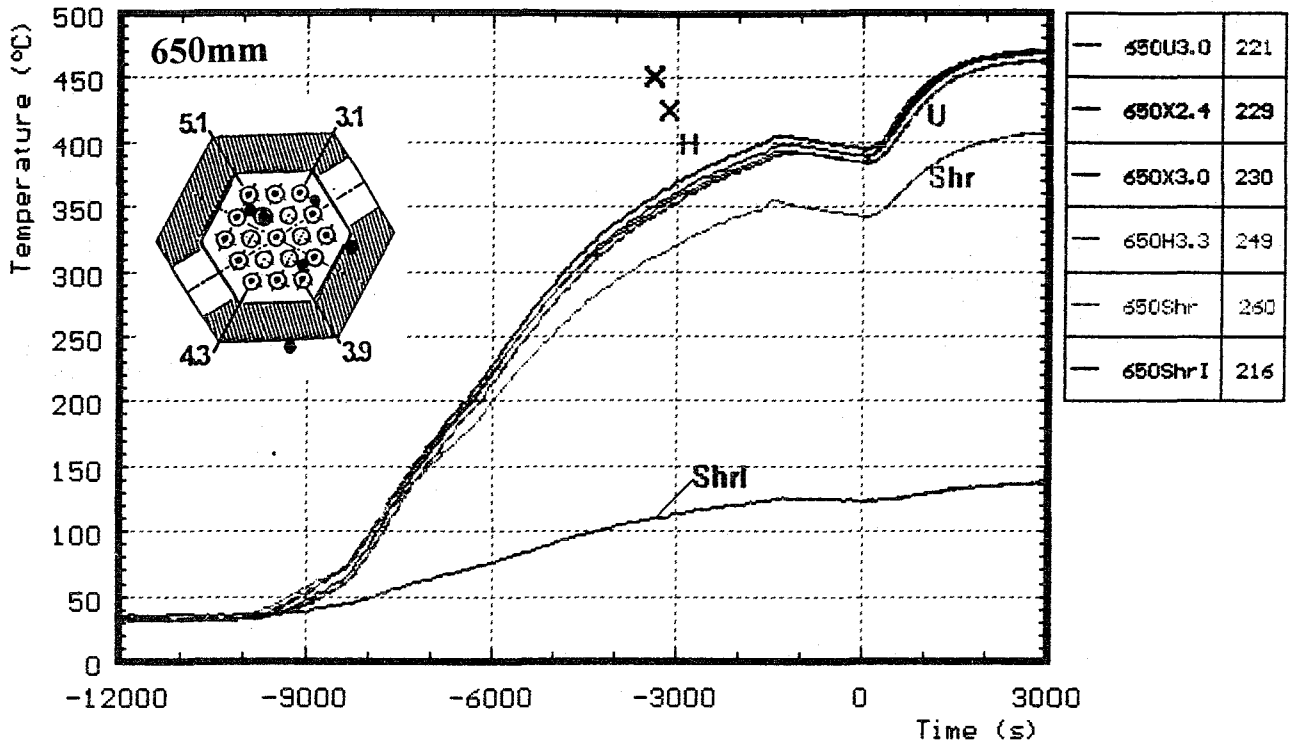
H : heated rods
 U : unheated rods
 X : on unheated rods
 Shr : on shroud
 ShrI : shroud insulation

Fig.A15: CORA-W1: Temperatures at fixed elevations, pre-heat phase (1050, 950 mm)



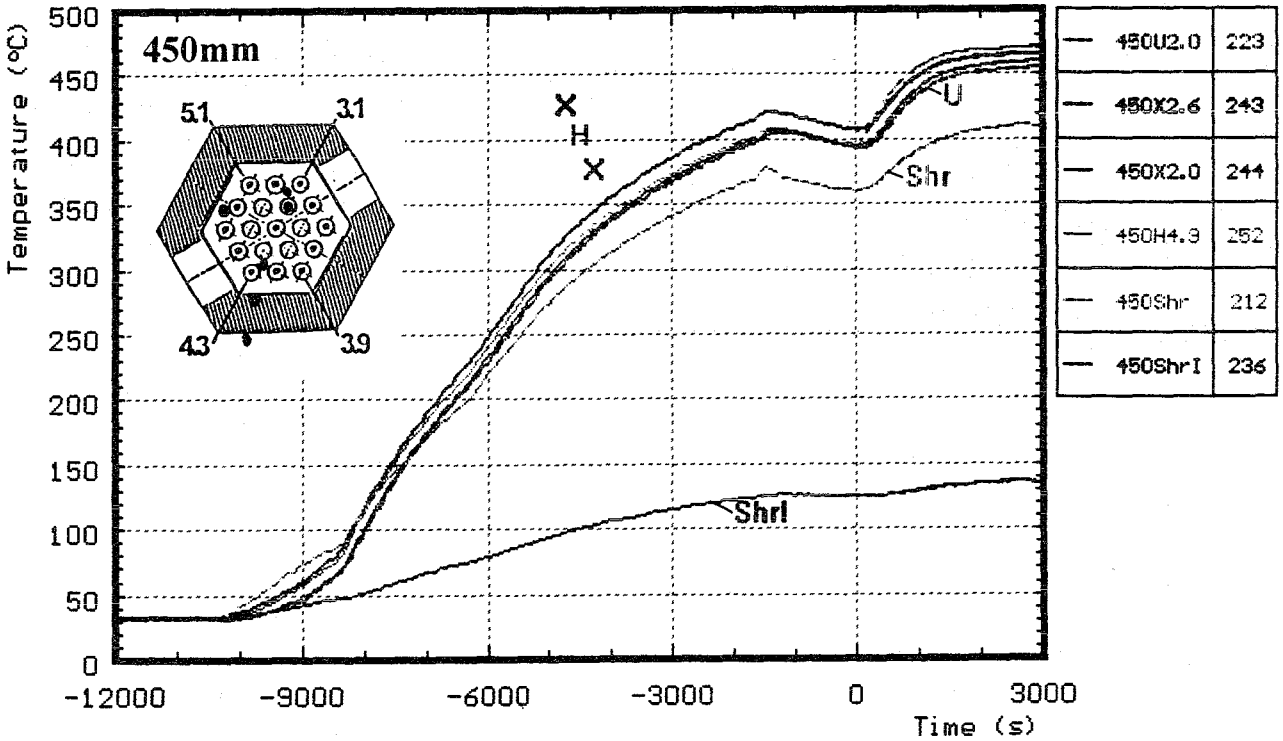
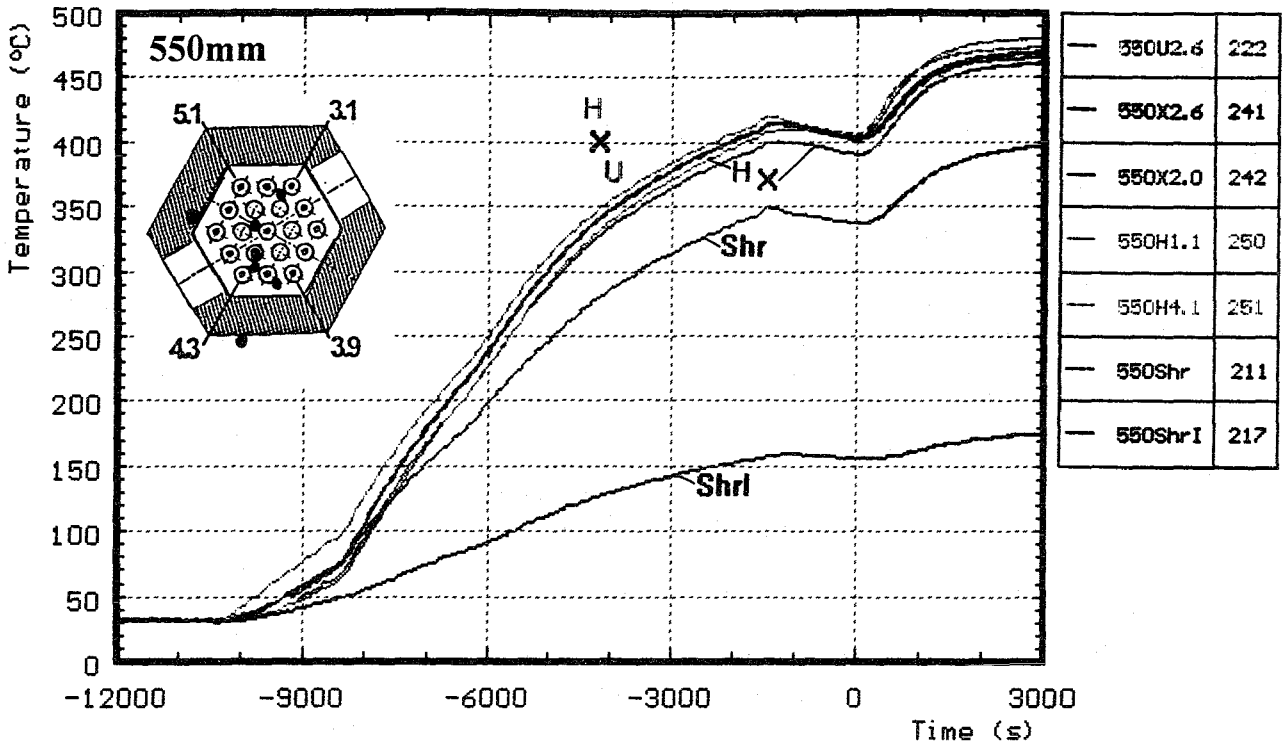
H : heated rods
 U : unheated rods
 X : on unheated rods
 Shr : on shroud
 ShrI : shroud insulation

Fig.A16: CORA-W1: Temperatures at fixed elevations, pre-heat phase (850, 750 mm)



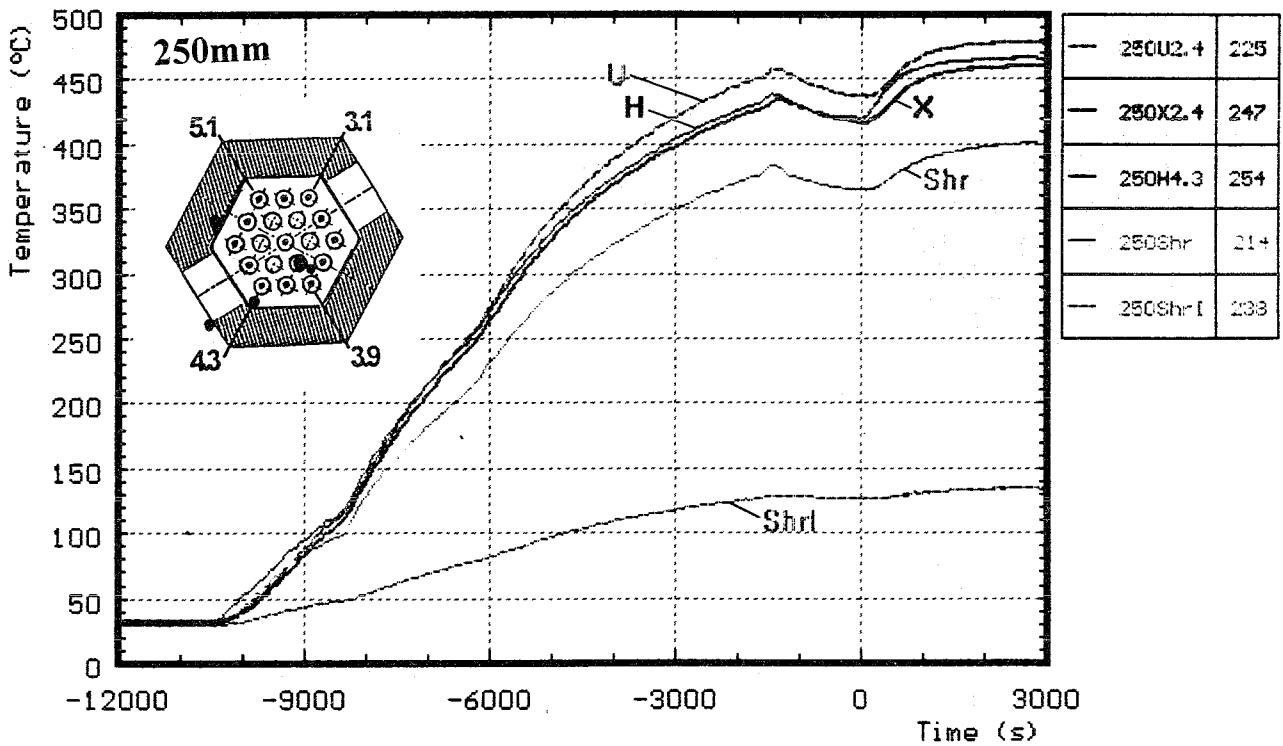
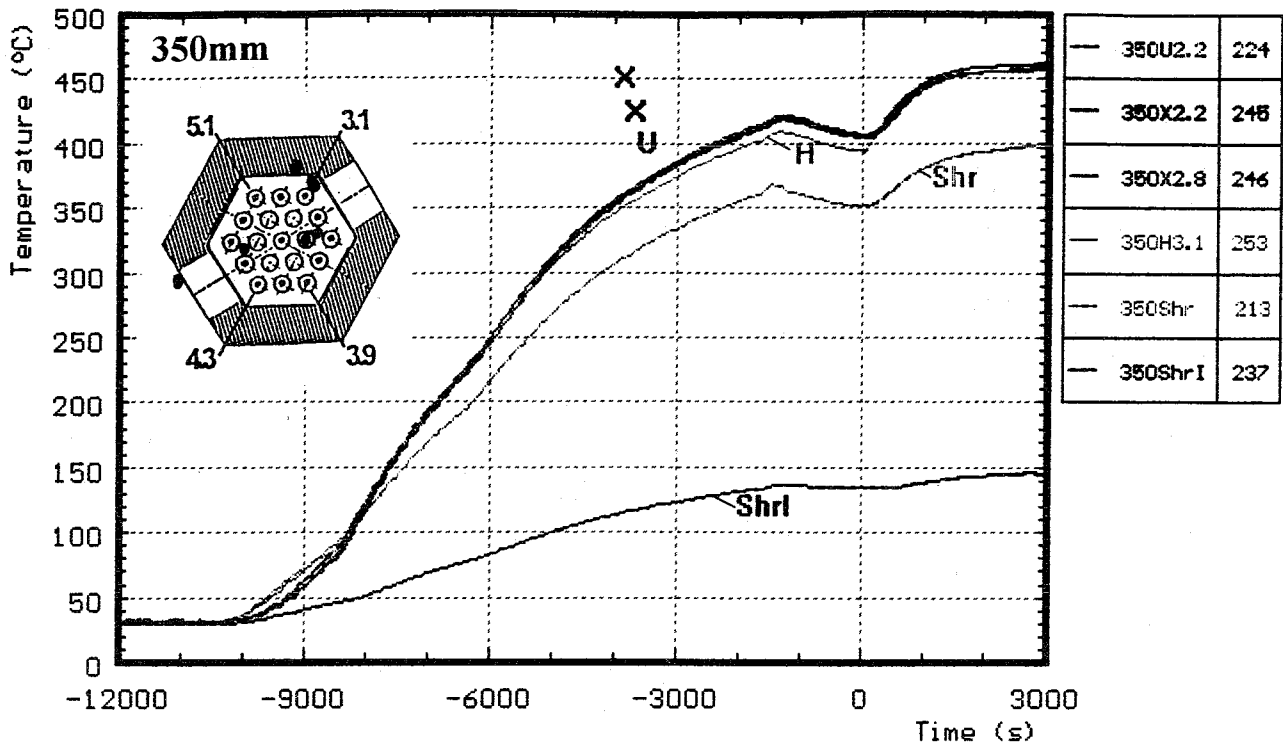
- H : heated rods
- U : unheated rods
- X : on unheated rods
- Sp : spacer
- Shr : on shroud
- ShrI : shroud insulation

Fig.A17: CORA-W1: Temperatures at fixed elevations, pre-heat phase (650, 600 mm)



H : heated rods
 U : unheated rods
 X : on unheated rods
 Shr : on shroud
 ShrI : shroud insulation

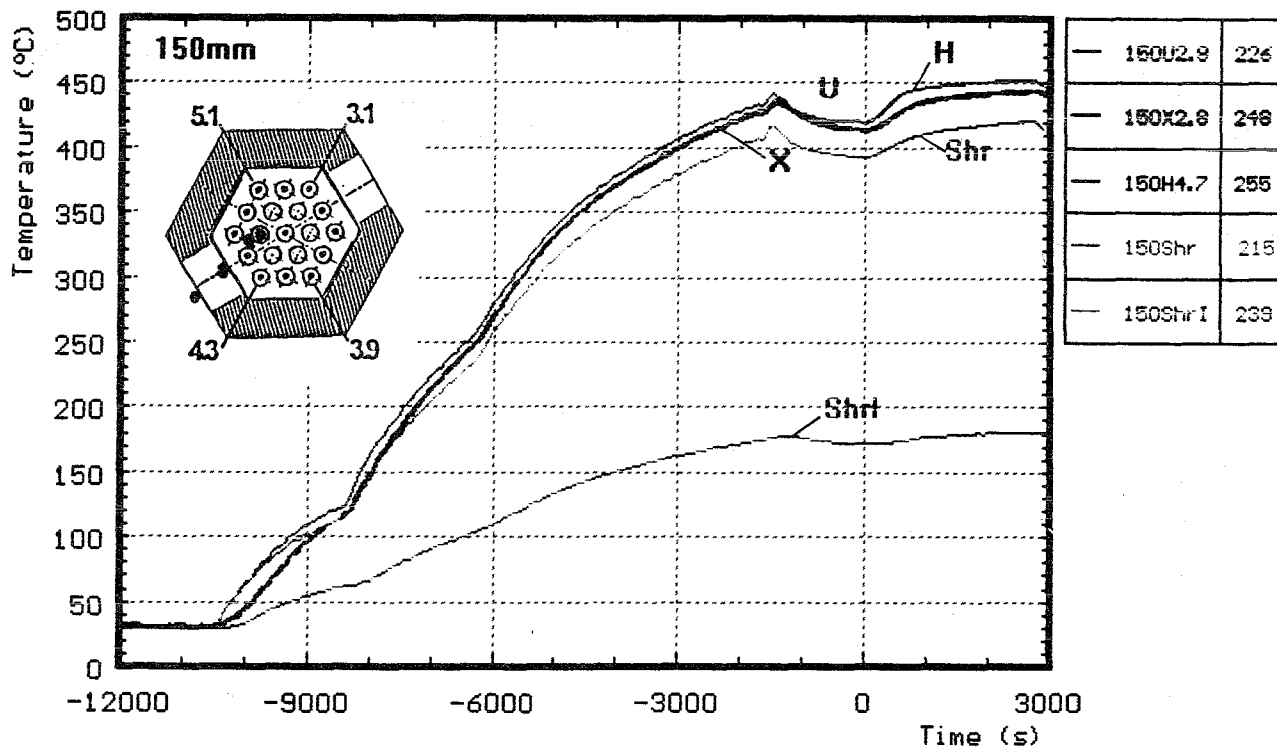
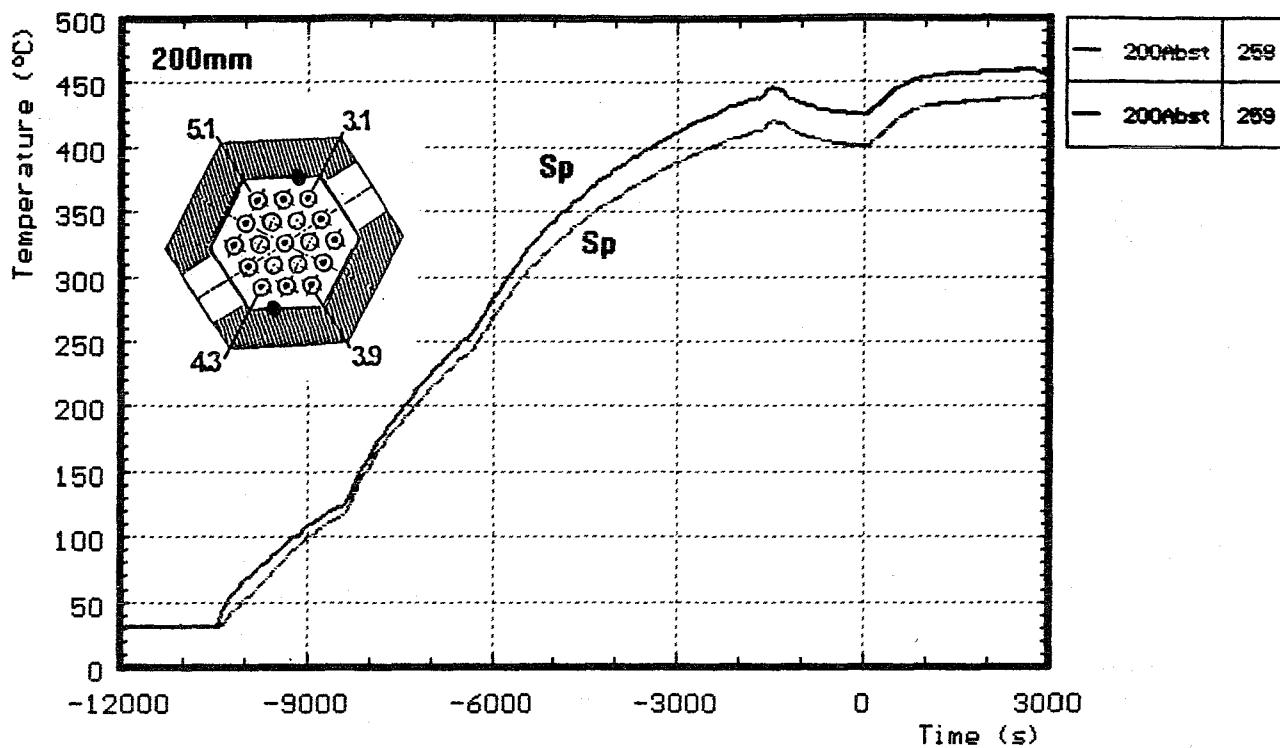
Fig.A18: CORA-W1: Temperatures at fixed elevations, pre-heat phase (550, 450 mm)



H : heated rods
 U : unheated rods
 X : on unheated rods

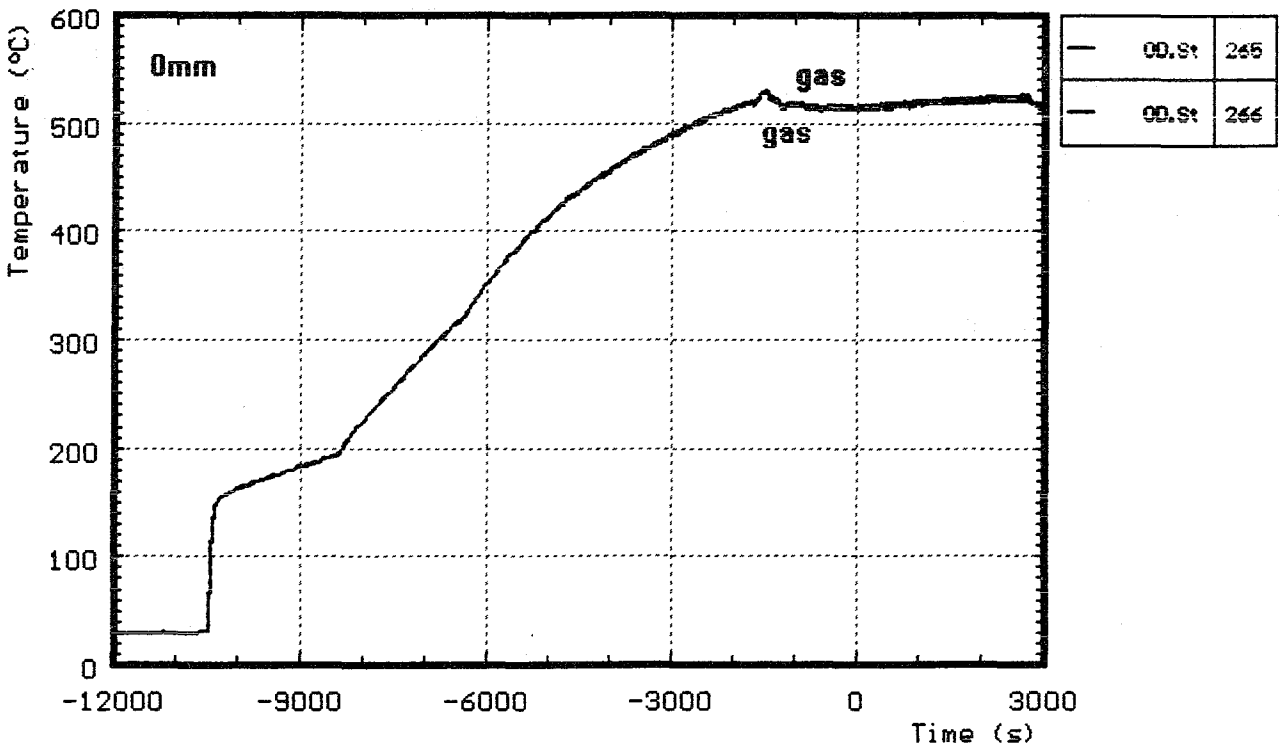
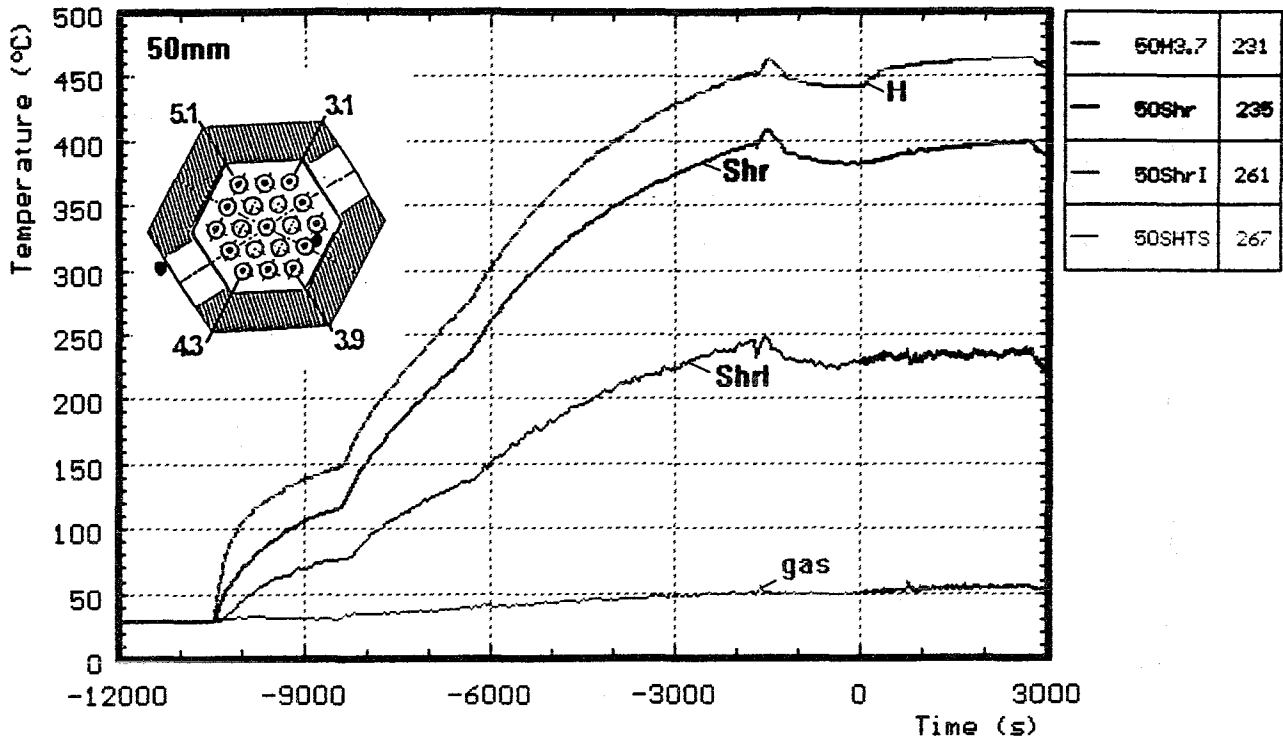
Shr : on shroud
 ShrI : shroud insulation

Fig.A19: CORA-W1: Temperatures at fixed elevations, pre-heat phase (350, 250 mm)



- | | | | |
|---|--------------------|------|---------------------|
| H | : heated rods | Sp | : spacer |
| U | : unheated rods | Shr | : on shroud |
| X | : on unheated rods | ShrI | : shroud insulation |

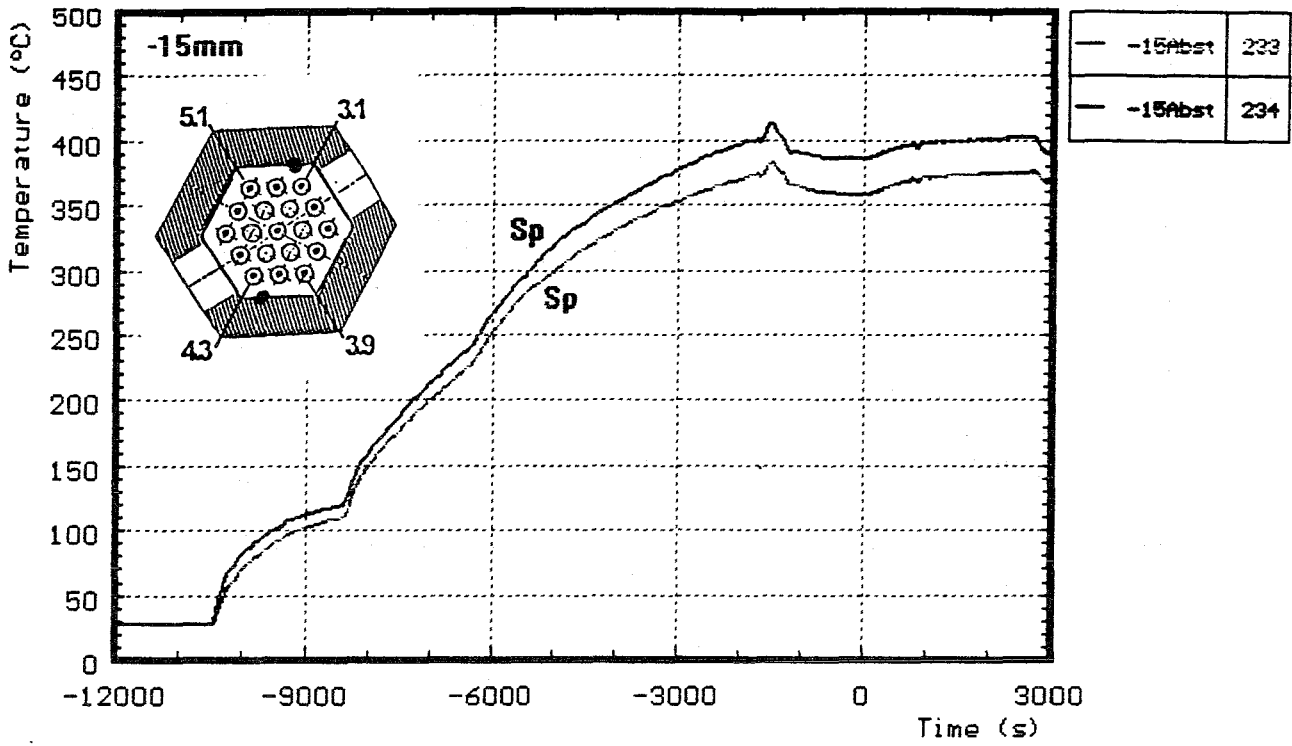
Fig.A20: CORA-W1: Temperatures at fixed elevations, pre-heat phase (200, 150 mm)



H : heated rods
 gas : gas temperature

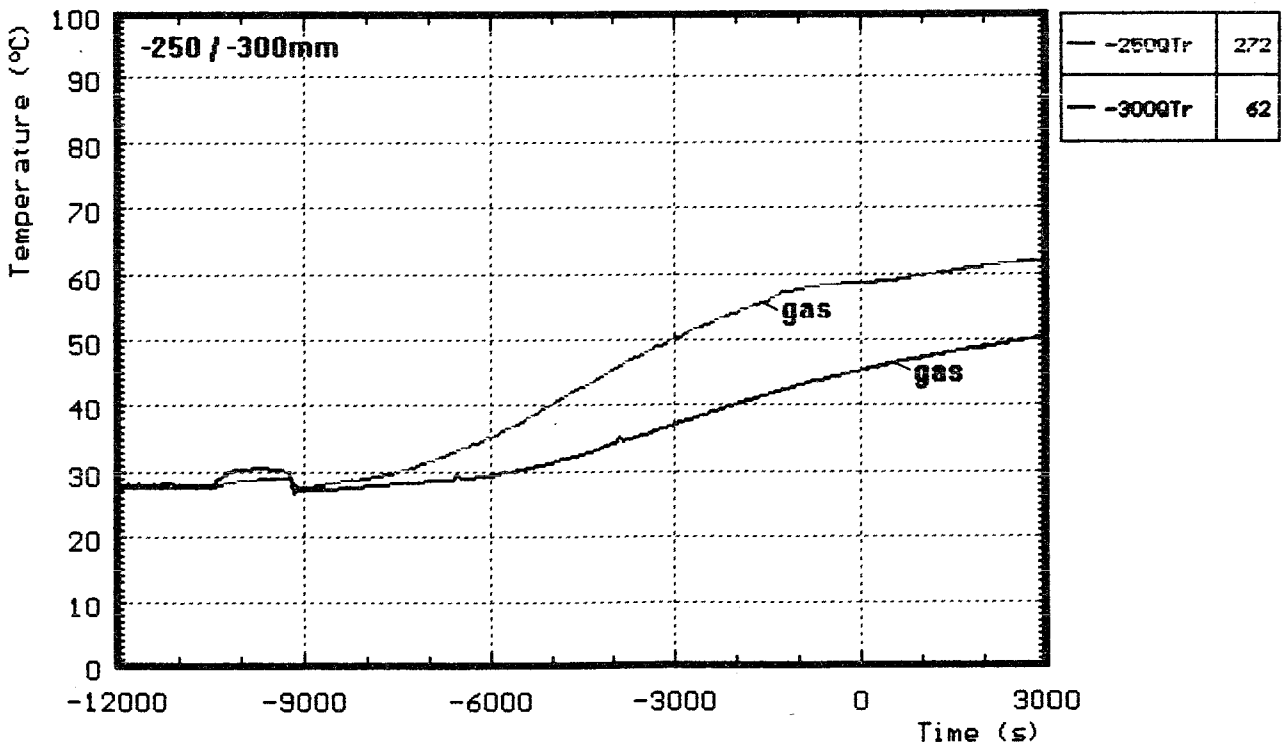
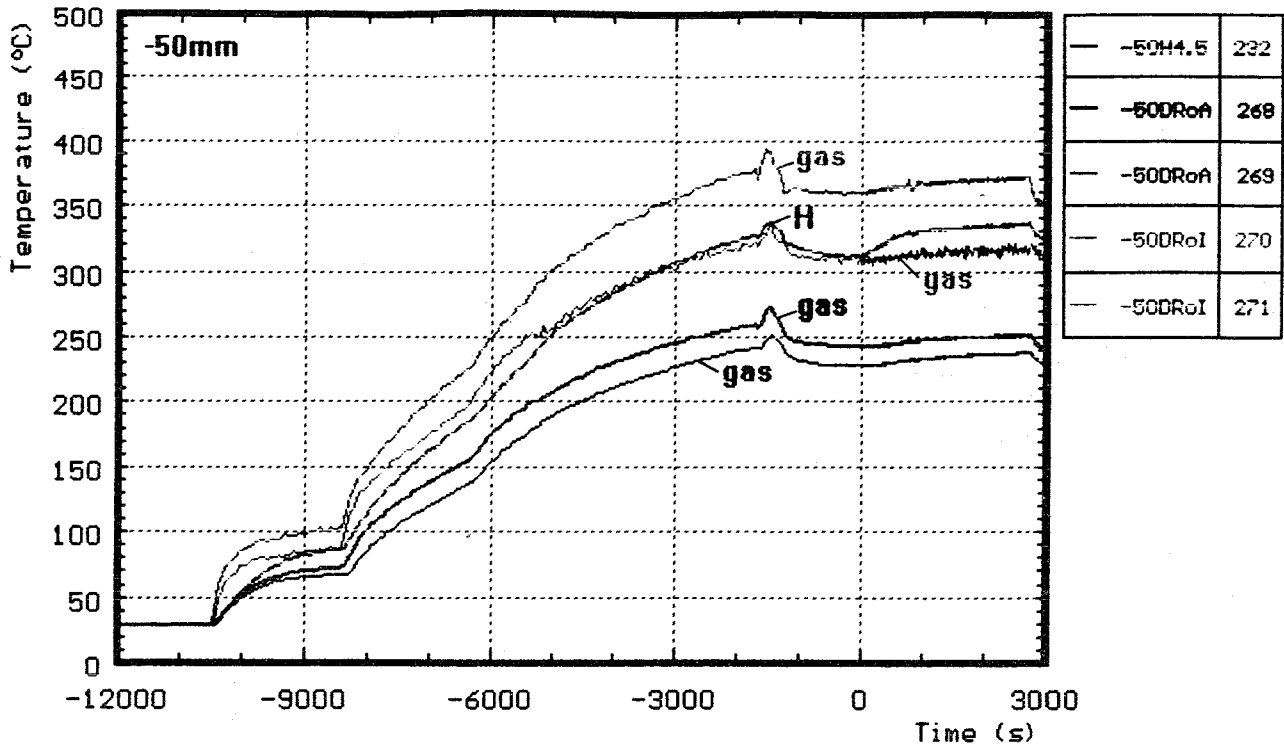
Shr : on shroud
 ShrI : shroud insulation

Fig.A21: CORA-W1: Temperatures at fixed elevations, pre-heat phase (50, 0 mm)



Sp : spacer

Fig.A22: CORA-W1: Temperatures at fixed elevations, pre-heat phase (-15 mm)



H : heated rods

gas : gas temperature

Fig.A23: CORA-W1: Temperatures at fixed elevations, pre-heat phase (-50, -200, -300 mm)